University at Buffalo
The State University of New York

Analytical and Numerical Studies of Seismic Fluid-Structure Interaction in Liquid-Filled Vessels

by
Ching-Ching Yu and Andrew S. Whittaker

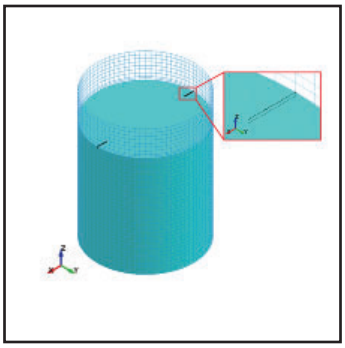
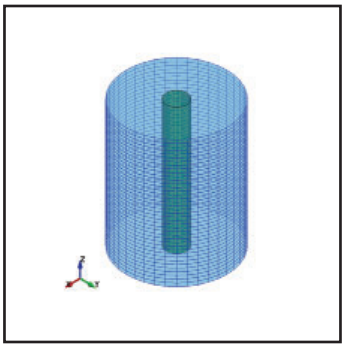

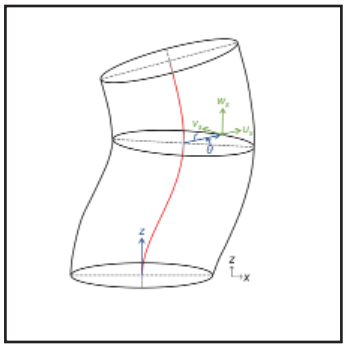

Technical Report MCEER-20-0003

Revision 01, April 16, 2021; originally published August 1, 2020

NOTICE

This report was prepared by the University at Buffalo, The State University of New York, as a result of research sponsored by MCEER. Neither MCEER, associates of MCEER, its sponsors, University at Buffalo, The State University of New York, nor any person acting on their behalf:

a. makes any warranty, express or implied, with respect to the use of any information, apparatus, method, or process disclosed in this report or that such use may not infringe upon privately owned rights; or

b. assumes any liabilities of whatsoever kind with respect to the use of, or the damage resulting from the use of, any information, apparatus, method, or process disclosed in this report.

Any opinions, findings, and conclusions or recommendations expressed in this publication are those of the author(s) and do not necessarily reflect the views of MCEER, the National Science Foundation or other sponsors.

University at Buffalo
The State University of New York

Analytical and Numerical Studies of Seismic Fluid-Structure Interaction in Liquid-Filled Vessels

by

Ching-Ching Yu[1] and Andrew S. Whittaker[2]

Revision 01 Publication Date: April 16, 2021
Publication Date: August 1, 2020
Submittal Date: July 20, 2020

Technical Report MCEER-20-0003

1. Postdoctoral Associate and former Graduate Student, Department of Civil, Structural and Environmental Engineering, University at Buffalo, The State University of New York
2 SUNY Distinguished Professor, Department of Civil, Structural and Environmental Engineering, University at Buffalo, The State University of New York

MCEER: Earthquake Engineering to Extreme Events
University at Buffalo, The State University of New York
212 Ketter Hall, Buffalo, NY 14260
mceer@buffalo.edu; *buffalo.edu/mceer*

Preface

MCEER is a national center of excellence dedicated to the discovery and development of new knowledge, tools and technologies that equip communities to become more disaster resilient in the face of earthquakes and other extreme events. MCEER accomplishes this through a system of multidisciplinary, multi-hazard research, in tandem with complimentary education and outreach initiatives.

Headquartered at the University at Buffalo, The State University of New York, MCEER was originally established by the National Science Foundation in 1986, as the first National Center for Earthquake Engineering Research (NCEER). In 1998, it became known as the Multidisciplinary Center for Earthquake Engineering Research (MCEER), from which the current name, MCEER, evolved.

Comprising a consortium of researchers and industry partners from numerous disciplines and institutions throughout the United States, MCEER's mission has expanded from its original focus on earthquake engineering to one which addresses the technical and socio-economic impacts of a variety of hazards, both natural and man-made, on critical infrastructure, facilities, and society.

The Center derives support from several Federal agencies, including the National Science Foundation, Federal Highway Administration, Department of Energy, Nuclear Regulatory Commission, and the State of New York, foreign governments and private industry.

This report presents a study on seismic fluid-structure-interaction (FSI) analysis, with a focus on liquid-filled nuclear reactors. Seismic design, qualification, and risk assessment of advanced reactors will rely on numerical models to calculate fluid-structure responses of the reactor vessel, contained liquid, and submerged components. These numerical models must be verified and validated. This study verifies and validates numerical models for seismic FSI analysis. The Arbitrary-Lagrangian-Eulerian and Incompressible Computational Fluid Dynamics solvers in LS-DYNA are used to seismically analyze tanks, fluid and submerged components. Specifically, this study 1) reviews and corrects, as needed, prior analytical solutions for base-supported tanks and submerged components, 2) develops analytical solutions for seismic FSI analysis of head-supported tanks, 3) verifies numerical models using the corrected and newly-developed solutions, and 4) validates the numerical models using data from earthquake-simulator experiments. Numerical models of submerged components are verified for calculating their lateral frequencies, and those of tanks are verified and validated for calculating fluid pressures and reactions at the support, but not for calculating wave heights in the contained liquid. The products of the study are broadly applicable to the seismic analysis of base- and head-supported liquid-filled vessels.

Erratum: The revision updates equations and their descriptions in Section 3 and text on pages 232, 235, and 237 in Section 5. The updated equations include (3.11), (3.12), (3.13),

(3.33), (3.34), (3.35), (3.49), (3.61), (3.62), (3.63), (3.82), (3.83), (3.84), (3.107), (3.108), (3.109), (3.120), (3.136), (3.137), (3.138) and (3.141). On pages 232, 235 and 237, a_{14}, a_{41}, and a_{11} are changed to f_{14}, f_{41}, and f_{11}, respectively. Equations (5.28) and (5.29), which are related to the above-mentioned changes in Section 5, are correct as written.

ABSTRACT

A liquid metal reactor includes a vessel, and internal components submerged in a liquid metal coolant. Earthquake shaking of this liquid (fluid)-filled reactor induces fluid-structure interaction (FSI) between the vessel, the submerged components, and the contained coolant. Seismic design, qualification, and risk assessment of the reactor must consider response due to FSI, the actual geometries and support conditions, and three-directional seismic inputs of a site-specific intensity, none of which can be accommodated using analytical solutions. Physical testing of reactor vessels and internal components for seismic qualification is also not feasible because of the large scales involved. These limitations on analytical solutions and physical testing leave numerical simulations as the only plausible pathway for seismic design and qualification of fluid-filled reactors. However, reliable numerical models for FSI analysis that are both verified and validated are not available at the time of this writing.

Numerical models can be verified by comparing predictions with analytical solutions and then validated using data from physical testing. This report performs 1) verification and validation studies on numerical models for rigid and flexible, cylindrical vessels (tanks), supported at either the base or the top (head); and 2) a verification study on numerical models for flexible, submerged internal components. Two solvers capable of predicting nonlinear fluid responses are used to perform seismic FSI analysis in LS-DYNA: Arbitrary-Lagrangian-Eulerian and Incompressible Computational Fluid Dynamics. Analytical solutions, both extracted from prior studies and developed in this report, are used for the verification. The prior analytical solutions are corrected as needed. Test data from earthquake-simulator tests for a base-supported cylindrical tank are used for validation.

In general, the ALE models of tanks are verified and validated for calculating fluid pressures on the tank wall and reactions (shear force and moment) at the support, and the ICFD models are verified and validated for calculating these responses, if the wave action is not significant. The ALE and ICFD models of tanks are not verified and validated for calculating wave heights. The ALE and ICFD models of submerged components are verified for calculating their lateral frequencies.

ACKNOWLEDGMENTS

The authors thank the researchers and design professionals who provided input, ideas and knowledge over the course of the research project, including Professors Michael Constantinou and Mettapalayam Sivaselvan, and Mr. Faizan Ul Haq Mir of the University at Buffalo, Mr. Michael Cohen, TerraPower, Bellevue, WA; Dr. George Abatt of Becht Engineering, Richland, WA; Mr. Greg Soules of McDermott International, Houston, TX; and Dr. Ben Kosbab, SGH, Atlanta, GA.

The research presented in this report was funded in part by the Advanced Research Projects Agency-Energy (ARPA-E), the U.S. Department of Energy, under Award Number DE-AR0000978, and in part by TerraPower, Bellevue, WA and the U.S. Department of Energy under CRADA 14CR04. This financial support is gratefully acknowledged. The views and opinions expressed in this report are those of the authors alone and do not necessarily reflect those of the U.S. Government or agency thereof, or of TerraPower.

TABLE OF CONTENTS

LIST OF FIGURES

LIST OF TABLES

SECTION 1
INTRODUCTION

1.1 Nuclear power reactors

The nuclear reaction used for energy generation at the time of this writing is the process of nuclear fission: a heavy nucleus[1], mostly in actinides[2], absorbs a neutron, and splits into lighter nuclei, with a release of energy and neutrons. The released energy is in the form of heat, transferred by a coolant to be used to produce electricity through other systems, including steam turbines and energy generators. The released neutrons are absorbed by other heavy nuclei and foster a chain fission reaction. Based on the kinetic energy of the neutrons sustaining the chain reaction (i.e., slow and fast neutrons), nuclear reactors can be parsed into thermal and fast reactors. A thermal reactor uses a moderator, such as light water, heavy water, or solid graphite, to slow the neutrons to fission the nuclei of enriched uranium[3], used as the nuclear fuel. Fast reactors use fast neutrons to fission the nuclei of a wider variety of actinides, including natural uranium[4] and plutonium-239 (^{239}Pu). The coolants used in the fast reactors do not substantially moderate (reduce) the kinetic energy of the fast neutrons. Liquid metals, such as liquid sodium, lead-bismuth, and their alloys, serve as the coolant in a fast reactor, with advantages of 1) high power density, 2) high thermal conductivity to transfer heat from the nuclear reaction to create electricity, 3) suitable melting and boiling points to remain liquid at the operating temperature of the reactor (American Society of Mechanical Engineers (ASME) 1979) with a high margin, and 4) low operating reactor pressures, avoiding the need for a thick-walled pressure vessel.

The first nuclear reactor in the world was Chicago Pile-1 (CP-1) (ASME 1979), operated by the University of Chicago from around 1942 to 1943. It was a thermal reactor, with a stack of solid graphite bricks as a moderator and no coolant (Figure 1.1a). The first fast reactor was Clementine (Figure 1.1b), using mercury as the primary coolant, operated by the Los Alamos

[1] Nucleus: the central core of an atom. A nucleus carries positive charges and contributes most of the mass of an atom.

[2] Actinide: fifteen radioactive metallic elements with atomic numbers from 89 to 103 in the periodic table of chemical elements.

[3] Enriched uranium: a type of uranium in which the composition of uranium-235 is increased to 3% to 5% by mass, by comparison to natural uranium[4].

[4] Natural uranium: 0.7% uranium-235 and 99.3% uranium-238 by mass.

National Laboratory from 1949 to 1952. Mercury proved not to be an appropriate coolant because of its poor thermal conductivity (Harvey 2004). In the 1940s, Enrico Fermi proposed breeding nuclear fuel in a fast reactor (International Atomic Energy Agency (IAEA) 2012). The first demonstration of fuel breeding was in the Experimental Breeder Reactor I (EBR-I) (Figure 1.1c), operated by the Argonne National Laboratory from around 1951 to 1963, on the site of what is now the Idaho National Laboratory (INL). This reactor used liquid sodium-potassium eutectic (NaK) as its primary coolant (ASME 1979). The construction of EBR-1 was followed by Enrico Fermi 1 (operated from 1963 to 1972,) and EBR-II (operated from 1963 to 1994, also on the site of INL), which both used liquid sodium as the primary coolant (Cochran et al. 2010). These pioneering fast reactors demonstrated the feasibility of using liquid metals as the primary coolant.

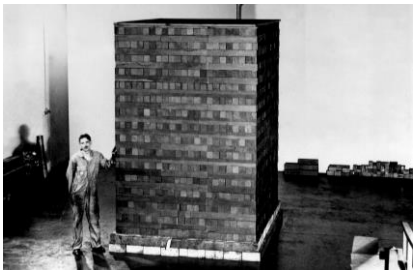

(a) CP-1 (Atomic Heritage Foundation (AHF) 2016)

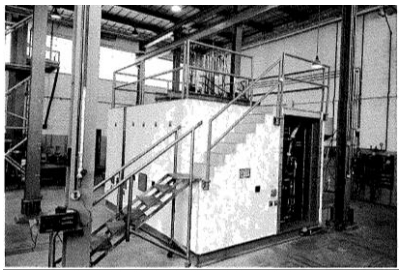

(b) Clementine (Harvey 2004)

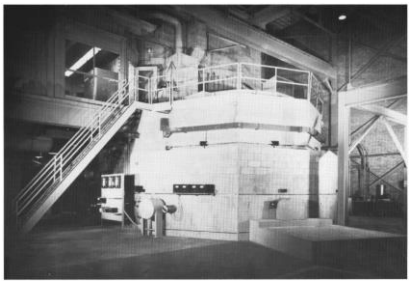

(c) EBR-I (ASME 1979)

Figure 1.1. Early nuclear reactors in the United States: the first thermal, fast, and fast breeder reactors

Sodium-cooled and lead-cooled fast reactors (SFR and LFR) are two of the six next-generation reactors selected by the Generation IV International Forum (GIF) (2002, 2014) for development. Both the SFR and the LFR use a liquid metal (i.e., liquid sodium and lead-bismuth) as the primary coolant. The six next-generation reactors were selected to meet three goals (Abram and Ion 2008): 1) improved safety and reliability, 2) efficiency and economic competitiveness, and 3) energy sustainability. The GIF established a Risk and Safety Working Group (RSWG) (2012) to address the goal of improved safety and reliability, where earthquake shaking was identified as one of the external hazards to be studied (Kelly 2014).

Figure 1.2 presents two cut-way views of a prototype liquid metal reactor, designed by General Electric Company, Boston, MA (Gluekler 1997). This reactor consists of a reactor vessel, a

containment or guard vessel, liquid sodium, and internal components, including an upper internal structure (UIS), intermediate heat exchangers (IHXs), primary pumps, and a nuclear core. The reactor vessel is filled with a liquid sodium and closed at its top by a shield or head, which supports many of the immersed internal components. The guard vessel surrounds the wall of the reactor vessel to capture the liquid sodium coolant in the event of a leak. The reactor vessel is supported at its head, at the top of a reactor vault, which is a cylindrical reinforced concrete structure supported on the basemat of the nuclear building.

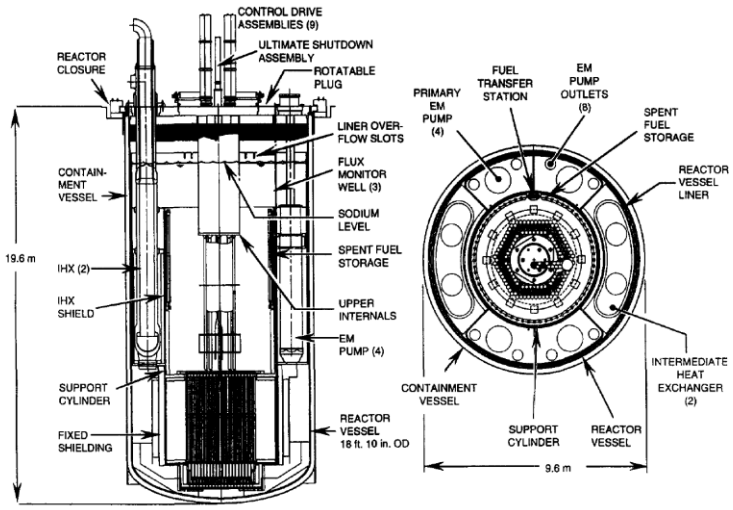

Figure 1.2. Prototype liquid metal reactor: reactor vessel, guard vessel, internal components, and liquid sodium coolant, designed by General Electric Company, Boston, MA (Gluekler 1997)

The low operating pressure in a liquid metal reactor enables design of thin-walled vessels containing the fluid and internal components. (Thick-walled vessels are needed for pressurized water reactors and boiling water reactors, which operate at pressures of approximately 150 and 75 atmospheres, respectively.) Chellapandi et al. (2008) reports that the diameter-to-thickness ratio for the vessel and internal components in a liquid metal reactor is typically between 500 and 800. The seismic capacity of a thin-walled vessel is less than its thick-walled counterpart, which is why seismic isolation was proposed for the liquid metal reactor of Figure 1.2: to enable an operationally efficient design with sufficient seismic capacity.

Nuclear reactors must be analyzed, designed, and qualified for site-specific, design basis earthquake shaking. Seismic probabilistic risk assessment (SPRA) is performed to demonstrate

that the mean annual frequency of core damage (CDF) and large early release (LERF) of radiation is acceptably small. The earthquake shaking of a liquid (fluid)-filled reactor induces interaction of the vessel, contained fluid, and components inside the vessel and immersed in the fluid. Seismic fluid-structure-interaction (FSI) analysis of the vessel-fluid-component system is needed to predict demands for design and SPRA.

1.2 Seismic FSI analysis of fluid-filled reactors

1.2.1 Legacy design methods and associated studies

Early reactor designs simplified seismic FSI analysis into: 1) interaction of the vessel (tank) and its contained fluid, and 2) interaction of the internal components and the surrounding fluid, both of which were calculated using analytical solutions. The early studies on seismic FSI analysis of tanks and submerged components, which were used to support the design of the first and second generations of nuclear reactors, are introduced below.

Analytical studies on seismic FSI of base-supported tanks began in the 1930s at the Vibration Laboratory at Stanford University (e.g., Hoskins and Jacobsen (1934); Morris (1938); Jacobsen (1949); Jacobsen and Ayre (1951)). Simplifying assumptions were made for developing analytical solutions. The tank was assumed to be rigid, and the fluid response was assumed to be linear and parsed into impulsive and convective components[5]. Hoskins and Jacobsen (1934) derived an analytical solution for impulsive pressures in a rectangular tank using the method of Westergaard (1933) for analyzing pressures on the wall of a dam. The solution was validated by earthquake-simulator tests presented in Figure 1.3, which were among the earliest (if not the first) seismic FSI experiments to the knowledge of the authors. Morris (1938) performed similar earthquake-simulator tests to study convective responses of rectangular and cylindrical tanks. Jacobsen (1949) used Bessel functions to derive the impulsive responses of a cylindrical tank, and those solutions were validated by Jacobsen and Ayre (1951) using earthquake-simulator tests.

[5] The impulsive response is generated by the part of the fluid accelerating with the tank (the so-called *added mass effect*) subjected to ground motion, and the convective response is generated by the part of the fluid assumed *not* to move with the tank but to oscillate vertically and form waves on the free surface. The hydrodynamic response in the tank is the sum of the impulsive and convective responses. See Section 3 for more information.

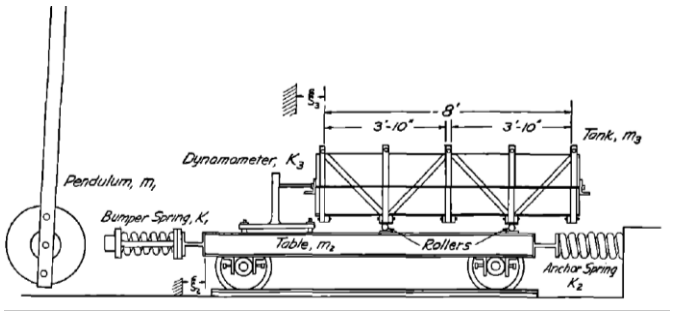

Figure 1.3. Experimental setup of the impulsive earthquake-simulator tests for a rectangular tank, Figure 1 in Hoskins and Jacobsen (1934)

Housner (1954, 1957) approximated impulsive and convective responses of rigid, base-supported, cylindrical tanks to avoid using Bessel functions in his analytical solutions. A mechanical analog was developed based on the approximate solutions and was widely accepted in early design practice (e.g., American Concrete Institute (ACI) (2006)). The U.S. Atomic Energy Commission (Thomas et al. 1963) provided information on seismic design and analysis for nuclear vessels and included the mechanical analog (Housner 1957) for calculating FSI responses. Early designs of fluid-filled vessels used this method (Fujita et al. 1984; Ma et al. 1982b) and ignored the internal components, the flexibility of the tank, and the head-supported boundary condition.

In the 1970s and early 1980s, Veletsos and two of his Ph.D. students, Yang and Tang, developed analytical solutions for rigid and flexible, base-supported, cylindrical tanks: 1) Veletsos and Yang (1977), Veletsos and Tang (1986, 1987), and Tang (1986) for impulsive responses; and 2) Veletsos and Yang (1977) and Yang (1976) for convective responses using the method of Abramson (1966) for analyzing sloshing of propellants in space vehicles. Veletsos, Yang, and Tang's solutions were presented, in part, in an American Society of Civil Engineers (ASCE) guideline (Veletsos 1984a) and a Department of Energy (DOE) guideline (Bandyopadhyay et al. 1995) for liquid storage tanks.

In the 1970s and 1980s, the Argonne National Laboratory (ANL) funded research on FSI analysis of submerged components for application to fluid-filled nuclear reactors (Chen et al. 1976; Chung and Chen 1976, 1977, 1984; Ma et al. 1983d, 1985b; Sakurai et al. 1989). Chen et al. (1976) and Chung and Chen (1976, 1977, 1984) derived solutions for the mass of fluid to be attached to submerged cylindrical pipes and rods (i.e., the so-called *added mass effect*) to calculate frequencies and damping ratios for seismic analysis. Ma et al. (1985b, 1983d) used

finite element models to address the impacts of internal components on pressures and wave heights of coolant in a reactor vessel; the response of the fluid was assumed to be linear. Sakurai et al. (1989) performed earthquake-simulator tests on a scaled model of a prototype liquid metal reactor with different arrangements of internal components for small-amplitude motions. The test results were used to validate Ma's models. Dong (1978) summarized studies on added mass and damping of submerged components in reactor vessels, including the studies performed at the ANL.

1.2.2 Modern methods

Modern seismic design and qualification of a fluid-filled advanced reactor must consider the interaction of the vessel, its internal components, and the contained fluid, the actual support conditions of the vessel, and three translational components (i.e., 2 horizontal, 1 vertical) of seismic input of site-specific intensity. Analytical solutions for seismic FSI analysis involve simplifying assumptions, which cannot accommodate 1) the geometries, boundary and support conditions, and interactions of a reactor vessel and its internal components, 2) simultaneous three-component seismic inputs, and 3) and nonlinear response of the fluid (e.g., large-amplitude sloshing, disengagement of fluid from the vessel wall, interaction of waves with the vessel head). Physical testing of reactors for seismic qualification is also not feasible because they are too large and too heavy to be tested on available earthquake simulators, and the spatial and temporal pressure loadings on the vessel and internal components are too complex to reproduce with physical testing equipment such as actuators. These limitations on analytical solutions and physical testing leave numerical simulation of reliable models as the only plausible pathway for seismic FSI design and qualification of advanced reactors.

Numerical models need to be verified and validated for analysis of nuclear structures. Figure 1.4 introduces verification and validation. A model can be verified by comparing the results of numerical simulations with those calculated using analytical solutions for identical assumptions. A verified model can then be validated by comparing the results of numerical solutions with those generated by physical testing. The dimensions, mechanical properties, and boundary conditions of the test specimen are used to build the numerical model for validation. The verified and validated model can then be used for seismic design, qualification, and probabilistic risk assessment.

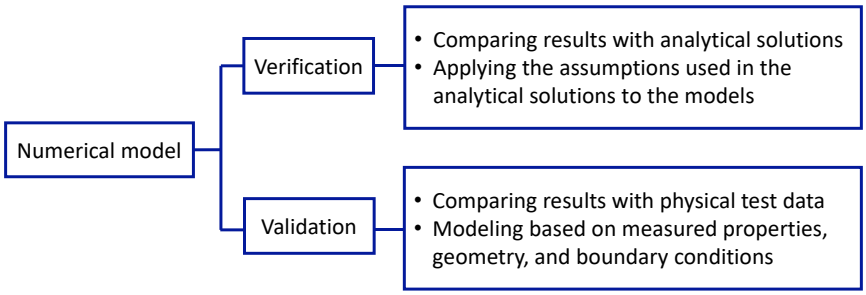

Figure 1.4. Verification and validation for a numerical model

1.3 Objectives of the report

Seismic FSI analysis of advanced nuclear reactors will be needed regardless of whether the reactor building or fluid-filled components inside the building are seismically isolated. The goal of this report is to enable such analysis by providing reliable numerical models and guidance for verification and validation. The goal is achieved by meeting six objectives:

1. To review, summarize, and correct as needed, prior analytical studies on seismic FSI analysis of base-supported cylindrical tanks (Jacobsen 1949; Chalhoub and Kelly 1988; Housner 1957, 1954; Veletsos 1984a) and submerged components (Chen and Rosenberg 1975).
2. To develop analytical solutions for seismic FSI responses of a head-supported cylindrical tank (see Figure 1.2), which is a support condition for a number of advanced reactor designs. The analytical solutions could be used for preliminary design of the reactor vessel and to support verification of numerical models.
3. To verify numerical models of tanks using prior analytical solutions for a base-supported boundary condition (Jacobsen 1949; Veletsos 1984a) and using newly developed analytical solutions for a head-supported boundary condition.
4. To validate verified models using data from earthquake-simulator tests on a base-supported cylindrical tank.
5. To verify models of components submerged in a fluid using prior analytical solutions (Chen and Rosenberg 1975).
6. To provide recommendations for developing verified and validated numerical models for fluid-filled advanced reactors.

1.4 Organization of the report

This report is organized into seven sections, a list of references, and three appendices.

Section 2 reviews analytical, numerical, and experimental studies on seismic fluid-structure interaction (FSI) analysis for tanks (vessels), submerged components, and nuclear reactors.

Section 3 summarizes analytical solutions from prior studies on base-supported cylindrical tanks and develops companion solutions for head-supported cylindrical tanks, with application to the boundary conditions and geometries similar to those proposed for fluid-filled advanced reactor vessels. The solutions address lateral frequencies of the tank, frequencies of waves, hydrodynamic pressures, reactions at the tank support, and wave heights of the contained fluid.

Section 4 develops numerical models for base- and head-supported cylindrical tanks and verifies them using analytical solutions presented in Section 3. Response-history analysis is performed using the Arbitrary Lagrangian-Eulerian (ALE) and Incompressible Computational Fluid Dynamics (ICFD) solvers in LS-DYNA (Livermore Software Technology Corporation (LSTC) 2018a). Guidance is provided for verification studies on numerical models of a reactor vessel.

Section 5 reviews analytical solutions for submerged internal components, develops ALE and ICFD models for internal components, and verifies the models using the reviewed solutions. Guidance is provided for verification studies on numerical models of submerged reactor components.

Section 6 describes earthquake-simulator tests on a base-supported cylindrical tank and validates the verified models constructed in Section 4 by comparing numerical and test results. Guidance is provided for validation studies on numerical models of a reactor vessel.

Section 7 summarizes the work in each section, presents conclusions drawn from the verification and validation studies performed in this report, and provides recommendations for developing verified and validated numerical models for fluid-filled advanced reactors.

A list of references and three appendices follow the body of this report.

Appendix A summarizes the derivations and analytical solutions for FSI responses of base- and head-supported cylindrical tanks that are presented in detail in Section 3.

Appendix B compares FSI responses of a flexible base-supported tank calculated using solutions from an analytical study (Veletsos 1984a) presented in Section 3 and a simplified procedure (Malhotra et al. 2000), which was based on the Veletsos study and has been widely used by industry in the United States.

Appendix C discusses challenges in outputting results for wave heights calculated using the ALE models in Section 4 to help engineers tasked with analyzing fluid-filled vessels, verifying and validating numerical models, and performing commercial grade dedication of software.

Appendix D presents a list of the input motions used for the earthquake-simulator tests on a base-supported cylindrical tank that support the validation studies of Section 6.

SECTION 2
LITERATURE REVIEW

2.1 Overview

This section summarizes the literature on analytical, numerical, and experimental studies related to seismic fluid-structure interaction (FSI) of tanks and fluid-filled reactors vessels[6]. Section 2.2 introduces studies on: 1) FSI analysis of vessels (tanks), excluding internal components, 2) FSI analysis of submerged components, and 3) FSI analysis of fluid-filled reactors, including tanks and internal components. Section 2.3 describes relevant experimental studies on tanks and fluid-filled reactors and the use of test data to validate analytical and numerical calculations.

2.2 Analytical and numerical studies on seismic FSI analysis

2.2.1 FSI analysis of tanks

Jacobsen (1949) developed analytical solutions for impulsive responses (see footnote 5 on page 4) of a base-supported cylindrical tank, excited by unidirectional horizontal motion of small amplitude. The impulsive responses included fluid pressure p_{imp} and reactions at the tank base (i.e., shear force F_{imp} and moment M_{imp}). The analytical solutions assumed the tank to be rigid, and the fluid to be ideal[7] and respond linearly. The effects of hydrostatic pressure[8] and fluid sloshing were not considered. A velocity potential[9] was derived for the fluid using three boundary conditions at the three surfaces enclosing the fluid: 1) zero pressure at the free surface, namely no wave action, 2) zero vertical velocity on the tank base, and 3) the fluid adjacent to the tank wall moved with the wall at the ground velocity. Boundary conditions 2) and 3) were defined based on the assumption that the contained fluid would not disengage from the inner surface of the tank. The impulsive pressure was derived using an assumed velocity potential for the contained fluid, and the impulsive reactions were derived to balance the resultant forces and moments generated by the impulsive pressure on the inner surface of the tank. Section 3 presents the derivation and calculates the impulsive responses of a tank using Jacobsen's solutions.

[6] Herein, *fluid* is used to refer to *liquid*.

[7] Ideal fluid: a fluid that is incompressible, irrotational, and inviscid.

[8] Hydrostatic pressure: pressure created by fluid at rest under gravity.

[9] Fluid responses can be fully defined using a velocity potential: 1) fluid velocity is the gradient of the velocity potential, and 2) fluid pressure is associated with the derivative of the velocity potential with respect to time.

Jacobsen (1949) validated his solutions using data from earthquake-simulator tests for a cylindrical tank, with a radius R of 0.3 m and filled with fluid with a range of depth H : $0.2 \leq H/R \leq 15$. The test tank was subjected to a horizontal impulse of $u_0'' =$ 0.12 g. Figure 2.1 presents the analytical results $F_{imp}/(u_0''m_l)$ (solid lines) and experimental data (open circles) for the normalized impulsive shear force $F_{imp}/(u_0''m_l)$ and the impulsive moment M_{imp} at the tank base, where m_l is the mass of the contained fluid. The analytical solutions were in excellent agreement with the experimental results.

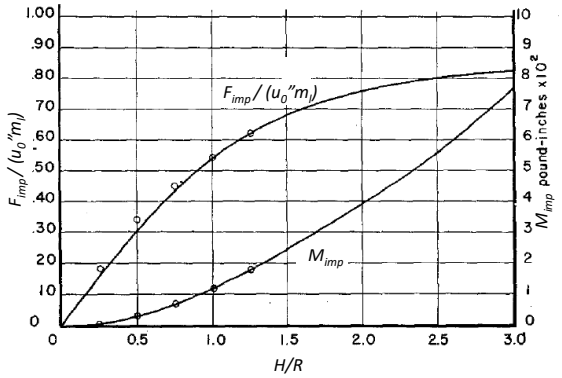

Figure 2.1. Analytical solutions (solid lines) and experimental data (open circles), normalized impulsive shear force $F_{imp}/(u_0''m_l)$ and moment M_{imp} at the tank base for $u_0'' = 0.12$ g, adapted from Jacobsen (1949)

Housner (1954, 1957) derived approximate analytical solutions for impulsive and convective responses (see footnote 5 on page 4) of rectangular, cylindrical, elliptical, and trapezoidal base-supported tanks subjected to unidirectional horizontal motion. The tank was assumed to be rigid, and the fluid was assumed to be ideal and respond linearly. His solutions addressed the impulsive and convective components of 1) fluid pressures, p_{imp} and p_{con}, 2) shear forces at the tank base, F_{imp} and F_{con}, and 3) moments at the tank base, M_{imp} and M_{con}, and convective frequencies f_{con} (i.e., frequencies of wave action) and wave heights d_w. The solutions were derived using discretized fluid in a vertical cross section of a tank, as presented in Figure 2.2. The impulsive responses were calculated using the vertically discretized fluid presented in Figure 2.2a. The analytical solution for p_{imp} of a fluid layer was derived by balancing its resultant force and the inertial force generated by the horizontal acceleration u_0'' of the tank. The analytical solutions for the impulsive reactions F_{imp} and M_{imp} at the tank base were derived using the resultant forces

and moments generated by p_{imp} on the inner surfaces of the tank. The convective responses were decoupled into modes. The convective pressure p_{con} in the first mode was calculated using the horizontally discretized fluid presented in Figure 2.2b. The fluid layers were free to rotate with respect to the axis normal to the cross section and generate the first modal wave shape on the free surface. The vertical displacement of the free surface, namely, the wave height d_w, was defined using the rotational angle ϕ of the top fluid layer. The analytical solution for the convective pressure was derived using Hamilton's Principle: balancing the kinetic and potential energies of the fluid layers, both of which were expressed using ϕ. The analytical solutions for the convective reactions F_{con} and M_{con} at the tank base were derived using the resultant forces and moments generated by the convective pressures on the inner surfaces of the tank. Section 3 presents Housner's derivation and calculates the impulsive and convective responses of a tank. Housner compared FSI responses calculated using his solutions with those calculated using solutions from other studies: Graham and Rodriquez (1951) for rectangular tanks, Jacobsen (1949) and Lamb (1932) for cylindrical tanks, and Jeffreys (1925) for elliptical tanks. The differences were less than 4%[10].

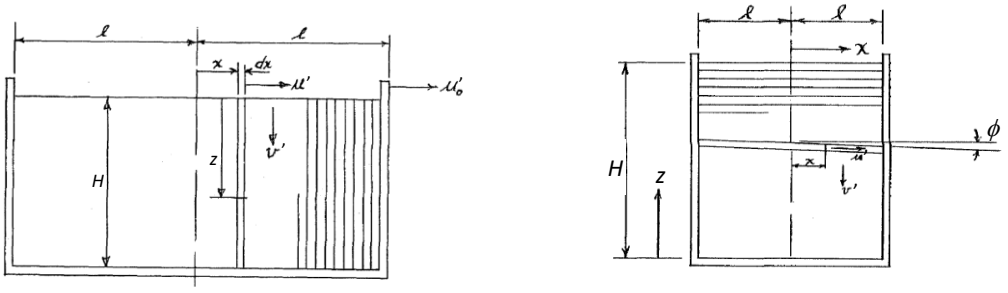

(a) impulsive response (b) convective response, first mode

Figure 2.2. Vertical cross section through a tank and discretized contained fluid, adapted from Housner (1954)

Housner (1957) then developed a mechanical analog based on his analytical solutions for seismic FSI analysis of rigid base-supported tanks. The mechanical analog is presented in Figure 2.3. The mechanical analog simulated the impulsive response using a lumped mass m_{imp} (termed impulsive mass hereafter), rigidly attached to the tank wall at a height of h_{imp} with respect to the tank base. The convective response was simulated using multiple lumped masses $m_{con,j}$ (j =1,

[10] The dimensions of the tank used for the comparison were not given.

2,…, n; termed convective mass hereafter), and each lumped mass $m_{con,j}$ was associated with a convective mode (i.e., j th mode). The lumped mass $m_{con,j}$ was attached to the tank wall using a set of elastic springs with a composite stiffness of $k_{con,j}$ at a height of $h_{con,j}$, with respect to the tank base.

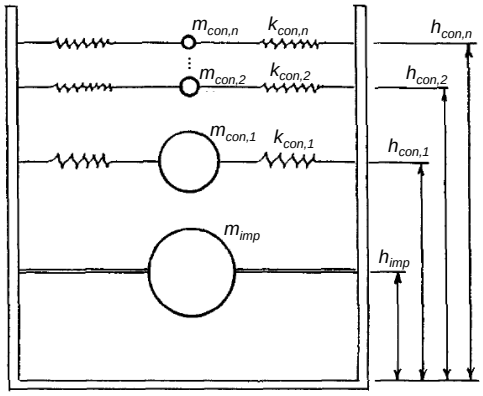

Figure 2.3. Mechanical analog for seismic FSI analysis of a rigid base-supported tank, adapted from Housner (1957)

The parameters used in the mechanical analog (m_{imp} , $m_{con,j}$, h_{imp} , $h_{con,j}$, and $k_{con,j}$) were developed by balancing the inertial forces of the lumped masses with the impulsive and convective reactions at the tank base calculated using the analytical solutions (Housner 1957). The lumped masses moved with the tank subjected to horizontal motion u_0'' . The impulsive mass m_{imp} was rigidly attached to and moved with the rigid tank at u_0'' . Each of the convective masses $m_{con,j}$ was assumed to oscillate at an acceleration $u_{con,j}''$. Their inertial forces balanced the impulsive and convective shear forces at the tank base, F_{imp} and $F_{con,j}$:

$$F_{imp} = m_{imp} \cdot u_0'' \tag{2.1}$$

$$F_{con,j} = m_{con,j} \cdot u_{con,j}'' \tag{2.2}$$

The heights of the impulsive and convective masses generated overturning moments at the tank base, which were balanced by M_{imp} and $M_{con,j}$:

$$M_{imp} = m_{imp} \cdot u_0'' \cdot h_{imp} \tag{2.3}$$

$$M_{con,j} = m_{con,j} \cdot u_{con,j}'' \cdot h_{con,j} \tag{2.4}$$

The stiffness $k_{con,j}$ of the springs for $m_{con,j}$ was related to the convective frequency $f_{con,j}$:

$$f_{con,j} = \frac{1}{2\pi}\sqrt{\frac{k_{con,j}}{m_{con,j}}} \tag{2.5}$$

The parameters m_{imp}, $m_{con.j}$, h_{imp}, $h_{con,j}$ and $k_{con,j}$ were derived using F_{imp}, $F_{con,j}$, M_{imp}, $M_{con,j}$, and $f_{con,j}$ calculated per Housner's solutions for Eqs. (2.1) to (2.5).

Housner (1963) simplified the mechanical analog of Figure 2.3 for seismic FSI analysis of a base-supported tank to a two-degree-of-freedom system presented in Figure 2.4a, including the impulsive mass m_{imp} and the convective mass of the first mode $m_{con,1}$. The simplified mechanical analog was adapted for elevated tanks as presented in Figure 2.4b. In this figure, m_f and k_f are the mass and the stiffness of the frame supporting the tank.

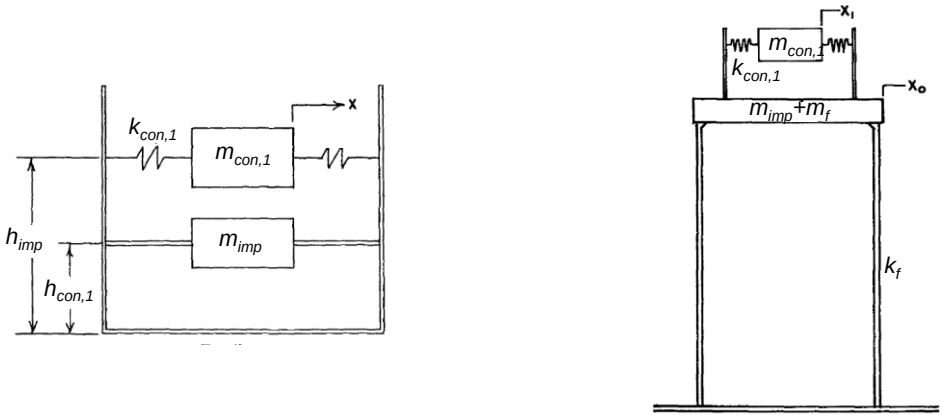

(a) base-supported tank (b) elevated tank

Figure 2.4. Simplified mechanical analog for seismic FSI analysis of base-supported and elevated rigid tanks, adapted from Housner (1963)

Veletsos (1974) and Chapter 3 of Yang (1976) derived analytical solutions for impulsive responses of a flexible, base-supported, cylindrical tank, subjected to unidirectional horizontal motion. The solutions addressed fluid pressure p_{imp}, and shear force F_{imp} and moment M_{imp} at the tank base, associated with an assumed lateral deformation of the tank. The lateral deformation of the tank along its height H_s was expressed using three shapes presented in Figure 2.5: 1) Mode A, linear, 2) Mode B, sinusoidal, and 3) Mode C, co-sinusoidal. The impulsive responses were calculated using the method of Jacobsen (1949) with a modification to the boundary condition assigned to the tank wall: the horizontal velocities of the tank wall and

the adjacent fluid were identical, expressed using the three deformed shapes of Figure 2.5. Figure 2.6 presents analytical results for the impulsive pressure p_{imp} on the wall of a flexible tank, given the three deformed shapes, together with results for a rigid tank, for $H/R = 0.5$ and 3. (The results for p_{imp} for a rigid tank are identical to those calculated using the solution of Jacobsen.) The pressures p_{imp} were normalized using $\rho H u''_{imp}$, where u''_{imp} is the acceleration of a single-degree-of-freedom system with the impulsive frequency of the tank for a seismic input. The impulsive reactions at the tank base were derived using the resultant forces and moments generated by the impulsive pressures on the wall of the tank. However, the impulsive frequency for the calculation of u''_{imp} was not derived, and so the analytical solutions of Veletsos (1974) and Chapter 3 of Yang (1976) were not complete.

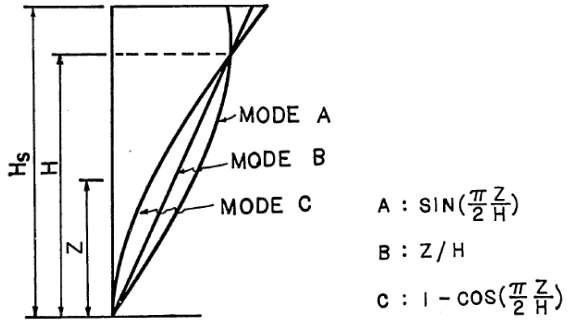

Figure 2.5. Three lateral deformed shapes along the height of the tank Yang (1976)

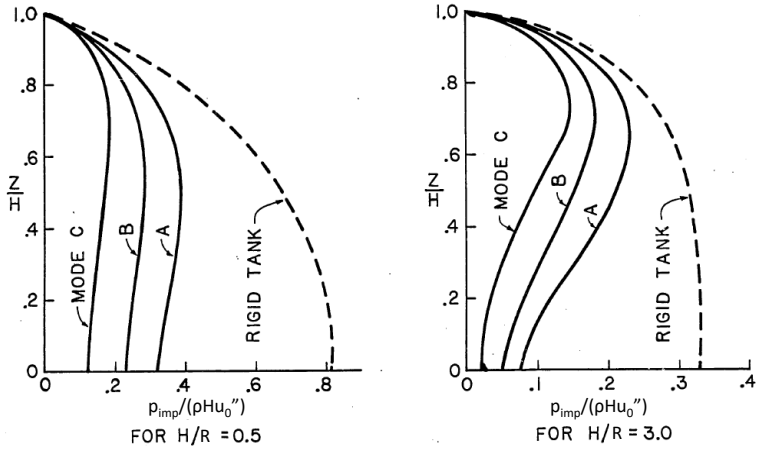

Figure 2.6. Normalized impulsive pressure $p_{imp} / \rho H u''_{imp}$ on the wall of a rigid tank and a flexible tank with the lateral deformed shapes presented in Figure 2.5, $H/R = 0.5$ and 3, adapted from Yang (1976)

Veletsos and Yang (1977) and Chapter 4 of Yang (1976) improved the analysis methodology of Veletsos (1974) and Chapter 3 of Yang (1976): impulsive response of a flexible tank was decoupled into modes and associated frequencies were derived. The tank was assumed to be full. The impulsive response was derived using the method presented in Veletsos (1974) and Chapter 3 of Yang (1976) with a modification to the boundary condition assigned to the tank wall: the horizontal velocities of the tank wall and the adjacent fluid were identical, expressed using a linear superposition of modal shapes of a vertical cantilever $\psi_i(z)$ developed by Young and Felgar (1949)[11]. The equation of motion for the tank, represented using a multi-degree-of-freedom system, was derived using the Lagrangian equation, including the strain and kinetic energies of the tank, the kinetic energy of the fluid, and the external work of seismic motion. The strain and kinetic energies of the tank and the kinetic energy of the fluid were derived using the velocity or displacement of the tank wall, which were functions of $\psi_i(z)$. The impulsive frequencies and responses can be calculated given the equation of motion of the tank. Veletsos and Yang (1977) and Chapter 4 of Yang (1976) presented the equation of motion but did not calculate either frequencies or responses.

Veletsos (1984a) and Tang (1986) used the equation of motion of Veletsos and Yang (1977) and Chapter 4 of Yang (1976) to compute impulsive frequencies f_{imp} of the first three modes and the associated modal responses, including pressure p_{imp}, and shear force F_{imp} and moment M_{imp} at the tank base. Section 3 of this report presents the derivation of the analytical solutions, extracted from Veletsos and Yang (1977), Chapter 4 of Yang (1976), Veletsos (1984a), and Tang (1986), and calculates the impulsive responses for flexible tanks using the solutions.

Tang and Chang (1994) and Padmanaban (1996) modified the assumed modal shapes for the full base-supported tank presented in Veletsos and Yang (1977) to calculate impulsive frequencies for partially filled tanks with different boundary conditions: 1) free, 2) hinged, or 3) roller-supported at its top, and fixed at its base. The first impulsive frequency $f_{imp,1}$ of the partially filled tank was calculated for the three boundary conditions and different tank dimensions: $0.5 \le H / H_s \le 1$ and $0.3 \le H_s / R \le 3$. The studies concluded that for a given tank radius R, the

[11] Young and Felgar (1949) developed lateral modal shapes for a prismatic beam with two ends 1) fixed and free (cantilever), 2) fixed and hinged, 3) fixed and roller-supported, and 4) fixed and fixed.

effect of the fluid height H on the impulsive frequency was much greater than that of the tank height H_s. At a given H/R, the difference in the impulsive frequencies for $0.5 \le H_s/R \le 1.5$ was insignificant.

A Department of Energy (DOE) guideline (Bandyopadhyay et al. 1995) for liquid storage tanks summarized the work of Veletsos and his co-workers (i.e., Yang, Tang, Padmanaban, and Chang).

Malhotra et al. (2000) developed a mechanical analog for seismic FSI analysis of flexible, base-supported, cylindrical tanks subjected to unidirectional horizontal motion. The mechanical analog is a two-degree-of-freedom system using one impulsive and one convective mass, m_{imp} and m_{con}, as presented in Figure 2.7. In this figure, the masses m_{imp} and m_{con} are attached to the tank wall using springs and dampers at heights of h_{imp} and h_{con} with respect to the tank base, respectively. The stiffnesses of the springs for m_{imp} and m_{con} are k_{imp} and k_{con}, respectively. The damping ratios of the dampers for m_{imp} and m_{con} are ζ_{imp} and ζ_{con}, respectively. Malhotra et al proposed ζ_{imp}=2% for a steel tank, ζ_{imp}=5% for a concrete tank, and ζ_{con}=0.5% for both steel and concrete tanks. Similar to the mechanical analog of Housner (1957), the parameters used in the Malhotra analog (i.e., m_{imp}, m_{con}, h_{imp}, h_{con}, k_{imp}, and k_{con} shown in Figure 2.7) were developed by balancing the inertial forces of the lumped masses with the impulsive and convective reactions at the tank base calculated using analytical solutions. The analytical solutions of Veletsos (1984) for flexible tanks were used to develop the mechanical analog, with modifications to enable calculating FSI responses using one impulsive mode and one convective mode: impulsive (convective) responses in the second and higher modes were added to that in the first mode. Appendix B presents the derivation of the parameters (i.e., m_{imp}, m_{con}, h_{imp}, and h_{con}) used in the mechanical analog. Malhotra compared shear forces and moments at the base of a tank and wave heights calculated using the mechanical analog and Veletsos' solutions, and the differences in the responses were less than 10%. Malhotra's procedure is widely accepted in industry and included in Eurocode 8 (European Committee for Standardization (CEN) 1998) and API 650 (American Petroleum Institute (API) 2012) for the seismic design and analysis of base-supported cylindrical tanks. Appendix B calculates the FSI responses using the mechanical

analog of Malhotra et al. and the analytical solutions of Veletsos (1984) for three tanks with different dimensions and three input motions.

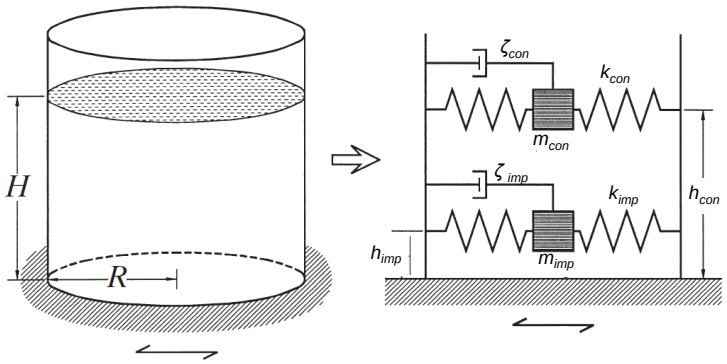

Figure 2.7. Mechanical analog for seismic FSI analysis of flexible base-supported cylindrical tanks subjected to unidirectional horizontal motion (Malhotra et al. 2000)

Haroun and Housner (Housner and Haroun 1980; Haroun 1980a, b, 1983; Haroun and Housner 1981a, b, 1982a, b) performed numerical and experimental seismic FSI analysis of flexible, base-supported, cylindrical tanks. Their work included three phases: 1) developing a numerical formulation for seismic FSI analysis of tanks, 2) performing ambient and forced vibration tests on three cylindrical water tanks, and 3) developing a mechanical analog based on FSI results of the formulation in (1). Phases (1) and (3) are introduced in this section (2.2.1) and phase (2) is introduced in Section 2.3.

The numerical formulation of Haroun and Housner combined the finite element method and an analytical solution of fluid pressure to calculate seismic FSI in flexible, base-supported cylindrical tanks, subjected to unidirectional horizontal seismic motion of a small amplitude. The tank wall was modeled using cylindrical shell elements, as presented in Figure 2.8a. Seven cylindrical shell elements are used for the tank wall in this figure. Each end of the cylindrical shell elements (i.e., top and bottom) had four degrees of freedom: axial $\bar{u}$, tangential $\bar{v}$, radial $\bar{w}$, and rotational $\hat{w}$, with respect to the axial axis. The impulsive response of the tank was modeled by applying an analytically-calculated impulsive pressure (i.e., traction) on the inner surface of the cylindrical elements. The degrees of freedom of the cylindrical elements enabled modeling impulsive responses associated with the lateral and circumferential modal shapes of the tank wall presented in Figures 2.8b and c, respectively. The circumferential modes included two

types of motions: 1) $\cos\theta-$ type and 2) $\cos n\theta-$ type. The shape of the $\cos\theta-$ type mode resulted in no deformation along the circumference of the wall, namely, the deformations of the tank were contributed by lateral modes only. The free surface of the fluid was modeled using concentric annular elements shown in Figure 2.9a to accommodate wave action (i.e., convective response). The concentric annular elements enabled deformations on the free surface associated with convective modes presented in Figure 2.9b. The numerical formation of Haroun and Housner was validated using test results generated in Phase (2) of the project, which is presented in Section 2.3.

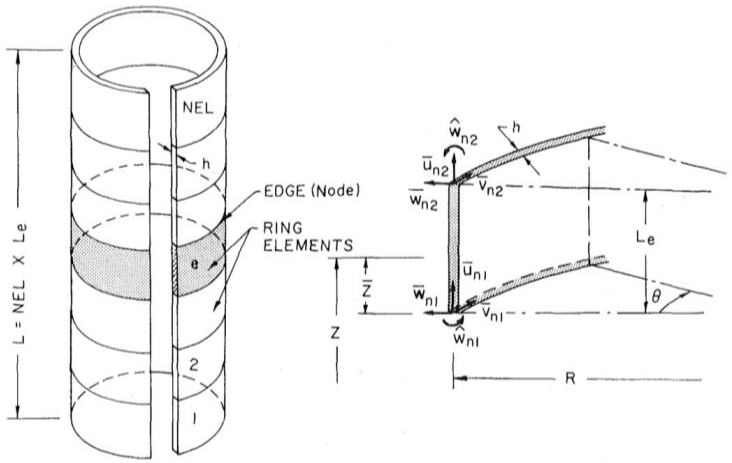

(a) flexible tank modeled using cylindrical shell elements

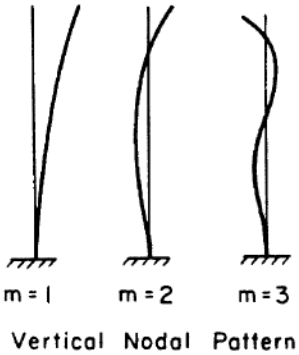

(b) lateral modal shapes

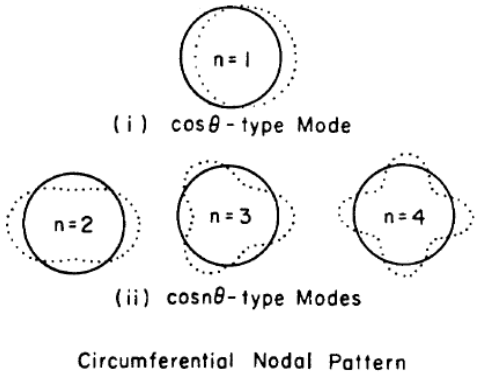

(c) circumferential modal shapes

Figure 2.8. Numerical model for seismic FSI analysis of flexible base-supported cylindrical tanks, impulsive response (Haroun 1980a, b)

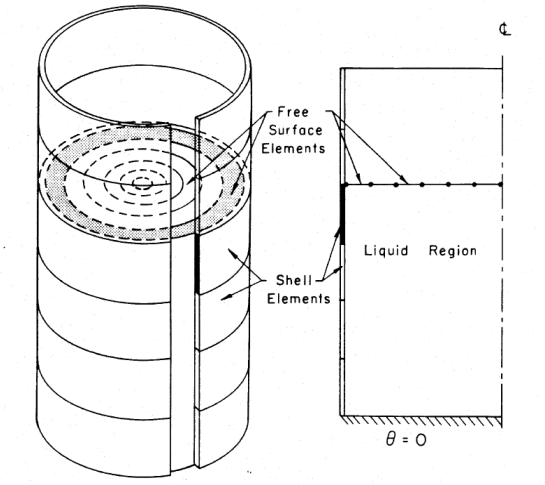

(a) free surface modeled using concentric annular elements

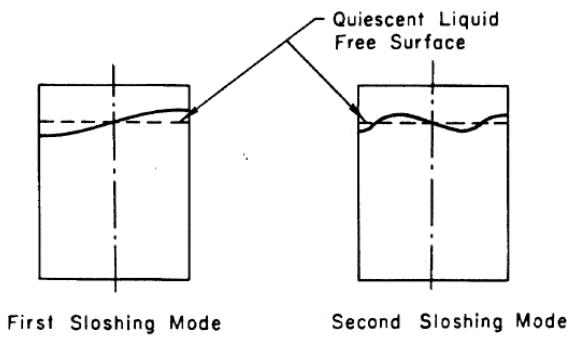

(b) convective modal shapes

Figure 2.9. Numerical model for seismic FSI analysis of flexible base-supported cylindrical tanks, convective response (Haroun 1980a, b)

Haroun proposed a mechanical analog for seismic FSI analysis of flexible, base-supported cylindrical tanks subjected to unidirectional horizontal motion. The mechanical analog was based on results of analysis of his numerical formulation. Figure 2.10 presents the mechanical analog. The lumped masses $m_{imp,r}$ and $m_{imp,f}$ were the parts of the fluid contributing to the impulsive response generated by rigid-body motion and lateral deformation of the tank, respectively. The lumped mass m_{con} was the part of the fluid contributing to the convective response. The lumped masses were located at the corresponding heights, $h_{imp,r}$, $h_{imp,f}$, and h_{con}, with respect to the tank base. The stiffness of the springs k_{imp} (k_{con}) that attached the lumped mass $m_{imp,f}$ (m_{con}) to the tank wall was associated with the first impulsive frequency $f_{imp,1}$ (convective frequency $f_{co,1}$). The parameters used in the mechanical analog (i.e., $m_{imp,r}$, $m_{imp,f}$, m_{con}, $h_{imp,r}$, $h_{imp,f}$, h_{con}, k_{imp}, and k_{con}) were developed by balancing the inertial forces of the lumped masses with the impulsive and convective reactions at the tank base calculated using the numerical formulation. The values of the parameters were presented in charts, for a range of tank dimensions, in Haroun and Housner (1981b) and Haroun (1983).

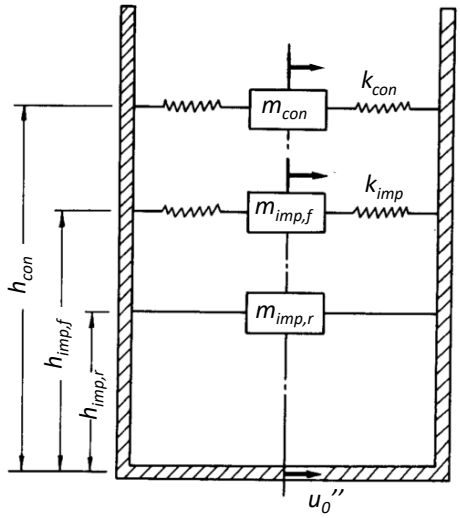

Figure 2.10. Mechanical analog for seismic FSI analysis of flexible, base-supported, cylindrical tanks subjected to unidirectional horizontal motion, adapted from Haroun and Housner (1981b)

Ma et al. (1982a) studied the effect of tank flexibility on seismic FSI response of base-supported cylindrical tanks using FLUSTR (Liu 1980, 1981; Liu and Belytschko 1982). FLUSTR was a finite element code for seismic FSI analysis developed by the Argonne National Laboratory in the 1980s for application to liquid metal reactors. The fluid response was assumed to be linear. Response-history analysis was performed for six finite element models of a tank with $H/R = 1.7$. One of the six models was rigid, and the other five models were flexible, with first impulsive frequencies $f_{imp,1}$ of 10, 7, 5, 2.5, and 1.5 Hz, achieved by varying the elastic modulus of the tank material. The first convective frequency $f_{con,1}$ of the rigid tank was 4.8 seconds (0.2 Hz), estimated using an analytical solution (Housner 1957). A 10-second, unidirectional horizontal ground motion of with peak ground acceleration (PGA) of 0.5 g was input at the tank base in each model. Response-history analysis was performed for 10 seconds for the five flexible tanks and 60 seconds for the rigid tank to investigate free-vibration wave response after the shaking had ended. Hydrodynamic pressure on the tank wall, where the face was normal to the direction of the seismic input, and wave heights along the diameter parallel to the input were compared for the six models. Ma et al. observed that 1) fluid pressures on the wall of the five flexible tanks were greater than that of the rigid tank, 2) the greatest fluid pressure occurred in the tank with $f_{imp,1}$ close to the frequency of the peak spectral acceleration of the input motion, 3) wave heights

increased with increasing tank flexibility[12], namely with reducing $f_{imp,1}$, and 4) the amplitude of wave heights in the rigid tank in the last 50 seconds was greater than that in the first 10 seconds by 20%: post-earthquake wave action was significant.

Ma et al. (1983a; 1983b) studied the effect of boundary conditions for flexible cylindrical tanks on seismic FSI responses. Response-history analysis was performed for a base-supported and a head-supported tank using FLUSTER. The dimensions of the two tanks were identical: $H/R = 1.7$. The bases of the two tanks were flat: rigid for the base-supported tank and flexible for the head-supported tank. A 10-second, unidirectional horizontal motion with a PGA of 0.5 g was input to the tank support, either base or head. Ma et al. observed the time series of hydrodynamic pressures on the tank wall and base of the two tanks, and approximated the period of the first impulsive mode using the time between every two consecutive crests in the time series. For the base-supported tank, the first impulsive frequency associated with the lateral vibration of the tank was identified using the pressure on the wall. For the head-supported tank, the impulsive frequencies associated with the lateral vibration of the tank and the vertical vibration of its base were identified using the pressure on the wall above the mid-height and on the base near the center, respectively. The pressure history near the wall-base intersection was affected by vibrations of both the wall and the base. The frequency for the lateral vibration of the head-supported tank was lower than that of the base-supported tank, and so the head-supported boundary condition increased the lateral flexibility of the tank. The frequency for the lateral vibration of the head-supported tank was significantly higher than that for the vertical vibration of its base. Ma et al. concluded that this outcome was due to the small bending stiffness of the tank base and the large mass of the fluid supported by and attached to the base. Wave heights along the diameter parallel to the input motion were compared for the two models, which were almost identical. Ma et al. concluded that wave action was independent of the location of the support (base or top).

Ma and Chang (1985a, 1985b)[13] studied the effect of horizontal seismic isolation on wave heights in a liquid metal reactor vessel. The seismic isolators were installed beneath the

[12] Sakurai et al. (1989) disagree with this observation, as noted in Section 2.3: tank flexibility did not affect wave heights.

foundation of the reactor building that housed the reactor. The vessel was assumed to be a flexible base-supported tank with $H/R = 1.4$. No internal components were included in the vessel. A stick model was built for the reactor building, and a finite element model was built for the reactor. The fundamental frequency of the building was 3 Hz, and the first convective frequency of the vessel was 0.25 Hz. (The first impulsive frequency of the vessel was not reported.) Three isolation systems with different periods were designed for the nuclear building: 1, 1.25, and 1.7 seconds (i.e., 1, 0.8, 0.6 Hz). Response-history analysis was first performed for the stick model of the reactor building using a unidirectional horizontal motion with a PGA of 0.3 g, for four models, one conventionally founded and three isolated. The acceleration time series at the location of the support of the reactor was then extracted and applied to its finite element models. The maximum fluid pressure on the wall of the vessel was reduced by around 80% with the use of the isolation of all three periods. The maximum wave height increased with all three isolation systems, with a maximum increase of 80% for the isolated period of 1.7 seconds. Ma and Chang concluded that the use of the horizontal seismic isolation for the reactor building significantly reduced hydrodynamic pressures on the reactor vessel in the building, but increased wave height, especially if the isolation period was close to the first convective frequency.

Malhotra (1997) performed seismic FSI analysis for conventionally founded and seismic isolated tanks to study the effectiveness of base isolation. A broad steel tank of $H/R = 0.60$ and a slender steel tank of $H/R = 1.85$ were used in the analysis. The first impulsive and convective frequencies of the broad tank were 9 and 0.12 Hz (i.e., periods of 0.25 and 8 seconds), respectively. The first impulsive and convective frequencies of the slender tank were 6.4 and 0.27 Hz (i.e., periods of 0.16 and 3.7 seconds), respectively. Malhotra applied 60 and 12 translational base isolators to the broad and slender tanks, respectively, and employed viscous dampers to prevent large horizontal displacements. The isolated periods for the broad and slender tanks were about 2.2 and 2.5 seconds, respectively. Seismic FSI analysis was performed using a mechanical analog per 3-D-BASIS-M (Tsopelas et al. 1991) for each tank. The mechanical

[13] Ma and Chang (1985a, 1985b) repeated the work of Ma et al. (1985a, 1985b) on seismic FSI analysis of internal components in a liquid sodium reactor. The section of Ma and Chang (1985a, 1985b) related to seismic isolation is summarized here. Ma et al. (1985a, 1985b), which includes the section of Ma and Chang (1985a, 1985b) related to internal components, is summarized in Section 2.2.2.

analog modeled the fluid using one impulsive and one convective mode, identical to that proposed in Malhotra's later study (Malhotra et al. (2000)), and the parameters used for the two modes were extracted from Veletsos and Tang (1990). Since the mechanical analog can only accommodate unidirectional horizontal input, responses to two horizontal components were calculated separately and combined using the method of the square root of the sum of the squares (SRSS). Malhotra compared reactions at the tank base and wave heights in the conventionally founded and seismic isolated tanks. For both the broad and the tall tanks, the use of the horizontal seismic isolation reduced the maximum base shear and moment by 80%, but increased the maximum wave height of the contained fluid by about 45%. The maximum axial force on the isolators was calculated using the maximum moment at the tank base and the weight of the tank and fluid, assumed to be evenly distributed to all isolators. The maximum tensile force on the isolators of the slender tank was significantly greater than that of the broad tank. Malhotra concluded that 1) horizontal seismic isolation was effective at reducing the reactions at the tank base without a significant increase in wave heights, 2) the tensile forces in the isolators due to the overturning moment would have to be considered in the design of the isolation system, especially for tall tanks.

Christovasilis and Whittaker (2008) performed seismic FSI analysis for a conventionally founded and two horizontally seismic isolated cylindrical tanks using a finite element model and a mechanical analog (Malhotra et al. 2000). The finite element model was built using ANSYS (2005) and the mechanical analog was built using RUAUMOKO (Carr 2004). The results of the analysis were used to judge the utility of the mechanical analog for the preliminary design of the tank and the effectiveness of employing seismic isolation. The dimensions of the conventionally founded and seismic isolated tanks were identical: $H/R = 0.87$. The translational periods of the isolation systems were 2 and 3 seconds. The impulsive and convective periods of the conventionally founded tank calculated using the finite element model and the mechanical analog were identical: 0.5 and 9 seconds, respectively. Response-history analysis of the three tanks (i.e., the conventionally founded, 2-second isolated, and 3-second isolated) was performed using the finite element model and the mechanical analog. Five unidirectional horizontal motions were used in the response-history analysis, and they were spectrally matched to the design spectrum at an assumed site. Seismic responses calculated using the finite element model and the

mechanical analog were compared, in terms of the maximum shear force and moment at the tank base and the maximum wave height. The two numerical methods differed in these seismic responses to the five input motions by the average of 6% for the conventionally founded tank and 1% for the isolated tanks. The seismic responses of the conventionally founded and isolated tanks were also compared. The maximum shear force and moment at the tank base were reduced by approximately 80% if isolation was used. The effect of the isolation on wave heights of the contained fluid was insignificant because the isolated periods were well separated from the period of the fundamental convective mode. Christovasilis and Whittaker concluded that the mechanical analog was a suitable tool for the preliminary design of a connectionally founded and seismic isolated cylindrical tank, and seismic isolation with an appropriate design period was effective for substantially mitigating seismic demands on the tank.

2.2.2 FSI analysis of submerged components

Chen (1975a, 1975b, 1977) derived analytical solutions for the mass of fluid contributing to hydrodynamic pressures on a row or an array of cylindrical rods subjected to seismic motions. The rods were parallel and submerged in an infinite fluid domain, and the seismic input was assumed to be unidirectional and perpendicular to their axial axis. The dimensions and boundary conditions of the rods in a row or an array were identical, and the distance between two adjacent rods was a constant, as presented in Figure 2.11: a row of 6 rods and arrays of 7 and 37 rods. The analytical solutions assumed the rods to be elastic, and the fluid to be ideal and respond linearly. The effects of hydrostatic pressure and fluid sloshing were not considered. The fluid contributing to the hydrodynamic pressures was assumed to be attached to and move with the rods. The mass of the attached fluid (i.e., added mass, m_{add}) reduced the lateral frequencies of the rods. A velocity potential was derived for the fluid using a boundary condition: each rod and its adjacent fluid moving at an identical velocity. Given the velocity potential, the hydrodynamic pressures on all rods in a row or an array could be calculated (see footnote 9 on page 11). The added mass m_{add} attached to and moving with the rod at an acceleration u'' was derived by balancing the inertial force, $m_{add} \cdot u''$, and the resultant force F_{hydro} associated with its hydrodynamic pressure: $F_{hydro} = m_{add} \cdot u''$. The added mass on each rod in a row or an array was a function of the rod radius R_i, the clear distance d_i between adjacent rods, and the density of the fluid ρ. Chen calculated

added masses for rows or arrays of rods using a range of R_i and d_i. In general, a smaller ratio of d_i / R_i added a greater mass to the rod, leading to lower lateral frequencies.

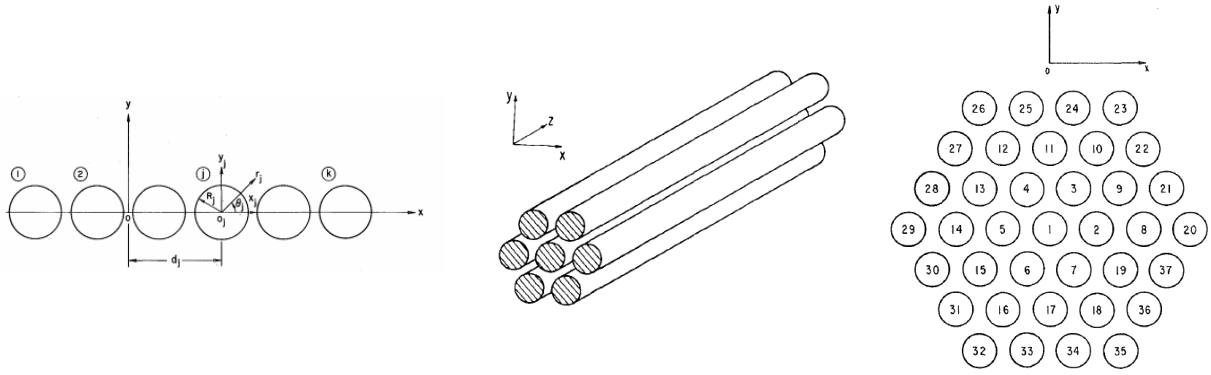

(a) a row of 6 rods (b) an array of 7 rods (a) an array of 37 rods

Figure 2.11. Row or array of parallel cylindrical rods in an infinite fluid space (Chen 1975b, 1977)

Chen and Rosenberg (1975) derived solutions for frequencies of two concentric pipes, with fluid filling the inner pipe and the annulus between the two pipes. The lateral, circumferential, and axial modes of the pipes were considered in the analysis. The two pipes were considered to be subjected to a unidirectional translational motion. The fluid contributing to the hydrodynamic pressures on the surfaces of the pipes was assumed to be attached to and move with the pipes as an added mass, and so the frequencies of the pipes were reduced. Solutions were derived using a method and assumptions similar to those of Chen (1975a, 1975b, 1977): elastic pipes, ideal fluids, identical lengths and boundary conditions for the two pipes, and neglecting hydrostatic pressure and sloshing. Section 5 presents the derivation and calculates the lateral frequencies of two concentric pipes with a range of dimensions using the solutions. In general, given a radius of the inner pipe, the frequencies of the two pipes both reduced with a smaller radius of the outer pipe (i.e., smaller clear distance between the two pipes).

Chung and Chen (1976, 1977) developed a computer code, AMASS, to calculate the added mass on cylindrical rods submerged in a fluid confined by a pipe (e.g., tank wall). The added mass was calculated using the method of Chen (1975a, 1975b, 1977) and Chen and Rosenberg (1975): a velocity potential of the fluid was derived and used for calculating hydrodynamic pressures on

the rods generated by unidirectional translational seismic input. The computer code was capable of calculating added masses for a group of rods with arbitrary dimensions and clear distances.

Chen and Chung (1976) provided a guideline for seismic FSI analysis of submerged components that summarized added masses for cylindrical rods and pipes extracted from their prior studies (e.g., Chen (1975a, 1975b) and Chen and Rosenberg (1975)). Chung and Chen (1984) provided a companion guideline for submerged components with various geometries, including rods of cylindrical, elliptical, semi-circular, triangle, rectangular, or hexagonal cross sections. Data presented in Chung and Chen (1984) were extracted from studies published in the 1930s to 1980s (e.g., Yu (1945) and Patton (1965)).

2.2.3 FSI analysis of fluid-filled advanced reactors

Ma et al. (1983c, 1983d) and Ma (1985b, 1985a) performed seismic FSI analysis for a submerged cylindrical pipe concentrically mounted on the base of a cylindrical tank using FLUSTR. Ma et al. and Ma mapped the cylindrical tank to a liquid metal reactor vessel and the submerged pipe to a cylindrical shield[14] for the reactor core, termed a core barrel in the studies. The effects of the presence of the core barrel and its dimensions on the FSI response of the tank were studied. A unidirectional horizontal motion with a PGA of 0.5 g was input at the base of the tank. Ma et al. (1983c, 1983d) performed the analysis using 2-D models, as presented in Figure 2.12a. In this figure, $H = 60$ ft, $R = 24$ ft, $H_b = 36$ ft, and $R_b = 8$ ft. The 2-D models were constructed for a tank of $H/R = 2.5$, and a core barrel of height H_b and different radii R_b: $H_b/H = 0.6$ and $R_b/R = 0.17$, 0.3, 0.5, and 0.7. Ma (1985b, 1985a) used 3-D models for the tank, barrel, and contained fluid, as presented in Figure 2.12b. The models took advantage of symmetry: only one half of the tank and barrel was modeled, and the horizontal motion was parallel to the plane of symmetry. The 3-D models were constructed for a tank of $H/R = 2$, and a core barrel of height H_b and different radii R_b: $H_b/H = 0.6$ and $R_b/R = 0.3$, 0.5, and 0.7. Both the tank and the barrel were flexible. The results of analysis presented in Ma et al. (1983c, 1983d) and Ma (1985b, 1985a) are in good agreement and so are summarized together here. First, the radius of the core barrel affected the first impulsive frequency of the base-supported tank.

[14] The cylindrical shield for the reactor core of a prototype liquid sodium reactor is presented in Figure 1.2 (Gluekler 1997).

The impulsive frequencies of the tank reduced as the radius of the barrel was increased, namely, the gap between the walls of the tank and barrel was reduced. Second, for all models, hydrodynamic pressures on the inner surface of the core barrel were significantly smaller than those on the outer surface. Third, the presence of the core barrel reduced the first convective frequency of the tank. Ma et al. observed that the first convective frequency of a tank with a core barrel, calculated using the numerical models, was similar to the analytical results per Housner (1957), calculated using the tank radius R and a fluid height of $H - H_b$: the fluid depth at the level of the top of the barrel. Accordingly, Ma et al. concluded that the fluid below the level of the top of the core barrel, including that inside the barrel and between the barrel and the tank wall, did not affect the convective response of the tank.

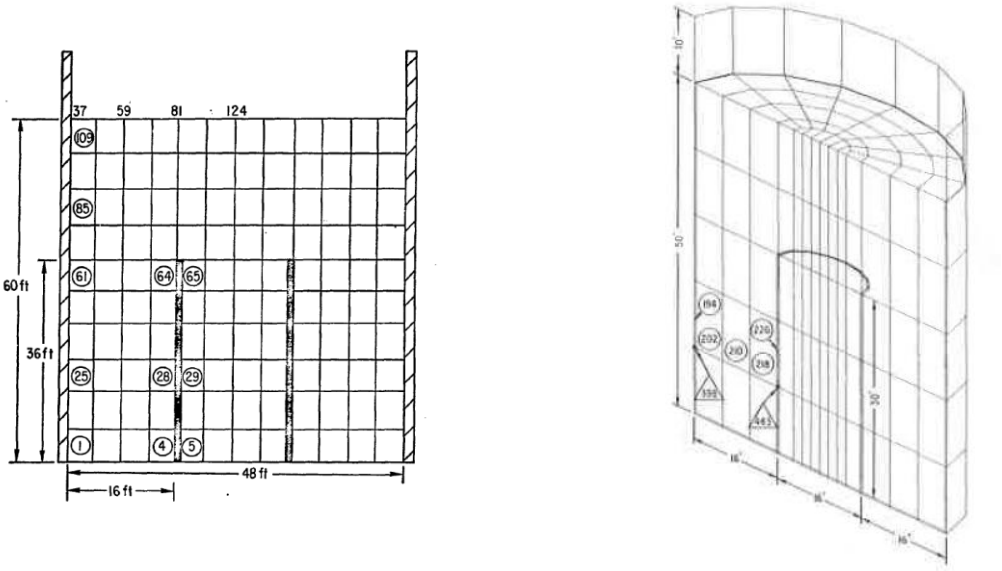

(a) 2-D model (Ma et al. 1983c) (b) 3-D model (Ma 1985b)

Figure 2.12. Numerical models for seismic FSI analysis of a core barrel in a tank, FLUSTR

Ma et al. (1985b, 1985a) investigated the effects of central and non-centered internal components on convective response in a liquid sodium reactor subjected to unidirectional horizontal motion. The reactor vessel and the internal components were assumed to be rigid and supported at their tops. Two 3-D finite element models were built: 1) a half reactor vessel with a central internal component, representing an upper internal structure (UIS)[15], as shown in Figure 2.13a; and 2) a

[15] Drawings of an upper internal structure (UIS), an intermediate heat exchanger (IHX), and a pump used in a prototype liquid sodium reactor are presented in Figure 1.2 (Gluekler 1997).

half reactor vessel with a central and 6 off-center components, representing 3 intermediate heat exchangers (IHXs)[15] and 3 pumps[15], as shown in Figure 2.13b. The models of the reactor took advantage of symmetry: only one half of the reactor was modeled, and the horizontal motion was parallel to the plane of symmetry. Only the upper part of the reactor was included in the models of Figure 2.13 because Ma et al. believed that the excluding part of the reactor did not affect wave action, which was the focus of the studies. A 10-second seismic motion with a PGA of 1 g was used for each model. Response-history analysis was performed for 60 seconds to investigate free-vibration wave action after the shaking had ended. Maximum wave heights calculated using the two models were compared. The maximum wave height in the two models occurred at different locations, noted using the red circles shown in Figures 2.13a and b. Without off-center components (Figure 2.13a), the maximum wave height occurred near the vessel wall. The maximum wave height occurred near component #6 in the model that included off-center components (Figure 2.13b). The maximum wave height in the vessel that included the off-center components was 40% smaller than in the vessel with only a central component. Ma et al. (1985a, 1985b) concluded that the presence of off-center components changed the shapes of the waves and significantly reduced the maximum wave heights.

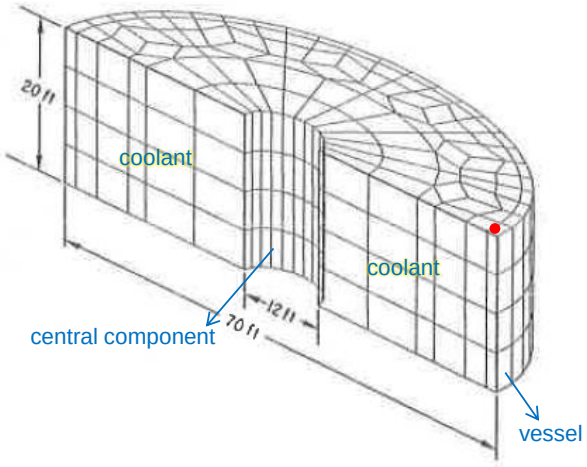

(a) vessel, coolant, and central component

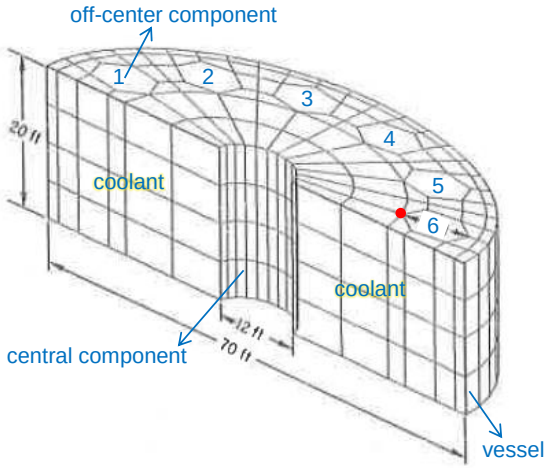

(b) vessel, coolant, central component, and six off-center components

Figure 2.13. Finite element models for a liquid sodium reactor, adapted from Ma et al. (1985b, 1985a)

Chellapandi et al. (2012)[16] performed seismic FSI analysis of a prototype liquid sodium reactor subjected to operating basis earthquake (OBE) shaking at an assumed site, with the consideration of a leak of the coolant. Figure 2.14a presents the liquid sodium reactor used in the study. In the event of a leak, the coolant would be retained in a space between the reactor vessel and the guard vessel. A 2-D and a 3-D model was constructed for the reactor, and seismic FSI analysis was performed using a finite element code, CAST3M (Commissariat Français à l'Energie Atomique (CEA) 2003). The analysis was performed to 1) judge the accuracy of the 2-D model by comparing results with the 3-D model, and 2) investigate the response of the guard vessel under OBE, after the main vessel leak and before decommissioning during relatively long shutdown condition. Figure 2.14b presents the 2-D and 3-D models, each including the reactor vessel, guard vessel, internal components, reactor vault, and liquid sodium in the reactor vessel and between the reactor and guard vessels. The 2-D model was computationally efficient and took advantage of axisymmetric geometries, and assumed the seismic shaking was either in the vertical direction or in the horizontal direction parallel to the plane of the model. The modal properties of the 2-D and 3-D models were characterized using their free-vibration response. The frequencies and modal shapes associated with global vibrations of the reactor and guard vessels calculated using the two models were in good agreement, but the 2-D model was unable to correctly identify local vibrations of the internal components.

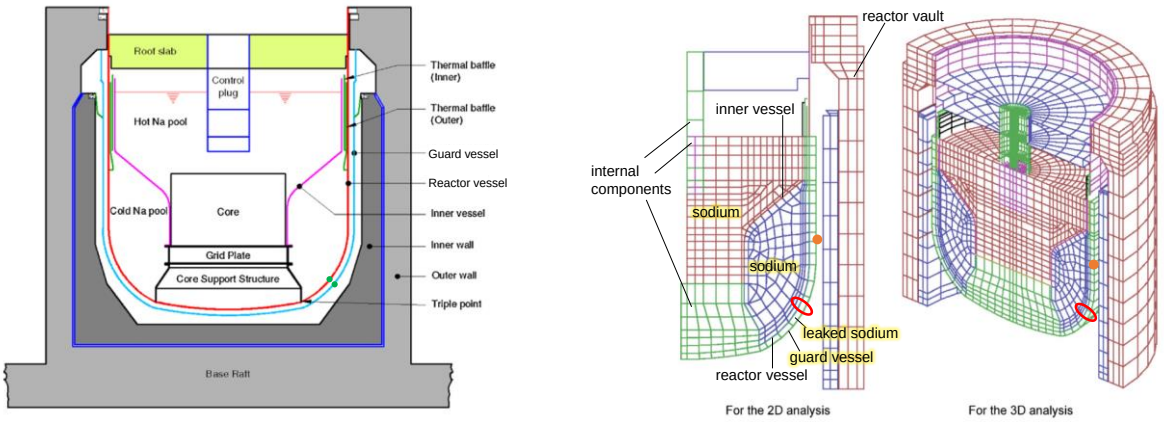

(a) prototype liquid sodium reactor (b) 2-D axisymmetric and 3-D models

Figure 2.14. Prototype liquid sodium reactor and the numerical models, adapted from Chellapandi et al. (2012)

[16] Chellapandi et al. (2012) also performed bucking analysis at the support of the guard vessel on the reactor vault. This work is not related to the focus of this report, and so is not summarized here.

Response-history analysis was performed for the 2-D and 3-D models using OBE shaking. Since the 2-D model could only accommodate unidirectional input motion, the horizontal and the vertical components of the OBE shaking were input separately for both 2-D and 3-D models, to enable a comparison of results. Results were compared for 1) absolute and relative displacements of the reactor and guard vessels, at their crown-knuckle junctions, around the red ellipses drawn in Figure 2.14b, 2) reactions at the support of the guard vessel on the reactor vault, and 3) hydrodynamic pressures on the wall and at the mid-height of the guard vessel, at the orange solid circles denoted in Figure 2.14b. The time series of the reactions (i.e., shear force and moment) calculated using the two models were in good agreement, in both amplitude and frequency content. The time series of the displacement and hydrodynamic pressure calculated using the two models differed in their frequency contents but the maximum values were similar. The maximum relative displacements of the guard and reactor vessels around the red ellipses (see Figure 2.14b) generated using the horizontal input was insignificant (<3.2 mm), and that generated using the vertical input was negligible, by comparison with the nominal clear distance (∼250 mm). Chellapandi et al. (2012) concluded that the 2-D model predictions for the peak responses were reasonable by comparison with that of the 3-D model, and the guard and reactor vessels would not impact under the simultaneous occurrence of a coolant leak and OBE shaking.

2.3 Experimental and validation studies on seismic FSI analysis of tanks and fluid-filled reactors

Haroun and Housner (Haroun 1980a, b, 1983; Housner and Haroun 1980) performed ambient and forced vibration tests on base-supported, cylindrical, steel tanks filled with water. This experimental study was Phase 2 of their research project on seismic FSI analysis of tanks. Test data were used to validate the numerical models developed in Phase 1 of the project. (Phases 1 and 3 are introduced in Section 2.2.1.)

Figure 2.15 presents the three tanks used for the experiments, each of which was essentially full and close at its top by a tank roof. The radii R of the three tanks were 7, 9, and 9 m, and the height-to-radius ratios H/R ranged between 2 and 3. Seismometers were used to measure the velocity on the tanks in both ambient and forced vibration tests. A vibration generator (i.e., shaker) was used to generate horizontal sinusoidal motions for the forced vibration tests. Figure 2.16 presents the test setup for Tank No. (1) presented in Figure 2.15. Per Figure 2.16, the

vibration generator was anchored to the concrete slab supporting the tank and resting on the ground. Six seismometers (denoted as 1 to 6 in Figure 2.16) were attached to the tank wall at 6 different heights to measure motions in a horizontal direction (parallel to the input motion from the vibration generator in the forced vibration tests). Two seismometers (denoted as 7 and 8 in Figure 2.16) were placed on the concrete slab supporting the tank to measure vertical velocities associated with rocking motions of the tank due to horizontal excitation. Per detail (b) in Figure 2.16, three seismometers were used to measure velocities in three orthogonal directions at a point on the tank roof. This set of three seismometers was moved from point to point to record data at 10 different locations around the perimeter of the tank roof.

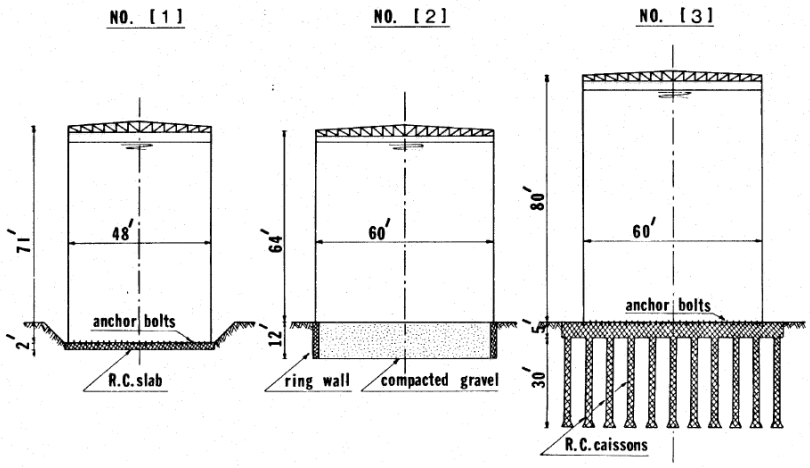

Figure 2.15. Base-supported cylindrical tanks used for ambient and forced vibration tests (Haroun 1980b)

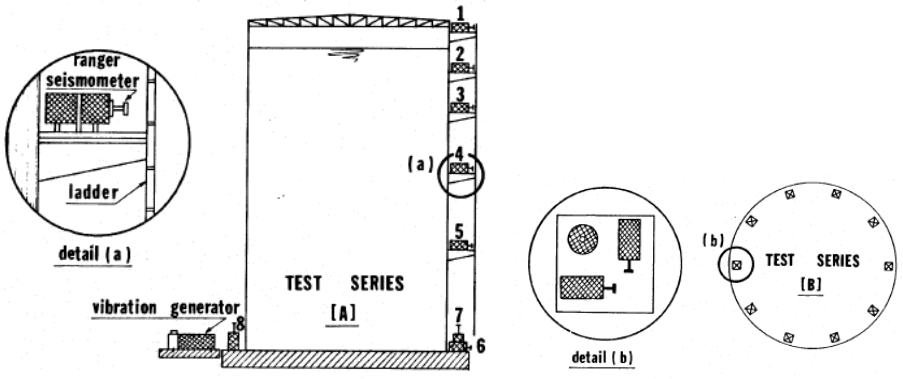

Figure 2.16. Setup of seismometers for the ambient and forced vibration tests for Tank No. (1) presented in Figure 2.15, and vibration generator for the forced vibration tests, adapted from Haroun (1980b)

The frequencies of the lateral modes of the tank (see Figure 2.8b) were identified using data from the six seismometers on the tank wall, and those of the circumferential modes (see Figure 2.8c) were identified using seismometer data around the perimeter of the tank roof, generated from both ambient and forced vibration tests. The lateral frequencies of each tank measured from the ambient and forced vibration tests were lower than those calculated using the numerical formulation presented in Section 2.2.1. Haroun concluded that the reason for the lower frequencies measured in the tests was due to foundation flexibility. The frequencies of the $\cos\theta-$ and $\cos n\theta-$ types circumferential modes of each tank calculated using the numerical formulation agreed well with measurements from the ambient tests if the hydrostatic pressure of the fluid on the tank wall and the stiffness of the tank roof were considered in the numerical calculations. The frequencies of the $\cos n\theta-$ type circumferential modes could not be identified from the forced vibration tests because the motion of the tank generated by the vibration generator was dominated by lateral deformation and the circumferential deformations associated with $\cos n\theta$-type modal shapes were insignificant. Haroun concluded that 1) the numerical models calculated using his formulation were validated, and 2) foundation flexibility, hydrostatic pressure, and stiffness of the tank roof played an important role in the modal properties of the tanks.

Chalhoub and Kelly (1988, 1990) performed earthquake-simulator tests to investigate the effectiveness of horizontal seismic isolation on reducing the FSI response of base-supported tanks. Two rigid steel tanks with similar dimensions were tested. The radius and height of the tanks were both around 0.6 m, the wall thickness was 1 mm, and the height of the contained water was 0.45 m. As presented in Figure 2.17, tank #1 was anchored to the earthquake simulator and tank #2 was anchored to the base plate of a seismically isolated steel fame supported on the simulator. The steel frame was a 1/4th-scale, 9-story structure. Eight elastomeric isolators were installed beneath the steel frame. Weights were attached to each floor of the frame to achieve an isolated frequency of 0.7 Hz.

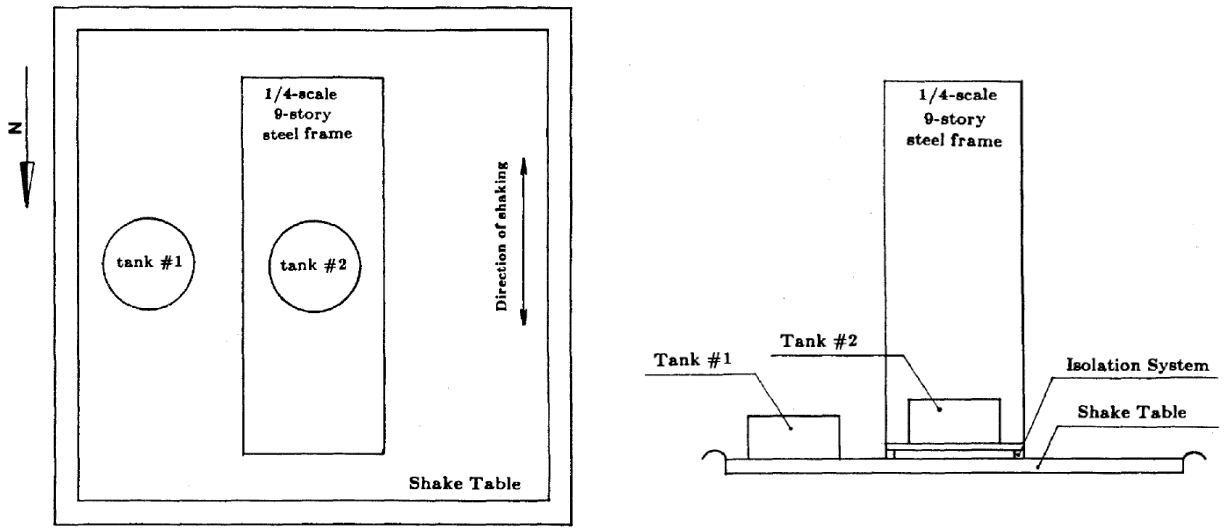

(a) plane view (b) side view from south

Figure 2.17. Earthquake-simulator tests on two rigid, base-supported, cylindrical tanks filled with water, each anchored to the simulator or a base-isolated steel frame

Time series of sinusoidal motions and earthquake records, with peak ground accelerations ranging between 0.07 g and 0.3 g, were input in the north direction identified in Figure 2.17. Identical instrumentation was used for each tank. Eight pressure gauges were installed on the wall of each tank: three gauges on each of the north and south faces of the tank wall at three different depths and one gauge on each of the east and west faces at the mid-height of the tank. One accelerometer was installed on each of the north and west faces of the wall and near the top for each tank. Two water level gauges were used to measure wave heights adjacent to the north and south faces of the wall of each tank.

Convective frequencies were determined from Fourier amplitude spectra of the measured wave heights in the two tanks. The first convective frequency was 0.83 Hz for both tanks, which was very close to the isolated frequency of the steel frame supporting the tank (i.e., 0.7 Hz). Hydrodynamic pressures, accelerations, and wave heights measured for the two tanks were presented and compared for seven input motions. The peak hydrodynamic pressures and accelerations on the tank supported on the base plate of the isolated frame (i.e., tank #2) were 15% to 80% smaller than those on the tank anchored to the simulator (i.e., tank #1) for the seven input motions. However, the peak wave heights measured in tank #2 were greater than those in tank #1 by 3% to 47%. Chalhoub and Kelly concluded that the use of seismic isolation reduced

the accelerations and hydrodynamic pressures of the base-supported tank but increased wave heights, which could be addressed by selecting an isolated frequency that was well separated from the first convective frequency.

Data from the earthquake-simulator tests were also used to validate analytical solutions developed by Chalhoub and Kelly for FSI responses of a rigid, base-supported, cylindrical tank. The solutions addressed hydrodynamic pressures and wave heights. (Section 3 presents the derivation and calculates the FSI responses for a range of tank dimensions using the solutions.) The test and analytical results for hydrodynamic pressures and wave heights were compared for the two tanks and five earthquake records. The test and analytical results were in phase but differed in maximum pressures and wave heights by an average of 15% and 3%, respectively, for the two tanks and the five motions. The maximum differences in responses were not reported. Chalhoub and Kelly (1988, 1990) concluded that the test data and analytical results for the seismic FSI responses were in good agreement.

Fujita et al. (1984) performed experiments for two scaled models of a loop-type[17] liquid sodium nuclear reactor presented in Figure 2.18a. The goals of the tests were to 1) investigate seismic FSI response, 2) judge the effectiveness of a sloshing suppressing system used in the vessel, and 3) validate a beam-column model and an in-house linear finite element model. The test specimens were a 1/8th-scale steel vessel and a 1/4th-scale plastic vessel, as presented in Figures 2.18b and c, respectively.

The 1/8th-scale vessel was tested using an electromagnetic shaker as presented in Figure 2.19a. The shapes and frequencies of the lateral and circumferential modes were identified for the vessel as empty and filled with water. The 1/8th-scale vessel did not include internal components. As presented in Figure 2.19a, the vessel was supported at both top and bottom: the top was supported by a head and the bottom was supported using a column to mimic the boundary conditions of the reactor vessel of Figure 2.18a. Test results for the shapes and frequencies of the lateral and circumferential modes of the vessel generated using the electromagnetic shaker showed good agreement with those calculated using analytical solutions (Fujita 1981).

[17] Loop-type: the coolant pump and the heat exchanger are located outside the reactor vessel, in contrary to pool-type (e.g., the prototype liquid metal reactor of Figure 1.2 (Gluekler 1997)).

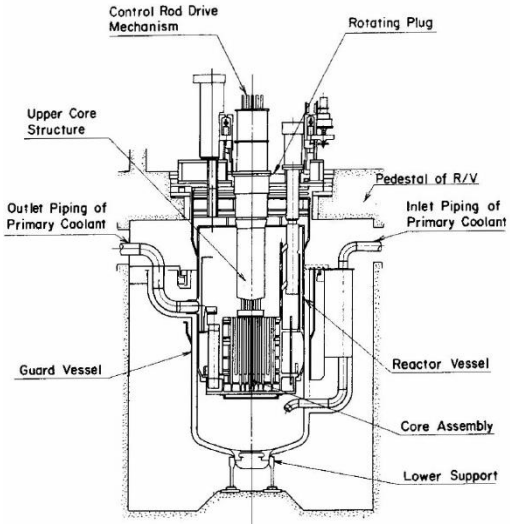

(a) loop-type liquid sodium

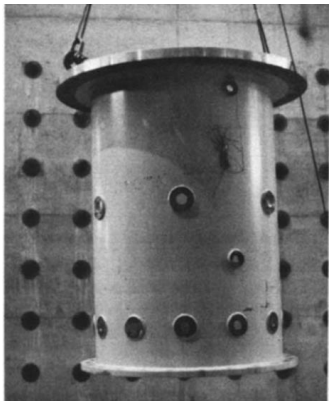

(b) 1/8th-scale steel vessel

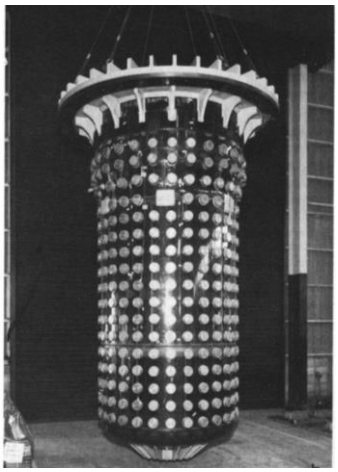

(c) 1/4th-scale plastic vessel

Figure 2.18. Loop-type liquid sodium reactor, 1/8th- and 1/4th-scale test models, filled with water (Fujita et al. 1984)

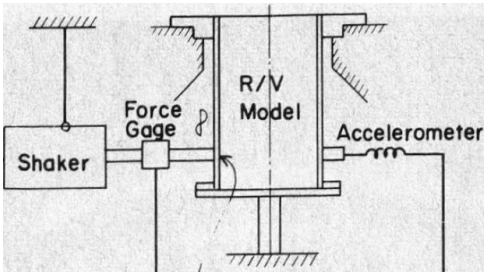

(a) test setup for the 1/8th-scale steel vessel

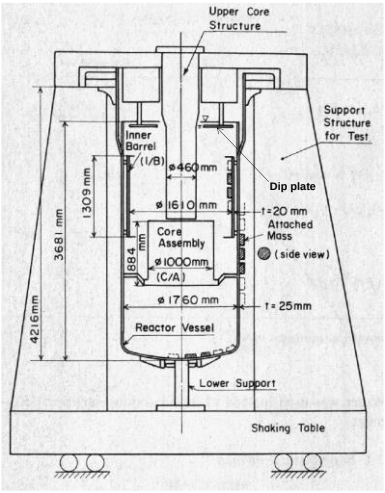

(b) test setup for the 1/4th-scale plastic vessel

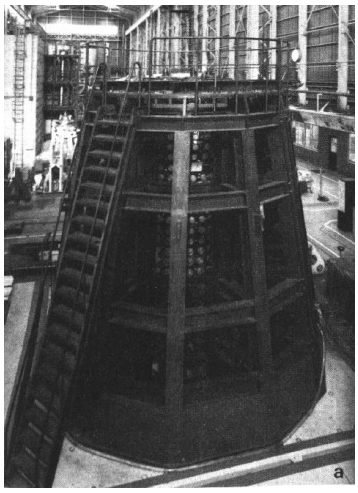

(c) 1/4th-scale vessel supported by a steel frame on an earthquake simulator

Figure 2.19. Test setups for the 1/8th- and 1/4th-scale test models filled with water (Fujita et al. 1984)

The 1/4th-scale vessel was supported at its top by a head on a frame, which was anchored to an earthquake simulator, as presented in Figures 2.19b and c. The base of the vessel was supported by a column attached to the simulator. As presented in Figure 2.19b, the 1/4th-scale vessel included a sloshing suppressing system (termed dip plate in the study) and internal components, representing a nuclear core, an upper structure, and an inner barrel. The modal shapes and frequencies of the lateral modes of the vessel, including the internal components and the dip plate, were identified as empty and filled with water. The circumferential modes of the vessel were not considered. The fluid sloshing in the vessel, generated by a horizontal harmonic motion, were investigated for three test configurations: 1) vessel only, 2) vessel, including all internal components and excluding the dip plate, and 3) vessel, including all internal components and the dip plate. Wave heights were measured adjacent to the tank wall. Results for the three test configurations were compared. Wave heights measured in Configuration 2 were significantly smaller than those in Configuration 1: the presence of the internal components reduced wave heights. When the dip plate was installed in the vessel (Configuration 3), the wave heights were too small to be measured. The convective frequencies in the first three modes were identified using Fourier amplitude spectra of wave heights measured for all three configurations. The convective frequencies for Configuration 2 were lower than those for Configuration 1: the internal components reduced the convective frequencies of the vessel. The convective frequencies for Configuration 3 (including the dip plate) could not be identified because the measured wave heights were too small to be measured, as noted above.

A beam-column model and a finite element model was constructed for the 1/4th-scale vessel, as presented in Figure 2.20. In the beam-column model, the vessel and its internal components were modeled using beam-column elements and the contained water was modeled as a distributed mass attached to these elements. Springs were used to model the boundary conditions of the vessel and internal components. The dip plate was not included in the beam-column model. The finite element model was developed and analyzed using an in-house code. The vessel, contained water, internal components, and dip plate were included in the finite element model.

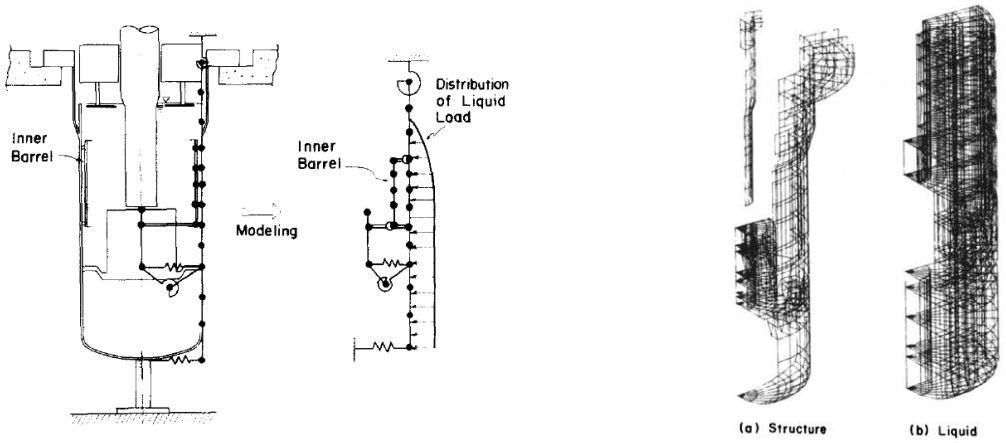

(a) beam-column model (b) finite element model

Figure 2.20. Numerical models for the 1/4th-scale plastic vessel filled with water (Fujita et al. 1984)

The modal shapes and frequencies of the first lateral modes of the 1/4th-scale vessel, empty and water-filled, were calculated using the beam-column and finite element models. The modal properties calculated using the models were both in good agreement with the test results: the differences in the frequencies were less than 10%. The convective frequencies of the 1/4th-scale vessel, excluding the internal components and dip plate, were calculated using the finite element model. The numerical results for the first three convective frequencies were essentially identical to those measured in the tests. Wave heights adjacent to the wall were calculated using the finite element model for horizontal motions used in the tests for 1) vessel, excluding internal components and the dip plate (Configuration 1), and 2) vessel, including the internal components and the dip plate (Configuration 3). The numerical results and the test data were compared. Figure 2.21[18] presents results for a harmonic input: the predicted wave height was inaccurate.

[18] The analytical results for wave heights presented in Figure 2.21a were calculated using solutions developed in a document written in Japanese, and so are not described here.

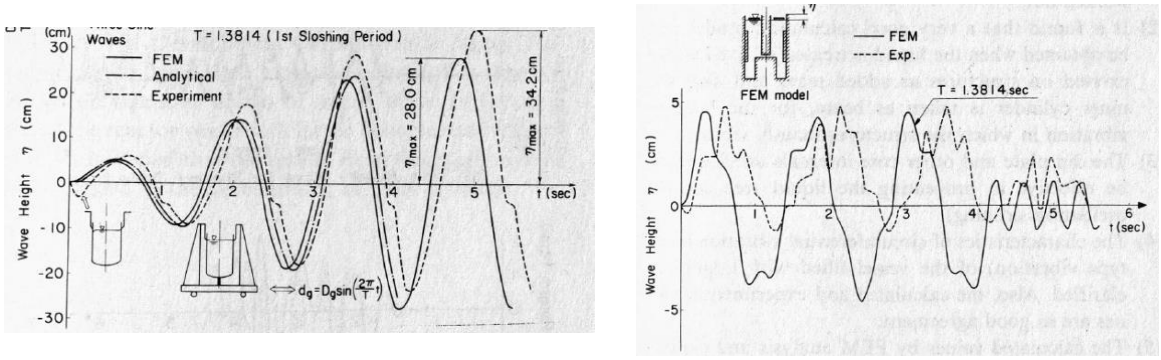

(a) configuration 1 (b) configuration 3

Figure 2.21. Wave heights in the 1/4th-scale vessel calculated using the finite element model and measured in the earthquake-simulator tests (Fujita et al. 1984)

Sakurai et al. (1989)[19] used the 1/l0th-scale model presented in Figure 2.22a for earthquake-simulator testing of a prototype pool-type liquid sodium reactor. The model included a) a 6 mm thick cylindrical tank (termed *rigid*) to represent the reactor vessel, b) a 1.2 mm thick cylinder (termed *flexible*) to represent a thermal baffle, and c) submerged components. The gap between the rigid and flexible vessels was 50 mm. The vessel, thermal baffle, and submerged components were head supported by a frame, which was anchored to an earthquake simulator. Tests were performed in the five configurations of Figure 2.22b. In configurations 3 and 4, water was contained by the *flexible* inner cylinder (which was presumably sealed at its base). The earthquake-simulator experiments were performed for the five configurations to investigate sloshing of the coolant, including the effects of wall flexibility and submerged components on wave action.

Sinusoidal motions and an earthquake record were used as unidirectional horizontal inputs in the tests. Convective frequencies and damping ratios were determined using results for wave heights generated by sinusoidal motions. Wave heights were measured for the earthquake simulation at 6 locations on the free surface, along the diameter in the direction of the input motion. The first convective frequencies and wave heights were compared for the five configurations. In general, the effect of wall flexibility on the frequencies and damping ratios in the convective modes and wave heights was insignificant. The presence of the submerged components reduced the

[19] Sakurai et al. (1989) also performed experiments for a 1/3rd-scale model of the hot pool of a 1000 MWe reactor. The test data were used for bucking analysis of the pool. This work is not related to the focus of this report, and so is not summarized here.

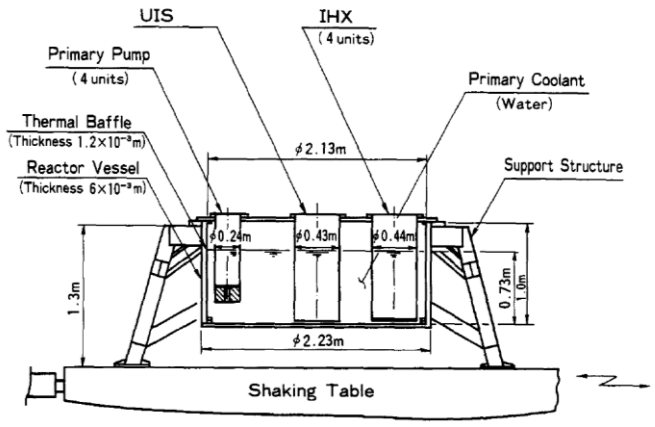

(a) side view of the 1/10th-scale vessel, thermal baffle, and submerged components, supported at top

Test Model Configurations

No.	Configuration	Feature
1		Rigid Wall
2		Rigid Wall and Internals
3		Flexible Wall
4		Flexible Wall and Internals
5		Water in the Annulus

(b) test configurations

Figure 2.22. 1/10th-scale vessel for earthquake simulation tests (Sakurai et al. 1989)

convective frequencies by about 5% and the maximum wave heights by about 40%. The damping ratios of the first convective mode of the vessel, excluding and including the submerged components, were 0.1% and 0.4% of critical, respectively: the presence of the internal components increased the damping ratios.

SECTION 3
ANALYTICAL SOLUTIONS FOR SEISMIC FLUID-STRUCTURE INTERACTION RESPONSES OF CYLINDRICAL TANKS

3.1 Introduction

Earthquake shaking of a liquid metal nuclear reactor induces fluid-structure interaction (FSI) between the reactor vessel, the internal components, and the liquid metal coolant. As noted in Section 1, early reactor designs ignored the interaction between the vessel and the internal components to simplify the seismic analysis, which enabled FSI to be parsed into: 1) interaction of the vessel and its contained fluid and 2) interaction of the internal components and the surrounding fluid. This section addresses the first interaction and provides analytical solutions for seismic FSI responses, including modal properties of the vessel, hydrodynamic pressures on the vessel generated by the fluid, and global reactions at the vessel supports. (The second interaction is addressed in Section 5.) The analytical solutions are suitable for preliminary design and seismic qualification for vessels containing fluid, such as liquid metal reactors and other nuclear reactors that contain a large volume of fluid (e.g., pressurized water and boiling water reactors). The analytical solutions also support verification of the numerical models presented in Section 4.

A liquid metal reactor vessel is generally cylindrical with a dish-shaped base. The tank is filled with fluid and closed by an air-tight head that supports the tank at its top. Analytical solutions for the seismic response of such head-supported cylindrical tanks have not been published at the time of this writing, but companion solutions for base-supported tanks have been developed in prior studies. Analytical solutions are derived in this section for head-supported cylindrical tanks, achieved by modifying published derivations for seismic response of base-supported cylindrical tanks and addressing the change in the boundary conditions (i.e., base- to head-supported). The shaped base is ignored in the derivations and the bottom of the tank is assumed to be flat and rigid.

This section introduces a number of prior analytical studies of base-supported cylindrical tanks subjected to small-amplitude, unidirectional horizontal motion. The studies assumed the tank to be either rigid or elastic (flexible), the thickness of the tank wall to be constant, and the

contained fluid to be ideal[20]. The fluid adjacent to the wall and the base of the tank was attached to these surfaces because the amplitude of the input motion was assumed to be small. The analytical studies parsed the seismic response of a base-supported cylindrical tank into an impulsive and a convective component, which are introduced next.

Impulsive response is generated by the part of the fluid accelerating with the tank. This fluid behaves like a distributed mass attached to the wall and the base of the tank, following the movement and deformation of the tank. The impulsive response is also described as an *added mass effect* on the tank. The impulsive response disregards fluid waves and assumes the pressure on the initial free surface[21] to be zero as atmospheric pressure is not considered. Convective response is generated by the part of the fluid assumed theoretically *not* to move with the tank horizontally but oscillates vertically. The vertical oscillation is a wave action that induces vertical displacements of the free surface. The convective response considers the pressures generated by wave actions, and together with the impulsive response completes the hydrodynamic pressures in the tank.

The analytical solutions for seismic FSI response of a head-supported cylindrical tank developed here adopt the same assumptions used previously for studies of base-supported cylindrical tanks. The assumptions include 1) rigid or elastic (flexible) tank, 2) constant thickness of the tank wall, 3) ideal fluid, 4) fluid attached to the tank, and 5) small-amplitude, unidirectional horizontal input motion. Identical to the studies on base-supported tanks, the seismic response of a head-supported tank is also parsed into impulsive and convective components. The analytical solutions for a head-supported cylindrical tank are derived by modifying the boundary condition used for the analysis of a base-supported cylindrical tank: 1) the seismic input is at the head of the tank, and 2) the base of the tank is free to vibrate when the deformation of the tank is taken into account.

Section 3.2 introduces analytical solutions for the seismic FSI response of both rigid and flexible, base-supported, cylindrical tanks as derived previously. Seismic FSI responses calculated using the analytical solutions are compared for such tanks with a range of dimensions (i.e., height of

[20] Ideal fluid: a fluid that is incompressible, irrotational, and inviscid.

[21] Initial free surface: open surface of a fluid at rest.

contained fluid and tank radius). Section 3.3 develops analytical solutions for seismic FSI responses of rigid and flexible, head-supported cylindrical tanks. Seismic FSI responses are calculated using the proposed analytical solutions for head-supported tanks with a range of dimensions and the results enable preliminary seismic design and qualification of such tanks (e.g., nuclear reactor vessels) by others at a later time.

Appendix A summarizes the derivations and analytical solutions presented in this section, including governing equations, boundary conditions, and separation of variables.

3.2 Base-supported cylindrical tank

3.2.1 Impulsive responses

3.2.1.1 Introduction

Figure 3.1 illustrates impulsive responses in a vertical cross section through a base-supported cylindrical tank accelerating in the x direction. The contained fluid is attached to the inner surfaces of the tank (i.e., wall and base) and generates impulsive pressures, p_{imp}, in the fluid and on the inner surfaces. The fluid adjacent to the $+x$ side of the wall and the base tends to be expanded by the tank accelerating to the x direction, which generates a negative p_{imp} on these surfaces; the fluid adjacent to the $-x$ side of the wall and the base tends to be compressed by the accelerating tank, which generates a positive p_{imp} on these surfaces. These impulsive pressures, p_{imp}, on the inner surfaces of the tank are mechanically equilibrated by global impulsive reactions, including the impulsive shear force and moments, at the base of the tank, which is assumed to be rigid. The resultant force of the horizontal p_{imp} on the wall (orange arrows) is balanced by the impulsive shear force at the base, F_{imp}, in the x direction. The impulsive moment at the base is composed of: 1) $M_{imp,w}$, which balances the moment at the center of the base (red solid circle) generated by p_{imp} on the wall (orange arrows); and 2) $M_{imp,b}$, which balances the moment at the center of the base generated by p_{imp} on the base (pink arrows). The impulsive moments, $M_{imp,w}$ and $M_{imp,b}$, act in a clockwise direction about the y axis.

The impulsive responses are generated by the fluid accelerating with the wall and the base of the tank, under seismic motion of the base. The seismic response of the wall includes rigid-body displacements and deformations due to tank flexibility. Consequently, the flexibility of the wall

of the tank may play an important role in the calculation of the impulsive responses. Section 3.2.1.2 introduces and compares analytical solutions for the impulsive responses of rigid tanks developed in a number of prior studies, in which deformation of the wall of the tank was ignored. Section 3.2.1.3 introduces analytical solutions for the impulsive responses of flexible tanks developed in a prior study, and the results are compared introduced in Section 3.2.1.2 with those of rigid tanks.

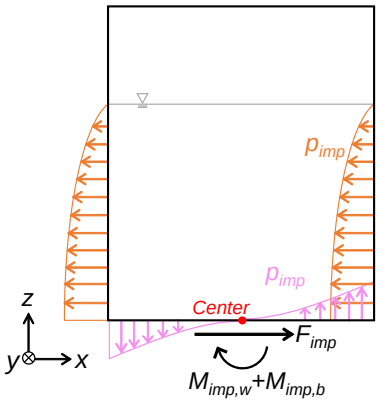

Figure 3.1. Impulsive responses: impulsive pressure, p_{imp}, on the walls and base of a tank; impulsive shear force at the base, F_{imp}; and impulsive moments at the base, $M_{imp,w}$ and $M_{imp,b}$; shown in a vertical cross section through a base-supported cylindrical tank accelerating in the x direction

3.2.1.2 Rigid tank

This section presents the analytical solutions for impulsive responses developed by 1) Jacobsen (1949), 2) Chalhoub and Kelly (1988), and 3) Housner (1957), for a rigid, base-supported cylindrical tank subjected to unidirectional horizontal motion of a small amplitude. Table 3.1 lists the impulsive responses analytically derived in each of the three studies.

Jacobsen, and Chalhoub and Kelly derived *exact* analytical solutions for the impulsive responses using similar methodologies, with both assuming a velocity potential for the ideal fluid in the tank. Different assumptions regarding the boundary conditions assigned to the contained fluid were made for solving the equation of the velocity potential, which led to different analytical solutions for the impulsive responses. Housner derived *approximate* analytical solutions for the impulsive responses using a 2-dimensional vertical cross section through a base-supported

cylindrical tank. He discretized the fluid in the vertical cross section into multiple vertical thin layers and derived the impulsive responses using Newton's second law.

The exact solutions per Jacobsen, and Chalhoub and Kelly are first summarized in this section, followed by the approximate solutions of Housner. Accordingly, the summary is not chronological. The equations used in the derivations and the solutions presented here are not identical to those in the original documents to enable use of a consistent set of variables and coordinate systems.

Table 3.1. Impulsive responses of a rigid, base-supported cylindrical tank subjected to unidirectional horizontal seismic motion of a small amplitude, analytically derived in the studies listed in the first column

	p_{imp}	F_{imp}	$M_{imp,w}$	$M_{imp,b}$
Jacobsen (1949)[1]	✓	✓	✓	✓
Chalhoub and Kelly (1988)	✓			
Housner (1957)[2]	✓	✓	✓	✓

1. The paper contains calculation errors. The correct analytical solutions and their derivations presented in this section follow those in Yang (1976), Veletsos (1984), and Tang (1986)
2. The paper contains calculation errors. The correct analytical solutions and their derivations presented in this section follow those in Thomas et al. (1963)

Figure 3.2 introduces the variables for the analytical solutions used herein, shown on two cut-away views of a base-supported cylindrical tank, together with a Cartesian coordinate system (x, y, z) and a cylindrical coordinate system (r, θ, z). The radius of the tank is R and the height of the contained fluid is H. The tank moves with the rigid foundation at a horizontal displacement, velocity, and acceleration, $u_0(t)$, $u_0'(t)$, and $u_0''(t)$, in the x direction, which generates impulsive responses on the tank and in the fluid. The velocities of an arbitrary point (pt) in the fluid are u', v', and w' along the cylindrical coordinates, r, θ, and z, respectively.

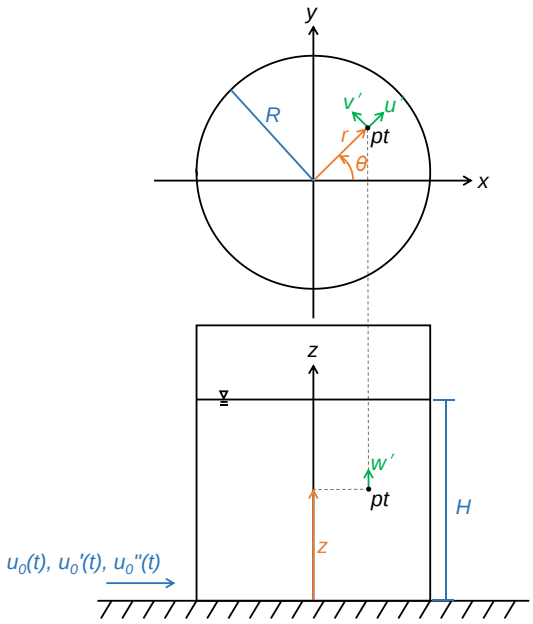

Figure 3.2. Variables used in the analytical solutions of impulsive response shown on two cut-away views of a base-supported cylindrical tank, a Cartesian coordinate system, and a cylindrical coordinate system

Jacobsen (1949)

Jacobsen derived analytical solutions for the impulsive responses listed in the second row of Table 3.1. The effects of hydrostatic pressure and fluid sloshing were not considered. A velocity potential was first assumed for the contained fluid because mechanical behaviors of a fluid (whether hydrostatic or hydrodynamic) can be fully defined given a velocity potential. The pressure, p, and the velocity, vel, of the contained fluid are related to the velocity potential, Φ, in the following:

$$p(r,\theta,z) = -\rho \frac{\partial \Phi}{\partial t} \tag{3.1}$$

$$vel(r,\theta,z) = \nabla\Phi = \frac{\partial \Phi}{\partial r}\vec{r} + \frac{1}{r}\frac{\partial \Phi}{\partial \theta}\vec{\theta} + \frac{\partial \Phi}{\partial z}\vec{z} \tag{3.2}$$

where ρ is the density of the fluid, t is time, and ∇ is the gradient operator with respect to a cylindrical coordinate system (r, θ, z). The fluid velocity, vel, includes the vectors of radial, angular, and vertical velocities. The pressure, p, and the velocity, vel, calculated using Φ are functions of r, θ, and z, which enable the determination of the responses for the contained

fluid. The velocity potential for the impulsive response, Φ_{imp}, derived by Jacobsen was a function of four variables: the three components of the cylindrical coordinate system (r, θ, z) shown in Figure 3.2 and the velocity of the horizontal seismic motion $u_0'(t)$, which was a function of time, t. The velocity potential was the product of the four unknown functions, $\tilde{R}$, $\tilde{\Theta}$, $\tilde{Z}$, $\tilde{T}$, associated with the four variables, r, θ, z, t, respectively, since these variables were independent:

$$\Phi_{imp}(r,\theta,z,t) = \tilde{R}(r)\cdot\tilde{\Theta}(\theta)\cdot\tilde{Z}(z)\cdot\tilde{T}(t) \tag{3.3}$$

The velocity potential, Φ_{imp}, of the contained ideal fluid satisfied Laplace's equation, $\nabla\cdot\nabla\Phi = 0$[22]:

$$\frac{\tilde{R}''}{\tilde{R}} + \frac{1}{r}\frac{\tilde{R}'}{\tilde{R}} + \frac{1}{r^2}\frac{\tilde{\Theta}''}{\tilde{\Theta}} + \frac{\tilde{Z}''}{\tilde{Z}} = 0 \tag{3.4}$$

Three boundary conditions were assumed for the impulsive responses of the fluid to solve the functions $\tilde{R}$, $\tilde{\Theta}$, $\tilde{Z}$, and $\tilde{T}$:

1) Disregarding fluid waves on the free surface, the impulsive pressure on the initial free surface, $p_{imp}(z=H)$, was zero:

$$p_{imp}(z=H) = -\rho\left.\frac{\partial\Phi_{imp}}{\partial t}\right|_{z=H} = 0 \tag{3.5}$$

where the impulsive pressure, p_{imp}, was calculated using Eq. (3.1).

2) The fluid adjacent to the wall of the tank moved with the tank at the same radial velocity, $u'(r=R)$, because the fluid was attached to the wall:

$$u'(r=R) = \left.\frac{\partial\Phi_{imp}}{\partial r}\right|_{r=R} = u_0'(t)\cos\theta \tag{3.6}$$

[22] Laplace's equation: $\nabla\cdot\nabla\Phi$ equals $\nabla\cdot vel$ based on Eq. (3.2), defined as the divergence of the velocity in a fluid domain of interest. The divergence of the fluid velocity is zero when the fluid domain has no volume change, namely no inlet, outlet, and change of fluid density (i.e., incompressibility).

where $u_0'(t)\cos\theta$ is the radial velocity of the rigid tank, and the radial velocity of the fluid, u', was calculated using Eq. (3.2).

3) The vertical velocity of the fluid at the base of the tank, $w'(z=0)$, was zero because the fluid was attached to the base of the tank, which was rigidly connected to the foundation that was subjected to horizontal motion only:

$$w'(z=0) = \left.\frac{\partial \Phi_{imp}}{\partial z}\right|_{z=0} = 0 \tag{3.7}$$

where the vertical velocity of the fluid, w', was calculated using Eq. (3.2).

Solving functions, $\tilde{R}$, $\tilde{\Theta}$, $\tilde{Z}$, and $\tilde{T}$, using Eqs. (3.4), (3.5), (3.6), and (3.7) yields the velocity potential for the impulsive responses, Φ_{imp}:

$$\Phi_{imp} = u_0'(t) H \cos\theta \sum_{i=1}^{\infty} \frac{8(-1)^{i+1}}{\left[(2i-1)\pi\right]^2} \frac{I_1\left[(2i-1)\frac{\pi}{2}\frac{r}{H}\right]}{I_1'\left[(2i-1)\frac{\pi}{2}\frac{R}{H}\right]} \cos\left[(2i-1)\frac{\pi}{2}\frac{z}{H}\right] \tag{3.8}$$

where i is the order of the terms in the infinite summation, I_1 is the modified Bessel function of the first kind with an integer order of 1, and I_1' is the first derivative of I_1 with respect to its variable $(2i-1)\frac{\pi}{2}\frac{R}{H}$. The variables are defined in Figure 3.2.

Given the velocity potential per Eq. (3.8), the impulsive pressure, p_{imp}, at an arbitrary location in the fluid or on the inner surfaces of the tank (i.e., wall and base) was determined using Eq. (3.1). The impulsive pressure on the wall of the tank (i.e., at $r = R$), along the vertical and the circumferential directions, z and θ, was:

$$p_{imp,w} = p_{imp}(r=R) = -u_0''(t)\rho H \cos\theta \sum_{i=1}^{\infty} \frac{8(-1)^{i+1}}{\left[(2i-1)\pi\right]^2} \frac{I_1\left[(2i-1)\frac{\pi}{2}\frac{R}{H}\right]}{I_1'\left[(2i-1)\frac{\pi}{2}\frac{R}{H}\right]} \cos\left[(2i-1)\frac{\pi}{2}\frac{z}{H}\right] \tag{3.9}$$

The impulsive pressure on the base of the tank (i.e., at $z = 0$), along the radial and the circumferential directions, r and θ, was:

$$p_{imp,b} = p_{imp}(z=0) = -u_0''(t)\rho H \cos\theta \sum_{i=1}^{\infty} \frac{8(-1)^{i+1}}{\left[(2i-1)\pi\right]^2} \frac{I_1\left[(2i-1)\frac{\pi}{2}\frac{r}{H}\right]}{I_1'\left[(2i-1)\frac{\pi}{2}\frac{R}{H}\right]} \tag{3.10}$$

The impulsive shear force at the base of the tank, F_{imp}, in the x direction, which was the direction of seismic input, equilibrated the resultant force generated by $p_{imp,w}$ on the wall of the tank. The resultant force was the integral of $p_{imp,w} \cdot \cos\theta$ over the area of the wall, A_w. The impulsive shear force was given by:

$$F_{imp} = -\iint_{A_w} p_{imp,w} \cdot \cos\theta \cdot dA_w = u_0''(t) m_l \frac{H}{R} \sum_{i=1}^{\infty} \frac{16}{\left[(2i-1)\pi\right]^3} \frac{I_1\left[(2i-1)\frac{\pi}{2}\frac{R}{H}\right]}{I_1'\left[(2i-1)\frac{\pi}{2}\frac{R}{H}\right]} \tag{3.11}$$

where m_l is the mass of the contained fluid. The impulsive pressure on the wall of the tank, $p_{imp,w}$, with vertical distance z above the base, created a moment about the y axis at the center of the base (see Figure 3.1), which was equilibrated by the impulsive moment at the base of the tank, $M_{imp,w}$:

$$M_{imp,w} = -\iint_{A_w} p_{imp,w} \cdot \cos\theta \cdot z \cdot dA_w = u_0''(t) m_l \frac{H^2}{R} \sum_{i=1}^{\infty} \frac{16}{\left[(2i-1)\pi\right]^3} \frac{I_1\left[(2i-1)\frac{\pi}{2}\frac{R}{H}\right]}{I_1'\left[(2i-1)\frac{\pi}{2}\frac{R}{H}\right]} \left[1 - \frac{2(-1)^{i+1}}{(2i-1)\pi}\right] \tag{3.12}$$

Similarly, the impulsive pressure on the base of the tank, $p_{imp,b}$, with horizontal distance $r \cdot \cos\theta$ from the center of the base, created a moment about the y axis at the center, which was equilibrated by the impulsive moment at the base of the tank, $M_{imp,b}$:

$$M_{imp,b} = -\iint_{A_b} p_{imp,b} \cdot r \cdot \cos\theta \cdot dA_b = u_0''(t) m_l H \sum_{i=1}^{\infty} \frac{16(-1)^{i+1}}{\left[(2i-1)\pi\right]^3} \frac{I_2\left[(2i-1)\frac{\pi}{2}\frac{R}{H}\right]}{I_1'\left[(2i-1)\frac{\pi}{2}\frac{R}{H}\right]} \tag{3.13}$$

where A_b is the area of the base of the tank. Note that Eqs. (3.12) and (3.13), as written in Jacobsen, contain calculation errors.

Chalhoub and Kelly (1988)

Chalhoub and Kelly used an assumed velocity potential to determine seismic FSI responses of a rigid, base-supported cylindrical tank, under unidirectional horizontal seismic motion of a small amplitude. Unlike Jacobsen, Chalhoub and Kelly derived a velocity potential, Φ_h, with considerations of both the impulsive and convective components of hydrodynamic response. The hydrostatic pressure generated by fluid *below* the level of the initial free surface was not considered, but the hydrostatic pressure *at* the level of the initial free surface generated by the fluid above the surface due to wave action was accounted for in the derivations. The solutions of the impulsive pressure are presented in this section and those of the convective responses are presented in Section 3.2.2.2.

Chalhoub and Kelly assumed Φ_h to be a function of the three components of the cylindrical coordinate system (r, θ, z) in Figure 3.2 at any given time, t. The velocity potential was the product of the three unknown functions, $\tilde{R}$, $\tilde{\Theta}$, and $\tilde{Z}$ associated with the three variables r, θ, and z, respectively, because these variables were independent:

$$\Phi_h = \tilde{R}(r) \cdot \tilde{\Theta}(\theta) \cdot \tilde{Z}(z) \tag{3.14}$$

The velocity potential, Φ_h, satisfied Laplace's equation since the ideal fluid was incompressible, which led to Eq. (3.4) used in Jacobsen (1949). Three boundary conditions were assumed for the hydrodynamic response of the fluid, including impulsive and convective components, to solve for $\tilde{R}$, $\tilde{\Theta}$, and $\tilde{Z}$. Different from the assumption made by Jacobsen in Eq. (3.5), in which the pressure on the initial free surface was zero, one of the three boundary conditions assumed by Chalhoub and Kelly accounted for the pressure on the initial free surface induced by wave actions. The vertical acceleration of the waves was assumed to be negligible. The vertical displacement of the free surface, d_w, which was the height of the wave above the initial free surface, generated a hydrostatic pressure, p_s, at the initial free surface:

$$p_s = \rho g d_w \tag{3.15}$$

where g is the gravitational acceleration. The hydrostatic pressure, $\rho g d_w$, calculated using Eq. (3.1) was:

$$\rho g d_w = -\rho \frac{\partial \Phi_h}{\partial t}\bigg|_{z=H} \tag{3.16}$$

Equation (3.16) was partially differentiated with respect to t and the vertical velocity of the free surface, $\frac{\partial d_w}{\partial t}$, was calculated using Eq. (3.2):

$$g \frac{\partial \Phi_h}{\partial z} = -\frac{\partial^2 \Phi_h}{\partial t^2}, \text{ at } z = H \tag{3.17}$$

The other two boundary conditions used by Chalhoub and Kelly were identical to the boundary conditions of Eqs. (3.6) and (3.7) used in Jacobsen. These two boundary conditions were applied based on the assumption that the fluid was attached to the wall and the base of the tank. The functions, $\tilde{R}$, $\tilde{\Theta}$, and $\tilde{Z}$, were solved using the three boundary conditions of Eqs. (3.6), (3.7), and (3.17), and Φ_h was determined:

$$\Phi_h = \sum_{i=1}^{\infty} \chi_i \left[\int_0^t u_0''(t) \cos \lambda_i (t-\tau) d\tau \right] \cdot J_1(n_i \frac{r}{R}) \frac{\cosh n_i \frac{z}{R}}{\cosh n_i \frac{H}{R}} \cos\theta + u_0'(t) r \cos\theta \tag{3.18}$$

$$\chi_i = \frac{2R}{J_1(n_i) \cdot (1 - n_i^2)} \tag{3.19}$$

$$\lambda_i = \sqrt{\frac{n_i g}{R} \cdot \tanh(n_i \frac{H}{R})} \tag{3.20}$$

where i is the order of the terms in the infinite summation, J_1 is the Bessel function of the first kind with an integer order of 1, and n_i is a root (solution) of $J_1'(n_i) = 0$. The values of n_i for i =1 to 10 are listed in Table 3.2. The other variables are defined in Figure 3.2.

Table 3.2. Values of n_i for i =1 to 10, used in Eqs. (3.18) to (3.24)

i	1	2	3	4	5
n_i	1.84118	5.33144	8.53632	11.70600	14.86359
i	6	7	8	9	10
n_i	18.01553	21.16437	24.31133	27.45705	30.60192

Given the velocity potential in Eq. (3.18), the hydrodynamic pressure, p_d, including impulsive and convective components, was determined using Eq. (3.1), at any location in the fluid or on the inner surfaces of the tank:

$$p_d(r,\theta,z,t) = -u_0''(t)\rho\cos\theta\cdot\left[\sum_{i=1}^{\infty} B_i + r\right] + \rho\cos\theta\sum_{i=1}^{\infty} B_i\lambda_i\int_0^t u_0''(\tau)\sin\lambda_i(t-\tau)d\tau \qquad (3.21)$$

$$B_i = \frac{2R}{1-n_i^2}\frac{\cosh(n_i\frac{z}{R})}{\cosh(n_i\frac{H}{R})}\frac{J_1(n_i\frac{r}{R})}{J_1(n_i)} \qquad (3.22)$$

where λ_i is defined in Eq. (3.20). Although Chalhoub and Kelly did not parse p_d of Eq. (3.21) into impulsive and convective pressures, the first term on the right-hand side of Eq. (3.21) is assumed here to be the impulsive pressure p_{imp}, since the impulsive response of a rigid tank is associated with the fluid moving with the tank at the ground acceleration $u_0''(t)$. (The second term in the right-hand side of Eq. (3.21) is associated with the convective pressure and is discussed in Section 3.2.2). The impulsive pressure on the wall of the tank (i.e., at $r = R$) along the vertical and the circumferential directions, z and θ, was given as:

$$p_{imp,w} = p_{imp}(r=R) = -u_0''(t)\rho R\cos\theta\left[1+\sum_{i=0}^{\infty}\frac{2}{1-n_i^2}\frac{\cosh n_i\frac{z}{R}}{\cosh n_i\frac{H}{R}}\right] \qquad (3.23)$$

The impulsive pressure on the base of the tank (i.e., at $z = 0$) along the radial and the circumferential directions, r and θ, was given as:

$$p_{imp,b} = p_{imp}(z=0) = -u_0''(t)\rho R\cos\theta\left[\frac{r}{R} + \sum_{i=0}^{\infty}\frac{2}{1-{n_i}^2}\frac{1}{\cosh n_i\frac{H}{R}}\frac{J_1(n_i\frac{r}{R})}{J_1(n_i)}\right] \quad (3.24)$$

Housner (1957)

Housner developed approximate analytical solutions for the impulsive responses listed in the fourth row of Table 3.1, which avoided the use of an infinite series of Bessel functions for calculating a velocity potential for the contained fluid (i.e., Jacobsen (1949) and Chalhoub and Kelly (1988)). The effects of hydrostatic pressure and fluid sloshing were not considered. The solutions were first derived for a broad tank with the ratio of fluid height to tank radius less than or equal to 1.5 (i.e., $H/R \le 1.5$), and the derivation was modified for a slender tank with $H/R > 1.5$. Housner derived solutions for $H/R \le 1.5$ based on a 2-dimensional (2-D) vertical cross section through a cylindrical tank with a radius of R, filled with fluid to a height of H. The 2-D configuration is presented in Figure 3.3, showing a vertical cross section of width $2R\cos\theta$ through the tank, a Cartesian coordinate system (x, y, z), and a cylindrical coordinate system (r, θ, z). The horizontal ground motion was input in the x direction, parallel to the vertical cross section. The horizontal and vertical accelerations at an arbitrary point in the fluid on the vertical cross section were u_x'' and u_z'', respectively, shown in Figure 3.3. Housner expressed u_x'' and u_z'' as functions of both x and z, which determined the acceleration field for all the fluid on the vertical cross section.

The fluid in the vertical cross section was divided into multiple vertical layers of width *dx* as shown in Figure 3.3. Figure 3.4a shows the horizontal and vertical accelerations on the four edges of the fluid in a single layer. The right side of the layer moved faster than the left side by a horizontal acceleration of $\frac{\partial u_x''}{\partial x}dx$. The difference between the horizontal accelerations at the two sides changed the thickness (width) of the layer. Because the volume of the incompressible ideal fluid was conserved, the height of the fluid in the layer changed at a vertical acceleration, u_z''. The horizontal and vertical accelerations of the fluid in the layer were related as follows:

$$u_z'' \cdot dx = \frac{\partial u_x''}{\partial x}dx \cdot z \quad (3.25)$$

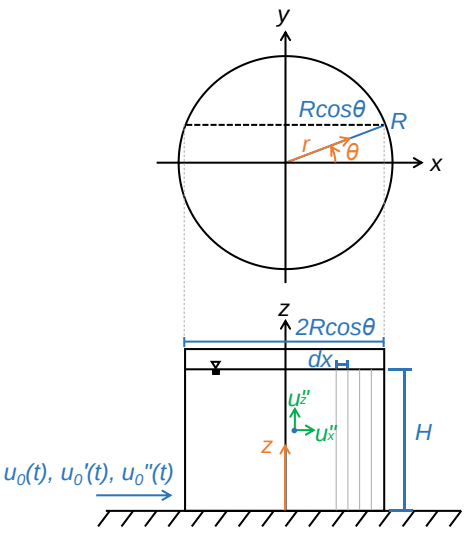

Figure 3.3. A base-supported cylindrical tank, showing the 2-D configuration used in the derivations of impulsive responses for $H/R \leq 1.5$ in Housner, adapted from Figure F.8 in Thomas et al. (1963)

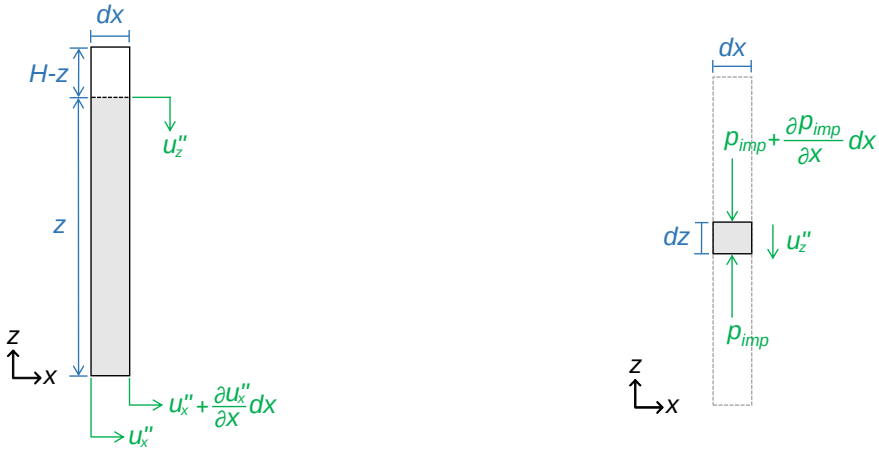

(a) accelerations on the four edges of the fluid in a fluid layer

(b) impulsive pressures and a vertical acceleration of a fluid element in a fluid layer

Figure 3.4. Responses of the fluid in a fluid layer, adapted from Figures F.2 and F.3 in Thomas et al. (1963)

Figure 3.4b is a free-body diagram of a fluid element in a layer, showing the vertical impulsive pressures acting on the element and the acceleration of the element in the z direction. The difference in the impulsive pressures on the top and the base of the element, $\frac{\partial p_{imp}}{\partial z} dz$, created a

force in the z direction. The equilibrium of forces in the z direction was calculated using Newton's second law associated with the mass of the fluid element, $\rho dxdz$, and its vertical acceleration, u_z'':

$$\frac{\partial p_{imp}}{\partial z} dz \cdot dx = \rho dxdz \cdot u_z'' \tag{3.26}$$

The vertical acceleration, u_z'', was related to the horizontal acceleration, u_x'', using Eq. (3.25). By taking the indefinite integral of Eq. (3.26) with respect to z and adopting the boundary condition of zero pressure at $z = H$, the impulsive pressure was determined:

$$p_{imp} = -\frac{\rho}{2}(H^2 - z^2)\frac{du_x''}{dx} \tag{3.27}$$

The equation for p_{imp} was a function of x and z on the vertical cross section in Figure 3.3. Noting that $x = r\cos\theta$, p_{imp} could be calculated at any location in the fluid or on the inner surfaces of the tank. The total horizontal force in a fluid layer generated by the impulsive pressure was the integral of p_{imp} with respect to z over the height of the layer:

$$P_{imp,layer} = \int_0^H p_{imp} \cdot \cos\theta \; dz = -\rho H^3 \frac{1}{3}\frac{du_x''}{dx} \tag{3.28}$$

The horizontal force, $P_{imp,layer}$, balanced the inertial force of the fluid layer in Figure 3.4a. The inertial force was calculated using Newton's second law associated with the mass of the fluid in the layer, ρHdx, and its horizontal acceleration ignoring higher order terms, u_x'':

$$P_{imp,layer} = -\rho Hdx \cdot u_x'' \tag{3.29}$$

Equating the right-hand sides of Eqs. (3.28) and (3.29) gave a second-order differential equation for u_x''. The solution of u_x'' was derived with the boundary conditions that the fluid adjacent to the wall of the tank (i.e., at $x = \pm R\cos\theta$) moved with the tank at the horizontal ground acceleration $u_0''(t)$:

$$u_x'' = u_0''(t)\frac{\cosh\sqrt{3}\frac{x}{H}}{\cosh\sqrt{3}\frac{R\cos\theta}{H}} \tag{3.30}$$

The horizontal acceleration of the fluid per Eq. (3.30) enabled the determination of p_{imp} in Eq. (3.27). The impulsive pressure on the wall of the tank (i.e., at $x = R\cos\theta$), along the vertical and the circumferential directions, z and θ, was given as:

$$p_{imp,w} = p_{imp}(x = R\cos\theta) = -u_0''(t)\frac{\sqrt{3}}{2}\frac{\rho}{H}(H^2 - z^2)\tanh(\sqrt{3}\frac{R\cos\theta}{H}) \tag{3.31}$$

The impulsive pressure on the base of the tank (i.e., at $z = 0$), along the radial and the circumferential directions, r and θ, was given as:

$$p_{imp,b} = p_{imp}(z = 0) = -u_0''(t)\frac{\sqrt{3}}{2}\rho H\frac{\sinh\sqrt{3}\frac{r\cos\theta}{H}}{\cosh\sqrt{3}\frac{R\cos\theta}{H}} \tag{3.32}$$

The impulsive shear force at the base of the tank, F_{imp}, in the x direction equilibrated the resultant force generated by $p_{imp,w}$ on wall of the tank. The resultant force was the integral of $p_{imp,w}\cdot\cos\theta$ over the area of the wall A_w. The impulsive shear force was:

$$F_{imp} = -\iint_{A_w} p_{imp,w}\cdot\cos\theta\cdot dA_w = u_0''(t)\frac{1}{\sqrt{3}}\rho\pi RH^2\tanh(\sqrt{3}\frac{R}{H}) \tag{3.33}$$

The impulsive pressure on the wall of the tank, $p_{imp,w}$, at a vertical distance z above the base, created a moment about the y axis at the center of the base, which was equilibrated by the impulsive moment at the base of the tank, $M_{imp,w}$:

$$M_{imp,w} = -\iint_{A_w} p_{imp,w}\cdot\cos\theta\cdot z\cdot dA_w = F_{imp}\frac{3}{8}H \tag{3.34}$$

Similarly, the impulsive pressure on the base of the tank, $p_{imp,b}$, at a horizontal distance $r\cdot\cos\theta$ from the center of the base, created a moment about the y axis at the center, which was equilibrated by the impulsive moment at the base of the tank $M_{imp,b}$:

$$M_{imp,b} = -\iint_{A_b} p_{imp,b} \cdot r \cdot \cos\theta \cdot dA_b = F_{imp} \frac{1}{2} \left(\frac{\sqrt{3}\frac{R}{H}}{\tanh(\sqrt{3}\frac{R}{H})} - 1 \right) H \tag{3.35}$$

where A_b is the area of the base of the tank.

Figure 3.5 presents the modification made for slender tanks with $H/R > 1.5$. The fluid in the upper $1.5R$ of the tank (shown in green) was discretized into vertical layers as those used for the derivation for $H/R \geq 1.5$. The impulsive pressure in this fluid and the associated reactions at the tank base were derived using boundary conditions and method identical to those used for the fluid in the broad tank shown in Figure 3.3. The fluid in the lower part of the slender tank of Figure 3.5 (shown in yellow), from the base to a height of $H - 1.5R$, was assumed to move with the tank as a rigid body. The pressure in the *discretized fluid* (green) at a height immediately above $H - 1.5R$ (the interface of the two fluids) was applied to the top of the *rigid fluid* (yellow), and the pressure in the rigid fluid was identical along the height. The resultant force and moment at the tank base generated by the rigid fluid were calculated per the inertial force associated with its acceleration and mass: $u_0''(t) \cdot \rho\pi R^2 (H - 1.5R)$. The reactions at the base of the slender tank ($H/R > 1.5$) balanced the total resultant forces and moments contributed by both the discretized (green) and rigid (yellow) fluids in Figure 3.5. Housner did not provide analytical solutions for $H/R > 1.5$. Solutions for $H/R > 1.5$ are derived here by the authors based on the modification to the derivation noted in Housner (1957). The analytical solutions of p_{imp}, F_{imp}, $M_{imp,w}$, and $M_{imp,b}$ for $H/R > 1.5$ are given as:

$$p_{imp} = \begin{cases} -u_0''(t) \cdot 0.745 \cdot \rho R \cdot \sinh(\frac{\sqrt{3}}{1.5}\frac{r}{R}) \cos\theta, & 0 \leq z \leq H - 1.5R \\ -u_0''(t) \cdot 0.33 \cdot \frac{\rho}{R} (3R + z - H)(-z + H) \sinh(\frac{\sqrt{3}}{1.5}\frac{r}{R}) \cos\theta, & H - 1.5R < z \leq H \end{cases} \tag{3.36}$$

$$F_{imp} = u_0''(t) \rho\pi R^2 (H - 0.44R) \tag{3.37}$$

$$M_{imp,w} = u_0''(t) \rho\pi R^2 \left(0.5H^2 + R \cdot (0.13R - 0.44H) \right) \tag{3.38}$$

$$M_{imp,b} = u_0''(t) \cdot 0.327 \cdot \rho\pi R^4 \tag{3.39}$$

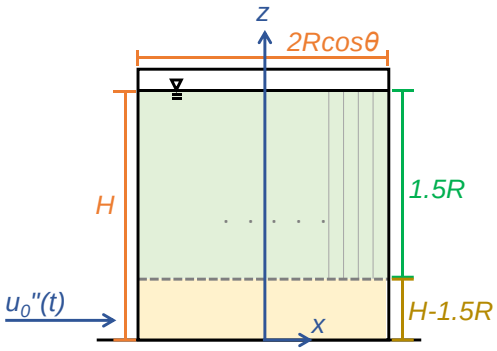

Figure 3.5. analytical solutions for $H/R>1.5$, modified from those for $H/R\le 1.5$ derived by Housner

Discussion

Jacobsen (1949), Chalhoub and Kelly (1988), and Housner (1957) developed analytical solutions for impulsive responses of rigid, base-supported cylindrical tanks, subjected to unidirectional horizontal motion of a small amplitude. The three studies assumed that the contained fluid was ideal and was attached to the tank. Table 3.1 lists the derived impulsive responses. These impulsive responses include impulsive pressure, p_{imp}, impulsive shear force at the base of the tank, F_{imp}, and the two components of impulsive moment at the base of the tank: $M_{imp,w}$, which is generated by $p_{imp,w}$ on the wall, and $M_{imp,b}$, which is generated by $p_{imp,b}$ on the base. Jacobsen, and Chalhoub and Kelly both derived exact analytical solutions for the impulsive responses using a velocity potential for the fluid. However, they made different assumptions regarding the pressure at the free surface of the fluid to solve for the velocity potential, leading to different exact solutions for the impulsive responses. Housner derived approximate analytical solutions for the impulsive responses by using Newton's second law for discretized fluid in the tank. This section has presented the analytical solutions derived in the three studies, and their equation numbers assigned in this report are listed in Table 3.3.

Below, impulsive responses are calculated and compared using the analytical solutions derived by Jacobsen, Chalhoub and Kelly, and Housner for rigid, base-supported cylindrical tanks with a range of dimensions. Time series of small-amplitude unidirectional horizontal ground acceleration, $u_0''(t)$, is input at the base of the tank in the x direction. The impulsive pressures on the wall and the base of the tank, $p_{imp,w}$ and $p_{imp,b}$, respectively, are calculated for $H/R=0.5$, 1,

Table 3.3. Equation numbers of the analytical solutions for impulsive responses of a rigid, base-supported cylindrical tank subjected to unidirectional horizontal motion of a small amplitude, derived in the studies listed in the first column

	$p_{imp,w}$	$p_{imp,b}$	F_{imp}	$M_{imp,w}$	$M_{imp,b}$
Jacobsen (1949)	(3.9)	(3.10)	(3.11)	(3.12)	(3.13)
Chalhoub and Kelly (1988)[1]	(3.23)	(3.24)	--	--	--
Housner (1957)	(3.31) (3.36)	(3.32) (3.36)	(3.33) (3.37)	(3.34) (3.38)	(3.35) (3.39)

1. Analytical solutions for global impulsive reactions, F_{imp}, $M_{imp,w}$, and $M_{imp,b}$, were not presented in Chalhoub and Kelly (1988).

and 2. The global reactions at the base of the tank, F_{imp}, $M_{imp,w}$, and $M_{imp,b}$, are calculated for $0.2 \le H/R \le 3$. The impulsive responses presented here are normalized to be unitless, which makes the amplitude of the input motion, u_0''; the dimensions of the tank and the fluid, R and H; and the density of the fluid, ρ, independent of the normalized results. The only variable for the normalized impulsive responses is the unitless ratio describing the dimensions of the tank, H/R. Consequently, R, H, and ρ do not need to be defined for calculating the normalized responses, although these variables are shown in the analytical solutions.

As the tank accelerates to the x direction, the greatest positive and negative impulsive pressures on the wall and the base of the tank are shown at angular directions $\theta = 180°$ and 0°, respectively. Values of impulsive pressures at $\theta = 180°$ are presented here. The impulsive pressures on the wall of the tank, $p_{imp,w}$, along the z direction, at $r = R$ and $\theta = 180°$, are calculated using Eqs. (3.9), (3.23), (3.31), and (3.36). Figures 3.6a, b, and c show values of $p_{imp,w}$ normalized by $\rho R u_0''$, for $H/R = 0.5$, 1, and 2, respective. The z direction in these figures is normalized by H. The solutions of Jacobsen and Chalhoub and Kelly are almost identical over the entire height of the fluid in the tank for the three values of H/R. The tiny differences between these two solutions close to the free surface (i.e., $z/H \approx 1$) are due to the use of different assumptions regarding the pressure at the free surface. These differences in $p_{imp,w}$ are further diminished with

increasing H/R. The approximate analytical solution of Housner generally underestimates $p_{imp,w}$ for $z/H \geq 0.5$ (upper half of the fluid) and overestimates it for $z/H \leq 0.5$ (lower half of the fluid), by comparison to the exact analytical solutions of Jacobsen and Chalhoub and Kelly. These differences increase with increasing H/R. At each value of H/R (i.e., 0.5, 1, or 2), the impulsive pressures on the wall of the tank, $p_{imp,w}$, increase with decreasing z: the minimum and maximum $p_{imp,w}$ are at the levels of the free surface (i.e., at $z = H$) and the base (i.e., at $z = 0$), respectively. Comparing the results for the three values of H/R from each study, the values of $p_{imp,w}/\rho R u_0''$ along the entire fluid height are always greater at a larger value of H/R. This comparison indicates that impulsive pressures on the wall of a tank with a given radius, R, are generally greater when the tank is filled with fluid to a greater height, H. This outcome is expected because a greater volume of fluid (achieved by a greater H and a constant R) attached to and accelerating with the wall of the tank, will generate a greater inertial force and apply greater impulsive pressures to the wall.

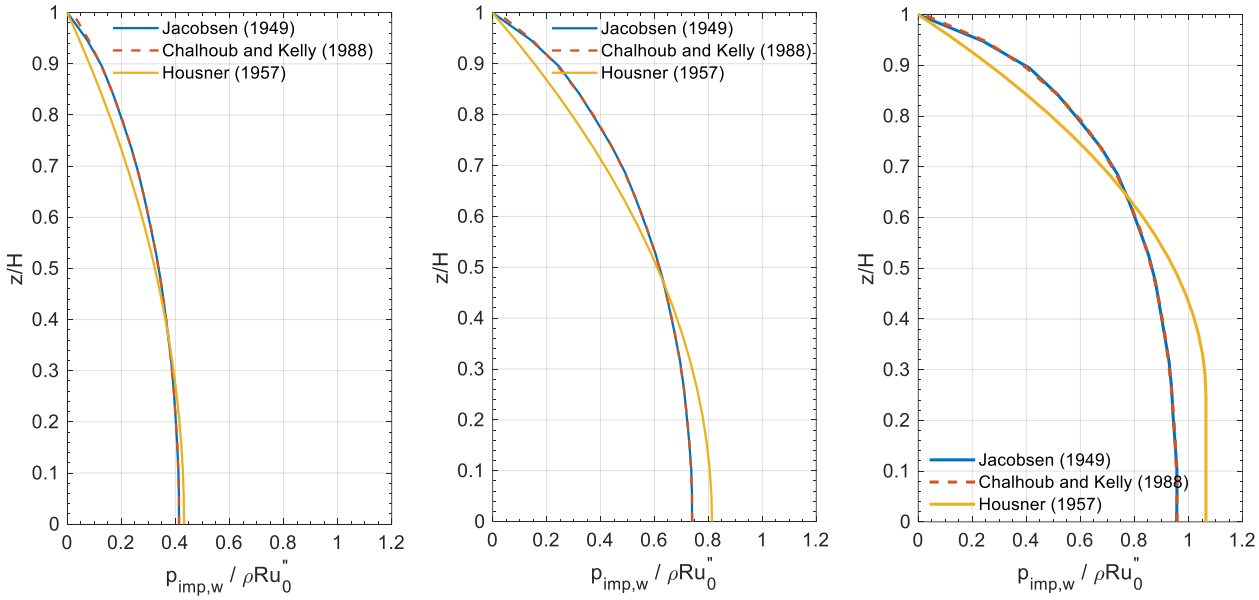

(a) $H/R = 0.5$ (b) $H/R = 1$ (c) $H/R = 2$

Figure 3.6. Normalized impulsive pressures on the wall of a tank, $p_{imp,w}/\rho R u_0''$, along the normalized vertical direction, z/H, at $r = R$ and $\theta = 180°$, for $H/R = 0.5$, 1, and 2, calculated using Eqs. (3.9), (3.23), (3.31), and (3.36)

The impulsive pressures on the base of the tank, $p_{imp,b}$, along the r direction, at $z = 0$ and $\theta = 180°$, are calculated using Eqs. (3.10), (3.24), (3.32), and (3.36). Figures 3.7a, b, and c show the values of $p_{imp,b}$ normalized by $\rho R u_0''$, for $H/R = 0.5$, 1, and 2, respectively; the distance r is normalized by R. The solutions of Jacobsen, and Chalhoub and Kelly, are identical. Housner's solution generally overestimates $p_{imp,b}$ in the fluid close to the wall of the tank, namely at $r/R \approx 1$, with respect to the exact solutions. For $0 \le r/R \le 0.9$, $p_{imp,b}$ is underestimated by Housner for the tanks with smaller H/R (i.e., 0.5 and 1) and overestimated for the tank with greater H/R (i.e., 2), again with respect to the exact solutions. At each value of H/R, the impulsive pressures on the base of the tank, $p_{imp,b}$, increase with increasing r: the minimum and maximum $p_{imp,b}$ are at the center of the base (i.e., at $r = 0$) and adjacent to the wall (i.e., at $r = R$), respectively. Comparing the results of each study for the three values of H/R considered here (i.e., 0.5, 1, and 2), the values of $p_{imp,b}/\rho R u_0''$ along the entire radius are always greater at a larger value of H/R. Similar to $p_{imp,w}$, impulsive pressures on the base, $p_{imp,b}$, of a tank with a given radius, R, are generally greater when the tank is filled with fluid to a greater height, H.

Jacobsen and Housner derived solutions for the global reactions at the base of the tank associated with impulsive loadings. (Chalhoub and Kelly did not address global reactions.) The global reactions included impulsive shear force, F_{imp}, and the two components of impulsive moment, $M_{imp,w}$ and $M_{imp,b}$. The impulsive shear forces, F_{imp}, for $0.2 \le H/R \le 3$ in the x direction are calculated using Eqs. (3.11) and (3.33) or (3.37). Figure 3.8 presents the values of F_{imp} normalized by u_0'' and the mass of the contained fluid, m_l. Housner's approximate solution slightly underestimates F_{imp} for $H/R \le 1$ but overestimates it for $H/R \ge 1$, with respect to the exact solution of Jacobsen. The normalized impulsive force $F_{imp}/m_l u_0''$ increases with increasing H/R. This indicates that given a mass of contained fluid, m_l, (i.e., given a volume of fluid) the impulsive shear force, F_{imp}, at the base of a slender tank (i.e., with greater H/R) is greater than that of a broad tank (i.e., with smaller H/R). The two components of the impulsive moment at the base of the tank, $M_{imp,w}$ and $M_{imp,b}$, about the y axis are calculated for $0.2 \le H/R \le 3$.

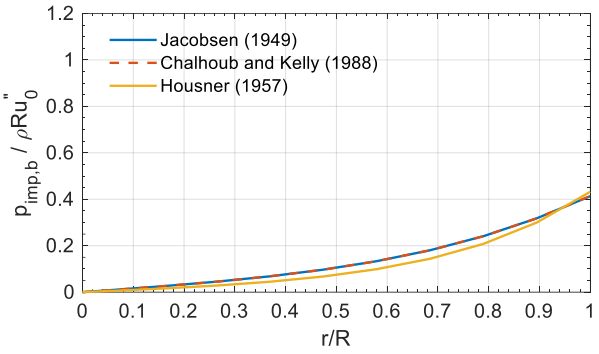

(a) H/R=0.5

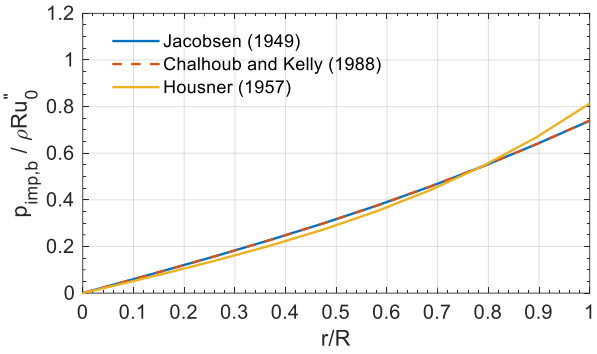

(b) H/R=1

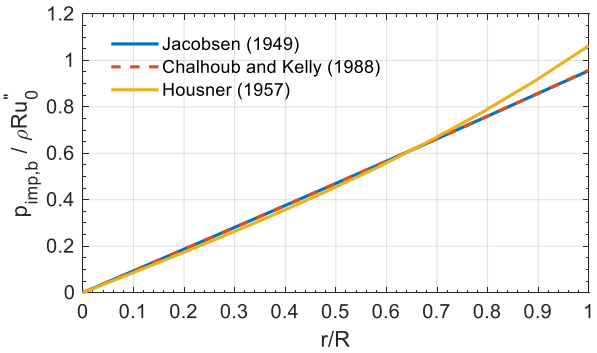

(c) H/R=2

Figure 3.7. Normalized impulsive pressures on the base of a tank, $p_{imp,b}/\rho R u_0''$, along the normalized radial direction, r/R, at $z=0$ and $\theta=180°$, for $H/R=0.5$, 1, and 2, calculated using Eqs. (3.10), (3.24), (3.32), and (3.36)

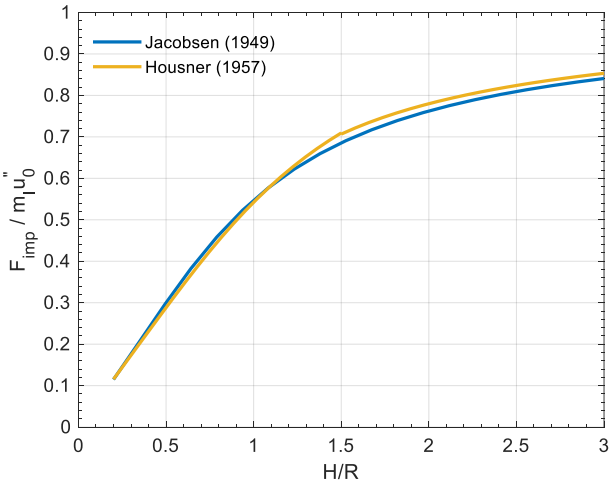

Figure 3.8. Normalized impulsive shear forces at the base of a tank, $F_{imp}/m_l u_0''$, in the x direction, for $0.2 \le H/R \le 3$, calculated using Eqs. (3.11), (3.33), and (3.37)

Figure 3.9a shows $M_{imp,w}$ calculated using Eqs. (3.12) and (3.34) or (3.38); and Figure 3.9b shows $M_{imp,b}$ calculated using Eqs. (3.13) and (3.35) or (3.39), all normalized by $m_l H u_0''$. Housner's approximate solutions generally underestimate $M_{imp,w}$ but overestimate $M_{imp,b}$ for the range of H/R considered here, again with respect to the exact solutions of Jacobsen. In terms of the total impulsive moment at the base of the tank, results in Figure 3.9 indicate that the contribution of $M_{imp,w}$ increases and the contribution of $M_{imp,b}$ decreases with increasing H/R.

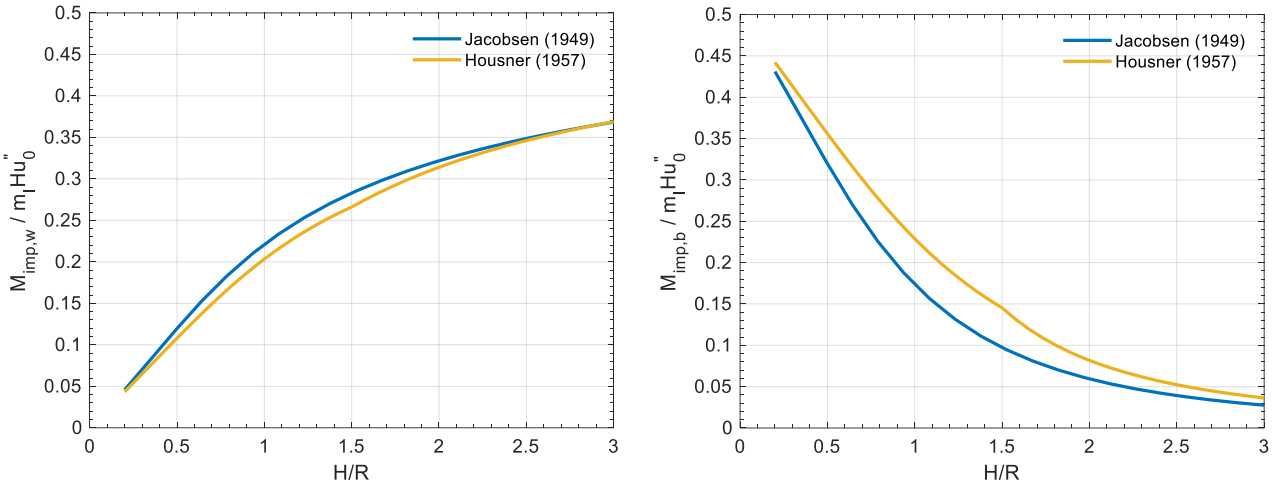

(a) $M_{imp,w}/m_l Hu_0''$, calculated using Eqs. (3.12), (3.34), and (3.38)

(b) $M_{imp,b}/m_l Hu_0''$, calculated using Eqs. (3.13), (3.35), and (3.39)

Figure 3.9. Normalized impulsive moments at the base of a tank, $M_{imp,w}/m_l Hu_0''$ and $M_{imp,b}/m_l Hu_0''$, about the y axis, for $0.2 \le H/R \le 3$

3.2.1.3 Flexible tank

This section introduces the analytical solutions of Veletsos (1984) for impulsive responses of a flexible, base-supported cylindrical tank subjected to horizontal seismic motion of a small amplitude. The impulsive responses addressed by Veletsos included impulsive frequency, f_{imp}; impulsive pressure, p_{imp}; impulsive shear force at the base of the tank, F_{imp}, and the two components of impulsive moment at the base of the tank, $M_{imp,w}$ and $M_{imp,b}$. A free-body diagram for these impulsive responses was introduced in Figure 3.1. The analytical solutions were drawn from the derivations in the dissertations of two of Veletsos' PhD students, Yang (1976) and Tang (1986). The two dissertations included procedures similar to those in Jacobsen

(1949), which assumed a velocity potential for the contained fluid to derive impulsive responses of the tank, but the velocity potential was modified to account for the deformation of the tank. The derivations of Yang and Tang are summarized and the calculation errors contained therein are corrected in this section. The equations used in the derivations and the solutions presented here are not identical to those in the original documents to enable use of a consistent set of variables and coordinate systems presented in Section 3.2.1.2 (see Figure 3.2).

Veletsos (1984)

Veletsos presented analytical solutions for impulsive responses of a flexible, base-supported cylindrical tank subjected to unidirectional horizontal motion of a small amplitude. The wall of the tank was assumed to be elastic with a constant thickness[23]. The freeboard and the circumferential deformation[24] of the tank were ignored.

The analytical solutions represented *modal* impulsive responses. The modal responses were derived in Yang and Tang by performing modal analysis of the equation of motion for the impulsive responses of the tank. Lagrange's equation was used to develop the equation of motion, considering virtual works (energies): 1) the kinetic energy of the fluid, K_l, 2) the kinetic energy of the tank, K_s, 3) the strain energy of the tank, S_s, and 4) the external energy associated with the input ground motion, W_{ext}. The four virtual works/energies were expressed using assumed displacements on the wall of the tank. The assumed displacements were *kinematically admissible*, which accommodated the boundary condition of the tank. (More information about kinematically admissible displacements in the principles of virtual work can be found in Chapter 5 of Hjelmstad (2010).) A potential velocity was derived for calculating the responses of the fluid, which were also related to the displacements of the wall of the tank.

To calculate the displacements on the wall of the tank, lateral displacements on the axial centerline of the tank were first assumed and were then extrapolated to the wall of the tank. Yang and Tang assumed the lateral displacements of the axial centerline, $u_{ac,x}(z)$, in the direction of

[23] In practice, the thickness of the wall of a base-supported cylindrical tank decreases with the height from the base to the top (API 650 (American Petroleum Institute 2012) and Soules (2018)). An average value of varied thicknesses along the height can be used in Veletsos' analytical solutions (Malhotra et al. 2000).

[24] Although Yang (1976) addressed effects of circumferential deformation on impulsive responses, the analytical solutions presented in both Veletsos (1984) and Tang (1986) did not take the effects into account.

seismic motions (i.e., in the x direction) to be a linear superposition of multiple modal shapes, ψ_i, of a vertical cantilever with a length equal to the height of the tank, fixed at its base and free at its tip. The modal shapes of the cantilever, $\psi_i(z)$, were those documented in Young and Felgar (1949). An example of superposing $\psi_i(z)$ to be the lateral displacements of the axial centerline, $u_{ac,x}(z)$, is given in Figure 3.10. Note that this example is *not* based on a theoretical calculation but illustrates the generation of an assumed $u_{ac,x}(z)$. The red line in Figure 3.10a represents the lateral displacements of the axial centerline, $u_{ac,x}(z)$, of a base-supported cylindrical tank in the x direction. Figure 3.10b presents the first and the second modal shapes of a cantilever (i.e., $\psi_1(z)$ and $\psi_2(z)$), with a length identical to the height of the tank in Figure 3.10a and fixed at the lower end. The $u_{ac,x}(z)$ of Figure 3.10c is the sum of twice the first modal shape and the second modal shape of the cantilever (i.e., $2\cdot\psi_1+\psi_2$).

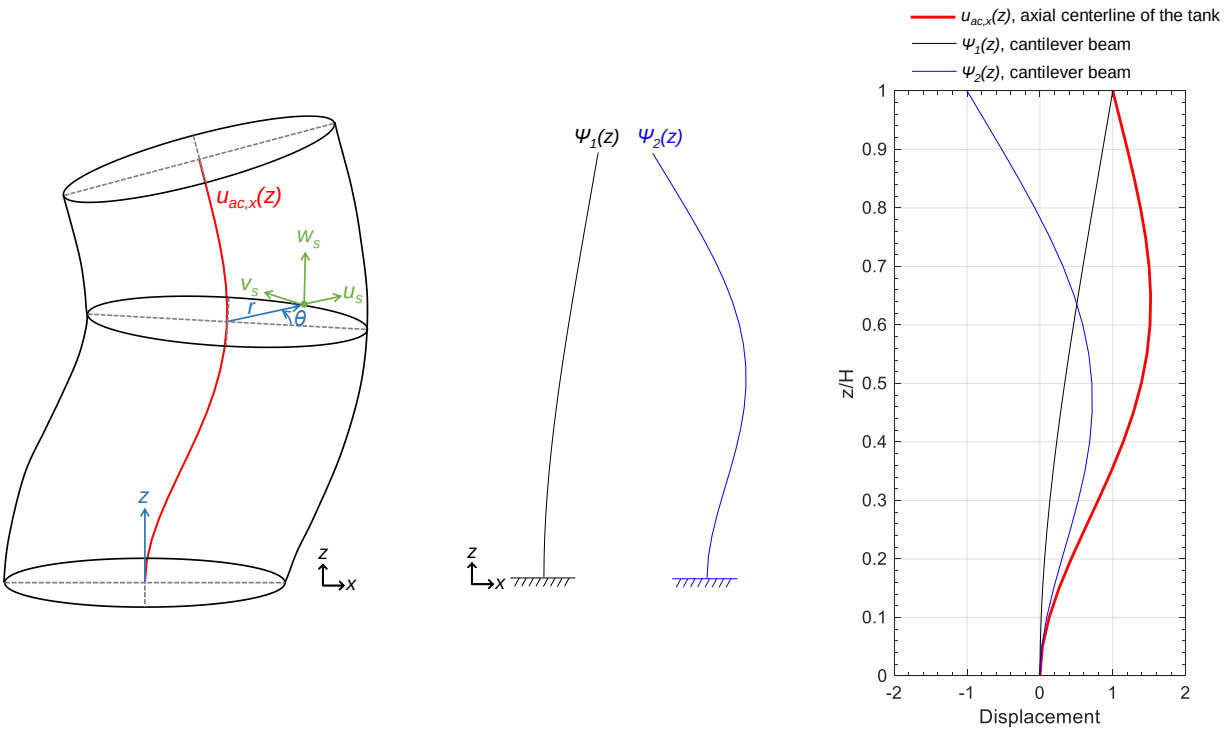

(a) deformations of the tank, displacements of the axial centerline and the wall

(b) first and second modal shapes of the cantilever

(c) axial centerline in panel (a) and superposition of the modal shapes in panel (b)

Figure 3.10. Lateral displacements on the axial centerline of a flexible, base-supported cylindrical tank in the x direction, assumed to be a linear superposition of multiple modal shapes of a cantilever with a length identical to the height of the tank

The radial, tangential and axial displacements, u_s, v_s, and w_s, on the wall of the tank, shown in Figure 3.10a, were calculated based on the lateral displacements of the axial centerline in the x direction, projected on the wall along the three components of the cylindrical coordinate system, r, θ, z. The calculations assumed that the horizontal cross sections of the tank remained plane and circular as the tank deformed laterally.

$$u_s(t,z,\theta) = \sum_{i=1}^{\infty} U_i(t)\psi_i(z)\cos\theta \tag{3.40}$$

$$v_s(t,z,\theta) = \sum_{i=1}^{\infty} V_i(t)\psi_i(z)\sin\theta \tag{3.41}$$

$$w_s(t,z,\theta) = \sum_{i=1}^{\infty} W_i(t)\psi_i'(z)\cos\theta \tag{3.42}$$

where the infinite series represent the linear superposition of the modal shapes, $\psi_i(z)$, of a cantilever with a length equal to the height of the tank; $\psi_i(z)$ is the i th modal shape of the cantilever; $\psi_i'(z)$ is the first derivative of $\psi_i(z)$ with respective to z; U_i, V_i, and W_i are coefficients for the modal shapes in the i th mode for the linear superposition; and $\sin\theta$ and $\cos\theta$ project the displacements of the axial centerline in the x direction to the wall in the cylindrical coordinates shown in Figure 3.10a. Other parameters have been defined previously.

The equation of motion represented the impulsive responses of the tank and the contained fluid as a multi-degree of freedom system. Note that the degrees of freedom in the equation of motion used in Yang and Tang did not represent the considered motions (displacements, velocities, or accelerations) in different directions or at different locations on the wall of the tank. Each degree of freedom in Yang and Tang's equation of motion represented a coefficient (i.e., U_i, V_i, or W_i) for a modal shape, $\psi_i(z)$, for the superposition. The motions of the tank were determined by solving U_i, V_i, and W_i in the equation of motion and applying them in Eqs. (3.40), (3.41), and (3.42).

The four energies, K_l, K_s, S_s, and W_{ext} were calculated as follows to construct the equation of motion:

1) The kinetic energy of the fluid, K_l, was associated with the velocities of the fluid, u', v', and w', in the whole fluid volume, V_l:

$$K_l = \frac{\rho}{2}\iiint_{V_l}(u'^2 + v'^2 + w'^2)dV_l \tag{3.43}$$

where the velocities of the fluid were calculated using Eq. (3.2) with a velocity potential. The velocity potential for the impulsive responses of the fluid, Φ_{imp}, was derived by modifying the methodology of Jacobsen to account for the flexibility of the tank. Yang and Tang assumed the fluid adjacent to the wall of the tank (i.e., at $r = R$) to move with the wall at the same radial velocity. The radial velocity of the fluid u' was calculated using Eq. (3.2) and the radial velocity of the tank was the first derivative of u_s in Eq. (3.40) with respect to t:

$$u'(r = R) = \left.\frac{\partial \Phi_{imp}}{\partial r}\right|_{r=R} = U_i'(t)\psi_i(z)\cos\theta \tag{3.44}$$

The other two boundary conditions used for deriving Φ_{imp} in Yang and Tang were identical to the boundary conditions of Eqs. (3.5) and (3.7) used in Jacobsen (1949), which assumed zero pressure on the initial free surface and zero vertical velocity in the fluid adjacent to the base of the tank, respectively. The velocity potential for the impulsive responses, Φ_{imp}, was derived using Eqs. (3.44), (3.5) and (3.7) as follows:

$$\Phi_{imp} = H\cos\theta\sum_{i=1}^{\infty}U_i''(t)\sum_{j=1}^{\infty}\frac{4}{(2j-1)\pi}\frac{I_1\left[(2j-1)\frac{\pi}{2}\frac{r}{H}\right]}{I_1'\left[(2j-1)\frac{\pi}{2}\frac{R}{H}\right]}\cos\left[(2j-1)\frac{\pi}{2}\frac{z}{H}\right]\cdot\alpha_{ij} \tag{3.45}$$

$$\alpha_{ij} = \frac{1}{H}\int_0^H \psi_i(z)\cdot\cos\left[(2j-1)\frac{\pi}{2}\frac{z}{H}\right]dz \tag{3.46}$$

where i and j are the order of the terms in each of the infinite summations. Other parameters in Φ_{imp} have been defined previously. Given the velocity potential of Eq. (3.45), the velocities of the fluid were calculated using (3.2), and then K_l was determined per Eq. (3.43).

2) The kinetic energy of the tank, K_s, was associated with the velocities on the wall of the tank:

$$K_s = \frac{\rho_s}{2} \iiint_{V_s} (u_s'^2 + v_s'^2 + w_s'^2) dV_s \tag{3.47}$$

where V_s is the volume of the wall of the tank (the thickness of the wall was considered), and u_s', v_s', and w_s' are the radial, tangential, and axial velocities at an arbitrary location on the wall calculated by differentiating Eqs. (3.40), (3.41), and (3.42) with respect to t, respectively.

3) The strain energy of the tank, S_s, was calculated by assuming the wall of the tank to be a thin cylindrical shell, which obeyed the plane stress constitutive law:

$$S_s = \frac{E}{2(1-\upsilon^2)} \iiint_{V_s} \left[\varepsilon_z^2 + \varepsilon_\theta^2 + \frac{1-\mu}{2} \gamma_{z\theta}^2 + 2\mu\varepsilon_z\varepsilon_\theta \right] dV_s \tag{3.48}$$

where E and υ are the elastic modulus and Poisson's ratio of the material forming the wall of the tank, respectively; ε_z is the axial normal strain, ε_θ is the tangential normal strain, and $\gamma_{z\theta}$ is the shear strain on the wall of the tank. The strain energy expressions for thin cylindrical shells in Bleich and DiMaggio (1952) were used to relate the strains ε_z, ε_θ, and $\gamma_{z\theta}$ to the displacements of the wall of the tank, u_s, v_s, and w_s. Those expressions are not repeated here, but are documented in Eqs. (2) and (3) in Bleich and DiMaggio.

4) The external energy, W_{ext}, created by the ground motion, $u_0''(t)$, was calculated using the principle of virtual work assuming the tank to be rigid. The external energy comprised the virtual work generated by external forces acting on the tank and the contained fluid, calculated using the inertial force of the tank and the impulsive pressure on the wall of the tank:

$$W_{ext} = \rho_s \iiint_{V_s} \left[u_0''(t)\delta u_s \cos\theta - u_0''(t)\delta v_s \sin\theta \right] dV_s + \iint_{A_w} \left[-p_{imp,r} \cdot \delta u_s \right] dA_w \tag{3.49}$$

where the first term in the right-hand side, which is the integral with respect to V_s, is the virtual work generated by the inertial force of the tank in the x direction, associated with the virtual radial displacement, δu_s, and the virtual tangential displacements, δv_s, on the wall. The second term, which is the integral with respect to the area of the wall, A_w, is the virtual work generated

by the impulsive pressure $p_{imp,r}$ on the wall associated with δu_s, where $p_{imp,r}$ was calculated using Eq. (3.9) since the tank was assumed to be rigid.

The equation of motion of the tank was derived using Lagrange's equation, including K_l, K_s, S_s, and W_{ext}:

$$\frac{d}{dt}\frac{\partial(K_l+K_s)}{\partial d_i'}-\frac{\partial(K_l+K_s)}{\partial d_i}+\frac{\partial S_s}{\partial d_i}=\frac{\partial W_{ext}}{\partial d_i} \tag{3.50}$$

where d_i represents the degrees of freedom in the equation of motion, U_i, V_i, and W_i; and d_i' is the first derivative of d_i with respect to time, t. The number of degrees of freedom depended on the number of the modal shapes, $\psi_i(z)$, considered in u_s, v_s, and w_s (Eqs. (3.40), (3.41), and (3.42)). Considering N_1 modes for u_s, N_2 modes for v_s, and N_3 modes for w_s, the general form of the equation of motion calculated using Eq. (3.50) was:

$$\begin{bmatrix} \quad M \quad \end{bmatrix}_{N\times N}\begin{Bmatrix} U_i'' \\ V_i'' \\ W_i'' \end{Bmatrix}_{N\times 1}+\begin{bmatrix} \quad K \quad \end{bmatrix}_{N\times N}\begin{Bmatrix} U_i \\ V_i \\ W_i \end{Bmatrix}_{N\times 1}=u_0''(t)\begin{Bmatrix} P_{ext} \end{Bmatrix}_{N\times 1} \tag{3.51}$$

where $N=N_1+N_2+N_3$, $[M]$ and $[K]$ are the mass and stiffness matrices of the tank, $u_0''(t)\{P_{ext}\}$ is the external force vector associated with the ground motion, and $U_i=\{U_1,U_{2,}...,U_{N_1}\}^T$, $V_i=\{V_1,V_{2,}...,V_{N_2}\}^T$, and $W_i=\{W_1,W_{2,}...,W_{N_3}\}^T$. Given the mass and stiffness matrices, the frequencies and modal shapes of impulsive modes of the tank were calculated as follows:

$$[K]\{\phi_k\}=\left(\frac{f_{imp,k}}{2\pi}\right)^2[M]\{\phi_k\} \tag{3.52}$$

where $f_{imp,k}$ and $\{\phi_k\}$ are the frequency and modal shape in the kth impulsive mode.

To perform modal analysis for the impulsive responses of the tank, the degrees of freedom, d_i, namely U_i, V_i, and W_i, in the equation of motion of Eq. (3.51) were transformed to modal coordinates, q_k, using the modal shape, ϕ_{ik}:

$$d_i = \phi_{ik} \cdot q_k \tag{3.53}$$

Transforming the degrees of freedom, U_i, V_i, and W_i, in the equation of motion in Eq. (3.51) to the modal coordinates using Eq. (3.53), $[M]$ and $[K]$ were diagonalized to the *modal* mass and *modal* stiffness matrices, respectively, and $u_0''(t)\{P_{ext}\}$ was transformed to the *modal* force vector, to represent multiple independent impulsive modes. As the equation of motion was decoupled into modes, q_k was calculated using Duhamel's integral:

$$q_k = e_k \frac{1}{\omega_{imp,k}} \int_0^t u_0''(\tau) \cdot \sin \omega_{imp,k}(t-\tau) d\tau \tag{3.54}$$

where e_k is the modal participation factor:

$$e_k = \frac{\{\phi_k\}^T \{P_{ext}\}}{\{\phi_k\}^T [M] \{\phi_k\}} \tag{3.55}$$

The second derivation of the modal coordinate, q_k'', was approximated using a pseudo quantity back calculated from q_k:

$$q_k'' \approx \omega_{imp,k}{}^2 \cdot q_k = e_k \cdot A_k(t) \tag{3.56}$$

$$A_k(t) = \omega_{imp,k} \int_0^t u_0''(\tau) \cdot \sin \omega_{imp,k}(t-\tau) d\tau \tag{3.57}$$

where $\omega_{imp,k}$ is $f_{imp,k} / 2\pi$; $A_k(t)$ is the acceleration time series of a single degree-of-freedom (SDOF) system with a natural frequency of $f_{imp,k}$, subjected to the ground motion, $u_0''(t)$. (More information about modal analysis for multi-degree-of-freedom system can be found in Chapter 12 of Chopra (2012)). The acceleration calculated per Eq. (3.57) provided in Veletsos assumed zero damping in the impulsive modes. However, in practice, damping ratios of 2% and 5% are recommended for calculating the impulsive responses of steel and concrete tanks, respectively (Malhotra et al. 2000). Appendix B presents calculations using the Veletsos solutions adjusted for non-zero damping in the impulsive modes.

According to Eqs. (3.53) and (3.56), d_i'' was related to q_k'' as the following:

$$d_i'' = \phi_{ik} \cdot q_k'' \approx \phi_{ik} \cdot e_k \cdot A_k(t) \tag{3.58}$$

The velocity potential associated with the k th impulsive mode was computed by substituting Eq. (3.58) for U_i'' in Eq. (3.45). The impulsive pressure p_{imp} at an arbitrary location in the fluid and on the wall and the base of the tank were determined using Eq. (3.1). The impulsive pressure on the wall (i.e., at $r = R$) of the tank associated with the k th mode, along the vertical and the circumferential directions, z and θ, was given as:

$$p_{imp,w,k} = -A_k(t) \cdot \rho H \cos\theta e_k \sum_{i=1}^{N_1} \phi_{ik} \sum_{j=1}^{\infty} \frac{4}{(2j-1)\pi} \frac{I_1\left[(2j-1)\frac{\pi}{2}\frac{R}{H}\right]}{I_1'\left[(2j-1)\frac{\pi}{2}\frac{R}{H}\right]} \cos\left[(2j-1)\frac{\pi}{2}\frac{z}{H}\right] \cdot \alpha_{ij} \tag{3.59}$$

where α_{ij} is defined in Eq. (3.46). The impulsive pressure on the base of the tank (i.e., at $z = 0$) associated with the k th mode, along the radial and the circumferential directions, r and θ, was given as:

$$p_{imp,b,k} = -A_k(t) \cdot \rho H \cos\theta e_k \sum_{i=1}^{N_1} \phi_{ik} \sum_{j=1}^{\infty} \frac{4}{(2j-1)\pi} \frac{I_1\left[(2j-1)\frac{\pi}{2}\frac{r}{H}\right]}{I_1'\left[(2j-1)\frac{\pi}{2}\frac{R}{H}\right]} \cdot \alpha_{ij} \tag{3.60}$$

where e_k is defined in Eq. (3.55). The impulsive shear force at the base of the tank, $F_{imp,k}$, associated with the k th mode in the x direction, equilibrated the resultant force generated by $p_{imp,w,k}$ on wall of the tank. The resultant force was the integral of $p_{imp,k,w} \cdot \cos\theta$ over the area of the wall, A_w. The impulsive shear force in the k th mode was:

$$F_{imp,k} = -\iint_{A_w} p_{imp,w,k} \cdot \cos\theta \cdot dA_w = A_k(t) \cdot m_l \frac{H}{R} e_k \sum_{i=1}^{N_1} \phi_{ik} \sum_{j=1}^{\infty} \frac{8(-1)^{j+1}}{\left[(2j-1)\pi\right]^2} \frac{I_1\left[(2j-1)\frac{\pi}{2}\frac{R}{H}\right]}{I_1'\left[(2j-1)\frac{\pi}{2}\frac{R}{H}\right]} \cdot \alpha_{ij} \tag{3.61}$$

where m_l is the mass of the contained fluid. The impulsive pressure on the wall of the tank, $p_{imp,w,k}$, at a vertical distance z above the base, created a moment about the y axis at the center

of the base (see Figure 3.1), which was equilibrated by the impulsive moment at the base of the tank, $M_{imp,w,k}$:

$$M_{imp,w,k} = -\iint_{A_w} p_{imp,w,k} \cdot \cos\theta \cdot z \cdot dA_w$$

$$= A_k(t) \cdot m_l \frac{H^2}{R} e_k \sum_{i=1}^{N_1} \phi_{ik} \sum_{j=1}^{\infty} \frac{8(-1)^{j+1}}{\left[(2j-1)\pi\right]^2} \frac{I_1\left[(2j-1)\frac{\pi}{2}\frac{R}{H}\right]}{I_1'\left[(2j-1)\frac{\pi}{2}\frac{R}{H}\right]} \left[1 - \frac{2(-1)^{j+1}}{(2j-1)\pi}\right] \cdot \alpha_{ij} \quad (3.62)$$

Similarly, the impulsive pressure on the base of the tank, $p_{imp,b,k}$, at a horizontal distance $r \cdot \cos\theta$ from the center of the base, created a moment about the y axis at the center, which was equilibrated by the impulsive moment at the base of the tank, $M_{imp,b,k}$:

$$M_{imp,b,k} = -\iint_{A_b} p_{imp,b,k} \cdot r \cdot \cos\theta \cdot dA_b = A_k(t) \cdot m_l H e_k \sum_{i=1}^{N_1} \phi_{ik} \sum_{j=1}^{\infty} \frac{8}{\left[(2j-1)\pi\right]^2} \frac{I_2\left[(2j-1)\frac{\pi}{2}\frac{R}{H}\right]}{I_1'\left[(2j-1)\frac{\pi}{2}\frac{R}{H}\right]} \cdot \alpha_{ij} \quad (3.63)$$

where A_b is the area of the base of the tank.

Discussion

Veletsos (1984) presented analytical solutions for impulsive responses of a flexible, base-supported cylindrical tank, subjected to unidirectional horizontal motion of a small amplitude. The impulsive responses were decoupled into modal contributions and solutions were provided for each mode. Solutions were provided for impulsive frequency, f_{imp}, impulsive pressure, p_{imp}, impulsive shear force at the base of the tank, F_{imp}, and the two components of impulsive moment at the base of the tank: $M_{imp,w}$, generated by $p_{imp,w}$ on the wall of the tank, and $M_{imp,b}$, generated by $p_{imp,b}$ on the base. This section presented the analytical solutions of these impulsive responses with equation numbers listed in Table 3.4.

Table 3.4. Equation numbers of the analytical solutions of Veletsos for impulsive responses of a flexible, base-supported cylindrical tank subjected to unidirectional horizontal motion of a small amplitude

f_{imp}	$p_{imp,w}$	$p_{imp,b}$	F_{imp}	$M_{imp,w}$	$M_{imp,b}$
(3.52)	(3.59)	(3.60)	(3.61)	(3.62)	(3.63)

Impulsive responses are calculated below using Veletsos' solutions for flexible, base-supported cylindrical tanks with a range of dimensions. Results are presented and compared with those of Jacobsen. Impulsive responses are calculated for a flexible tank with multiple values of H/R: $p_{imp,w}$ and $p_{imp,b}$ are calculated for $H/R = 0.5$, 1, and 2; f_{imp}, F_{imp}, $M_{imp,w}$, and $M_{imp,b}$ are calculated for $0.2 \le H/R \le 3$. The tank with typical dimensions is used in the calculations: a radius R of 30 m and a thickness of the wall h of $0.001\,R$. Per Table K-1a of API 650 (American Petroleum Institute (API) 2012), a radius, R, between 25 m to 60 m and a ratio of wall thickness to radius, h/R, of the order of 0.001 are practical for a steel base-supported cylindrical tank. The tank used here is assumed to be fabricated from carbon steel and the contained fluid is assumed to be water. The mechanical properties used in the calculations are listed in Table 3.5, including the elastic modulus, E, Poisson's ratio, υ, and density, ρ_s, of the steel, and the density of the contained fluid, ρ. The impulsive responses presented here are appropriately normalized to be unitless, which makes the results *insensitive*[25] to the dimensions (i.e., h, R, and H) and the mechanical properties (i.e., E, υ, ρ_s, and ρ) of the tank and the fluid, and independent of the modal acceleration time series, A_k, at the impulsive frequency, $f_{imp,k}$. The only variable considered for the normalized impulsive responses is the unitless dimension of the tank, H/R. Normalizing the impulsive responses enables the results to be generalized.

[25] The normalization assumes $\rho_s \gg \rho$ and $\upsilon^2 \ll 1$ and disregards the effect of ρ_s and υ in the results. The normalized results are not fully independent of but insensitive to the dimensions and the mechanical properties of the tank and the fluid.

Table 3.5. Mechanical properties of the tank and the contained fluid used for the calculations of impulsive responses

Carbon steel	Elastic modulus, E	1.94×10^{11} (N/m^2)
	Poisson's ratio, υ	0.27
	Density, ρ_s	7875 (kg/m^3)
Water	Density, ρ	1000 (kg/m^3)

Figure 3.11a shows the impulsive frequencies, $f_{imp,k}$, associated with the first three modes (i.e., $k=1$ to 3), for the carbon steel tank with $R=30$ m, $h/R=$ 0.001, and $0.2\le H/R\le 3$. The impulsive frequency in each mode, $f_{imp,k}$, reduces with increasing H/R, namely, $f_{imp,k}$ is lower when the tank is filled with fluid to a greater height H. The first impulsive frequencies, $f_{imp,1}$, are between 1.5 Hz and 7 Hz (i.e., first impulsive period, $T_{imp,1}$, ranges from 0.14 sec to 0.7 sec), and those in the higher mode (i.e., $f_{imp,2}$ and $f_{imp,3}$) are between 2 Hz and 16 Hz, for the range of H/R considered here.

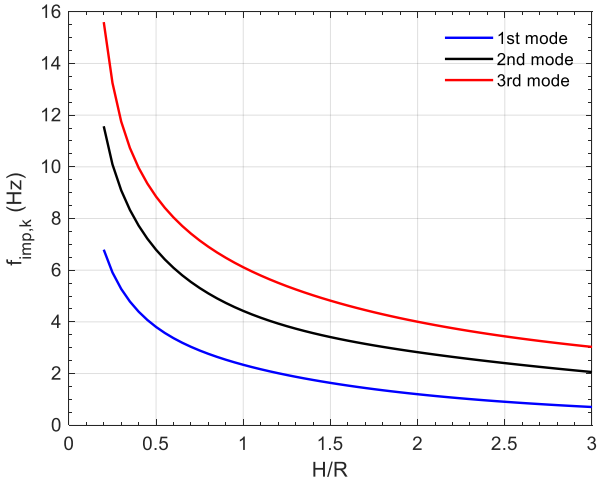

(a) $f_{imp,k}$, R =30m, h =0.001 R, and the mechanical properties listed in Table 3.5, calculated using Eq. (3.52)

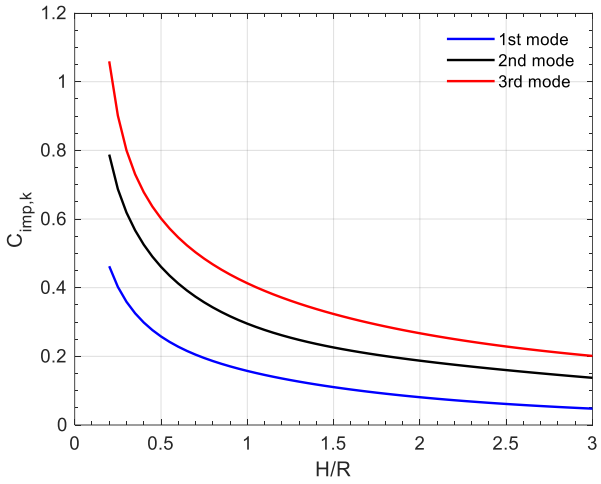

(b) $C_{imp,k}$, calculated using Eq. (3.64) and $f_{imp,k}$ in panel (a)

Figure 3.11. Impulsive frequencies, $f_{imp,k}$, and coefficients of impulsive frequency, $C_{imp,k}$, associated with the first three impulsive modes (i.e., $k=1$ to 3), for $0.2\le H/R\le 3$

For the purpose of generalizing over different mechanical properties and dimensions of the tank and the contained fluid, the impulsive frequency of each mode is expressed as follows:

$$f_{imp,k} = C_{imp,k} \frac{1}{R} \sqrt{\frac{Eh}{\rho R}} \tag{3.64}$$

where $C_{imp,k}$ is the coefficient of the impulsive frequency in the kth mode. The coefficient is a function of H/R, unitless and insensitive to h, E, υ, ρ_s, and ρ (see footnote 25 on page 75). Figure 3.11b presents values of $C_{imp,k}$ for the first three impulsive modes (i.e., $k = 1$ to 3) calculated using Eq. (3.64) with results presented in Figure 3.11a.

Two important observations can be drawn from Eq. (3.64) and Figure 3.11. First, $C_{imp,k}$ in each mode reduces with increasing H/R. For a given value of R, $f_{imp,k}$ calculated per Eq. (3.64) reduces with increasing H, indicating that $f_{imp,k}$ in a mode of a tank with a given radius, R, reduces when the tank is filled with fluid to a greater height, H. Second, per Eq. (3.64) the impulsive frequency, $f_{imp,k}$, in a mode is inversely proportional to R when the mechanical properties of the tank and the contained fluid (i.e., E and ρ) and h/R are held constant. For example, the impulsive frequency of a water-filled carbon-steel tank with $R = 60$ m and $h/R = 0.001$ can be calculated by multiplying $f_{imp,k}$ for $R = 30$ m (see Figure 3.11a) by the reciprocal of the ratio of their radii, namely 1/2 (=30/60). As a result, the values of the first impulsive frequency, $f_{imp,1}$, are between 0.75 Hz and 3.5 Hz (i.e., $T_{imp,1}$ ranges from 0.3 sec to 1.3 sec) for $R = 60$ m and $0.2 \le H/R \le 3$.

The impulsive pressure on the wall of the tank, $p_{imp,w,k}$, and that on the base, $p_{imp,w,b}$, are calculated using Eqs. (3.59) and (3.60), respectively, for $H/R = 0.5$, 1, and 2. Figure 3.12 presents $p_{imp,w,k}$ in the first three modes (i.e., $k = 1$ to 3), along the z direction, at $r = R$ and $\theta = 180°$; and Figure 3.13 presents $p_{imp,b,k}$ in the first three modes ($k = 1$ to 3), along the r direction, at $z = 0$ and $\theta = 180°$. The values of $p_{imp,w,k}$ and $p_{imp,b,k}$ in the figures are each normalized by $\rho H A_k$, the z direction in Figure 3.12 is normalized by H, and the r direction in Figure 3.13 is normalized by R.

Given an order of the impulsive mode (i.e., $k=1$, 2, or 3), the maximum value of the normalized impulsive pressure on the wall, $p_{imp,w,k}/\rho RA_k$, increases with increasing of H/R, whereas the results for $p_{imp,b,k}/\rho RA_k$ do not show this trend. Consider $p_{imp,w,k}/\rho RA_k$ in each of the first three modes, for each H/R in Figure 3.12. The amplitude in the first mode is the greatest over the height of the fluid. Similarly, in Figure 3.13, the amplitude of $p_{imp,b,k}/\rho RA_k$ is the greatest in the first mode, across the radius of the tank, for each value of H/R. Namely, $p_{imp,1}/\rho RA_1 > p_{imp,2}/\rho RA_2 > p_{imp,3}/\rho RA_3$ for $0 \le z/H \le 1$ on the wall and $0 \le r/R \le 1$ on the base. However, this comparison of the amplitudes for the normalized impulsive pressures, $p_{imp,k}/\rho RA_k$, in the first three modes must not be used to compare the amplitudes of the impulsive pressures, $p_{imp,k}$, since the values of A_k used for the normalization will be different. The value of A_k is associated with the impulsive frequency, $f_{imp,k}$, in the mode of interest and the input motion, $u_0''(t)$. A greater (smaller) value of $p_{imp,k}/\rho RA_k$ does not necessarily result in a greater (smaller) value of $p_{imp,k}$.

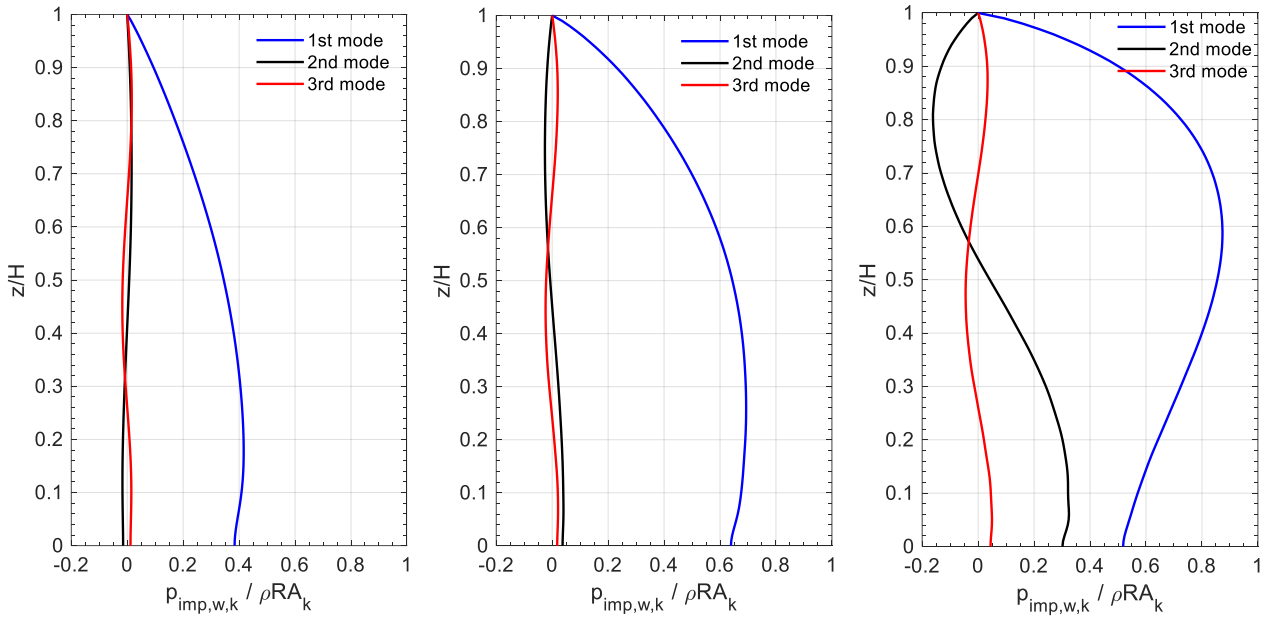

(a) H/R=0.5 (b) H/R=1 (c) H/R=2

Figure 3.12. Normalized impulsive pressures on the wall of a tank, $p_{imp,w,k}/\rho RA_k$, associated with the first three modes (i.e., $k=1$ to 3), along the normalized vertical direction, z/H, at $r=R$ and θ=180°, for $H/R=0.5$, 1, and 2, calculated using Eq. (3.59)

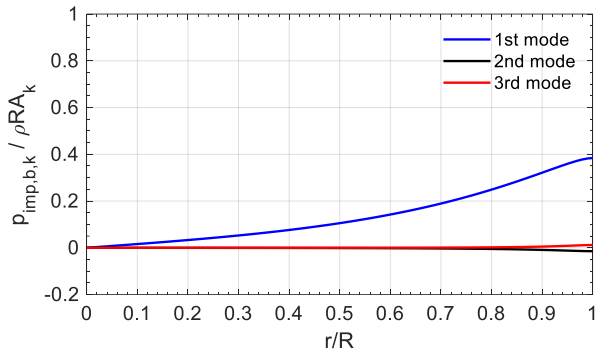

(a) H/R=0.5

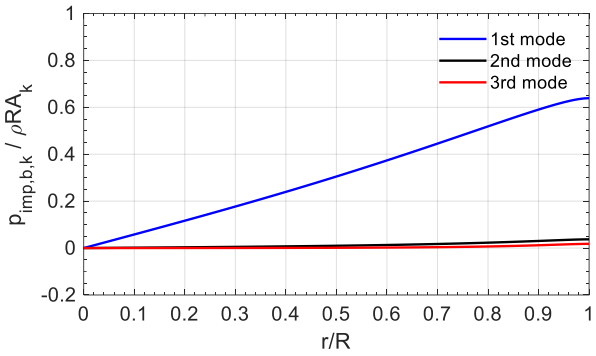

(b) H/R=1

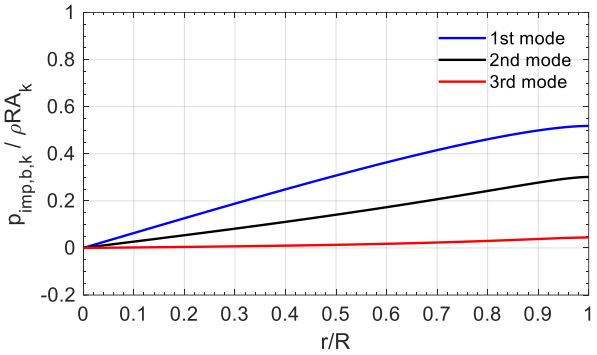

(c) H/R=2

Figure 3.13. Normalized impulsive pressure on the base of a tank, $p_{imp,b,k}/\rho RA_k$, associated with the first three modes (i.e., $k=1$ to 3), along the normalized radial direction, r/R, at $z=0$ and $\theta=180°$, for $H/R=0.5$, 1, and 2, calculated using Eq. (3.60)

The impulsive shear force and the two components of the impulsive moment at the base of the tank, F_{imp}, $M_{imp,w}$, and $M_{imp,b}$, are calculated using Eqs. (3.61), (3.62), and (3.63), respectively, for $0.2 \le H/R \le 3$. Figure 3.14 shows $F_{imp,k}$ in the first three impulsive modes, in the x direction, normalized by $m_l A_k$. Figures 3.15a and b show $M_{imp,w,k}$ and $M_{imp,b,k}$, respectively, in the first three impulsive modes, about the y axis, normalized by $m_l H A_k$. Identical to the discussion above on the impulsive pressure, $p_{imp,k}$, the normalized data presented in Figures 3.14 and 3.15 must be interpreted carefully because A_k will be different in each mode. A discussion of the modal contributions of impulsive responses calculated using the solutions of Veletsos is presented in Appendix B.

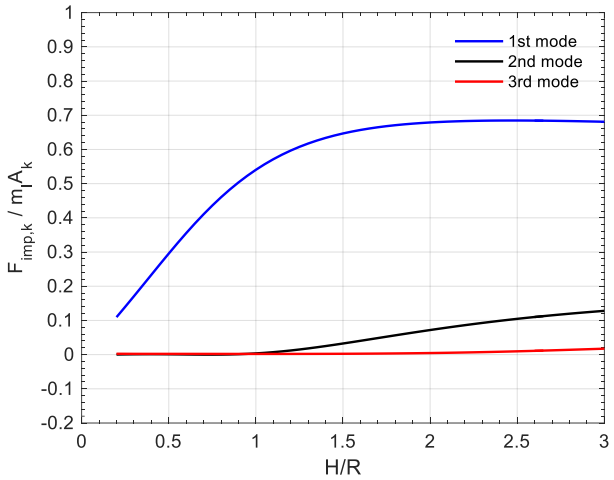

Figure 3.14. Normalized impulsive shear force at the base of a tank, $F_{imp,k} / m_I A_k$, associated with the first three modes (i.e., $k = 1$ to 3), in the x direction for $0.2 \le H/R \le 3$, calculated using Eq. (3.61)

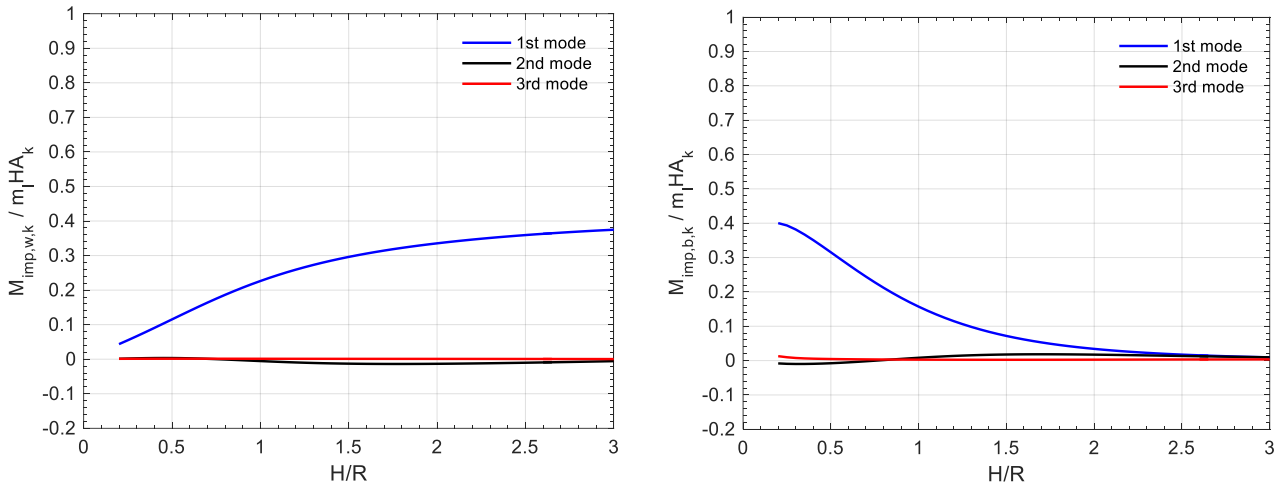

(a) $M_{imp,w,k} / m_I HA_k$, calculated using Eq. (3.62) (b) $M_{imp,b,k} / m_I HA_k$, calculated using Eq. (3.63)

Figure 3.15. Normalized impulsive moments at the base of a tank, $M_{imp,w,k} / m_I HA_k$ and $M_{imp,b,k} / m_I HA_k$, associated with the first three modes (i.e., $k = 1$ to 3), about the y axis for $0.2 \le H/R \le 3$

The analytical solutions of Veletsos (1984) for a flexible tank and the analytical solutions of Jacobsen (1949) for a rigid tank are compared below. Impulsive responses are calculated using both sets of solutions for a rigid and a flexible tank for the same range of H/R. The mechanical properties listed in Table 3.5 and the thickness of the wall, $h = 0.001\,R$, are used in the calculations for the flexible tank. The results of impulsive responses presented here are normalized using the methods identical to those used in Section 3.2.1.2 for a rigid tank and those used earlier in this section for a flexible tank, to make the normalized results dependent on only one variable, H/R. Consequently, normalizations associated with acceleration responses of the rigid and the flexible tanks are different: the results of the rigid tank are normalized by the input motion, u_0''; and the results of the flexible tank are normalized by the acceleration time series, A_k, at the impulsive frequency, $f_{imp,k}$.

Figures 3.16 to 3.19 present normalized impulsive responses of a rigid tank and those of a flexible tank in multiple modes. The variable A shown in the label for the horizontal or vertical axes of each figure for normalizing results is $u_0''(t)$ for the rigid tank and $A_k(t)$ for the flexible tank. The normalized impulsive responses of a flexible tank are algebraic sums of normalized, modal responses composed of 1) the first impulsive mode ($k = 1$) only, 2) the first three impulsive modes ($k = 1$ to 3), and 3) the first 10 impulsive modes ($k = 1$ to 10). The impact of normalized, responses in the 11th and higher impulsive modes is negligible in the algebraic sums for the range of H/R presented here. Figure 3.16 presents the normalized impulsive pressures on the wall of the tank, $p_{imp,w}/\rho HA$, along the z/H direction at $r = R$ and $\theta = 180°$; and Figure 3.17 presents the normalized impulsive pressures on the base, $p_{imp,b}/\rho HA$, along the r/R direction at $z = 0$ and $\theta = 180°$, both for $H/R = 0.5$, 1, and 2. Figure 3.18 presents the normalized, impulsive shear forces, $F_{imp}/m_l A$, and Figure 3.19 presents the normalized, impulsive moments, $M_{imp,w}/m_l HA$ and $M_{imp,b}/m_l HA$, at the base of a tank for $0.2 \le H/R \le 3$. The results shown in the figures indicate that as more modes are included in the algebraic sum, the normalized, modal impulsive responses of a flexible tank gradually recover the corresponding impulsive responses of a rigid tank. The algebraic sums of the normalized impulsive responses in the first ten modes of the flexible tank (red lines) are almost identical to the corresponding normalized impulsive responses of the rigid tank (black dashed lines) for the

values of H/R considered here. If the acceleration time series used to normalize the modal responses data in Figures 3.16 to 3.19 are assumed to be identical, namely $A_1(t) = A_2(t) ... = A_{10}(t) = acc(t)$, the algebraic sum of the modal impulsive responses in the first ten modes recovers the impulsive responses of the corresponding rigid tank accelerating at $acc(t)$.

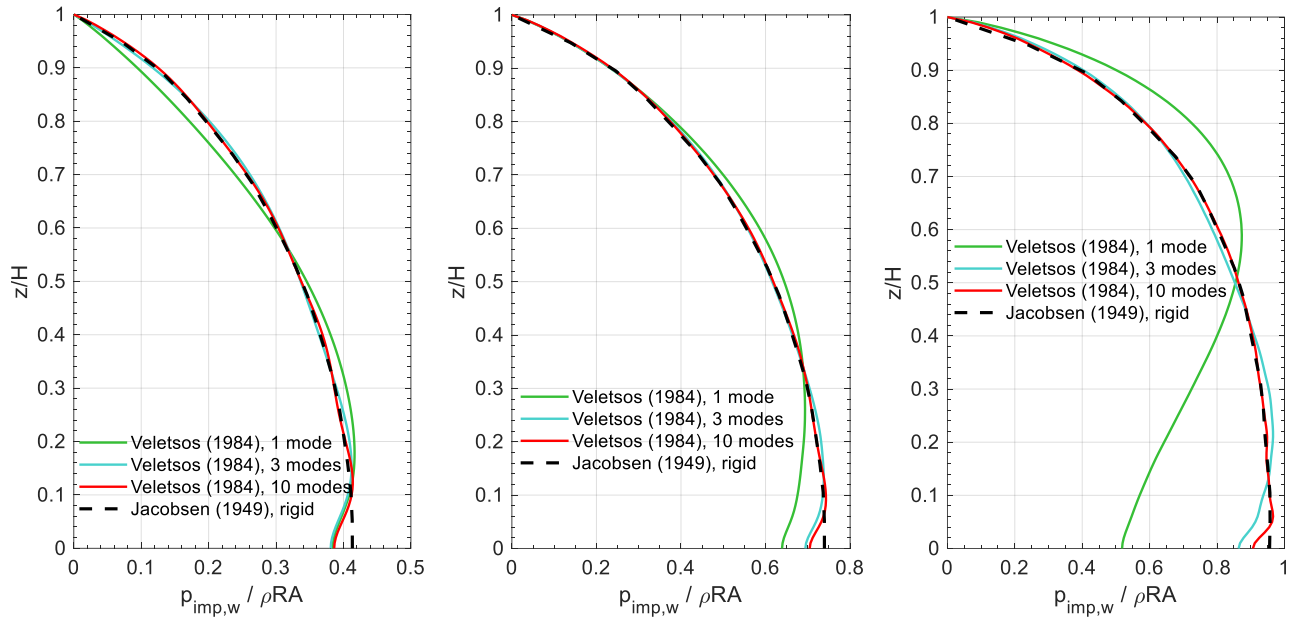

(a) $H/R = 0.5$ (b) $H/R = 1$ (c) $H/R = 2$

Figure 3.16. Impulsive responses of a flexible tank (Veletsos) and those of a rigid tank (Jacobsen), in terms of normalized impulsive pressure on the wall of the tank, $p_{imp,w}/\rho RA$, along the normalized vertical direction, z/H, at $r = R$ and $\theta = 0°$, for $H/R = 0.5$, 1, and 2

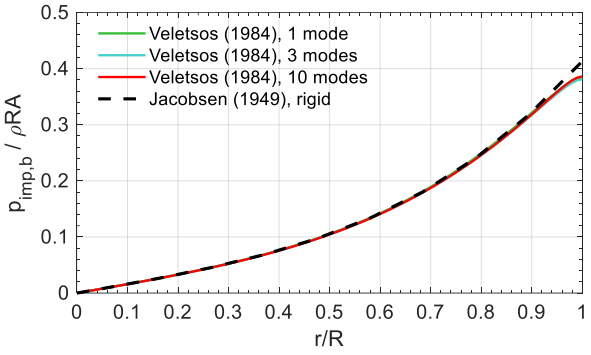

(a) $H/R=0.5$

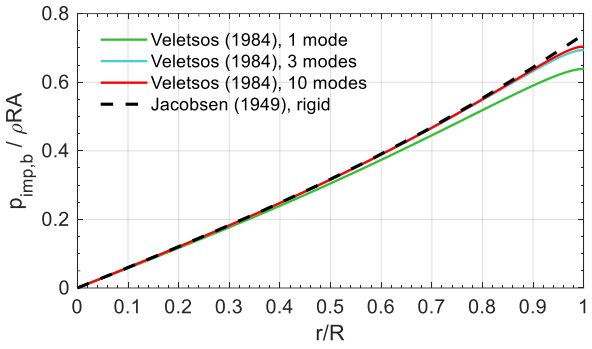

(b) $H/R=1$

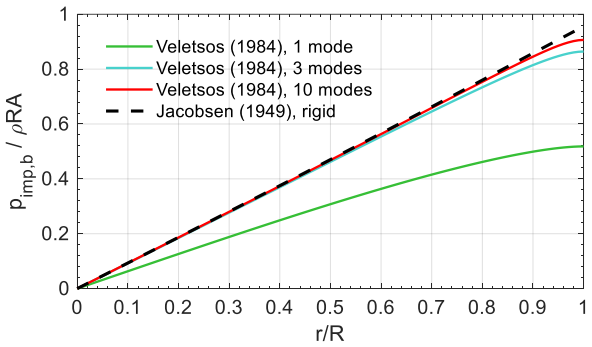

(c) $H/R=2$

Figure 3.17. Impulsive responses of a flexible tank (Veletsos) and those of a rigid tank (Jacobsen), in terms of normalized impulsive pressure on the base of the tank, $p_{imp,b}/\rho RA$, along the normalized radial direction, r/R, at $z=0$ and $\theta=0°$, for $H/R=0.5$, 1, and 2

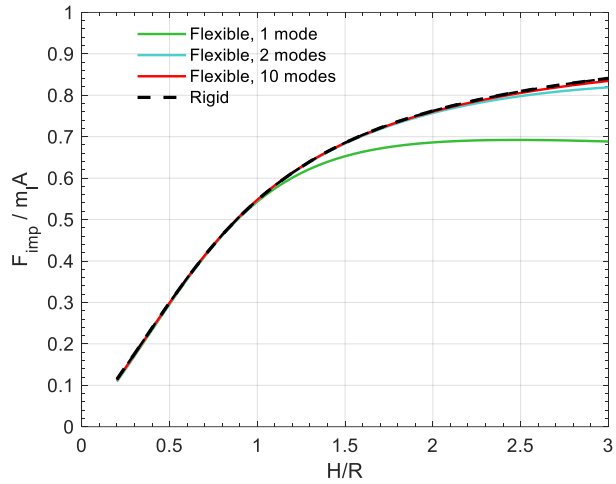

Figure 3.18. Impulsive responses of a flexible tank (Veletsos) and those of a rigid tank (Jacobsen), in terms of normalized impulsive shear force at the base of the tank, $F_{imp} / m_l A$, in the x direction for $0.2 \le H/R \le 3$

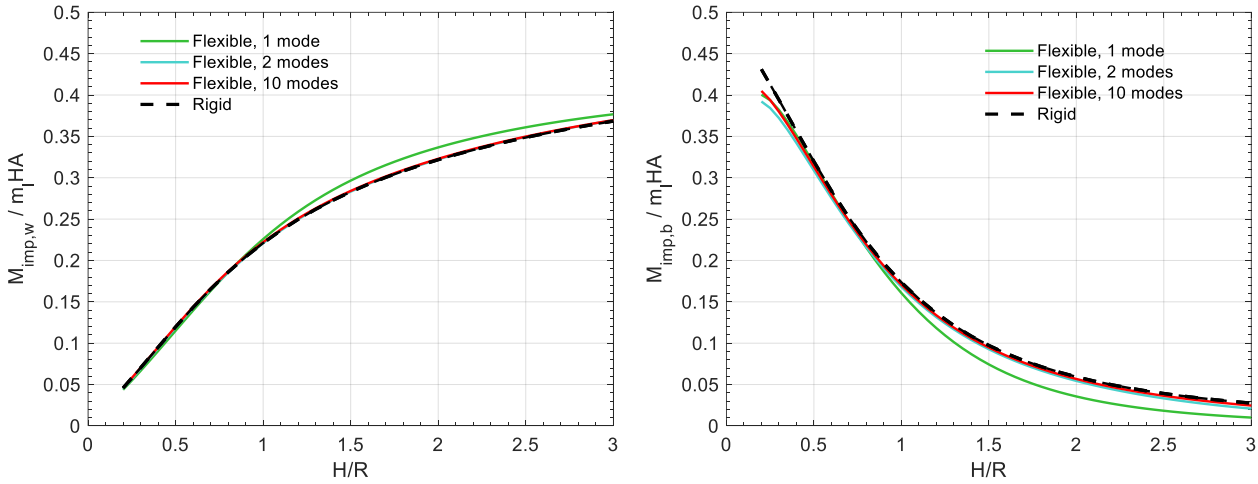

(a) $M_{imp,w} / m_l HA$ (b) $M_{imp,b} / m_l HA$

Figure 3.19. Impulsive responses of a flexible tank (Veletsos) and those of a rigid tank (Jacobsen), in terms of normalized impulsive moments at the base of the tank, $M_{imp,w} / m_l HA$ and $M_{imp,b} / m_l HA$, about the y axis for $0.2 \le H/R \le 3$

3.2.2 Convective responses

3.2.2.1 Introduction

Figure 3.20 shows convective responses in a vertical cross section through a base-supported cylindrical tank accelerating in the x direction. Waves are generated in the contained fluid: the free surface of the fluid oscillates vertically at a convective frequency, f_{con}, with a small displacement, d_w. This displacement also describes the height of a wave above the initial free surface. The wave action induces convective pressures, p_{con}, in the fluid and on the inner surfaces of the tank (i.e., the wall and the base). The part of the free surface with a negative vertical displacement reduces the depth of the fluid (with respect to the base) at the $+x$ side of the tank and generates a negative p_{con} on the wall and the base. The part of the free surface with a positive displacement increases the depth of the fluid at the $-x$ side of the tank and generates a positive p_{con} on the wall and the base. Similar to the impulsive responses in the base-supported tank, these convective pressures, p_{con}, on the inner surfaces of the tank are mechanically equilibrated by global convective reactions at the base, including a convective shear force and moments. The resultant force of the horizontal p_{con} on the wall (green arrows) is balanced by the convective shear force at the base, F_{con}, in the x direction. The convective pressure on the wall (green arrows) and that on the base (blue arrows) generate resultant moments at the center of the base (solid red circle), which are balanced by the convective moments, $M_{con,w}$ and $M_{con,b}$, in a clockwise direction about the y axis, respectively.

The convective responses of a tank subjected to small-amplitude horizontal seismic motion are generated by the part of the fluid assumed theoretically *not* to move horizontally with the tank but to oscillate vertically to form waves on the free surface. Since this part of the fluid does not follow the movement or the deformation of the tank, the convective responses are considered independent of the flexibility of the wall of the tank (Haroun 1980; Veletsos 1984). Consequently, this section introduces analytical solutions for convective responses of rigid tanks developed in a number of prior studies, but these solutions can also be applied to flexible tanks.

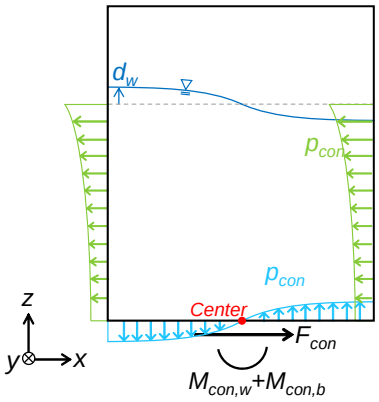

Figure 3.20. Convective responses: vertical displacement of the free surface, d_w; convective frequency, f_{con}; convective pressure, p_{con}, on the walls and base of a tank; convective shear force, F_{con}, at the base; and convective moments, $M_{con,w}$ and $M_{con,b}$, at the base; shown in a vertical cross section through a base-supported cylindrical tank accelerating in the x direction

3.2.2.2 Rigid tank

This section presents the analytical solutions for convective responses developed by 1) Veletsos (1984), 2) Chalhoub and Kelly (1988), and 3) Housner (1957) for a rigid, base-supported cylindrical tank subjected to unidirectional horizontal motion of a small amplitude. All three studies assumed that the contained fluid is ideal (footnote 20 on page 11). The damping of the fluid was not considered in the analytical solutions because an ideal fluid is inviscid. In inviscid flow, the viscous forces (or damping) are very small in comparison with the inertial forces. Table 3.6 lists the convective responses analytically derived in each of the three studies, including f_{con}, p_{con}, d_w, F_{con}, $M_{con,w}$, and $M_{con,b}$.

Veletsos' analytical solutions were drawn from the derivations in the PhD dissertation of Yang (1976). (The dissertation also derived the analytical solutions of impulsive responses of a flexible tank; see Section 3.2.1.3). A velocity potential was assumed for the convective responses of the fluid subjected to harmonic motion, and then the *exact* solutions for the convective responses generated by earthquake shaking were derived using a frequency-domain method. Chalhoub and Kelly derived analytical solutions for the convective responses using procedures different from those used in Veletsos but the two solutions were identical. Housner derived *approximate* analytical solutions for the convective responses using a 2-dimensional vertical cross section through a base-supported cylindrical tank. He discretized the fluid in the vertical cross section

into multiple thin horizontal layers, which were free to rotate with respect to the axis normal to the cross section (e.g., the y axis for the vertical cross section of the tank presented in Figure 3.20). The analytical solutions were derived using Newton's second law on the inertial forces and Hamilton's principle on the kinetic and potential energies the motion of these horizontal fluid layers.

Table 3.6. Convective responses of a rigid, base-supported cylindrical tank subjected to unidirectional horizontal seismic motion of a small amplitude, addressed in the studies listed in the first column

	f_{con}	p_{con}	d_w	F_{con}	$M_{con,w}$	$M_{con,b}$
Veletsos (1984)[1]	✓	✓	✓	✓	✓	✓
Chalhoub and Kelly (1988)	✓	✓	✓			
Housner (1957)[2]	✓	✓	✓	✓	✓	✓

1. This paper did not present complete derivations for the analytical solutions. The derivations in Yang (1976) are used in this section.
2. The paper contains calculation errors. The correct analytical solutions and their derivations presented in this section in part follow those in Housner (1954) and Thomas et al. (1963).

These analytical solutions and their derivations are not introduced chronologically in this section: the exact solutions of Veletsos, and Chalhoub and Kelly are summarized first, followed by the approximate solutions of Housner. The equations used in the derivations and the solutions presented here are not identical to those in the original documents to enable the use of a consistent set of variables and coordinate systems.

The variables used in this section are the same as those used in the derivations and the solutions for impulsive responses, shown in Figure 3.2, including: radius of the tank, R; height of the contained fluid, H; horizontal ground displacement, $u_0(t)$, velocity, $u_0'(t)$, and acceleration, $u_0''(t)$; velocities of an arbitrary point, pt, in the fluid, u', v', and w', along the three components of a cylindrical coordinate system (r, θ, z); and a Cartesian coordinate system (x, y, z).

Veletsos (1984)

Veletsos presented analytical solutions for the convective responses listed in the second row of Table 3.6. The analytical solutions represented *modal* convective responses derived in Yang. The derivations assumed the tank to be rigid and the contained fluid to be ideal. The vertical displacement of the free surface (i.e., the heights of waves above the free surface) was assumed to be small. Hydrostatic pressure generated by fluid *below* the level of the initial free surface was not considered, whereas hydrostatic pressure *at* the level of the initial free surface generated by the fluid above the surface due to wave action was accounted for in the derivations of the convective responses.

The analytical solutions were derived in three steps: 1) using a velocity potential, Φ_{con}, to derive the steady-state convective pressure, $p_{con,h}$, in a tank subjected to unidirectional, horizontal harmonic motion of a unit amplitude, 2) applying an inverse Fourier transform on $p_{con,h}$ to calculate the convective pressure, $p_{con,\delta}$, of the tank subjected to a unidirectional, horizontal impulse with a unit amplitude, and 3) using Duhamel's integral on $p_{con,\delta}$ to calculate the convective responses of the tank subjected to small-amplitude, unidirectional, horizontal seismic motion. Herein, the derivations in Yang are reworked for reasons of clarity.

The unit-amplitude harmonic motion is ground acceleration time series, $e^{i\omega t}$, with an excitation radial frequency of ω. The velocity potential, Φ_{con}, for convective responses of the fluid subjected to the harmonic input motion was assumed to be a function of four variables: the three components of the cylindrical coordinate system, r, θ, and z, shown in Figure 3.2, and the velocity of the horizontal ground motion $(1/i\omega)e^{i\omega t}$. The velocity potential was the product of the four unknown functions, $\tilde{R}$, $\tilde{\Theta}$, $\tilde{Z}$, and $\tilde{T}$, associated with the four variables, r, θ, z, and t, respectively, since these variables were independent:

$$\Phi_{con}(r,\theta,z,t) = \tilde{R}(r)\cdot\tilde{\Theta}(\theta)\cdot\tilde{Z}(z)\cdot\tilde{T}(t) \tag{3.65}$$

The velocity potential, Φ_{con}, satisfied Laplace's equation since the ideal fluid was incompressible, which led to Eq. (3.4) used in Jacobsen (1949). Three boundary conditions were

assumed for the fluid in the tank subjected to the horizontal harmonic motion to solve $\tilde{R}$, $\tilde{\Theta}$, $\tilde{Z}$, and $\tilde{T}$:

1) The pressure on the initial free surface was induced by wave actions. The vertical acceleration of the waves was assumed to be negligible. The vertical displacement of the free surface, d_w, which was the height of the wave above the initial free surface, generated hydrostatic pressure, p_s, at the initial free surface:

$$p_s = \rho g d_w \tag{3.66}$$

where ρ is the density of the fluid and g is the gravitational acceleration. The hydrostatic pressure, p_s, (i.e., $\rho g d_w$) calculated using Eq. (3.1) was:

$$\rho g d_w = -\rho \left. \frac{\partial \Phi_{con}}{\partial t} \right|_{z=H} \tag{3.67}$$

Equation (3.67) was partially differentiated with respect to t, and the term, $\frac{\partial d_w}{\partial t}$, on the left-hand side of the equation was the vertical velocity of the free surface (i.e., at $z = H$). The fluid velocity at $z = H$ was calculated using Eq. (3.2) with the velocity potential of impulsive and convective responses, Φ_{imp} and Φ_{con}:

$$g \left. \frac{\partial \left(\Phi_{imp} + \Phi_{con} \right)}{\partial z} \right|_{z=H} = - \left. \frac{\partial^2 \Phi_{con}}{\partial t^2} \right|_{z=H} \tag{3.68}$$

where Φ_{imp} was calculated per Eq. (3.8) and $u_0'(t)$ used in the equation was the velocity of the harmonic motion, $(1/i\omega)e^{i\omega t}$.

2) The radial velocity of the fluid adjacent to the wall, $u'(r = R)$, was zero because the fluid was assumed not to move horizontally with the tank:

$$u'(r = R) = \left. \frac{\partial \Phi_{con}}{\partial r} \right|_{r=R} = 0 \tag{3.69}$$

where Eq. (3.2) was used for the calculation of the radial velocity of the fluid, u'.

3) The vertical velocity of the fluid at the base of the tank, $w'(z=0)$, was zero because the fluid was attached to the base, rigidly connected to the foundation that was subjected to horizontal motion only:

$$w'(z=0) = \left.\frac{\partial \Phi_{con}}{\partial z}\right|_{z=0} = 0 \tag{3.70}$$

where Eq. (3.2) was used for the calculation of the vertical velocity of the fluid, w'.

Solving $\tilde{R}$, $\tilde{\Theta}$, $\tilde{Z}$, and $\tilde{T}$, using Eqs. (3.68), (3.69), and (3.70) yielded the velocity potential, Φ_{con}:

$$\Phi_{con} = \frac{g}{i\omega} e^{i\omega t} \cos\theta \frac{2}{\frac{n_j g}{R}\tanh(n_j \frac{H}{R}) - \omega^2} \frac{n_j}{{n_j}^2 - 1} \frac{J_1(n_j \frac{r}{R})}{J_1(n_j)} \frac{\cosh(n_j \frac{z}{R})}{\cosh(n_j \frac{H}{R})} \tanh(n_j \frac{H}{R}) \tag{3.71}$$

where J_1 is the Bessel function of the first kind with an integer order of 1, and n_j is a root (solution) of $J_1'(n_j) = 0$. The values of n_j for $j = 1$ to 10 are listed in Table 3.2, which were also used by Chalhoub and Kelly (1988) (see Section 3.2.1.2). The other parameters were defined previously.

Given the velocity potential per Eq. (3.71), the convective pressure, $p_{con,h}$, at an arbitrary location in the fluid or on the inner surfaces of the tank (i.e., wall and base), subjected to the unit-amplitude harmonic motion (i.e., $u_0''(t) = e^{i\omega t}$) was determined using Eq. (3.1):

$$p_{con,h} = -g \cdot e^{i\omega t} \rho \cos\theta \frac{2}{\frac{n_j g}{R}\tanh(n_j \frac{H}{R}) - \omega^2} \frac{n_j}{{n_j}^2 - 1} \frac{J_1(n_j \frac{r}{R})}{J_1(n_j)} \frac{\cosh(n_j \frac{z}{R})}{\cosh(n_j \frac{H}{R})} \tanh(n_j \frac{H}{R}) \tag{3.72}$$

When the excitation radial frequency of the harmonic motion, ω, was identical to a natural radial frequency of a convective mode, $\omega_{con,j}$ (or $2\pi f_{con,j}$), the amplitude of the pressure, $p_{con,h}$, was theoretically unbounded (i.e., $\to \infty$). Per Eq. (3.72), the amplitude of $p_{con,h}$ is infinite when $\omega^2 = \frac{n_j g}{R}\tanh(n_j \frac{H}{R})$, and so the frequency of the convective mode was:

$$f_{con,j} = \frac{1}{2\pi}\sqrt{\frac{n_j g}{R}\tanh(n_j \frac{H}{R})} \tag{3.73}$$

where each value of n_j (see Table 3.2) refers to a frequency, $f_{con,j}$, associated with the j th convective mode.

Given $p_{con,h}$ per Eq. (3.72), a frequency-domain method was used to calculate the convective pressure, $p_{con,\delta}$, in the tank subjected to a unidirectional, horizontal impulse of a unit amplitude, $\delta(t)$. (More information can be found in the appendix A of Chopra (2012); per Eqs. (A.1.5) and (A.4.3) in Chopra (2012), $p_{con,\delta}$ and $\frac{p_{con,h}}{e^{i\omega t}}$ are a *Fourier transform pair*). The convective pressure, $p_{con,\delta}$, generated by $\delta(t)$ was the inverse Fourier transform of $\frac{p_{con,h}}{e^{i\omega t}}$:

$$p_{con,\delta} = \mathcal{F}^{-1}\left(\frac{p_{con,h}}{e^{i\omega t}}\right) \tag{3.74}$$

where $\mathcal{F}^{-1}$ is the operator of the inverse Fourier transform. The convective pressure, $p_{con,\delta}$, calculated using Eq. (3.74) was given as:

$$p_{con,\delta} = -g\cdot\rho\cos\theta\frac{2n_j}{{n_j}^2-1}\frac{J_1(n_j\frac{r}{R})}{J_1(n_j)}\frac{\cosh(n_j\frac{z}{R})}{\cosh(n_j\frac{H}{R})}\tanh(n_j\frac{H}{R})\cdot\omega_{con,j}\cdot\sin\omega_{con,j}t \tag{3.75}$$

Using Duhamel's integral on $p_{con,\delta}$, the convective pressure, p_{con}, in the tank subjected to unidirectional horizontal seismic acceleration of a small amplitude, $u_0''(t)$, was determined to be:

$$p_{con} = \int_0^t u_0''(\tau)\,p_{con,\delta}(t-\tau)d\tau \tag{3.76}$$

which yields:

$$p_{con,j} = -A_j(t)\cdot\rho R\cos\theta\frac{2}{{n_j}^2-1}\frac{\cosh(n_j\frac{z}{R})}{\cosh(n_j\frac{H}{R})}\frac{J_1(n_j\frac{r}{R})}{J_1(n_j)} \tag{3.77}$$

$$A_j(t) = \omega_{con,j} \int_0^t u_0''(\tau) \cdot \sin \omega_{con,j}(t-\tau) d\tau \tag{3.78}$$

where each value of n_j refers to $p_{con,j}$ associated with the j th convective mode; and $A_j(t)$ is the pseudo-acceleration time series in the j th convective mode, represented as a SDOF system with a natural frequency of $f_{con,j}$, subjected to the ground motion, $u_0''(t)$. The time series, $A_j(t)$, calculated per Eq. (3.78) provided in Veletsos assumed zero damping in the convective modes. However, in practice, a damping ratio of 0.5% is recommended for calculating the convective responses of steel and concrete tanks (Malhotra et al. 2000). Appendix B presents calculations using the Veletsos solutions adjusted for non-zero damping in the convective modes.

The convective pressure on the wall of the tank (i.e., at $r = R$) associated with the j th mode, along the vertical and the circumferential directions, z and θ, was given as:

$$p_{con,w,j} = p_{con,j}(r = R) = -A_j(t) \cdot \rho R \cos\theta \frac{2}{n_j{}^2 - 1} \frac{\cosh(n_j \frac{z}{R})}{\cosh(n_j \frac{H}{R})} \tag{3.79}$$

The convective pressure on the base of the tank (i.e., at $z = 0$) associated with the j th mode, along the radial and the circumferential directions, r and θ, was given as:

$$p_{con,b,j} = p_{con,j}(z = 0) = -A_j(t) \cdot \rho R \cos\theta \frac{2}{n_j{}^2 - 1} \frac{J_1(n_j \frac{r}{R})}{J_1(n_j)} \frac{1}{\cosh(n_j \frac{H}{R})} \tag{3.80}$$

The vertical displacement of the free surface, which was the height of the wave above the initial free surface, generated hydrostatic pressure at the initial free surface (see Eq. (3.66)). The hydrostatic pressure was the convective pressure at $z = H$. The vertical displacement of the free surface, $d_{w,j}$, associated with the j th mode, along the radial and the circumferential directions, r and θ, was given as:

$$d_{w,j} = \frac{p_{con,j}(z = H)}{\rho g} = -A_j(t) \cdot \frac{R}{g} \cos\theta \frac{2}{n_j{}^2 - 1} \frac{J_1(n_j \frac{r}{R})}{J_1(n_j)} \tag{3.81}$$

where $p_{con,j}(z=H)$ was calculated using Eq. (3.77).

The convective shear force at the base of the tank, $F_{con,j}$, associated with the j th mode in the x direction, equilibrated the resultant force generated by $p_{con,w,j}$ on wall of the tank. The resultant force was the integral of $p_{con,w,j}\cdot\cos\theta$ over the area of the wall, A_w. The convective shear force in the j th mode was:

$$F_{con,j} = -\iint_{A_w} p_{con,w,j}\cdot\cos\theta\cdot dA_w = A_j(t)\cdot m_l \frac{R}{H}\frac{2}{n_j(n_j^{\,2}-1)}\tanh(n_j\frac{H}{R}) \tag{3.82}$$

where m_l is the mass of the contained fluid. The convective pressure on the wall of the tank, $p_{con,w,j}$, at a vertical distance z above the base, created a moment about the y axis at the center of the base (see Figure 3.20), which was equilibrated by the convective moment at the base of the tank, $M_{con,w,j}$:

$$M_{con,w,j} = -\iint_{A_w} p_{con,w,j}\cdot\cos\theta\cdot z\cdot dA_w = A_j(t)\cdot m_l R\frac{2}{n_j(n_j^{\,2}-1)}\tanh(n_j\frac{H}{R})\left[1-\frac{R}{n_j H}\tanh(n_j\frac{H}{2R})\right] \tag{3.83}$$

Similarly, the convective pressure on the base of the tank, $p_{con,b,j}$, at a horizontal distance $r\cdot\cos\theta$ from the center of the base, created a moment about the y axis at the center, which was equilibrated by the convective moment at the base of the tank, $M_{con,b,j}$:

$$M_{con,b,j} = -\iint_{A_b} p_{con,b,j}\cdot r\cdot\cos\theta\cdot dA_b = A_j(t)\cdot m_l \frac{R^2}{H}\frac{2}{n_j(n_j^{\,2}-1)}\frac{J_2(n_j)}{J_1(n_j)}\frac{1}{\cosh(n_j\frac{H}{R})} \tag{3.84}$$

where A_b is the area of the base of the tank.

Chalhoub and Kelly (1988)

Chalhoub and Kelly determined FSI responses of a rigid, base-supported cylindrical tank, subjected to unidirectional horizontal seismic motion of a small amplitude by using a velocity potential, Φ_h, with considerations of both the impulsive and convective components. Section 3.2.1.2 presented the derivations of Φ_h and the analytical solutions of the impulsive pressure. This section presents the analytical solutions of convective responses, including convective

frequency, f_{con}, convective pressure, p_{con}, and vertical displacement of the free surface, d_w. The derivations are not repeated here.

As noted in Section 3.2.1.2, Chalhoub and Kelly did not parse hydrodynamic pressure, p_d, per Eq. (3.21) into impulsive and convective components, but here the first term on the right-hand side of Eq. (3.21) is considered to be the impulsive pressure, p_{imp}, and the second term the convective pressure, p_{con}:

$$p_{con} = \rho \cos\theta \sum_{j=1}^{\infty} \frac{2R}{1-n_j^{\,2}} \frac{\cosh(n_j \frac{z}{R})}{\cosh(n_j \frac{H}{R})} \frac{J_1(n_j \frac{r}{R})}{J_1(n_j)} \lambda_j \int_0^t u_0''(\tau) \sin\lambda_j (t-\tau) d\tau \tag{3.85}$$

$$\lambda_j = \sqrt{\frac{n_j g}{R} \cdot \tanh(n_j \frac{H}{R})} \tag{3.86}$$

The frequency of the convective mode was the frequency of the sinusoidal function in Eq. (3.85):

$$f_{con,j} = \frac{\lambda_j}{2\pi} = \frac{1}{2\pi} \sqrt{\frac{n_j g}{R} \cdot \tanh(n_j \frac{H}{R})} \tag{3.87}$$

The convective pressure per Eq. (3.85) was an algebraic sum of modal pressures for $j = 1$ to ∞. The convective pressure in the jth mode, with was the jth term in the infinite series in Eq. (3.85), was identical to Veletsos's analytical solution per Eq.(3.77). Therefore, the convective pressures on the wall and the base of the tank, $p_{con,w,j}$ and $p_{con,b,j}$, in the jth mode were identical to Eqs. (3.79) and (3.80), respectively. The vertical displacements of the free surface calculated using the convective pressure at $z = H$ were identical to Eq. (3.81). Those equations are not repeated herein.

Housner (1957)

Housner developed approximate analytical solutions for the convective responses listed in the fourth row of Table 3.6, which avoided having to use Bessel's functions for calculating a velocity potential for the contained fluid (e.g., Veletsos (1984) and Chalhoub and Kelly (1988)). The derivations assumed the tank to be rigid and the contained fluid to be ideal. The vertical displacements of the free surface were assumed to be small. Identical to the solutions of Veletsos,

and Chalhoub and Kelly, hydrostatic pressures below the level of the initial free surface were not considered, whereas the derivations accounted for the effect of hydrostatic pressure on the initial free surface due to wave actions. The analytical solutions were derived for the convective responses in the first mode. Some of these solutions were extended to the higher modes based on an assumption regarding wavelengths of fluid waves on the free surface. The solutions for convective responses were derived based on a 2-dimensional (2-D) vertical cross section through a cylindrical tank, but the fluid velocities in three orthogonal directions were all considered. Figure 3.21 presents a vertical cross section through a tank with radius R and filled with fluid to height H, a Cartesian coordinate system (x, y, z), and a cylindrical coordinate system (r, θ, z). The horizontal ground motion, $u_0''(t)$, was input in the x direction, parallel to the vertical cross section. The fluid in the vertical cross section was divided into multiple thin horizontal layers that were free to rotate with respect to the y axis. The rotational angle of a fluid layer, φ, was associated with the vertical displacement of the fluid due to wave actions. The velocities at an arbitrary point in the fluid were u_x', u_y' and u_z', in the x, y, and z directions, respectively, as shown in Figure 3.21. These velocities and rotational angle obeyed boundary conditions given as:

$$u_x'(x = \pm R\cos\theta) = 0 \tag{3.88}$$

$$\varphi(z = 0) = 0 \tag{3.89}$$

$$u_y'(y = 0) = 0 \tag{3.90}$$

The boundary conditions per Eqs. (3.88) and (3.89) were similar to those per Eqs. (3.69) and (3.70) used in Veletsos, which assumed the part of the fluid associated with convective responses not to move horizontally with the tank and the vertical velocity of the fluid adjacent to the base of the tank to be zero. The boundary condition per Eq. (3.90) assumed the velocity of the fluid in the y direction was zero on the plane of symmetry for the tank (i.e., the x-z plane) accelerating in the x direction.

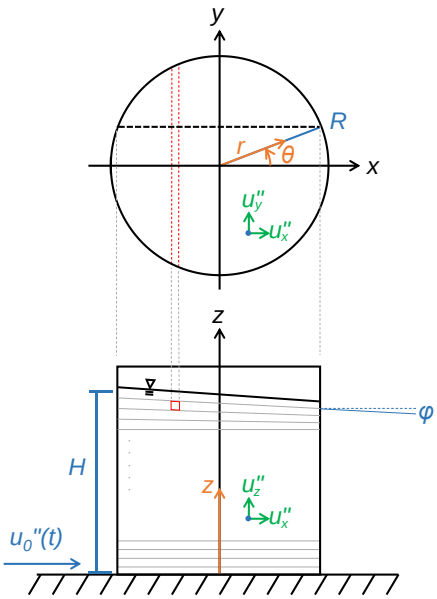

Figure 3.21. A base-supported cylindrical tank, showing the 2-D configuration used in the derivations of convective responses in Housner (1957), adapted from Figure F.4 in Thomas et al. (1963)

Housner used Hamilton's principle, including the kinetic energy of the fluid, K_l, and the potential energy of the fluid, P_l, to derive the convective responses:

$$\int (K_l - P_l)dt = 0 \tag{3.91}$$

$$K_l = \frac{1}{2}\iiint_{V_l} (u_x'^2 + u_y'^2 + u_z'^2)dV_l \tag{3.92}$$

$$P_l = \iiint_{V_l} \rho g u_z dV_l \tag{3.93}$$

where V_l is the volume of the contained fluid, and other parameters have been defined previously. The kinetic energy and the potential energy could be calculated given the velocities of the fluid, u_x', u_y' and u_z'. These velocities were functions of x, y, and z, which determined the velocity field for all of the fluid in the tank. Housner related these velocities to the rotational angles of the fluid layers, φ. The vertical velocity of the fluid, u_z', was given as:

$$u_z' = -x\varphi' \tag{3.94}$$

To determine u_x', Housner derived the mass balance for a fluid element in a horizontal layer, shown red in Figure 3.21. Figure 3.22 presents the horizontal and vertical velocities on the four edges of the fluid element, together with the dimensions of the fluid element. The fluid element was approximately rectangular with lengths dx, $2b$, and dz in the x, y, and z directions, respectively. The horizontal and vertical net volume flow rates of the fluid element shown in Figure 3.22b were $-2\frac{\partial}{\partial x}(u_x'b)dxdz$ and $-2b\frac{\partial u_z'}{\partial z}dxdz$, respectively. The volume of the incompressible ideal fluid was conserved. Accordingly, the sum of the net volume flow rates was zero, which related u_x' and u_z':

$$-\frac{\partial}{\partial x}(u_x'b)-b\frac{\partial u_z'}{\partial z}=0 \tag{3.95}$$

The velocity of the fluid in the x direction, u_x', was determined by taking indefinite integral Eq. (3.95) with respect to x and u_z' in the equation was expressed using Eq. (3.94):

$$u_x'=\frac{1}{b}\frac{\partial\varphi'}{\partial z}\int bxdx \tag{3.96}$$

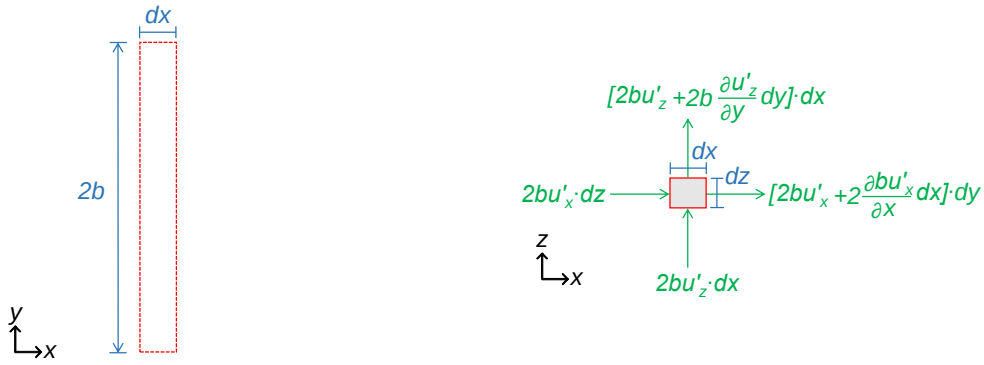

(a) dimensions, x - y plane (b) volume flow rates and dimensions, x - z plane

Figure 3.22. Volume flow rates and dimensions of a fluid element shown as red in Figure 3.21, adapted from Figures F.5 in Thomas et al. (1963)

Since the volume of the incompressible ideal fluid was conserved, the divergence of the velocities of the fluid was zero, $\nabla\cdot vel=0$ (see footnote 22 on page 49):

$$\frac{\partial u_x'}{\partial x}+\frac{\partial u_y'}{\partial y}+\frac{\partial u_z'}{\partial z}=0 \tag{3.97}$$

The velocity of the fluid in the y direction, u_y', was determined by taking indefinite integral for Eq. (3.97) with respect to y, and u_x' and u_z' in the equation were defined using Eqs. (3.96) and (3.94), respectively:

$$u_y'=y\frac{db}{dx}\frac{1}{b^2}\frac{\partial\varphi'}{\partial y}\int bxdx \tag{3.98}$$

The kinetic energy and the potential energy of the fluid, K_l and P_l, were calculated using, u_x', u_y', and u_z', determined in Eqs. (3.96), (3.98), and (3.94). Using Hamilton's principle per Eq. (3.91) and the boundary conditions per Eqs. (3.88), (3.89), and (3.90), the rotational acceleration of a horizontal layer of the fluid was determined to be a sinusoidal function:

$$\varphi''=\varphi_{H,a}\frac{\sinh(\sqrt{\frac{27}{8}}\frac{z}{R})}{\sinh(\sqrt{\frac{27}{8}}\frac{H}{R})}\sin\omega_{con,1}t \tag{3.99}$$

where $\varphi_{H,a}$ is the maximum rotational acceleration at the free surface (i.e., $z=H$), and $\omega_{con,1}$ is the radial frequency in the first convective mode given as:

$$\omega_{con,1}=\left[\frac{g}{R}\sqrt{\frac{27}{8}}\tanh(\sqrt{\frac{27}{8}}\frac{H}{R})\right]^{\frac{1}{2}} \tag{3.100}$$

and so the first convective frequency was:

$$f_{con,1}=\frac{1}{2\pi}\left[\frac{g}{R}\sqrt{\frac{27}{8}}\tanh(\sqrt{\frac{27}{8}}\frac{H}{R})\right]^{\frac{1}{2}} \tag{3.101}$$

The derivations for the convective pressures, $p_{con,1}$, in the first mode presented here follow those in Housner (1954) for simplicity, which considered only the accelerations of the fluid in the x direction, u_x'':

$$p_{con,1} = -\int_0^x \rho u_x'' dx \tag{3.102}$$

where u_x'' was determined per Eq. (3.96). The convective pressures, $p_{con,1}$, at an arbitrary location in the fluid or on the inner surfaces of the tank was given as:

$$p_{con,1} = -\varphi_{H,a} \cdot \sin \omega_{con,1} t \sqrt{\frac{3}{8}} \rho R^2 \left[\frac{x}{R} - \frac{1}{3} (\frac{x}{R})^3 \right] \frac{\cosh(\sqrt{\frac{27}{8}} \frac{z}{R})}{\sinh(\sqrt{\frac{27}{8}} \frac{H}{R})} \tag{3.103}$$

where $x = r\cos\theta$ based on the cylindrical coordinate system shown in Figure 3.21. The convective pressure on the wall of the tank (i.e., at $x = R\cos\theta$) associated with the first convective mode, along the vertical and the circumferential directions, z and θ, was given as:

$$p_{con,w,1} = -\varphi_{H,a} \cdot \sin \omega_{con,1} t \cdot \sqrt{\frac{3}{8}} \rho R^2 (1 - \frac{1}{3} \cos^2 \theta) \cos\theta \frac{\cosh(\sqrt{\frac{27}{8}} \frac{z}{R})}{\sinh(\sqrt{\frac{27}{8}} \frac{H}{R})} \tag{3.104}$$

The convective pressure on the base of the tank (i.e., at $z = 0$) associated with the first convective mode, along the radial and the circumferential directions, r and θ, was given as:

$$p_{con,b,1} = -\varphi_{H,a} \cdot \sin \omega_{con,1} t \cdot \sqrt{\frac{3}{8}} \rho R^2 (\frac{r}{R} - \frac{1}{3} \frac{r^3}{R^3} \cos^2 \theta) \cos\theta \frac{1}{\sinh(\sqrt{\frac{27}{8}} \frac{H}{R})} \tag{3.105}$$

The vertical displacement of the free surface, which was the height of the wave above the initial free surface, generated hydrostatic pressure at the initial free surface. Assuming the vertical acceleration of the free surface, $x\varphi''$, was negligible, the hydrostatic pressure was the convective pressure at $z = H$. The vertical displacement of the free surface, $d_{w,1}$, associated with the first mode, along the radial and the circumferential directions, r and θ, was given as:

$$d_{w,1} = \frac{p_{con,1}(z = H)}{\rho g} \tag{3.106}$$

where $p_{con,1}(z = H)$ was calculated using Eq.(3.103).

The convective shear force at the base of the tank, $F_{con,1}$, in the x direction equilibrated the resultant force generated by $p_{con,w,1}$ on the wall of the tank. The resultant force was the integral of $p_{con,w,1} \cdot \cos\theta$ over the area of the wall, A_w. The convective shear force was:

$$F_{con,1} = -\iint_{A_w} p_{con,w.1} \cdot \cos\theta \cdot dA_w = \varphi_{H,a} \cdot \sin\omega_{con,1} t \frac{1}{4}\sqrt{\frac{27}{8}}\rho R^4 \tag{3.107}$$

The convective pressure on the wall of the tank, $p_{con,w,1}$, at a vertical distance z above the base, created a moment about the y axis at the center of the base, which was equilibrated by the convective moment at the base of the tank, $M_{con,w,1}$:

$$M_{con,w,1} = -\iint_{A_w} p_{imp,w,1} \cdot \cos\theta \cdot z \cdot dA_w = F_{con,1} \cdot \left(H + R\sqrt{\frac{8}{27}} \frac{1-\cosh\sqrt{\frac{27}{8}}\frac{H}{R}}{\sinh\sqrt{\frac{27}{8}}\frac{H}{R}} \right) \tag{3.108}$$

Similarly, the convective pressure on the base of the tank, $p_{con,b,1}$, at a horizontal distance $r \cdot \cos\theta$ from the center of the base, created a moment about the y axis at the center, which was equilibrated by the convective moment at the base of the tank $M_{con,b,1}$:

$$M_{con,b,1} = -\iint_{A_b} p_{con,b,1} \cdot r \cdot \cos\theta \cdot dA_b = F_{con,1} \frac{\frac{5}{6}\sqrt{\frac{3}{8}}R}{\sinh(\sqrt{\frac{27}{8}}\frac{H}{R})} \tag{3.109}$$

where A_b is the area of the base of the tank. Note that Eq. (3.109) as written in Housner (1954) contains calculation errors.

The analytical solutions for the convective responses per Eqs. (3.103) to (3.106) included the variable, $\varphi_{H,a}$. To derive $\varphi_{H,a}$, Housner (1957) represented wave actions in the first convective mode using a SDOF system with a frequency of $f_{con,1}$, subjected to the ground motion, $u_0''(t)$. Unlike Veletsos, and Chalhoub and Kelly using Eq. (3.78), Housner assumed the acceleration of the SDOF system to be a sinusoidal function:

$$A_1(t) = A_m \sin\omega_{con,1} t \tag{3.110}$$

where the amplitude, A_m, was suggested to be considered to be the spectral acceleration, $Sa(f_{con,1})$, due to the ground motion, $u_0''(t)$. The inertial force of the part of the fluid associated with wave actions was assumed to equal the horizontal force generated by $p_{con,1,w}$:

$$m_{con} \cdot A(t) = \iint_{dA_w} p_{con,1,w} dA_w \tag{3.111}$$

where m_{con} is the mass of the part of the fluid associated with wave actions. The right-hand side of Eq. (3.111) was $-F_{con,1}$ per Eq. (3.107). The kinetic energy of m_{con} was assumed to equal the kinetic energy of the fluid in the horizontal layers, K_l, shown in Figure 3.21:

$$\frac{1}{2} m_{con} V(t)^2 = K_l \tag{3.112}$$

where $V(t)$ is the velocity of the SDOF system calculated by the integration of $A_1(t)$ with respect to t. Equation (3.92) was used to calculate K_l. Eqs. (3.111) and (3.112) related the maximum rotational acceleration at the free surface, $\varphi_{H,a}$, and the amplitude of the acceleration of the SDOF system, A_m:

$$\varphi_{H,a} = \sqrt{\frac{27}{8}} \frac{A_m}{R} \tanh \sqrt{\frac{27}{8}} \frac{H}{R} \tag{3.113}$$

The convective responses per Eqs. (3.103) to (3.106) were determined given $\varphi_{H,a}$.

To calculate the convective responses in higher modes, Housner assumed the wavelength of the fluid wave on the free surface in the j th mode was $1/(2j-1)$ of that of the first mode. Figure 3.23 presents the assumed shapes of the fluid wave in the second and third convective modes (i.e., $j = 2$ and 3) in a vertical cross section through a tank. The wavelengths in the second and third modes are 1/3 and 1/5 of the wavelength of the first convective mode (shown in Figure 3.21), respectively. The convective frequency and the global convective reactions at the base of the tank, $f_{con,j}$, $F_{con,j}$, $M_{con,w,j}$, and $M_{con,b,j}$, in the j th mode were computed by substituting $R/(2j-1)$ for R in the analytical solutions for $f_{con,1}$, $F_{con,1}$, $M_{con,w,1}$, and $M_{con,b,1}$, respectively:

$$f_{con,j} = \frac{1}{2\pi}\left[\frac{g(2j-1)}{R}\sqrt{\frac{27}{8}}\tanh\left(\sqrt{\frac{27}{8}}\frac{H(2j-1)}{R}\right)\right]^{\frac{1}{2}} \tag{3.114}$$

$$F_{con,j} = \varphi_{H,a}\cdot\sin\omega_{con,j}t\,\frac{1}{4}\sqrt{\frac{27}{8}}\rho\left(\frac{R}{2j-1}\right)^4 \tag{3.115}$$

$$M_{con,w,j} = F_{con,j}\cdot\left(H + \frac{R}{2j-1}\sqrt{\frac{8}{27}}\frac{1-\cosh\sqrt{\frac{27}{8}}\frac{H(2j-1)}{R}}{\sinh\sqrt{\frac{27}{8}}\frac{H(2j-1)}{R}}\right) \tag{3.116}$$

$$M_{con,b,j} = F_{con,j}\frac{\frac{5}{6}\sqrt{\frac{3}{8}}\frac{R}{2j-1}}{\sinh\left(\sqrt{\frac{27}{8}}\frac{H(2j-1)}{R}\right)} \tag{3.117}$$

$$\varphi_{H,a} = \sqrt{\frac{27}{8}}\frac{A_m(2j-1)}{R}\tanh\sqrt{\frac{27}{8}}\frac{H(2j-1)}{R} \tag{3.118}$$

The convective pressures and the vertical displacement of the free surface in the higher convective modes were not addressed.

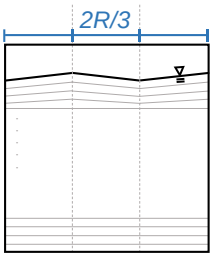

(a) second mode, $j=2$

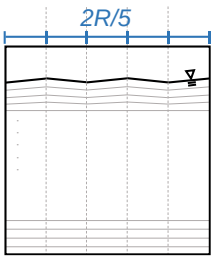

(b) third mode, $j=3$

Figure 3.23. Shapes of the fluid wave on the free surface shown in a vertical cross section through a tank

Discussion

Veletsos (1984), Chalhoub and Kelly (1988), and Housner (1957) developed analytical solutions for convective responses of rigid, base-supported cylindrical tanks subjected to unidirectional horizontal motion of a small amplitude. The derived convective responses include convective frequency, f_{con}; convective pressure, p_{con}; vertical displacement of the free surface (i.e., wave height above the initial free surface), d_w; convective shear force at the base of the tank, F_{con}; and the two components of convective moment, $M_{con,w}$ and $M_{con,b}$. Veletsos derived exact analytical solutions for the convective responses (i.e., f_{con}, p_{con}, d_w, F_{con}, $M_{con,w}$, and $M_{con,b}$) in different modes by using an assumed velocity potential for the fluid and a frequency-domain method. Chalhoub and Kelly derived analytical solutions for f_{con}, p_{con}, and d_w, which were identical to the corresponding solutions of Veletsos. Housner derived approximate analytical solutions for the convective responses by applying Newton's second law to the inertial forces and Hamilton's principle to the potential and kinetic energies of fluid discretized into multiple horizontal layers. The convective pressure, p_{con}, and the vertical displacement of the free surface, d_w, were only addressed for the first convective mode. Other convective responses, including f_{con}, F_{con}, $M_{con,w}$, and $M_{con,b}$, were addressed for different convective modes. This section has presented the analytical solutions derived in the three studies, and their equation numbers assigned in this report are listed in Table 3.7.

Table 3.7. Equation numbers of the analytical solutions for convective responses of a rigid, base-supported cylindrical tank subjected to unidirectional horizontal motion of a small amplitude, derived in the studies listed in the first column

	f_{con}	$p_{con,w}$	$p_{con,b}$	d_w	F_{con}	$M_{con,w}$	$M_{con,b}$
Veletsos (1984)	(3.73)	(3.79)	(3.80)	(3.81)	(3.82)	(3.83)	(3.84)
Chalhoub and Kelly (1988)[1]	(3.87)	(3.79)	(3.80)	(3.81)	--	--	--
Housner (1957)	(3.114)	(3.104)	(3.105)	(3.106)	(3.115)	(3.116)	(3.117)

1. The analytical solutions for $f_{con,w}$, $p_{con,w}$, $p_{con,d}$, and d_w in Chalhoub and Kelly were identical to those in Veletsos. Analytical solutions for global convective reactions, F_{con}, $M_{con,w}$, and $M_{con,b}$, were not presented in Chalhoub and Kelly.

Below, convective responses are calculated and compared using the analytical solutions derived by Veletsos, Chalhoub and Kelly, and Housner for a rigid tank subjected to small-amplitude ground motion, $u_0''(t)$, in the x direction. The convective responses calculated using the solutions of Veletsos, and Chalhoub and Kelly are presented just once because their equations are identical. Multiple values of H/R are considered in the calculations: $p_{con,w}$, $p_{con,b}$, and d_w are calculated for $H/R = 0.5$, 1, and 2; and f_{con}, F_{con}, $M_{con,w}$, and $M_{con,b}$ are calculated for $0.2 \le H/R \le 3$. The radius of the tank, R, is assumed to be 30 m. The contained fluid is assumed to be water, with a density, ρ, is 1000 kg/m^3. (The same values for R and ρ are assumed for calculating impulsive responses of a rigid and a flexible tank, presented in Sections 3.2.1.2 and 3.2.1.3, respectively). Other dimensions (e.g., thickness of the wall of the tank) and mechanical properties (e.g., density and elastic modulus of the material) of the tank do not need to be defined for the calculations because the tank is assumed to be rigid. The convective responses presented herein are normalized to be unitless. The normalized results are independent of the dimensions of the tank and the fluid, R and H, the density of the fluid, ρ, and the acceleration time series in the convective mode, A_j. The only variable for the normalized convective responses is the unitless ratio describing the dimensions of the tank, H/R. (The convective pressure is normalized using the same method used for the impulsive pressure, and the convective reactions are normalized using the same methods used for the corresponding impulsive reactions; see Sections 3.2.1.2 and 3.2.1.3 for the normalizations of impulsive responses).

Figure 3.24a shows the convective frequencies, $f_{con,j}$, associated with the first three convective modes (i.e., $j = 1$ to 3), calculated for a tank with $0.2 \le H/R \le 3$ using Eqs. (3.73) and (3.114). Per the two equations, the only two variables in $f_{con,j}$ are the radius of the tank, R, and the unitless ratio describing the dimensions of the tank, H/R. (Note that $f_{con,j}$ is independent of the density of the fluid, ρ). A radius of 30 m is used in the calculations. In the legend for the figure, "V and C&K" denotes Veletsos (1984) and Chalhoub and Kelly (1988), and the "H" denotes Housner (1957). The convective frequencies for the first mode calculated using the solution of Veletsos, and Chalhoub and Kelly and the solution of Housner are identical over the range of H/R considered here. The solution of Housner slightly overestimates the convective

frequencies in the second and the third modes for the range of H/R, with respect to the solution of Veletsos, and Chalhoub and Kelly. For the tank with $R = 30$ m, the values of $f_{con,1}$ range from 0.07 Hz to 0.12 Hz (i.e., the convective periods in the first mode range from 8 to 14 sec) for $0.2 \le H/R \le 0.9$; and the value of $f_{con,1}$ is 0.13 Hz for $0.9 \le H/R \le 3$. The values of $f_{con,2}$ range from 0.18 Hz to 0.21 Hz and of $f_{con,3}$ range from 0.26 Hz to 0.28 Hz for $0.2 \le H/R \le 3$.

For the purpose of generalizing over different tank radii, $f_{con,j}$ is expressed as follows:

$$f_{con,j} = C_{con,j}\sqrt{\frac{g}{R}} \tag{3.119}$$

where $C_{con,j}$ is the coefficient of the convective frequency in the j th convective mode. The coefficient is a function of H/R, unitless and independent of R. Figure 3.24b presents values of $C_{con,j}$ associated with the first three convective modes (i.e., $j = 1$ to 3), calculated based on the analytical solutions for $f_{con,j}$ in Veletsos, Chalhoub and Kelly, and Housner.

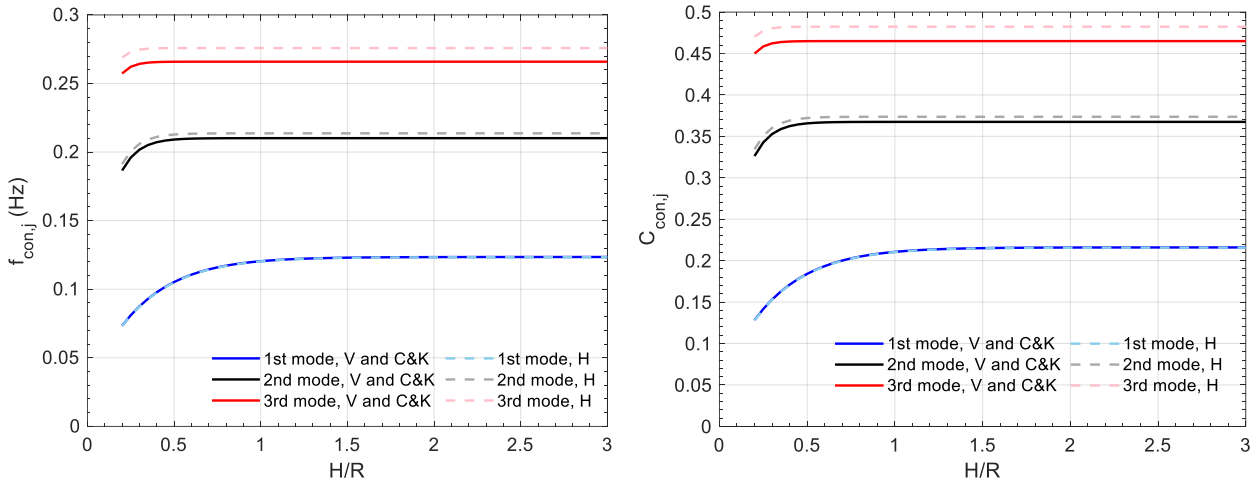

(a) $f_{con,j}$, R =30 m, calculated using Eqs. (3.73) and (3.114)

(b) $C_{con,j}$, calculated using Eq. (3.119) and $f_{con,j}$ in panel (a)

Figure 3.24. Convective frequencies, $f_{con,j}$, and coefficients of convective frequency, $C_{con,j}$, associated with the first three convective modes (i.e., $j = 1$ to 3), for $0.2 \le H/R \le 3$

Two important observations can be drawn from Eq. (3.119) and Figure 3.24. First, the height of the fluid, H, in a tank with a given R has an insignificant influence on the convective frequencies, $f_{con,j}$, when $H/R > 1$ because 1) the values of $C_{con,j}$ in each mode shown in Figure

3.24b are almost constant for $H/R > 1$ and 2) the relationship of $f_{con,j}$ and $C_{con,j}$ is independent of H per Eq. (3.119). Second, the convective frequency, $f_{con,j}$, in a given mode is inversely proportional to $\sqrt{R}$ per Eq. (3.119), namely, $f_{con,j}$ is lower for a tank with a greater R. For example, the convective frequency of a tank with $R = 60$ m can be calculated by multiplying $f_{con,j}$ for $R = 30$ m (see Figure 3.24a) by the reciprocal of the square root of the ratio of their radii, namely $1/\sqrt{2}$ ($= 1/\sqrt{30/60}$). As a result, the values of the first convective frequencies, $f_{con,1}$, are between 0.06 Hz and 0.09 Hz (i.e., $T_{con,1}$ ranges from 11 sec to 18 sec) for $R = 60$ m and $0.2 \le H/R \le 3$.

The first impulsive frequency, $f_{imp,1}$, shown in Figure 3.11a, decreases from 7 to 1.5 Hz and the first convective frequency, $f_{con,1}$, shown in Figure 3.24a, increases from 0.07 to 0.12 Hz, as H/R increases from 0.2 to 3 for a tank with $R = 30$ m. The value of $f_{imp,1}$ is greater than $f_{con,1}$ by a factor of about 20 at a given H/R for $R = 30$ m. As noted in Section 3.2.1.3, the impulsive frequency in a mode is inversely proportional to R per Eq. (3.64), and the convective frequency in a mode is inversely proportional to $\sqrt{R}$ per Eq. (3.119). As a result, for a wide range of tank radius, say 2 m $\le R \le$ 90 m (i.e., 1/15 to 3 times the radius of 30 m), $f_{imp,1}$ is expected to be greater than $f_{con,1}$ by a factor of between 12 and 77 (i.e., $20/\sqrt{3}$ and $20 \times \sqrt{15}$, in which $\sqrt{3}$ is the square root of the ratio of 90 m to 30 m and $\sqrt{15}$ is the square root of the ratio of 30 m to 2 m). The first impulsive mode is generally well separated from the first convective mode, in terms of frequency.

Veletsos, and Chalhoub and Kelly addressed convective pressures, p_{con}, and vertical displacements of the free surface, d_w, in all modes, whereas Housner only provided equations for the first mode. Below, Veletsos, and Chalhoub, and Kelly's solutions are used to calculate p_{con} and d_w in the first three modes, and Housner's solutions are used to calculate only those in the first mode.

Identical to the impulsive pressure, the greatest positive and negative convective pressures on the wall and the base of the tank are generated at $\theta = 180°$ and 0°, respectively, as the tank accelerates in the x direction. Values of the convective pressures at $\theta = 180°$ are presented here.

The convective pressures on the wall of the tank, $p_{con,w,j}$ along the z direction, at $r = R$ and θ=180°, are calculated using Eq. (3.79) for the first three modes (i.e., $j = 1$, 2, and 3) and Eq. (3.104) for the first mode (i.e., $j = 1$). Figures 3.25a, b, and c present values of $p_{con,w,j}$ normalized by ρRA_j, for $H/R = 0.5$, 1, and 2, respectively. The z direction in the figures is normalized by H. The approximate solution of Housner generally underestimates $p_{con,w,1}$ for the entire height of the fluid for all three values of H/R by comparison to the exact solution of Veletsos, and Chalhoub and Kelly. These differences reduce with increasing H/R. For a given value of H/R (i.e., 0.5, 1, or, 2) and an order of the convective mode (i.e., $j = 1$, 2, or, 3), the maximum convective pressure on the wall of the tank, $p_{con,w,j}$, is at the initial free surface (i.e., at $z = H$). The values of $p_{con,w,j}/\rho RA_j$ at $z = H$ in a given convective mode are identical for all three values of H/R, for both the approximate and exact solutions. The values of $p_{con,w,j}/\rho RA_j$ decrease with increasing distance from the free surface (i.e., at $z = H$), and the reduction is more significant for larger values of H/R (i.e., 2). The amplitudes of $p_{con,w,j}/\rho RA_j$ in the first convective mode are the greatest of the three over the height of the fluid (i.e., $p_{con,w,1}/\rho RA_1 > p_{con,w,2}/\rho RA_2 > p_{con,w,3}/\rho RA_3$), for each value of H/R.

The convective pressures on the base of the tank, $p_{con,b,j}$ along the r direction, at $z = 0$ and $\theta = 180°$, are calculated using Eq. (3.80) for the first three modes (i.e., $j = 1$, 2, and 3) and Eq. (3.105) for the first mode (i.e., $j = 1$). Figures 3.26a, b, and c present values of $p_{con,b,j}$ normalized by ρRA_j, for $H/R = 0.5$, 1, and 2, respectively. The r dimension in these figures is normalized by R. The approximate solution of Housner generally underestimates $p_{con,b,1}$ along the entire radius of the tank for all three values of H/R by comparison to the exact solution of Veletsos, and Chalhoub and Kelly. These differences decrease with increasing H/R. Given a value of H/R (i.e., 0.5, 1, or, 2) and an order of the convective mode (i.e., $j = 1$, 2, or, 3), the maximum convective pressure on the base of the tank, $p_{con,b,j}$, is adjacent to the wall (i.e., $r = R$). The amplitude of $p_{con,b,j}/\rho RA_j$ in a given mode (i.e., $j = 1$, 2, or 3) decreases with increasing H/R (i.e., 2). Identical to $p_{con,w,j}/\rho RA_j$, the normalized pressures on the base, $p_{con,b,j}/\rho RA_j$, for each H/R, are the greatest in the first mode across the radius of the tank (i.e.,

$p_{con,b,1} / \rho RA_1 > p_{con,b,2} / \rho RA_2 > p_{con,b,3} / \rho RA_3$). The comparison of the amplitudes for the normalized convective pressures, $p_{con,j} / \rho RA_j$, in the first three modes must not be used to compare the amplitudes of the convective pressures, $p_{con,j}$, since the values of A_j used for the normalization will be different. The value of A_j is associated with the convective frequency, $f_{con,j}$, in the mode of interest and the input motion, $u_0''(t)$. A greater (smaller) value of $p_{con,j} / \rho RA_j$ does not necessarily result in a greater (smaller) value of $p_{con,j}$.

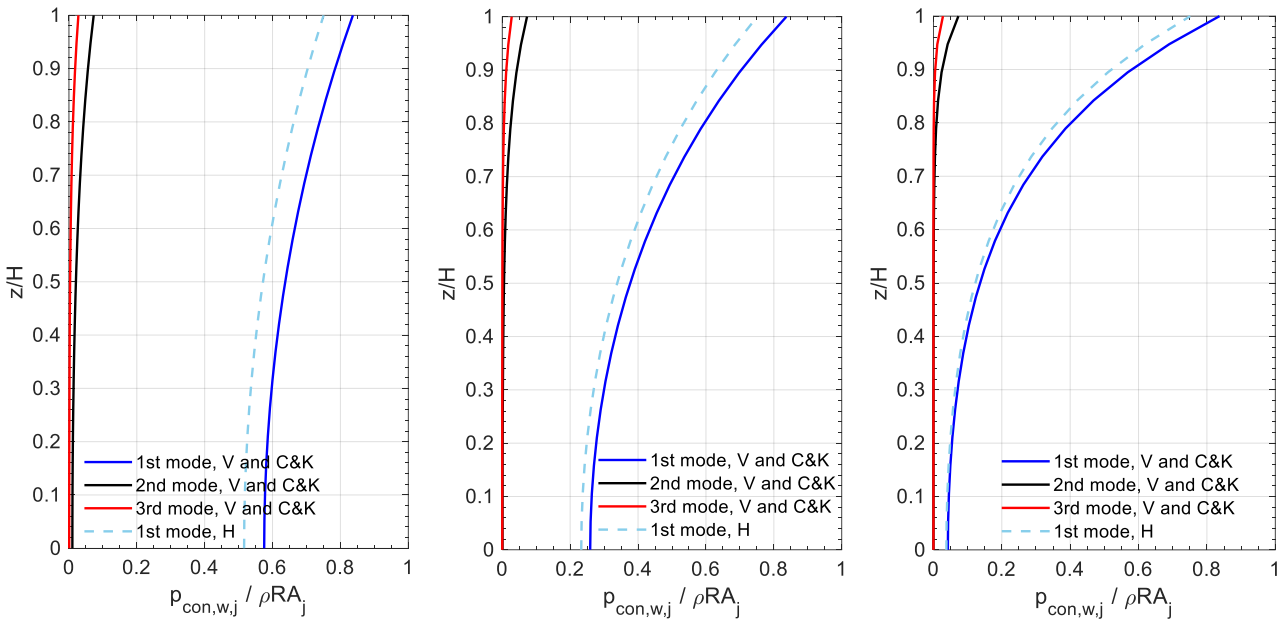

(a) H / R=0.5 (b) H / R=1 (c) H / R=2

Figure 3.25. Normalized convective pressures on the wall of a tank, $p_{con,w,j} / \rho RA_j$, associated with the first three modes (i.e., $j = 1$ to 3), along the normalized vertical direction, z / H, at $r = R$ and θ=180°, for $H / R = 0.5$, 1, and 2, calculated using Eqs. (3.79) and (3.104)

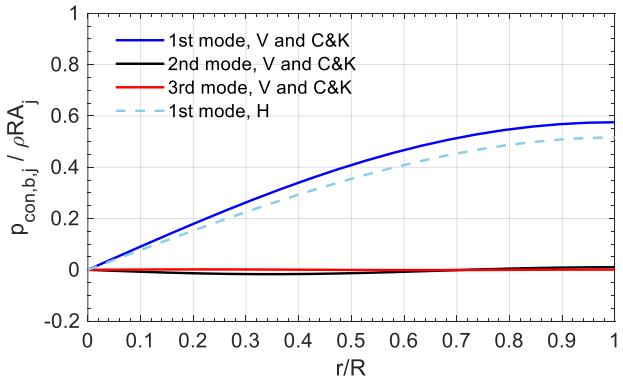

(a) H/R=0.5

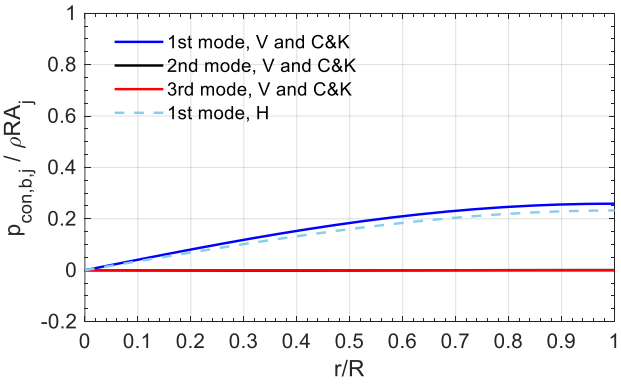

(b) H/R=1

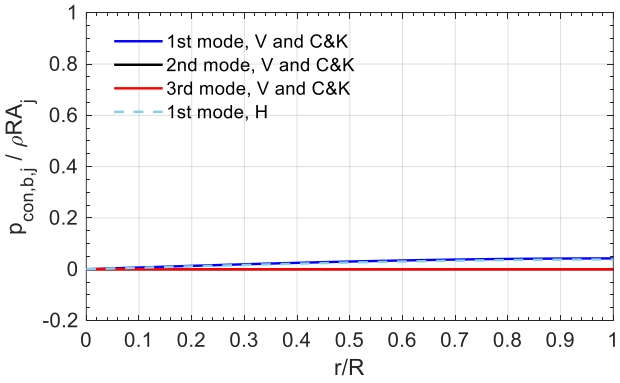

(c) H/R=2

Figure 3.26. Normalized convective pressures on the base of a tank, $p_{con,b,j}/\rho RA_j$, associated with the first three modes (i.e., $j=1$ to 3), along the normalized radial direction, r/R, at $z=0$ and $\theta=180°$, for $H/R=0.5$, 1, and 2, calculated using Eqs. (3.80) and (3.105)

The vertical displacements of the free surface, $d_{w,j}$, along the entire range of the r axis (i.e., $-R \le r \le R$), at θ=0°, are calculated using Eq. (3.81) for the first three modes (i.e., $j=1$, 2, and 3) and Eq. (3.106) for the first modes (i.e., $j=1$). Figures 3.27a, b, and c present values of $d_{w,j}$ normalized by $\rho RA_j/g$, for $H/R=0.5$, 1, and 2, respectively. Identical to $p_{con,w,1}$ and $p_{con,b,1}$, the approximate solution of Housner generally underestimates $d_{w,1}$ for all three values of H/R, by comparison to the *exact* solution. The values of $d_{w,j}\cdot g/RA_j$ in the jth convective mode are identical for all three values of H/R. These results agree with values of $p_{con,w,j}/\rho RA_j$ at $z=H$ that are identical for the three H/R presented in Figure 3.25 because $p_{con,j}(z=H)$ is a factor of

$d_{w,j}$ per Eqs. (3.81) and (3.106). The vertical displacements of the free surface shown in Figure 3.27 are antisymmetric with respect to the $r-z$ plane at $\theta=90°$ of the cylindrical coordinate system (see Figure 3.2). The wavelengths of $d_{w,j}$ in the first, second, and third modes (i.e., $j=1$, 2, and 3) are $4R$, $4R/3$, and $4R/5$, respectively. The amplitudes of $d_{w,j}$ in the second and third modes reduce from the center of the free surface (i.e., $r=0$) to the wall of the tank (i.e., $r=R$).

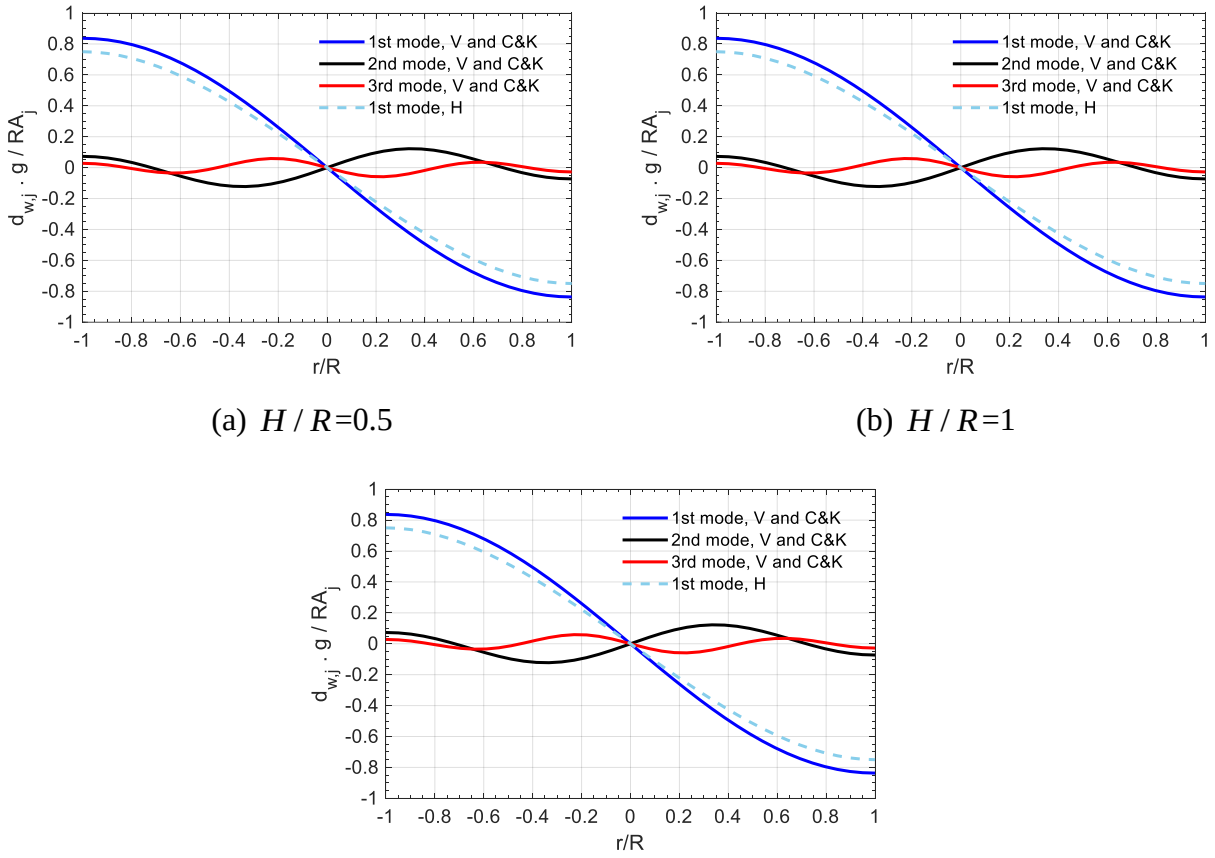

(a) H/R=0.5 (b) H/R=1

(c) H/R=2

Figure 3.27. Normalized vertical displacements of the free surface in a tank, $d_{w,j}\cdot g/RA_j$, associated with the first three modes (i.e., $j=1$ to 3), along the normalized radial direction, r/R, at $\theta=0°$, for $H/R=0.5$, 1, and 2, calculated using Eqs. (3.81) and (3.106)

Veletsos and Housner derived solutions for the global reactions on the foundation associated with the convective loadings in all modes, generated by unidirectional horizontal motion of a small amplitude. (Chalhoub and Kelly did not address global reactions.) The global reactions included convective shear force, $F_{con,j}$, and the two components of convective moment, $M_{con,w,j}$ and $M_{con,b,j}$. These global reactions associated with the first three convective modes (i.e., $j=1$, 2, and 3) are calculated here for a tank with $0.2 \le H/R \le 3$. Figure 3.28 shows $F_{con,j}$ in the x direction, calculated using Eqs. (3.82) and (3.115), normalized by $m_l A_j$. The values of $F_{con,j}$ in the first three modes calculated using the solutions of Veletsos and Housner are almost identical for the range of H/R considered here.

Equations (3.83) and (3.116) are used to calculate $M_{con,w,j}$ about the y axis; and Eqs. (3.84) and (3.117) are used to calculate $M_{con,b,j}$ about the y axis. Figures 3.29a and b show the calculated $M_{con,w,j}$ and $M_{con,b,j}$ normalized by $m_l H A_j$, respectively. The values of $M_{con,w,j}$ in the first three modes calculated using the solutions of Veletsos and Housner are almost identical for the range of H/R considered here. Veletsos and Housner's solutions are almost identical in $M_{con,b,1}$ for $0.2 \le H/R \le 3$ and in $M_{con,b,2}$ and $M_{con,b,3}$ for $H/R > 0.5$. Housner's solution overestimates $M_{con,b,2}$ and $M_{con,b,3}$ for $H/R < 0.5$, with respect to the Veletsos' solution.

Although these normalized, global convective reactions in a lower mode (i.e., $j=1$) seem to be greater than those in higher modes (i.e., $j=2$ and 3) in Figures 3.28 and 3.29, the amplitudes of lines in different modes should not be compared since A_j used for the normalization is different for each line. A discussion regarding modal contributions in convective responses calculated using Veletsos' solutions is presented in Appendix B.

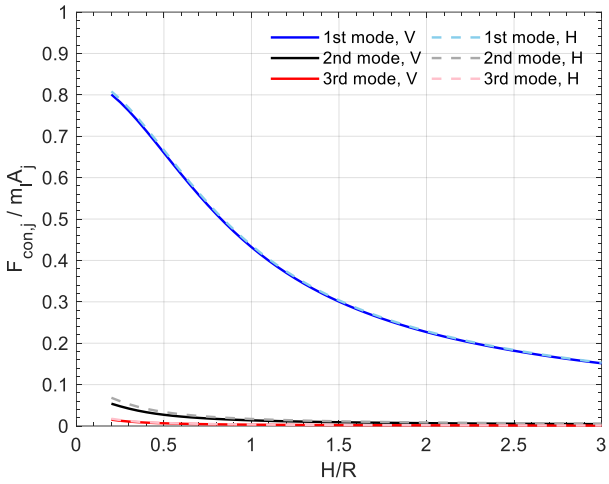

Figure 3.28. Normalized convective shear force at the base of a tank, $F_{con,j} / m_l A_j$, associated with the first three modes (i.e., $j = 1$ to 3), in the x direction for $0.2 \le H/R \le 3$, calculated using Eqs. (3.82) and (3.115)

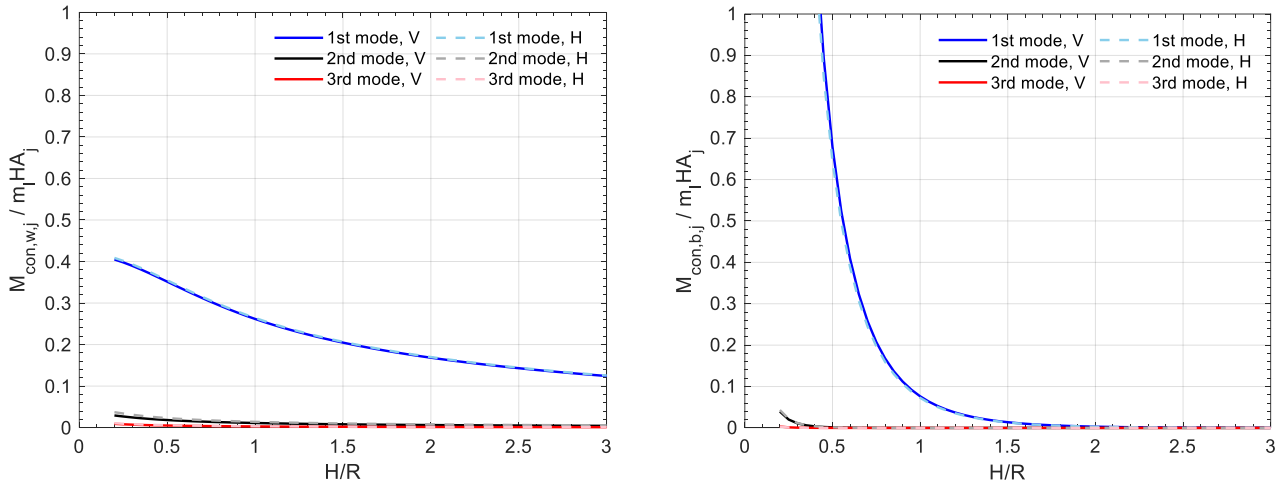

(a) $M_{con,w,j} / m_l HA_j$, calculated using Eqs. (3.83) and (3.116)

(b) $M_{con,b,j} / m_l HA_j$, calculated using Eqs. (3.84) and (3.117)

Figure 3.29. Normalized convective moments at the base of a tank, $M_{con,w,j} / m_l HA_j$ and $M_{con,b,j} / m_l HA_j$, associated with the first three modes (i.e., $j = 1$ to 3), about the y axis for $0.2 \le H/R \le 3$

3.2.3 Closing remarks

Section 3.2.1 presents analytical solutions for impulsive responses of a base-supported cylindrical tank subjected to unidirectional horizontal motion of a small amplitude. Section 3.2.1.2 presents and compares the solutions for the impulsive responses of a rigid tank developed by Jacobsen (1949), Chalhoub and Kelly (1988), and Housner (1957). The impulsive responses are calculated for tanks with different dimensions, in terms of the ratio of the height of the fluid to the radius of the tank, H/R. The impulsive pressures on the wall and the base of the tank are calculated for $H/R = 0.5$, 1, and 2; the impulsive shear force and moments at the base of the tank are calculated for $0.2 \le H/R \le 3$. The analytical solutions of Jacobsen, and Chalhoub and Kelly agree well for the range of H/R considered here. The analytical solutions of Housner are in reasonable agreement with the solutions of Jacobsen, and Chalhoub and Kelly, but differences increase with increasing values of H/R. The impulsive responses of a tank with a given radius, calculated using the three solutions, are generally greater when the tank is filled with fluid to a greater height. Section 3.2.1.3 presents the solutions for impulsive responses of a flexible tank developed by Veletsos (1984). The impulsive responses are calculated using Veletsos' solutions for a tank with different H/R: the impulsive pressures on the wall and the base of the tank are calculated for $H/R = 0.5$, 1, and 2; the impulsive frequency and the impulsive reactions including shear force and moments at the base of the tank are calculated for $0.2 \le H/R \le 3$. The amplitudes of the normalized impulsive responses (i.e., the pressures and reactions) in the first mode are greater than those in the second and third modes. The impulsive frequency in a mode of a tank: 1) decreases with increasing fluid height, H, as the radius and material of the tank and the fluid are constant and 2) decreases with increasing radius, R, of the tank within the range of H/R considered here. The impulsive frequency affects the acceleration of a flexible tank, which is generally greater than the ground, whereas a rigid tank is assumed to accelerate with the ground acceleration. Veletsos' solutions are compared with Jacobsen's solutions developed for rigid tanks. The acceleration of the flexible tank leads to greater impulsive responses than the rigid tank. If the accelerations of the flexible tank in different modes are assumed to be constant, the algebraic sum of the modal impulsive responses in the first ten modes recovers the impulsive response of the corresponding rigid tank.

Section 3.2.2 presents analytical solutions for convective responses of a rigid, base-supported cylindrical tank subjected to unidirectional horizontal motion of a small amplitude, developed by Veletsos (1984), Chalhoub and Kelly (1988), and Housner (1957). The convective responses are calculated using the solutions of the three studies for a tank with different H/R: the convective pressures on the wall and the base of the tank and the vertical displacement of the free surface are calculated for $H/R = 0.5$, 1, and 2; the convective frequency and the convective reactions including shear force and moments at the base of the tank are calculated for $0.2 \le H/R \le 3$. The solutions of Veletsos, and Chalhoub and Kelly are identical. The solutions of Housner show a reasonable agreement with the solutions of Veletsos, and Chalhoub and Kelly, for the values of H/R considered here. The amplitudes of the normalized convective responses (i.e., the pressures, vertical displacement of the free surface, and reactions) in the first mode are greater than those in the second and third modes. The convective frequency in a mode of a tank: 1) is loosely related to the fluid height, H, when the radius of the tank is given and 2) decreases with increasing radius, R, of the tank within the range of H/R considered here.

Veletsos (1984) presented solutions for fluid-structure responses, including the impulsive and convective frequencies, the impulsive and convective components of the pressure and the global reactions at the base of the tank, and the vertical displacement of the free surface in different modes. Based on the data in Veletsos, Malhotra et al. (2000) proposed a simplified procedure for analyzing seismic FSI responses of a flexible base-supported cylindrical tank. Veletsos' solutions were modified to enable the use of only one impulsive mode and one convective mode to calculate global reactions at the base of a tank for engineering applications. A discussion on the procedures and a comparison of responses calculated using Malhotra and Veletsos for tanks with different dimensions is presented in Appendix B.

3.3 Head-supported cylindrical tank

3.3.1 Impulsive responses

Figure 3.30 shows impulsive responses in a vertical cross section through a head-supported cylindrical tank accelerating in the x direction. Similar to a base-supported tank shown in Figure 3.1, the impulsive pressure, p_{imp}, is generated on the wall and the base of the tank and mechanically equilibrated by global impulsive reactions at the support. Different from a base-

supported tank, the location of the support moves from the base to the top. The resultant force of the horizontal p_{imp} acting on the wall (orange arrows) is balanced by the impulsive shear force at the top, F_{imp}, in the x direction. The impulsive pressure on the wall (orange arrows) generates a resultant moment at the center of the head (solid red circle) about the y axis (in a *clockwise* direction on the figure based on the right-hand rule), which is balanced by the impulsive moment, $M_{imp,w}$. The impulsive pressure on the base (pink arrows) generates a resultant moment at the center of the head in a *counterclockwise* direction, which is balanced by the impulsive moment, $M_{imp,b}$. Note that the impulsive moments, $M_{imp,w}$ and $M_{imp,b}$, in Figure 3.30 are both presented in a clockwise direction for reasons of consistency, although $M_{imp,w}$ has to be counterclockwise to balance the moment generated by p_{imp} on the wall. The analytical solutions of $M_{imp,w}$ presented in Sections 3.3.1.1 and 3.3.1.2 accommodate the direction defined in Figure 3.30, and so the values of $M_{imp,w}$ calculated using these solutions are generally negative.

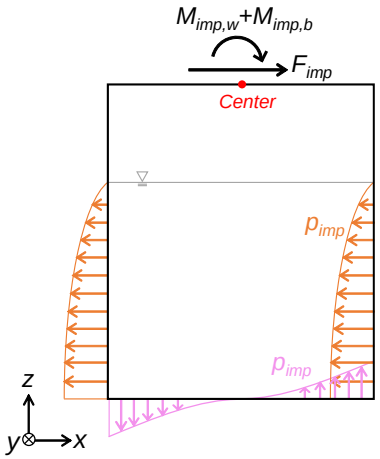

Figure 3.30. Impulsive responses: impulsive pressure, p_{imp}, on the walls and base of a tank; impulsive shear force at the top, F_{imp}; and impulsive moments at the top, $M_{imp,w}$ and $M_{imp,b}$; shown in a vertical cross section through a head-supported cylindrical tank accelerating in the x direction

Analytical solutions for the impulsive responses of a rigid and a flexible head-supported tank subjected to small-amplitude unidirectional horizontal motion are derived in this section, following the methodologies of Jacobsen (1949) and Veletsos (1984), respectively. A velocity potential for the contained fluid is used to derive exact solutions for both the rigid and flexible head-supported tanks. The fluid is assumed to be ideal. Modifications to Jacobsen's and Veletsos' methodologies are made to address the change in the boundary condition, where the support is moved from the base to the head. For a rigid tank, only the analytical solution for $M_{imp,w}$ is modified to accommodate the change in the vertical distance (i.e., the moment arm) from the center of p_{imp} on the wall to the support (i.e., base- to head-supported). For a flexible tank, the assumed lateral deformation of the tank used in the derivations is modified to recognize that the base is free to vibrate. This modification requires a complete analysis of the impulsive responses for the head-supported tank to derive the analytical solutions.

The variables used in this section are similar to those used in the derivations and the solutions for impulsive responses of a base-supported tank. The variables are presented here again in two views of a head-supported cylindrical tank in Figure 3.31, including: the radius of the tank, R; the height of the contained fluid, H; horizontal seismic motion input at the top, in terms of displacement, $u_0(t)$, velocity, $u_0'(t)$, and acceleration, $u_0''(t)$; velocities of an arbitrary point, pt, in the fluid, u', v', and w', along the three components of a cylindrical coordinate system (r, θ, z); and a Cartesian coordinate system (x, y, z). An additional variable used here is the height of the tank, H_s, which was not considered in the derivations for the impulsive responses of base-supported tanks in Jacobsen and Veletsos.

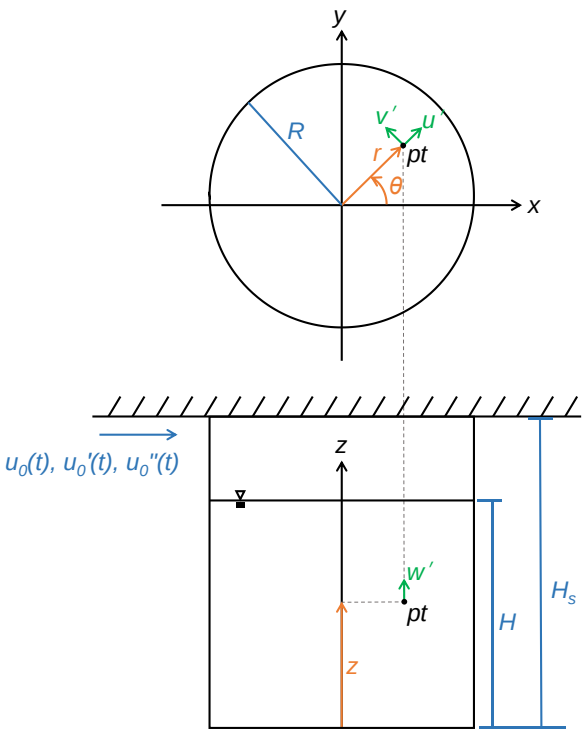

Figure 3.31. Variables used in the analytical solutions for impulsive response shown on two views of a head-supported cylindrical tank, a Cartesian coordinate system, and a cylindrical coordinate system

3.3.1.1 Rigid tank

Analytical solutions for the impulsive responses of a rigid, head-supported cylindrical tank are developed by modifying the solutions of Jacobsen (1949) for a rigid, base-supported cylindrical tank. The seismic input in the x direction at the support is moved from the base to the head of the tank. With no deformations in the rigid tank, the impulsive pressures on the inner surfaces of the tank are not affected by the location of the seismic input, and so the impulsive pressure on the wall and the base, $p_{imp,w}$ and $p_{imp,b}$, are identical to the solutions of Jacobsen per Eqs. (3.9) and (3.10) presented in Section 3.2.1.2, respectively. These impulsive pressures generate resultant forces and moments at the top of the tank. The impulsive shear forces at the top, F_{imp}, in the x direction equilibrates the resultant force calculated by integrating $p_{imp,w} \cdot \cos\theta$ over the area of the wall per Eq. (3.11). The impulsive moment at the top, $M_{imp,b}$, about the y axis equilibrates the resultant moment generated by the impulsive pressure on the base, $p_{imp,b}$. This resultant moment is the integral of $p_{imp,b}$ with a horizontal distance $r \cdot \cos\theta$ from the center of

the head over the area of the base, which makes $M_{imp,b}$ identical to Eq. (3.13). The impulsive moment at the top, $M_{imp,w}$, about the y axis equilibrates the resultant moment generated by the impulsive pressure on the wall, $p_{imp,w}$. The resultant moment is the integral of $p_{imp,w} \cdot \cos\theta$ with a vertical distance $(H_s - z)$ below the head over the area of the wall. The direction of $M_{imp,w}$ defined here is identical to the direction of the resultant moment generated by $p_{imp,w}$ (see Figure 3.30), and so $M_{imp,w}$ equals the resultant moment:

$$M_{imp,w} = \iint_{A_w} p_{imp,w} \cdot \cos\theta \cdot (H_s - z) \cdot dA_w = H_s \iint_{A_w} p_{imp,w} \cdot \cos\theta \cdot dA_w - \iint_{A_w} p_{imp,w} \cdot \cos\theta \cdot z \cdot dA_w \quad (3.120)$$

where the first integral on the right-hand side of Eq. (3.120) is $-F_{imp}$ per Eq. (3.11), and the second integral (including the minus sign at the front of the integral operator) is identical to $M_{imp,w}$ of a base-supported tank per Eq. (3.12). Applying Eqs. (3.11) and (3.12) to Eq. (3.120), the analytical solution of $M_{imp,w}$ is given as:

$$M_{imp,w} = u_0''(t) m_l \frac{H^2}{R} \sum_{i=1}^{\infty} \frac{16}{\left[(2i-1)\pi\right]^3} \frac{I_1\left[(2i-1)\frac{\pi}{2}\frac{R}{H}\right]}{I_1'\left[(2i-1)\frac{\pi}{2}\frac{R}{H}\right]} \cdot \left[-\frac{H_s}{H} + 1 - \frac{2(-1)^{i+1}}{(2i-1)\pi}\right] \quad (3.121)$$

Discussion

Impulsive responses are calculated using the analytical solutions for a rigid, head-supported cylindrical tank subjected to small-amplitude seismic motion, $u_0''(t)$, at the top in the x direction. The radius of the tank, R, is assumed to be 30 m. The contained fluid is assumed to be water, with a density, ρ, of 1000 kg/m^3. (The same values for R and ρ are assumed for calculating impulsive responses of a rigid, base-supported tank, presented in Section 3.2.1.2). Other dimensions (e.g., thickness of the wall of the tank) and mechanical properties (e.g., density and elastic modulus of the material) of the tank do not need to be defined for these calculations because the tank is rigid. The impulsive responses presented herein are normalized to be unitless using the method for normalizing the corresponding impulsive responses of the rigid base-supported tank in Section 3.2.1.2. The normalized results of $p_{imp,w}$, $p_{imp,b}$, F_{imp}, and $M_{imp,b}$ are independent of the dimensions of the tank and the fluid, H and R, the density of the fluid, ρ,

and the acceleration of the seismic motion, u_0''. The only variable for these normalized impulsive responses is the unitless ratio describing the dimensions of the tank and the fluid, H/R. However, the normalized results of $M_{imp,w}$ are independent of ρ and u_0'' but dependent on H and R because an additional variable representing the height of the tank, H_s, is introduced for the head-supported tank and makes the analytical solution of $M_{imp,w}$ not proportional to H and R (see Eq. (3.121)). The values of $M_{imp,w}$ are calculated and presented here for multiple dimensions of the tank and the fluid (i.e., H, R, and H_s) to populate the results.

The analytical solutions for $p_{imp,w}$, $p_{imp,b}$, F_{imp}, and $M_{imp,b}$ of a head-supported tank are identical to those of a base-supported tank derived in Jacobsen (1949), which the results were presented in Section 3.2.1.2 to be compared with other analytical solutions in prior studies (i.e., from Chalhoub and Kelly (1988), and Housner (1957)). These results are repeated here for the purpose of presenting a complete set of data for a head-supported cylindrical tank.

The impulsive pressures are calculated for a tank with $H/R = 0.5$, 1, and 2. Identical to the impulsive pressures in a base-supported tank, as the tank accelerates to the x direction, the greatest positive and negative impulsive pressures on the wall and the base of the tank are shown at $\theta = 180°$ and 0°, respectively. Values of the impulsive pressures at $\theta = 180°$ are presented here. The normalized impulsive pressures on the wall of the tank, $p_{imp,w}/\rho R u_0''$, along the normalized vertical direction, z/H, at $r = R$ and $\theta = 180°$, are presented in Figure 3.32a. The normalized impulsive pressures on the base of the tank, $p_{imp,b}/\rho R u_0''$, along the normalized radial direction, r/R, at $z = 0$ and $\theta = 180°$, are presented in Figure 3.32b.

The global impulsive reactions are calculated for a tank with $0.2 \le H/R \le 3$. The normalized impulsive shear forces at the top of the tank, $F_{imp}/m_l u_0''$, in the x direction are presented in Figure 3.33. The two components of the impulsive moments at the top of the tank, $M_{imp,w}$ and $M_{imp,b}$, about the y axis, normalized by $m_l H u_0''$, are presented in Figures 3.34a and b, respectively. The results of $M_{imp,w}$ in Figure 3.34a for a tank with $0.2 \le H/R \le 3$, are calculated based on two unitless variables: 1) H_s/R, which describes the dimensions of the tank (i.e., the aspect ratio of the tank), and 2) H/H_s, which is the ratio of the fluid height to the tank height,

termed hereafter the fill ratio of the tank. Six values of H_s / R in the range between 0.5 and 3 and nine values of H / H_s in the range between 0.2 and 1 (i.e., full tank) are considered in the calculation of $M_{imp,w}$. Given the dimensions of a tank, H_s and R, and ground motion, $u_0''(t)$, the impulsive moment, $M_{imp,w}$, at the top of the tank can be determined based on Figure 3.34a for a range of fluid heights, H.

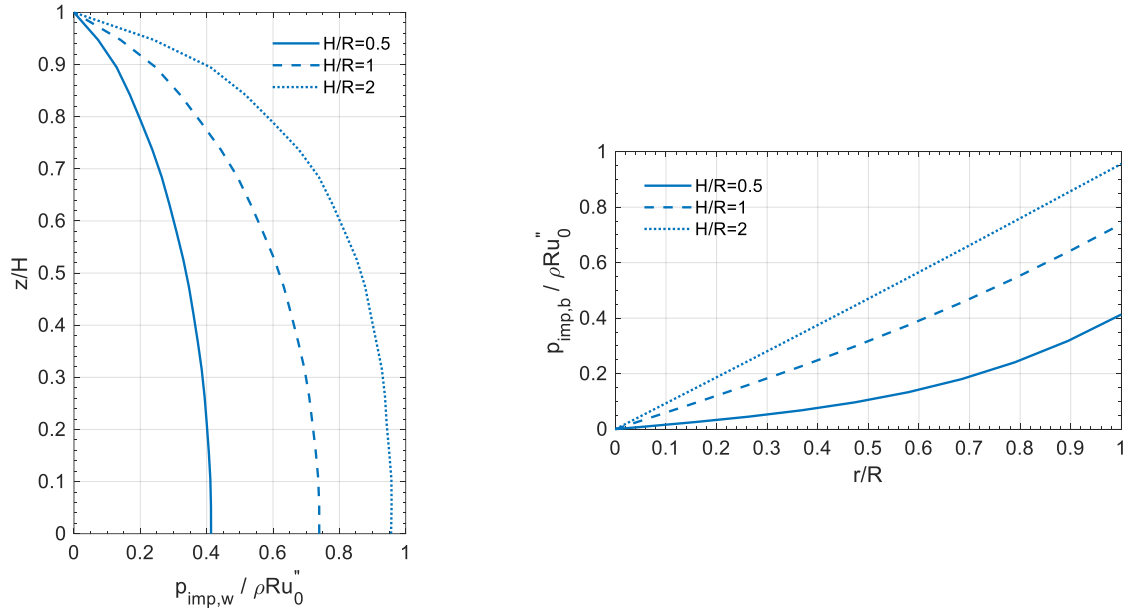

(a) $p_{imp,w} / \rho R u_0''$ along the normalized vertical direction, z / H, at $r = R$ and $\theta = 180°$, calculated using Eq. (3.9)

(b) $p_{imp,b} / \rho R u_0''$ along the normalized radial direction, r / R, at $z = 0$ and $\theta = 180°$, calculated using Eq. (3.10)

Figure 3.32. Normalized impulsive pressures on the wall and the base of a head-supported tank, $p_{imp,w} / \rho R u_0''$, and $p_{imp,b} / \rho R u_0''$, for $H / R = 0.5$, 1, and 2

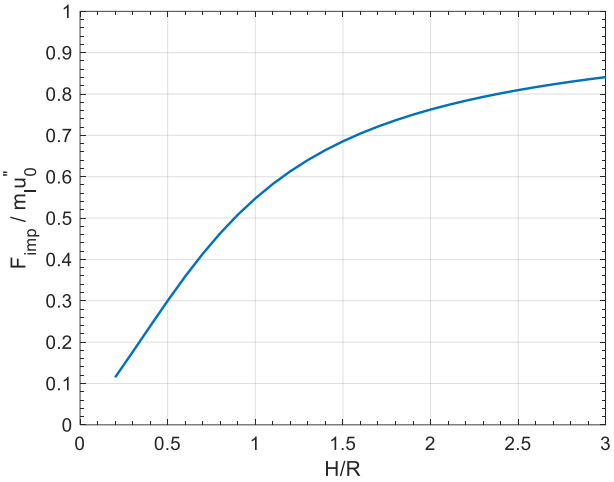

Figure 3.33. Normalized impulsive shear forces at the top of a head-supported tank, $F_{imp} / m_l u_0''$, in the x direction, for $0.2 \le H / R \le 3$, calculated using Eq. (3.11)

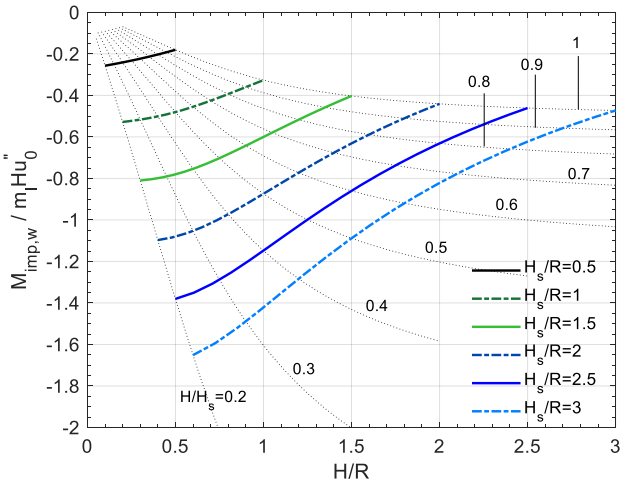

(a) $M_{imp,w} / m_l H u_0''$ for $0.2 \le H / H_s \le 1$ and $0.5 \le H_s / R \le 3$, calculated using Eq. (3.121)

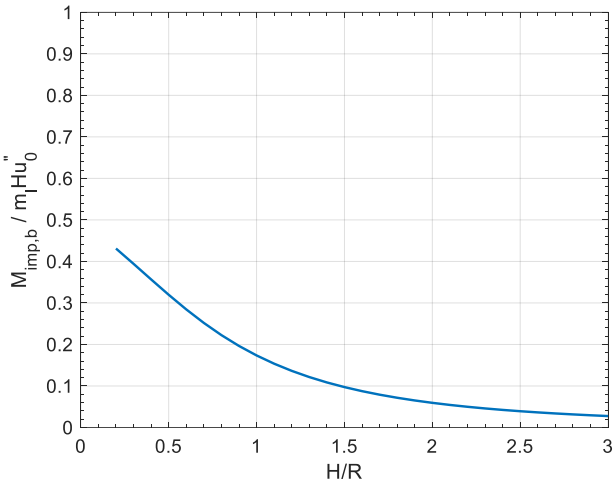

(b) $M_{imp,b} / m_l H u_0''$, calculated using Eq. (3.13)

Figure 3.34. Normalized impulsive moments at the top of a head-supported tank, $M_{imp,w} / m_l H u_0''$ and $M_{imp,b} / m_l H u_0''$, about the y axis, for $0.2 \le H / R \le 3$

3.3.1.2 Flexible tank

Analytical solutions for the impulsive responses of a flexible head-supported cylindrical tank are derived following the methodologies of Veletsos (1984) for a flexible base-supported cylindrical tank. Veletsos' methodology includes three main steps: 1) establishing an equation of motion for the impulsive responses of the tank, 2) decoupling the impulsive responses to modes using the equation of motion, and 3) deriving analytical solutions representing the modal impulsive responses. Moving the support from the base to the head changes the lateral deformation of the tank and the vertical distance (i.e., moment arm or lever arm) from the center of the impulsive pressure on the wall to the support, which generates a resultant moment at the top. The change in lateral deformation of the tank is addressed in the first step and the change in lever arm for generating moment at the support is addressed in the third step. The derivation presented here focuses on addressing these changes since a complete derivation for the flexible base-supported tank in Veletsos has been presented in Section 3.2.1.3.

The equation of motion for the impulsive responses of the head-supported tank is established using Lagrange's equation, considering 1) the kinetic energy of the fluid, K_l, 2) the kinetic energy of the tank, K_s, 3) the strain energy of the tank, S_s, and 4) the external energy associated with the input ground motion, W_{ext}. To calculate four energies using Eqs. (3.43), (3.47), (3.48), and (3.49), displacements of the wall of the tank need to be determined.

The radial, tangential and axial displacements, u_s, v_s, and w_s, on the wall of the head-supported tank are calculated by extrapolating the assumed lateral displacements of the axial centerline of the tank to the wall. The calculations assume that the horizontal cross section of the tank remains plane and circular as the tank deforms laterally. Veletsos assumed the lateral displacements of the axial centerline of a base-supported tank to be a linear superposition of multiple modal shapes of a cantilever, $\psi_i(z)$, fixed at the bottom, with a length identical to the height of the tank, presented in Figure 3.10. For a head-supported tank, the modal shapes of a cantilever fixed at the top, with a length identical to the height of the tank, are used in the calculation of the lateral displacements of the axial centerline of the tank. The modal shapes used for the base-supported tank in Veletsos are inverted for the head-supported tank, which is achieved by substituting $H_S - z$ for z in the function of the modal shapes, $\psi_i(z)$. The modal shapes used for the head-

supported tank, $\psi_i(H_s - z)$, in the first two modes (i.e., $i = 1$ and 2) are presented in Figure 3.35, together with $\psi_i(z)$ in the first two modes.

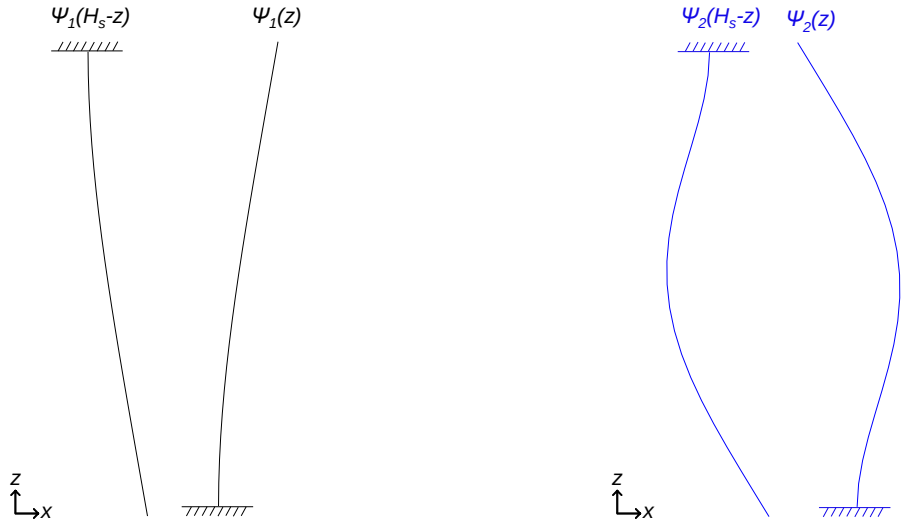

(a) first mode (b) second mode

Figure 3.35. Modal shapes of the cantilever for the displacement of the axial centerline of a head-supported tank, $\psi_i(H_s - z)$ and those of a base-supported tank, $\psi_i(z)$, used in Veletsos

Accordingly, the radial, tangential and axial displacements, u_s, v_s, and w_s, on the wall of the head-supported tank are calculated by substituting $\psi_i(H_s - z)$ for $\psi_i(z)$ in Eqs. (3.40), (3.41), and (3.42), respectively:

$$u_s(t, z, \theta) = \sum_{i=1}^{\infty} U_i(t)\psi_i(H_S - z)\cos\theta \tag{3.122}$$

$$v_s(t, z, \theta) = \sum_{i=1}^{\infty} V_i(t)\psi_i(H_S - z)\sin\theta \tag{3.123}$$

$$w_s(t, z, \theta) = \sum_{i=1}^{\infty} W_i(t)\psi_i'(H_S - z)\cos\theta \tag{3.124}$$

where U_i, V_i, and W_i are coefficients for the modal shapes in the i th mode for the linear superposition, which are the degrees of freedom in the equation of motion. The motions of the

tank are determined by solving U_i, V_i, and W_i in the equation of motion and applying them to Eqs. (3.122), (3.123), and (3.124). (More details can be found in Section 3.2.1.3).

The kinetic energy of the tank, K_s, the strain energy of the tank, S_s, and the external energy associated with the input ground motion, W_{ext} are calculated using the displacements of the wall (i.e., u_s, v_s, and w_s) through Eq. (3.47), (3.48), and (3.49), respectively. The velocities of the fluid, u', v', and w' are needed for the calculations of the kinetic energy of the fluid, K_l, per Eq. (3.43). A velocity potential for the impulsive response of the fluid, Φ_{imp}, is used to calculate the velocities of the fluid. The velocity potential, Φ_{imp}, is assumed to be the product of the four unknown functions, $\tilde{R}$, $\tilde{\Theta}$, $\tilde{Z}$, and $\tilde{T}$, associated with the four variables, r, θ, z, and t, respectively (i.e., three components of the cylindrical coordinate system and time). Three boundary conditions for the fluid are used to solve these four functions. The fluid adjacent to the wall of the tank (i.e., at $r = R$) is assumed to move with the wall at the same radial velocity. The radial velocity of the fluid u' is calculated using Eq. (3.2) and the radial velocity of the tank is the first derivative of u_s in Eq. (3.122) with respect to t:

$$u'(r=R) = \left.\frac{\partial \Phi_{imp}}{\partial r}\right|_{r=R} = U_i'(t)\psi_i(H_s - z)\cos\theta \tag{3.125}$$

The other two boundary conditions used here are identical to two of the boundary conditions used in Veletsos: 1) zero impulsive pressure on the initial free surface per Eq. (3.5), and 2) zero vertical velocity of the fluid adjacent to the base of the tank per Eq. (3.7), which is applied to the head-supported tank based on the assumption that the rocking motion of the base due to small-amplitude horizontal input motion at the head is negligible.

The functions, $\tilde{R}$, $\tilde{\Theta}$, $\tilde{Z}$, and $\tilde{T}$, are solved using Eqs. (3.125), (3.5) and (3.7), and the velocity potential for the impulsive responses, Φ_{imp}, is:

$$\Phi_{imp} = H\cos\theta \sum_{i=1}^{\infty} U_i''(t) \sum_{j=1}^{\infty} \frac{4}{(2j-1)\pi} \frac{I_1\left[(2j-1)\frac{\pi}{2}\frac{r}{H}\right]}{I_1'\left[(2j-1)\frac{\pi}{2}\frac{R}{H}\right]} \cos\left[(2j-1)\frac{\pi}{2}\frac{z}{H}\right] \cdot \alpha_{ij} \tag{3.126}$$

$$\alpha_{ij} = \frac{1}{H}\int_0^H \psi_i(H_s - z)\cdot\cos\left[(2j-1)\frac{\pi}{2}\frac{z}{H}\right]dz \tag{3.127}$$

Given the velocity potential, the velocities of the fluid are calculated using Eq. (3.2), and then K_l is determined through Eq. (3.43).

The equation of motion of the tank is derived using Lagrange's equation with the four virtual energies, K_l, K_s, S_s, and W_{ext}, per Eq. (3.50), where d_i in the equation represents a degree of freedom (i.e., U_i, V_i, or W_i). Given the mass and stiffness matrices of the equation of motion, $[M]$ and $[K]$, frequencies and modal shapes in different impulsive modes are calculated using Eq. (3.128).

$$[K]\{\phi_k\} = \left(\frac{f_{imp,k}}{2\pi}\right)^2 [M]\{\phi_k\} \tag{3.128}$$

where $f_{imp,k}$ and $\{\phi_k\}$ are the frequency and the modal shape in the k th impulsive mode, respectively. The modal shape, $\{\phi_k\}$, enables a transformation of the mass matrix, $[M]$, the stiffness matrix, $[K]$, and the external force vector (associated with the input motion), $u_0''(t)\{P_{ext}\}$, in the equation of motion to modal coordinates and yields the *modal* mass matrices, *modal* stiffness matrices, and the *modal* force vectors, respectively, to represent multiple independent impulsive modes. The degree of freedom, d_i, is related to the modal coordinate, q_i, using the modal shape, ϕ_{ik}, in the k th mode:

$$d_i = \phi_{ik}\cdot q_k = \phi_{ik}\cdot e_k \frac{1}{\omega_{imp,k}}\int_0^t u_0''(\tau)\cdot\sin\omega_{imp,k}(t-\tau)d\tau \tag{3.129}$$

where q_k is calculated using Duhamel's integral (the third term in the equation), $\omega_{imp,k}$ is $f_{imp,k}/2\pi$, and e_k is the modal participation factor:

$$e_k = \frac{\{\phi_k\}^T\{P_{ext}\}}{\{\phi_k\}^T[M]\{\phi_k\}} \tag{3.130}$$

According to Eq. (3.129), d_i'' is related to q_k'' per Eq. (3.131), and q_k'' is approximated using a pseudo quantity back calculated from q_k per Eq. (3.132):

$$d_i'' = \phi_{ik} \cdot q_k'' \tag{3.131}$$

$$q_k'' \approx \omega_{imp,k}{}^2 \cdot q_k = e_k \cdot A_k(t) \tag{3.132}$$

$$A_k(t) = \omega_{imp,k} \int_0^t u_0''(\tau) \cdot \sin \omega_{imp,k}(t-\tau) d\tau \tag{3.133}$$

The velocity potential associated in the kth impulsive mode is computed by substituting d_i'' per Eq. (3.131) for U_i'' in Eq. (3.126). The impulsive pressure, p_{imp}, at an arbitrary location in the fluid and on the wall or the base of the tank is determined using Eq. (3.1). The impulsive pressure on the wall (i.e., at $r = R$) of the tank associated with the kth mode, along the vertical and the circumferential directions, z and θ, is given as:

$$p_{imp,w,k} = -A_k(t) \cdot \rho H \cos\theta e_k \sum_{i=1}^{N_1} \phi_{ik} \sum_{j=1}^{\infty} \frac{4}{(2j-1)\pi} \frac{I_1\left[(2j-1)\frac{\pi}{2}\frac{R}{H}\right]}{I_1'\left[(2j-1)\frac{\pi}{2}\frac{R}{H}\right]} \cos\left[(2j-1)\frac{\pi}{2}\frac{z}{H}\right] \cdot \alpha_{ij} \tag{3.134}$$

where α_{ij} is defined in Eq. (3.127). The impulsive pressure on the base of the tank (i.e., at $z = 0$) associated with the kth mode, along the radial and the circumferential directions, r and θ, is given as:

$$p_{imp,b,k} = -A_k(t) \cdot \rho H \cos\theta e_k \sum_{i=1}^{N_1} \phi_{ik} \sum_{j=1}^{\infty} \frac{4}{(2j-1)\pi} \frac{I_1\left[(2j-1)\frac{\pi}{2}\frac{r}{H}\right]}{I_1'\left[(2j-1)\frac{\pi}{2}\frac{R}{H}\right]} \cdot \alpha_{ij} \tag{3.135}$$

The impulsive shear force at the top of the tank, $F_{imp,k}$, associated with the kth mode in the x direction, equilibrates the resultant force generated by $p_{imp,w,k}$ on wall of the tank:

$$F_{imp,k} = -\iint_{A_w} p_{imp,w,k} \cdot \cos\theta \cdot dA_w = A_k(t) \cdot m_l \frac{H}{R} e_k \sum_{i=1}^{N_1} \phi_{ik} \sum_{j=1}^{\infty} \frac{8(-1)^{j+1}}{\left[(2j-1)\pi\right]^2} \frac{I_1\left[(2j-1)\frac{\pi}{2}\frac{R}{H}\right]}{I_1'\left[(2j-1)\frac{\pi}{2}\frac{R}{H}\right]} \cdot \alpha_{ij} \tag{3.136}$$

where A_w is the area of the wall. The impulsive moment at the top of the tank, $M_{imp,b,k}$, in the kth mode about the y axis, equilibrates the resultant moment generated by $p_{imp,b,k}$ on the base of the tank with a horizontal distance $r \cdot \cos\theta$ from the center of the head:

$$M_{imp,b,k} = -\iint_{A_b} p_{imp,b,k} \cdot \cos\theta \cdot r \cdot dA_b = A_k(t) \cdot m_l H e_k \sum_{i=1}^{N_1} \phi_{ik} \sum_{j=1}^{\infty} \frac{8}{\left[(2j-1)\pi\right]^2} \frac{I_2\left[(2j-1)\frac{\pi}{2}\frac{R}{H}\right]}{I_1'\left[(2j-1)\frac{\pi}{2}\frac{R}{H}\right]} \cdot \alpha_{ij} \quad (3.137)$$

These analytical solutions for $p_{imp,w,k}$, $p_{imp,b,k}$, $F_{imp,k}$, and $M_{imp,b,k}$ of the head-supported tank presented here *seem* identical to the corresponding solutions of Veletsos for the base-supported tank per Eqs. (3.59), (3.60), (3.61), and (3.63), respectively. However, α_{ij} used in the solutions for the head-supported tank is associated with $\psi_i(H_s - z)$ per Eq. (3.127) and the values of e_k and ϕ_{ik} used in the solutions for the head-supported tank, which are calculated through modal analysis of the equation of motion, are different from those used for the base-supported tank. The results of $p_{imp,w,k}$, $p_{imp,b,k}$, $F_{imp,k}$, and $M_{imp,b,k}$ in Veletsos for the base-supported tank do not apply to the head-supported tank.

The impulsive moment at the top, $M_{imp,w,k}$, about the y axis equilibrates the resultant moment generated by the impulsive pressure on the wall, $p_{imp,w,k}$, with a vertical distance $H_s - z$ below the head. The direction of $M_{imp,w,k}$ defined here and the direction of the resultant moment are identical (see Figure 3.30), and so $M_{imp,w,k}$ equals the resultant moment:

$$M_{imp,w,k} = \iint_{A_w} p_{imp,w,k} \cdot \cos\theta \ (H_s - z) \cdot dA_w = H_s \iint_{A_w} p_{imp,w,k} \cos\theta \cdot dA_w - \iint_{A_w} p_{imp,w,k} \cos\theta \cdot z \cdot dA_w \quad (3.138)$$

The first integral on the right-hand side of Eq. (3.138) is $-F_{imp,k}$ per Eq. (3.136) and the second integral (including the minus sign at the front of the integral operator) is identical to $M_{imp,w,k}$ of a base-supported tank per Eq. (3.62). Substituting Eqs. (3.136) and (3.62) into Eq. (3.138), $M_{imp,w,k}$ of the head-supported tank is given as:

$$M_{imp,w,k} = A_k(t) \cdot m_l \frac{H^2}{R} e_k \sum_{i=1}^{N_1} \phi_{ik} \sum_{j=1}^{\infty} \frac{8(-1)^{j+1}}{\left[(2j-1)\pi\right]^2} \frac{I_1\left[(2j-1)\frac{\pi}{2}\frac{R}{H}\right]}{I_1'\left[(2j-1)\frac{\pi}{2}\frac{R}{H}\right]} \cdot \alpha_{ij} \cdot \left[-\frac{H_s}{H} + 1 - \frac{2(-1)^{j+1}}{(2j-1)\pi}\right] \quad (3.139)$$

Discussion

Impulsive responses are calculated using the analytical solutions for a flexible, head-supported cylindrical tank subjected to small-amplitude seismic motion, $u_0''(t)$, of the head in the x direction. The dimensions and mechanical properties of the tank and the fluid considered here are identical to those in the calculations of impulsive responses of a flexible, cylindrical base-supported tank presented in Section 3.2.1.3. The tank is assumed to be fabricated from carbon steel and the contained fluid is assumed to be water, for which the mechanical properties are listed in Table 3.5, including the elastic modulus, E, Poisson's ratio, υ, the density, ρ_s, of the steel, and the density of the contained fluid, ρ. The radius of the tank, R, is assumed to be 30 m, and the thickness of the wall of the tank, h, is assumed to be $0.001R$.

The impulsive responses presented herein are normalized to be unitless using the method for normalizing the corresponding impulsive responses of a flexible, base-supported tank in Section 3.2.1.3. The normalized results are *insensitive* (see footnote 25 on page 75) to the mechanical properties of the tank and the fluid (i.e, E, υ, ρ_s, and ρ) and independent of the acceleration time series, $A_k(t)$, of the kth impulsive mode associated with the seismic motion, $u_0''(t)$. The normalized results are dependent on the dimensions of the tank and the fluid, H and R, because the derivations for the head-supported tank include a variable representing the height of the tank, H_s, which makes the analytical solutions not proportional to H and R. The impulsive responses are calculated and presented here for multiple dimensions of the tank and the fluid (i.e., H, R, and H_s) to populate the results. The impulsive pressures, $p_{imp,w}$ and $p_{imp,b}$, are calculated for $H/R = 0.5$, 1, and 2; the impulsive frequency, f_{imp}, and a unitless coefficient, C_{imp}, representing f_{imp}, the impulsive shear force, F_{imp}, and the impulsive moments, $M_{imp,w}$ and $M_{imp,b}$, are calculated for $0.2 \le H/R \le 3$. For this range of H/R, six aspect ratios of the tank, H_s/R, between 0.5 and 3 and nine fill ratio, H/H_s, between 0.2 and 1 (i.e., full tank) are

considered in these calculations. This section presents values of $f_{imp,k}$, $C_{imp,k}$, $p_{imp,w,k}$, $p_{imp,b,k}$, $F_{imp,k}$, $M_{imp,w,k}$, and $M_{imp,b,k}$ in the first three modes (i.e., $k = 1$ to 3) for $H_s = H$ (i.e., $H / H_s = 1$, full tank). The coefficient of the impulsive frequency, $C_{imp,1}$, and the global impulsive reactions, $F_{imp,1}$, $M_{imp,w,1}$, and $M_{imp,b,1}$, in the first mode are presented for multiple values of H_s / R and H / H_s.

Figures 3.36a and b present the impulsive frequencies, $f_{imp,k}$, and the coefficients of the impulsive frequency, $C_{imp,k}$, respectively, associated with the first three impulsive modes (i.e., $k = 1$ to 3), calculated for a tank with $0.2 \le H / R \le 3$ and $H / H_s = 1$. The impulsive frequency, $f_{imp,k}$, in the kth mode is related to the coefficient, $C_{imp,k}$, as follows:

$$f_{imp,k} = C_{imp,k} \frac{1}{R} \sqrt{\frac{Eh}{\rho R}} \tag{3.140}$$

where $C_{imp,k}$ is unitless and dependent on only the variable H / R. Comparing the impulsive frequencies, $f_{imp,k}$, in the first three modes (i.e., $k = 1$ to 3) of a head-supported tank shown in Figure 3.36a and those of a base-supported tank shown in Figure 3.11a, with both tanks full ($H / H_s = 1$), $R = 30$ m, and $h = 0.001 R$, the values of $f_{imp,k}$ of the head-supported tank are generally lower than those of a base-supported tank for the range of H / R considered here. The coefficients of the impulsive frequency in the first mode, $C_{imp,1}$, for multiple values of H_s / R and H / H_s are presented in a linear format in Figure 3.37a, and also a linear-logarithmic format in Figure 3.37b to better differentiate results for different values of H / H_s.

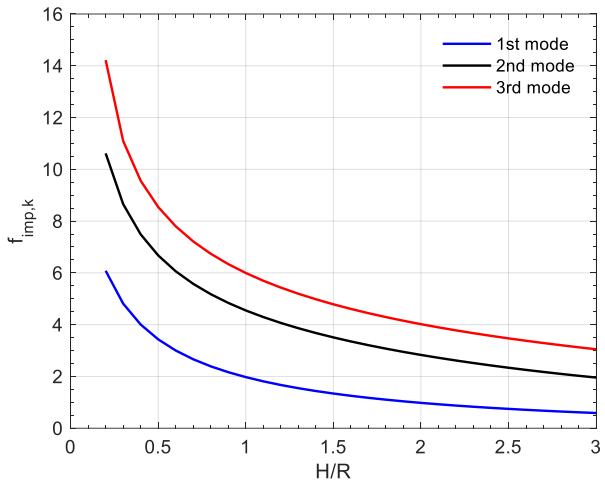

(a) $f_{imp,k}$, $R = 30$ m, $h = 0.001\,R$, and the mechanical properties listed in Table 3.5, calculated using Eq. (3.128)

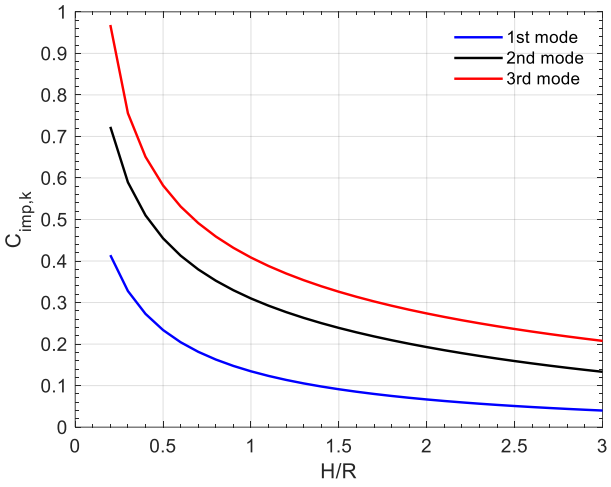

(b) $C_{imp,k}$, calculated using Eq. (3.140) and $f_{imp,k}$ in panel (a)

Figure 3.36. Impulsive frequencies, $f_{imp,k}$, and coefficients of impulsive frequency, $C_{imp,k}$, associated with the first three impulsive modes (i.e., $k = 1$ to 3), for $0.2 \le H/R \le 3$, $H/H_s = 1$, head-supported tank

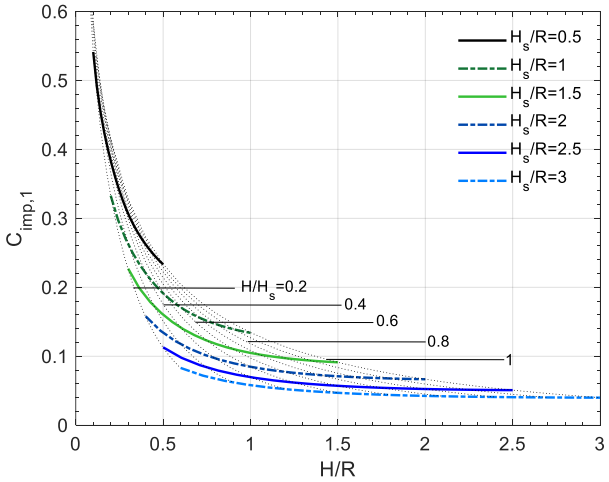

(a) linear scale

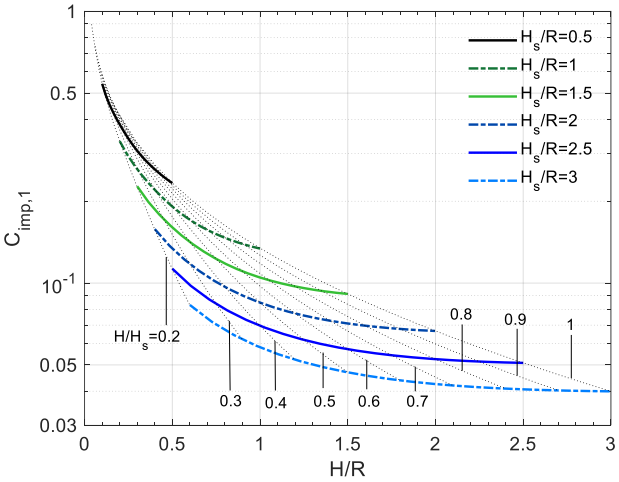

(b) linear-logarithmic scale

Figure 3.37. Coefficients of impulsive frequency in the first mode, $C_{imp,1}$, for $0.2 \le H/R \le 3$, $0.5 \le H_s/R \le 3$, $0.2 \le H/H_s \le 1$, head-supported tank

The impulsive pressures, $p_{imp,k}$, in the first three modes (i.e., $k=1$, 2, and 3) are presented in Figures 3.38 and 3.39 for a tank with $H/R=0.5$, 1, and 2 and $H/H_s=1$. The normalized impulsive pressures on the wall of the tank, $p_{imp,w,k}/\rho RA_k$, along the normalized vertical direction, z/H, at $r=R$ and $\theta=180°$, are presented in Figure 3.38. The normalized impulsive pressures on the base of the tank, $p_{imp,b,k}/\rho RA_k$, along the normalized radial direction, r/R, at $z=0$ and $\theta=180°$, are presented in Figure 3.39. The results presented in Figures 3.38 and 3.39 indicate that 1) given an order of the impulsive mode (i.e., $k=1$, 2, or 3), the amplitudes of $p_{imp,w,k}/\rho RA_k$ and $p_{imp,b,k}/\rho RA_k$ increase with increasing H/R, and 2) given a value of H/R (i.e., 0.5, 1, or 2), the amplitudes of $p_{imp,w,k}/\rho RA_k$ and $p_{imp,b,k}/\rho RA_k$ are the greatest in the first mode. These two conclusions are also drawn for the impulsive pressures on the wall and the base of a base-supported tank: see Figures 3.12 and 3.13. Different from the base-supported tank, the greatest impulsive pressures in the first mode of the head-supported tank are always at the edge of the wall and the base (i.e., $z=0$ and $r=R$) for all three values of H/R.

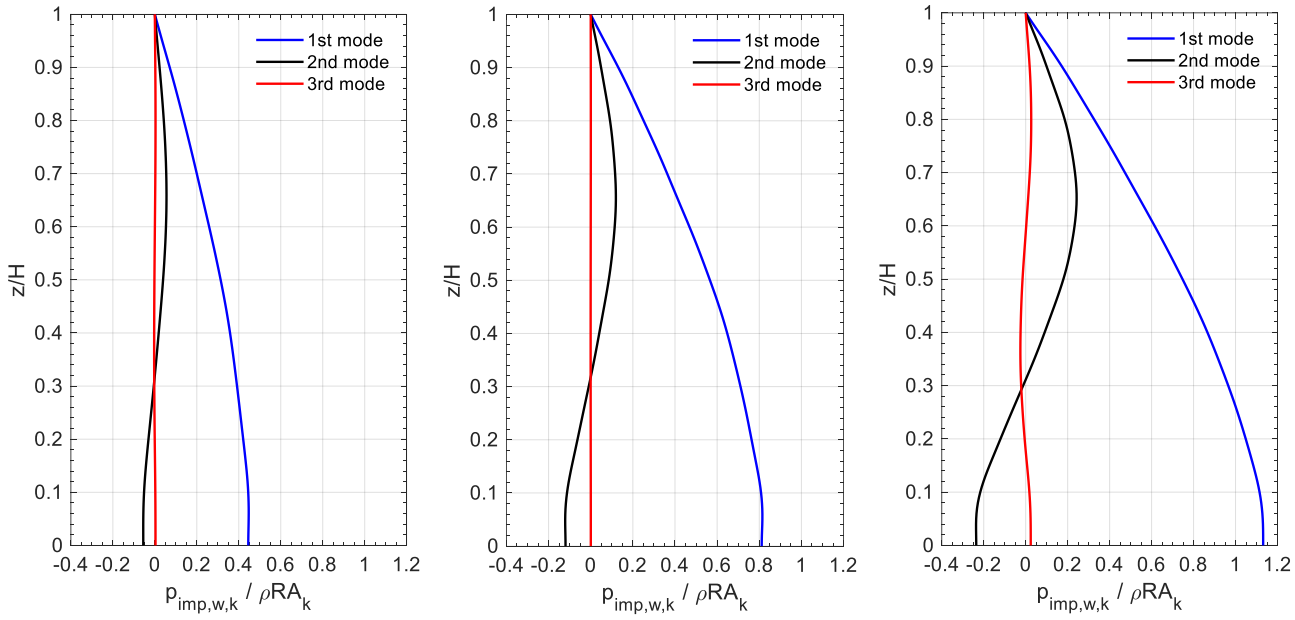

(a) H/R=0.5 (b) H/R=1 (c) H/R=2

Figure 3.38. Normalized impulsive pressures on the wall of a head-supported tank, $p_{imp,w,k}/\rho RA_k$, associated with the first three modes (i.e., $k=1$ to 3), along the normalized vertical direction, z/H, at $r=R$ and $\theta=180°$, for $H/R=0.5$, 1, and 2 and $H/H_s=1$, calculated using Eq. (3.134)

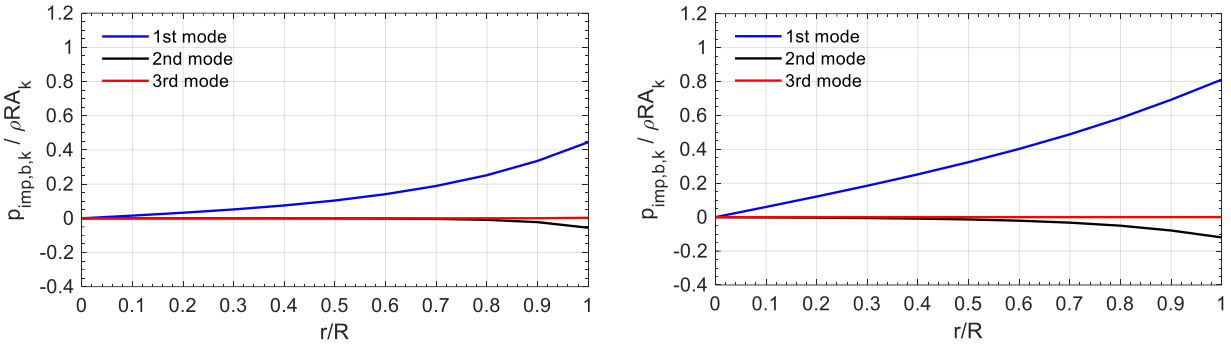

(a) H/R=0.5 (b) H/R=1

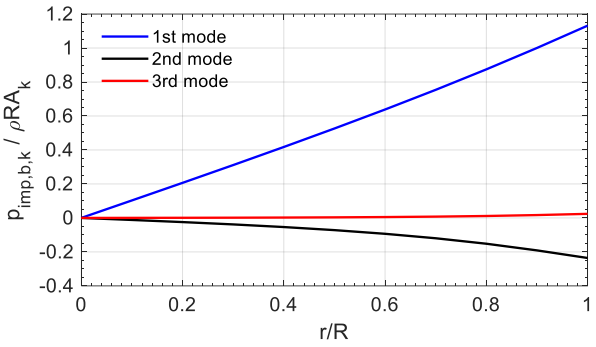

(c) H/R=2

Figure 3.39. Normalized impulsive pressure on the base of a head-supported tank, $p_{imp,b,k}/\rho RA_k$, associated with the first three modes (i.e., $k=1$ to 3), along the normalized radial direction, r/R, at $z=0$ and $\theta=180°$, for $H/R=0.5$, 1, and 2, and $H/H_s=1$, calculated using Eq. (3.135)

The global impulsive reactions, $F_{imp,k}$, $M_{imp,w,k}$, and $M_{imp,b,k}$, in the first three impulsive modes (i.e., $k=1$ to 3) are presented for a tank with $0.2 \le H/R \le 3$ and $H/H_s=1$ (i.e., full tank). The reactions in the first mode, $F_{imp,1}$, $M_{imp,w,1}$, and $M_{imp,b,1}$, are further presented for a tank with multiple aspect ratios, H_s/R, and fill retios, H/H_s. The normalized impulsive shear forces at the top of the tank, $F_{imp,k}/m_l A_k$, in the x direction are presented in Figure 3.40. Figure 3.40a presents results for the first three impulsive modes for a full tank and Figure 3.40b presents results in the first impulsive mode for multiple values of H_s/R and H/H_s. Figure 3.40b shows that the influence of H_s/R and H/H_s on $F_{imp,1}/m_l A_1$ is insignificant. Labels for $H/H_s<0.6$

are not shown in the figure. The impulsive moments at the top of the tank, $M_{imp,w,k}$ and $M_{imp,b,k}$, about the y axis, normalized by $m_l HA_k$, are presented in Figures 3.41 and 3.42, respectively. Figures 3.41a and 3.42a present results in the first three impulsive modes for a full tank. The results of $M_{imp,w,1}/m_l HA_1$ in the first impulsive mode for multiple values of H_s/R and H/H_s are presented in a linear format in Figure 3.41b, and also a linear-logarithmic format in Figure 3.41c to better differentiate results for $H/H_s = 0.8$, 0.9, and 1. Given the dimensions of a tank, H_s and R, and ground motion, $u_0''(t)$, the impulsive moment, $M_{imp,w,1}$, at the top of the tank can be determined using Figures 3.41b and c for a range of fluid heights, H. Figure 3.41b presents the normalized impulsive moments in the first mode, $M_{imp,b,1}/m_l HA_1$, calculated for multiple values of H_s/R and H/H_s. The results show that the influence of H_s/R and H/H_s on $M_{imp,b,1}/m_l HA_1$ to be negligible. Labels are presented only for H/H_s equal to 0.2 and 1 in the figure.

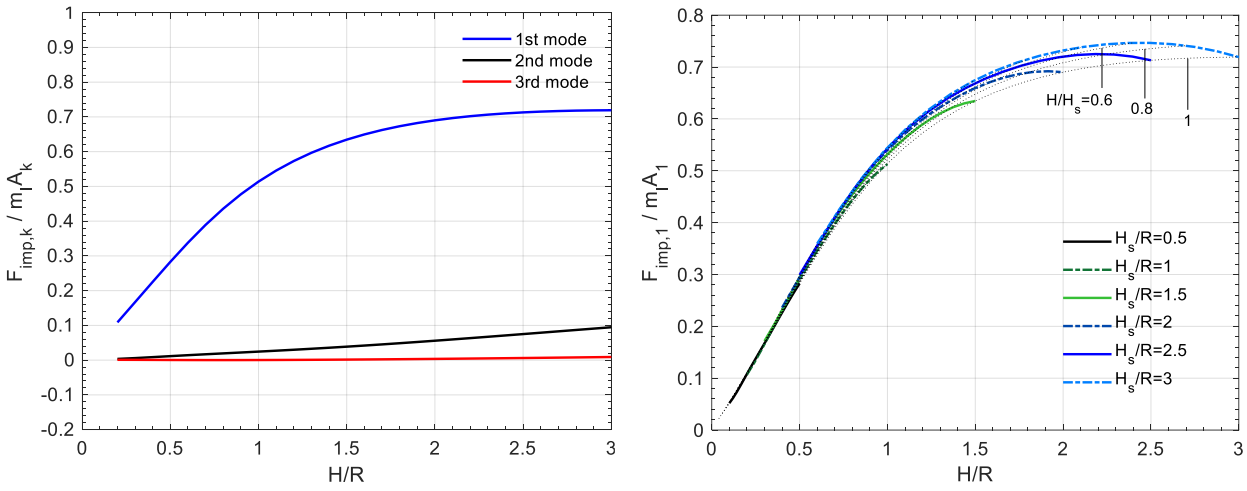

(a) first three modes ($k = 1$ to 3), $H/H_s = 1$

(b) first mode, for $0.5 \le H_s/R \le 3$ and $0.2 \le H/H_s \le 1$

Figure 3.40. Normalized impulsive shear force at the top of a head-supported tank, $F_{imp,k}/m_l A_k$, in the x direction for $0.2 \le H/R \le 3$, calculated using Eq. (3.136)

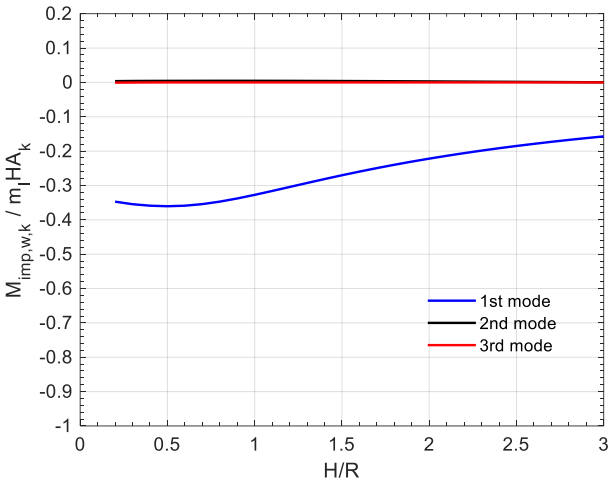

(a) first three modes ($k = 1$ to 3), $H / H_s = 1$

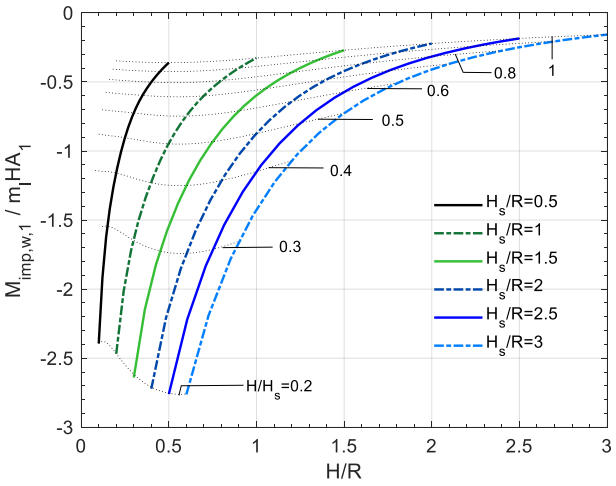

(b) first mode, linear scale, $0.5 \le H_s / R \le 3$ and $0.2 \le H / H_s \le 1$

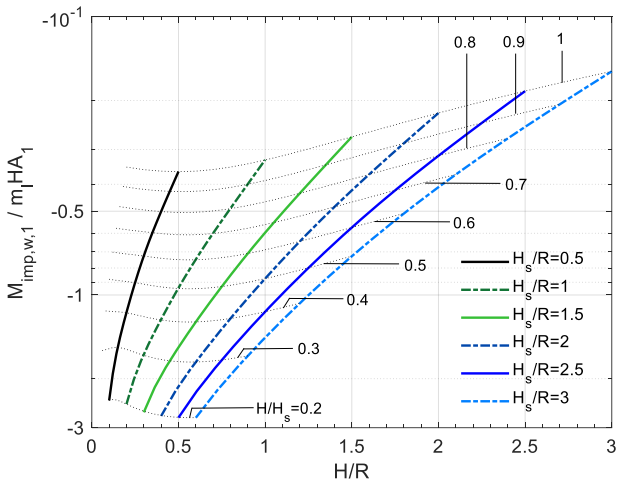

(c) first mode, linear-logarithmic scale, $0.5 \le H_s / R \le 3$ and $0.2 \le H / H_s \le 1$

Figure 3.41. Normalized impulsive moments at the top of a head-supported tank, $M_{imp,w,k} / m_l H A_k$, about the y axis for $0.2 \le H / R \le 3$, calculated using Eq. (3.139)

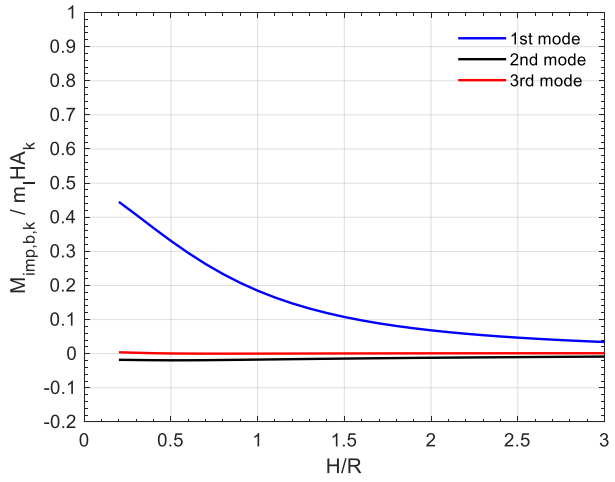

(a) first three modes ($k = 1$ to 3), $H / H_s = 1$

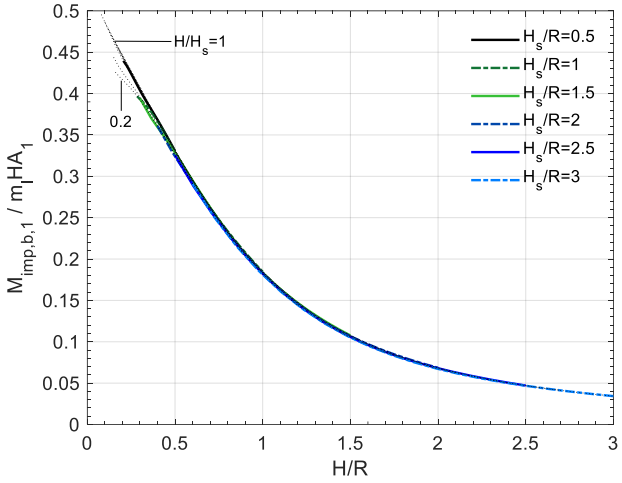

(b) first mode, $0.5 \le H_s / R \le 3$ and $0.2 \le H / H_s \le 1$

Figure 3.42. Normalized impulsive moments at the top of a head-supported tank, $M_{imp,b,k} / m_l HA_k$, about the y axis for $0.2 \le H / R \le 3$, calculated using Eq. (3.137)

3.3.2 Convective responses

Figure 3.43 shows convective responses in a vertical cross section through a head-supported cylindrical tank accelerating in the x direction. Similar to the base-supported tank shown in Figure 3.20, the free surface vertically displaces, d_w, and the convective pressure, p_{imp}, is generated on the wall and the base of the tank. Identical to the impulsive responses in a head-supported tank, these convective pressures, p_{con}, on the wall and the base of the tank are mechanically equilibrated by global convective reactions at the top. The resultant force of the horizontal p_{con} on the wall (green arrows) is balanced by the convective shear force at the top, F_{con}, in the x direction. The convective pressure on the wall (green arrows) and that on the base (blue arrows) generate resultant moments at the center of the head (solid red circle), which are balanced by the convective moments, $M_{con,w}$ and $M_{con,b}$, about the y axis (in a clockwise direction), respectively. The direction of $M_{con,w}$ is counterclockwise to balance the resultant moment at the top generated by p_{con} on the wall. The analytical solution of $M_{con,w}$ presented in Section 3.3.2.1 accommodates the direction defined in Figure 3.43, and so the values of $M_{con,w}$ calculated using this solution are negative.

Analytical solutions for the convective responses of a rigid, head-supported cylindrical tank subjected to unidirectional horizontal motion of a small amplitude are adapted from the solutions of Veletsos (1984) for a rigid, base-supported cylindrical tank. The convective pressures on the wall and the base of a rigid tank are not affected by the change of boundary conditions (i.e., base- to head-supported). Only the analytical solution for $M_{con,w}$ is modified to accommodate the change of the vertical distance (i.e., moment arm) from the center of p_{con} on the wall to the support. The analytical solutions developed for a rigid tank can also be applied to a flexible tank since convective responses are independent of the flexibility of the tank. The variables used in the solutions here are identical to those used in the solutions of impulsive responses shown in Figure 3.31.

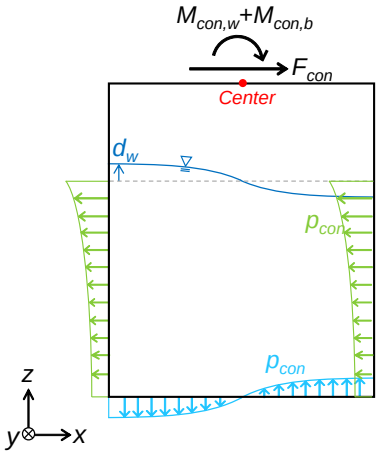

Figure 3.43. Convective responses: vertical displacement of the free surface, d_w; convective pressure, p_{con}, on the walls and base of a tank; convective shear force, F_{con}, at the top; and convective moments, $M_{con,w}$ and $M_{con,b}$, at the top; shown in a vertical cross section through a head-supported cylindrical tank accelerating in the x direction

3.3.2.1 Rigid tank

The analytical solutions for convective responses of a rigid, head-supported cylindrical tank are developed by modifying the solutions of Veletsos (1984) for a rigid, base-supported cylindrical tank. Only the analytical solution for the convective moment at the top generated by the convective pressure on the wall is affected by moving the support (i.e. base- to head-supported), due to the change in the lever arm. Other convective responses of the head-supported tank are identical to the corresponding solutions of Veletsos presented in Section 3.2.2.2, and so the

convective frequency of the head-supported tank, $f_{con,j}$ in the j th mode is Eq. (3.73); the convective pressure on the wall, $p_{con,w,j}$, is Eq. (3.79); the convective pressure on the base, $p_{con,b,j}$, is Eq. (3.80); the vertical displacement of the free surface, $d_{w,j}$, is Eq. (3.81); the convective shear force at the top of the tank, $F_{con,j}$, in the x direction is Eq. (3.82); the convective moment at the top of the tank, $M_{con,b,j}$, about the y axis that equilibrates the resultant moment generated by $p_{con,b,j}$ is Eq. (3.84). Those equations are not repeated here. The convective moment at the top, $M_{con,w,j}$, about the y axis equilibrates the resultant moment generated by $p_{con,w,j}$ with a vertical distance $(H_s - z)$ below the head. The direction of $M_{con,w,j}$ defined here is identical to the direction of the resultant moment (see Figure 3.43), and so $M_{con,w}$ is given as:

$$M_{con,w,j} = \iint_{A_w} p_{con,w,j} \cdot \cos\theta \cdot (H_s - z) \cdot dA_w = H_s \iint_{A_w} p_{con,w,j} \cdot \cos\theta \cdot dA_w - \iint_{A_w} p_{con,w,j} \cdot \cos\theta \cdot z \cdot dA_w \quad (3.141)$$

where the first integral on the right-hand side of Eq. (3.141) is $-F_{con,j}$ per Eq. (3.82), and the second integral (including the minus sign at the front of the integral operator) is identical to $M_{con,w,j}$ of a base-supported tank per Eq. (3.83). Applying Eqs. (3.82) and (3.83) to Eq. (3.141), the analytical solution of $M_{con,w,j}$ is given as:

$$M_{con,w,j} = A_j(t) \cdot m_l R \frac{2}{n_j(n_j{}^2 - 1)} \tanh(n_j \frac{H}{R}) \left[-\frac{H_s}{H} + 1 - \frac{R}{n_j H} \tanh(n_j \frac{H}{2R}) \right] \quad (3.142)$$

where $A_j(t)$ is the acceleration time series in the j th convective mode with a natural frequency of $f_{con,j}$.

Discussion

Convective responses are calculated using the analytical solutions for a rigid, head-supported cylindrical tank subjected to small-amplitude seismic motion, $u_0''(t)$, at the head in the x direction. The radius of the tank, R, is assumed to be 30 m. The contained fluid is assumed to be water, with a density, ρ, is 1000 kg/m^3. (The same values for R and ρ are assumed for calculating convective responses of a rigid base-supported tank, presented in Section 3.2.2.2).

Other dimensions (e.g., thickness of the wall of the tank) and mechanical properties (e.g., density and elastic modulus of the material) of the tank do not need to be defined for the calculations because the tank is assumed to be rigid. The convective responses presented herein are normalized to be unitless using the method for normalizing the corresponding convective responses of the base-supported tank in Section 3.2.2.2. The normalized results of the convective frequency, $f_{con,j}$, in the j th mode (i.e., the coefficient of the convective frequency, $C_{con,j}$); the convective pressures, $p_{con,w,j}$ and $p_{con,b,j}$; the vertical displacement of the free surface, $d_{w,j}$; the convective shear force, $F_{con,j}$; and the convective moment, $M_{con,b,j}$ is independent of the dimensions of the tank and the fluid, R and H, the density of the fluid, ρ, and the acceleration time series, $A_j(t)$, in the j th convective mode with respect to the seismic motion, $u_0''(t)$. The only variable for these normalized convective responses is the unitless ratio describing the dimensions of the tank and the contained fluid, H/R. Similar to $M_{imp,w}$ presented in Section 3.3.1.1, the normalized results of $M_{con,w,j}$ are independent of ρ and $A_j(t)$ but dependent on H and R because an additional variable representing the height of the tank, H_s, is introduced for the head-supported tank and makes the analytical solution of $M_{con,w,j}$ not proportional to H and R (see Eq. (3.142)). The values of $M_{con,w,j}$ are calculated and presented here for multiple dimensions of a tank and its fluid (i.e., H, R, and H_s) to populate the results.

The analytical solutions for $f_{con,j}$, $p_{con,w,j}$, $p_{con,b,j}$, $F_{con,j}$, and $M_{con,b,j}$ in the j th mode of a head-supported tank are identical to the solutions of Veletsos for a base-supported tank. Results are presented in Section 3.2.2.2 for comparison with other analytical solutions (i.e., from Chalhoub and Kelly (1988), and Housner (1957)). These results are repeated here for the purpose of presenting a complete set of data for the convective responses of a head-supported cylindrical tank.

Figures 3.44a and b present the convective frequencies, $f_{con,j}$, and the coefficients of the convective frequency, $C_{con,j}$, respectively, associated with the first three convective modes (i.e., $j=1$ to 3), calculated for a tank with $0.2 \le H/R \le 3$. The convective frequency, $f_{con,j}$, in the j th mode is related to the coefficient, $C_{con,j}$, as follows:

$$f_{con,j} = C_{con,j}\sqrt{\frac{g}{R}} \tag{3.143}$$

where $C_{con,j}$ is unitless and only dependent on H/R.

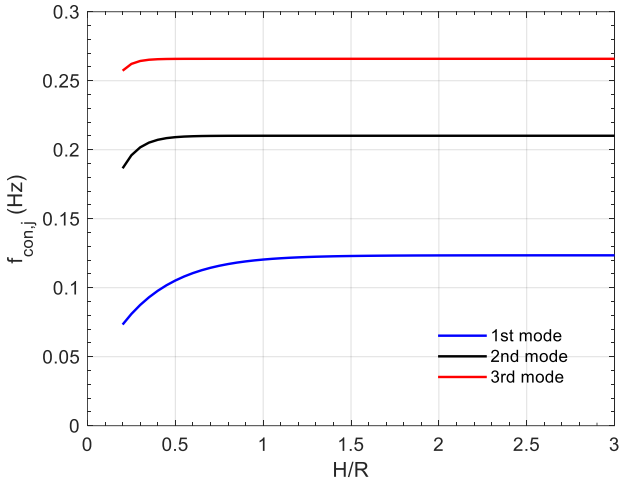

(a) $f_{con,j}$, R =30 m, calculated using Eq. (3.73)

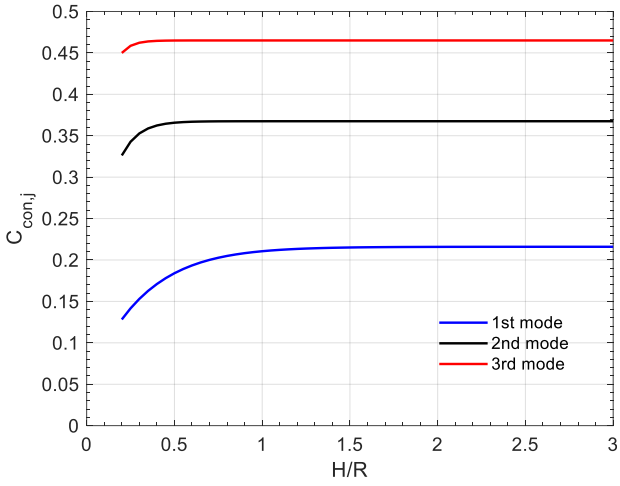

(b) $C_{con,j}$, calculated using Eq. (3.143) and $f_{con,j}$ in panel (a)

Figure 3.44. Convective frequencies, $f_{con,j}$, and coefficients of convective frequency, $C_{con,j}$, associated with the first three convective modes (i.e., $j = 1$ to 3), for $0.2 \le H/R \le 3$, head-supported cylindrical tank

The convective pressures in the first three modes (i.e., $j = 1$, 2, and 3) are presented for a tank with $H/R = 0.5$, 1, and 2. The normalized convective pressures on the wall of the tank, $p_{con,w,j}/\rho R A_j$, along the normalized vertical direction, z/H, at $r = R$ and $\theta = 180°$, are presented in Figure 3.45. The normalized convective pressures on the base of the tank, $p_{con,b,j}/\rho R A_j$, along the normalized radial direction, r/R, at $z = 0$ and $\theta = 180°$, are presented in Figure 3.46.

The normalized vertical displacements of the free surface, $d_{w,j} \cdot g/\rho R A_j$, in the first three modes (i.e., $j = 1$, 2, and 3) for $-1 \le r/R \le 1$, at $\theta = 0°$, are presented in Figure 3.47. (The values of $d_{w,j} \cdot g/\rho R A_j$ are independent of the value of H/R; see Figure 3.27 in Section 3.2.2.2.)

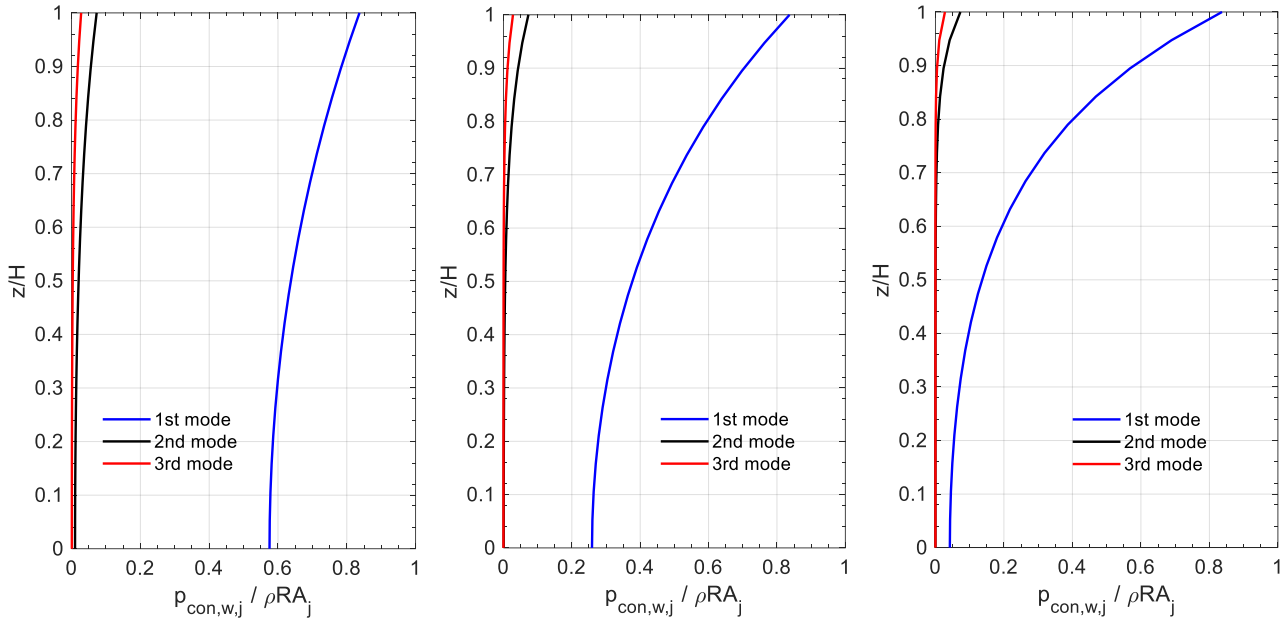

(a) H/R=0.5 (b) H/R=1 (c) H/R=2

Figure 3.45. Normalized convective pressures on the wall of a tank, $p_{con,w,j}/\rho RA_j$, associated with the first three modes (i.e., $j=1$ to 3), along the normalized vertical direction, z/H, at $r=R$ and θ=180°, for $H/R=0.5$, 1, and 2, calculated using Eq. (3.79), head-supported tank

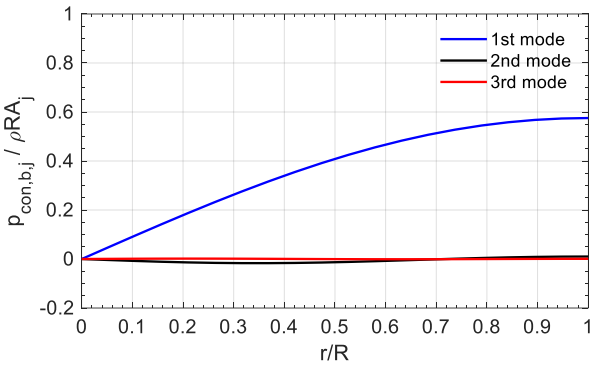

(a) H / R=0.5

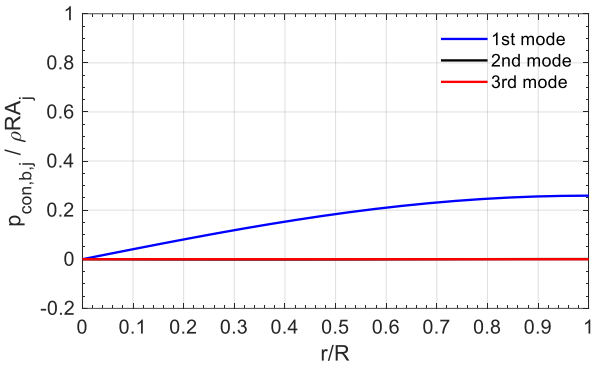

(b) H / R=1

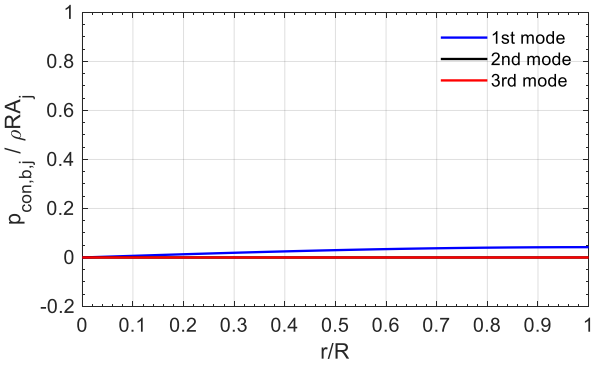

(c) H / R=2

Figure 3.46. Normalized convective pressures on the base of a tank, $p_{con,b,j} / \rho RA_j$, associated with the first three modes (i.e., $j = 1$ to 3), along the normalized radial direction, r / R, at $z = 0$ and $\theta = 180°$, for $H / R = 0.5$, 1, and 2, calculated using Eq. (3.80), head-supported tank

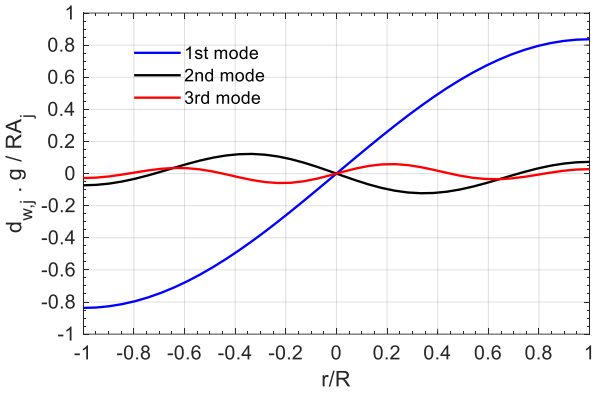

Figure 3.47. Normalized vertical displacements of the free surface in a head-supported tank, $d_{w,j} \cdot g / RA_j$, associated with the first three modes (i.e., $j = 1$ to 3), along the normalized radial axis, r / R, at $\theta = 0°$, calculated using Eqs. (3.81)

The global convective reactions in the first three modes ($j = 1$, 2, and 3) are presented for a tank with $0.2 \le H / R \le 3$. The normalized convective shear forces at the top of the tank, $F_{con,j} / m_l A_j$, in the x direction are presented in Figure 3.48. The convective moments at the top of the tank, $M_{con,w,j}$ and $M_{con,b,j}$, about the y axis, normalized by $m_l H A_j$, are presented in Figures 3.49a and b, respectively. The values of $M_{con,w,j}$ in the first three modes in Figure 3.49a are calculated for a full tank, namely, $H_s = H$ is used in Eq. (3.142). The values of the convective moment in the first mode, $M_{con,w,1}$, are calculated for six values of H_s / R in the range between 0.5 and 3 and nine values of H / H_s in the range between 0.2 and 1 (i.e., full tank). The values of the normalized convective moment in the first mode, $M_{con,w,1} / m_l H A_1$, are presented in a linear format in Figure 3.50a, and also a linear-logarithmic format in Figure 3.50b to better differentiate results for $H / H_s = 0.8$, 0.9, and 1.

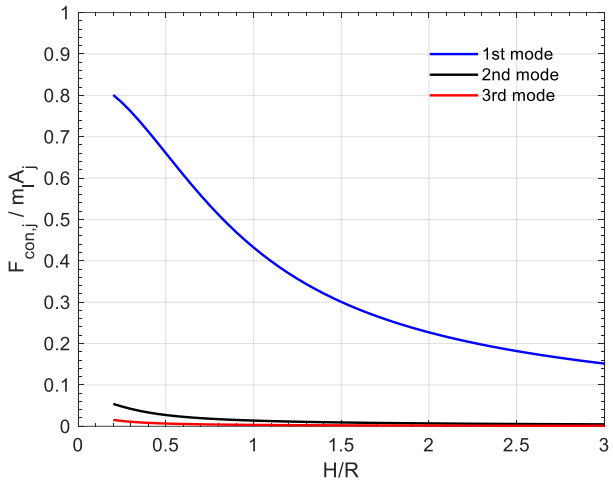

Figure 3.48. Normalized convective shear force at the top of a head-supported tank, $F_{con,j} / m_l A_j$, associated with the first three modes (i.e., $j = 1$ to 3), in the x direction for $0.2 \le H/R \le 3$, calculated using Eq. (3.82)

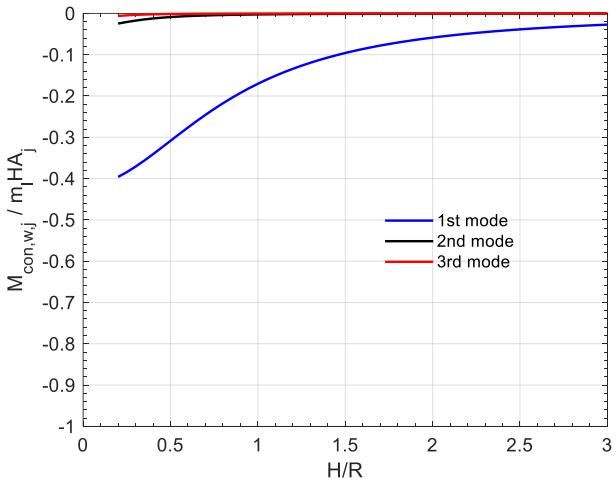

(a) $M_{con,w,j} / m_l HA_j$ for $H/H_s = 1$, calculated using Eq. (3.141)

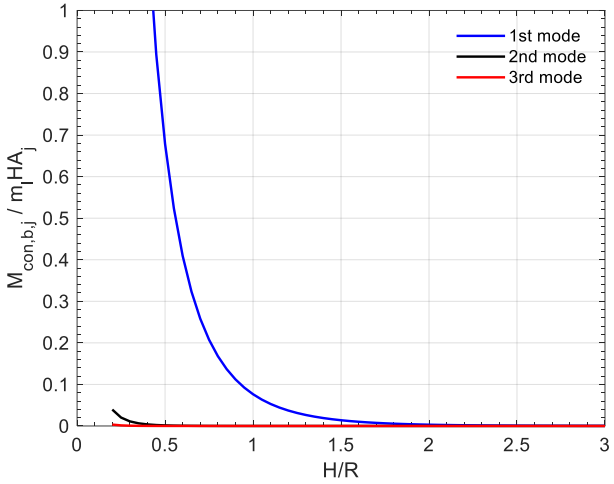

(b) $M_{con,b,j} / m_l HA_j$, calculated using Eq. (3.84)

Figure 3.49. Normalized convective moments at the top of a head-supported tank, $M_{con,w,j} / m_l HA_j$ and $M_{con,b,j} / m_l HA_j$, associated with the first three modes (i.e., $j = 1$ to 3), about the y axis for $0.2 \le H/R \le 3$

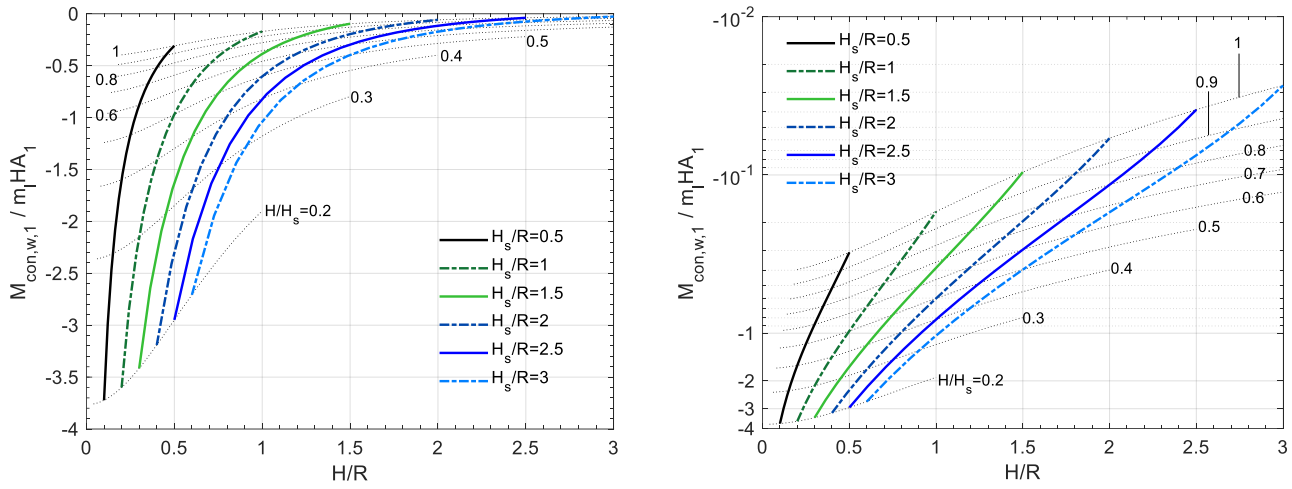

(a) linear scale (b) logrithmic scale

Figure 3.50. Normalized convective moments at the top of a head-supported tank in the first mode, $M_{con,w,1} / m_I HA_1$, about the y axis for $0.2 \le H/R \le 3$, $0.5 \le H_s/R \le 3$, and $0.2 \le H/H_s \le 1$, calculated using Eq. (3.141)

3.3.3 Closing remarks

Analytical solutions for FSI responses of head-supported cylindrical tanks subjected to small-amplitude, unidirectional, horizontal seismic motion are developed in Section 3.3. The solutions are derived using the work of prior studies on base-supported cylindrical tanks presented in Section 3.2 and address the change in the boundary condition (i.e., base- to head-supported). The FSI response is parsed into an impulsive and a convective component. Section 3.3.1 presents analytical solutions for impulsive responses: Section 3.3.1.1 develops solutions for rigid tanks using the method of Jacobsen (1949), and Section 3.3.1.2 developed those for flexible tanks using the method of Veletsos (1984). The analytical solutions address impulsive frequencies associated with lateral motions of the flexible tank, and impulsive pressures, shear force and moment at the head support (for both rigid and flexible tanks). Section 3.3.2 develops analytical solutions for convective responses of a rigid tank using the method of Veletsos (1984). The analytical solutions address convective frequencies, pressures, shear force and moment at the head support and wave heights.

The frequencies and responses are calculated for a tank with different dimensions, in terms of the ratio of the fluid height to the tank radius, H/R, the aspect ratios of the tank, H_s/R, and the

fill ratio, H / H_s. The results are normalized to be unitless, enabling their use for tanks and contained fluids with different dimensions and mechanical properties. In general, the impulsive frequency in a mode: 1) reduces with increasing fluid height H and tank height H_s for a given radius R, and 2) reduces proportionally with R if the material of the tank and length ratios, h / R, H / R, and H / H_s, are held constant. The convective frequency in a mode: 1) is loosely related to the fluid height H of a tank, for the considered range of H / R (i.e., between 0.2 and 3), and 2) reduces proportionally with $\sqrt{R}$ for a given H / R. The amplitudes of the normalized impulsive and convective responses (i.e., pressures, wave heights, and reactions) in the first mode are the greatest, in comparison with those in the higher modes (i.e., second and third). The impulsive component for the reactions at the head support increases and the convective component reduces with increasing H / R. Namely, the impulsive reactions are generally more significant in a tall tank (i.e., greater H / R), and the convective reactions are generally more significant in a broad tank (i.e., smaller H / R).

SECTION 4
VERIFICATION OF NUMERICAL MODELS FOR SEISMIC FLUID-STRUCTURE-INTERACTION ANALYSIS OF CYLINDRICAL TANKS

4.1 Introduction

Fluid-structure-interaction (FSI) analysis for seismic design and qualification of liquid-filled advanced nuclear reactors will rely on numerical models. There are no analytical solutions for FSI responses that can address realistic geometries and boundary conditions of the nuclear reactor and three-directional seismic input. If the reactor is subjected to extreme earthquake shaking, the responses of the fluid will be nonlinear, including sloshing and disengagement from the inner surfaces of the vessel, none of which can be calculated analytically. Numerical models that accommodate these nonlinear responses use fluid-mechanics solvers, including adaptive meshing routines or defining fluid in a control volume (fluid domain) without discretizing the fluid. Table 4.1 introduces solvers capable of simulating nonlinear fluid responses: Fluent and CFX, compatible with ANSYS (ANSYS Inc. 2005); Computational Fluid Dynamics (CFD) and Coupled Eulerian and Lagrangian (CEL), compatible with ABAQUS (Dassault Systèmes 2018); Arbitrary Lagrangian-Eulerian (ALE), Incompressible Computational Fluid Dynamics (ICFD), and Smoothed Particle Hydrodynamics (SPH), compatible with LS-DYNA (Livermore Software Technology Corporation (LSTC) 2018a); and the particle finite element method (PFEM) in OpenSeesPy (Zhu et al. 2018), which is an extension of the open-source code, OpenSees (Mazzoni et al. 2009). If fluid responses are linear, a structural mechanics solver compatible with fluid elements and/or fluid materials could be used for FSI analysis. The last column of Table 4.1 presents fluid elements and fluid materials in finite element codes for linear FSI analysis, including fluid elements, Fluid30, Fluid38, Fluid80, and Fluid130 in ANSYS; and fluid materials, MAT_ELASTIC_FLUID and MAT_ACOUSTIC in LS-DYNA. A challenge with the use of these fluid elements and materials is justifying the assumption of linear fluid response, which will depend on the intensity and frequency content of the input, the vessel dimensions, fluid freeboard, and the presence of components inside the vessel.

Table 4.1. Nonlinear and linear FSI analysis using computer codes, fluid-mechanics solvers, and fluid elements and materials used in a structural mechanics solver

Computer code	Fluid-mechanics solvers: nonlinear fluid response	Fluid elements and materials: linear fluid response
ANSYS	Fluent and CFX	Fluid30, Fluid38, Fluid80, and Fluid130
ABAQUS	CFD and CEL	--
LS-DYNA	ICFD, ALE, and SPH	MAT_ELASTIC_FLUID and MAT_ACOUSTIC
OpenSees	PFEM in OpenSeesPy	--

Numerical models for FSI analysis need to be first verified and validated before being used for seismic design and qualification of liquid-filled advanced reactors (or other nuclear facilities that contain a large volume of liquid; e.g., boiling water reactors and spent fuel pools). Numerical models can be verified by comparing analysis results with those generated using analytical solutions (e.g., Jacobsen (1949); Veletsos (1984a); Chen and Rosenberg (1975)). A verified numerical model can be validated using data from physical testing. This section presents the verification of numerical models of cylindrical tanks by comparing their FSI responses with those calculated using the analytical solutions presented in Section 3. To enable the comparison, simplifying assumptions used for the analytical solutions are applied to the models herein, including 1) rigid or elastic tank, 2) ideal fluid, 3) base- and head-supported boundary conditions, 4) small-amplitude, unidirectional, horizontal seismic motion, and 5) no interaction between the tank and its internal components. The verification of numerical models for internal components submerged in the fluid is presented in Section 5. Validation of the verified models is presented in Section 6, using data from earthquake-simulator tests of a base-supported cylindrical tank, fabricated from carbon steel and filled with water. Two solvers capable of predicting nonlinear fluid responses are considered: ALE and ICFD in the code LS-DYNA.

The first set of numerical models is used to predict fluid responses in a cylindrical vessel (or tank). Loosely based on a prototype advanced reactor and a length scale of around 1/10, the radius, R, of the test tank is 0.79 m, the height H_s is 2 m, and the wall thickness h is 7.92 mm.

(More information on the test tank and the experiment are presented in Section 6.2.) The first impulsive frequency of the test tank, assumed to be full (i.e., fluid height $H = H_s$, $H/R = 2.5$), is 108 Hz, estimated using Eq. (3.64)[26] (Veletsos 1984). The test tank is very stiff based on this frequency, and so the numerical models of the tank are constructed assuming a rigid material, and the numerical results are compared using analytical solutions for rigid tanks. Two boundary conditions are considered for the analysis: base- and head-supported.

The second set of numerical models is used to predict fluid responses in a flexible cylindrical vessel (or tank). The models are verified using analytical solutions developed for flexible tanks. The height and radius of the tank are identical to those used in the first set of models (i.e., $R = 0.79$ m and $H_s = 2$ m), but the wall thickness h is reduced to 0.4 mm to achieve flexibility[27]. Although this wall thickness is too thin to be used for physically constructing a tank, the use of $h = 0.4$ mm for the tank in the models results in a first impulsive frequency, which is reasonable by comparison with a 1/10th-length-scale model of an advanced reactor vessel. The first impulsive frequency of the flexible tank ($R = 0.79$ m, $H_s = 2$ m, and $h = 0.4$ mm), assumed to be full ($H = 2$ m) and supported at the base, is 24.1 Hz per Eq. (3.64)[26] (Veletsos 1984), and that supported at the head is 20.2 Hz, per Eq. (3.140)[26]. Figure 4.1 presents the prototype fast reactor (PFR) in Dounreay, Scotland, including a head-supported vessel with $H_s/R = 2.5$, similar to the test tank. The first impulsive frequency of the PFR vessel is about 5.4. Hz, estimated using Eq. (3.140)[28]. If a 1/10 length scale is used for the PFR vessel, the frequencies are scaled by a factor of $\sqrt{10}$: 17.2 Hz. The first impulsive frequencies of the flexible tank (i.e., 24.1 Hz for base-supported and 20.2 Hz for head-supported) used for the numerical models here are comparable to that of the 1/10th-scale PFR vessel (i.e., 17.2 Hz).

---

[26] Calculated using a water density of 1000 kg/m^3 and the following mechanical properties of carbon steel: elastic modulus of 2×10^{11} N/m^2, Poisson's ratio of 0.27, and density of 7850 kg/m^3.

[27] There are different numerical methods to increase the flexibility of the tank wall, including 1) reducing the elastic modulus, 2) increasing the density, and 3) reducing the wall thickness. However, reducing the elastic modulus increases the run time of the analysis significantly, and increasing the density increases the inertial force of the tank, which is not considered in the analytical solutions used for the verification herein.

[28] Calculated using the dimensions of the vessel (i.e., $R = 6.1$ m, $H_s = 15.2$ m, $H \doteq 0.9 H_s = 13.7$ m, and $h = 12.7$ mm), a liquid-sodium density of 968 kg/m^3, and the following mechanical properties of stainless steel: elastic modulus of 1.9×10^{11} N/m^2, Poisson's ratio of 0.3, and density of 8000 kg/m^3.

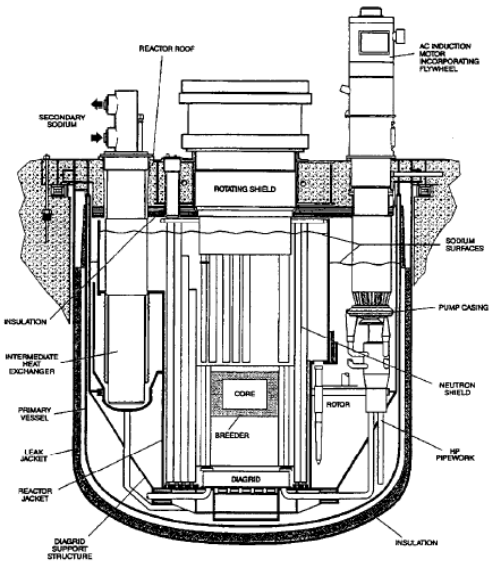

Figure 4.1. Prototype fast reactor (PFR), Dounreay, Scotland, constructed using stainless steel and filled with liquid sodium; dimensions of the vessel: $R = 6.1$ m, $H_s = 15.2$ m, $H \doteq 0.9\,H_s = 13.7$ m, and $h = 12.7$ mm (International Atomic Energy Agency (IAEA) 2012; Jensen and Ølgaard 1995)

The response-history analysis for the rigid and flexible tanks are performed using the ALE and the ICFD solvers in LS-DYNA (2018b, 2019)[29], both capable of calculating nonlinear FSI responses. The ALE solver uses an explicit analysis and models fluids using Eulerian elements. These elements do not deform with the fluid; rather, they serve together as a grid for the fluid domain through which the fluid can flow. Integration points for calculating fluid responses are located in each grid cell (i.e., each Eulerian element). Accordingly, the Eulerian elements are not distorted by large deformation of the fluid. The ICFD solver adopts an implicit analysis to model fluids using Lagrangian elements. These elements can deform to a defined tolerance, and then a number of smaller elements are automatically generated by an adaptive meshing routine to accommodate large deformation of the fluid.

Sections 4.2 and 4.3 verify the numerical models for the rigid and the flexible tanks, respectively, by comparing results with the analytical solutions presented in Section 3. The tanks are subjected to small-amplitude, unidirectional, horizontal motions. The sources of the analytical solutions used in this section are listed in Table 4.2, for rigid and flexible cylindrical tanks with the two

[29] Different versions of LS-DYNA are used here: SMP_d_Dev_126632 (2018b) is used for the ALE analysis and SMP_d_R11_139066 (2019) is used for the ICFD analysis.

boundary conditions, base- and head-supported. Each of the two sections (4.2 and 4.3) presents descriptions for the numerical models, input motions for response-history analysis, and FSI results for verification.

Table 4.2. Sources of analytical solutions for rigid and flexible cylindrical tanks subjected to unidirectional horizontal motion of a small amplitude, base- and head-supported, impulsive and convective components

		Impulsive	Convective
Base-supported	Rigid	Jacobsen (1949) per Section 3.2.1.2.	Veletsos (1984) per Section 3.2.2.2
	Flexible	Veletsos (1984) per Section 3.2.1.3	--
Head-supported	Rigid	Derived in Section 3.3.1.1	Derived in Section 3.3.2.1
	Flexible	Derived in Section 3.3.1.2	--

4.2 Rigid tank

Numerical models of rigid, base- and head-supported cylindrical tanks are developed. The response-history analysis is performed using the ALE and ICFD solvers for x-directional seismic inputs, based on the coordinate system of Figure 4.2. (Other information shown in Figure 4.2 will be presented and used in Sections 4.2.3 and 4.3.3.) Numerical results of FSI responses are compared to those calculated using analytical solutions, in terms of hydrodynamic pressures[30], reactions (i.e., shear forces and moments) at the support (i.e., base or head), and wave heights.

[30] Hydrodynamic pressure: the load applied by a fluid to surrounding structures, generated by dynamic motions, including earthquake shaking.

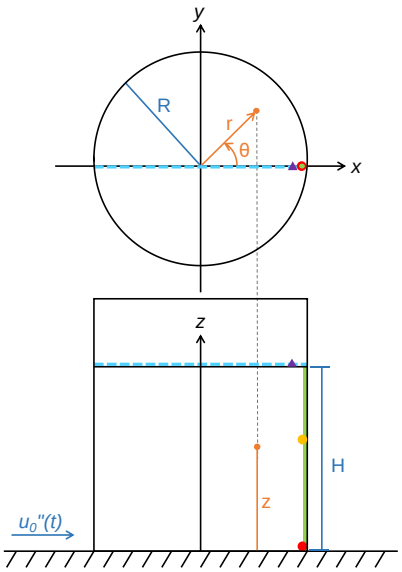

Figure 4.2. Cartesian coordinates and cylindrical coordinates shown on two cut-away views of a base-supported cylindrical tank, together with locations for reporting responses: hydrodynamic pressures at the red and yellow solid circles and along the green line, and vertical displacements of the free surface at the purple triangle and along the blue dashed line

4.2.1 Numerical models

Numerical models are constructed for a rigid cylindrical tank, with $R = 0.79$ m and $H_s = 2$ m, and filled with water to heights H of 1.2 and 1.8 m. With no deformation in the rigid tank, the responses of the contained fluid are not affected by the location of the support for horizontal seismic input, whether at the base or top. Accordingly, one set of models is used for the analysis of the base- and head-supported tanks, but their support reactions are output at different locations (i.e., base or head). Figure 4.3 presents the ALE models and global coordinates (x, y, z) consistent with those in Figure 4.2. Figures 4.3a, b, and c present different parts of the model for the tank filled with water to a depth of 1.2 m. Figures 4.3d, e, and f present parts of the tank filled with water to a depth of 1.8 m. The tank is shown in blue, and the water is shown in yellow. A vacuum space shown in grey is built above the water. The water and vacuum in each model together define a fluid domain. Air is not included in the models since the analytical solutions used for the verification (see Table 4.2 and Section 3) do not consider the effect of the atmospheric pressure on the FSI responses. The nodes of the tank, water, and vacuum are merged on their interfaces.

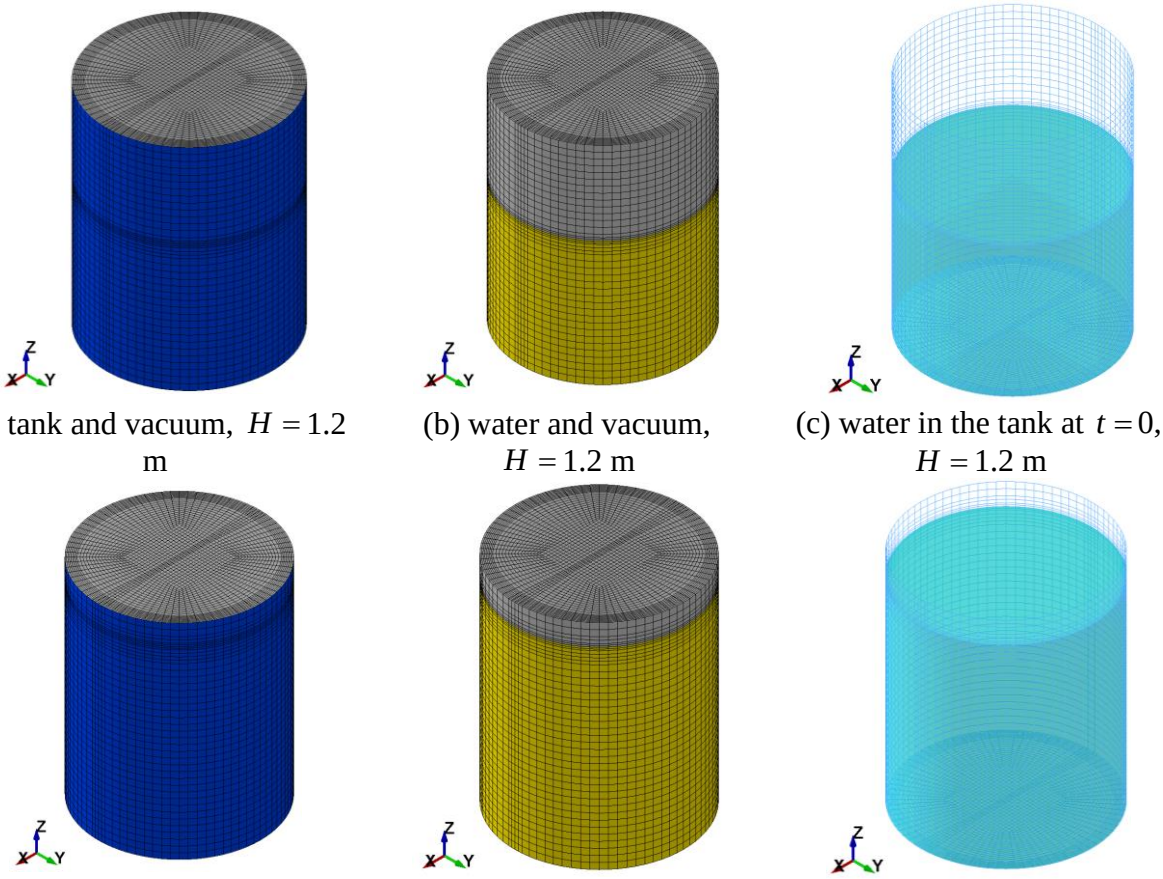

(a) tank and vacuum, $H = 1.2$ m

(b) water and vacuum, $H = 1.2$ m

(c) water in the tank at $t = 0$, $H = 1.2$ m

(d) tank and vacuum, $H = 1.8$ m

(e) water and vacuum, $H = 1.8$ m

(f) water in the tank at $t = 0$, $H = 1.8$ m

Figure 4.3. ALE models of a rigid cylindrical tank with $R = 0.79$ m, $H_s = 2$ m, and $H = 1.2$ and 1.8 m, isometric view

The sizes of the elements shown in Figures 4.3a, b, d, and e are optimized, resulting in smaller elements for the fluid domain adjacent to the tank wall, around the boundary between the water and the vacuum (i.e., free surface), and along the direction of the seismic input (i.e., x direction) across the diameter of the tank. The tank is modeled using Lagrangian, four-node, shell elements (i.e., quadrilateral elements), and the water and vacuum are modeled using Eulerian, eight-node, solid elements (i.e., brick elements). The types and numbers of elements used for the ALE models are listed in Table 4.3 for $H = 1.2$ and 1.8 m. Figures 4.3c and f present the contained water with depths of 1.2 and 1.8 m, respectively, at the first step of the analysis (i.e., time $t = 0$).

Table 4.3. Types and numbers of elements used in the ALE models shown in Figure 4.3

	Tank	Water	Vacuum
Element type	Lagrangian four-node shell	Eulerian eight-node solid	Eulerian eight-node solid
$H = 1.2$ m	5732	56928	37952
$H = 1.8$ m	5816	80648	14232

Figure 4.4 presents the ICFD models and the global coordinate system (x, y, z). The model of the tank presented in Figure 4.4a is used for both the analyses for $H = 1.2$ and 1.8 m. Three surfaces are used to define a fluid domain for the contained fluid. Figure 4.4b (d) presents a half domain for the water of $H = 1.2$ m (1.8 m) built using surfaces: 1) adjacent to the tank base (shown in pink), 2) adjacent to the tank wall (shown in yellow), and 3) horizontally closing the top of the domain (shown in grey). The domain provides sufficient height for wave actions. The height of the fluid domain shown in Figure 4.4b is 1.4 m for $H = 1.2$ m and that shown in Figure 4.4d is 2 m for $H = 1.8$ m, providing a freeboard of 0.2 m. (The vertical displacement of the free surface in the tank subjected to small motions is expected to be significantly less than 0.2 m; see results presented in Figures 4.16 and 4.17.) The tank and the fluid surfaces do not share nodes at their interfaces. The interaction between the tank and water is activated by the *ICFD_BOUNDARY_FSI card in the LS-DYNA deck.

An ICFD model with a finer mesh for fluid surfaces results in more accurate FSI responses but also a longer analysis time. The mesh shown in Figures 4.4b and d is determined by a trade-off between the accuracy of results and the analysis time, which is bounded by around two weeks for a 13-second input motion, namely the longest motion shown in Figure 4.5d used in this section. (Information of the analysis computer: 7th Gen (i7) 4-core Intel processor, 32 GB RAM, and 512 GB SSD.) Smaller elements are used along the direction of the seismic input (i.e., x direction) across the diameter of the fluid domain. Both the tanks and the fluid surfaces are models using Lagrangian three- or four-node shell elements. The initial height of the free surface (i.e., $H = 1.2$ m or 1.8 m) is defined using the *ICFD_INITIAL_LEVELSET card. The finite element model of the water enclosed by the yellow and pink surfaces in Figures 4.4b and d and the free surface

defined in the *ICFD_INITIAL_LEVELSET card is automatically generated by the ICFD solver at the first step of the analysis (i.e., $t = 0$). The water is constructed using four-node solid elements (i.e., tetrahedral elements), as shown in Figures 4.4c and e for $H = 1.2$ and 1.8 m, respectively. The *MESH_BL card is used to generate finer water elements adjacent to the inner surfaces of the tank. The types and numbers of elements used for the ICFD models are listed in Table 4.4.

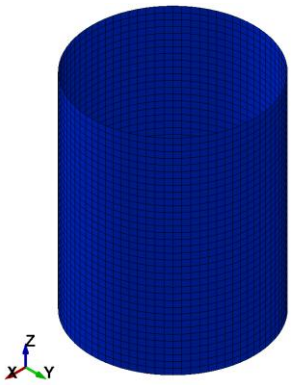

(a) tank

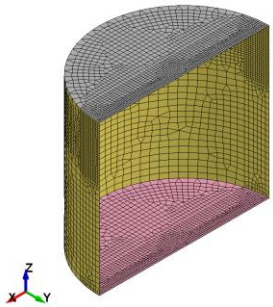

(b) surfaces for a half fluid domain with a height of 1.4 m, $H = 1.2$ m

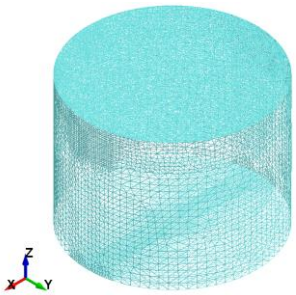

(c) water, $H = 1.2$ m, $t = 0$

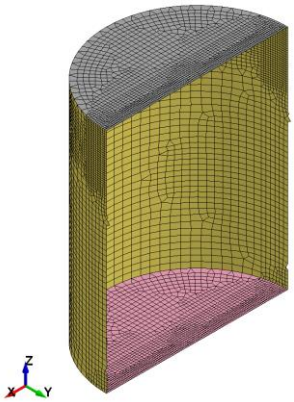

(d) surfaces for a half fluid domain with a height of 2 m, $H = 1.8$ m

(e) water, $H = 1.8$ m, $t = 0$

Figure 4.4. ICFD models of a rigid cylindrical tank with $R = 0.79$ m, $H_s = 2$ m, and $H = 1.2$ and 1.8 m, isometric view

Table 4.4. Types and numbers of elements used for the ICFD models shown in Figure 4.4

	Tank	Fluid surface	Water
Element type	Lagrangian three/four-node shell	Lagrangian three/four-node shell	Lagrangian four-node solid
$H = 1.2$ m	4761	12688	Automatically generated by the solver
$H = 1.8$ m	4761	14030	

The results of the response-history analysis are compared with the analytical solutions for hydrodynamic pressures, reactions at the support (i.e., base or head), and wave heights. The analytical solutions address the reactions at the support associated with hydrodynamic loadings and do not consider those associated with the inertial force of the tank. Accordingly, the inertial force of the tank in the numerical models must be removed to generate reactions consistent with those analytically calculated. To make the inertial force negligible, a tiny thickness, h, of 0.5 mm and a tiny density, ρ_s, of 100 kg/m^3 is assigned to the shell elements, both of which reduce the mass of the tank. Although the tank used in the earthquake simulation tests is built using 7.92 mm-thick carbon steel, of which the generic density is 7850 kg/m^3, the reduced thickness and density used in the numerical analysis in this section (4.2.1) do not affect the responses since the tank is assumed to be rigid. Other mechanical properties consistent with carbon steel are assigned to the elements of the tank, including the elastic modulus E_s of 2×10^{11} N/m^2 and Poisson's ratio υ_s of 0.27. These values do not affect the responses of the rigid tank but must be defined in the models. No damping is applied to the tank (i.e., damping ratio=0).

The analytical solutions assumed the fluid is ideal, which is inviscid and incompressible. A density ρ_w of 1000 kg/m^3 and a viscosity μ_w of 0 is assigned to the water elements in the ALE models shown as yellow in Figure 4.3 and the pink and yellow fluid surfaces in the ICFD models shown in Figure 4.4. The ICFD solver can accommodate only incompressible fluids, whereas the ALE solver addresses the compressibility of the fluid through the *EOS_LINEAR_POLYNOMIAL card. To achieve incompressibility, the bulk modulus, K_w, defined in the card (termed $C1$) for the water must be sufficiently large. A sensitivity analysis is

performed for the bulk modulus using values of 2.15×10^9 N/m^2 (i.e., the bulk modulus of water at 25°C), 5×10^9 N/m^2, and 2×10^{10} N/m^2. The differences in the results are negligible, but the run time of the analysis significantly increases with an increasing value of the bulk modulus, and so the value consistent with water, 2.15×10^9 N/m^2, is used for the ALE models. The analytical solutions did not consider the effect of the atmospheric pressure on the FSI responses. The elements of the vacuum space in the ALE models shown as grey in Figure 4.3 are assigned void properties through the *INITIAL_VOID card. The elements of the top surface of the fluid domain in the ICFD models, shown as grey in Figure 4.4, are assigned *vacuum properties* with zero density and viscosity (i.e., $\rho_a = 0$ and $\mu_a = 0$). The mechanical properties assigned to the elements in the numerical models of the tank, water, and vacuum are listed in Table 4.5. The masses of the numerical models are listed in Table 4.6. The gravitational acceleration g of 9.81 m/s^2 is assigned to the z direction.

Table 4.5. Mechanical properties assigned to the elements in the numerical models of the tank, water, and vacuum, the ALE and ICFD models

		ALE	ICFD
Tank	Density, ρ_s	100 kg/m^3	
	Elastic modulus, E_s	2×10^{11} N/m^2	
	Poisson's ratio, υ_s	0.27	
Water	Density, ρ_w	1000 kg/m^3	
	Viscosity, μ_w	0	
	Bulk modulus, K_w	2.15×10^9 N/m^2	--[1]
Vacuum	Density, ρ_a	--[2]	0
	Viscosity, μ_a		0

1. The ICFD solver analyzes only incompressible fluids, and so K_w is not used in the models.
2. The vacuum is assigned void properties through the *INITIAL_VOID card for the ALE analysis.

Table 4.6. Masses the tank and water in the ALE and ICFD models

Component	Mass (kg)	
	$H = 1.2$ m	$H = 1.8$ m
Tank (including the wall and the base)	0.6	
Water	2352	3527

4.2.2 Input motions

Four input motion time series are used for the response-history analysis of the rigid tanks in the x direction: two sinusoidal motions, S-1 and S-2, and two earthquake motions, E-1 and E-2. The four motions are all small-amplitude, unidirectional, and horizontal, to accommodate assumptions used for the analytical solutions and enable verification. Their time series are presented in Figure 4.5, and information is listed in Table 4.7.

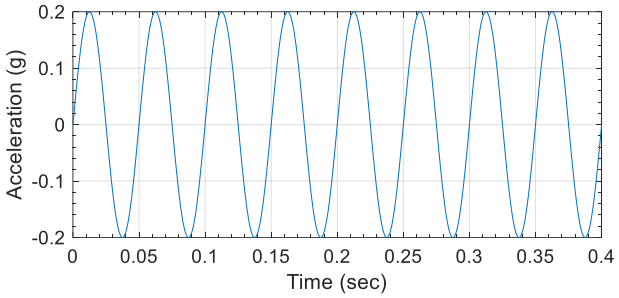

(a) sinusoidal motion, S-1, PGA=0.2 g

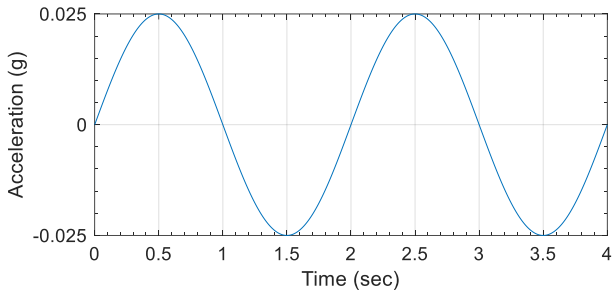

(b) sinusoidal motion, S-2, PGA=0.025 g

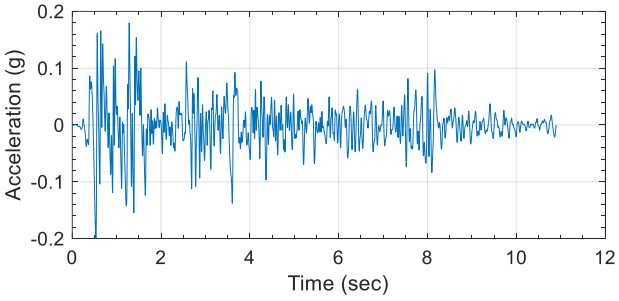

(c) earthquake motion, E-1, time scale of $1/\sqrt{10}$, PGA=0.2 g

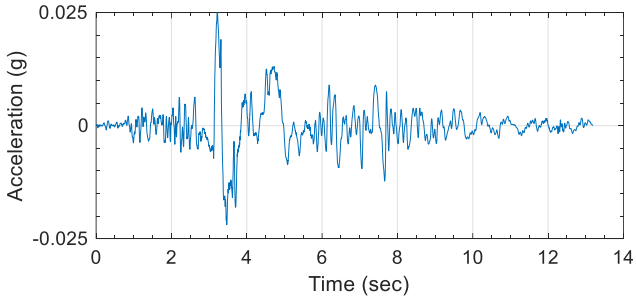

(d) earthquake motion, E-2, time scale of $1/\sqrt{10}$, PGA=0.025 g

Figure 4.5. Unidirectional, horizontal input for the response-history analysis of the rigid tanks

Table 4.7. Information on the time series shown in Figure 4.5 for the response-history analysis of the rigid tanks

a. sinusoidal motions

	Frequency (Hz)	Amplitude/PGA (g)	Number of cycles
S-1	20	0.2	8
S-2	0.5	0.025	2

b. earthquake motion records[1]

	Event	Year	Station	Direction	Original PGA (g)	Scaled PGA (g)	Time scale
E-1	El Centro Earthquake (Imperial Valley-02)	1940	El Centro Array #9	180	0.28	0.2	$1/\sqrt{10}$
E-2	Chi-Chi Earthquake	1999	TCU052	EW	0.36	0.025	$1/\sqrt{10}$

1. Ground motions are extracted from the PEER Ground Motion Database (http://ngawest2.berkeley.edu/, accessed on March 18, 2019), Pacific Earthquake Engineering Research (PEER) Center, University of California, Berkeley, CA.

Figures 4.6a and b show typical, horizontal acceleration spectra in black, at a site in the U.S., in the period and the frequency axes, respectively. Per the U.S. Geological Survey (https://earthquake.usgs.gov/hazards/interactive/, accessed on Dec 11, 2018), horizontal acceleration spectra generally have a peak value at a period of between 0.1 and 0.2 second (i.e., frequency of 5 to 10 Hz), as shown in Figure 4.6. To be consistent with the 1/10 length scale for the tank, the period axis of a spectrum is compressed by a factor of $\sqrt{10}$, and the peak spectral acceleration is between periods of 0.03 and 0.06 second after scaling, namely, at frequencies between 16 and 30 Hz, as shown in the red spectra in Figure 4.6. The frequency of motion S-1 is chosen accordingly: 20 Hz. Motion S-1 includes eight cycles of a 20-Hz sine wave with an amplitude (i.e., peak ground acceleration, PGA) of 0.2 g.

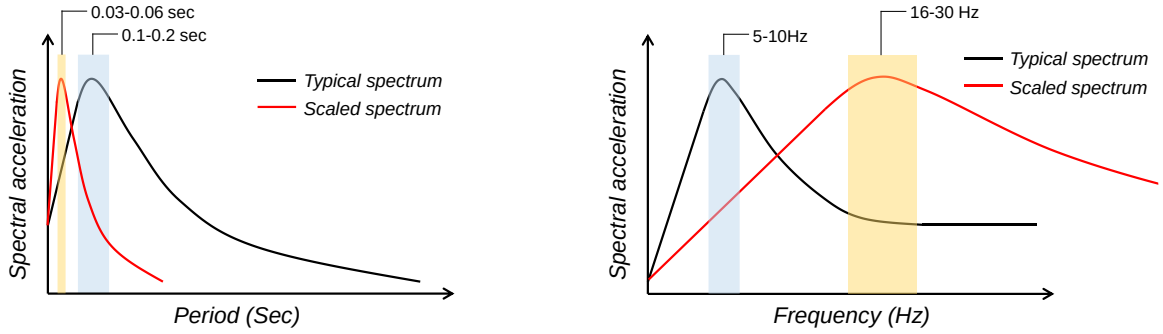

(a) period axis (a) frequency axis

Figure 4.6. Typical horizontal acceleration spectra and scaled acceleration spectra based on the 1/10 length scale: period axis compressed and frequency axis expanded by a factor of $\sqrt{10}$

The sinusoidal motion, S-2, is used to drive wave actions of the contained fluid. Accordingly, a frequency of 0.5 Hz is selected to be sufficiently close to the first convective frequency of the tank of 0.76 Hz, estimated using Eq. (3.119)[26] (Veletsos 1984). (A frequency of the sinusoidal motion greater than 0.5 Hz and closer to the first convective frequency could induce sloshing instability, for which numerical results cannot be verified by the analytical solution derived based on linear response (Veletsos).) Motion S-2 includes two cycles of a 0.5-Hz sine wave with an amplitude of 0.025 g. This wave-driving motion uses a tiny PGA of 0.025 g to reduce the vertical accelerations of the free surface in the numerical models since the analytical solution used herein for verification assumed this acceleration to be zero.

The two earthquake motion time series, E-1 and E-2, are records of the 1940 El Centro earthquake in California, U.S. and the 1999 Chi-Chi earthquake in Taiwan, respectively. Consistent with the length scale of the tank, the time scale of each earthquake motion is compressed by a factor of $\sqrt{10}$. The PGAs of E-1 and E-2 are scaled to 0.2 g and 0.025 g, respectively. Figure 4.7 presents spectral accelerations for both E-1 and E-2 with the time scale and the amplitude scale, calculated using a damping ratio of 2%, with respect to period in a linear format and frequency in a logarithmic-linear format. These two ground motions have very different frequency contents and their peak spectral accelerations are well separated in terms of period/frequency. Identical to S-2, the PGA of E-2 is scaled to 0.025 g since the spectral acceleration around the first convective frequency (i.e. 0.76 Hz) is relatively high, which could

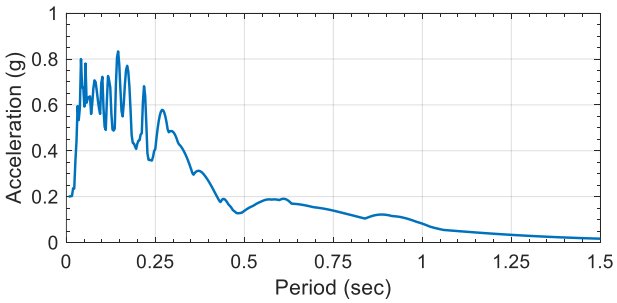

(a) E-1, PGA=0.2g, period axis in a linear format

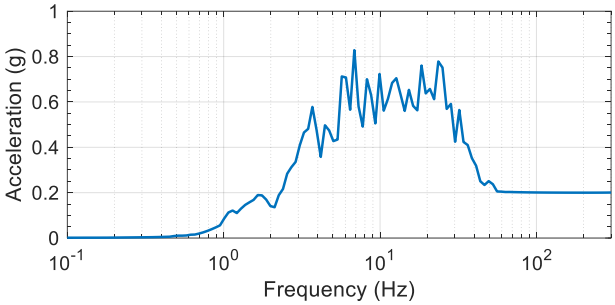

(b) E-1, PGA=0.2g, frequency axis in a logarithmic format

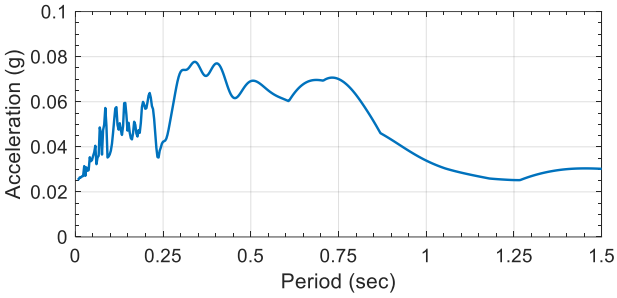

(c) E-2, PGA=0.025g, period axis in a linear format

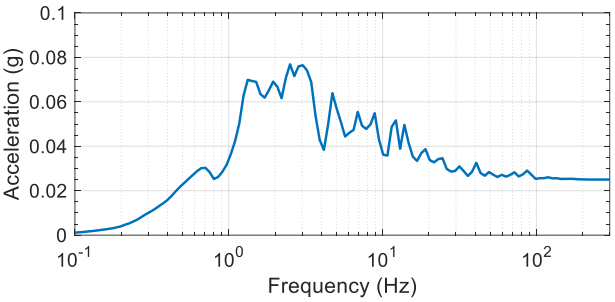

(d) E-2, PGA=0.025g, frequency axis in a logarithmic format

Figure 4.7. Spectral accelerations of the earthquake motion time series, E-1 and E-2, shown in Figures 4.5c and d, time scale of $1/\sqrt{10}$, damping ratio of 2%

induce intense waves with large vertical accelerations that need to be avoided for verification, for the reason given above.

4.2.3 Results and verification

Seismic responses of the rigid, base- and head-supported cylindrical tanks with two fluid heights are extracted from the response-history analysis calculated using the ALE and ICFD models presented in Section 4.2.1. The response-history analysis of each tank is performed for the four motions listed in Table 4.7 in the x direction, and the analysis continues for 1 to 2 seconds after the seismic shaking has ended to investigate the post-shaking sloshing response.

4.2.3.1 Base-supported tank

The analytical solutions used to verify the numerical models of the rigid, base-supported tank ($R = 0.79$ m, $H_s = 2$ m, $H = 1.2$ and 1.8 m) were derived by Jacobsen and Veletsos for impulsive

and convective responses, respectively, per Table 4.2. These analytical solutions were derived based on the cylindrical coordinate system (r , θ , z) shown in Figure 4.2. The impulsive responses (Jacobsen, Section 3.2.1.2) include the pressure on the inner surfaces of the tank, p_{imp} , shear force at the base of the tank, F_{imp} , and two components of the moment at the base of the tank: $M_{imp,w}$, generated by $p_{imp,w}$ on the wall, and $M_{imp,b}$, generated by $p_{imp,b}$ on the base. The convective responses (Veletsos, Section 3.2.2.2) were decoupled into modal contributions. The solutions address the convective frequency, $f_{con,j}$, of the j th mode ($j = 1, 2, \ldots \infty$) and the modal convective responses including $p_{con,w,j}$, $p_{con,b,j}$, $F_{con,j}$, $M_{con,w,j}$, and $M_{con,b,j}$ (counterparts of $p_{imp,w}$, $p_{imp,b}$, F_{imp} , $M_{imp,w}$, and $M_{imp,b}$, respectively), and the vertical displacement of the free surface, $d_{w,j}$. The equation numbers used in Section 3.2.1.2 for the impulsive responses are listed in Table 4.8a, and those used in Section 3.2.2.2 for the modal convective response are listed in Table 4.8b.

Table 4.8. Equation numbers of the analytical solutions for rigid, base-supported tanks

a. impulsive responses (Jacobsen 1949)

$p_{imp,w}$	$p_{imp,b}$	F_{imp}	$M_{imp,w}$	$M_{imp,b}$
(3.9)	(3.10)	(3.11)	(3.12)	(3.13)

b. modal convective responses (Veletsos 1984)

$p_{con,w}$	$p_{con,b}$	d_w	F_{con}	$M_{con,w}$	$M_{con,b}$
(3.79)	(3.80)	(3.81)	(3.82)	(3.83)	(3.84)

The time series of the hydrodynamic pressure, p_w , on the tank wall, the shear force, F , at the tank base in the x direction, the moment, M_{wb} , at the tank base about the y axis, and the vertical displacement of the free surface, d_w , calculated using the numerical models are compared with those calculated using the analytical solutions. The analytical solutions for the impulsive and convective components of p_w , F , and M_{wb} were derived separately (Veletsos 1984; Jacobson 1949), but numerical analysis combines both components. To compare the analytical and numerical results, the analytical solution of each impulsive response and that of

the corresponding convective response are algebraically summed. Note that each convective response is the infinite algebraic sum of modal responses (i.e., $j = 1$ to ∞).

$$p_w(\theta, z, t) = p_{imp,w} + \sum_{j=1}^{N} p_{con,w,j} \tag{4.1}$$

$$F(t) = F_{imp} + \sum_{j=1}^{N} F_{con,j} \tag{4.2}$$

$$M_{wb}(t) = M_w + M_b = (M_{imp,w} + \sum_{j=1}^{N} M_{con,w,j}) + (M_{imp,b} + \sum_{j=1}^{N} M_{con,b,j}) \tag{4.3}$$

$$d_w(r, \theta, t) = \sum_{j=1}^{N} d_{w,j} \tag{4.4}$$

where the impulsive responses $p_{imp,w}$, F_{imp}, $M_{imp,w}$ and $M_{imp,b}$ are calculated using the equations listed in Table 4.8a; and the modal convective responses $p_{con,w,j}$, $F_{con,j}$, $M_{con,w,j}$, $M_{con,b,j}$, and $d_{w,j}$ are calculated using the equations listed in Table 4.8b. The moment at the tank base, M_{wb}, calculated by numerical analysis includes the components, M_w and M_b, associated with both the hydrodynamic pressures on the wall and the base, respectively. Accordingly, Eq. (4.3) sums the analytical solutions of M_w and M_b to be consistent with the numerical results. (Equation (4.3) is also used for a rigid head-supported tank in Section 4.2.3.2, but $M_{imp,w}$, $M_{imp,b}$, $M_{con,w,j}$, and $M_{con,b,j}$ are calculated per the equations listed in Table 4.12.) Per Eqs. (4.1) to (4.4), the algebraic sums for the convective responses include N modes. Theoretically, an infinite number of convective modes are required (i.e., $N = \infty$, $j = 1$ to ∞), but only the first ten modes (i.e., $N = 10$) are included in the calculation herein since the contributions of the eleventh and higher modes are negligible for the tanks and the ground motions used for this analysis.

Hydrodynamic pressure

The time series of hydrodynamic pressure, p_w, calculated using the numerical models and Eq. (4.1) are compared at the location of the red solid circle on the tank presented in Figure 4.2. The cylindrical coordinates of the circle are used for Eq. (4.1): $(r, \theta, z) = (0.79 \text{ m}, 0, 0)$. Figure 4.8 enables a comparison of ALE model results and analytical solutions for the two fluid heights (i.e.,

$H = 1.2$ or 1.8 m) and the four input motions (i.e. S-1, S-2, E-1, or E-2). Figure 4.9 presents companion results for the ICFD models.

The distributions of p_w calculated using the numerical models and Eq. (4.1) are compared along the green line on the tank wall shown in Figure 4.2. The cylindrical coordinates of the green line are used for Eq. (4.1): $(r, \theta, z) = (0.79 \text{ m}, 0, 0 \text{ to } H)$, where $H = 1.2$ or 1.8 m. Figures 4.10a to h present the comparison at the time step t of peak response in the p_w time series for the ALE: see the open red circles in the corresponding panels of Figure 4.8. Figure 4.11 presents the comparison at the time step of peak response in the p_w time series for the ICFD models: see the open red circles in panels of Figure 4.9.

Reactions: shear force and moment at the base

The time series of shear force, F, in the x direction at the tank base, calculated using the numerical models can be compared with the solutions of Eq. (4.2) in Figures 4.12 and 4.13. Figure 4.12 enables a comparison for the ALE models for the two fluid heights (i.e., $H = 1.2$ and 1.8 m) and the four input motions (i.e. S-1, S-2, E-1, and E-2). Figure 4.13 presents companion results for the ICFD models. The time series of moment, M_{wb}, about the y axis at the tank base, calculated using the numerical models can be compared with the results of Eq. (4.3) in Figures 4.14 and 4.15. Figure 4.14 enables a comparison for the ALE models for the two fluid heights (i.e., $H = 1.2$ and 1.8 m) and the four input motions (i.e. S-1, S-2, E-1, and E-2). Figure 4.15 presents companion results for the ICFD models.

Vertical displacement of the free surface, wave height

The vertical displacement of the free surface, d_w, is the height of the wave above the initial free surface at $z = H$. As noted in Section 3.2.2.2, Veletsos (1984) derived $d_{w,j}$ in the jth mode by assuming 1) the vertical acceleration of the wave to be zero, generating a hydrostatic pressure[31] at $z = H$, and 2) the hydrostatic pressure to be equal to the convective pressure $p_{con,j}$ at $z = H$. As a result, $p_{con,j}$ is related to the depth of the fluid $d_{w,j}$ above the initial free surface at $z = H$ as $p_{con,j} = \rho g d_{w,j}$, where ρ is the density of the fluid, and g is the gravitational acceleration.

[31] Hydrostatic pressure: pressure created by fluid at rest under gravity.

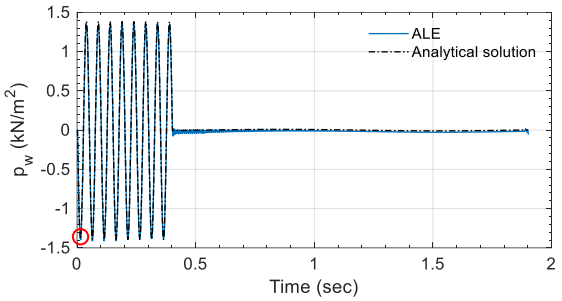

(a) S-1, $H = 1.2$ m

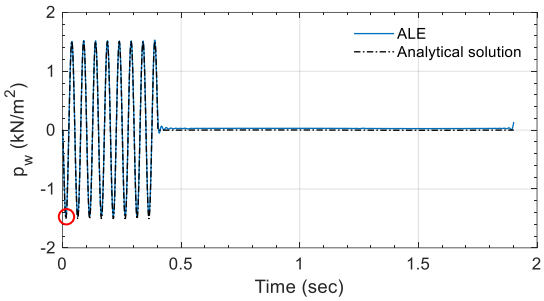

(b) S-1, $H = 1.8$ m

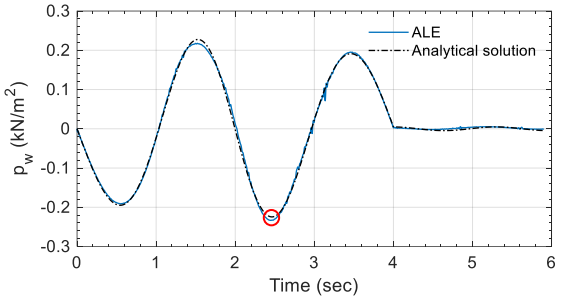

(c) S-2, $H = 1.2$ m

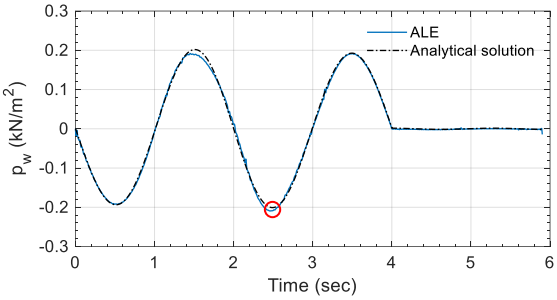

(d) S-2, $H = 1.8$ m

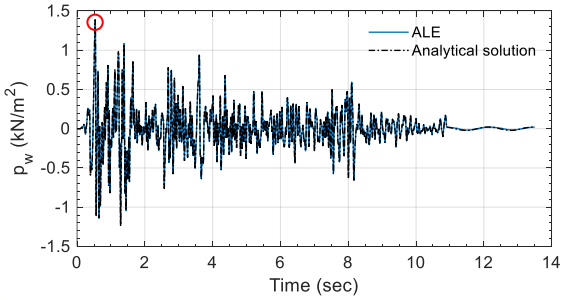

(e) E-1, $H = 1.2$ m

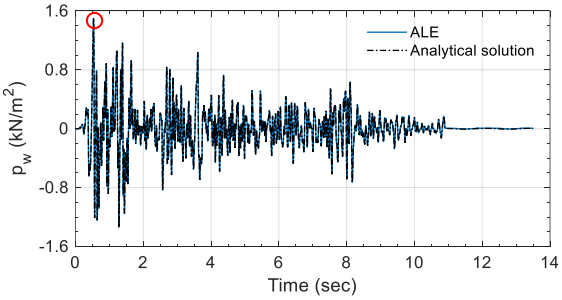

(f) E-1, $H = 1.8$ m

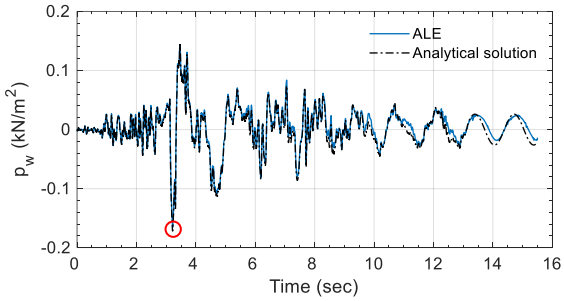

(g) E-2, $H = 1.2$ m

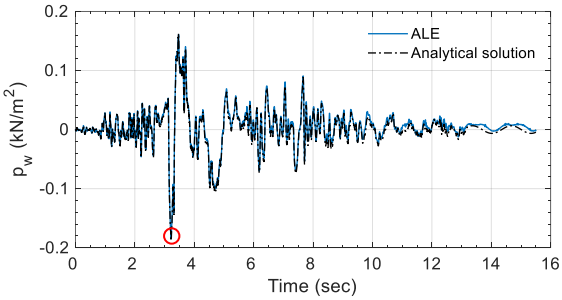

(h) E-2, $H = 1.8$ m

Figure 4.8. Time series of the hydrodynamic pressure, p_w, at the location of the red solid circle shown in Figure 4.2, calculated using the ALE models and Eq. (4.1)

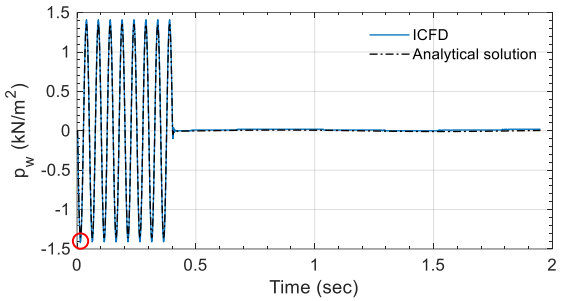

(a) S-1, $H = 1.2$ m

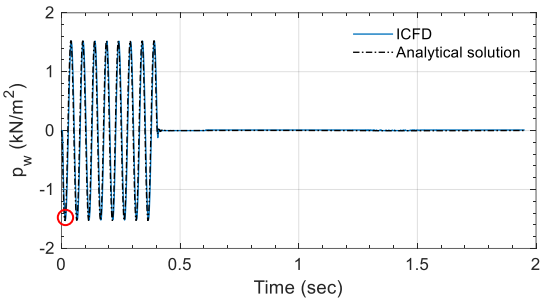

(b) S-1, $H = 1.8$ m

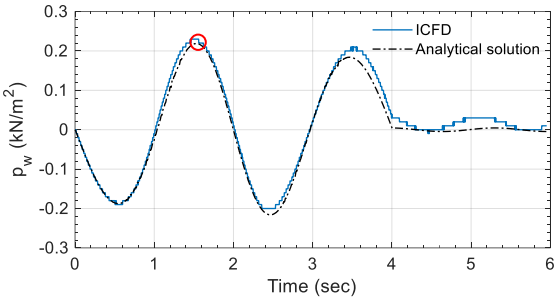

(c) S-2, $H = 1.2$ m

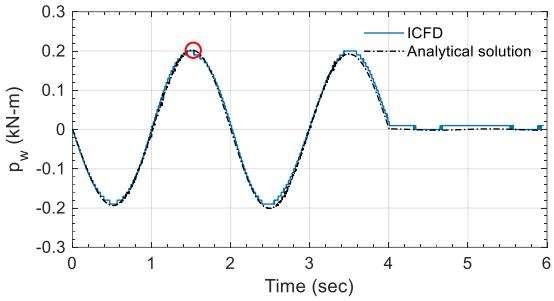

(d) S-2, $H = 1.8$ m

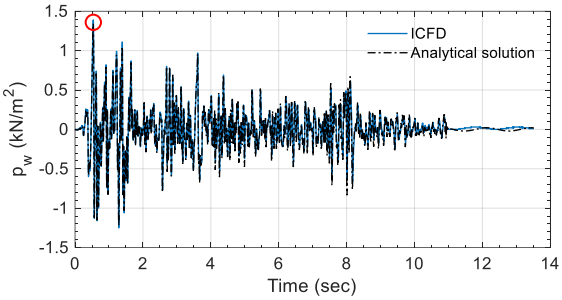

(e) E-1, $H = 1.2$ m

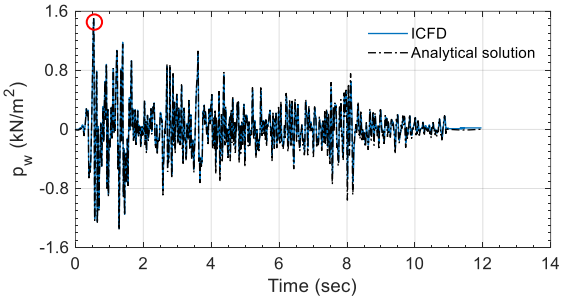

(f) E-1, $H = 1.8$ m

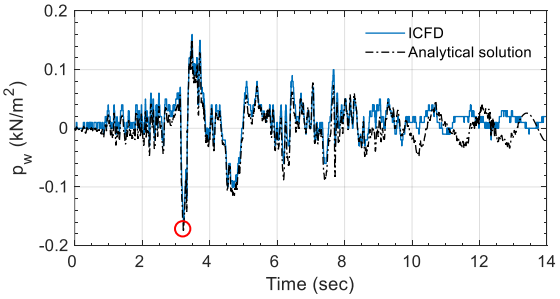

(g) E-2, $H = 1.2$ m

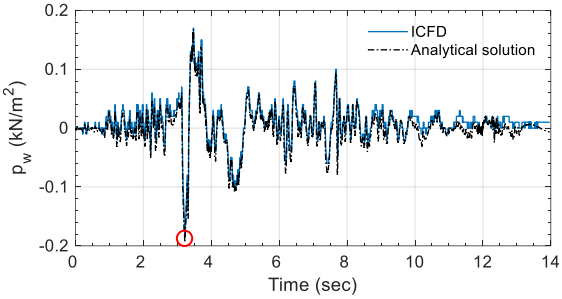

(h) E-2, $H = 1.8$ m

Figure 4.9. Time series of the hydrodynamic pressure, p_w, at the location of the red solid circle shown in Figure 4.2, calculated using the ICFD models and Eq. (4.1)

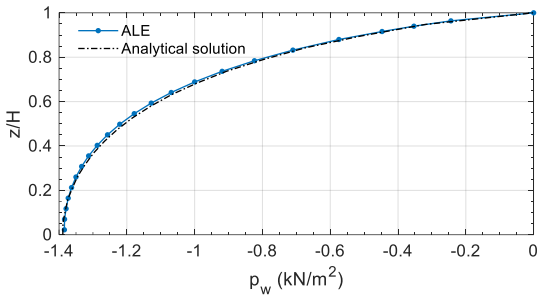

(a) S-1, $H = 1.2$ m, $t = 0.0125$ sec

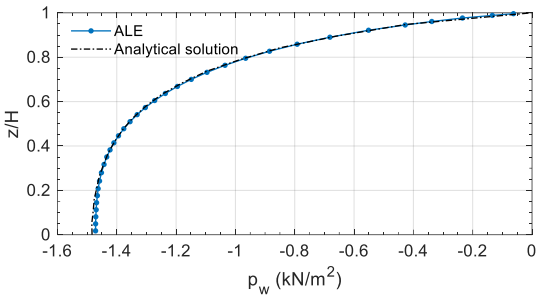

(b) S-1, $H = 1.8$ m, $t = 0.0125$ sec

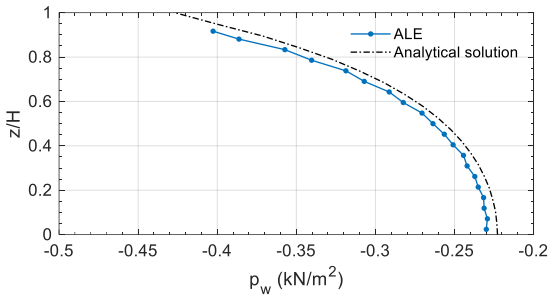

(c) S-2, $H = 1.2$ m, $t = 2.45$ sec

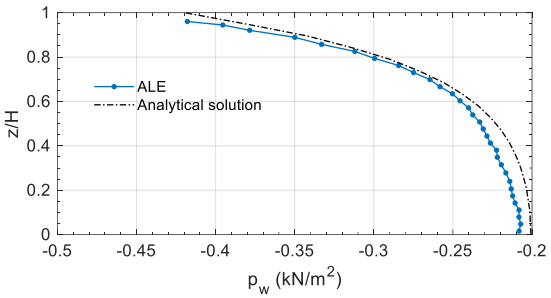

(d) S-2, $H = 1.8$ m, $t = 2.45$ sec

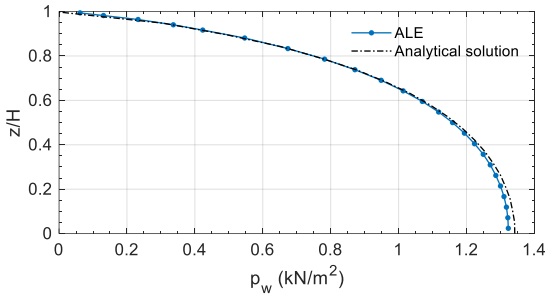

(e) E-1, $H = 1.2$ m, $t = 0.53$ sec

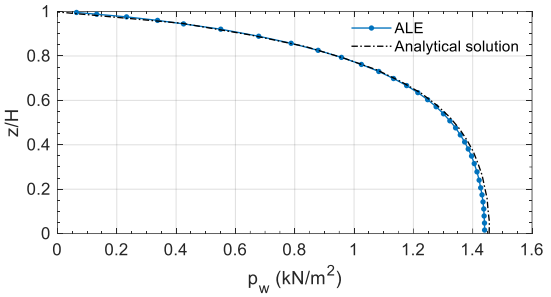

(f) E-1, $H = 1.8$ m, $t = 0.53$ sec

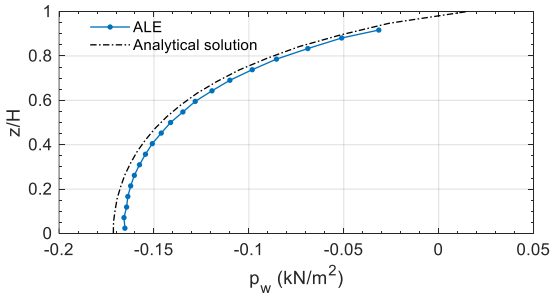

(g) E-2, $H = 1.2$ m, $t = 3.22$ sec

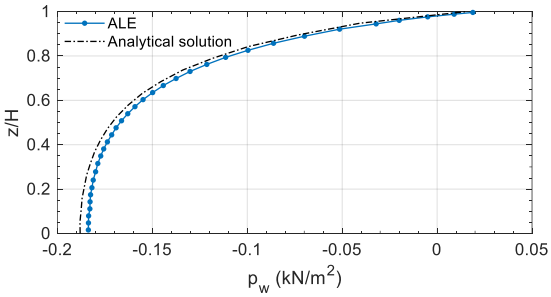

(h) E-2, $H = 1.8$ m, $t = 3.22$ sec

Figure 4.10. Distributions of the hydrodynamic pressure, p_w, along the green line on the tank wall shown in Figure 4.2, at the time step of a peak response (open red circle) shown in the corresponding panels of Figure 4.8, calculated using the ALE models and Eq. (4.1)

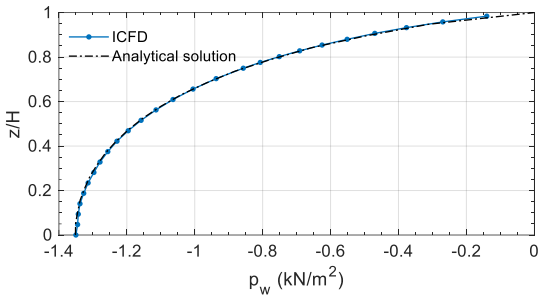

(a) S-1, $H = 1.2$ m, $t = 0.013$ sec

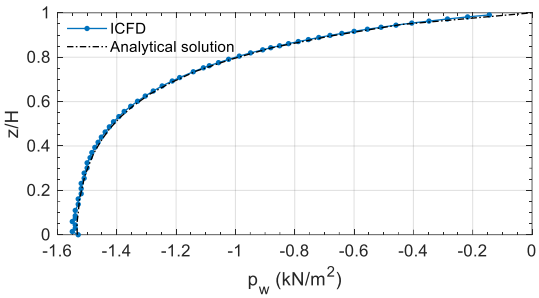

(b) S-1, $H = 1.8$ m, $t = 0.013$ sec

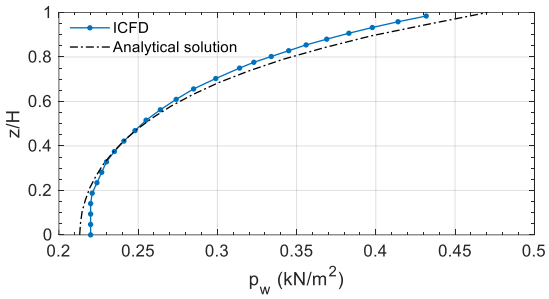

(c) S-2, $H = 1.2$ m, $t = 1.55$ sec

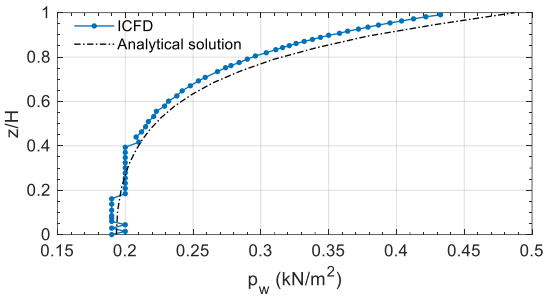

(d) S-2, $H = 1.8$ m, $t = 1.55$ sec

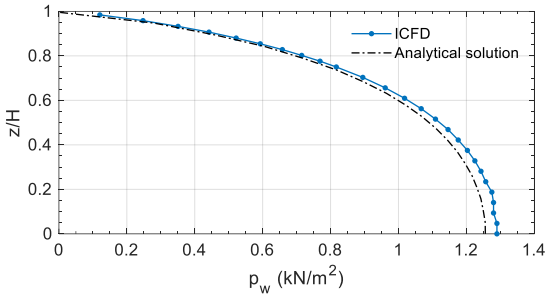

(e) E-1, $H = 1.2$ m, $t = 0.53$ sec

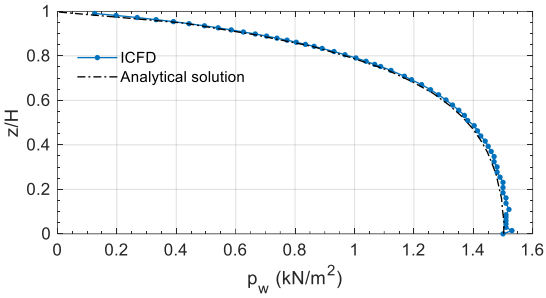

(f) E-1, $H = 1.8$ m, $t = 0.53$ sec

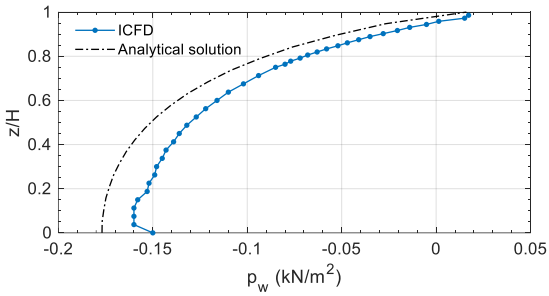

(g) E-2, $H = 1.2$ m, $t = 3.22$ sec

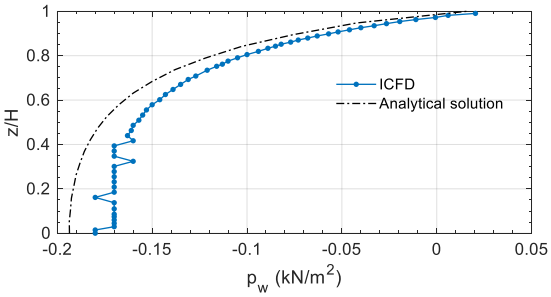

(h) E-2, $H = 1.8$ m, $t = 3.22$ sec

Figure 4.11. Distributions of the hydrodynamic pressure, p_{imp}, along the green line on the tank wall shown in Figure 4.2, at the time step of a peak response (open red circle) shown in the corresponding panels of Figure 4.9, calculated using the ICFD models and Eq. (4.1)

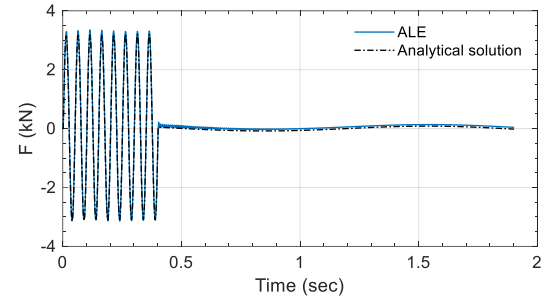

(a) S-1, $H = 1.2$ m

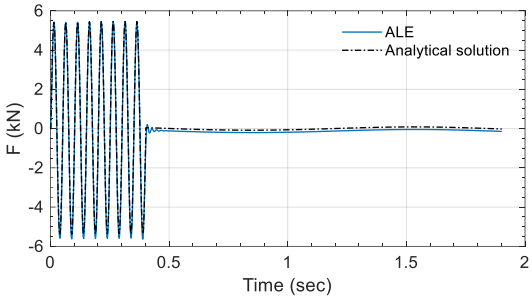

(b) S-1, $H = 1.8$ m

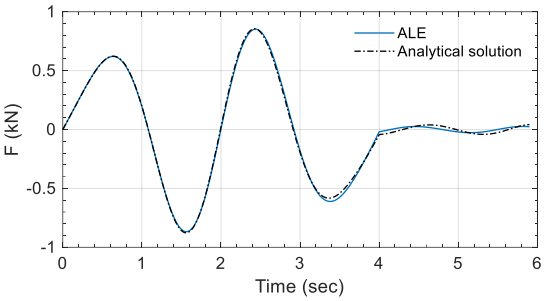

(c) S-2, $H = 1.2$ m

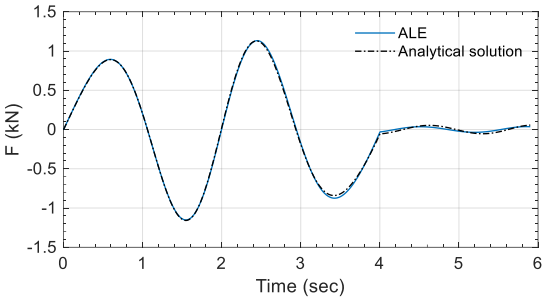

(d) S-2, $H = 1.8$ m

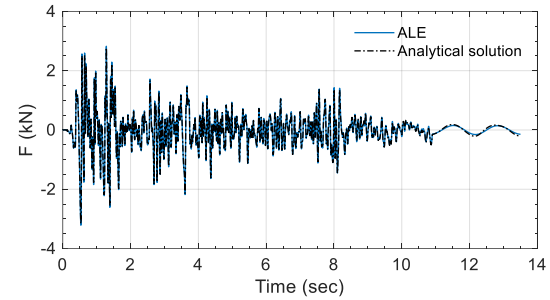

(e) E-1, $H = 1.2$ m

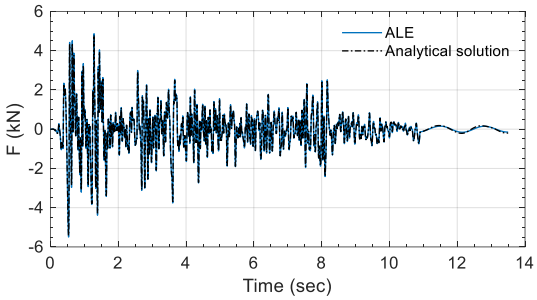

(f) E-1, $H = 1.8$ m

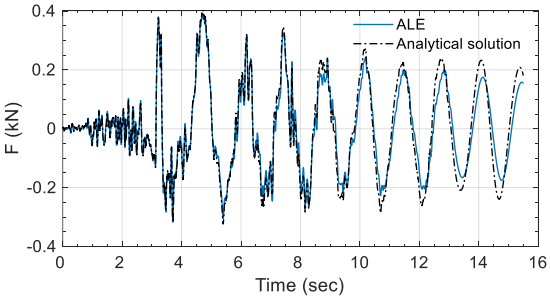

(g) E-2, $H = 1.2$ m

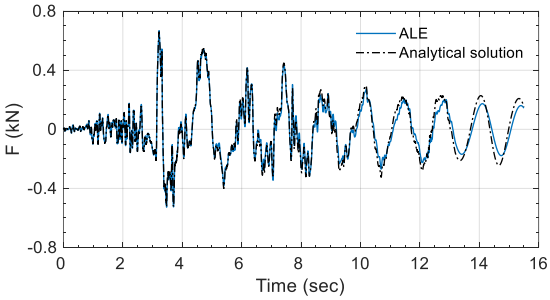

(h) E-2, $H = 1.8$ m

Figure 4.12. Time series of the shear force, F, in the x direction at the tank base, calculated using the ALE models and Eq. (4.2)

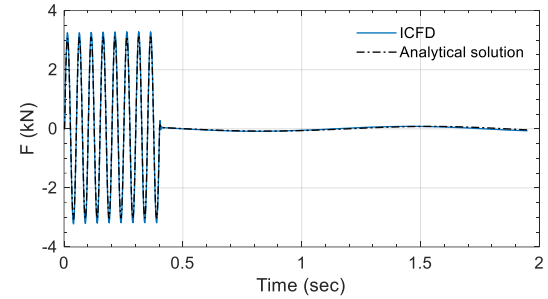

(a) S-1, $H = 1.2$ m

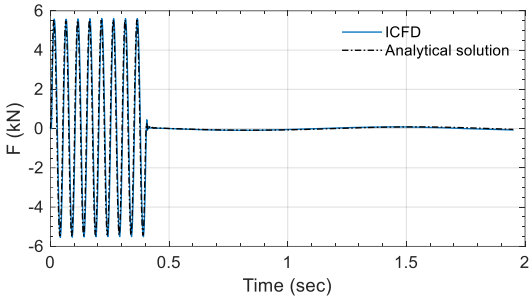

(b) S-1, $H = 1.8$ m

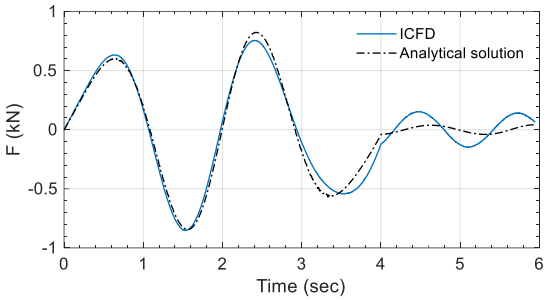

(c) S-2, $H = 1.2$ m

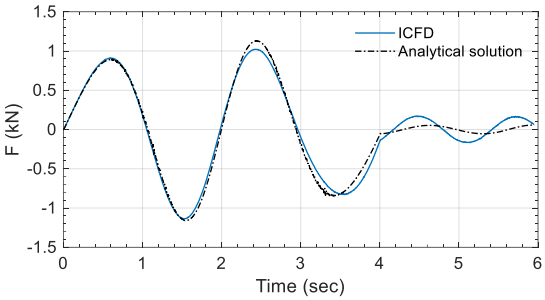

(d) S-2, $H = 1.8$ m

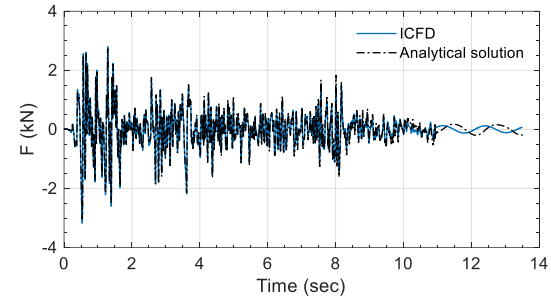

(e) E-1, $H = 1.2$ m

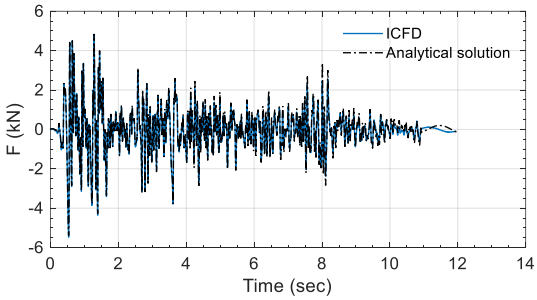

(f) E-1, $H = 1.8$ m

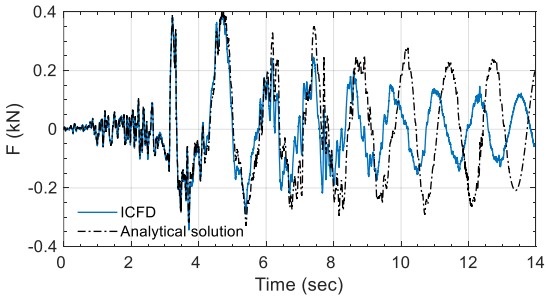

(g) E-2, $H = 1.2$ m

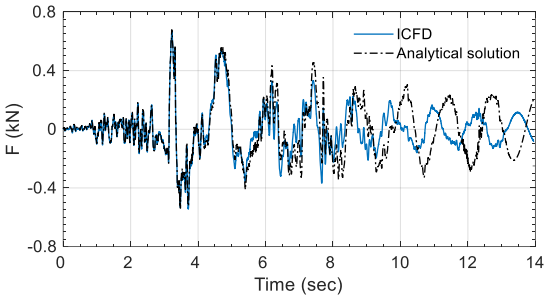

(h) E-2, $H = 1.8$ m

Figure 4.13. Time series of the shear force, F, in the x direction at the tank base, calculated using the ICFD models and Eq. (4.2)

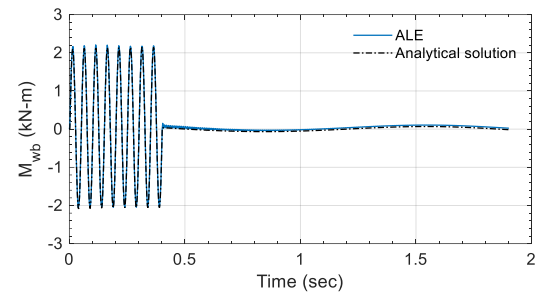

(a) S-1, $H = 1.2$ m

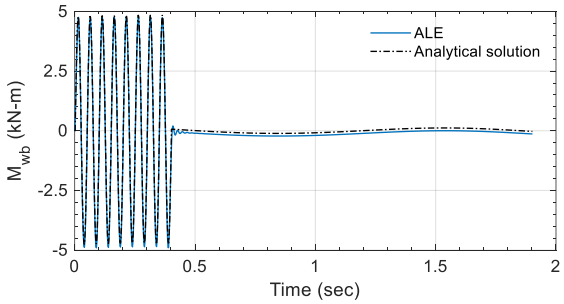

(b) S-1, $H = 1.8$ m

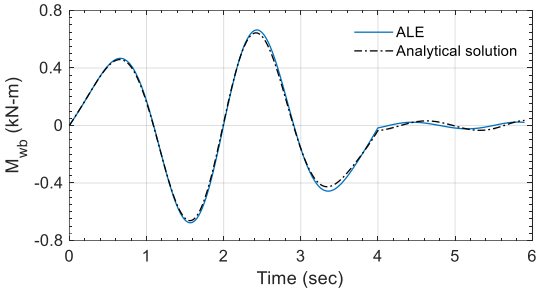

(c) S-2, $H = 1.2$ m

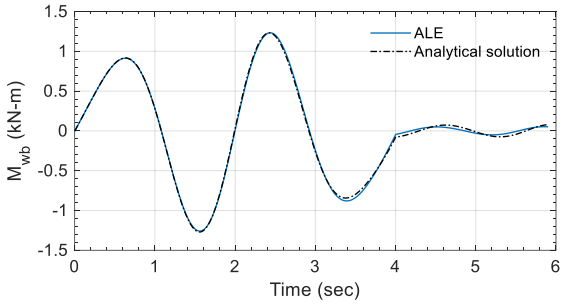

(d) S-2, $H = 1.8$ m

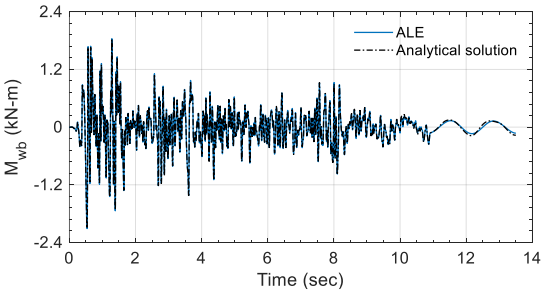

(e) E-1, $H = 1.2$ m

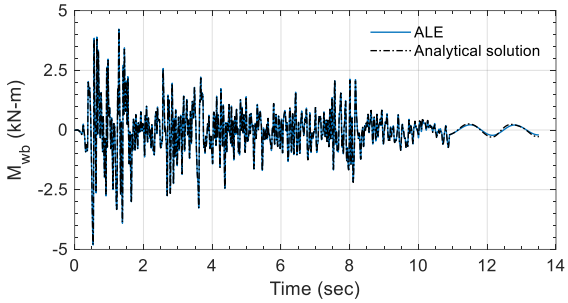

(f) E-1, $H = 1.8$ m

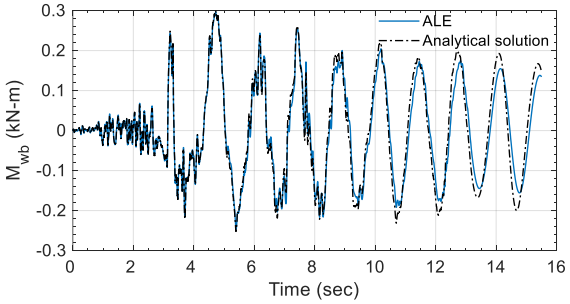

(g) E-2, $H = 1.2$ m

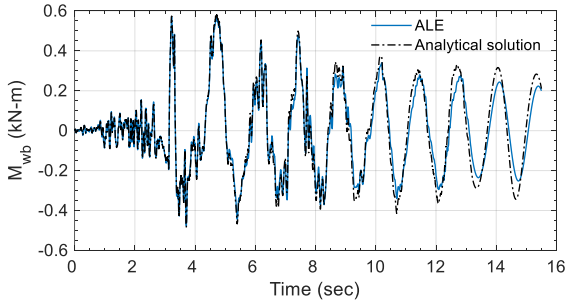

(h) E-2, $H = 1.8$ m

Figure 4.14. Time series of the moment, M_{wb}, about the y axis at the tank base, calculated using the ALE models and Eq. (4.3)

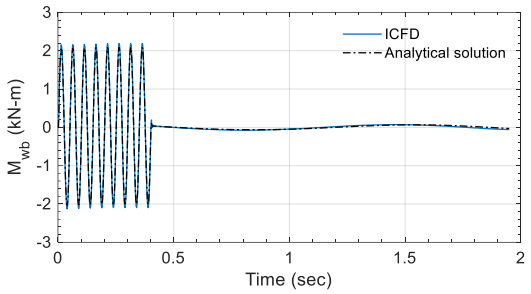

(a) S-1, $H = 1.2$ m

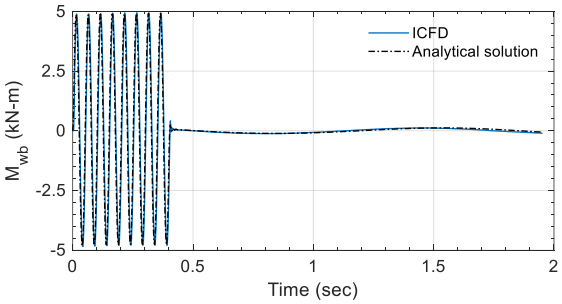

(b) S-1, $H = 1.8$ m

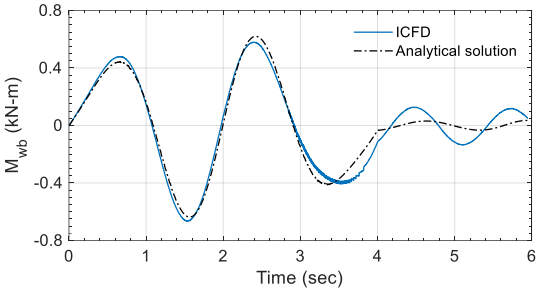

(c) S-2, $H = 1.2$ m

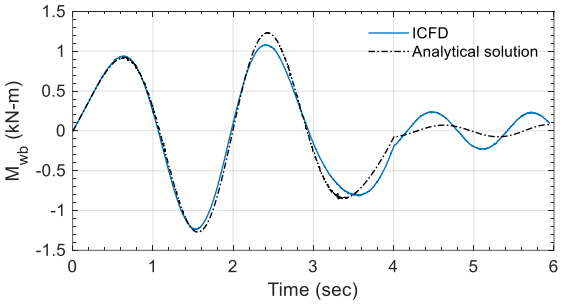

(d) S-2, $H = 1.8$ m

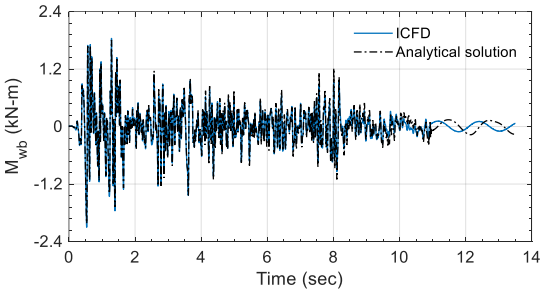

(e) E-1, $H = 1.2$ m

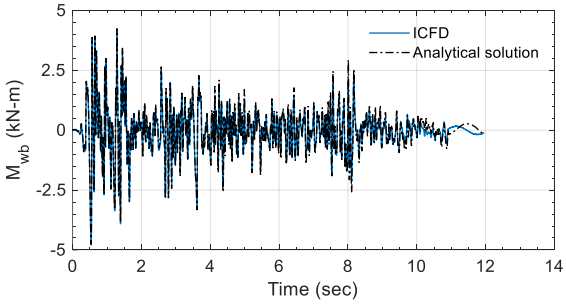

(f) E-1, $H = 1.8$ m

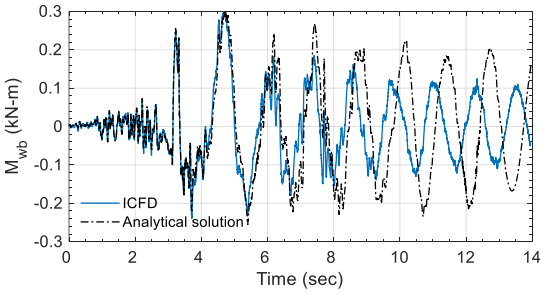

(g) E-2, $H = 1.2$ m

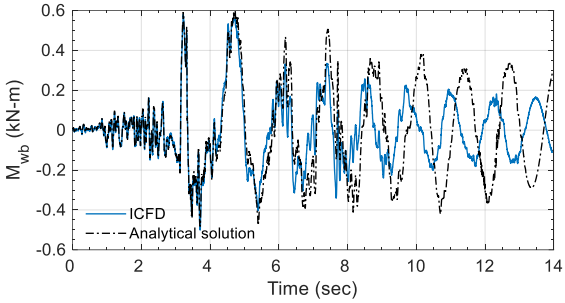

(h) E-2, $H = 1.8$ m

Figure 4.15. Time series of the moment, M_{wb}, about the y axis at the tank base, calculated using the ICFD models and Eq. (4.3)

For numerical calculations, it is not physically possible to generate waves without vertical accelerations, but the accelerations can be reduced by scaling down the amplitude of the input motion. As noted in Section 4.2.2, the input motions, S-2 and E-2, are expected to induce significant vertical motions on the free surface, and so their amplitudes are both scaled to a tiny PGA, namely, 0.025 g.

The relationship between $p_{con,j}$ and $d_{w,j}$ assumed by Veletsos (i.e., $p_{con,j} = \rho g d_{w,j}$ at $z = H$) is not valid in the numerical models as the free surface moves downward (i.e., $d_{w,j} < 0$) because there is no fluid existing at $z = H$ to produce the pressure, $p_{con,j}$. The vertical displacements of the free surface are tracked in the ALE models through the *DATABASE_TRACER card. The card records the time series of the coordinates (x, y, z) of assigned points that float on the free surface and move with the velocities of the fluid in the three directions. For the ICFD analysis, the *Floater* option in the graphical user interface (GUI) of LS-Prepost (2018c) is used to create points that are fixed at the assigned x and y coordinates and float on the free surface. The GUI is used to output the time series of the z coordinates of the assigned points. The vertical displacements of the free surface, d_w, in the ALE and ICFD models are calculated using the z coordinates of a set of floating points assigned along the direction of the seismic input (i.e., x direction) across the diameter of the tank.

The time series of d_w calculated using the numerical models and Eq. (4.4) are presented at the location of the purple triangle on the free surface shown in Figure 4.2. The purple triangle is located $0.1R$ from the tank wall because the ALE and ICFD solvers cannot properly calculate the position of the free surface at the boundary of the fluid domain (i.e., interface of the fluid and the tank wall; more details will be presented together with Figures 4.18 and 4.19). The purple triangle is located at the cylindrical coordinates $(r, \theta, z) = (0.7 \text{ m}, 0, H)$, used in Eq. (4.4), and at the global coordinates $(x, y, z) = (0.7 \text{ m}, 0, H)$, at $t = 0$, used for extracting numerical results. The x coordinate of the purple triangle changes in the numerical analysis with the horizontal displacement of the tank subjected to seismic motions. Wave heights at the purple triangle are calculated by interpolating the z coordinates of its two adjacent floating points at each time step. Figure 4.16 enables a comparison of the time series of d_w for the ALE models for the two fluid

heights (i.e., $H = 1.2$ or 1.8 m) and the four input motions (i.e. S-1, S-2, E-1, or E-2). Figure 4.17 presents companion information for the ICFD models.

The distributions of d_w calculated using the numerical models and Eq. (4.4) are presented along the blue dashed line on the free surface shown in Figure 4.2. Numerical results are calculated using the z coordinates of the floating points assigned across the diameter of the tank in the x direction. The coordinates of the blue line are used in Eq. (4.4): $(r, \theta, z) =$ (-0.79 to 0.79 m, 0, H), where $H = 1.2$ or 1.8 m. Figures 4.18a to h present distributions of d_w at the time of peak response, identified using an open red circle in the time series for the ALE models, shown in the corresponding panels of Figure 4.16. (For each of the E-1 and E-2 time series presented in Figures 4.16e to h, the open red circle is at a peak in the first 5 seconds because thereafter the ALE results gradually diverge from the analytical results, as discussed on pages 221 through 226.) Figure 4.19 presents distributions of d_w at the time of the peak response, identified using an open red circle in the time series for the ICFD models, shown in each panel of Figure 4.17. (The open red circle is at a peak in an early stage of each time series when the ICFD and analytical results are in-phase. The accuracy of the ICFD predictions of wave height is discussed on pages 226 and 227.) The blue dots in each panel of Figures 4.18 and 4.19 present the vertical displacements of floating points on the free surface at a time step. In Figure 4.18, the vertical displacements of the free surface at $r / R = \pm 1$ (i.e., interface of the fluid and the wall) calculated using the ALE models are all zero for the two fluid heights and the four input motions. The vertical displacements of the free surface fluctuate near $r / R = \pm 1$ due to the boundary effect of the fluid velocity calculated by the ALE solver (Do 2019) and gradually stabilize by $r / R = \pm 0.9$. In Figure 4.19, which presents results of analysis of the ICFD models, the vertical displacements of the free surface adjacent to the tank wall (i.e., $r / R = \pm 1$) are zero. No fluctuation is seen in the ICFD results near the wall (i.e., $0.9 \le \pm r / R \le 1$).

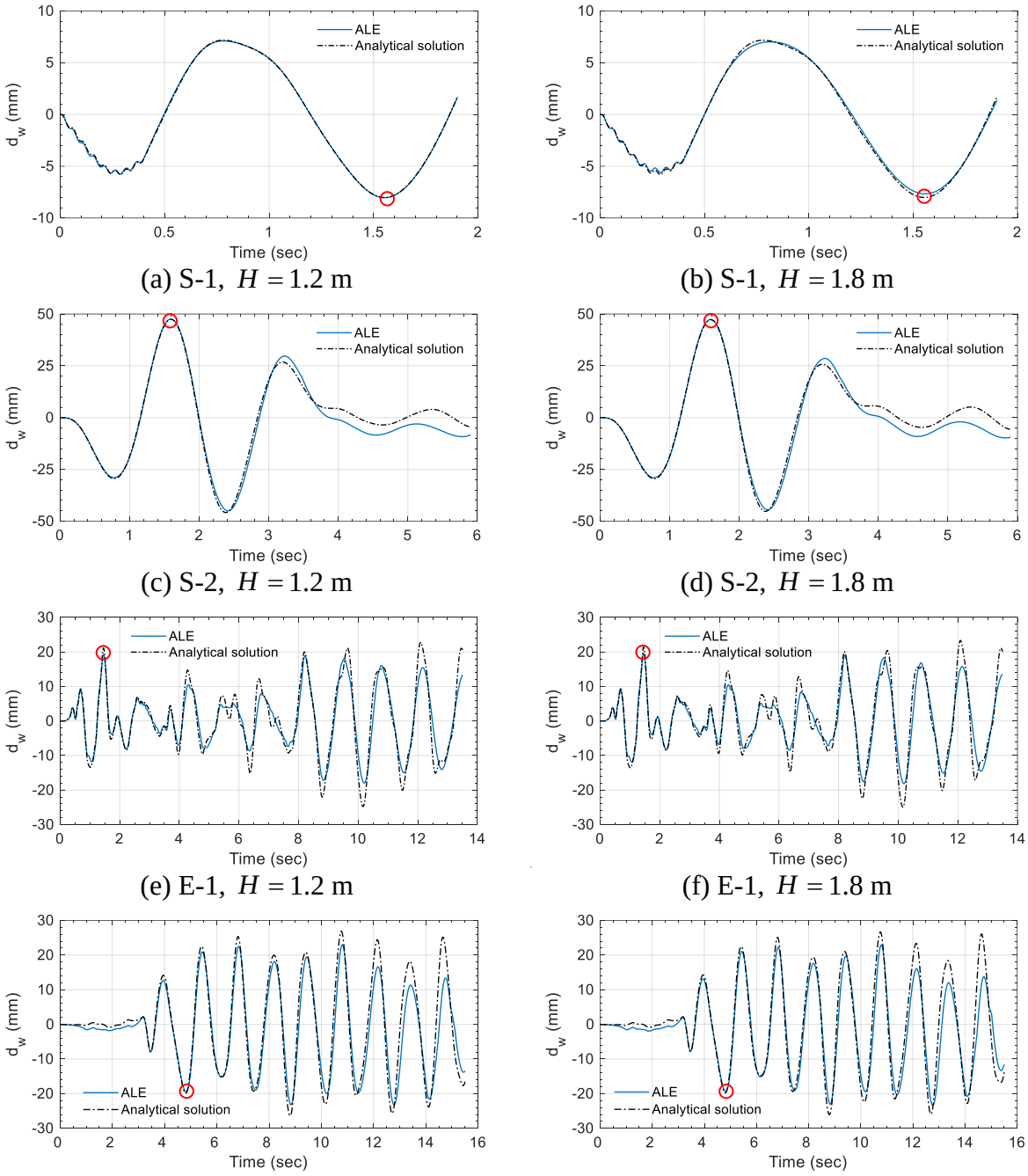

(a) S-1, $H = 1.2$ m (b) S-1, $H = 1.8$ m

(c) S-2, $H = 1.2$ m (d) S-2, $H = 1.8$ m

(e) E-1, $H = 1.2$ m (f) E-1, $H = 1.8$ m

(g) E-2, $H = 1.2$ m (h) E-2, $H = 1.8$ m

Figure 4.16. Time series of the vertical displacement of the free surface, d_w, at the location of the purple triangle presented in Figure 4.2, calculated using the ALE models and Eq. (4.4)

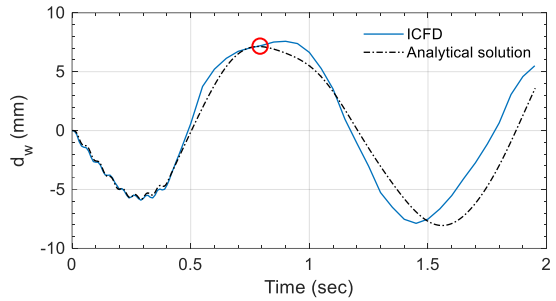

(a) S-1, $H = 1.2$ m

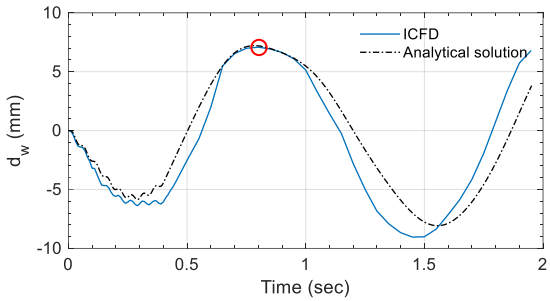

(b) S-1, $H = 1.8$ m

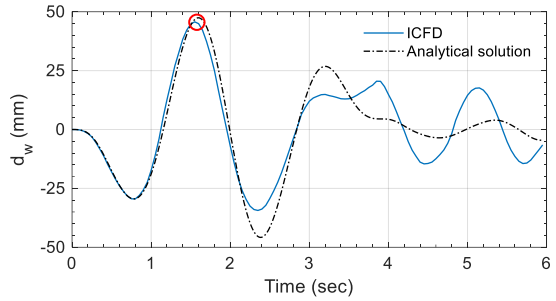

(c) S-2, $H = 1.2$ m

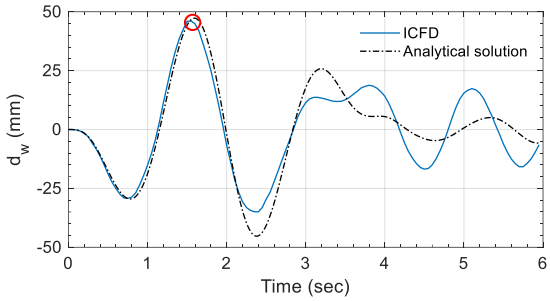

(d) S-2, $H = 1.8$ m

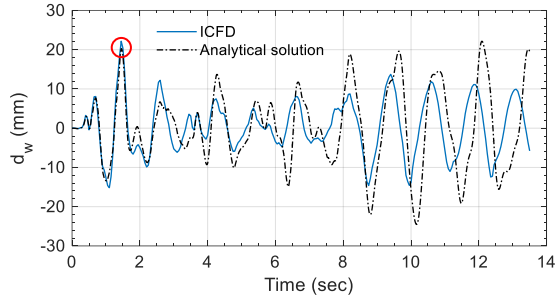

(e) E-1, $H = 1.2$ m

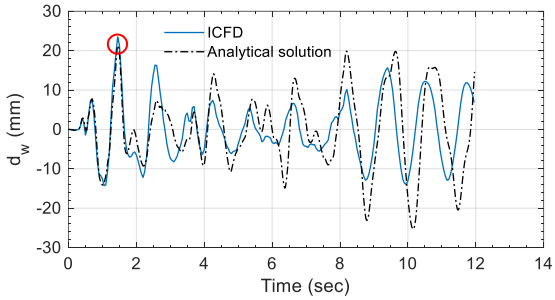

(f) E-1, $H = 1.8$ m

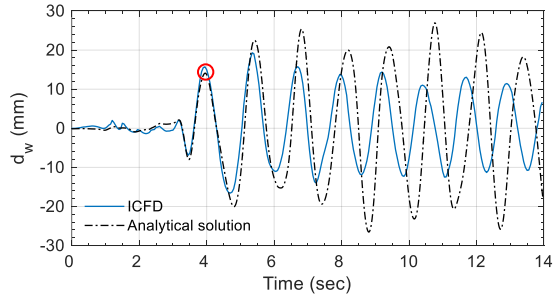

(g) E-2, $H = 1.2$ m

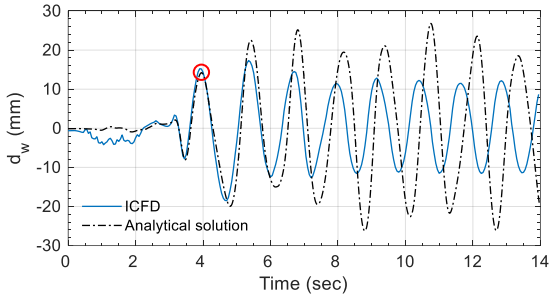

(h) E-2, $H = 1.8$ m

Figure 4.17. Time series of the vertical displacement of the free surface, d_w, at the location of the purple triangle presented in Figure 4.2, calculated using the ICFD models and Eq. (4.4)

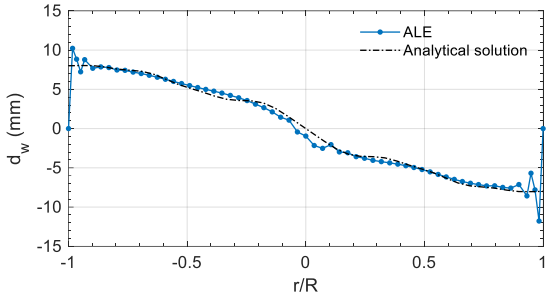

(a) S-1, $H = 1.2$ m, $t = 1.56$ sec

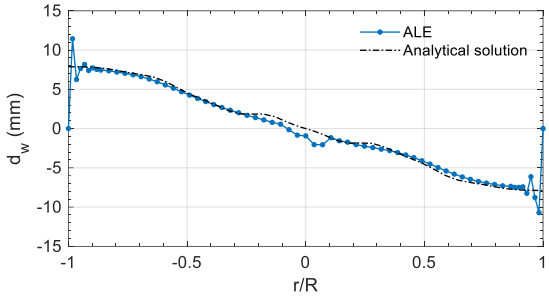

(b) S-1, $H = 1.8$ m, $t = 1.56$ sec

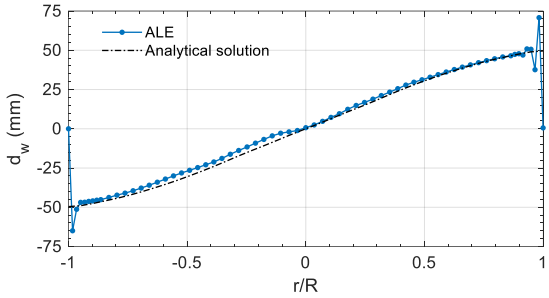

(c) S-2, $H = 1.2$ m, $t = 1.61$ sec

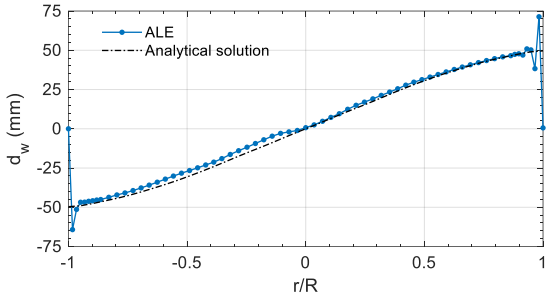

(d) S-2, $H = 1.8$ m, $t = 1.61$ sec

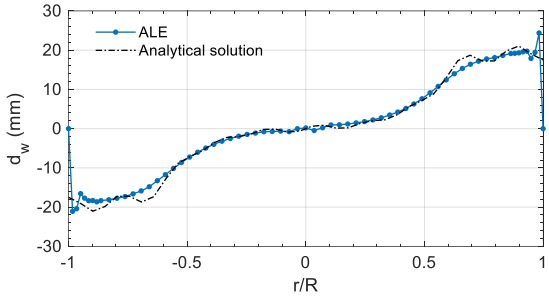

(e) E-1, $H = 1.2$ m, $t = 1.45$ sec

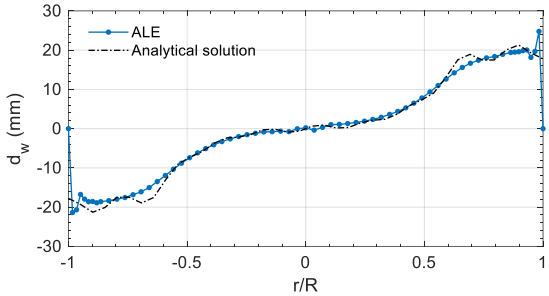

(f) E-1, $H = 1.8$ m, $t = 1.45$ sec

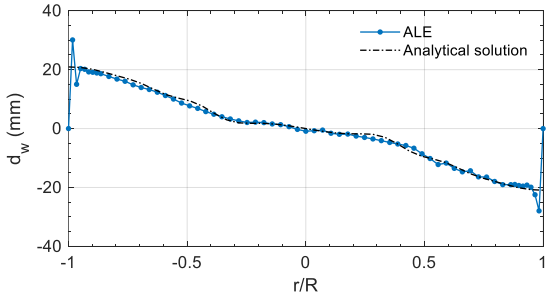

(g) E-2, $H = 1.2$ m, $t = 4.82$ sec

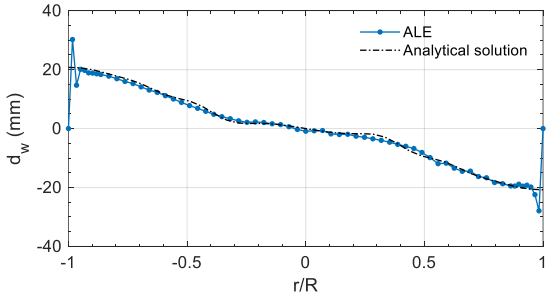

(h) E-2, $H = 1.8$ m, $t = 4.82$ sec

Figure 4.18. Distribution of the vertical displacement of the free surface, d_w, along the blue dashed line shown in Figure 4.2, at the time step of a peak response (open red circle) shown in the corresponding panels of Figure 4.16, calculated using the ALE models and Eq. (4.4)

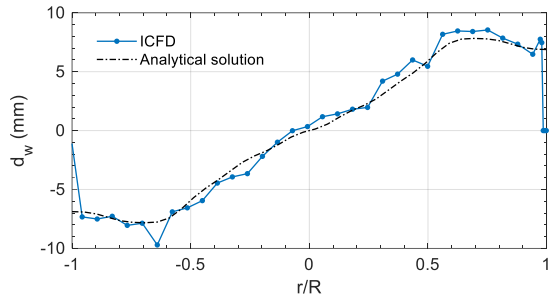

(a) S-1, $H = 1.2$ m, $t = 0.8$ sec

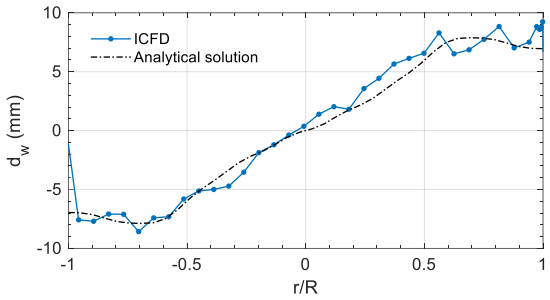

(b) S-1, $H = 1.8$ m, $t = 0.8$ sec

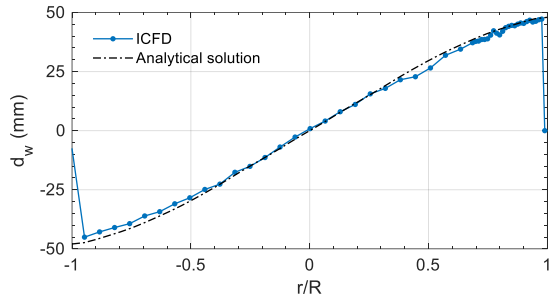

(c) S-2, $H = 1.2$ m, $t = 1.59$ sec

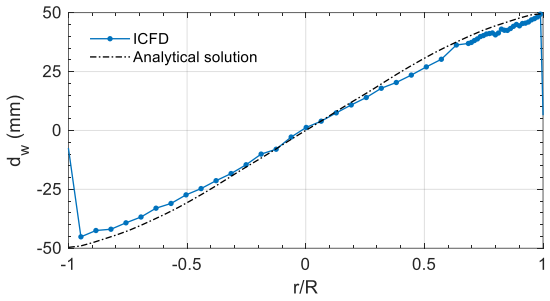

(d) S-2, $H = 1.8$ m, $t = 1.59$ sec

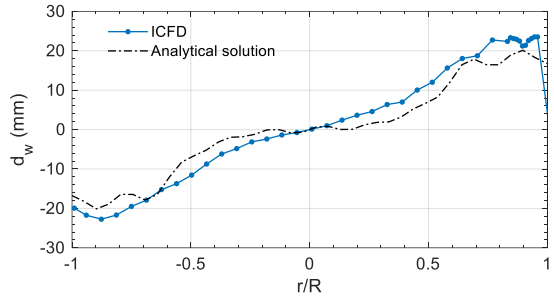

(e) E-1, $H = 1.2$ m, $t = 1.45$ sec

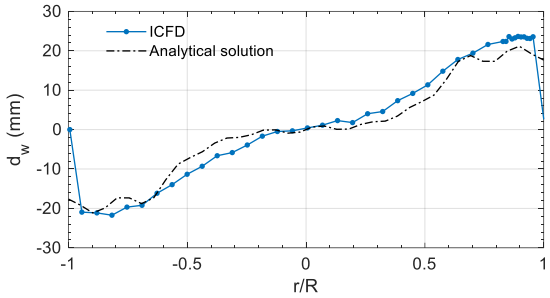

(f) E-1, $H = 1.8$ m, $t = 1.45$ sec

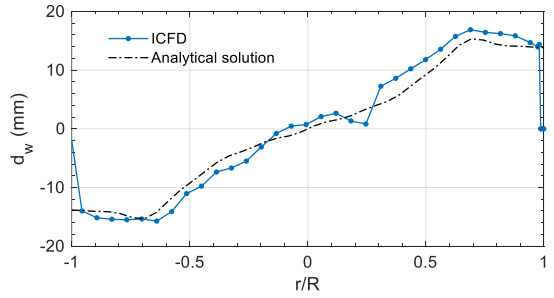

(g) E-2, $H = 1.2$ m, $t = 3.95$ sec

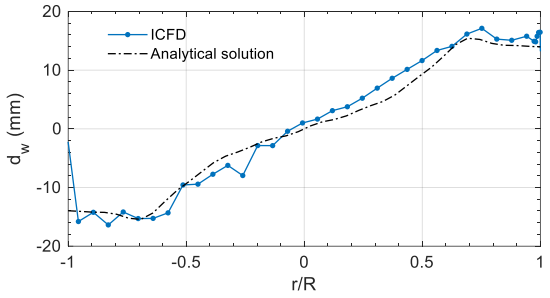

(h) E-2, $H = 1.8$ m, $t = 3.95$ sec

Figure 4.19. Distribution of the vertical displacement of the free surface, d_w, along the blue dashed line shown in Figure 4.2, at the time step of a peak response (open red circle) shown in the corresponding panels of Figure 4.17, calculated using the ICFD models and Eq. (4.4)

Discussion

Figures 4.8 to 4.19 enable comparisons of the numerical and analytical FSI responses of a rigid, base-supported, cylindrical tank ($R = 0.79$ m, $H_s = 2$m), filled with water to depths of $H = 1.2$ and 1.8 m, and subjected to input motions S-1, S-2, E-1, and E-2. The four motions are small-amplitude, unidirectional, and horizontal. The reported FSI responses include p_w at the location of the red circle and along the green line shown in Figure 4.2, F and M_{wb} at the tank base, and d_w at the location of the purple triangle and along the blue dashed line shown in Figure 4.2. Table 4.9 presents the maximum absolute values (amplitudes) of the analytical, ALE, and ICFD results of p_w, F, M_{wb}, and d_w, for the two fluid heights and the four motions. The results are extracted from the time series presented in Figures 4.8, 4.9, and 4.12 to 4.17. The percentage differences between the ALE (and ICFD) and analytical results are presented in parentheses in Table 4.9.

Per Table 4.9, for an ALE or ICFD model and an input motion, the listed percentage differences of each response (p_w, F, M_{wb}, or d_w) for the two fluid heights (1.2 and 1.8 m) are similar. This outcome indicates that the effect of the fluid height (volume) on the degree of accuracy of the ALE and ICFD models used here is insignificant.

The ALE and analytical results for p_w, F, and M_{wb} for each of the four motions are in excellent agreement, as seen in Figures 4.8, 4.10, 4.12, and 4.14. Per Table 4.9, the differences of the ALE and analytical results in these responses are less than $\pm 5\%$. For d_w, per Figures 4.16 and 4.18, the ALE and analytical results are in excellent agreement for S-1 and S-2 (in panels a to d), and their percentage differences, listed in Table 4.9, are small ($\leq \pm 4\%$). However, as shown in Figure 4.16, the E-1 and E-2 time series of d_w (in panels e to h) calculated using the ALE models are reasonable for the first 5 to 8 seconds, but thereafter the amplitudes diverge from the analytical results. The ALE models underestimate the peak amplitudes of d_w for E-1 and E-2 by -12% to -22%, as presented in Table 4.9. The underestimation of the amplitudes for the longer duration motions, E-1 and E-2, is in part due to the limitation of outputting wave heights using floating points for the ALE analysis. This limitation is discussed in Appendix C. Although the

Table 4.9. Maximum absolute FSI responses of the rigid base-supported tank calculated using the numerical models and the analytical solutions, extracted from Figures 4.8, 4.9, and 4.12 to 4.17, $H = 1.2$ and 1.8 m, input motions S-1, S-2, E-1, and E-2

Motion	Response	$H = 1.2$ m			$H = 1.8$ m		
		A.S.[1]	ALE (diff)[2]	ICFD (diff)[2]	A.S.[1]	ALE (diff)[2]	ICFD (diff)[2]
S-1	p_w (kN/m^2)	1.4	1.41 (1%)	1.44 (4%)	1.5	1.53 (1%)	1.53 (0%)
	F (kN)	3.2	3.35 (5%)	3.29 (5%)	5.5	5.63 (3%)	5.61 (1%)
	M_{wb} (kN-m)	2.1	2.21 (3%)	2.19 (5%)	4.9	4.91 (1%)	4.94 (1%)
	d_w (mm)	8.0	7.92 (-1%)	7.88 (-2%)	8.0	7.66 (-4%)	9.05 (12%)
S-2	p_w (kN/m^2)	0.2	0.23 (3%)	0.23 (5%)	0.2	0.21 (4%)	0.20 (-1%)
	F (kN)	0.9	0.87 (-1%)	0.85 (1%)	1.2	1.15 (-1%)	1.14 (-2%)
	M_{wb} (kN-m)	0.7	0.68 (2%)	0.67 (4%)	1.3	1.26 (-1%)	1.24 (-3%)
	d_w (mm)	47.4	47.56 (0%)	45.73 (-4%)	47.3	47.36 (0%)	46.08 (-3%)
E-1	p_w (kN/m^2)	1.4	1.37 (-2%)	1.37 (4%)	1.5	1.49 (-1%)	1.50 (0%)
	F (kN)	3.2	3.22 (2%)	3.17 (4%)	5.4	5.50 (1%)	5.48 (2%)
	M_{wb} (kN-m)	2.1	2.11 (0%)	2.10 (4%)	4.8	4.82 (0%)	4.80 (1%)
	d_w (mm)	24.8	19.31 (-22%)	22.15 (-10%)	24.9	19.59 (-21%)	23.48 (-4%)
E-2	p_w (kN/m^2)	0.2	0.17 (-4%)	0.16 (-10%)	0.2	0.18 (-2%)	0.18 (-7%)
	F (kN)	0.4	0.39 (-3%)	0.39 (-3%)	0.7	0.67 (1%)	0.67 (-1%)
	M_{wb} (kN-m)	0.3	0.30 (-1%)	0.30 (0%)	0.6	0.57 (-3%)	0.58 (-2%)
	d_w (mm)	26.9	23.24 (-14%)	19.32 (-28%)	26.7	23.40 (-12%)	18.50 (-31%)

1. Analytical solution
2. Percentage difference of FSI responses calculated using the numerical models with respect to those calculated using the analytical solutions, to the nearest 1%

amplitudes of d_w are underestimated for E-1 and E-2 (after 5 to 8 seconds of the analysis) by the ALE models, the phases of the time series shown in Figures 4.16e to h are in good agreement with the analytical solution. The phases of the time series are associated with the periods/frequencies of waves (i.e., convective periods/frequencies). The first three convective frequencies, $f_{con,j}$, of the tank in the ALE models are identified from the times series of d_w for E-1 and E-2, at 18 locations across the tank diameter in the x direction at $\pm 0.1R$, $\pm 0.2R$, …, $\pm 0.9R$. The time series are transformed into the frequency domain using the Fast Fourier Transform (FFT). The convective frequencies are identified from the Fourier amplitude spectra. Figure 4.20 presents spectra for the two input motions (E-1 and E-2), the two fluid heights (1.2 and 1.8 m), and the 18 locations, together, normalized by their maximum ordinates, for frequencies ranging between 0 and 3 Hz. The peaks identified using open red circles are associated with the first three convective modes. (These spectra are presented together in one figure because the convective frequencies are independent of seismic motions, fluid heights[32], and locations on the free surface if the amplitude of the input motion is small.) Table 4.10 presents the frequencies calculated using the analytical solution per Eq. (3.73) (Veletsos 1984) and the ALE models. The percentage differences are tiny (i.e., $\leq 2\%$).

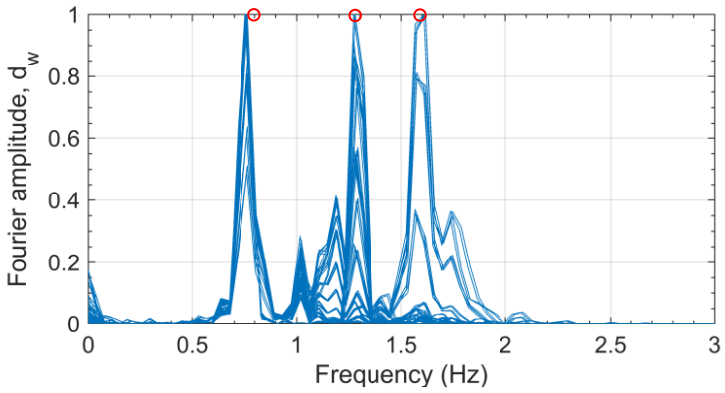

Figure 4.20. Normalized Fourier amplitude spectra for wave heights, d_w, at 18 locations along the x direction, $H = 1.2$ and 1.8 m, motions E-1 and E-2, calculated using the ALE models

[32] The effect of fluid height H on the convective frequencies in a tank with a given radius R is negligible if $H / R > 1$; see Figure 3.24.

Table 4.10. Convective frequencies, $f_{con,j}$, of the base-supported tank, calculated using Eq. (3.73) and the ALE models, and their percentage differences

	Frequency (Hz)		
Mode	Analytical solution	ALE models	Difference[1] (%)
First	0.76	0.76	0
Second	1.29	1.27	-2
Third	1.64	1.61	-2

1. Percentage differences of the numerical results with respect to those calculated using the analytical solution

Table 4.11 compares the maximum absolute values of d_w in the first 5 seconds of each time series presented in Figure 4.16, for which the amplitudes calculated using the ALE models and the analytical solution are consistent. (All results for S-1 and S-2 are used here because the durations of both motions are less than 5 seconds. Consequently, those data presented in Tables 4.9 and 4.11 are identical.) Using the percentage differences listed in Table 4.11, the greatest underestimation reduces to -9% from -22% (see Table 4.9).

Table 4.11. Maximum absolute values of d_w in the first 5 seconds of the time series presented in Figure 4.16, ALE and analytical results, $H = 1.2$ and 1.8 m, input motions S-1, S-2, E-1, and E-2

	d_w (mm)			
	1.2 m		1.8 m	
Motion	Analytical solution	ALE (diff)[1]	Analytical solution	ALE (diff)[1]
S-1	8.0	7.9 (-1%)	8.0	7.7 (-4%)
S-2	47.4	47.6 (0%)	47.3	47.4 (0%)
E-1	21.1	19.3 (-9%)	21.4	19.6 (-8%)
E-2	19.9	19.5 (-2%)	19.8	19.4 (-2%)

1. Percentage difference of FSI responses calculated using the numerical models with respect to those calculated using the analytical solutions, to the nearest 1%

In the E-1 time series of d_w, shown in Figures 4.16e and f, the analytical solution for $5 \le t \le 8$ seconds includes higher mode response, which is not predicted by the ALE models. This higher mode response is identified using green circles in Figure 4.21a, which is repeated from Figure 4.16f. The two consecutive crests of the higher mode response are separated (i.e., period) by 0.6 second, which is associated with the third convective mode that has a frequency of approximately 1.6 Hz (see Table 4.10). The absence of response in the third convective mode in the ALE results could be associated with 1) the use of linear interpolation of the z coordinates of the floating points for calculating wave heights, and/or 2) suppression of the higher modes by numerical damping.

Wave heights are calculated here by interpolating between the z coordinates of the two floating points on the free surface closest to each monitoring location (i.e., $r = 0.7$ m; purple triangle presented in Figure 4.2) at each time step. The interpolation assumes a linear change in the free surface displacement between two floating points. Per Figure 3.27, the wavelength of the vertical displacement of the free surface in the third convective mode is $4R/5 = 632$ mm. The maximum distance between two floating points adjacent to the location of the purple triangle is 22 mm, for $0 \le t \le 14$ seconds. The wavelength of 632 mm is significantly longer than the maximum distance (= 22 mm) between the two floating points adjacent to $r = 0.7$ m. The use of linear interpolation for calculating wave heights is therefore not the reason why the third mode response is suppressed in the ALE analysis. For additional information, Figure 4.21b presents the $z-$displacement history of the floating point that was located at $r = 0.7$ m at time $t = 0$ second. This point moves with the velocity of the fluid in three directions, and at 5 and 8 seconds has moved 24 mm and 47 mm horizontally, respectively, from its original position (at $r = 0.7$ m) toward the center of the free surface. The analytical results are output at the same spatial coordinate of the floating point at each time step. The third mode response is also suppressed at $t \approx 5$ seconds in the ALE prediction of d_w in this alternate presentation.

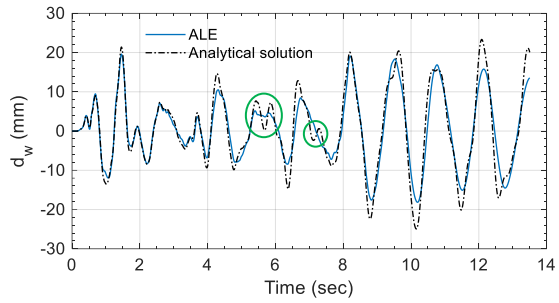

(a) d_w at $r = 0.7$ m, Figure 4.16f

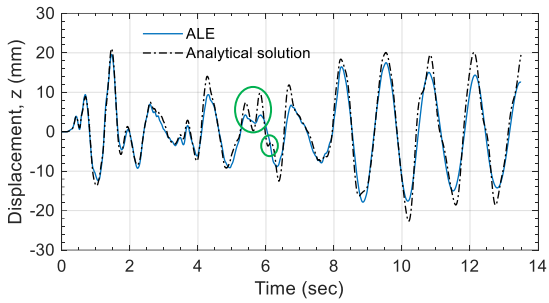

(b) z – displacement of the floating point initially at $r = 0.7$ m at time $t = 0$ second

Figure 4.21. Time series of d_w at $r = 0.7$ m (the location of the purple triangle presented in Figure 4.2) and z – displacement of the floating point initially located at $r = 0.7$, calculated using the ALE model and Eq. (4.4)

Figure 4.22 presents Fourier amplitude spectra of the time series of d_w for E-1, at 18 locations across the tank diameter in the x direction at $\pm 0.1R$, $\pm 0.2R$, …, $\pm 0.9R$, calculated using the ALE model and Eq. (4.4). The amplitudes are normalized by their maximum ordinates for frequencies ranging between 0 and 3 Hz. The ALE and analytical spectra are enveloped using blue and grey dashed lines, respectively. The three significant peaks in the enveloped spectra are associated with the first three convective modes, with frequencies noted in Table 4.10. The width of a peak is associated with the damping ratio (Chopra 2012): the greater the width of a peak, the greater the damping ratio. As shown in Figure 4.22, the widths of the peaks calculated using the ALE model and the analytical solution are similar for the first and second modes (at 0.76 and 1.3 Hz). The width of the peak associated with the third mode (at 1.6 Hz) calculated using the ALE model is broader than that calculated using the analytical solution. Consequently, numerical damping is the most likely cause of the suppression of higher mode response of d_w in the ALE analysis. In this case, the higher mode response does not affect the maximum amplitude of d_w.

On the basis of the comparisons presented above, the authors concludes that the ALE models of the rigid base-supported tank are verified for calculating p_w, F, M_{wb}, and $f_{con,j}$, but are limited to the analysis of short duration (i.e., 5 to 8 seconds in the analysis here) motions for calculating d_w, until the issues discussed in Appendix C are resolved.

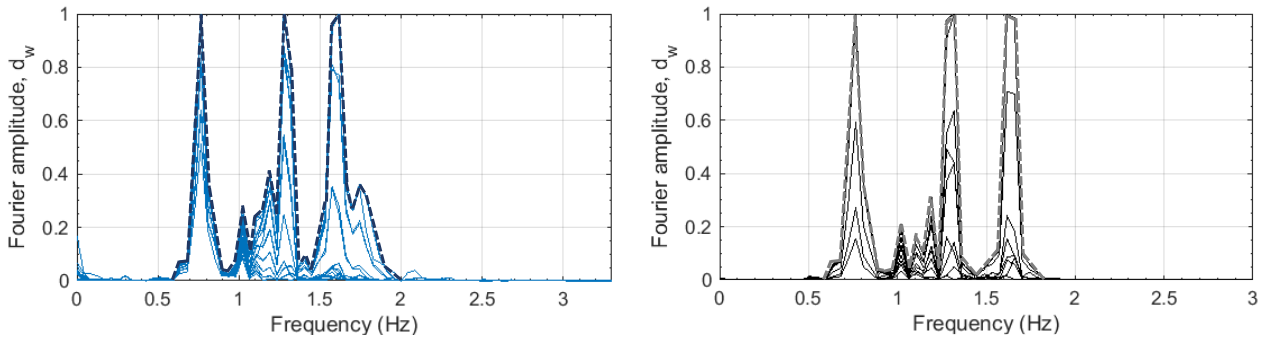

(a) ALE (b) analytical solution Eq. (4.4)

Figure 4.22. Normalized Fourier amplitude spectra for wave heights, d_w, at 18 locations along the x direction, $H = 1.8$ m, E-1, calculated using the ALE model and Eq. (4.4)

As presented in Figures 4.9, 4.11, 4.13, and 4.15, the ICFD and analytical results of p_w, F, and M_{wb} for motions S-1, S-2, and E-1 are in excellent agreement, but those for E-2 agree reasonably only for the first 6 seconds. (The maximum absolute values of p_w, F, and M_{wb} for E-2 are attained in the first 6 seconds.) Per Table 4.9, the differences between the ICFD and analytical results are less than $\pm$ 10%. Per Figure 4.17, the ICFD results for the time series of d_w are reasonably consistent with the analytical results for the first cycle (i.e., a crest and a trough) only: the first 1.2, 2, 1.6, and 4.5 seconds for S-1, S-2, E-1 and E-2, respectively. Subsequently, the amplitudes and periods of waves are generally underestimated by the ICFD models. Per Table 4.9, the differences between the ICFD and analytical results range between -31% and 12%. The differences between the ICFD and analytical results for p_w, F, and M_{wb} and motion E-2, as presented in panels g and h of Figures 4.9, 4.13, and 4.15, are linked to the inaccurate calculation of d_w and the long duration of the analysis (i.e., 14 seconds). Motion E-2 drives waves in the tank (see Section 4.2.2), and so p_w, F, and M_{wb} include a significant convective component. The inaccurate d_w calculated by the ICFD solver affects the results of p_w, F, and M_{wb}, and their inaccuracies (errors) accumulate with time. For the ICFD analysis, the free surface is defined through *ICFD_INITIAL_LEVELSET and its mesh is automatically generated by the solver. The calculation of wave actions on the free surface is a subject of LSTC development at the time of this writing (Caldichoury 2020). Accordingly, at the time of this writing, the ICFD models of the rigid base-supported tank are verified for calculating p_w, F,

and M_{wb}, if the wave action is not significant (e.g., for S-1, S-2, and E-1). The ICFD models are not verified for calculating waves (neither heights d_w nor frequencies).

4.2.3.2 Head-supported tank

The analytical solutions used to verify the numerical models of the rigid, head-supported tank ($R = 0.79$ m, $H_s = 2$ m, $H = 1.2$ and 1.8 m) are derived in Sections 3.3.1.1 and 3.3.2.1 for the impulsive and the convective responses, respectively, per Table 4.2. As noted in those two sections, the location of the seismic input, whether at the base or the top, does not affect the hydrodynamic pressures in a rigid tank, with no deformation of its wall. For a head-supported tank, hydrodynamic pressures on its inner surfaces generate a resultant force and moment at the head support. The shear force, F, which balances the resultant force of the pressure on the wall, p_w, is identical to that of a base-supported tank. The moment at the head support, M_{wb}, includes two components: M_w and M_b. The moment, M_w, which balances the pressure on the wall, p_w, is dependent on the location of the support (i.e., base or head). Moving the supported from the base to the top changes the vertical lever arm from the center of p_w to the support. The moment, M_b, which balances the pressures on the base, p_b, with horizontal lever arm to the center of the head, is identical to that at the base of a base-supported tank. The wave height, d_w, is generated by the hydrodynamic pressure on the initial free surface, and so is not affected by the change in the boundary condition (i.e., base- to head-supported). Consequently, this section compares M_{wb} at the head of the tank calculated using the numerical models and the analytical solutions. Other responses, namely, p_w, F, and d_w, are identical to those presented in Section 4.2.3.1 for the base-supported tank and are not repeated here.

Reaction: moment at the head

As noted in Section 4.2.3.1, the moment at the support, M_{wb}, calculated using the numerical models cannot be separated into M_w and M_b, nor can the impulsive and convective components of these moments (i.e., $M_{imp,w}$, $M_{con,w}$, $M_{imp,b}$, and $M_{con,b}$) be identified. Consequently, the analytical solutions for M_w and M_b, including their impulsive and convective components, must be summed for a comparison with numerical results: Eq. (4.3). The impulsive moments, $M_{imp,w}$

and $M_{imp,b}$, and the convective moments, $M_{con,w,j}$ and $M_{con,b,j}$, used for Eq. (4.3) are calculated using the solutions developed in Sections 3.3.1.1 and 3.3.2.1, and their equation numbers are listed in Table 4.12.

Table 4.12. Equation numbers for the analytical solutions for impulsive and convective moments at the head of a rigid, head-supported cylindrical tank

$M_{imp,w}$	$M_{imp,b}$	$M_{con,w,j}$	$M_{con,b,j}$
(3.121)	(3.13)	(3.141)	(3.84)

The time series of M_{wb} about the y axis at the head of the tank calculated using the numerical models and Eq. (4.3) are presented in Figures 4.23 and 4.24. Figure 4.23 enables a comparison for the ALE models, the two fluid heights (i.e., $H = 1.2$ and 1.8 m), and the four input motions (i.e. S-1, S-2, E-1, and E-2). Figure 4.24 presents companion information for the ICFD models.

Discussion

The numerical (both ALE and ICFD) and analytical results for the time series of M_{wb} at the head of the rigid head-supported tank ($R = 0.79$ m, $H_s = 2$ m) are presented in Figures 4.23 and 4.24, for fluid heights $H = 1.2$ and 1.8 m and input motions S-1, S-2, E-1, and E-2. The numerical and analytical results agree well, except for those shown in Figure 4.24g and h, for the ICFD models and E-2. These M_{wb} time series for E-2 agree reasonably for the first 6 seconds only; subsequently, the ICFD results are smaller than and out of phase, with those calculated using the analytical solution. As identified in Section 4.2.3.1: E-2 drives significant convective response and the calculation of wave height by the ICFD solver is challenged. (Software developers at LSTC are seeking to improve this predictive capability (Caldichoury 2020).) Table 4.13 presents the maximum absolute values of the analytical, ALE, and ICFD results extracted from Figures 4.23 and 4.24. The percentage differences between the ALE (and ICFD) and analytical results are presented in parentheses in Table 4.13. The differences are less than $\pm$ 5%. (The listed percentage differences for the ICFD models and E-2 are small because the maximum absolute values of M_{wb} occur in the first 6 seconds of the time series, for which agreement with the analytical solution is reasonable.)

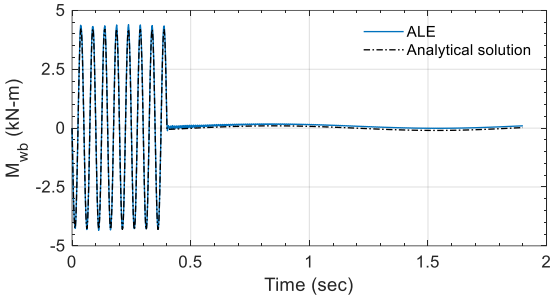

(a) S-1, $H = 1.2$ m

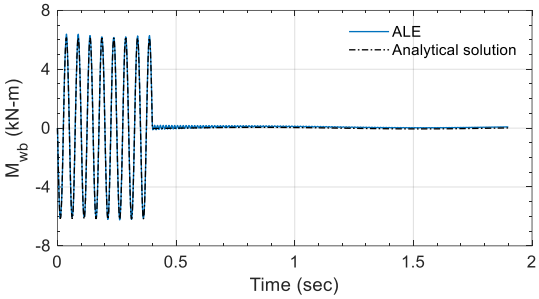

(b) S-1, $H = 1.8$ m

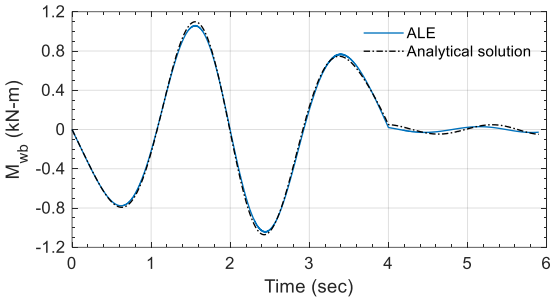

(c) S-2, $H = 1.2$ m

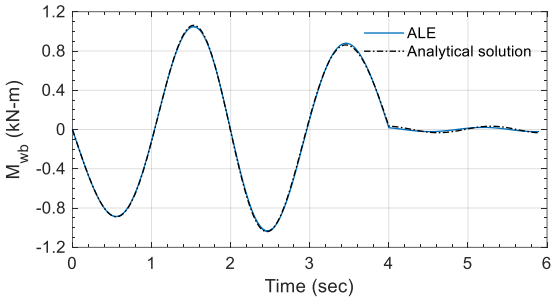

(d) S-2, $H = 1.8$ m

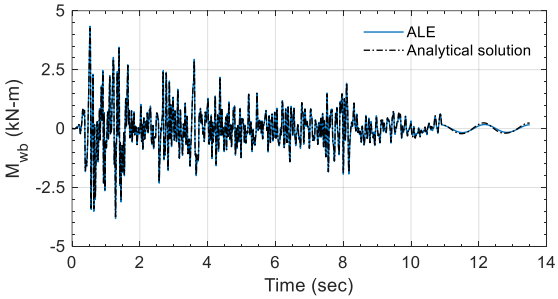

(e) E-1, $H = 1.2$ m

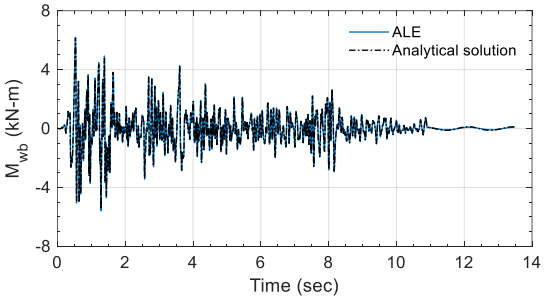

(f) E-1, $H = 1.8$ m

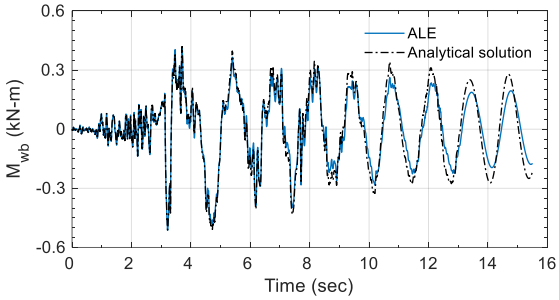

(g) E-2, $H = 1.2$ m

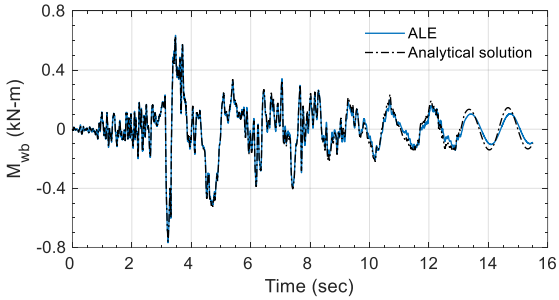

(h) E-2, $H = 1.8$ m

Figure 4.23. Time series of the moment, M_{wb}, about the y axis at the head of the tank, calculated using the ALE models and Eq. (4.3)

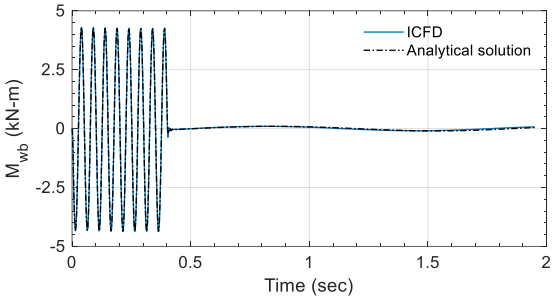

(a) S-1, $H = 1.2$ m

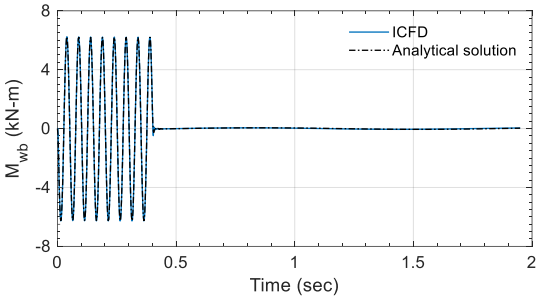

(b) S-1, $H = 1.8$ m

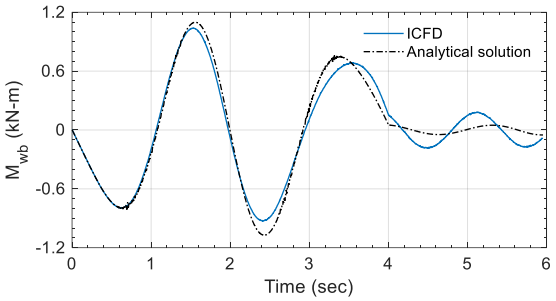

(c) S-2, $H = 1.2$ m

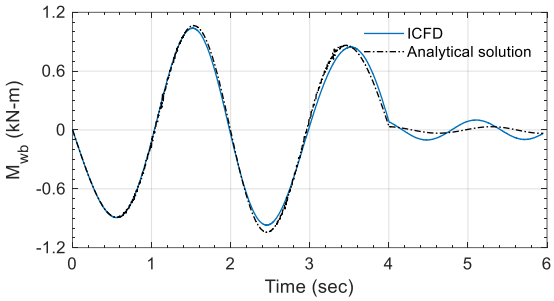

(d) S-2, $H = 1.8$ m

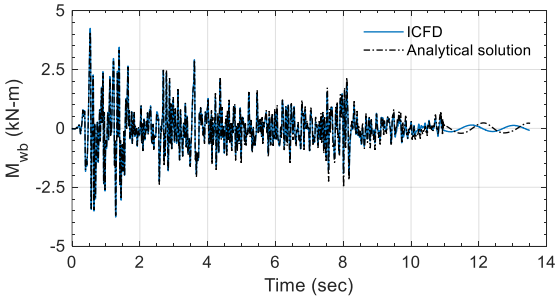

(e) E-1, $H = 1.2$ m

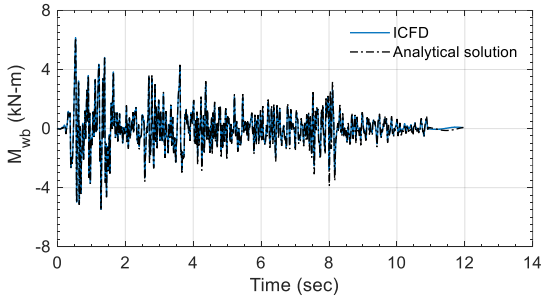

(f) E-1, $H = 1.8$ m

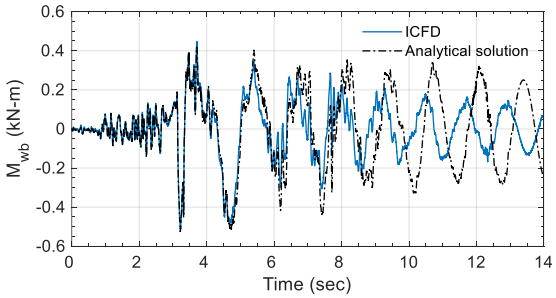

(g) E-2, $H = 1.2$ m

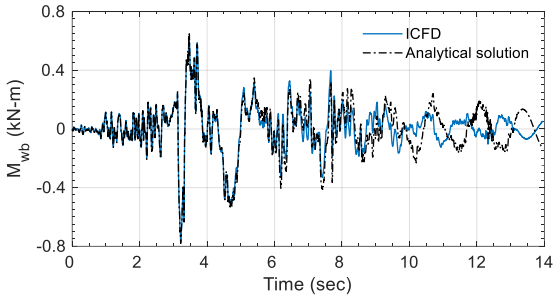

(h) E-2, $H = 1.8$ m

Figure 4.24. Time series of the moment, M_{wb}, about the y axis at the head of the tank, calculated using the ICFD models and Eq. (4.3)

Table 4.13. Maximum absolute moments, M_{wb}, at the head of the head-supported tank calculated using the numerical models and the analytical solutions, extracted from Figures 4.23 and 4.24, H = 1.2 and 1.8 m, input motions S-1, S-2, E-1, and E-2

	M_{wb} (kN-m)					
Motion	1.2 m			1.8 m		
	Analytical solution	ALE (diff)[1]	ICFD (diff)[1]	Analytical solution	ALE (diff)[1]	ICFD (diff)[1]
S-1	4.4	4.39 (1%)	4.38 (0%)	6.3	6.39 (2%)	6.28 (0%)
S-2	1.1	1.06 (-3%)	1.04 (-5%)	1.1	1.05 (-1%)	1.04 (-2%)
E-1	4.3	4.34 (2%)	4.25 (0%)	6.2	6.20 (1%)	6.16 (0%)
E-2	0.5	0.51 (0%)	0.51 (-3%)	0.8	0.77 (1%)	0.76 (-3%)

1. Percentage difference of FSI responses calculated using the numerical models with respect to those calculated using the analytical solutions, to the nearest 1%

The differences in M_{wb} calculated using the numerical models and the analytical solution here are similar to those for the rigid base-supported tank presented in Section 4.2.3.1. Other responses, namely, p_w, F, and d_w, for the rigid head-supported tank here are identical to those for the rigid base-supported tank in Section 4.2.3.1. Consequently, the conclusions drawn in Section 4.2.3.1 are appropriate here, namely, 1) the ALE models are verified for calculating p_w, F, and M_{wb}, but are limited to short-duration analysis for calculating d_w; and 2) the ICFD models are not verified for calculating d_w, but are verified for calculating p_w, F, and M_{wb}, if the wave action is not significant.

4.3 Flexible tank

Numerical models of flexible, base-supported and head-supported cylindrical tanks subjected to x-directional seismic motion of a small amplitude are analyzed using the ALE and ICFD solvers. The models are verified using the analytical solutions with the sources listed in Table 4.2: the solutions developed by Veletsos (1984) presented in Section 3.2.1.3 for base-supported tanks and those developed in Section 3.3.1.2 for head-supported tanks. These analytical solutions address only the impulsive component of FSI responses for flexible tanks. To the knowledge of the

authors, no prior analytical has work addressed convective responses in flexible tanks[33]. To enable comparisons between the numerical and analytical results, the convective component in the FSI responses is disregarded using a numerical method, for which details are presented in Section 4.3.1. The numerical results of the impulsive pressures and reactions (i.e., shear forces and moments) at the support (i.e., base or head) are compared with those calculated using the analytical solutions.

4.3.1 Numerical models

Numerical models are constructed for a flexible, base- and head-supported, cylindrical tank, with $R = 0.79$ m, $H_s = 2$ m, and $h = 0.4$ mm. The analytical solutions for base-supported tanks (Veletsos 1984) used for the verification here assumed the tank to be full, while the analytical solutions for head-supported tanks account for freeboard (i.e., not required to be full). Accordingly, fluid heights of $H = 2$ and 1.8 m are used for the base- and head-supported tanks, respectively. The numerical models are analyzed using the ALE and ICFD solvers, and the numerical results are compared with those calculated using the analytical solutions. Figures 4.25 and 4.26 present the ALE models for the base- and head-supported tanks, respectively, and the global coordinates (x, y, z). The tank is shown in blue, the water is shown in yellow. A 0.2-m deep vacuum space shown in grey is modeled at the top of the water. With the presence of a vacuum space, a free surface is formed at the top of the water, where the pressure is zero as the atmospheric pressure not considered. Since the base-supported tank is full, the vacuum space is modeled beyond the height of the tank, as shown in Figure 4.25a. The nodes of the tank, water, and vacuum are merged at their interfaces. The sizes of the elements shown in Figures 4.25 and 4.26 are similar to those used for the rigid tanks presented in Figure 4.3: smaller fluid elements adjacent to the tank wall and along the direction of the seismic input (i.e., x direction) across the diameter of the tank. The types and numbers of elements used for the ALE models are listed in Table 4.14 for the base- and head-supported tanks. Figures 4.25c and 4.26c present the water in the base- and head-supported tanks, respectively, at the first step of the analysis ($t = 0$).

[33] Analytical studies (e.g. Veletsos (1984), and Chalhoub and Kelly (1988)) assumed that the convective response of a tank subjected to a small-amplitude, horizontal motion is generated by the part of the fluid not moving horizontally with the tank but oscillating vertically to form waves. Since this part of the fluid was assumed not to follow the movement or the deformation of the tank, the convective response was independent of the flexibility of the tank wall. Consequently, the analytical solutions were derived for rigid tanks only.

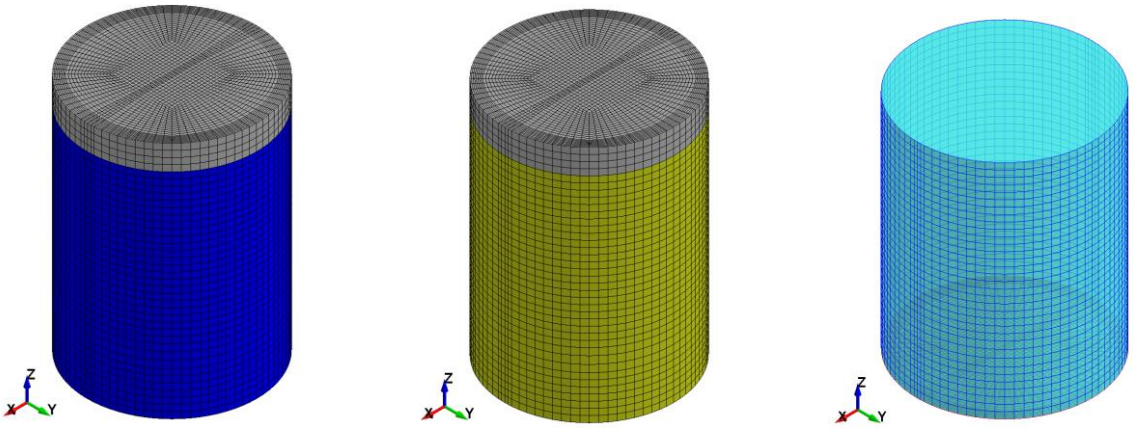

(a) tank and vacuum (b) water and vacuum (c) water in the tank at $t = 0$

Figure 4.25. ALE model of a flexible base-supported tank with $R = 0.79$ m, $H_s = 2$ m, and $H = 2$ m, isometric view

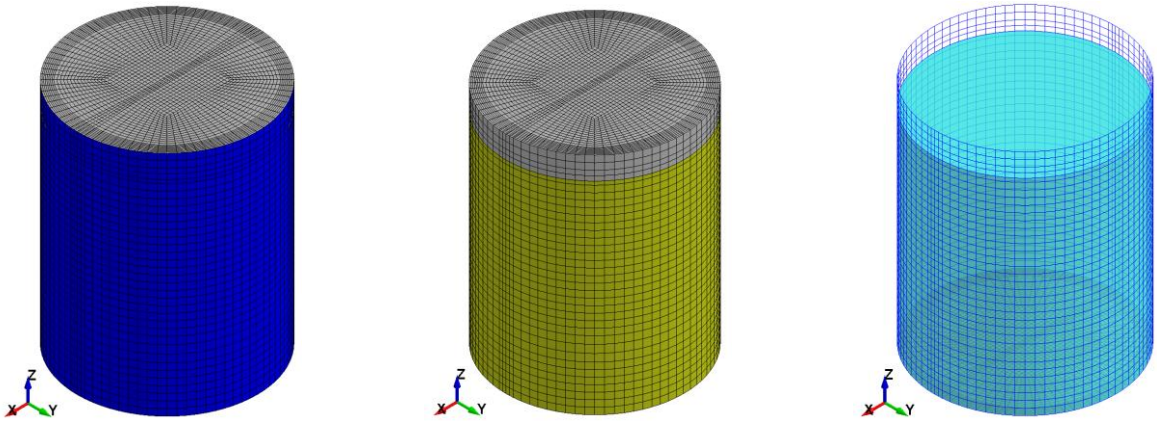

(a) tank and vacuum (b) water and vacuum (c) water in the tank at $t = 0$

Figure 4.26. ALE model of a flexible head-supported tank with $R = 0.79$ m, $H_s = 2$ m, and $H = 1.8$ m, isometric view

Table 4.14. Types and numbers of elements used in the ALE models shown in Figures 4.25 and 4.26, base- and head-supported tanks

	Tank	Water	Vacuum
Element type	Lagrangian four-node shell	Eulerian eight-node solid	Eulerian eight-node solid
Base-supported	5228	80648	9488
Head-supported	5312	73532	9488

Figures 4.27 and 4.28 present the ICFD models for the base- and head-supported tanks, respectively. The models of the tanks are shown in blue in Figures 4.27a and 4.28a. Figures 4.27b and 4.28b present half domains for the fluid, each defined using three surfaces: 1) adjacent to the tank base (shown in pink), 2) adjacent to the tank wall (shown in yellow), and 3) horizontally closing the top of the domain (shown in grey). The tank and the fluid surfaces do not share nodes at their interfaces. The interaction between the tank and water is activated by the *ICFD_BOUNDARY_FSI card in the LS-DYNA deck.

The sizes of the elements for these fluid surfaces are larger than those used for the rigid tanks presented in Figure 4.4 because wave action, which requires fine meshes, is not included for the analysis of the flexible tanks here. The height of the fluid domain of Figure 4.27b for the base-supported tank is 2.2 m and that shown in Figure 4.28b for the head-supported tank is 2 m, namely a freeboard of 0.2 m is provided. Different from the models for the rigid tanks (Figure 4.4), the freeboard here is not used for developing waves, but providing a vacuum space so that a free surface of zero pressure is generated on the top of the water. The height of the free surface (i.e., H = 2 m or 1.8 m) is defined using the *ICFD_INITIAL_LEVELSET card. The *MESH_BL is assigned to the yellow and pink surfaces in Figures 4.27b and 4.28b to generate finer water elements adjacent to the inner surfaces of the tank. Four-node solid elements for the water are automatically generated by the ICFD solver at the first step of the analysis (i.e., $t = 0$), as shown in Figures 4.27c and 4.28c. The types and numbers of elements used for the ICFD model are listed in Table 4.15 for the base- and head-supported tanks.

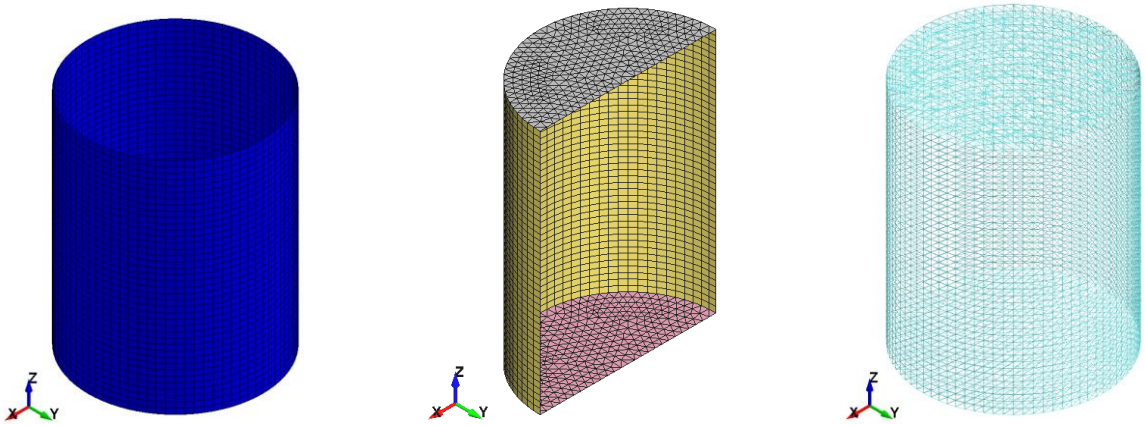

(a) tank (b) surfaces for a half fluid domain with a height of 2.2 m (c) water, $t = 0$

Figure 4.27. ICFD model of a flexible base-supported tank with $R = 0.79$ m, $H_s = 2$ m, $H = 2$ m, isometric view

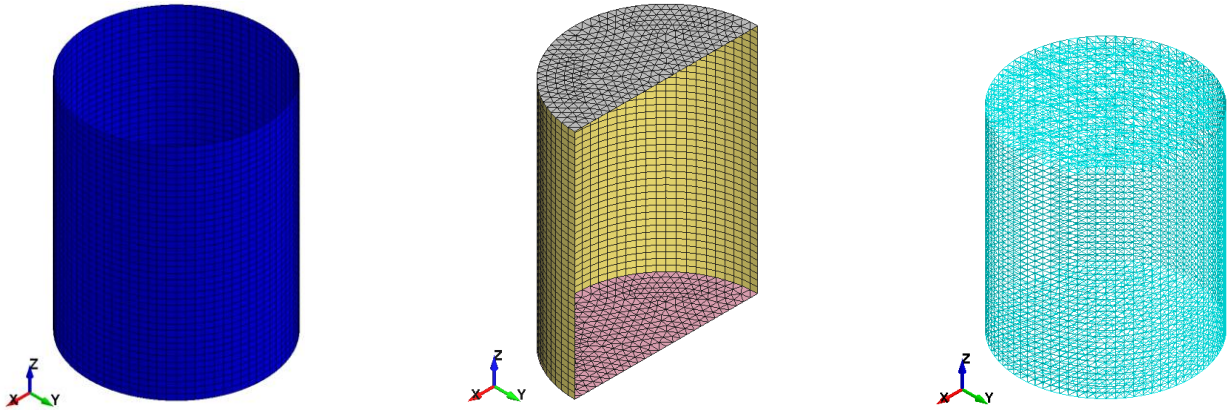

(a) tank (b) surfaces for a half fluid domain with a height of 2 m (c) water, $t = 0$

Figure 4.28. ICFD model of a flexible head-supported tank with $R = 0.79$ m, $H_s = 2$ m, $H = 1.8$ m, isometric view

Table 4.15. Types and numbers of elements used for in the ICFD models shown in Figures 4.27 and 4.28, base- and head-supported tanks

	Tank	Fluid surfaces	Water
Element type	Lagrangian three/four-node shell	Lagrangian three/four-node shell	Lagrangian four-node solid
Base-supported	4448	6016	Automatically generated by the solver
Head-supported	4448	5696	

Seismic motions are input in the x direction at the nodes of the base for the base-supported tank and at the top of the wall for the head-supported tank. These nodes are constrained in the y and z directions and the rotational directions with respect to x, y, and z axes.

The analytical solutions used for the verification assume the wall of the tank is elastic and the base is rigid. The elements of the wall and base are assigned elastic and rigid materials, respectively, with the mechanical properties consistent with carbon steel, including the density ρ_s of 7850 kg/m^3, the elastic modulus E_s of 2×10^{11} N/m^2, and Poisson's ratio υ_s of 0.27. (The values of E_s and υ_s do not affect the responses of the rigid base but must be defined in the models.) A damping ratio of 2% is assigned to the elements of the wall for a frequency range of 15 to 250 Hz using the *DAMPING_FREQUENCY_RANGE_DEFORM card (Huang et al. 2019). (Variables assigned in the card are: $CDAM = 0.02$, $FLOW = 15$, and $FHIGH = 250$.) The assigned frequency range covers the first five impulsive modes of the base- and head-supported tanks (i.e., 21 Hz to 160 Hz, estimated using the analytical solutions). The damping model implemented by the card is a function of frequency (Huang 2019). Figure 4.29 presents the damping achieved by the card (blue line), which is used for the numerical calculation of both the ALE and ICFD models, and the assigned damping (red line), namely 2% for 15 to 250 Hz. This frequency-dependent damping model shown in blue is used for the analytical solutions in Section 4.3.3 to enable a comparison with numerical results. (No damping is applied to the tank base since it is rigid; damping ratio=0.)

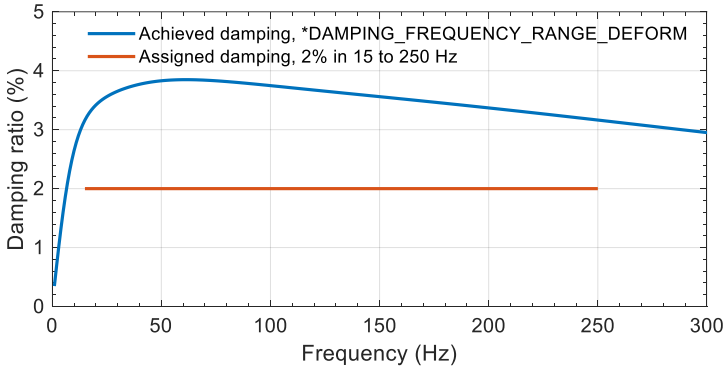

Figure 4.29. Damping ratio achieved by *DAMPING_FREQUENCY_RANGE_DEFORM card and used for the numerical calculation, damping ratio of 2% for 15 to 250 Hz assigned in the card

The models of the water are assigned the mechanical properties identical to those described in Section 4.2.1 for the analysis of the rigid tanks, and so are not repeated here. Table 4.16 lists the mechanical properties assigned to the elements in the numerical models of the tank, water, and vacuum. The masses of the numerical models are listed in Table 4.17. Note that the analytical solutions used to verify the models address the reactions at the support associated with hydrodynamic loadings and do not consider those associated with the inertial force of the tank. Per Table 4.17, the mass of the tank is less than 1% of that of the water for the numerical models. Accordingly, the contribution of the inertial force of the tank to the reactions calculated using the models is negligible.

Table 4.16. Mechanical properties assigned to the elements in the numerical models of the base- and head-supported tanks, ALE and ICFD models

		ALE	ICFD
Tank	Density, ρ_s	7850 kg/m^3	
	Elastic modulus, E_s	2×10^{11} N/m^2	
	Poisson's ratio, υ_s	0.27	
Water	Density, ρ_w	1000 kg/m^3	
	Viscosity, μ_w	0	
	Bulk modulus, K_w	2.15×10^9 N/m^2	--[1]
Vacuum	Density, ρ_a	--[2]	0
	Viscosity, μ_a		0

1. The ICFD solver analyzes only incompressible fluids, and so K_w is not used in the models.
2. The vacuum is assigned void properties through the *INITIAL_VOID card for the ALE analysis.

Table 4.17. Masses of the tank and water in the ALE and ICFD models

Component	Mass (kg)	
	Base-supported	Head-supported
Tank (including the wall and the base)	38	
Water	3921	3527

The analytical solutions used here address only the impulsive component of FSI responses. The convective component must be removed from the numerical analysis to generate results consistent with those analytically calculated. Convective responses are generated by the part of the fluid oscillates vertically in a tank. The vertical oscillation changes the potential energy of the fluid[34], which is transformed from the kinetic energy generated by fluid velocities. The potential energy can only appear if the gravitational acceleration g exists[35]. Accordingly, to remove the convective component from the FSI responses, g is not assigned in the numerical model.

4.3.2 Input motions

Three small-amplitude time series are used for the response-history analysis of the tanks in the x direction: a sine-sweep motion, S-S, a sinusoidal motion, S-1, and an earthquake motion, E-1. The sine-sweep motion is used for calculating the impulsive frequencies of the tanks, and S-1 and E-1 are used for calculating impulsive responses, including pressures and reactions. Table 4.18 presents information on the three motions.

The frequencies of the tanks are identified from the responses for the sine-sweep motion, S-S, since the ALE and ICFD solvers cannot perform eigenvalue analysis. The frequency band of S-S ranges between 0.25 and 150 Hz, and enables identification of the first three impulsive frequencies for the base- and head-supported tanks (i.e., 21 to 105 Hz, estimated using the analytical solutions). The identified frequencies are compared with those calculated using the analytical solutions. The fourth and higher modes are not identified because fluid-structure responses in these modes are considered *rigid* and not affected by the calculated frequencies, which are greater than 100 Hz. Figures 4.30a and b present the time series and the Fourier amplitude spectrum of S-S, respectively.

[34] The potential energy is generated by an object elevating in a gravity field. For the fluid in a tank, the potential energy increases as the wave going upwards and decreases as the wave going downwards.

[35] Per Eqs. (3.73), (3.87), and (3.114) derived by Veletsos (1984), Chalhoub and Kelly (1988), and Housner (1957), respectively, the analytical solutions for the convective frequencies include the gravitational acceleration g.

Table 4.18. Unidirectional, horizontal ground motion time series for the response-history analysis of the flexible tanks

a. sine-sweep motion

	Frequency band (Hz)	Amplitude/PGA (g)
S-S	0.25 to 150	0.2

b. sinusoidal motion

	Frequency (Hz)	Amplitude/PGA (g)	Number of cycles
S-1	20	0.02	8

c. earthquake motion record[1]

	Event	Year	Station	Direction	Original PGA (g)	Scaled PGA (g)	Time scale
E-1	El Centro Earthquake (Imperial Valley-02)	1940	El Centro Array #9	180	0.28	0.05	$1/\sqrt{10}$

1. Ground motions are extracted from the PEER Ground Motion Database (http://ngawest2.berkeley.edu/, accessed on March 18, 2019), Pacific Earthquake Engineering Research (PEER) Center, University of California, Berkeley, CA.

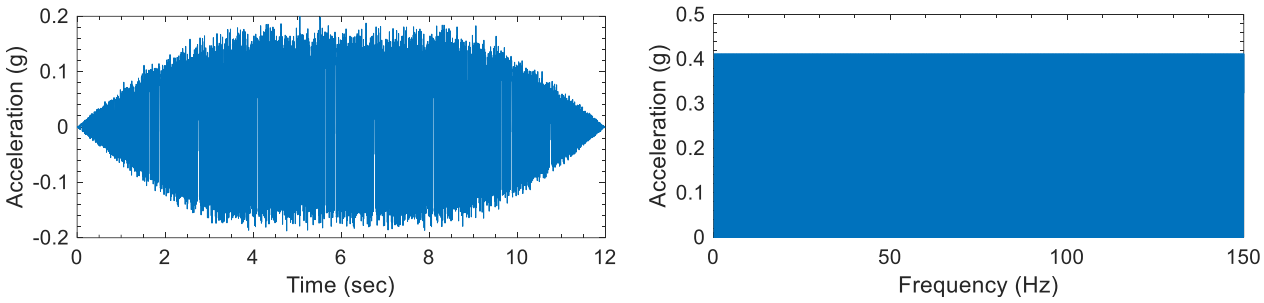

(a) time series (b) Fourier amplitude spectrum

Figure 4.30. Sine-sweep motion, S-S, unidirectional horizontal input, PGA=0.2g

The time series of motions S-1 and E-1 are presented in Figure 4.31, both of which are used for the analysis of the rigid tanks presented in Section 4.2, but their amplitudes are reduced to smaller values in this section (4.3). Motion S-1 is a sinusoidal function with a frequency of 20 Hz, which is close to the first impulsive mode of the base- and head-supported tanks (i.e., 25 and 21 Hz, respectively) and could induce nonlinear responses or instability that cannot be verified

using analytical solutions. Consequently, the amplitude of S-1 is reduced to a very small value (i.e., 0.02 g). Motion E-1 is a record of the 1940 El Centro Earthquake in California, U.S. The time scale of E-1 is compressed by a factor of $\sqrt{10}$ to be consistent with the length scale for the tank, and the PGA is scaled to 0.05 g. Figure 4.32 presents the acceleration response spectra for the time- and amplitude-scaled E-1, calculated using a damping ratio of 2%, using a linear period axis and a logarithmic frequency axis. The spectral acceleration around the first impulsive modes (i.e., 25 and 21 Hz, respectively) is relatively high, which could induce nonlinear responses or instability, and so a small PGA (i.e., 0.05 g) is used here. (Motions S-2 and E-2, which are used in Section 4.2 to drive waves in the rigid tanks, are not used because convective responses are not the subject of inquiry here for flexible tanks.)

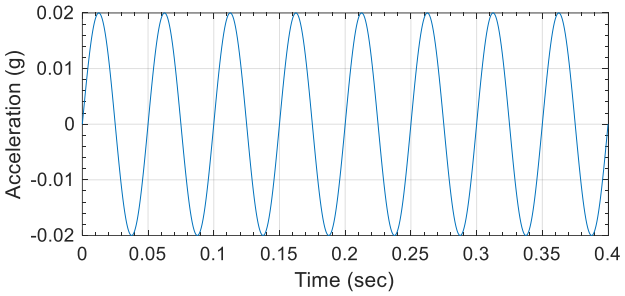

(a) sinusoidal motion, S-1, PGA=0.02 g

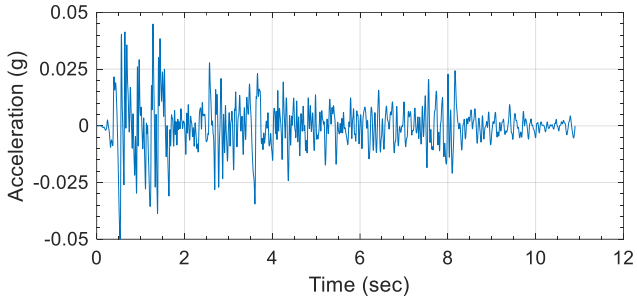

(b) earthquake motion, E-1, time scale of $1/\sqrt{10}$, PGA=0.05 g

Figure 4.31. Unidirectional, horizontal input motion time series for the response-history analysis of the flexible tanks

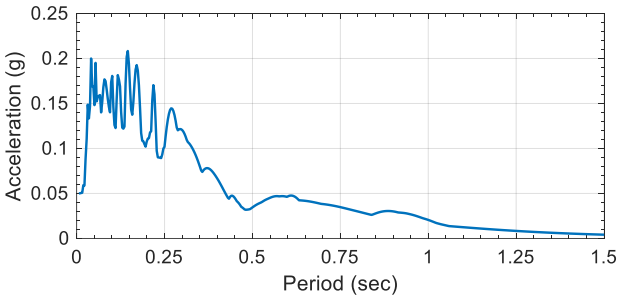

(a) period axis in a linear format

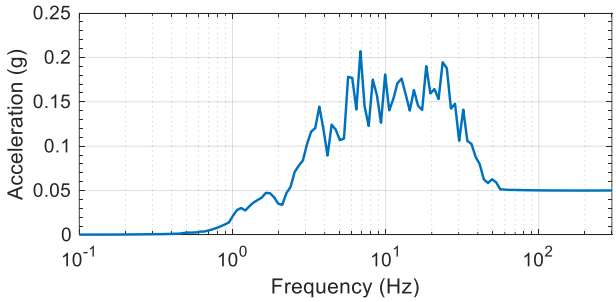

(b) frequency axis in a logarithmic format

Figure 4.32. Spectral accelerations of the earthquake motion time series, E-1, shown in Figure 4.31b, time scale of $1/\sqrt{10}$, PGA=0.05 g, damping ratio of 2%

4.3.3 Results and verification

Response-history analysis is performed for the ALE and ICFD models of the flexible, base- and head-supported cylindrical tanks presented in Section 4.3.1. The motions listed in Table 4.18 are input to the x direction of the models, including a sine-sweep motion, S-S, a sinusoidal motion, S-1, and an earthquake motion, E-1. Motion S-S is used for calculating the impulsive frequencies of the tanks, and S-1 and E-1 are used for calculating impulsive responses, including pressures and reactions. As noted previously, convective responses are not considered in this section (4.3).

4.3.3.1 Base-supported tank

The analytical solutions used to verify the ALE and ICFD models of the flexible, base-supported tank ($R = 0.79$ m, $H = H_s = 2$ m, $h = 0.4$ mm) shown in Figures 4.25 and 4.27, respectively, were derived by Veletsos for impulsive responses presented in Section 3.2.1.3, per Table 4.2. These analytical solutions were derived based on the cylindrical coordinate system (r, θ, z) shown in Figure 4.2. Veletsos decoupled each impulsive response into modal contributions and provided a solution for each mode. The solutions address the impulsive frequency, $f_{imp,k}$ of the kth mode ($k = 1, 2, \ldots \infty$), and the associated modal responses, including the pressure on the inner surfaces of the tank, $p_{imp,k}$, shear force at the tank base, $F_{imp,k}$, and two components of the moment at the tank base: $M_{imp,w,k}$, which is generated by $p_{imp,w,k}$ on the wall, and $M_{imp,b,k}$, which is generated by $p_{imp,b,k}$ on the base. The equation numbers used in Section 3.2.1.3 for the frequency and the modal responses are listed in Table 4.19.

Table 4.19. Equation numbers of the analytical solutions of Veletsos for the impulsive frequency of the kth mode and the modal responses for flexible, base-supported cylindrical tanks

$f_{imp,k}$	$p_{imp,w,k}$	$p_{imp,b,k}$	$F_{imp,k}$	$M_{imp,w,k}$	$M_{imp,b,k}$
(3.52)	(3.59)	(3.60)	(3.61)	(3.62)	(3.63)

Per the equations listed in Table 4.19, the modal responses are functions of a time series, $A_k(t)$, which is the acceleration of a single degree-of-freedom (SDOF) system with a frequency $f_{imp,k}$, subjected to a horizontal motion, $u_0''(t)$. The acceleration, $A_k(t)$, is calculated using Duhamel's integral:

$$A_k(t) = \frac{\omega_{imp,k}^2}{\omega_{imp,d,k}} \int_0^t u_0''(\tau) \cdot e^{-\zeta_k \cdot \omega_{imp,k} \cdot (t-\tau)} \cdot \sin \omega_{imp,d,k}(t-\tau) d\tau \tag{4.5}$$

where τ is a time variable, ζ_k, $\omega_{imp,k}$, and $\omega_{imp,d,k}$ are the damping ratio, radial frequency, and damped radial frequency of the k th impulsive mode, respectively (i.e., $\omega_{imp,k} = 2\pi f_{imp,k}$; $\omega_{imp,d,k} = \omega_{imp,k}\sqrt{1-\zeta_k^2}$). To enable the verification, the damping ratio, ζ_k, used in Eq. (4.5) here is consistent with the damping model used for the numerical calculation shown as the blue line in Figure 4.29. The value of ζ_k for the k th impulsive mode is extracted from the blue line per the analytically calculated frequency $f_{imp,k}$.

The first three impulsive frequencies, $f_{imp,k}$, of the base-supported tank calculated using the numerical models and Eq. (3.52) are compared. The frequencies of the tank in the numerical models are identified from the hydrodynamic pressure, $p_{imp,w}$, for sine-sweep motion S-S, at the yellow solid circle presented in Figure 4.2. The yellow solid circle is at a height of $0.6H$ (with respect to the tank base) where the impulsive pressure is expected to be the greatest along the tank wall per the first modal response shown in Figure 3.12c, calculated using the analytical solution of Veletsos for $H/R = 2$. The pressure time series at the yellow circle calculated using the ALE and ICFD models are transformed into the frequency domain using the Fast Fourier Transform (FFT). The impulsive frequencies are identified from the Fourier amplitude spectrum. Figures 4.33a and b present the spectrum for the ALE model, normalized by its maximum ordinate, for frequencies ranging between 0 and 120 Hz, in a linear format and a linear-logarithmic format, respectively. Figures 4.33c and d present those calculated using the ICFD model. The peaks in the spectra at the three lowest frequencies are associated with the first three impulsive modes. The third mode cannot be identified from the ICFD result, but the fluid-structure responses in the mode (90.2 Hz per the analytical solution) are considered *rigid* and not affected by the calculated frequency. Table 4.20 presents the frequencies calculated using Eq. (3.52) and the numerical models, and their percentage differences. The results are essentially identical.

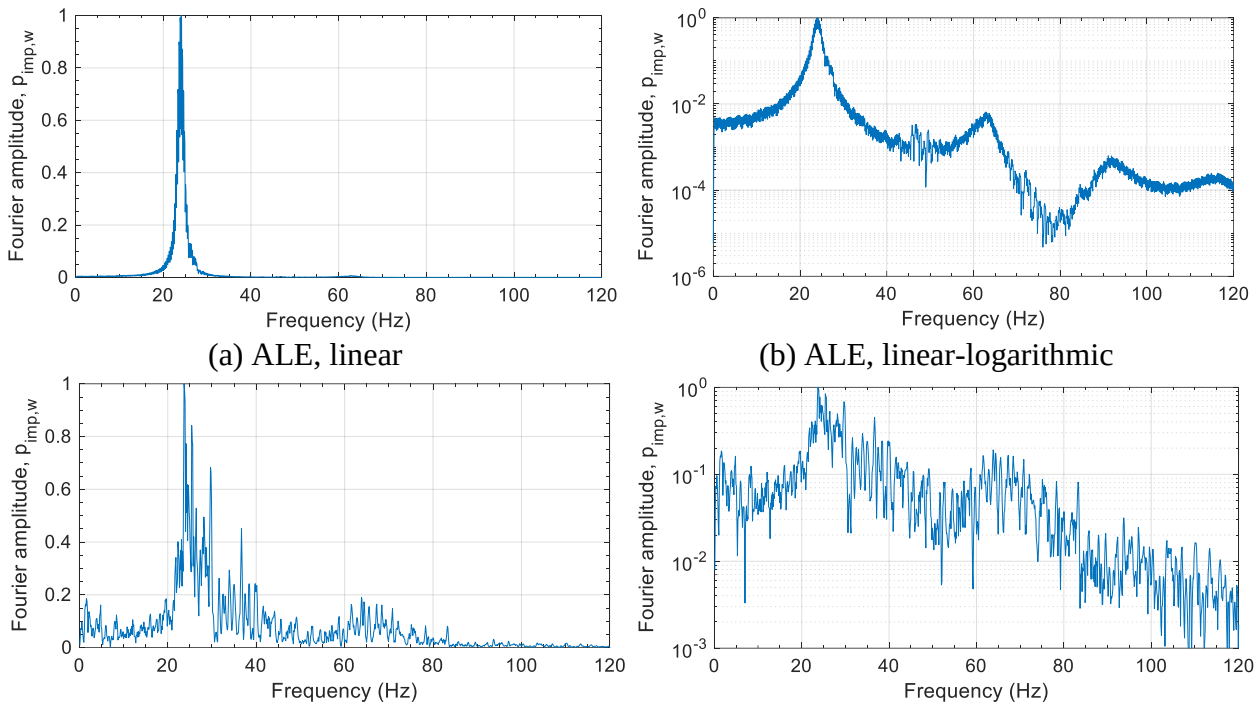

Figure 4.33. Normalized Fourier amplitude spectra for the hydrodynamic pressure, $p_{imp,w}$, at the location of the yellow solid circle shown in Figure 4.2, calculated using the ALE and ICFD models

Table 4.20. Impulsive frequencies of the flexible base-supported tank, calculated using Eq. (3.52) and the ALE and ICFD models, and their percentage differences

Mode	Frequency (Hz)			Difference[1] (%)	
	Analytical solution	ALE model	ICFD model	ALE model	ICFD model
First	24.1	24.1	24.4	0	4
Second	62.9	62.8	63.8	0	1
Third	90.2	91.1	--	1	--

1. Percentage differences of the numerical results with respect to those calculated using the analytical solution

The time series of the impulsive pressure, $p_{imp,w}$, on the tank wall, the shear force, F_{imp}, at the tank base in the x direction, and the moment, $M_{imp,wb}$, at the tank base about the y axis calculated using the numerical models are compared with those calculated using the analytical

solutions. Each impulsive response is the infinite algebraic sum of the modal responses (i.e., $k=1$ to ∞):

$$p_{imp,w}(\theta,z,t)=\sum_{k=1}^{N}p_{imp,w,k} \tag{4.6}$$

$$F_{imp}(t)=\sum_{k=1}^{N}F_{imp,k} \tag{4.7}$$

$$M_{imp,wb}(t)=M_{imp,b}+M_{imp,b}=\sum_{k=1}^{N}M_{imp,w,k}+\sum_{k=1}^{N}M_{imp,b,k} \tag{4.8}$$

where the modal responses $p_{imp,w,k}$, $F_{imp,k}$, $M_{imp,w,k}$ and $M_{imp,b,k}$ are calculated using the equations listed in Table 4.19. The moment at the tank base, $M_{imp,wb}$, calculated using the numerical models includes the components, $M_{imp,w}$ and $M_{imp,b}$, associated with the hydrodynamic pressures on the wall and the base, respectively. Accordingly, Eq. (4.8) sums the analytical solutions of $M_{imp,w}$ and $M_{imp,b}$, to be consistent with the numerical results. (Equations (4.6) to (4.8) are also used for the flexible head-supported tank in Section 4.3.3.2, but $p_{imp,w,k}$, $F_{imp,k}$, $M_{imp,w,k}$ and $M_{imp,b,k}$ are calculated per the equations listed in Table 4.22.)

Per Eqs. (4.6) to (4.8), the algebraic sums for the impulsive responses include N modes. Theoretically, infinite impulsive modes are required (i.e., $N=\infty$, $k=1$ to ∞), but only the first ten modes (i.e., $N=10$) are included in the calculations herein since the contributions of the eleventh and higher modes are negligible for the tanks and the ground motions used in the analysis.

Impulsive pressure

The time series of $p_{imp,w}$ calculated using the numerical models and Eq. (4.6) are presented at the location of the yellow solid circle on the tank wall shown in Figure 4.2. The cylindrical coordinates of the circle are used for Eq. (4.6): $(r,\theta,z)=$(0.79 m, 0, 1.2 m). Figure 4.34 enables a comparison of results for the ALE model and the analytical solution for the two input motions (i.e. S-1 and E-1). As seen in Figure 4.34b, significant response to motion E-1 is realized in the first 2 seconds. To reduce run time, the ICFD analysis for E-1 is performed for 2.5 seconds only.

(The run time of this analysis is about 8 days.) Figure 4.35 enables a comparison of results for the ICFD model and the analytical solution for S-1 and (the first 2.5 seconds of) E-1.

The distributions of $p_{imp,w}$ calculated using the numerical models and Eq. (4.6) are presented using the green line on the tank wall shown in Figure 4.2. The cylindrical coordinates of the green line are used for Eq. (4.6): $(r,\theta,z)=$(0.79 m, 0, 0 to 2 m). Figures 4.36a and b present results at peak response in the $p_{imp,w}$ time series for the ALE model: see the open red circles in the corresponding panels of Figure 4.34. Figure 4.37 presents results at peak response in the $p_{imp,w}$ time series for the ICFD model: see the open red circles in panels of Figure 4.35. The presented distributions in Figures 4.36 and 4.37 confirm that the greatest $p_{imp,w}$ on the wall is at a height of around $0.6H$, where the yellow solid circle is located.

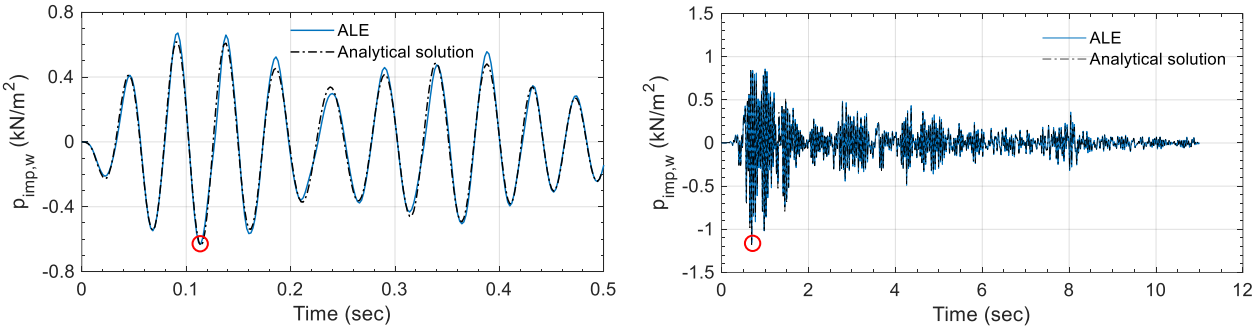

(a) S-1 (b) E-1

Figure 4.34. Time series of the impulsive pressure, $p_{imp,w}$, at the location of the yellow solid circle shown in Figure 4.2, calculated using the ALE model and Eq. (4.6)

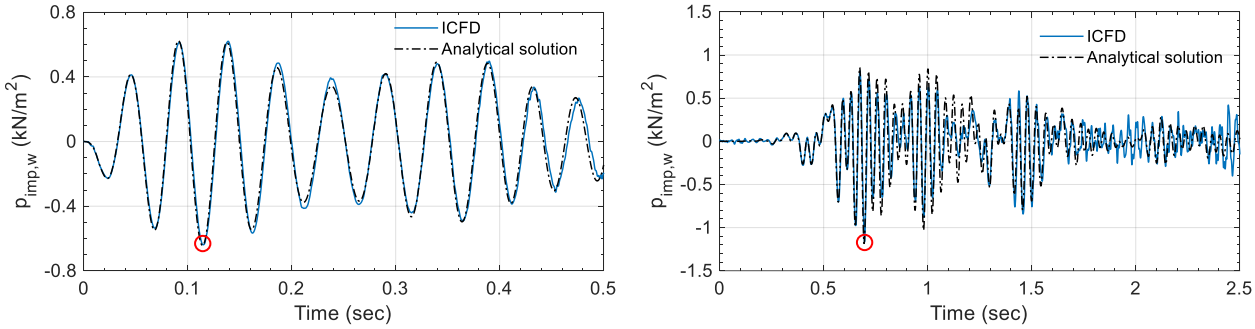

(a) S-1 (b) E-1

Figure 4.35. Time series of the impulsive pressure, $p_{imp,w}$, at the location of the yellow solid circle shown in Figure 4.2, calculated using the ICFD model and Eq. (4.6)

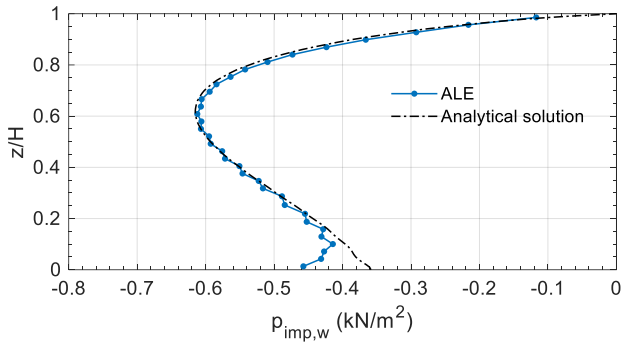

(a) S-1, $t = 0.112$ sec

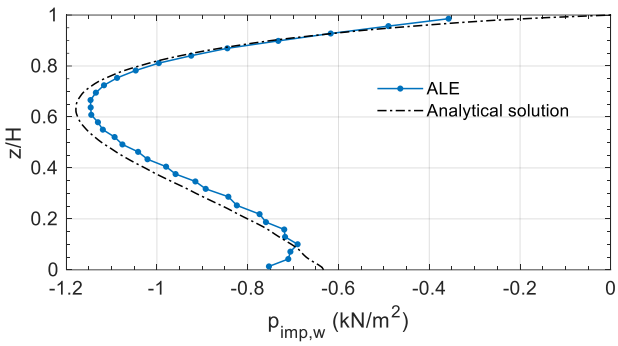

(b) E-1, $t = 0.694$ sec

Figure 4.36. Distributions of the impulsive pressure, $p_{imp,w}$, along the green line on the tank wall shown in Figure 4.2, at the time step of a peak response (open red circle) shown in the corresponding panels of Figure 4.34, calculated using the ALE model and Eq. (4.6)

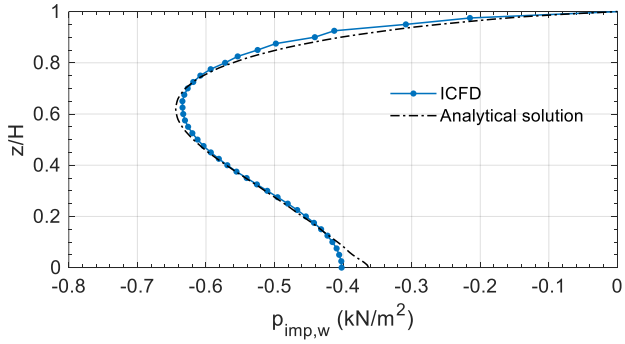

(a) S-1, $t = 0.114$ sec

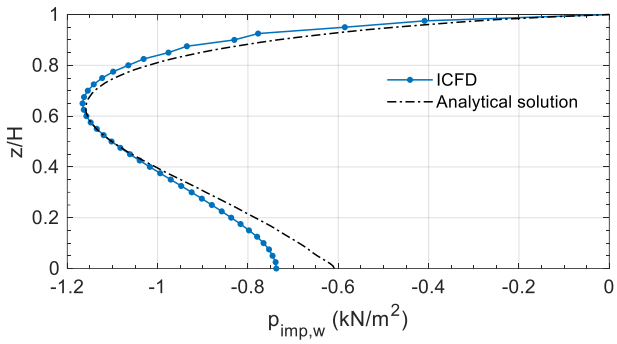

(b) E-1, $t = 0.696$ sec

Figure 4.37. Distributions of the impulsive pressure, $p_{imp,w}$, along the green line on the tank wall shown in Figure 4.2, at the time step of a peak response (open red circle) shown in the corresponding panels of Figure 4.35, calculated using the ICFD model and Eq. (4.6)

Reactions: shear force and moment at the base

The time series of F_{imp} in the x direction at the tank base, calculated using the numerical models and Eq. (4.7), are presented in Figures 4.38 and 4.39. Figure 4.38 presents results for the ALE model and the two input motions (i.e. S-1 and E-1). Figure 4.39 presents companion data for the ICFD model. For the reason given above (in the section on impulsive pressure), only the first 2.5 seconds of motion E-1 is used.

The time series of $M_{imp,wb}$ about the y axis at the tank base calculated using the numerical models and Eq. (4.8), are presented in Figures 4.40 and 4.41. Figure 4.40 presents results for the

ALE model and the two input motions (i.e. S-1 and E-1). Figure 4.41 presents companion data for the ICFD model. Again, only the first 2.5 seconds of motion E-1 is used.

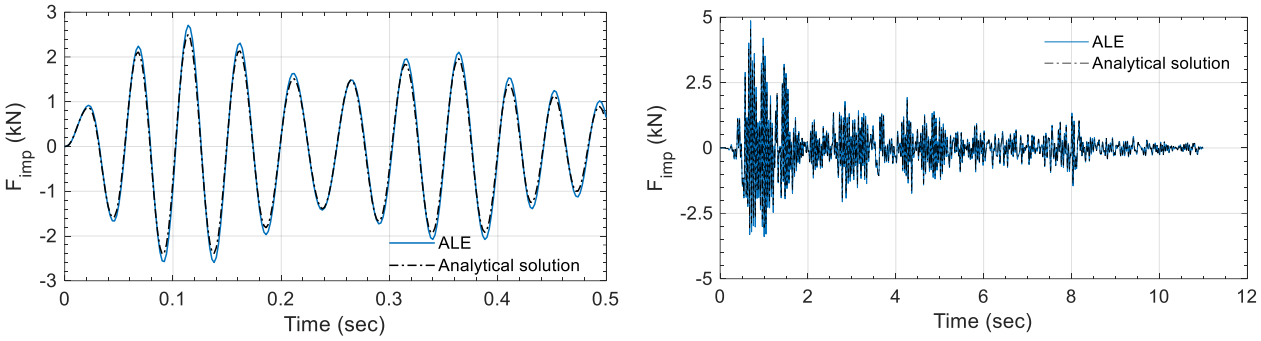

(a) S-1 (b) E-1

Figure 4.38. Time series of the impulsive shear force, F_{imp}, in the x direction at the tank base, calculated using the ALE model and Eq. (4.7)

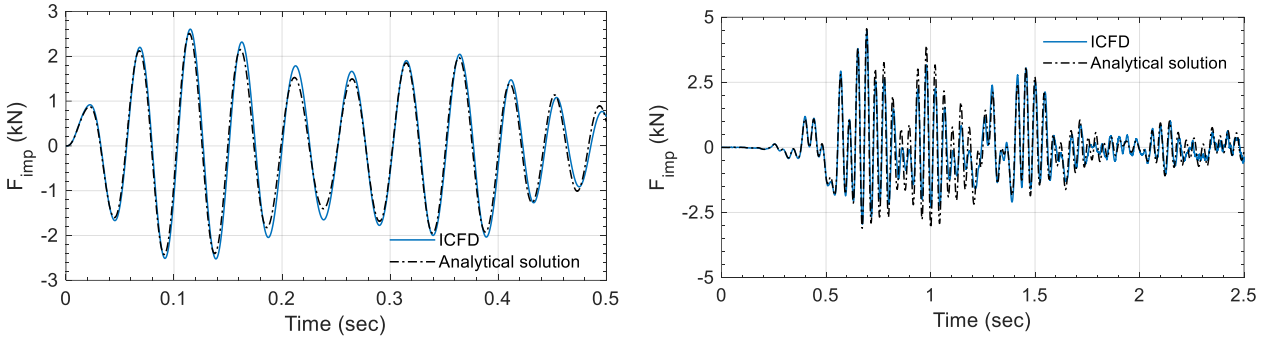

(a) S-1 (b) E-1

Figure 4.39. Time series of the impulsive shear force, F_{imp}, in the x direction at the tank base, calculated using the ICFD model and Eq. (4.7)

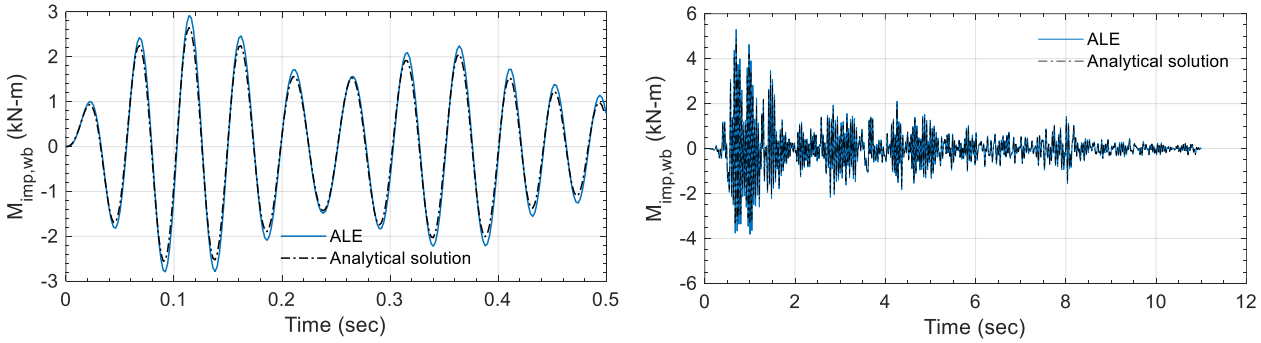

(a) S-1 (b) E-1

Figure 4.40. Time series of the impulsive moment, $M_{imp,wb}$, about the y axis at the tank base, calculated using the ALE model and Eq. (4.8)

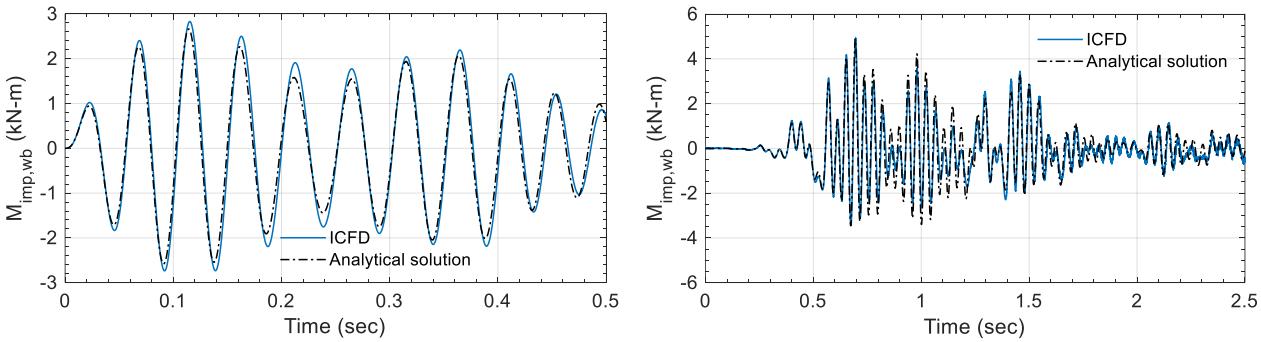

(a) S-1 (b) E-1

Figure 4.41. Time series of the impulsive moment, $M_{imp,wb}$, about the y axis at the tank base, calculated using the ICFD model and Eq. (4.8)

Discussion

To verify the ALE and ICFD models, Figures 4.34 through 4.41 present results for the numerical and analytical impulsive responses of a flexible, base-supported, cylindrical tank ($R = 0.79$ m, $H_s = 2$m, $h = 0.4$ mm), fully filled with fluid, and subjected to small-amplitude, unidirectional, horizontal motions, S-1 and E-1. The reported impulsive responses include $p_{imp,w}$ at the location of the yellow circle and along the green line in Figure 4.2, and F_{imp} and $M_{imp,wb}$ at the tank base. For the time series presented in Figures 4.34, 4.35, and 4.38 to 4.41, the results of the analysis using the ALE and ICFD models are in excellent agreement with the analytical results for both input motions. For the distributions of $p_{imp,w}$ presented in Figures 4.36 and 4.37, the ALE and ICFD results show reasonable agreement with the analytical results along the wall, but both slightly overestimate $p_{imp,w}$ near the base.

Table 4.21 presents the maximum absolute values of the analytical, ALE, and ICFD responses for $p_{imp,w}$, F_{imp} and $M_{imp,wb}$, and the two motions. The results are extracted from the time series presented in Figures 4.34, 4.35, and 4.38 to 4.41. The percentage differences between the ALE (and ICFD) and analytical results are presented in parentheses in Table 4.21. The percentage differences are all less than $\pm 10\%$. Accordingly, the ALE and ICFD models are verified for calculating impulsive responses of a flexible base-supported cylindrical tank subjected to unidirectional horizontal motion of a small amplitude.

Table 4.21. Maximum absolute impulsive responses of the flexible base-supported tank calculated using the numerical models and the analytical solutions, extracted from Figures 4.34, 4.35, and 4.38 to 4.41, input motions S-1, and E-1

Motion	Response	Analytical solution	ALE (diff)[1]	ICFD (diff)[1]
S-1	$p_{imp,w}$ (kN/m^2)	0.64	0.67 (4%)	0.64 (-1%)
	F_{imp} (kN)	2.51	2.71 (8%)	2.60 (4%)
	$M_{imp,wb}$ (kN-m)	2.66	2.92 (10%)	2.83 (6%)
M-1	$p_{imp,w}$ (kN/m^2)	1.18	1.16 (-2%)	1.16 (-2%)
	F_{imp} (kN)	4.56	4.86 (7%)	4.49 (-2%)
	$M_{imp,wb}$ (kN-m)	4.88	5.30 (9%)	4.93 (1%)

1. Percentage difference of FSI responses calculated using the numerical models with respect to those calculated using the analytical solutions, to the nearest 1%

4.3.3.2 Head-supported tank

The analytical solutions used to verify the ALE and ICFD models of the flexible, head-supported tank ($R = 0.79$ m, $H_s = 2$ m, $H = 1.8$ m, $h = 0.4$ mm) shown in Figures 4.26 and 4.28, respectively, are derived in Section 3.3.1.2 for impulsive responses, per Table 4.2. Similar to Veletsos (1984) for flexible base-supported tanks, the solutions used here address the impulsive frequency, $f_{imp,k}$ of the k th mode ($k = 1, 2, \ldots \infty$), and the associated modal responses, including the pressure on the inner surfaces of the tank, $p_{imp,k}$, shear force at the head of the tank, $F_{imp,k}$, and two components of the moment at the head: $M_{imp,w,k}$, generated by $p_{imp,w,k}$ on the wall, and $M_{imp,b,k}$, generated by $p_{imp,b,k}$ on the base. The equation numbers used in Section 3.3.1.2 for the analytical solutions of the frequency and the modal responses are listed in Table 4.22.

Table 4.22. Equation numbers of the analytical solutions for the impulsive frequency of the k th mode and the modal responses for flexible, head-supported cylindrical tanks, developed in Section 3.3.1.2

$f_{imp,k}$	$p_{imp,w,k}$	$p_{imp,b,k}$	$F_{imp,k}$	$M_{imp,w,k}$	$M_{imp,b,k}$
(3.128)	(3.134)	(3.135)	(3.136)	(3.139)	(3.137)

Identical to the solutions of Veletsos (1984), the equations listed in Table 4.22 for modal responses are functions of an acceleration time series, $A_k(t)$ per Eq. (4.5). The damping ratio, ζ_k, used for calculating $A_k(t)$ is extracted from the blue line in Figure 4.29, per the analytically calculated frequency $f_{imp,k}$. The blue line is the damping model implemented for the numerical calculation (see Section 4.3.1).

The first three impulsive frequencies, $f_{imp,k}$, of the tank calculated using the numerical models and Eq. (3.128) are compared. The frequencies of the tank in the numerical models are identified from the hydrodynamic pressure, $p_{imp,w}$, for sine-sweep motion S-S, at the red solid circle presented in Figure 4.2. The red solid circle is on the edge of the base and the wall of the tank, where the impulsive pressure is expected to be the greatest along the tank wall per the first modal response shown in, calculated per Eq. (3.134) for $H/R = 2$. The impulsive frequencies are identified from the Fourier amplitude spectrum of $p_{imp,w}$ calculated using Fast Fourier Transform (FFT). Figures 4.42a and b present the spectrum for the ALE model, normalized by its maximum ordinate, for frequencies ranging between 0 and 120 Hz, in a linear format and a linear-logarithmic format, respectively. Figures 4.42c and d present those calculated using the ICFD model. The peaks in the spectra at the three lowest frequencies are associated with the first three impulsive modes. The second and third modes cannot be identified from the ICFD result, but the fluid-structure responses in the two modes (68 and 103.1 Hz per the analytical solution) are considered *rigid* and not affected by the calculated frequencies. Table 4.23 presents the frequencies calculated using Eq. (3.128) and the numerical models. The differences are less than 4%.

The time series of the impulsive pressure, $p_{imp,w}$, on the tank wall, the shear force, F_{imp}, at the head of the tank in the x direction, and the moment, $M_{imp,wb}$, at the head about the y axis calculated using the numerical models are compared with those calculated using the analytical solutions per Eqs. (4.6) to (4.8), in which $p_{imp,w,k}$, $F_{imp,k}$, $M_{imp,w,k}$ and $M_{imp,b,k}$ are calculated per the equations listed in Table 4.22.

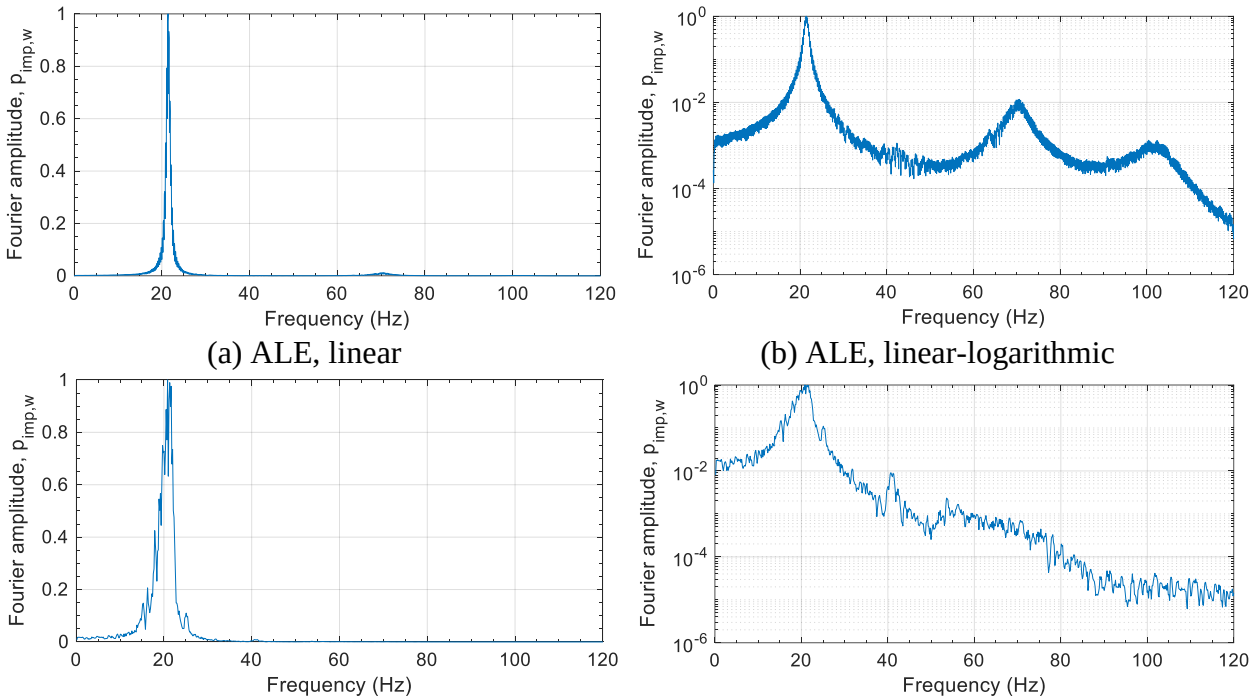

Figure 4.42. Normalized Fourier amplitude spectra for the hydrodynamic pressure, $p_{imp,w}$, at the location of the red solid circle shown in Figure 4.2, calculated using the ALE and ICFD models

Table 4.23. Impulsive frequencies of the flexible head-supported tank calculated using Eq. (3.128) and the ALE and ICFD models, and their percentage differences

Mode	Frequency (Hz)			Difference[1] (%)	
	Analytical solution	ALE model	ICFD model	ALE model	ICFD model
First	20.9	21.4	20.8	2	0
Second	68.0	70.4	--	4	--
Third	103.1	102.3	--	-1	--

1. Percentage differences of the numerical results with respect to those calculated using the analytical solution

Impulsive pressure

The time series of $p_{imp,w}$ calculated using the numerical models and Eq. (4.6) are presented at the location of at the red solid circle on the tank shown in Figure 4.2. The cylindrical coordinates of the circle are used for Eq. (4.6): $(r,\theta,z)=(0.79\text{ m}, 0, 0)$. Figure 4.43 presents results for the ALE model and the two input motions (i.e. S-1 and E-1). As seen in Figure 4.43b, significant response to motion E-1 is realized in the first 2.5 seconds. To reduce run time, the ICFD analysis for E-1 is performed for 3 seconds only. (The run time of this analysis is about 9 days.) Figure 4.44 enables a comparison of results for the ICFD model and the analytical solution for S-1 and (the first 3 seconds of) E-1.

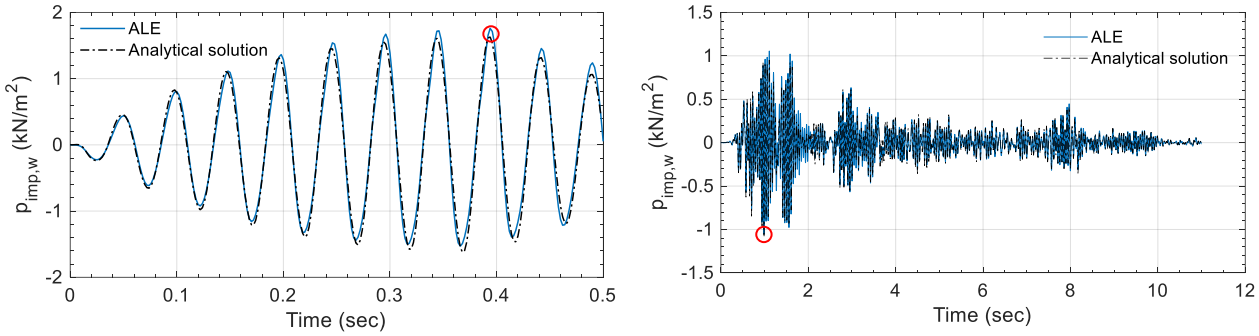

(a) S-1 (b) E-1

Figure 4.43. Time series of the impulsive pressure, $p_{imp,w}$, at the location of the red solid circle shown in Figure 4.2, calculated using the ALE model and Eq. (4.6)

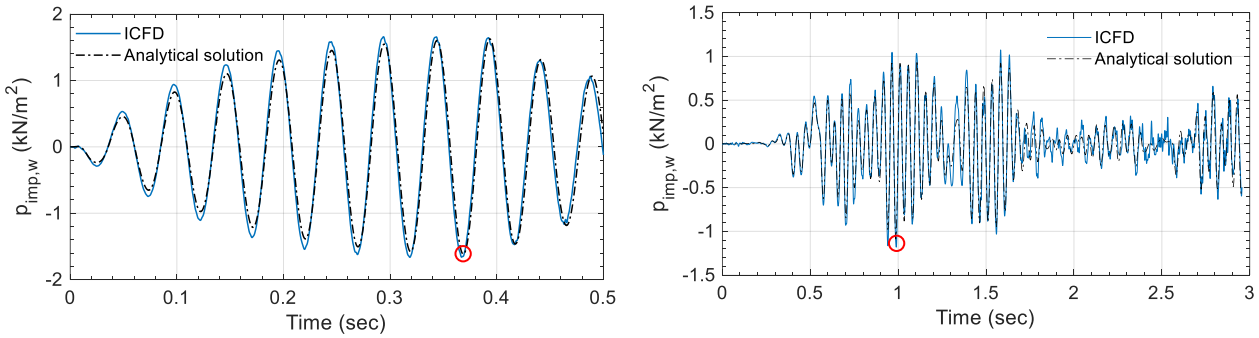

(a) S-1 (b) E-1

Figure 4.44. Time series of the impulsive pressure, $p_{imp,w}$, at the location of the red solid circle shown in Figure 4.2, calculated using the ICFD model and Eq. (4.6)

The distributions of $p_{imp,w}$ calculated using the numerical models and Eq. (4.6) are presented using the green line on the tank wall shown in Figure 4.2. The cylindrical coordinates of the green line are used for Eq. (4.6): $(r,\theta,z)=$(0.79 m, 0, 0 to 1.8 m). Figures 4.45a and b present results at peak response in the $p_{imp,w}$ time series for the ALE model: see the open red circles in the corresponding panels of Figure 4.43. Figure 4.46 presents results at peak response in the $p_{imp,w}$ time series for the ICFD model: see the open red circles in panels of Figure 4.44.

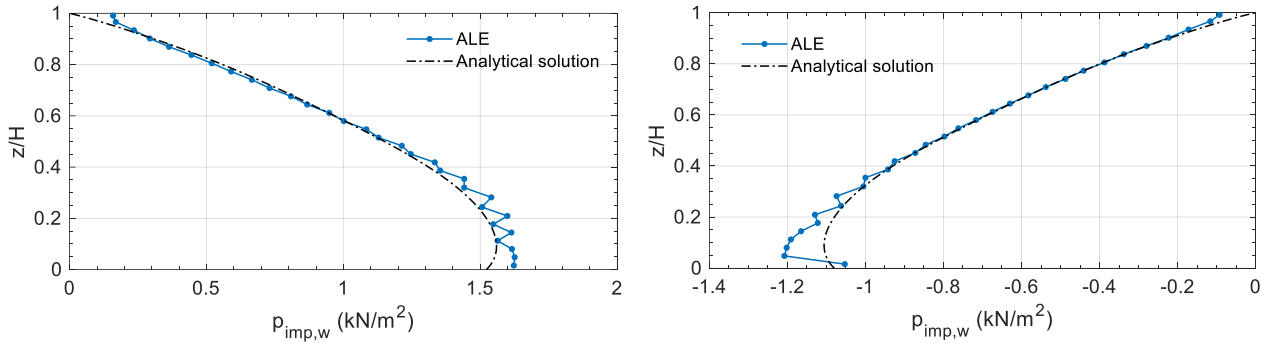

(a) S-1, $t=0.395$ sec (b) E-1, $t=0.986$ sec

Figure 4.45. Distributions of the impulsive pressure, $p_{imp,w}$, along the green line on the tank wall shown in Figure 4.2, at the time step of a peak response shown in the corresponding panels of Figure 4.43, calculated using the ALE model and Eq. (4.6)

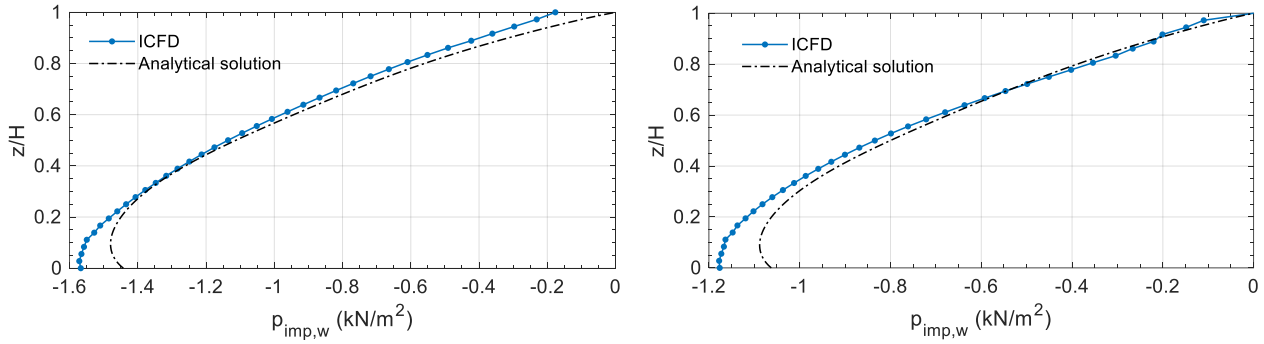

(a) S-1, $t=0.365$ sec (b) E-1, $t=0.988$ sec

Figure 4.46. Distributions of the impulsive pressure, $p_{imp,w}$, along the green line on the tank wall shown in Figure 4.2, at the time step of a peak response shown in the corresponding panels of Figure 4.44, calculated using the ICFD model and Eq. (4.6)

Reactions: shear force and moment at the head

The time series of F_{imp} in the x direction at the head of the tank calculated using the numerical models and Eq. (4.7), are presented in Figures 4.47 and 4.48. Figure 4.47 presents results for the ALE model and the two input motions (i.e. S-1 and E-1). Figure 4.48 presents companion data for the ICFD model. For the reason given above (in the section on impulsive pressure), only the first 3 seconds of motion E-1 is used.

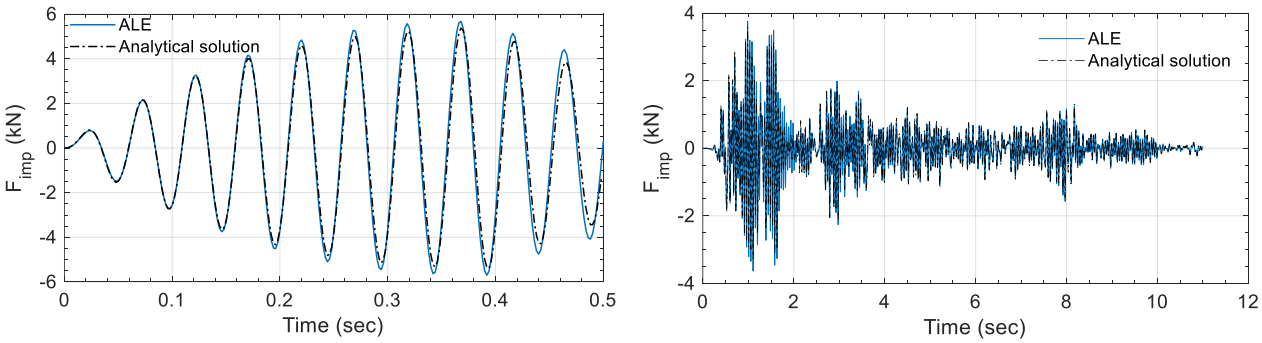

(a) S-1 (b) E-1

Figure 4.47. Time series of the impulsive shear force, F, in the x direction at the head of the tank, calculated using the ALE model and Eq. (4.7)

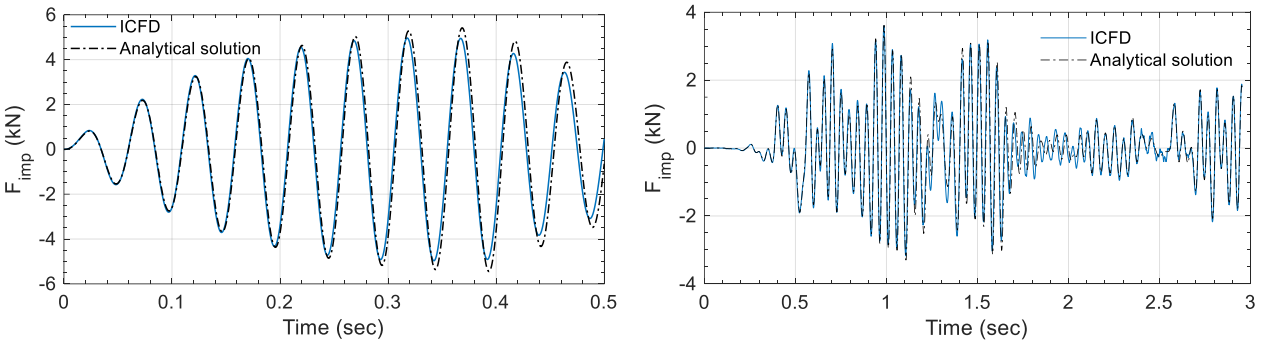

(a) S-1 (b) E-1

Figure 4.48. Time series of the impulsive shear force, F, in the x direction at the head of the tank, calculated using the ICFD model and Eq. (4.7)

The time series of $M_{imp,wb}$ about the y axis at the head of the tank calculated using the numerical models and Eq. (4.8), are presented in Figures 4.49 and 4.50. Figure 4.49 presents results for the ALE model and the two input motions (i.e. S-1 and E-1). Figure 4.50 presents companion data for the ICFD model. Again, only the first 3 seconds of motion E-1 is used.

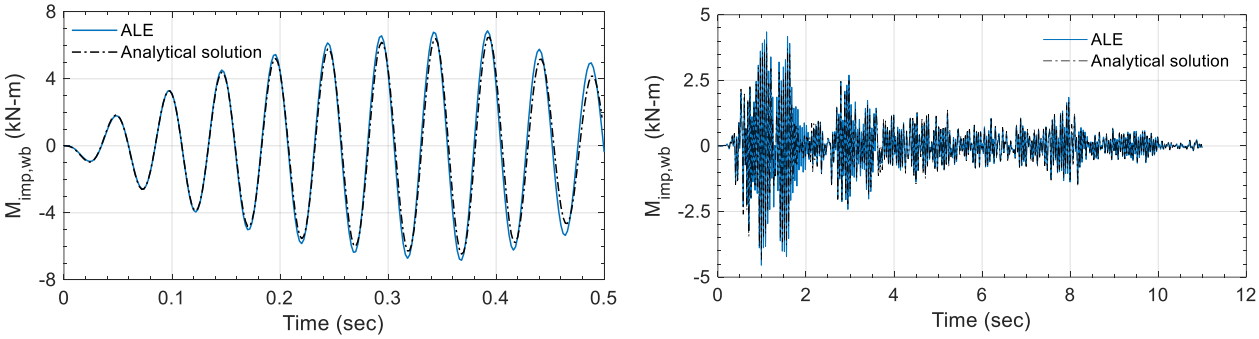

(a) S-1 (b) E-1

Figure 4.49. Time series of the moment, $M_{imp,wb}$, about the y axis at the head of the tank, calculated using the ALE model and Eq. (4.8)

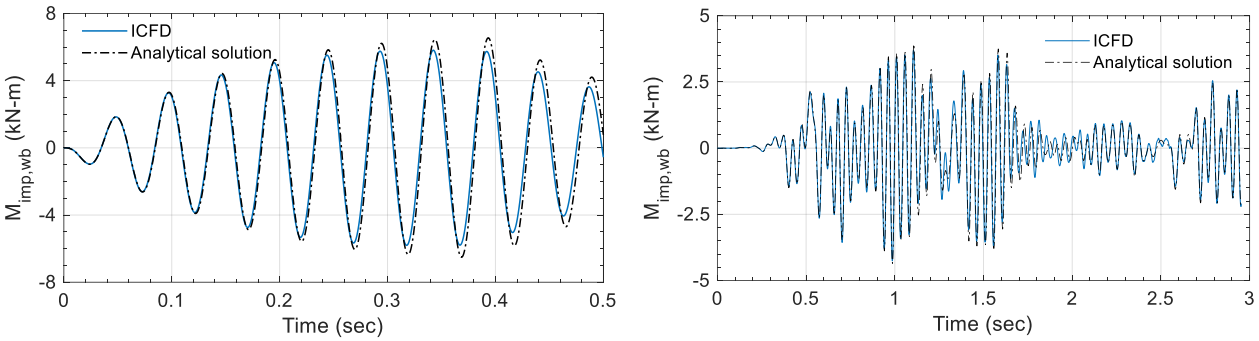

(a) S-1 (b) E-1

Figure 4.50. Time series of the impulsive moment, $M_{imp,wb}$, about the y axis at the head of the tank, calculated using the ICFD model and Eq. (4.8)

Discussion

Figures 4.43 through 4.50 enable comparisons of numerical and analytical FSI responses to verify the ALE and ICFD models of a flexible, head-supported, cylindrical tank ($R = 0.79$ m, $H_s = 2$ m, $h = 0.4$ mm), filled with fluid to $H = 1.8$ m and subjected to small-amplitude, unidirectional, horizontal motions S-1 and E-1. The reported FSI responses include $p_{imp,w}$ at the location of the red circle and along the green line shown in Figure 4.2, and F_{imp} and $M_{imp,wb}$ at the head. Similar to the comparisons made for the flexible base-supported tank presented in Section 4.3.3.1, the results of the analysis using the ALE and ICFD models are in excellent agreement with the analytical solutions, as shown in Figures 4.45 to 4.46.

Table 4.24 presents the maximum absolute values of the analytical, ALE, and ICFD responses for $p_{imp,w}$, F_{imp} and $M_{imp,wb}$, for the two input motions, extracted from the time series in Figures

4.43, 4.44, and 4.47 to 4.50. The percentage differences between the ALE (and ICFD) and the analytical results are presented in parentheses in Table 4.24. The percentage differences are all less than $\pm 10\%$. Accordingly, the ALE and ICFD models are verified for calculating impulsive responses of a flexible head-supported cylindrical tank subjected to unidirectional horizontal motion of a small amplitude.

Table 4.24. Maximum absolute impulsive responses of the flexible head-supported tank calculated using the numerical models and the analytical solutions, extracted from Figures 4.43, 4.44, and 4.47 to 4.50, input motions S-1, and E-1

Motion	Response	Analytical solution	ALE (diff)[1]	ICFD (diff)[1]
S-1	$p_{imp,w}$ (kN/m^2)	1.63	1.76 (8%)	1.66 (2%)
	F_{imp} (kN)	5.39	5.70 (6%)	4.98 (-8%)
	$M_{imp,wb}$ (kN-m)	6.48	6.86 (6%)	5.81 (-10%)
M-1	$p_{imp,w}$ (kN/m^2)	1.09	1.06 (-3%)	1.18 (8%)
	F_{imp} (kN)	3.59	3.77 (5%)	3.60 (0%)
	$M_{imp,wb}$ (kN-m)	4.32	4.55 (5%)	4.26 (-2%)

1. Percentage difference of FSI responses calculated using the numerical models with respect to those calculated using the analytical solutions, to the nearest 1%

4.4 Closing remarks

Earthquake shaking of a fluid (liquid)-filled advanced reactor induces fluid-structure interaction (FSI) between the reactor vessel, the submerged internal components, and the contained fluid. Verified and validated numerical models for FSI analysis will be required for the seismic design and qualification of the advanced reactors. Many prototype advanced reactor vessels are cylindrical and filled with liquid: the PFR of Figure 4.1 (International Atomic Energy Agency (IAEA) 2012; Jensen and Ølgaard 1995) and the liquid sodium reactor of Figure 1.2 (Gluekler 1997). In this section, fluid-filled cylindrical tanks are analyzed using the ALE and ICFD solvers in LS-DYNA (2018a), and the numerical models are verified using analytical solutions presented in Section 3. (Verification of ALE and ICFD models for internal components are presented in Section 5.)

To verify the ALE and ICFD models, this section compares numerical and analytical results for impulsive and convective components of hydrodynamic pressures, reactions (i.e., shear forces and moments) at the support (i.e., base or head), and wave heights in tanks. Response-history analysis of the tanks is performed for unidirectional horizontal input motion of a small amplitude. No internal components are included in the analysis, namely, the interaction of the tank and its internal components due to the presence of the contained fluid is not considered here. The tank is supported at either the base or the top, and its wall is either rigid or flexible. The material used for the tank is carbon steel, and the contained liquid is water. According to the comparisons presented in Sections 4.2.3 and 4.3.3, the ALE models are verified for calculating hydrodynamic pressures, reactions, and convective frequencies for rigid and flexible cylindrical tanks, but are limited to short-duration analysis (e.g., 5 seconds) for calculating wave heights. The ICFD models are not verified for calculating waves (neither heights nor frequencies) but verified for calculating hydrodynamic pressures and reactions for rigid and flexible cylindrical tanks, if the wave action is not significant. Accordingly, the use of ICFD models is limited to FSI analysis with no wave action (e.g., full tank) or for input motions with frequency contents not significant at the first convective mode of the tank.

Figure 4.1 presents the PFR, for which the vessel was constructed using stainless steel and filled with liquid sodium. The vessel includes multiple internal components, which are not considered in the verification studies of this section. Accordingly, to develop a numerical model for the seismic design and qualification of this reactor, a verification study would have to be performed beforehand, and separately, for models of: 1) fluid-structure responses of the vessel (excluding the internal components), and 2) interaction responses of the vessel and its internal components. Verification for (1) can follow the work of this section and the recommendation presented below, and information on verification for (2) is presented in Section 5. To verify a model for the fluid-structure responses (i.e., model (1)), the dimensions, geometries, and materials of the vessel of Figure 4.1 must be idealized to accommodate the assumptions used for the analytical solutions. Per Table 4.2, the analytical solutions presented in Sections 3.3.1.1, 3.3.2.1, and 3.3.1.2 are suitable for this head-supported vessel, and their assumptions include 1) rigid or elastic vessel, 2) ideal fluid, and 3) small-amplitude unidirectional horizontal motions. The vessel (tank), idealized in the model to accommodate the assumptions, would be constructed using a rigid/elastic

material assigned the mechanical properties of the stainless steel, and filled with an ideal fluid with the density of the liquid sodium at the assumed operating temperature. The geometries and dimensions used for the idealized tank should represent the vessel and be adapted for the analytical solutions. The analytical solutions use constant values for dimensions (e.g., R, h, H_s, and H), and so the dish-shaped base shown in Figure 4.1 would be set aside from the model of the idealized tank. The dimensions of the idealized tank (that represent the vessel and accommodate the solutions) would be the radius R at the head support of the vessel, its thinnest wall thickness h, the maximum height of the vessel H_s, and the greatest depth of the contained fluid H. Fluid-structure responses (i.e., hydrodynamic pressures, reactions at the support, and wave heights) of the idealized tank subjected to small-amplitude, unidirectional, horizontal motions would be calculated using the model and compared with the analytical solutions. If the differences are less than $\pm$ 10%, the model should be considered to be verified.

After verifying the model of the idealized tank (and models for interaction responses of the vessel and its internal components; see Section 5), a validation study would have to be performed using data from physical testing on a specimen representing the reactor of Figure 4.1. (Information on validation study is presented in Section 6.) Thereafter, a comprehensive numerical model for the reactor (including internal components) could be developed using the realistic boundary conditions and geometries shown in Figure 4.1. This comprehensive model would be used for calculating fluid-structure responses to three-directional seismic inputs for seismic design, qualification, and probabilistic risk assessment.

SECTION 5
VERIFICATION OF NUMERICAL MODELS FOR SEISMIC FLUID-STRUCTURE-INTERACTION ANALYSIS OF SUBMERGED COMPONENTS

5.1 Introduction

Figures 5.1a (Gluekler 1997) and 5.1b (TerraPower 2018) show cutaway views of prototype advanced reactors, each including a reactor vessel (i.e., vertical cylindrical tank), a contained fluid, and components internal to the vessel. Earthquake shaking of such fluid-filled advanced reactors induces interactions between the vessel, the contained fluid, and the internal components. Seismic design and qualification of the advanced reactors will require verified and validated numerical models for fluid-structure-interaction (FSI) analysis. These numerical models need to accommodate 1) realistic geometries and boundary conditions of the vessel and internal components, 2) three-directional seismic input, and 3) nonlinear responses of the fluid, none of which is possible with analytical solutions. The Arbitrary Lagrangian-Eulerian (ALE) and Incompressible Computational Fluid Dynamics (ICFD) solvers in LS-DYNA (Livermore Software Technology Corporation (LSTC) 2018) are capable of nonlinear FSI calculations for three-directional seismic loading.

Section 4 presented seismic analysis using the two solvers for numerical models of vertical cylindrical tanks. The numerical models of the tanks were verified using the analytical solutions presented in Section 3, and are validated using data from earthquake-simulator tests of a 1/10th-scale base-supported cylindrical tank, as presented in Section 6. This section develops ALE and ICFD models for components internal to a cylindrical tank and submerged in the contained fluid. Numerical results are compared with those calculated using analytical solutions to verify the models. Validation of the verified models will be presented in Mir (in progress), using data from earthquake-simulator tests of the 1/10th-scale tank including internal components supported at the head of the tank.

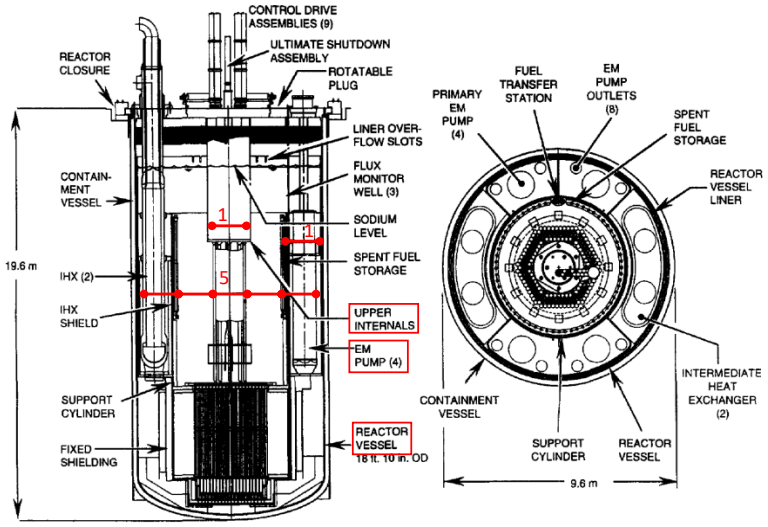

(a) liquid metal reactor, General Electric Company, Boston, MA, Figure 5 in Gluekler (1997)

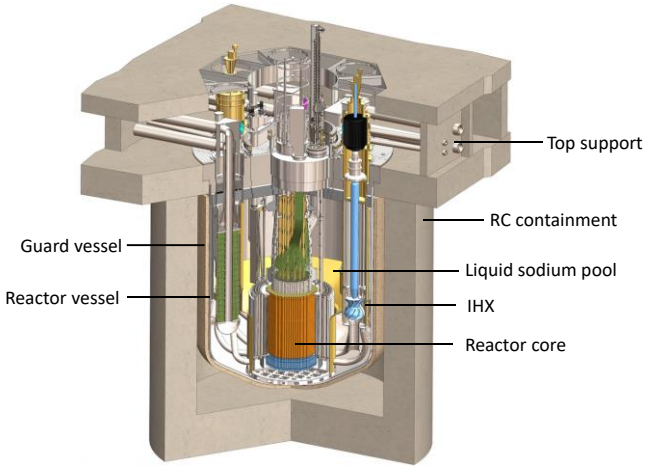

(b) liquid metal reactor, TerraPower, Bellevue, WA, http://terrapower.com/technologies/twr, accessed on July 4, 2018

Figure 5.1. Prototype advanced reactors, each including a reactor vessel, internal components, and a contained fluid

Per Figure 5.1, internal components are generally vertical, cylindrical, pipe-type structures, such as the upper internal[36], the immediate heat exchanger (IHX)[37], and electromagnetic (EM) pumps[38]. For application to design and analysis of components in a nuclear reactor, Chen and Rosenberg (1975) derived analytical solutions for frequencies of two concentric pipes filled with fluid, as shown in Figure 5.2. The inner pipe is an internal component, and the outer pipe refers to the wall of the reactor vessel. The lengths and boundary conditions of the two pipes are identical. The pipes are filled fully: there is no free surface. When the pipes displace (e.g., due to seismic motions), the fluid adjacent to them generates hydrodynamic pressures on their surfaces. The solutions assumed the mass of the fluid contributing to the hydrodynamic pressures to be attached to and move with the pipes, which reduced their frequencies (i.e., the so-called *added mass effect*). Although 1) a reactor vessel and its internal components are generally not concentric, 2) their boundary conditions and lengths are not identical, and 3) the fluid does not fully fill the vessel, Chen and Rosenberg provided the most relevant information for design and analysis of internal components in an advanced reactor[39], to the knowledge of the authors of this report.

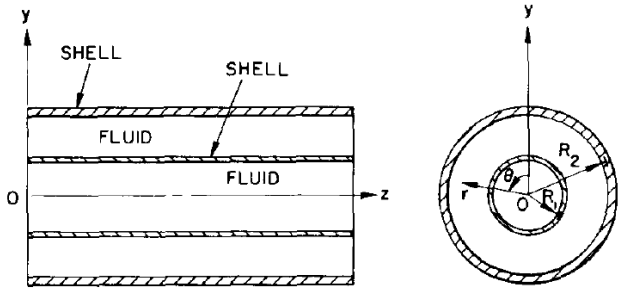

Figure 5.2. Two concentric cylindrical pipes with fluid fully filling the inside of the inner pipe and the annulus between the two pipes (Figure 1 in Chen and Rosenberg (1975))

To use the analytical solutions (Chen and Rosenberg) to verify numerical models herein, each model is composed of two fluid-filled concentric cylindrical pipes. To adopt the assumptions

[36] Upper internal: to suspend control rods above the reactor core; the control rods can be inserted to the reactor core to adjust the rate of nuclear fission; see Section 1.1 for information on nuclear fission

[37] Immediate heat exchanger (IHX): to transfer hot sodium from the reactor core to other systems (e.g., steam turbines and energy generators) to produce electricity and transfer cold sodium to cool the core

[38] Electromagnetic (EM) pump: to circulate sodium in the reactor

[39] Section 3.6 of ASCE/SEI 4-16 (2017) uses the analytical solutions of Chen and Rosenberg, in part, to provide guidance for the analysis and design of submerged nuclear components.

used in the study (Chen and Rosenberg), the two pipes in each model are both top-supported, which is similar to the boundary condition of the vessel and the internal components of some advanced reactors (see Figure 5.1), and their heights (i.e., lengths) are identical. Two sets of numerical models of two fluid-filled concentric pipes with different dimensions are analyzed. In the first set of the models, denoted M1, the dimensions are based on those of the 1/10th-scale tank and the central internal component used for the earthquake-simulator tests. Loosely based on a prototype advanced reactor, the radius of the 1/10th-scale test tank is 0.79 m, the height is 2 m, and the wall thickness is 7.92 mm: the outer pipe in M1. (The height and radius were also used for the numerical models of the tanks in Section 4.) The central internal component used for the earthquake-simulator tests is a round HSS 12.75×0.25 steel pipe (American Institute of Steel Construction (AISC) 2011) with a radius of 0.162 m (i.e., 12.75/2=6.375 inches) and a wall thickness of 6.35 mm (i.e., 0.25 inch). This radius is about 1/5th of that of the test tank (i.e. $0.162/0.79 = 0.205 \approx 1/5$), selected based on the dimensions used for prototype advanced reactors. Per Figure 5.1a, the ratio of the radii of the internal components (e.g., EM pump and upper internal) to the containing vessel is about 1/5, identified using red lines. The radius and the wall thickness of the inner pipe in M1 are identical to those of the central internal component used for the tests: 0.162 m and 6.35 mm, respectively. The height of the inner pipe in M1 is 2 m, which is identical to that of the outer pipe to be consistent with the assumption used for the analytical solutions. Figure 5.3a illustrates the dimensions and boundary condition of M1.

If the radii of the two concentric pipes are similar, the fluid-filled annulus is narrow and the frequencies of the inner pipe are significantly affected by the movement of the outer pipe (Chen and Rosenberg). Two *coupled* frequencies describe the motions of the two pipes displacing laterally in either the same or opposite directions. Additional information on the coupled frequencies is presented in Section 5.2.1. The second set of the models, denoted as M2, enables calculations of the coupled frequencies of a submerged pipe internal to an outer pipe with a similar radius. The inner pipe is identical to that used for M1: the radius, height, and wall thickness are 0.162 m, 2 m, and 6.35 mm, respectively. The height and the wall thickness of the outer pipe are identical to those used for M1 (i.e., 2 m and 7.92 mm, respectively), but the radius is reduced to 0.2 m. Figure 5.3b illustrates the dimensions and boundary conditions for M2.

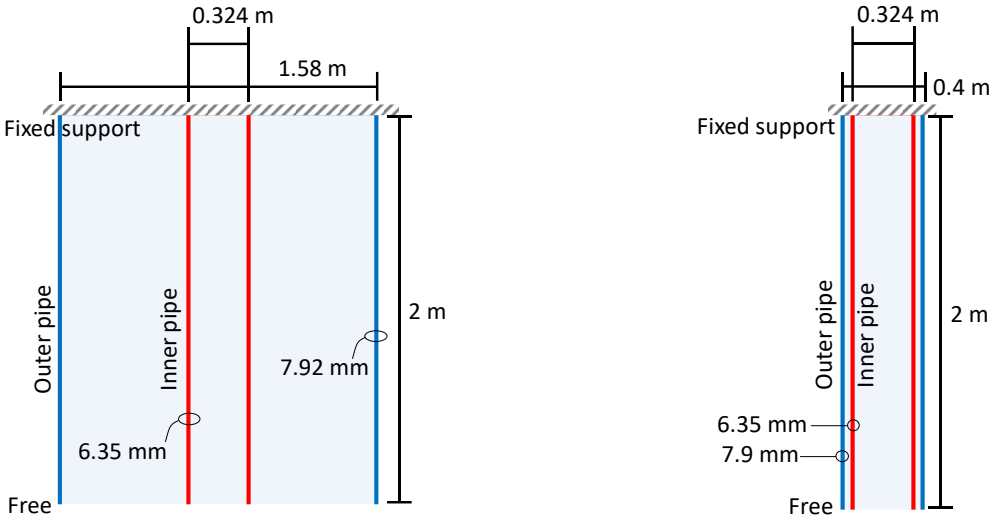

(a) M1 (b) M2

Figure 5.3. Dimensions and boundary conditions for two sets of numerical models of two fluid-filled concentric pipes

The frequencies of the internal component (i.e., inner pipe) in both M1 and M2 are calculated by FSI analysis using the ALE and ICFD solvers in LS-DYNA. The two solvers cannot perform eigenvalue analysis. Rather, the frequencies are identified from the response history of the inner pipe undergoing free vibration. To achieve free vibration response, a small horizontal displacement is applied at the free (i.e., bottom) end of the inner pipe, and the pipe is then released to vibrate. Since this displacement generates the first lateral modal shape of the inner pipe, the associated frequencies are the focus of the analysis and verification. The circumferential, axial, and torsional modes are not considered. If the fluid is not included in the models, the frequencies of the inner pipe (involving no fluid) are dependent on its mass and stiffness. The frequencies of the submerged inner pipe (involving fluid), as shown in Figure 5.3, are dependent on its mass and stiffness, and also the added mass contributed by hydrodynamic pressures. To benchmark the analysis for structures (without fluid) prior to the FSI analysis, numerical models for the inner pipe used for M1 and M2 involving no fluid are prepared. The models are verified by comparing the first lateral frequencies of the inner pipe (involving no fluid) calculated using eigen analysis numerically and the analytical solutions with the fluid

density assigned to zero[40], as presented in Table 5.1. (The models for the inner pipe (involving no fluid) are presented in Section 5.3; see Figures 5.16a, d and 5.17a, d. The eigen analysis is not presented.) Accordingly, for the submerged inner pipe, if the frequencies calculated using the numerical models and the analytical solutions are in good agreement, the added mass contributed by the hydrodynamic pressures on their surfaces is correctly calculated. The models that calculate the pressures correctly are considered verified here since other seismic FSI responses are all generated by the pressures: the hydrodynamic shear force and moment at the support of the inner pipe are associated with the integration of the pressure with respect to its surface. Since the free surface and the base of the pipes are not included in the numerical and analytical calculations, wave heights and pressures on the base are not available for a comparison.

Section 5.2 presents the analytical solutions of Chen and Rosenberg. Calculation errors made in Chen and Rosenberg are corrected, and the revised analytical solutions are used hereafter in this section. Analytical solutions for lateral frequencies of submerged cylindrical pipes are calculated, including those used for M1 and M2 in Figure 5.2. Section 5.3 presents the ALE and ICFD models for M1 and M2. Section 5.4 verifies the models of Section 5.3 by comparing the numerically calculated frequencies of the inner pipes with those calculated using the analytical solutions (Section 5.2). Section 5.5 identifies and quantifies the calculation errors made in Chen and Rosenberg. Section 5.6 presents closing remarks for this section.

Table 5.1. First lateral frequency of the inner pipe[1], no fluid involved, used for M1 and M2 shown in Figure 5.3, numerical models and analytical solution

Numerical models[2]: eigen analysis	78.4 Hz
Analytical solutions[3]	78.4 Hz
Difference	0%

1. Dimensions shown in Figure 5.3 and generic mechanical properties of carbon steel are used for the analysis.
2. The frequencies of the inner pipe in the models presented in Figures 5.16a, d and 5.17a, d are almost identical.
3. See footnote 40 on page 224.

[40] The analytical solutions of Chen and Rosenberg for the frequencies of the pipes presented in Figure 5.2 involved the use of the densities of the fluids: ρ_1 for the fluid inside the inner pipe and ρ_2 for the fluid in the annulus between the two pipes. Assigning to for both densities achieves the frequencies for the pipes involving no fluid, namely, only the mechanical properties of the pipes are used in the calculation. See Section 5.2 for more information on the analytical solutions.

5.2 Analytical solutions

Chen and Rosenberg (1975) derived analytical solutions for frequencies of two fluid-filled concentric pipes shown in Figure 5.2. The lengths and the boundary conditions of the two pipes are identical. The pipes are filled fully: there is no free surface. When the pipes displace (e.g., due to seismic motions), the fluid adjacent to them generates hydrodynamic pressures on their surfaces. The solutions assumed the mass of the fluid contributing to the hydrodynamic pressures to be attached to and move with the pipes, which reduced their frequencies (i.e., the so-called *added mass effect*). The hydrostatic pressure on the pipes was not included in the analysis because gravity was not considered. The pipes were assumed to be either elastic or rigid with a constant thickness; the fluid was assumed to be ideal, namely, inviscid and incompressible. Chen and Rosenberg derived the analytical solutions for the frequencies of lateral, circumferential, axial, and torsional motions of the pipes. However, only the frequencies of lateral motions are discussed herein, to be used to verify the results of the numerical models. Section 5.2.1 presents the derivation of the analytical solutions, and the calculation errors made in Chen and Rosenberg are identified and corrected. Section 5.2.2 presents the results calculated using the analytical solutions for two fluid-filled concentric pipes with a range of dimensions. Section 5.2.3 exercises the calculation of frequencies using the analytical solutions for three sets of two fluid-filled concentric pipes. The three examples are associated with typical nuclear components in an advanced reactor and those used in the numerical models presented in Section 5.3.

5.2.1 Derivation

Figure 5.4 presents the concentric pipes in two cutaway views and introduces the variables used in the derivation for the analytical solutions, together with a Cartesian coordinate system (x, y, z) and a cylindrical coordinate system (r, θ, z). In the figure, "Pipe 1" refers to the inner pipe, "Pipe 2" refers to the outer pipe, "Fluid 1" refers to the fluid filling the inside of the inner pipe, and "Fluid 2" refers to the fluid filling the annulus between the two pipes. This numbering system is consistent with the subscripts of the variables using in the derivation here and those in Chen and Rosenberg. For the inner pipe (i.e., Pipe 1), the radius, height, and wall thickness are R_1, H_1, and h_1, respectively; for the outer pipe (i.e., Pipe 2), the radius, height, and wall thickness are R_2, H_2, and h_2, respectively. Since the heights of the two pipes are identical, a variable H is used for both pipes (i.e., $H = H_1 = H_2$). The radial, tangential, and axial

displacements (i.e., along the r, θ, and z coordinates) on the wall of the inner pips are u_{s1}, v_{s1}, and w_{s1}, respectively, and the counterparts for the outer pipe are u_{s2}, v_{s2}, and w_{s2}. The radial, tangential, and axial velocities in the fluid inside the inner pipe (i.e., Fluid 1) are u_1', v_1', and w_1', respectively, and the counterparts for the fluid between the two pipes (i.e., Fluid 2) are u_2', v_2', and w_2'[41].

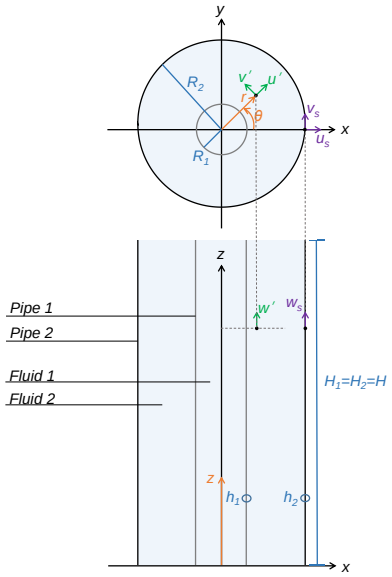

Figure 5.4. Variables used in the analytical solutions shown on two cutaway views of two concentric pipes, a Cartesian coordinate system, and a cylindrical coordinate system

Chen and Rosenberg used the equations of equilibrium for cylindrical shells provided by Flugge (1960) to relate the displacements of the pipes to the inertial forces and hydrodynamic forces (i.e., resultant forces of hydrodynamic pressures) on the pipes. Flugge equilibrated the stresses of and external forces on a unit area of a cylindrical shell using three differential equations[42] (Eq. (13a-c) on page 219 in Flugge):

[41] In Chen and Rosenberg (1975), the radial, tangential, and axial displacements along the r, θ, and z coordinates were denoted as w, v, and u, respectively. However, in this report, u, v, and w, respectively, are used (i.e., u and w are exchanged) for the purpose of consistency with the derivations for FSI responses of cylindrical tanks presented in Section 3.

[42] In Flugge (1960), the radial, tangential, and axial displacements along the r, θ, and z coordinates were denoted as w, v, and u, respectively. However, in this report, u, v, and w are used, respectively.

$$[\frac{1}{R^2}+\frac{h^2}{12R^4}+\frac{h^2}{12}\frac{\partial^4}{\partial z^4}+\frac{h^2}{6R^2}\frac{\partial^4}{\partial z^2\partial\theta^2}+\frac{h^2}{12R^4}\frac{\partial^4}{\partial\theta^4}+\frac{h^2}{6R^4}\frac{\partial^2}{\partial\theta^2}]u_s+$$
$$[-\frac{(3-\upsilon)h^2}{24R^2}\frac{\partial^3}{\partial\theta\partial z^2}+\frac{1}{R^2}\frac{\partial}{\partial\theta}]v_s+[-\frac{h^2}{12R}\frac{\partial^3}{\partial z^3}+\frac{\upsilon}{R}\frac{\partial}{\partial z}+\frac{(1-\upsilon)h^2}{24R^3}\frac{\partial^3}{\partial\theta\partial z^2}]w_s=-F_u\frac{1-\upsilon^2}{Eh} \quad (5.1)$$

$$[\frac{1}{R^2}\frac{\partial}{\partial\theta}-\frac{(3-\upsilon)h^2}{24R^2}\frac{\partial^3}{\partial\theta\partial z^2}]u_s+[\frac{1}{R^2}\frac{\partial^2}{\partial\theta^2}+\frac{1-\upsilon}{2}(1+\frac{h^2}{4R^2})\frac{\partial^2}{\partial z^2}]v_s+\frac{1+\upsilon}{2R}\frac{\partial^2}{\partial z\partial\theta}w_s=F_v\frac{1-\upsilon^2}{Eh} \quad (5.2)$$

$$[\frac{1}{R^2}\frac{\partial}{\partial\theta}-\frac{(3-\upsilon)h^2}{24R^2}\frac{\partial^3}{\partial\theta\partial z^2}]u_s+[\frac{1}{R^2}\frac{\partial^2}{\partial\theta^2}+\frac{1-\upsilon}{2}(1+\frac{h^2}{4R^2})\frac{\partial^2}{\partial z^2}]v_s+\frac{1+\upsilon}{2R}\frac{\partial^2}{\partial z\partial\theta}w_s=F_w\frac{1-\upsilon^2}{Eh} \quad (5.3)$$

where E, υ, R, and h are the elastic modulus, Poisson's ratio, radius, and wall thickness of the cylindrical shell; u_s, v_s, and w_s are displacements of the shell along the r, θ, and z coordinates, respectively; and F_u, F_v, and F_w are forces per unit area on the shell along the r, θ, and z coordinates, respectively. Eqs. (5.1) to (5.3) can be used for any general cylindrical shell. In the derivation of Chen and Rosenberg, for the inner pipe shown in Figure 5.4, E, υ, R, h, u_s, v_s, w_s, F_u, F_v, and F_w in the equations were replaced by E_1, υ_1, R_1, h_1, u_{s1}, v_{s1}, w_{s1}, F_{u1}, F_{v1}, and F_{w1} (e.g., a subscript "1" was added for each variable), respectively. The corresponding variables for the outer pipe in Figure 5.4 were E_2, υ_2, R_2, h_2, u_{s2}, v_{s2}, w_{s2}, F_{u2}, F_{v2}, and F_{w2} (e.g., a subscript "2" was added for each variable).

The forces (per unit area) on the inner and outer pipes included inertial forces (per unit area) and hydrodynamic pressures. The inertial forces were associated with the accelerations of the pipes in the r, θ, and z coordinates. The hydrodynamic pressures generated by the fluid were in the r direction normal to the walls of the pipes, and so were included in F_{u1} and F_{u2}. Accordingly, F_{u1}, F_{v1}, and F_{w1} of the inner pipe were:

$$F_{u1}=-\rho_{s1}h_1\cdot u''_{s1}+p_{1,1}-p_{1,2} \quad (5.4)$$

$$F_{v1}=-\rho_{s1}h_1\cdot v''_{s1} \quad (5.5)$$

$$F_{w1}=-\rho_{s1}h_1\cdot w''_{s1} \quad (5.6)$$

where ρ_{s1} is the density of the material of the inner pipe; u''_{s1}, v''_{s1}, and w''_{s1} are the accelerations of the inner pipe; and $p_{1,1}$ is the hydrodynamic pressure on the inner surface of the inner pipe

exerted by Fluid 1, and $p_{1,2}$ is that on the outer surface exerted by Fluid 2. Figure 5.5 shows $p_{1,1}$ and $p_{1,2}$ on a cutaway view of the two pipes accelerating in the x direction. The forces F_{u2}, F_{v2}, and F_{w2} on the outer pipe were:

$$F_{u2} = -\rho_{s2} h_1 \cdot u''_{s2} + p_{2,2} \tag{5.7}$$

$$F_{v2} = -\rho_{s2} h_2 \cdot v''_{s2} \tag{5.8}$$

$$F_{w2} = -\rho_{s2} h_2 \cdot w''_{s2} \tag{5.9}$$

where ρ_{s2} is the density of the material of the outer pipe; u''_{s2}, v''_{s2}, and w''_{s2} are the accelerations of the outer pipe; and $p_{2,2}$ is the hydrodynamic pressure on the inner surface of the outer pipe exerted by Fluid 2, as shown in Figure 5.5.

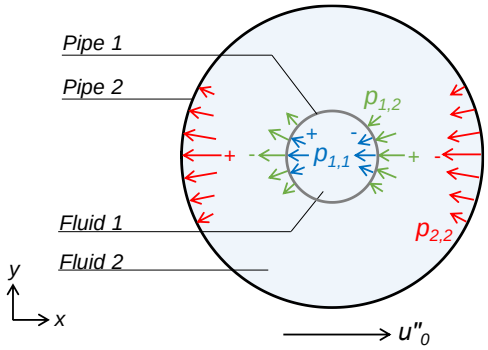

Figure 5.5. Hydrodynamic pressures generated by Fluids 1 and 2 on Pipes 1 and 2, accelerating in the x direction

The accelerations of the inner and outer pipes (i.e., u''_{s1}, v''_{s1}, w''_{s1}, u''_{s2}, v''_{s2}, and w''_{s2}) were the second derivatives of corresponding displacements with respect to time. The radial, tangential, and axial displacements, u_{s1}, v_{s1}, and w_{s1}, on the wall of the inner pipe were assumed to be:

$$u_{s1}(t,z,\theta) = \bar{u}_{s1} \cdot \cos\theta \cdot e^{i(\omega t - \frac{2\pi z}{l})} \tag{5.10}$$

$$v_{s1}(t,z,\theta) = \bar{v}_{s1} \cdot \sin\theta \cdot e^{i(\omega t - \frac{2\pi z}{l})} \tag{5.11}$$

$$w_{s1}(t,z,\theta) = \bar{w}_{s1} \cdot \cos\theta \cdot e^{i(\omega t - \frac{2\pi z}{l})} \tag{5.12}$$

where $\bar{u}_{s1}$, $\bar{v}_{s1}$, and $\bar{w}_{s1}$ are coefficients for the displacements; ω and l are the angular frequencies and the wavelength[43] of the pipe in a given eigen mode. The displacements, u_{s2}, v_{s2}, and w_{s2}, on the wall of the outer pipe were expressed by replacing the subscript "1" of each variable in Eqs. (5.10) to (5.12) with "2":

$$u_{s2}(t,z,\theta) = \bar{u}_{s2} \cdot \cos\theta \cdot e^{i(\omega t - \frac{2\pi z}{l})} \tag{5.13}$$

$$v_{s2}(t,z,\theta) = \bar{v}_{s2} \cdot \sin\theta \cdot e^{i(\omega t - \frac{2\pi z}{l})} \tag{5.14}$$

$$w_{s2}(t,z,\theta) = \bar{w}_{s2} \cdot \cos\theta \cdot e^{i(\omega t - \frac{2\pi z}{l})} \tag{5.15}$$

As noted in Section 3, the responses of a fluid can be defined using a velocity potential. The pressure, p, and the velocity, vel, of the fluid are related to its velocity potential, Φ, per Eqs. (3.1) and (3.2), respectively. Eqs. (3.1) and (3.2) are repeated here:

$$p(r,\theta,z) = -\rho \frac{\partial \Phi}{\partial t} \tag{5.16}$$

$$vel(r,\theta,z) = \nabla\Phi = \frac{\partial \Phi}{\partial r}\vec{r} + \frac{1}{r}\frac{\partial \Phi}{\partial \theta}\vec{\theta} + \frac{\partial \Phi}{\partial z}\vec{z} \tag{5.17}$$

---

[43] The wavelength l of a pipe is not the length (e.g., height) of the pipe, which was misused in many prior studies. The wavelength represents the shape in a given mode of an elastic beam with a uniform cross section. Timoshenko (1937) derived wavelengths in different lateral modes for a beam with the two ends 1) pinned-pinned (i.e., simply supported), 2) fixed-fixed, 3) fixed-free (i.e., cantilever beam), and 4) fixed-pinned. The wavelengths of the first lateral modal shapes (blue) of a cantilever and a simply-supported beam (black) are illustrated below:

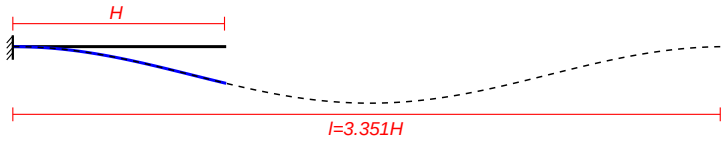

(a) cantilever beam, $l = 3.351\,H$

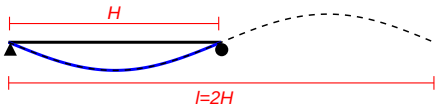

(b) simple-supported beam, $l = 2\,H$

where ρ is the density of the fluid, t is time, and ∇ is the gradient operator with respect to a cylindrical coordinate system (r, θ, z). The fluid velocity, *vel*, includes the vectors of radial, angular, and vertical components. The pressure, p, and the velocity, *vel*, calculated using Φ are functions of r, θ, and z, which enables the determination of the responses for any location in the fluid. Given assumed fluid velocities (i.e., boundary conditions), Eqs. (5.16) and (5.17) were used by Chen and Rosenberg to derive the velocity potentials for the fluids filling the two concentric pipes (see Figure 5.2) and to calculate the fluid pressures. Chen and Rosenberg assumed the expression of the velocity potentials to be the form of the radial displacements of the pipes (i.e., u_{s1} and u_{s2}). The velocity potentials for Fluids 1 and 2, Φ_1 and Φ_2, respectively, were:

$$\Phi_1 = \bar{\Phi}_1(r) \cdot \cos\theta \cdot e^{i(\omega t - \frac{2\pi z}{l})} \tag{5.18}$$

$$\Phi_2 = \bar{\Phi}_2(r) \cdot \cos\theta \cdot e^{i(\omega t - \frac{2\pi z}{l})} \tag{5.19}$$

where $\bar{\Phi}_1$ and $\bar{\Phi}_2$ are functions of r, to be solved using the assumed fluid velocities. Since Fluids 1 and 2 were assumed to be incompressible, Φ_1 and Φ_2 must satisfy Laplace's equation, $\nabla \cdot \nabla \Phi_1 = \nabla \cdot \nabla \Phi_2 = 0$ (see footnote 22 on page 49). Subjected to small-amplitude seismic motions, the fluids immediately adjacent to the wall of the pipes (i.e., at $r = R_1$ or R_2) were assumed to move with the wall at the same radial velocities:

$$u_1'(r = R_1) = \left.\frac{\partial \Phi_1}{\partial r}\right|_{r=R_1} = u_{s1}' \tag{5.20}$$

$$u_2'(r = R_1) = \left.\frac{\partial \Phi_2}{\partial r}\right|_{r=R_1} = u_{s1}' \tag{5.21}$$

$$u_2'(r = R_2) = \left.\frac{\partial \Phi_2}{\partial r}\right|_{r=R_2} = u_{s2}' \tag{5.22}$$

where u_1' and u_2' are the radial velocities of the two fluids calculated using Eq. (5.17), which leads to the second terms of Eqs. (5.20) to (5.22); u_{s1}' and u_{s2}' are the radial velocities of the wall

of the inner and outer pipes, respectively. Applying the boundary conditions per Eqs. (5.20) to (5.22), $\bar{\Phi}_1$ and $\bar{\Phi}_2$ were solved, and the velocity potentials Φ_1 and Φ_2 were then calculated:

$$\Phi_1 = \frac{I(\gamma)}{I'(\alpha_1)} i\omega \cdot \bar{w}_{s1} \cdot \cos\theta \cdot e^{i(\omega t - \frac{2\pi z}{l})} \tag{5.23}$$

$$\Phi_2 = \left(\frac{I_1(\gamma)K_1'(\alpha_2) - K_1(\gamma)I_1'(\alpha_2)}{I_1'(\alpha_1)K_1'(\alpha_2) - K_1'(\alpha_1)I_1'(\alpha_2)} \bar{w}_{s1} + \frac{K_1(\gamma)I_1'(\alpha_1) - I_1(\gamma)K_1'(\alpha_1)}{I_1'(\alpha_1)K_1'(\alpha_2) - K_1'(\alpha_1)I_1'(\alpha_2)} \bar{w}_{s2}\right) \cos\theta \cdot e^{i(\omega t - \frac{2\pi z}{l})} \tag{5.24}$$

where $\alpha_1 = 2\pi R_1 / l$, $\alpha_2 = 2\pi R_2 / l$, and $\gamma = 2\pi r / l$; I_1 and K_1 are modified Bessel's functions of the first and second kind, respectively; I_1' and K_1' are the first derivatives of I_1 and K_1 with respect to r, respectively (i.e., $I_1'(\gamma) = \frac{2\pi}{l}\frac{\partial I_1(\gamma)}{\partial \gamma}$ and $K_1'(\gamma) = \frac{2\pi}{l}\frac{\partial K_1(\gamma)}{\partial \gamma}$). The hydrodynamic pressure $p_{1,1}$ generated by Fluid 1 was calculated using Φ_1 per Eq. (5.16):

$$p_{1,1} = -\rho_1 \left.\frac{\partial \Phi_1}{\partial t}\right|_{r=R_1} = \rho_1 \omega^2 \frac{I_1(\alpha_1)}{I_1'(\alpha_1)} \cdot \bar{u}_{s1} \cdot \cos\theta \cdot e^{i(\omega t - \frac{2\pi z}{l})} \tag{5.25}$$

where ρ_1 is the density of Fluid 1. The hydrodynamic pressures $p_{1,2}$ and $p_{2,2}$ generated by Fluid 2 were calculated using Φ_2 per Eq. (5.16):

$$\begin{aligned} p_{1,2} &= -\rho_2 \left.\frac{\partial \Phi_2}{\partial t}\right|_{r=R_1} \\ &= \rho_2 \omega^2 \left(\frac{I_1(\alpha_1)K_1'(\alpha_2) - K_1(\alpha_1)I_1'(\alpha_2)}{I_1'(\alpha_1)K_1'(\alpha_2) - K_1'(\alpha_1)I_1'(\alpha_2)} \bar{u}_{s1} + \frac{K_1(\alpha_1)I_1'(\alpha_1) - I_1(\alpha_1)K_1'(\alpha_1)}{I_1'(\alpha_1)K_1'(\alpha_2) - K_1'(\alpha_1)I_1'(\alpha_2)} \bar{u}_{s2}\right) \cos\theta \cdot e^{i(\omega t - \frac{2\pi z}{l})} \end{aligned} \tag{5.26}$$

$$\begin{aligned} p_{2,2} &= -\rho_2 \left.\frac{\partial \Phi_2}{\partial t}\right|_{r=R_2} \\ &= \rho_2 \omega^2 \left(\frac{I_1(\alpha_2)K_1'(\alpha_2) - K_1(\alpha_2)I_1'(\alpha_2)}{I_1'(\alpha_1)K_1'(\alpha_2) - K_1'(\alpha_1)I_1'(\alpha_2)} \bar{u}_{s1} + \frac{K_1(\alpha_2)I_1'(\alpha_1) - I_1(\alpha_2)K_1'(\alpha_1)}{I_1'(\alpha_1)K_1'(\alpha_2) - K_1'(\alpha_1)I_1'(\alpha_2)} \bar{u}_{s2}\right) \cos\theta \cdot e^{i(\omega t - \frac{2\pi z}{l})} \end{aligned} \tag{5.27}$$

where ρ_2 is the density of Fluid 2. Equation (5.26) includes both $\bar{u}_{s1}$ and $\bar{u}_{s2}$, namely, the hydrodynamic pressure $p_{1,2}$ on the inner pipe is associated with the radial displacements of both the inner pipe and the outer pipe. Similarly, Eq. (5.27) includes both $\bar{u}_{s1}$ and $\bar{u}_{s2}$, and so $p_{2,2}$ on the outer pipe is associated with the radial displacements of both the inner pipe and the outer

pipe. Accordingly, the hydrodynamic pressure on each pipe generated by the fluid in the annulus (i.e., $p_{1,2}$ and $p_{2,2}$ in Fluid 2) is affected by the response of the other pipe, which indicates that Fluid 2 couples the responses of the two pipes. (If there is no fluid in the annulus between the two pipes, the responses of the two pipes are independent.)

Given the displacements u_{s1}, v_{s1}, and w_{s1} (Eqs. (5.10) to (5.12)) and the forces F_{u1}, F_{v1}, and F_{w1} (Eqs. (5.4) to (5.6)), Chen and Rosenberg derived three equations of equilibrium for the inner pipe using Flugge's equation per Eqs. (5.1) to (5.3). Similarly, given the displacements u_{s2}, v_{s2}, and w_{s2} (Eqs. (5.13) to (5.15)) and the forces F_{u2}, F_{v2}, and F_{w2} (Eqs. (5.7) to (5.9)), three equations of equilibrium for the outer pipe were yielded. The six equations of equilibrium were then reformatted as Eq. (5.28). The first three rows of matrix $[F]$ in Eq. (5.28) are associated with the inner pipe and the last three rows are associated with the outer pipe:

$$[F]_{6\times 6}\cdot\begin{Bmatrix}\overline{u}_{s1}\\ \overline{v}_{s1}\\ \overline{w}_{s1}\\ \overline{u}_{s2}\\ \overline{v}_{s2}\\ \overline{w}_{s2}\end{Bmatrix}=\begin{bmatrix} f_{11} & f_{12} & f_{13} & f_{14} & 0 & 0\\ f_{12} & f_{22} & f_{23} & 0 & 0 & 0\\ f_{13} & f_{23} & f_{33} & 0 & 0 & 0\\ f_{41} & 0 & 0 & f_{44} & f_{45} & f_{46}\\ 0 & 0 & 0 & f_{45} & f_{55} & f_{56}\\ 0 & 0 & 0 & f_{46} & f_{56} & f_{66}\end{bmatrix}\cdot\begin{Bmatrix}\overline{u}_{s1}\\ \overline{v}_{s1}\\ \overline{w}_{s1}\\ \overline{u}_{s2}\\ \overline{v}_{s2}\\ \overline{w}_{s2}\end{Bmatrix}=0 \tag{5.28}$$

To explain the composition and arrangement of the entries in $[F]$, the matrix is parsed here into two 3×3 submatrices, $[F_1]$ and $[F_2]$, and other two nonzero entries, f_{14} and f_{41}:

$$[F]_{6\times 6}=\begin{bmatrix}\begin{bmatrix}&&\\ &F_1&\\ &&\end{bmatrix} & \begin{matrix} f_{14} & 0 & 0\\ 0 & 0 & 0\\ 0 & 0 & 0\end{matrix}\\ \begin{matrix} f_{41} & 0 & 0\\ 0 & 0 & 0\\ 0 & 0 & 0\end{matrix} & \begin{bmatrix}&&\\ &F_2&\\ &&\end{bmatrix}\end{bmatrix} \tag{5.29}$$

Matrices $[F_1]$ and $[F_2]$ are symmetric. Matrix $[F_1]$ relates the inertial forces on Pipe 1 to its displacements, u_{s1}, v_{s1}, and w_{s1}, and relates the hydrodynamic pressures, $p_{1,1}$ and $p_{1,2}$, to the

radial displacement u_{s1} through f_{11}. All entries in $[F_1]$ are functions of the dimensions and mechanical properties of Pipe 1. Entry f_{11} also includes dimensions and densities of Fluids 1 and 2, both of which generate hydrodynamic pressures on Pipe 1. The entries in $[F_1]$ are:

$$f_{11} = 1 + \frac{h_1^2(\alpha_1^4 + 2\alpha_1^2)}{12R_1^2} - \frac{\omega^2 R_1^2 \rho_{s1}(1-\upsilon_1^2)}{E_1} \cdot \left(1 + \frac{\rho_1}{h_1\rho_{s1}} \frac{I_1(\alpha_1)}{I_1'(\alpha_1)} - \frac{\rho_2}{h_1\rho_{s1}} \frac{I_1(\alpha_1)K_1'(\alpha_2) - K_1(\alpha_1)I_1'(\alpha_2)}{I_1'(\alpha_1)K_1'(\alpha_2) - K_1'(\alpha_1)I_1'(\alpha_2)}\right) \quad (5.30)$$

$$f_{12} = 1 + \frac{h_1^2}{24R_1^2}(3-\upsilon_1)\alpha_1^2 \quad (5.31)$$

$$f_{13} = -i \cdot \left(\upsilon_1\alpha_1 + \frac{h_1^2}{12R_1}\left(\alpha_1^3 - \frac{1-\upsilon_1}{2}\alpha_1\right)\right) \quad (5.32)$$

$$f_{22} = 1 + \alpha_1^2\left(\frac{1-\upsilon_1}{2}\right)\left(1 + \frac{h_1^2}{4R_1^2}\right) - \omega^2 \cdot \frac{R_1^2\rho_{s1}(1-\upsilon_1^2)}{E_1} \quad (5.33)$$

$$f_{23} = -i \cdot \alpha_1 \frac{1+\upsilon_1}{2} \quad (5.34)$$

$$f_{33} = -\alpha_1^2 - \frac{1-\upsilon_1}{2}\left(1 + \frac{h_1^2}{12R_1^2}\right) + \omega^2 \cdot \frac{R_1^2\rho_{s1}(1-\upsilon_1^2)}{E_1} \quad (5.35)$$

Matrix $[F_2]$ relates the inertial forces on Pipe 2 to its displacements, u_{s2}, v_{s2}, and w_{s2}, and relates the hydrodynamic pressures, $p_{2,2}$, to the radial displacement u_{s2} through f_{44}. All entries in $[F_2]$ are functions of the dimensions and mechanical properties of Pipe 2, and the form of f_{44} further includes the dimensions and density of Fluid 2. Entry f_{44} is:

$$f_{44} = 1 + \frac{h_2^2}{12R_2^2}(\alpha_2^4 + 2\alpha_2^2) - \frac{\omega^2 R_2^2 \rho_{s2}(1-\upsilon_2^2)}{E_2} \cdot \left(1 + \frac{\rho_2}{h_2\rho_{s2}} \frac{K_1(\alpha_2)I_1'(\alpha_1) - I_1(\alpha_2)K_1'(\alpha_1)}{I_1'(\alpha_1)K_1'(\alpha_2) - K_1'(\alpha_1)I_1'(\alpha_2)}\right) \quad (5.36)$$

Entries f_{45}, f_{46}, f_{55}, f_{56}, and f_{66} in $[F_2]$ are counterparts of f_{12}, f_{13}, f_{22}, f_{23}, and f_{33} in $[F_1]$, respectively. Accordingly, entries f_{45}, f_{46}, f_{55}, f_{56}, and f_{66} are calculated by replacing the dimensions and mechanical properties of Pipe 1 in Eqs. (5.31) to (5.35) with those of Pipe 2 (i.e., substituting the subscript "1" of each variable with "2").

Entries f_{14} and f_{41} couple the responses of the two pipes due to the presence of Fluid 2 in the annulus between them. Entry f_{14} relates the hydrodynamic pressure on Pipe 1 to the radial displacement u_{s2} of Pipe 2, which is associated with the second term in the second line of $p_{1,2}$ per Eq. (5.26):

$$f_{14} = \frac{\omega^2 R_1^2 \rho_{s1}(1-\upsilon_1^2)}{E_1} \frac{\rho_2}{h_1 \rho_{s1}} \frac{K_1(\alpha_1) I_1'(\alpha_1) - I_1(\alpha_1) K_1'(\alpha_1)}{I_1'(\alpha_1) K_1'(\alpha_2) - K_1'(\alpha_1) I_1'(\alpha_2)} \tag{5.37}$$

Similarly, entry f_{41} relates the hydrodynamic pressure on Pipe 2 to the radial displacement u_{s1} of Pipe 1, which is associated with the first term in the second line of $p_{2,2}$ per Eq. (5.27):

$$f_{41} = -\frac{\omega^2 R_2^2 \rho_{s2}(1-\upsilon_2^2)}{E_2} \cdot \frac{\rho_2}{h_2 \rho_{s2}} \frac{I_1(\alpha_2) K_1'(\alpha_2) - K_1(\alpha_2) I_1'(\alpha_2)}{I_1'(\alpha_1) K_1'(\alpha_2) - K_1'(\alpha_1) I_1'(\alpha_2)} \tag{5.38}$$

Note that Eqs. (5.30), (5.36), (5.37), and (5.38), as written in Chen and Rosenberg, contain calculation errors. These errors are identified and quantified in Section 5.5.

The entries in $[F]$ are rearranged here into a mass matrix, $[M]$, and a stiffness matrix, $[K]$, for the two fluid-filled concentric pipes:

$$[F]_{6\times6} = [K]_{6\times6} - \omega^2 [M]_{6\times6} \tag{5.39}$$

The mass matrix, $[M]$, includes the masses of the pipes and the added masses attached to the pipes generated by the hydrodynamic pressures. The stiffness matrix, $[K]$, is formed by the two pipes only since the fluids have no stiffness. A wavelength, l, is used for the entries of $[F]$ based on the modal shape of interest for the two pipes (see footnote 43 on page 229). (Because the modal shapes of the two pipes are identical, one value of l is used in $[F]$.) The angular frequencies, ω, of the two fluid-filled pipes can be calculated using either Eq. (5.40), which was used by Chen and Rosenberg, or Eq. (5.41), which is an alternative introduced here:

$$det([F(\omega)]) = 0 \tag{5.40}$$

$$eig\left([M]^{-1}[K]\right) \rightarrow (\omega^2, \phi) \tag{5.41}$$

where *det*(·) is the operator for calculating the determinant of a matrix, and *eig*(·) is the operator for calculating the eigenvalues and eigenvectors of a matrix. The determinant of $[F(\omega)]$ is a six-degree polynomial function of ω and so Eq. (5.40) generates six roots (solutions) for the angular frequencies ω of the two fluid-filled pipes. The dimensions of $[M]^{-1}[K]$ are 6×6, and so Eq. (5.41) generates six eigenvalues and six eigenvectors. The square roots of the eigenvalues are the angular frequencies ω of the pipes, and the corresponding frequencies are $f = \omega / 2\pi$. The six values of ω calculated using Eqs. (5.40) and (5.41) are identical. Chen and Rosenberg calculated ω using Eq. (5.40), but the use of Eq. (5.41) is recommended here because it is computationally more efficient and provides six eigenvectors ϕ, which are the modal shapes of the two fluid-filled pipes. The modal shapes, ϕ, account for the interaction of the pipes and the fluids. The modal shapes, ϕ, associated with the lowest two values of ω involve coupled lateral movements of the two pipes due to entries f_{14} and f_{41} in $[F]$. Entry f_{14} (f_{41}) relates the hydrodynamic pressure on Pipe 1 (Pipe 2) to the radial displacement of Pipe 2 (Pipe 1). These two modes, with the two lowest values of ω, are termed "coupled modes" hereafter. The other four modal shapes are associated with axial and torsional motions of each pipe, which are not the focus of this section and not discussed further. The shapes of the first and second coupled modes involve *out-of-phase* and *in-phase* motions of the two pipes, respectively. The motions of the two pipes accommodate the lateral deformations associated with the assumed wavelength l. Figure 5.6 illustrates the two coupled modes given eigenvectors per Eq. (5.41) using an example: two concentric pipes supported at their tops with $l = 3.351\,H$ (i.e., the first wavelength for a cantilever; footnote 43 on page 229). In the out-of-phase mode (first coupled mode; Figure 5.6a), the inner pipe displaces opposite to and more than the outer pipe. In the in-phase mode (second coupled mode; Figure 5.6b), the two pipes displace in the same direction with amplitudes that are effectively identical. Additional discussion on the modal lateral displacements of the two pipes in the two coupled modes is presented in Section 5.2.2 and Figure 5.13.

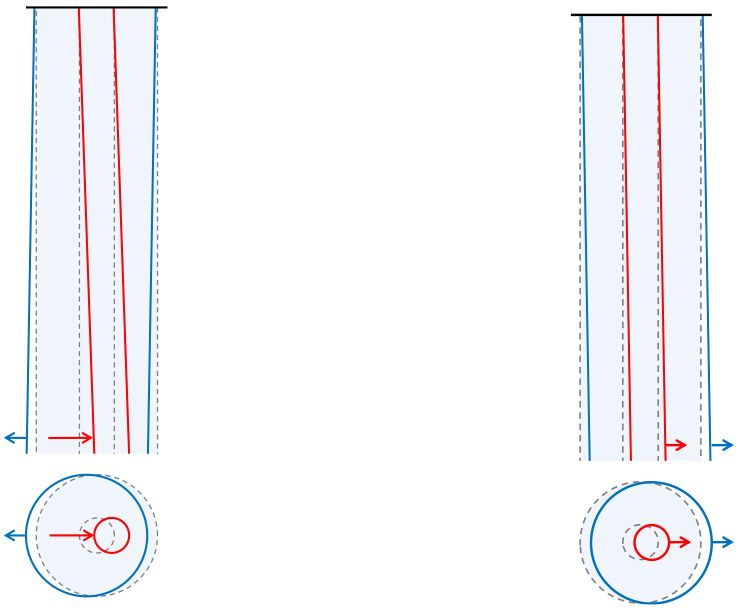

(a) out-of-phase (b) in-phase

Figure 5.6. Modal shapes of coupled lateral motions, out-of-phase and in-phase, two fluid-filled concentric pipes, supported at the tops, $l = 3.351\,H$

If the outer pipe is rigid relative to the inner pipe[44], the degrees-of-freedom of the outer pipe (i.e., $\bar{u}_{s2}$, $\bar{v}_{s2}$, and $\bar{w}_{s2}$) in the equations of equilibrium per Eq. (5.28) are set to zero. Accordingly, the submatrix $[F_1]$ (see Eq. (5.29)), which is extracted from $[F]$ and associated with the degrees-of-freedom of the inner pipe (i.e., $\bar{u}_{s1}$ $\bar{v}_{s1}$, and $\bar{w}_{s1}$), is used for the calculation of the frequencies. The dimensions of $[F_1]$ are 3×3, and so three values for ω are generated per Eqs. (5.40) or (5.41). The lowest value of ω is associated with a lateral mode of the inner pipe and the other two are associated with an axial and a torsional mode. The frequencies of the inner pipe are affected only by the added mass generated by the hydrodynamic pressures due to its movement because the rigid outer pipe does not displace and induce hydrodynamic pressures. Although $[F_1]$ does not consider the degrees-of-freedom of the rigid outer pipe, the calculation of the frequencies of the inner pipe involves the use of the radius of the outer pipe: R_2 is involved in

[44] This assumption is made in ASCE 4-16 for FSI analysis of internal components (i.e., inner pipe) submerged in a fluid contained in a tank or reactor vessel (i.e., outer pipe). The tank/vessel is assumed to be rigid relative to the internal components.

the entries of $[F_1]$ (see α_2 in f_{11} per Eq. (5.30)). Figure 5.7 shows two sets of two fluid-filled concentric pipes, including identical flexible inner pipes and rigid outer pipes with different radii. The frequencies of the two inner pipes are different, and depend on the radii of the outer pipes, which defines the dimensions of the fluid in the annulus. The frequency of the inner pipe of Figure 5.7b is lower than that of Figure 5.7a due to a greater added mass, although the volume of the annular fluid of Figure 5.7b is smaller (i.e., R_2 / R_1 is smaller). Additional discussion is presented in Section 5.2.2: frequencies and added masses for a range of R_2 / R_1 are calculated and compared.

(a) greater outer pipe (b) smaller outer pipe

Figure 5.7. Two sets of two concentric pipes, including identical inner pipes and rigid outer pipes with different radii

5.2.2 Results

The corrected analytical solutions of Chen and Rosenberg are used herein to calculate frequencies for two fluid-filled, concentric, cylindrical pipes, as shown in Figure 5.2. Two boundary conditions are considered for the two concentric pipes: 1) both cantilever and 2) both simply-supported. Since the focus of this section is to verify numerical models for internal components undergoing free vibration of the first lateral modal shape, the associated frequencies are calculated. The first wavelengths l for the cantilever and simply-supported pipes are $3.351\,H$ and $2\,H$, respectively (see footnote 43 on page 229). The lateral frequencies are calculated for 1) the two coupled modes of the two pipes (out-of-phase and in-phase) and 2) the uncoupled mode of the inner pipe considering the outer pipe is rigid. To calculate the frequencies of the two coupled modes, the 6×6 matrix $[F]$ per Eq. (5.29) is used in Eq. (5.41) to solve for the eigenvalues, and their square roots are the angular frequencies of the pipes, ω. Six values of

ω are obtained, and the smallest two are associated with the two coupled lateral modes, and denoted as ω_{lat}. To calculate the frequencies of the uncoupled mode of the inner pipe, the 3×3 submatrix $\left[F_1\right]$ per Eq. (5.29) is used in Eq. (5.41). Three values of ω are obtained, and the smallest frequency is associated with the uncoupled lateral mode, ω_{lat}.

The two pipes are assumed to be fabricated using an identical material. This assumption is reasonable for fluid-filled advanced reactors because the vessels (the outer pipe here) and their internal components (referred to as inner pipes) are generally fabricated using stainless and alloy steels (e.g., Gluekler (1997) and Chellapandi et al. (2010)), for which the mechanical properties considered in the analytical solutions are almost identical. Consequently, the subscripts "1" and "2" for the mechanical properties of the inner and outer pipes, respectively, used in the analytical solutions are set aside hereafter in this section (i.e., $E_1 = E_2 = E$, $\upsilon_1 = \upsilon_2 = \upsilon$, $\rho_{s1} = \rho_{s2} = \rho_s$). The inner pipe is submerged in a fluid confined by the outer pipe, and so the densities of Fluids 1 and 2 used in the analytical solutions are identical and noted as ρ (i.e., $\rho_1 = \rho_2 = \rho$).

To generalize the analytical results for different dimensions and mechanical properties of pipes and fluids, the frequencies of the lateral modes are expressed as follows:

$$f_{lat} = \frac{\omega_{lat}}{2\pi} = C_{lat}\frac{1}{R_1}\sqrt{\frac{Eh_1}{\rho R_1}} \tag{5.42}$$

where C_{lat} is a coefficient for lateral frequencies. Other variables in Eq. (5.42) were introduced previously. Per Eq. (5.42), the coefficient, C_{lat}, is a *unitless frequency* normalized using the elastic modulus and dimensions of the inner pipe (i.e., E, R_1, and h_1) and the density of the fluid (i.e., ρ). (Equation (5.42) relates f_{lat} and C_{lat} using the form for the impulsive frequency and its coefficient for a cylindrical tank presented in Section 3.2.1.) The density of the pipes, ρ_s, is not included in this normalization because f_{lat} and C_{lat} are not sensitive to their masses. Although ρ_s is involved in the calculation of f_{lat} (see the entries in $\left[F\right]$ per Eqs. (5.29) to (5.38)), the masses of the pipes are negligible by comparison to the added mass generated by the fluid, for the dimensions and mechanical properties used for a nuclear vessel (i.e., outer pipe) and its

internal component (i.e., inner pipe). Additional discussion on the added mass is presented later in this section (5.2.2) and Figure 5.11.

The coefficient, C_{lat}, is *insensitive*[45] to or independent of the mechanical properties (i.e., E, υ, ρ_s, and ρ) of the pipes and the fluid, but dependent on the radii and height of the pipes (i.e., R_1, R_2, and H). Accordingly, the values of C_{lat} are presented here for a range of radius ratios, R_2 / R_1, and height-to-radius ratios, H / R_1: $5 \le H / R_1 \le 30$, and $R_2 / R_1 = 1.2$, 2, 5, and 10.

Table 5.2 lists the radius ratios for internal components and the reactor vessel, R_2 / R_1, (see red, greed, and purple lines in Figure 5.8) and the height-to-radius ratios for the internal components, H / R_1 (see orange and blue lines in Figure 5.8), for the prototype advanced reactor shown in Figure 5.8 (Gluekler 1997). For the ratios listed in Table 5.2, the ranges, $5 \le H / R_1 \le 30$ and $R_2 / R_1 = 1.2$, 2, 5, and 10, used for the calculations here are practical. The ratios of wall thickness to radius for reactor vessels and the internal components typically range between 0.0025 and 0.004 (i.e., ratios of diameter to wall thickness are between 500 and 800 (Chellapandi et al. 2008)). Accordingly, h_1 / R_1 and h_2 / R_2 used in the calculation of C_{lat} are both assumed to be 0.003. However, for the dimensions (i.e., $5 \le H / R_1 \le 30$, and $R_2 / R_1 = 1.2$, 2, 5, and 10) and the boundary conditions (i.e., cantilever and simply-supported) considered here, the values of C_{lat} are not sensitive to thickness-to-radius ratios ranging from 0.0005 to 0.008[46], if an identical ratio is used for both pipes (i.e., $h_1 / R_1 = h_2 / R_2$). The two concentric pipes used here are assumed to be fabricated from stainless steel and the contained fluid is assumed to be water, for which the mechanical properties used in the calculations are listed in Table 5.3. Again, C_{lat}, is insensitive to or independent of the mechanical properties of the pipes and the fluid, and so the results presented here can be applied to pipes of a different material, and filled with a different fluid.

---

[45] The normalization assumes the density of the pipes is significantly greater than the density of the fluid (i.e., $\rho_{s1} = \rho_{s2} \gg \rho_1 = \rho_2$) and square of Poission's ratios of the pipes is significantly smaller than one (i.e., ${\upsilon_{s1}}^2 = {\upsilon_{s2}}^2 \ll 1$). The effects of ρ_{s1} (ρ_{s2}) and υ_{s1} (υ_{s2}) in the normalized results are negligible. The normalized results are not fully independent of but rather are insensitive to the dimensions and the mechanical properties of the pipes and the fluid.

[46] Given a value of H / R_1 and R_2 / R_1 and a boundary condition, the difference in the values of C_{lat} calculated using wall thickness-to-radius ratios of 0.0005 and 0.008 is less than 10%.

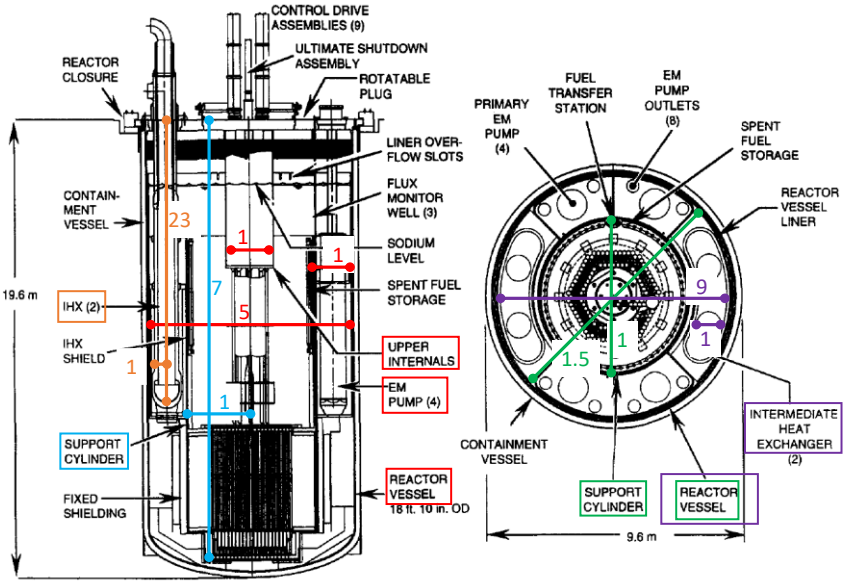

Figure 5.8. Prototype advanced reactor (Gluekler 1997), showing the radius ratios for the internal components to the reactor vessel (R_2 / R_1; red, green, and purple lines), and the height-to-radius ratios for the internal components (H / R_1; orange and blue lines)

Table 5.2. Radius ratios for the internal components to the reactor vessel, R_2 / R_1, and height-to-radius ratios for the internal components, H / R_1, for the advanced reactor of Figure 5.8

Internal component	Support cylinder (blue)		Immediate heat exchanger (IHX) (orange)	
H / R_1	7		23	
Internal component	Upper internal (red)	EM pump (red)	Support cylinder (green)	IHX (purple)
R_2 / R_1	5	5	1.5	9

Table 5.3. Mechanical properties of the pipes and the fluid used for the analytical solutions of Chen and Rosenberg

Carbon steel	Elastic modulus, E	1.9×10^{11} (N/m^2)
	Poisson's ratio, υ	0.27
	Density, ρ_s	8000 (kg/m^3)
Water	Density, ρ	1000 (kg/m^3)

Figures 5.9 and 5.10 present the values of C_{lat} for two cantilever and simply-supported, fluid-filled, concentric pipes, respectively. Each panel in Figures 5.9 and 5.10 presents results for the two coupled modes (out-of-phase and in-phase) and the uncoupled mode, given a value of R_2 / R_1 (i.e., 1.2, 2, 5, or 10) and $5 \le H / R_1 \le 30$. The frequencies of the out-of-phase modes (red solid lines) are appreciably lower than those of the in-phase modes (blue solid lines). The values of C_{lat} for the uncoupled modes (i.e., black dotted lines) lie between the values of the two coupled modes, at a given H / R_1 and R_2 / R_1.

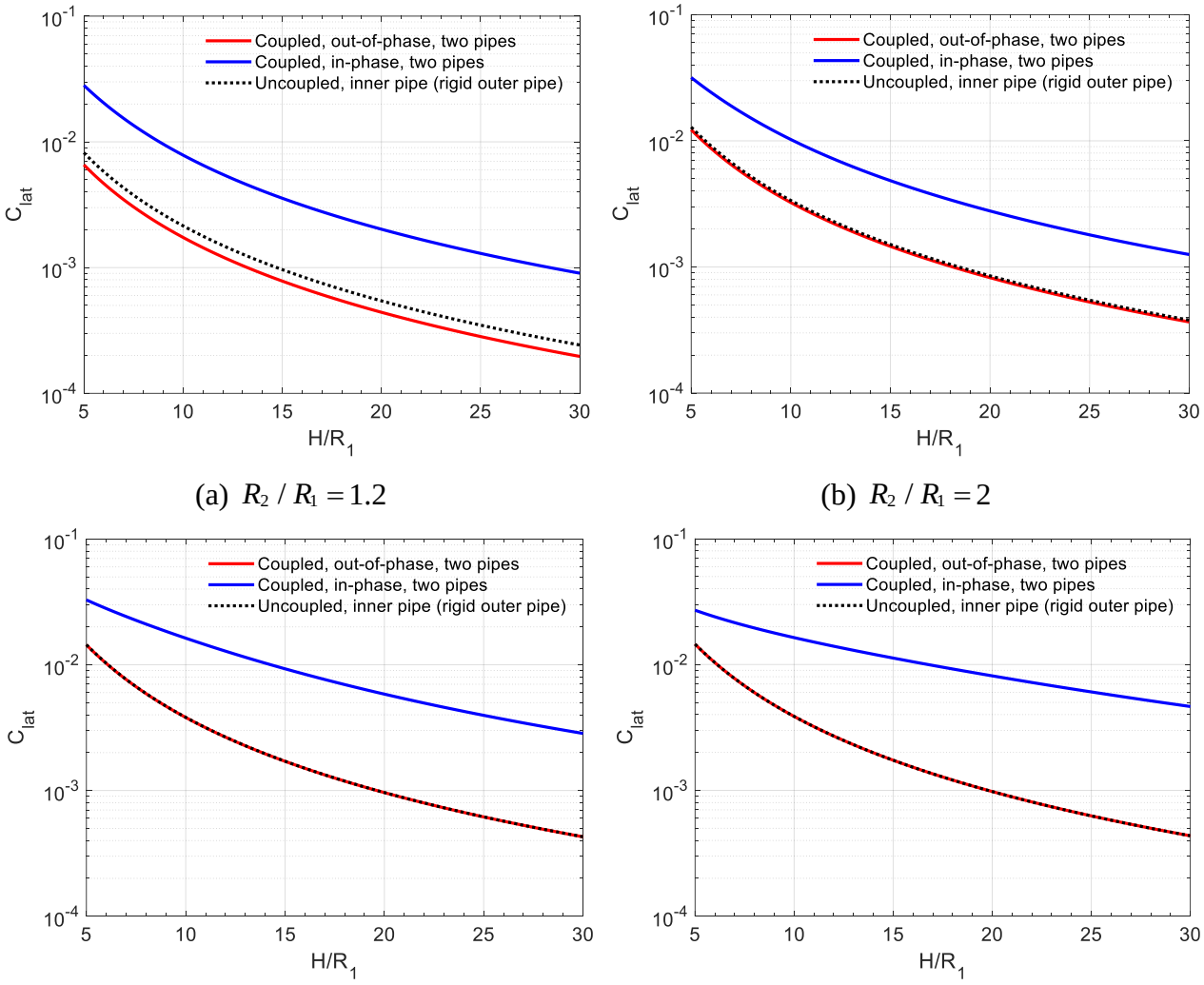

(a) $R_2 / R_1 = 1.2$ (b) $R_2 / R_1 = 2$

(c) $R_2 / R_1 = 5$ (d) $R_2 / R_1 = 10$

Figure 5.9. Frequency coefficients for two fluid-filled concentric pipes, cantilever, the first wavelength $l = 3.351\,H$, coupled modes and uncoupled mode of the inner pipe

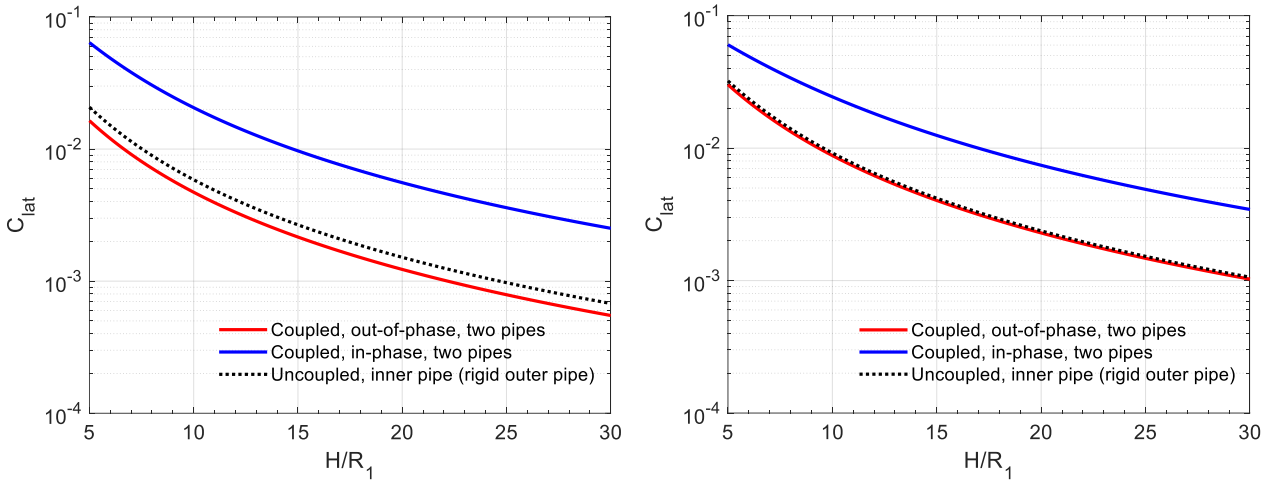

(a) $R_2 / R_1 = 1.2$ (b) $R_2 / R_1 = 2$

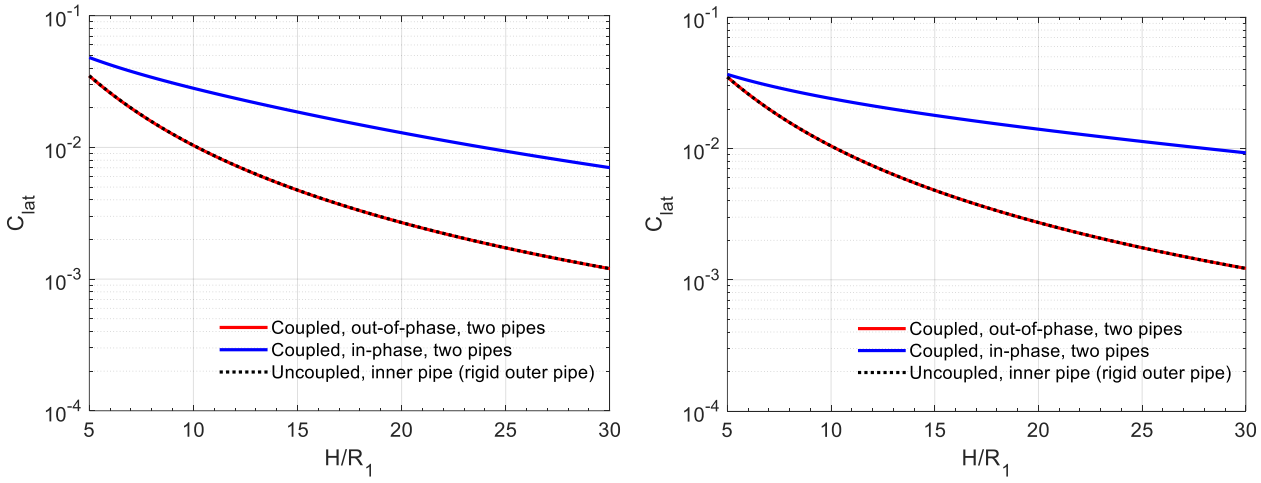

(c) $R_2 / R_1 = 5$ (d) $R_2 / R_1 = 10$

Figure 5.10. Frequency coefficients for two fluid-filled concentric pipes, simply-supported, the first wavelength $l = 2H$, coupled modes and uncoupled mode of the inner pipe

For all three modes (i.e., two coupled and one uncoupled) and a given R_2 / R_1, the frequency reduces with increasing H / R_1. This outcome is expected because the stiffness of a slenderer pipe (i.e., greater H / R_1) is smaller and so the frequency is lower. Given a value of H / R_1, the frequency increases with increasing R_2 / R_1 for all three modes. Accordingly, for a given inner pipe of a radius R_1, the frequencies are higher if the radius of the outer pipe is increased (i.e., greater R_2). The added masses on the pipes generated by the hydrodynamic pressures are

calculated to investigate the reason why the frequency increases with increasing R_2 / R_1. As presented in Figure 5.5, if the two pipes displace in the $+x$ direction, the hydrodynamic pressures, $(p_{1,1} - p_{1,2})$ on the inner pipe and $p_{2,2}$ on the outer pipe, generate resultant shear forces in the $-x$ direction (i.e., against the movement of the pipes). These hydrodynamic shear forces (i.e., contribution of the inertial forces on the pipes are not included) per unit length on the inner and outer pipes, termed $V_{1,x}$ and $V_{2,x}$, respectively, are the integrals of the pressures with respect to their perimeters:

$$V_{1,x} = \int_0^{2\pi} (p_{1,1} - p_{1,2}) R_1 \cos\theta d\theta \tag{5.43}$$

$$V_{2,x} = \int_0^{2\pi} p_{2,2} R_2 \cos\theta d\theta \tag{5.44}$$

Given $p_{1,1}$, $p_{1,2}$, and $p_{2,2}$ per Eqs. (5.25), (5.26), and (5.27), respectively, $V_{1,x}$ and $V_{2,x}$ are calculated and both functions of the radial displacements of the two pipes, u_{s1} and u_{s2}. The hydrodynamic shear forces, which are opposite in sign to the movement of the pipes, are equivalent to the inertial forces of the fluid that is attached to and accelerates with the pipes in the x direction[47]. The mass of this involved fluid is the added mass on the pipes, which reduces their lateral frequencies. Accordingly, the hydrodynamic shear forces (per unit length), $V_{1,x}$ and $V_{2,x}$, are related to the added masses (per unit length) and the x-directional accelerations of the pipes, $u''_{s1} / \cos\theta$ and $u''_{s2} / \cos\theta$:

$$V_{1,x} = M_{1,1} \cdot u''_{s1} / \cos\theta + M_{1,2} \cdot u''_{s2} / \cos\theta \tag{5.45}$$

$$V_{2,x} = M_{2,1} \cdot u''_{s1} / \cos\theta + M_{2,2} \cdot u''_{s2} / \cos\theta \tag{5.46}$$

where $M_{1,1}$, $M_{1,2}$, $M_{2,1}$, and $M_{2,2}$ are the added masses. Both $M_{1,1}$ and $M_{1,2}$ contribute to the shear force on the inner pipe, $V_{1,x}$, and are associated with the motion of the inner pipe and its interaction with the outer pipe, respectively. Similarly, the shear force on the outer pipe, $V_{2,x}$, is a

[47] Per Newton's law, the direction of the inertial force on a moving mass, m, is opposite to that of its acceleration, a. If the mass accelerates in the $+x$ direction, the inertial force, $F = ma$, is in the $-x$ direction.

function of $M_{2,1}$ and $M_{2,2}$, which are associated with its interaction with the inner pipe and the motion of the outer pipe, respectively.

Per Eqs. (5.43), (5.44), (5.45), and (5.46), these added masses are calculated here for $H / R_1 = 20$ and $1.2 \le R_2 / R_1 \le 10$. Consistent with the calculation for C_{lat} in Figures 5.9 and 5.10, h_1 / R_1 and h_2 / R_2 of 0.003 and the mechanical properties listed in Table 5.3 are used for calculating the added masses. Two boundary conditions are considered for the two concentric pipes: cantilever and simply-supported, for which the first wavelengths, l, are $3.351H$ and $2H$, respectively. Figure 5.11 presents the ratios of the added mass to the mass of the corresponding pipe (termed hereafter the added-mass ratio). The masses of the inner and outer pipes (per unit length) are $m_{s1} = 2\pi R_1 h_1 \rho_s$ and $m_{s2} = 2\pi R_2 h_2 \rho_s$, respectively. Per Figure 5.11, $M_{1,1}$ and $M_{2,2}$ are positive, and $M_{1,2}$ and $M_{2,1}$ are negative: the added mass on each pipe associated with its motion is positive, and that associated with the interaction with the other pipe is negative. Accordingly, if a pipe moves in the $+x$ direction (i.e., positive $u_{s1}'' / \cos\theta$ or $u_{s1}'' / \cos\theta$), the added mass on this pipe (i.e., $M_{1,1}$ or $M_{2,2}$) generates a positive inertial force, and that on the other pipe (refers to $M_{1,2}$ or $M_{2,1}$) generates a negative inertial force. The positive and negative inertial forces are in the $-x$ and $+x$ directions (see footnote 47 on page 239). The absolute values of the added-mass ratios, $M_{1,1} / m_{s1}$, $M_{1,2} / m_{s1}$, $M_{2,1} / m_{s2}$, and $M_{2,2} / m_{s2}$, all reduce with increasing R_2 / R_1. Accordingly, the frequencies, for which the coefficients C_{lat} are presented in Figures 5.9 and 5.10, increase with increasing R_2 / R_1 due to the reduced added-mass ratio. The added masses (per unit length) are calculated for the upper internal of Figure 5.8, assumed here to be submerged in a fluid contained by a cylindrical tank (i.e., outer pipe) with a range of radius. The radius, R_1, of the upper internal (i.e., inner pipe) is around 1 m, the radius, R_2, of the outer pipe is assumed to range between 1.2 m and 5 m, the heights of the two pipes are assumed to be 20 m. (The radius and height of the reactor vessel of Figure 5.8 are around 5 m and 20 m, respectively.) Again, $h_1 / R_1 = h_2 / R_2 = 0.003$ and the mechanical properties listed in Table 5.3 are used for the calculation. Both the inner and outer pipes are assumed to be head-supported, and the first modal wavelength for cantilevers is used for the calculation: $l = 3.351H$. Figure 5.12 presents the added masses (per unit length): $M_{1,1}$ and $M_{1,2}$ for the upper internal (i.e., inner pipe), and $M_{2,1}$,

and $M_{2,2}$ for the outer pipe, together with their summation (i.e., total added mass; $(M_{1,1}+M_{1,2}+M_{2,1}+M_{2,2})$, shown as a black dash-dotted line. The total added mass increases with increasing R_2/R_1 due to the greater volume of the fluid in the annulus between the pipes. The total added mass is almost identical to but less than the total fluid mass (per unit length), $\rho\pi R_2^2$, shown as a light blue line in Figure 5.12: a significant fraction of the fluid is involved in the first modal motion of the two pipes. The absolute values of $M_{1,1}$, $M_{1,2}$, and $M_{2,1}$ all reduce with increasing R_2/R_1, whereas $M_{2,2}$ increases significantly and is the greatest of the four. Accordingly, a majority mass of the involved fluid contributes to the hydrodynamic shear force on the outer pipe.

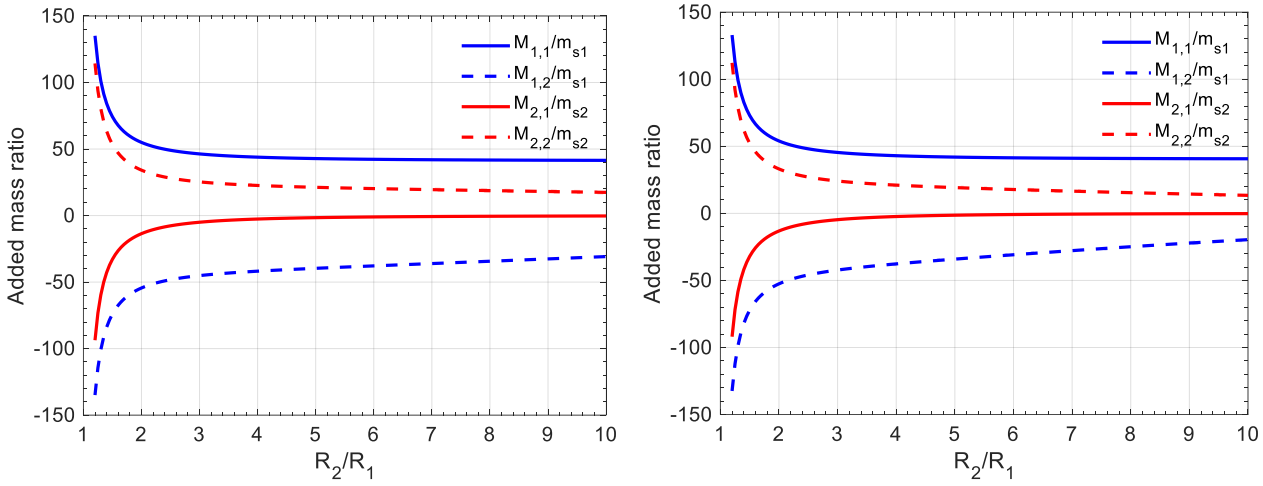

(a) cantilever, $l=3.351\,H$ (b) simply-supported, $l=2\,H$

Figure 5.11. Ratios of the added masses to the masses of the pipes ($m_{s1}=2\pi R_1 h_1 \rho_s$ and $m_{s2}=2\pi R_2 h_2 \rho_s$), $1.2\le R_2/R_1\le 10$, $H/R_1=20$, $h_1/R_1=h_2/R_2=0.003$, mechanical properties per Table 5.3

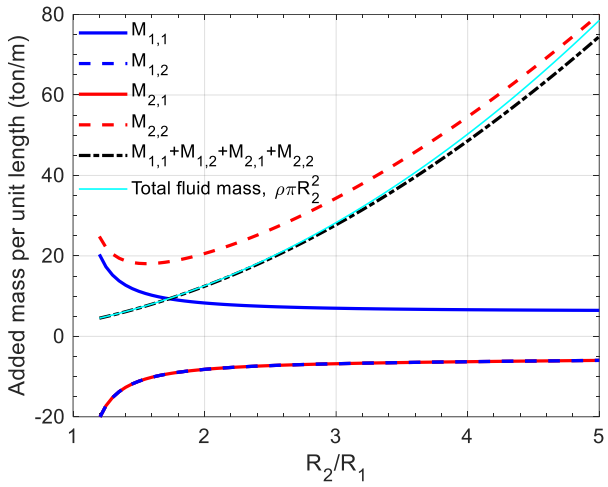

Figure 5.12. Added mass per unit length, $R_1 = 1$ m, $H = 20$ m, 1.2 m$\le R_2 \le 5$ m, $h_1 / R_1 = h_2 / R_2 = 0.003$, mechanical properties per Table 5.3, $l = 3.351\,H$

Per Figures 5.9 and 5.10, the values of C_{lat} for the out-of-phase coupled mode move closer to those of the uncoupled mode with increasing values of R_2 / R_1 and becomes identical at $R_2 / R_1 = 5$ and 10, for both boundary conditions. To investigate why the frequency (calculated using C_{lat} per Eq. (5.42)) of the out-of-phase coupled mode is similar to that in the uncoupled mode with $R_2 / R_1 \ge 5$, the lateral displacements of the pipes in these two modes are compared. The amplitudes of the modal lateral displacements (see Eqs. (5.10) and (5.13)) are the $\bar{u}_{s1}$- and $\bar{u}_{s2}$-components of the eigenvectors (i.e., modal shapes). Figure 5.13 presents the amplitudes of the two pipes in the out-of-phase coupled mode (red solid and dashed lines) and the inner pipe in the uncoupled mode (black dotted lines) for $H / R_1 = 20$ and $1.2 \le R_2 / R_1 \le 10$, together with those in the in-phase coupled mode (blue solid and dashed lines). For each boundary condition, the presented amplitudes of the modal lateral displacements are normalized by the value for the inner pipe in the uncoupled mode at a given R_2 / R_1. (Consequently, the amplitudes for the inner pipe in the uncoupled mode are unity.) For each boundary condition, in the out-of-phase mode, the amplitude of the inner pipe (red solid line) is greater than that of the outer pipe (red dashed line). The amplitude of the modal lateral displacement of the inner pipe in the out-of-phase mode increases and moves closer to that in the uncoupled mode (black dotted line), whereas the displacement of the outer pipe reduces to zero for $R_2 / R_1 \ge 4$. Consequently, the outer pipe can

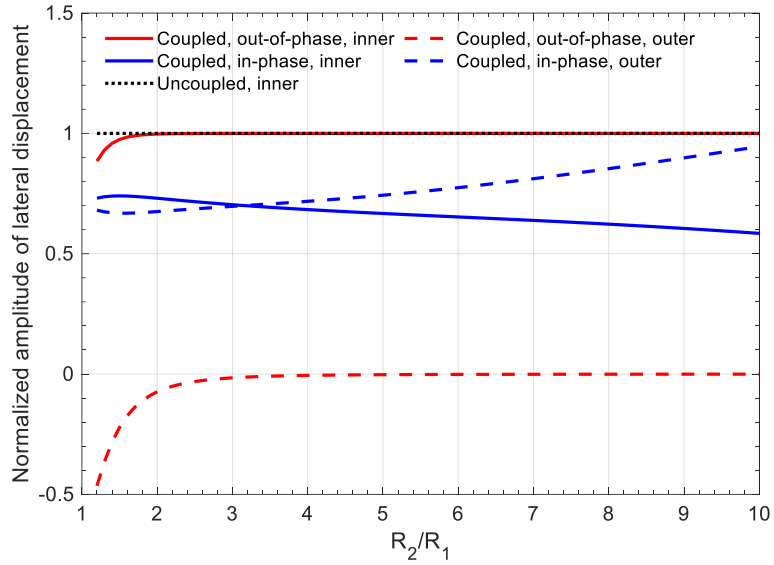

(a) cantilever, $l = 3.351\,H$

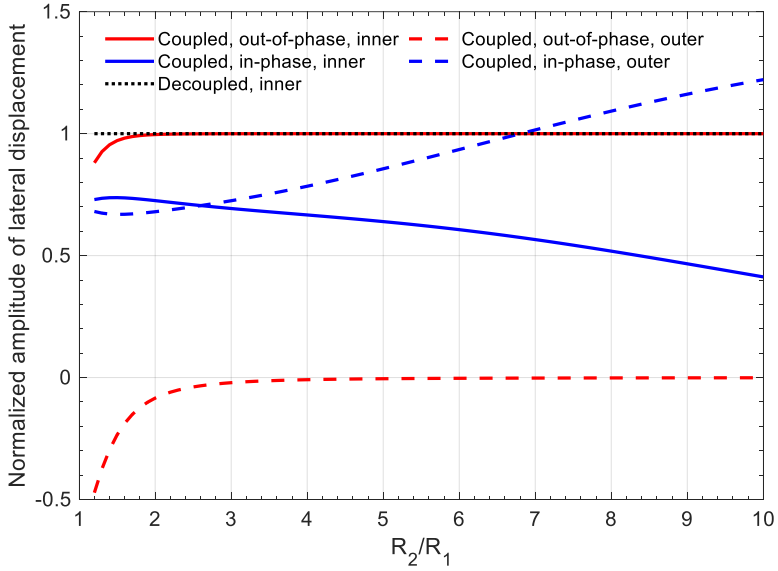

(b) simply-supported, $l = 2\,H$

Figure 5.13. Normalized amplitudes of modal lateral displacements of the two fluid-filled concentric pipes, out-of-phase coupled, in-phase coupled, and uncoupled modes, $H / R_1 = 20$ and $1.2 \le R_2 / R_1 \le 10$, the first wavelength

be considered as rigid if $R_2 / R_1 \ge 4$. (The directions of the lateral movements of the two pipes in the out-of-phase mode are opposite, as shown in Figure 5.6a, and so the amplitudes of the inner pipe are positive and those of the outer pipe are negative for both boundary conditions.) In the in-phase mode, the amplitudes of the two pipes shown in Figure 5.13 are similar for a small value

of R_2 / R_1 (e.g., $R_2 / R_1 < 4$). The amplitude of the outer pipe (blue dashed lines) increases, but that of the inner pipe (blue solid lines) decreases with increasing R_2 / R_1. Consequently, the movement of the outer pipe becomes more significant with respect to that of the inner pipe with increasing R_2 / R_1.

If the value of R_2 / R_1 for two flexible concentric pipes is greater than 4, namely, the distance between the walls of the two pipes is significant, the hydrodynamic pressure on the inner pipe is not affected by the motion of the outer pipe. Accordingly, the entries f_{14} and f_{41} in $[F]$ (see Eq. (5.29)), which couple the responses of the two pipes due to the hydrodynamic pressures of Fluid 2, can be disregarded:

$$[F] = \begin{bmatrix} \begin{bmatrix} & & \\ & F_1 & \\ & & \end{bmatrix} & \begin{matrix} 0 & 0 & 0 \\ 0 & 0 & 0 \\ 0 & 0 & 0 \end{matrix} \\ \begin{matrix} 0 & 0 & 0 \\ 0 & 0 & 0 \\ 0 & 0 & 0 \end{matrix} & \begin{bmatrix} & & \\ & F_2 & \\ & & \end{bmatrix} \end{bmatrix} \tag{5.47}$$

Per Eq. (5.47), the three equations of equilibrium (see Eq. (5.28)) for the inner pipe, which are associated with the first three rows of $[F]$, are then independent of those for the outer pipe, which are associated with the last three rows of $[F]$. Since there is no seismic interaction between the two pipes, the outer pipe can be considered as rigid to calculate the frequency of the inner pipe. Consequently, if the radii of two flexible concentric pipes are significantly different, the frequency (see Figures 5.9 and 5.10) and modal amplitude (see Figure 5.13) of the inner pipe of the first coupled mode are identical to those of the uncoupled mode.

5.2.3 Calculations of frequencies for submerged components

In this section, the lateral frequencies for three sets of two fluid-filled, concentric, cylindrical pipes are calculated using the corrected analytical solutions of Chen and Rosenberg. The lateral frequencies associated with the first modal shape of the pipes are calculated for 1) the two coupled modes, and 2) the uncoupled mode of the inner pipe (assuming the outer pipe to be rigid). The two pipes in the first set are based on sample nuclear components: a reactor vessel

and a reactor jacket[48] in the prototype fast reactor (PFR) in Dounreay, Scotland, presented in Figure 5.14a. The other two sets are identical to the pipes used for the numerical models presented in Section 5.3: M1 and M2, for which the schematic views were presented in Figure 5.3. Analytical results for M1 and M2 are used to verify the corresponding numerical models.

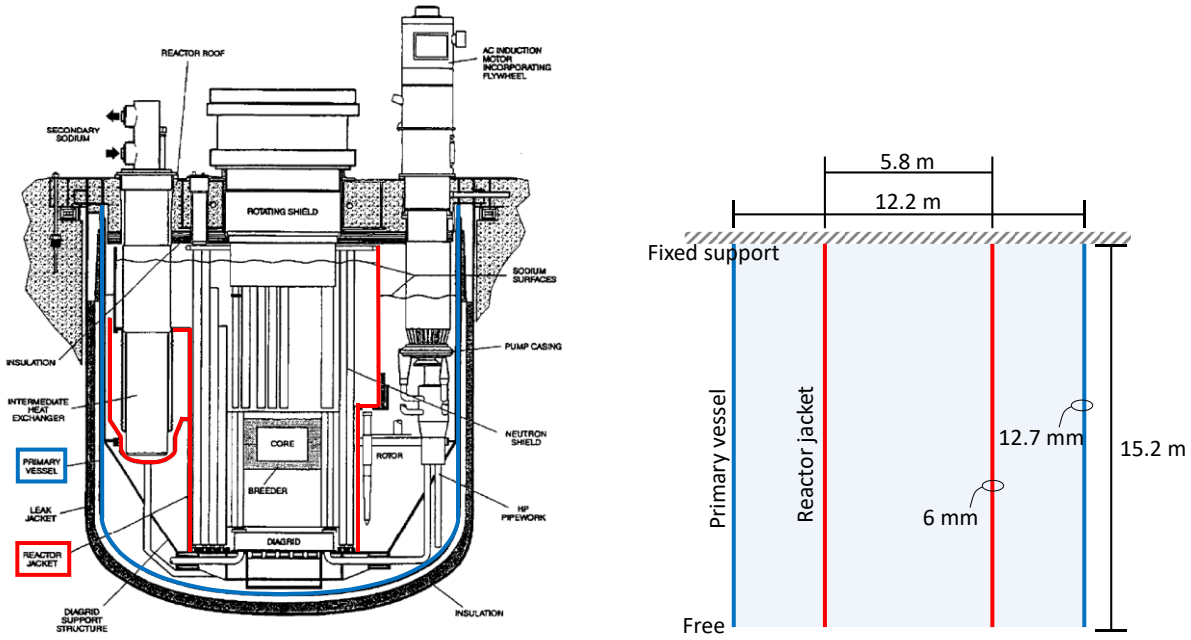

(a) PFR, Dounreay, Scotland (Figure 2.44 in IAEA (2012))

(b) N1, simplifying the reactor vessel and reactor jacket in panel (a)

Figure 5.14. Sample nuclear components and their simplified geometries and boundary conditions used for the analytical solutions

The reactor vessel and the reactor jacket in the PFR are identified in blue and red, respectively, in Figure 5.14a. The reactor vessel was constructed using stainless steel with a diameter of 12.2 m, a height of 15.2 m, and a wall thickness of 12.7 mm, and was filled with liquid sodium (Jensen and Ølgaard 1995). The reactor vessel was supported at its top by a head. The reactor jacket in the reactor vessel was a stainless steel shell (Jensen and Ølgaard 1995). The dimensions and boundary condition of the reactor jacket were not available in prior studies and documents, to the knowledge of the authors, but the dimensions can be estimated based on the drawing of Figure 5.14a. More information on the PFR can be found in Jensen and Ølgaard (1995) and

[48] The reactor jacket in the PFR of Figure 5.14a separates the hot liquid sodium surrounding the reactor core and the cold liquid sodium released from the intermediate heat exchanger shown in Figure 5.14a (Jensen and Ølgaard 1995).

IAEA (2012). To employ the corrected analytical solutions of Chen and Rosenberg, the geometries of the reactor vessel and the reactor jacket of the PFR are simplified to two fluid-filled, concentric, cylindrical pipes shown in Figure 5.14b, denoted here as N1. Other components internal to the reactor vessel are ignored, and the free surface of the liquid sodium is not considered. The dimensions and the mechanical properties of the two pipes used in the analytical solutions are listed in Tables 5.4 and 5.5, respectively. Generic mechanical properties for stainless steel are used for the two pipes (i.e., $E_1 = E_2 = 1.9 \times 10^{11}$ N/m^2, $\rho_{s1} = \rho_{s2} = 8000$ kg/m^3, and $\upsilon_{s1} = \upsilon_{s2} = 0.3$); the density of liquid sodium is assigned to the fluid (i.e., $\rho_1 = \rho_2 = \rho = 968$ kg/m^3). The radius, height, and wall thickness of the reactor vessel of the PFR are applied to the outer pipes (i.e., $R_2 = 6.1$ m, $H_2 = 15.2$ m, and $h_2 = 12.7$ mm). The radius of the inner pipe, R_1, is assumed to be 2.9 m, estimated based on the bottom end of the reactor jacket in the drawing of Figure 5.14a. The wall thickness of the reactor jacket is not available in Figure 5.14a. Somewhat arbitrarily, the wall thickness of the inner pipe, h_1, is assumed to be 6 mm, to achieve a wall thickness-to-radius ratio identical to that of the outer pipe (i.e., $h_1 / R_1 = h_2 / R_2 = 0.0021$). To be consistent with the assumptions used in the analytical solutions, the height of the inner pipe H_1 is 15.2 m, identical to that of the outer pipe (i.e., $H_1 = H_2 = H = 15.2$ m). The boundary conditions for the outer and inner pipes must be identical for comparison with analytical solutions. Given that the reactor vessel is supported at its head, the two pipes in N1 are top-supported, namely, cantilevers fixed at the top end and free at the bottom end. The first wavelength, l, of the two cantilever pipes is $3.351\,H$ (Timoshenko 1937).

Table 5.4. Dimensions used for the analytical solutions for three sets of two fluid-filled concentric pipes shown in Figures 5.14 and 5.3

	R_1 (m)	R_2 (m)	h_1 (mm)	h_2 (mm)	H (m)	R_2 / R_1	H / R_1	h_1 / R_1
N1	2.9	6.1	6	12.7	15.2	2.1	5.2	0.0021
M1	0.162	0.79	6.35	7.92	2	5.2	12.3	0.04
M2	0.162	0.2	6.35	7.92	2	1.3	12.3	0.04

Table 5.5. Mechanical properties used for the analytical solutions for three sets of two fluid-filled concentric pipes shown in Figures 5.14 and 5.3

	E_1, E_2 (N/m^2)	ρ_{s1}, ρ_{s2} (kg/m^3)	υ_{s1}, υ_{s2}	ρ (kg/m^3)
N1	1.9×10^{11}	8000	0.3	968
M1	2×10^{11}	7850	0.27	1000
M2	2×10^{11}	7850	0.27	1000

The dimensions, mechanical properties, and boundary conditions of the numerical and analytical models for M1 and M2 are identical for the calculation of lateral frequencies. The dimensions of M1 and M2 are listed in Table 5.4, which are taken from Figure 5.3. The mechanical properties are listed in Table 5.5: the two concentric pipes in each of M1 and M2 are of carbon steel (i.e., $E_1 = E_2 = 2\times10^{11}$ N/m^2, $\rho_{s1} = \rho_{s2} = 7850$ kg/m^3, and $\upsilon_{s1} = \upsilon_{s2} = 0.27$), and the fluid is water (i.e., $\rho = 1000$ kg/m^3). The pipes in both M1 and M2 are top-supported (i.e., cantilever), and so the first wavelength $l = 3.351\,H$. More information on the numerical models of M1 and M2 can be found in Section 5.3.

Below, the lateral frequencies of two fluid-filled concentric pipes are calculated for N1, M1, and M2 shown in Figures 5.14 and 5.3. The frequency coefficient, C_{lat}, presented in Section 5.2.2, which is suitable for reactor components with typical wall thickness-to-radius ratios (i.e., 0.0005 to 0.008; see footnote 46 on page 239), is used to calculate the frequencies of N1, for which h_1 / R_1 is 0.0021 (see Table 5.4). The two pipes in N1 are cantilevers and the radius ratio, R_2 / R_1, is 2.1 (see Table 5.4), and so results for C_{lat} in Figure 5.9b are used, presented here again in Figure 5.15. Based on the height-to-radius ratio, H / R_1, of 5.2 (see Table 5.4), the values of C_{lat} are extracted from Figure 5.15: the vertical green line. The values for C_{lat} are listed in Table 5.6 for 1) the out-of-phase mode, 2) the in-phase mode, and 3) the uncoupled mode of the inner pipe. Given these values of C_{lat}, the corresponding frequencies, f_{lat}, are calculated per Eq. (5.42), and listed in Table 5.6.

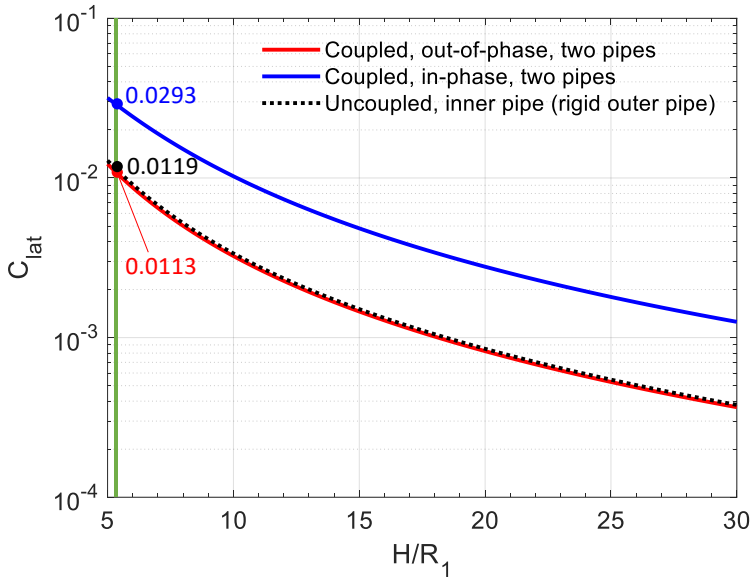

Figure 5.15. Extracted frequency coefficients for N1 from Figure 5.9b, the coupled modes and the uncoupled mode of the inner pipe, associate with the first wavelength, $l = 3.351\,H$

Table 5.6. Lateral frequencies of the two fluid-filled concentric pipes shown in Figures 5.14 and 5.3, associated with the first wavelength

Mode	Coupled, out-of-phase		Coupled, in-phase		Uncoupled, inner pipe	
Coefficient and frequency	C_{lat}	f_{lat} (Hz)	C_{lat}	f_{lat} (Hz)	C_{lat}	f_{lat} (Hz)
N1	0.0113	2.5	0.0293	6.6	0.0119	2.6
Frequency	f_{lat} (Hz)		f_{lat} (Hz)		f_{lat} (Hz)	
M1	37.9		98.9		38.0	
M2	20.9		63.7		24.7	

The frequency coefficients, C_{lat}, presented in Section 5.2.2 do not apply to M1 and M2 because their ratio $h_1 / R_1 = 0.04$, which is about an order of magnitude greater than those of nuclear components[49], and beyond the range of h_1 / R_1 considered in C_{lat} (i.e., 0.0005 to 0.008). The frequencies of M1 and M2 are calculated using the analytical process presented in Section 5.2.1. Matrices $[F]$ and $[F_1]$ are constructed for each of M1 and M2 using the entries per Eqs. (5.30) to (5.38). For the two coupled modes, $[F]$ is used in Eq. (5.41) to perform eigenvalue analysis. The angular frequencies, ω, of the two pipes are the square roots of the eigenvalues. The smallest ω is the out-of-phase angular frequency, and the second smallest ω is the in-phase angular frequency. For the uncoupled mode, $[F_1]$ is used, and the smallest ω calculated from the eigenvalue analysis is the uncoupled angular frequency of the inner pipe. The calculated frequencies for the two coupled modes and the uncoupled mode are listed in Table 5.6. These results are used to verify the corresponding numerical models presented in Section 5.3.

5.3 Numerical models and analysis

Numerical models of two fluid-filled, concentric, cylindrical pipes are analyzed: M1 and M2, as shown in Figure 5.3. Both pipes in each model are top-supported. Fluid-structure interaction (FSI) analysis for each of M1 and M2 is performed using the ALE and ICFD solvers in LS-DYNA to calculate lateral frequencies of the submerged (i.e., inner) pipes. The third and the fourth rows of Table 5.4 lists the dimensions of M1 and M2, respectively, consistent with those shown in Figure 5.3. Figure 5.16 presents the ALE models and the global coordinate system (x, y, z). Figures 5.16a and d present the finite element meshes for the pipes in the ALE models of M1 and M2, respectively. The outer pipe is shown in dark blue and the inner pipe is shown in green for each model. Figures 5.16b and e present the finite element meshes for the fluid, shown in yellow, for M1 and M2, respectively. The pipes and the fluid share nodes at their interfaces. The pipes are modeled using Lagrangian, four-node, shell (i.e., quadrilateral) elements, and the fluid is modeled using Eulerian, eight-node, solid (i.e., brick) elements. The types and numbers of

[49] The dimensions of M1 and M2 are based on the 1/10th-scale tank and its central internal component (i.e., cylindrical pipe) used in the earthquake-simulator tests. The 1/10th-scale test tank and the internal component are constructed using available steel cylindrical pipes. The dimensions of the pipes are selected based on the height-to-radius ratio of a prototype advanced reactor, but their thicknesses are not consistent with the 1/10th length scale.

elements used for the ALE models are listed in Table 5.7. As noted in Section 4.1, Eulerian elements define a grid of integration points for the fluid domain. The fluid response is calculated at the integration points in each grid cell. Figures 5.16c and f present the fluid filling in the pipes for M1 and M2, respectively, at the first step of the analysis (i.e., time $t = 0$).

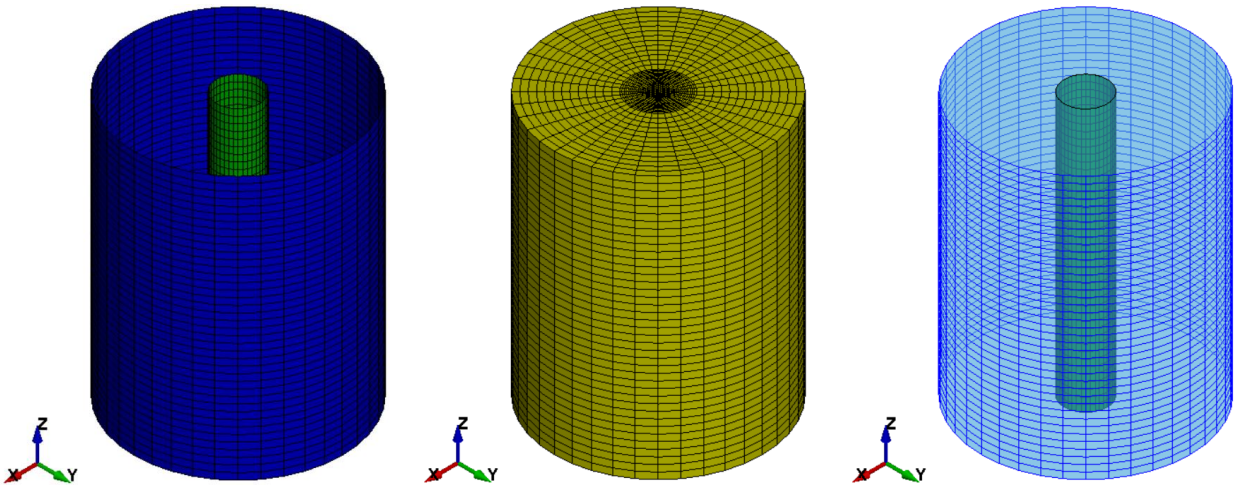

(a) pipes, M1 (b) fluid, M1 (c) pipes and fluid, M1, $t = 0$

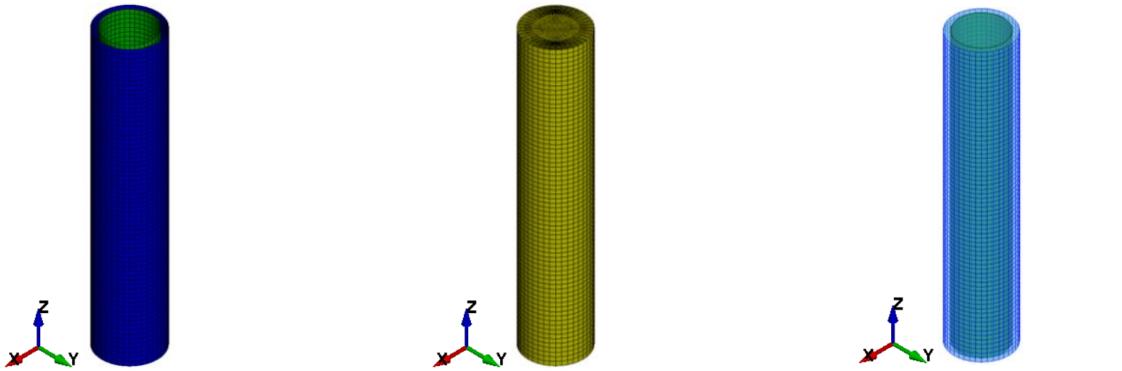

(d) pipes, M2 (e) fluid, M2 (f) pipes and fluid, M2, $t = 0$

Figure 5.16. ALE models, two fluid-filled concentric pipes, M1 and M2

Table 5.7. Types and numbers of elements for the pipes and fluid in the ALE models

	Inner pipe	Outer pipe	Fluid
Element type	Lagrangian four-node shell		Eulerian eight-node solid
M1	1600	1600	45600
M2	2800	2800	60200

Figure 5.17 presents the ICFD models and the global coordinate system (x, y, z). Figures 5.17a and d show the finite element meshes for the pipes in M1 and M2, respectively: inner pipes in blue and the outer pipes in green. The models of the fluid are defined by its boundary surfaces. Figures 5.17b and e present half models to show the fluid surfaces in M1 and M2, respectively. The fluid domain in each model is defined using four surfaces: 1) adjacent to the outer pipe (yellow), 2) adjacent to the inner pipe (light blue), 3) horizontally at the top of the two pipes (pink), and 4) horizontally at the base of the two pipes (dark blue). The pipes are constructed using Lagrangian four-node shell elements, and the fluid surfaces are constructed using Lagrangian three-node shell (i.e., triangular) elements. The types and numbers of elements used for the ICFD models are listed in Table 5.8. The pipes and the fluid surfaces do not share nodes

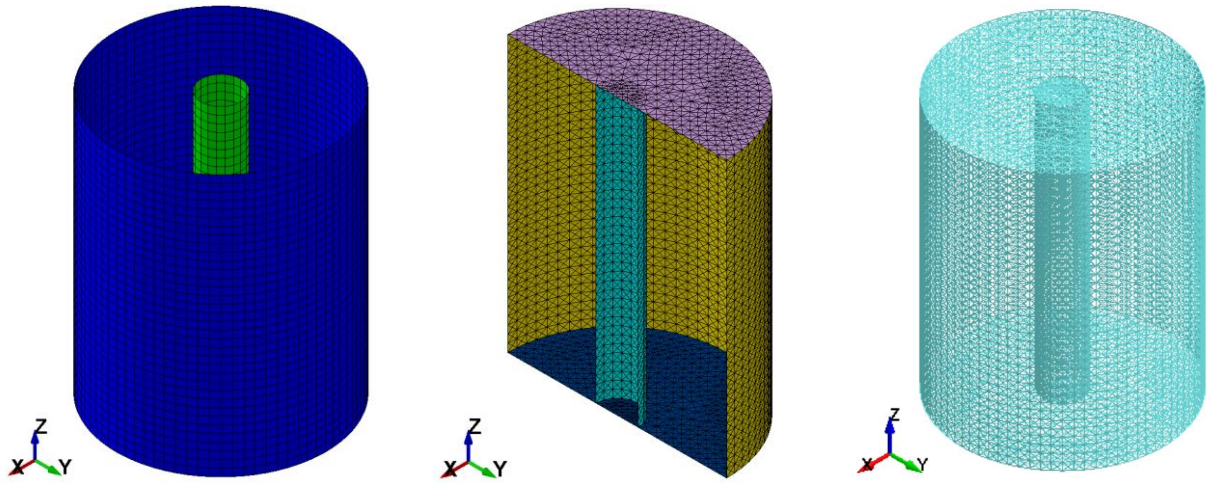

(a) pipes, M1 (b) fluid surfaces, M1 (c) fluid, M1, $t = 0$

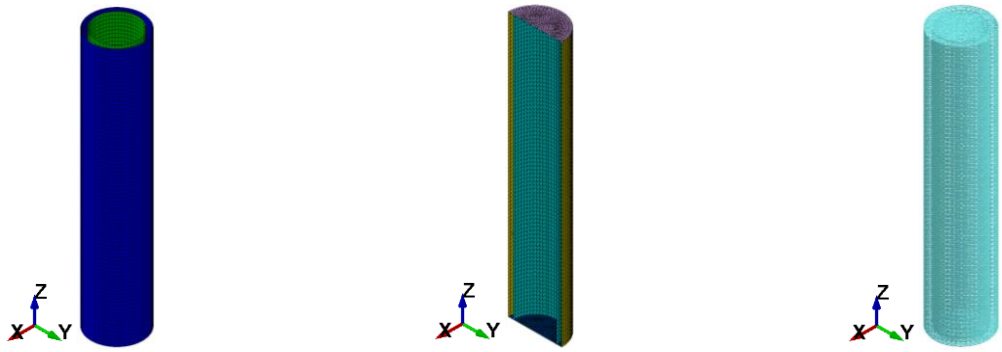

(d) pipes, M2 (e) fluid surfaces, M2 (f) fluid, M2, $t = 0$

Figure 5.17. ICFD models, two fluid-filled concentric pipes, M1 and M2

Table 5.8. Types and numbers of elements for the pipes and fluid surfaces in the ICFD models

	Inner pipe	Outer pipe	Fluid surfaces
Element type	Lagrangian four-node shell		Lagrangian three-node shell
M1	700	2800	19120
M2	2800	3360	27424

at their interfaces. To model fluid-structure response, the *ICFD_BOUNDARY_FSI card in the LS-DYNA deck is assigned to the fluid surfaces adjacent to the pipes: yellow and light blue in Figures 5.17b and e. The *MESH_EMBEDSHELL card is assigned to the light blue fluid surface to model the fluid domain separated by the submerged shell elements of the inner pipe. The fluid domain is automatically meshed using Lagrangian, four-node, solid (i.e., tetrahedral) elements by the ICFD solver at the first step of the analysis (i.e., $t = 0$): see Figures 5.17c and f for M1 and M2, respectively.

Frequencies are calculated using each model (i.e., ALE and ICFD models for M1 and M2) for 1) the two modes involving coupled movements of the two pipes (i.e., out-of-phase and in-phase modes; see Figure 5.6), and 2) the uncoupled mode of the inner pipe. To calculate the two coupled frequencies, the elements of both pipes in each model are assigned to be elastic. To calculate the uncoupled frequency, the elements of the inner pipe in each model are assigned to be elastic and those of the outer pipe are assigned to be rigid. Mechanical properties consistent with carbon steel are used for both elastic and rigid pipes, including a density ρ_s of 8000 kg/m^3, an elastic modulus E_s of 2×10^{11} N/m^2, and a Poisson's ratio υ_s of 0.27. Although the response of the elements assigned a rigid material is not affected by the elastic modulus and Poisson's ratio, LS-DYNA requires these mechanical properties to be defined. No damping is applied to the pipes.

The corrected analytical solutions (Chen and Rosenberg) used to verify the numerical models were developed for ideal fluids, which were inviscid and incompressible (see Section 5.2). The properties of the fluid used in the numerical models must be consistent with those used in the analytical solutions. Accordingly, the fluid in each model is assigned the density of water,

namely $\rho_w = 1000$ kg/m^3, and a viscosity μ_a of 0 to be inviscid. A bulk modulus K_w of 2.15×10^9 N/m^2, consistent with water, is used for the ALE models, and implemented using the *EOS_LINEAR_POLYNOMIAL card (termed $C1$ in the card). The bulk modulus of water is sufficiently large to achieve incompressibility, based on the results of a sensitivity analysis presented in Section 4.3.1. The bulk modulus is not used in the ICFD analysis because the solver can only accommodate incompressible fluids. Table 5.9 lists mechanical properties assigned to the elements in the ALE and ICFD models for both M1 and M2. The mass of each component of the numerical models is listed in Table 5.10. No gravitational acceleration is assigned to the models since gravity was not considered in the analytical solutions.

Table 5.9. Mechanical properties assigned to the elements of the pipes and water, ALE and ICFD models

		ALE	ICFD
Pipes	Density, ρ_s	8000 kg/m^3	
	Elastic modulus, E_s	2×10^{11} N/m^2	
	Poisson's ratio, υ_s	0.27	
Water	Density, ρ_w	1000 kg/m^3	
	Viscosity, μ_w	0	
	Bulk modulus, K_w	2.15×10^9 N/m^2	--[1]

1. The ICFD solver analyzes only incompressible fluids and so K_w is not used.

Table 5.10. Mass of each component of the ALE and ICFD models, pipes and water, M1 and M2

Components	Mass (kg)	
	M1	M2
Outer pipe	629	159
Inner pipe	103	103
Water	3921	251

The ALE and ICFD solvers cannot perform eigenvalue analysis, and so frequencies are identified from the response histories of the submerged component (i.e., inner pipe) undergoing free vibration. To achieve free vibration response, the displacement time series shown in Figure 5.18 is applied at the free end (i.e., bottom) of the inner pipe in each model in the x direction, and the

pipe is then released to vibrate. The peak displacement is 15 mm, which is less than 1% of the height of the inner pipe ($0.01H = 20$ mm). This displacement generates the first lateral modal shape of the inner pipe, and the associated frequencies (i.e., two coupled and one uncoupled) are the focus of the analysis and verification. The circumferential, axial, and torsional modes are not considered. A rigid diaphragm is assigned to the nodes at the free end of the inner pipe in each model through *CONSTRAINT_NODAL_RIGID_BODY card, and the displacement time series is applied at the center of the diaphragm. The rigid diaphragm makes the assigned set of nodes translate and rotate as a rigid body, and prevents circumferential deformation due to the applied displacement. Figure 5.19 shows the rigid diaphragm at the free end of the inner pipe (shown as yellow lines) in the ICFD model for M1. Response-history analysis for the ALE and ICFD models is performed for about 2 seconds after the pipe is released (i.e., at 0.03 sec in Figure 5.18) to vibrate freely. The displacement time series of the free vibration at the center of the rigid diaphragm is transformed into the frequency domain using the Fast Fourier Transform (FFT). The frequencies of the inner pipe associated with the first lateral modal shape are identified from the Fourier amplitude spectrum. The results calculated using the ALE and ICFD models are presented in Section 5.4 and compared with those calculated using the analytical solutions (Section 5.2.3) to verify the numerical models.

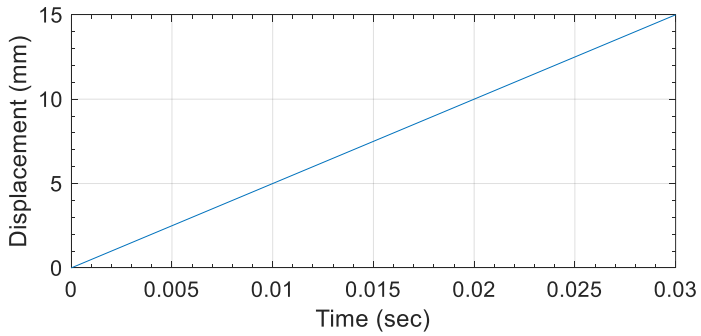

Figure 5.18. Displacement applied at the free end of the inner pipe in the x direction

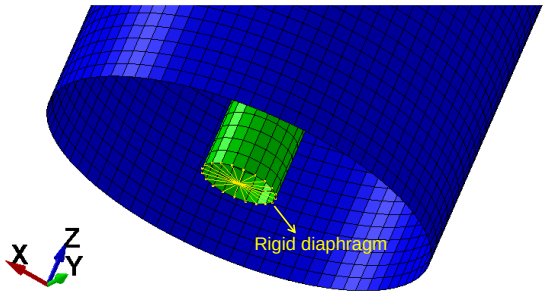

Figure 5.19. Rigid diaphragm (yellow lines) at the free end of the inner pipe, the ICFD model for M1

5.4 Results and verification

Figures 5.20a and b present Fourier amplitude spectra for the displacement at the center of the rigid diaphragm of the inner pipe in M1 and M2, respectively, calculated using the ALE models. Figures 5.21a and b present those calculated using the ICFD models for M1 and M2, respectively. Each Fourier amplitude spectrum shown in the figures is normalized by its maximum ordinate. The blue and red spectra are calculated using the displacement of the inner pipe, as the outer pipe is assigned to be elastic and rigid, respectively. Accordingly, the peaks in the blue spectra are associated with the coupled frequencies, and those in the red spectra are associated with the uncoupled frequencies. Table 5.11 lists the frequencies identified from the spectra for both M1 and M2, analyzed using the ALE and ICFD models.

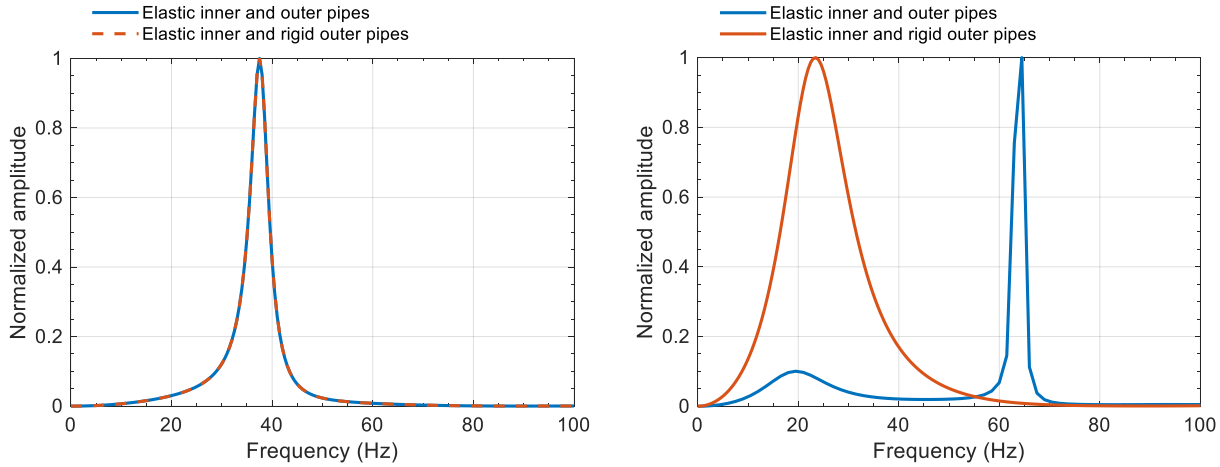

(a) M1, $R_2 / R_1 = 5.2$ (b) M2, $R_2 / R_1 = 1.3$

Figure 5.20. Normalized Fourier amplitude spectra for the displacement at the center of the rigid diaphragm of the inner pipes, ALE models for M1 and M2

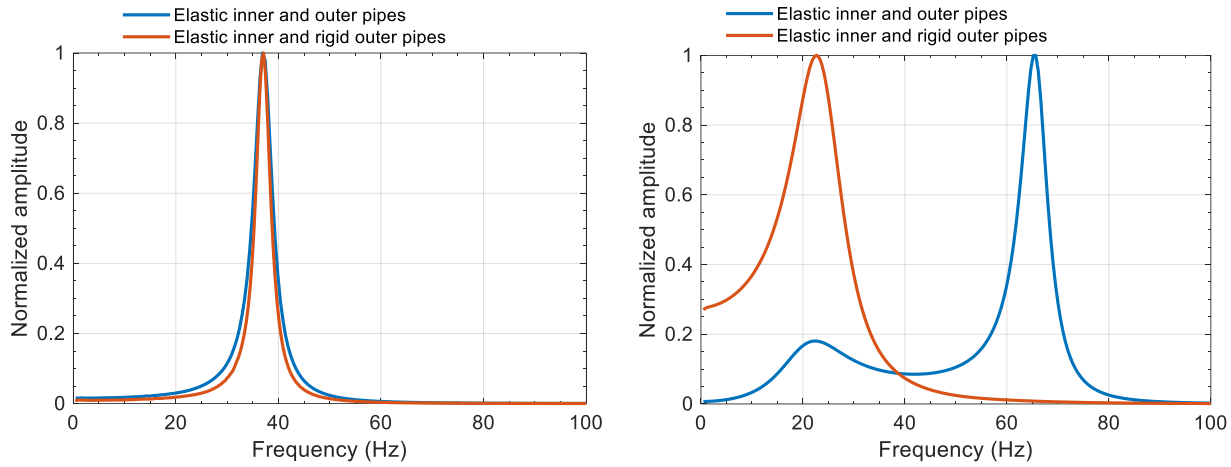

(a) M1, $R_2 / R_1 = 5.2$ (b) M2, $R_2 / R_1 = 1.3$

Figure 5.21. Normalized Fourier amplitude spectra for the displacement at the center of the rigid diaphragm of the inner pipes, ICFD models for M1 and M2

Table 5.11. Coupled and uncoupled lateral frequencies of the inner pipes, calculated using the ALE and ICFD models and the analytical solutions, M1 and M2

Model	Mode	Frequency[1] (Hz)			Difference[2] (%)	
		ALE model	ICFD model	Analytical solutions	ALE model	ICFD model
M1	First coupled, out-of-phase	38	37	38	-1	-2
	Second coupled, in-phase	--	--	99	--	--
	Uncoupled	38	37	38	-1	-2
M2	First coupled, out-of-phase	20	22	21	-3	4
	Second coupled, in-phase	64	65	64	1	2
	Uncoupled	24	24	25	-4	-5

1. Frequencies of coupled and uncoupled modes identified through the blue and red spectra, respectively, shown in Figures 5.20 and 5.21. Coupled modes: 1) lower frequency, out-of-phase; 2) higher frequency, in-phase
2. Percentage differences of the numerical results with respect to those calculated using the analytical solutions

Per Figures 5.20a and 5.21a and Table 5.11, for M1 ($R_2 / R_1 = 5.2$), the frequencies of the first coupled and uncoupled modes are identical: 38 Hz for the ALE models and 37 Hz for the ICFD models. As noted in Section 5.2.2, if the radii of two flexible fluid-filled pipes are significantly different (e.g., $R_2 / R_1 > 4$), the frequency of the first coupled mode (i.e., the out-of-phase mode) is identical to that of the uncoupled mode. (See Figure 5.9: C_{lat} in the first coupled and

uncoupled modes are identical for $R_2 / R_1 = 5$ and 10). The frequency of the second coupled mode cannot be identified from the blue spectra because the displacement amplitude in the mode is too small.

Per Figures 5.20b and 5.21b for M2 ($R_2 / R_1 = 1.3$), two peaks at different frequencies are shown in each blue spectrum, which are associated with the two coupled modes. Per the blue spectra, the two coupled frequencies calculated using the ALE model are 20 and 64 Hz, and those calculated using the ICFD model are 22 and 65 Hz, listed in Table 5.11. The uncoupled frequency is 24 Hz, identified from the red spectra presented in Figures 5.20b and 5.21b for the ALE and ICFD models, respectively. The uncoupled frequency calculated using each model lies between the two coupled frequencies, which is consistent with the analytical results shown in Figure 5.9 for $R_2 / R_1 \leq 2$.

The widths of the peaks in the presented spectra are associated with a damping effect on the fluid-filled pipes. Since the fluid is inviscid and no damping is assigned to the elements of the pipes in the numerical models, the damping effect is only associated with the fluid pressure that is opposite to and reduces the movement of the free-vibrating inner pipe (i.e., the so-called *pressure drag*). The half-power bandwidth method is used to calculate the damping ratio associated with each mode for the inner pipe in M1 and M2. Figure 5.22 (Chopra 2012) illustrates the use of the half-power bandwidth method on a displacement spectrum. The damping ratio, ζ , is calculated using the frequency associated with the peak, f_n, and the two frequencies, f_a and f_b, with respect to the ordinates at $1/\sqrt{2}$ th of the spectral amplitude. Applying this method to Figures 5.20a and 5.21a, the damping ratios for the uncoupled and out-of-phase modes of M1 (i.e., $R_2 / R_1 = 5.2$) are both around 3%. Calculating using Figures 5.20b and 5.21b for M2 (i.e., $R_2 / R_1 = 1.3$), the damping ratios for the out-of-phase, in-phase, and uncoupled modes are around 25%, 3%, and 20%, respectively. Accordingly, the damping effect is greater with smaller R_2 / R_1: an internal component (e.g., inner pipe) submerged in a fluid confined by a relatively small container (e.g., outer pipe).

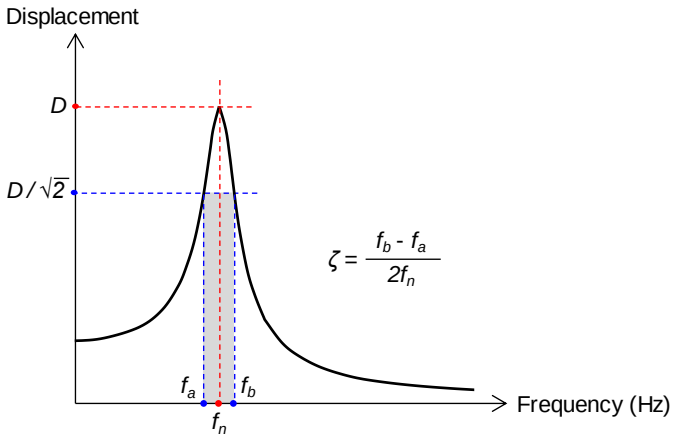

Figure 5.22. Half-power bandwidth method for calculating a damping ratio, ζ, using a displacement spectrum (adapted from Figure 3.2.9 in Chopra (2012))

To verify the ALE and ICFD models, the frequencies of the inner pipes in M1 and M2 calculated using the models and the analytical solutions are compared. The fifth column of Table 5.11 lists the analytically calculated frequencies, which are extracted from Table 5.6. The differences between the numerical and the analytical results are very small, and listed in the sixth and seventh columns of Table 5.11 for the ALE and ICFD models, respectively. These small differences enable the authors to conclude that the ALE and ICFD models are verified for cylindrical pipes submerged in fluid.

5.5 Identification and quantification of errors in Chen and Rosenberg

This section identifies the calculation errors presented in the derivation and the analytical solutions developed by Chen and Rosenberg. The analytical solutions address the frequencies of two fluid-filled concentric pipes. The corrected solutions and the original solutions that involve errors are compared for a range of dimensions of the two pipes and N1 presented in Figure 5.14b, which is a simplified model for the reactor vessel and jacket of the PFR, Dounreay, Scotland (Figure 5.14a). The solutions are presented here using the variables and coordinate systems defined in Figure 5.4.

The frequencies of two fluid-filled concentric pipes are calculated using $[F]$ per Eq. (5.28), which is a matrix presenting the equations of equilibrium for the pipes. Mistakes were made in the derivation for entries f_{11}, f_{44}, f_{14}, and f_{41} in $[F]$. Per $[F]$ in Eq. (5.28), all these four

entries relate the inertial and hydrodynamic forces on the pipes (per unit area) to their radial displacements, $\bar{u}_{s1}$ and $\bar{u}_{s2}$.

Table 5.12 lists the four original entries that involve errors and those corrected in this section per Eqs. (5.30), (5.36), (5.37), and (5.38). The listed entries are expressed using unitless parameters defined in Chen and Rosenberg: $\delta_1 = \frac{h_1}{R_1}$, $\delta_2 = \frac{h_2}{R_2}$, $\mu_1 = \frac{\rho_1 R_1}{\rho_{s1} h_1}$, $\mu_2 = \frac{\rho_2 R_2}{\rho_{s2} h_2}$, $\Omega_1 = R_1 \omega \sqrt{\frac{\rho_{s1}(1-\upsilon_1^2)}{E_1}}$, and $\Omega_2 = R_2 \omega \sqrt{\frac{\rho_{s2}(1-\upsilon_2^2)}{E_2}}$. The corrected parts of the entries are bolded Table 5.12, which are all factors for terms associated with modified Bessel's functions (i.e., I_1, K_1, I_1', and K_1'). These Bessel's functions are used for calculating hydrodynamic pressures on the pipes shown in Figure 5.5: $p_{1,1} - p_{1,2}$ on the inner pipe and $p_{2,2}$ on the outer pipe. Accordingly, Chen and Rosenberg calculated these hydrodynamic pressures incorrectly.

An error was made to a sign used for f_{11}; see the factor for the last fraction described using Bessel's functions. Entry f_{11} relates $p_{1,1} - p_{1,2}$ on the inner pipe to its radial displacement $\bar{u}_{s1}$, but Chen and Rosenberg incorrectly used $p_{1,1} + p_{1,2}$ in the calculation. The wrong direction (i.e., sign) defined for $p_{1,2}$ by Chen and Rosenberg makes the pipes unstable and results in imaginary values for their frequencies. Other errors were made in the use of the chain rule for the derivative of two Bessel functions with respect to r (i.e., I_1', and K_1'). Factors of $1/R_1$ or $1/R_2$ were omitted incorrectly in the original entries listed in Table 5.12, as shown bolded.

The original and corrected entries are used in $[F]$ and $[F_1]$ per Eq. (5.29) herein to calculate lateral frequencies, f_{lat}, for two fluid-filled, concentric, cylindrical pipes. The matrix $[F]$ is used for calculating the two coupled frequencies (out-of-phase and in-phase), and $[F_1]$ is used for calculating the uncoupled frequency of the inner pipe. Consistent with results presented in Figures 5.9 and 5.10, f_{lat} are calculated here for a range of dimensions: $5 \le H/R_1 \le 30$ and $R_2/R_1 = 1.2$, 2, 5, and 10. Two boundary conditions are used: 1) cantilever and 2) simply-supported, for which the first wavelengths l are $3.351H$ and $2H$, respectively (see footnote 43

Table 5.12. Entries f_{11}, f_{44}, f_{14}, and f_{41} in $[F]$ per Eq. (5.28): presented in Chen and Rosenberg (1975) (termed C&R in this table) and corrected in this section (errors and corrections bolded)

f_{11}	$1+\frac{\delta_1^2}{12}(\alpha_1^4+2\alpha_1^2)-\Omega_1^2\cdot(1+\boldsymbol{\mu_1}\frac{I_1(\alpha_1)}{I_1'(\alpha_1)}+\boldsymbol{\mu_1}\frac{\boldsymbol{\rho_2}}{\boldsymbol{\rho_1}}\frac{I_1(\alpha_1)K_1'(\alpha_2)-K_1(\alpha_1)I_1'(\alpha_2)}{I_1'(\alpha_1)K_1'(\alpha_2)-K_1'(\alpha_1)I_1'(\alpha_2)})$	termed a_{16} per Eq. (15) in C&R
	$1+\frac{\delta_1^2}{12}(\alpha_1^4+2\alpha_1^2)-\Omega_1^2\cdot(1+\frac{\boldsymbol{\mu_1}}{\boldsymbol{R_1}}\frac{I_1(\alpha_1)}{I_1'(\alpha_1)}-\frac{\boldsymbol{\mu_1}}{\boldsymbol{R_1}}\frac{\boldsymbol{\rho_2}}{\boldsymbol{\rho_1}}\frac{I_1(\alpha_1)K_1'(\alpha_2)-K_1(\alpha_1)I_1'(\alpha_2)}{I_1'(\alpha_1)K_1'(\alpha_2)-K_1'(\alpha_1)I_1'(\alpha_2)})$	Eq. (5.30) in Section 5.2.1
f_{44}	$1+\frac{\delta_2^2}{12}(\alpha_2^4+2\alpha_2^2)-\Omega_2^2\cdot(1+\boldsymbol{\mu_2}\frac{K_1(\alpha_2)I_1'(\alpha_1)-I_1(\alpha_2)K_1'(\alpha_1)}{I_1'(\alpha_1)K_1'(\alpha_2)-K_1'(\alpha_1)I_1'(\alpha_2)})$	termed a_{26} per Eq. (15) in C&R
	$1+\frac{\delta_2^2}{12}(\alpha_2^4+2\alpha_2^2)-\Omega_2^2\cdot(1+\frac{\boldsymbol{\mu_2}}{\boldsymbol{R_2}}\frac{K_1(\alpha_2)I_1'(\alpha_1)-I_1(\alpha_2)K_1'(\alpha_1)}{I_1'(\alpha_1)K_1'(\alpha_2)-K_1'(\alpha_1)I_1'(\alpha_2)})$	Eq. (5.36) in Section 5.2.1
f_{14}	$\Omega_1^2\boldsymbol{\mu_1}\frac{\boldsymbol{\rho_2}}{\boldsymbol{\rho_1}}\frac{\boldsymbol{R_2}}{\boldsymbol{R_1}}\frac{K_1(\alpha_1)I_1'(\alpha_1)-I_1(\alpha_1)K_1'(\alpha_1)}{I_1'(\alpha_1)K_1'(\alpha_2)-K_1'(\alpha_1)I_1'(\alpha_2)}$	termed a_{17} per Eq. (15) in C&R
	$\Omega_1^2\frac{\boldsymbol{\mu_1}}{\boldsymbol{R_1}}\frac{\boldsymbol{\rho_2}}{\boldsymbol{\rho_1}}\frac{K_1(\alpha_1)I_1'(\alpha_1)-I_1(\alpha_1)K_1'(\alpha_1)}{I_1'(\alpha_1)K_1'(\alpha_2)-K_1'(\alpha_1)I_1'(\alpha_2)}$	Eq. (5.37) in Section 5.2.1
f_{41}	$-\Omega_2^2\cdot\boldsymbol{\mu_2}\frac{\boldsymbol{R_1}}{\boldsymbol{R_2}}\frac{I_1(\alpha_2)K_1'(\alpha_2)-K_1(\alpha_2)I_1'(\alpha_2)}{I_1'(\alpha_1)K_1'(\alpha_2)-K_1'(\alpha_1)I_1'(\alpha_2)}$	termed a_{27} per Eq. (15) in C&R
	$-\Omega_2^2\cdot\frac{\boldsymbol{\mu_2}}{\boldsymbol{R_2}}\frac{I_1(\alpha_2)K_1'(\alpha_2)-K_1(\alpha_2)I_1'(\alpha_2)}{I_1'(\alpha_1)K_1'(\alpha_2)-K_1'(\alpha_1)I_1'(\alpha_2)}$	Eq. (5.38) in Section 5.2.1

on page 229). Figures 5.23 and 5.24 present the frequency coefficients, C_{lat}, calculated per Eq. (5.42) and f_{lat}. Each panel in Figures 5.23 and 5.24 presents results for the two coupled modes and the uncoupled mode, given a value of R_2 / R_1 and H / R_1. The orange, light blue, and gray thin lines describe C_{lat} calculated using the original solutions for out-of-phase, in-phase, and uncoupled modes, respectively; the red, blue, and black thick lines describe their counterparts calculated using the corrected solutions, which are identical to the those shown in Figures 5.9 and 5.10. The results calculated using the original solutions are complex values due to the

mistake in a sign used for f_1, which makes the pipes unstable. Only the real part of the results is presented in Figures 5.23 and 5.24, and the imaginary part is ignored. If C_{lat} is an imaginary value (i.e., real part is zero), no result is presented (e.g., light blue line in Figure 5.23c is not presented for $H / R_1 \geq 7$). As shown in Figures 5.23 and 5.24, for a given mode and a value of R_2 / R_1, the differences between (the real part of) C_{lat} calculated using the original and corrected solutions increases with increasing H / R_1.

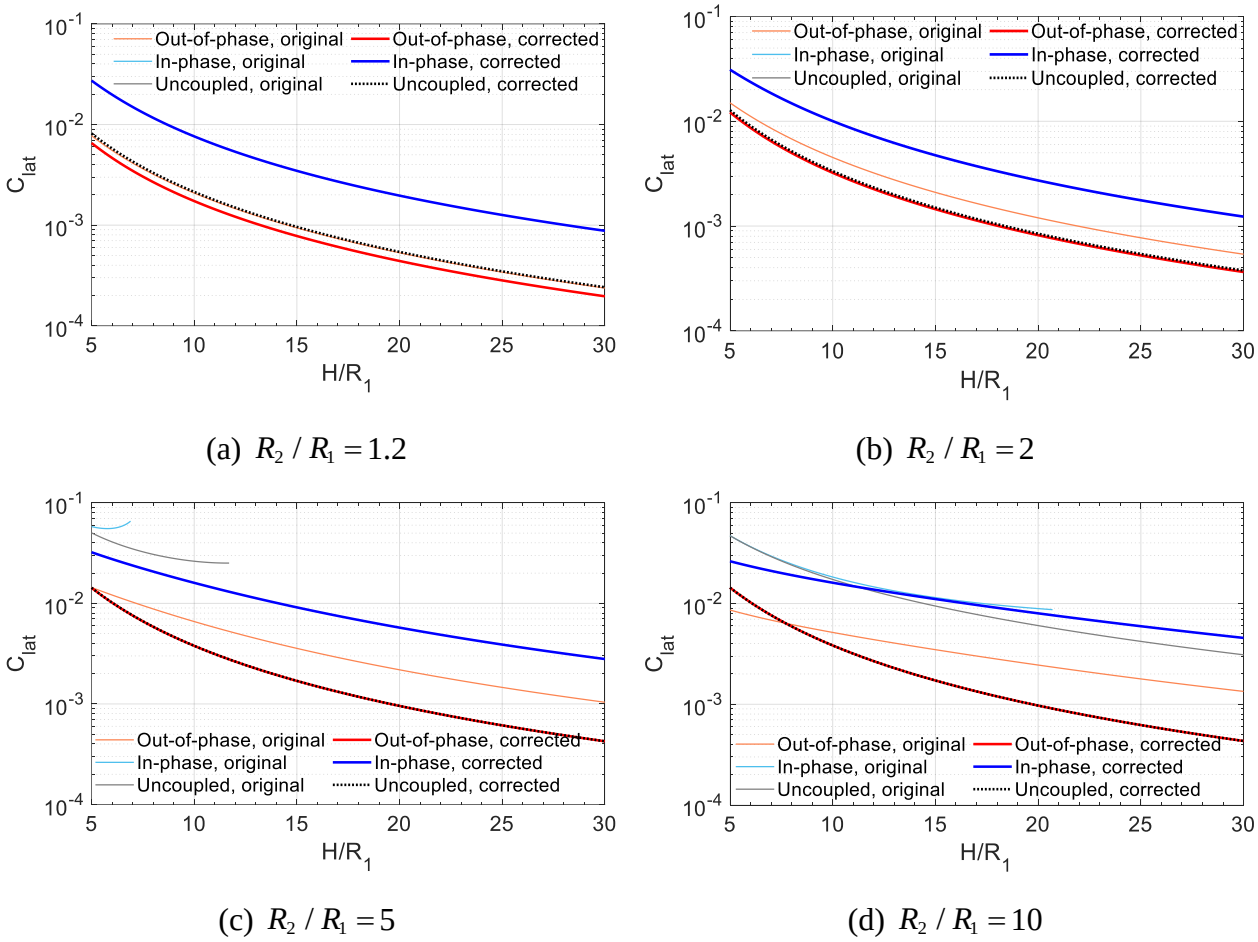

(a) $R_2 / R_1 = 1.2$ (b) $R_2 / R_1 = 2$

(c) $R_2 / R_1 = 5$ (d) $R_2 / R_1 = 10$

Figure 5.23. Frequency coefficients for two fluid-filled concentric pipes, cantilever, first wavelength $l = 3.351\,H$, coupled modes and uncoupled mode of the inner pipe, calculated using the original and corrected entries f_{11}, f_{44}, f_{14}, and f_{41} for $[F]$ listed in Table 5.12

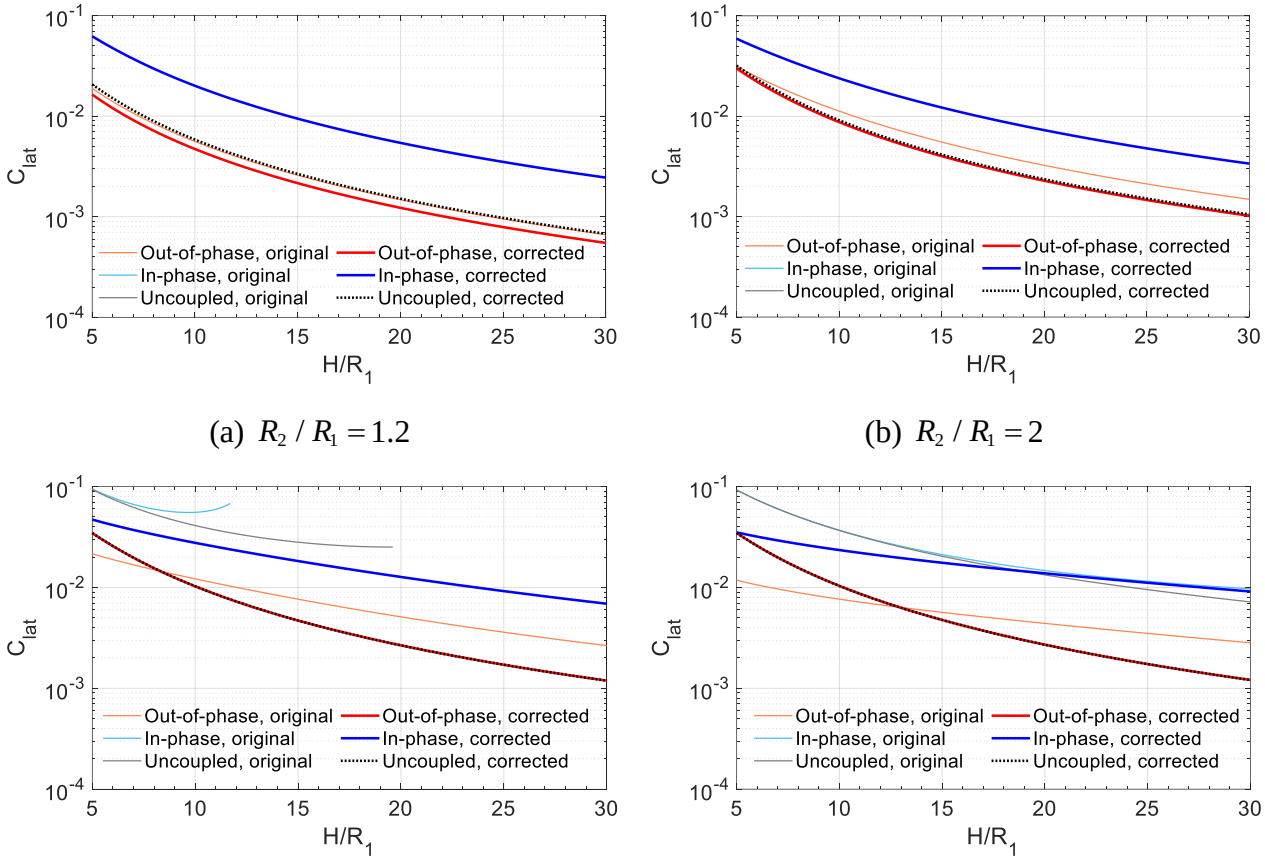

(a) $R_2 / R_1 = 1.2$ (b) $R_2 / R_1 = 2$

(c) $R_2 / R_1 = 5$ (d) $R_2 / R_1 = 10$

Figure 5.24. Frequency coefficients for two fluid-filled concentric pipes, simply-supported, first wavelength $l = 2H$, coupled modes and uncoupled mode of the inner pipe, calculated using the original and corrected entries f_{11}, f_{44}, f_{14}, and f_{41} for $[F]$ listed in Table 5.12

The frequencies are calculated using the original and corrected solutions for the two fluid-filled concentric pipes in N1 presented in Figure 5.14b. Both pipes are assumed to be head-supported (i.e., cantilever), with the first wavelength $l = 3.351\,H$. The dimensions and the mechanical properties of the two pipes used in the analytical solutions are listed in Tables 5.4 and 5.5, respectively. Per the listed dimensions, $R_2 / R_1 = 2.1$ and $H / R_1 = 5.2$. The values for C_{lat} at $H / R_1 = 5.2$ extracted from Figure 5.23b are listed in Table 5.13 for the two coupled modes (out-of-phase and in-phase) and the uncoupled mode. The results of C_{lat} for the in-phase and uncoupled modes calculated using the original solutions are not listed because they are

imaginary values and not shown in Figure 5.23b. Given the listed C_{lat}, the corresponding frequencies, f_{lat}, are calculated per Eq. (5.42), and listed in Table 5.6. The frequencies of the three modes calculated using the corrected solutions are identical to those listed in Table 5.6 for N1. The frequency of the out-of-phase mode calculated using the original solutions is 3.1 Hz, with a difference of 25% from 2.5 Hz calculated using the corrected solutions. The original solutions are not available for the in-phase and uncoupled frequencies due to the imaginary values of C_{lat}.

Table 5.13. Lateral frequencies of the two fluid-filled concentric pipes N1 presented in Figure 5.14b, $l = 3.351\,H$

Mode	Coupled, out-of-phase		Coupled, in-phase		Uncoupled, inner pipe	
Original	C_{lat}	f_{lat} (Hz)	C_{lat}	f_{lat} (Hz)	C_{lat}	f_{lat} (Hz)
	0.0141	3.1	--	--	--	--
Corrected	C_{lat}	f_{lat} (Hz)	C_{lat}	f_{lat} (Hz)	C_{lat}	f_{lat} (Hz)
	0.0113	2.5	0.0293	6.6	0.0119	2.6

5.6 Closing remarks

Earthquake shaking of a fluid-filled advanced reactor induces fluid-structure interaction (FSI) between the reactor vessel, the submerged internal components, and the contained fluid. Verified and validated numerical models for FSI analysis will be required for seismic design and qualification of the advanced reactors. This section verifies ALE and ICFD models for internal components using corrected analytical solutions of Chen and Rosenberg.

The solutions were developed for frequencies of two concentric pipes filled with fluid, as shown in Figure 5.2. The inner pipe is an internal component, and the outer pipe refers to the wall of the reactor vessel. The lengths and boundary conditions of the two pipes are identical. To be consistent with the solutions and enable verification, the numerical models are developed for two fluid-filled concentric pipes: M1 and M2 presented in Figure 5.3. The material used for the pipes is carbon steel, and the fluid is water. The frequencies of the inner pipes in M1 and M2 calculated using the models and the (corrected) analytical solutions are compared. The differences between the numerical and analytical results are very small (i.e., $\leq 5\%$), which enable

the authors to conclude that the ALE and ICFD models are verified for cylindrical pipes submerged in fluid.

However, as presented in Figure 5.1a, the reactor vessel and internal components are not concentric, prismatic, cylindrical pipes, their boundary conditions and lengths are not identical, and the vessel is not fully filled. To verify numerical models representing the internal components shown in Figure 5.1a, models of two concentric pipes can be developed based on the components that are pipe-type structures, including the vessel, the upper internal, and the intermediate heat exchanger (IHX) and its shield. Examples are models for inner and outer pipes based on 1) the upper internal and the vessel, respectively, and 2) the IHX and its shield, respectively. The two pipes in a model are assigned the mechanical properties, boundary conditions, and dimensions representing those used for the components shown in Figure 5.1a and yet adapting to the assumptions used for the solutions, to enable the verification. For example, the thinnest wall thicknesses and the radii around the head support of each component (referring to h_1, h_2, R_1, and R_2) and the greatest height of the two components (referring to H). After verifying the models of two concentric pipes using the (corrected) solutions for frequencies (Chen and Rosenberg), a comprehensive model for the reactor including its components can then be developed using the realistic boundary conditions and geometries shown Figure 5.1a. This comprehensive model can be used for calculating fluid-structure responses (e.g., shear force and moment at the support) for seismic design and qualification. (The model would have to be validated after the verification.)

SECTION 6
VALIDATION OF NUMERICAL MODELS FOR SEISMIC FLUID-STRUCTURE-INTERACTION ANALYSIS OF CYLINDRICAL TANKS

6.1 Introduction

Verified numerical models for fluid-structure-interaction (FSI) analysis of fluid (liquid)-filled advanced reactors must be validated before being used for seismic design and qualification. Guidance for verification studies is provided in Sections 4 and 5, in which numerical results for cylindrical tanks and submerged internal components, respectively, are compared with analytical solutions. This section validates numerical models using data generated in earthquake-simulator tests of a base-supported cylindrical tank. The models are modified from those used in Section 4. Validation of models including both tank and components submerged in the contained fluid will be presented in Mir (in progress).

Section 4 presents a verification study on FSI models of cylindrical tanks analyzed using Arbitrary Lagrangian-Eulerian (ALE) and Incompressible Computational Fluid Dynamics (ICFD) solvers in LS-DYNA (2018b, 2019)[50]. Unidirectional horizontal seismic motion of a small amplitude is used for the response-history analysis. Both ALE and ICFD models are *partially* verified in Section 4, by comparing numerical results with those calculated using analytical solutions in Section 3. The ALE models are verified for calculating hydrodynamic pressures and reactions at the support of the tank. Time series of wave heights are in reasonable agreement with the analytical solution only in the first 5 to 8 seconds due to the limitation of the method used to output ALE results (see Appendix C). The ICFD models are verified for calculating hydrodynamic pressures and reactions for the tank, if the wave action of the contained fluid is insignificant. The ICFD models do not predict wave heights accurately. A finer fluid mesh would improve the calculation of wave actions but increases analysis time. The ICFD models in Section 4 use a fluid mesh that limits the analysis time to two weeks for a 13-second input motion, on a computer with 7th Gen (i7) 4-core Intel processor, 32 GB RAM, and 512 GB SSD.

[50] Different versions of LS-DYNA are used here: SMP_d_Dev_126632 (2018b) is used for the ALE analysis and SMP_d_R11_139066 (2019) is used for the ICFD analysis.

The goals of this section are: 1) validating the *partially* verified numerical models of a cylindrical tank presented in Section 4, 2) improving the capability of the models for calculating wave height, and 3) providing guidance for validation studies on seismic FSI models of advanced reactors. The ALE and ICFD models presented in this section are validated using data of a base-supported cylindrical tank tested on an earthquake simulator for uni-, two-, and three-directional seismic motions. The test tank was fabricated from carbon steel and filled with water. The length scale of the tank is around 1/10, and its dimensions and geometries are loosely based on those of prototype advanced reactors. The numerical models here are developed using the realistic geometries, dimensions, mechanical properties, and boundary conditions of the test tank. To improve the predictions of wave height calculated using the ALE and ICFD models presented in Section 4, modifications are made here: 1) additional monitoring locations for outputting wave heights in the ALE model, and 2) a finer fluid mesh around the free surface in the ICFD model. Per the outcomes of Section 4, ALE results for wave heights are reasonable for short-duration analysis, and a finer fluid mesh in an ICFD model significantly increases run time, and so shorter motions, of 5 to 7 seconds duration, are used here for validation. The numerical and test results are compared for fluid-structure responses: hydrodynamic pressures on the wall, shear forces and moments at the tank base, and wave heights.

Section 6.2 describes the earthquake-simulator tests, including the test tank, instrumentation, and input motions. Section 6.3 presents the ALE and ICFD models of the test tank. Section 6.4 presents input motions used in the numerical models, generated using the acceleration at the tank base measured in the tests. Section 6.5 validates the models of Section 6.3 by comparing the numerical and test results of hydrodynamic pressures, reactions at the tank base, and wave heights. Section 6.6 presents closing remarks.

6.2 Earthquake-simulator tests for a base-supported tank

A base-supported, cylindrical tank was tested using an earthquake simulator at the University at Buffalo. The tank is a model of an advanced reactor vessel, at a length scale of approximately 1/10. Figure 6.1 presents the tank and the simulator, together with coordinates (x, y, z) and cardinal directions (N, S, E, W) in panel c. Per Figure 6.1b, the tank is composed of a square base plate and a cylindrical pipe served as a tank wall. The height of the tank, H_s, is 2 m and the

radius, R, is 0.76 m. The thickness of the tank wall, h, is 7.92 mm. The width of the square base plate is 2 m, and the thickness is 45 mm. A 76.2 mm-wide and 25.4 mm-thick flange is provided at the top of the tank. The tank is filled with fluid to a height, H, of 1.6 m.

(a) tank: view from the south

(b) tank containing water (dyed to green): view from the south and top

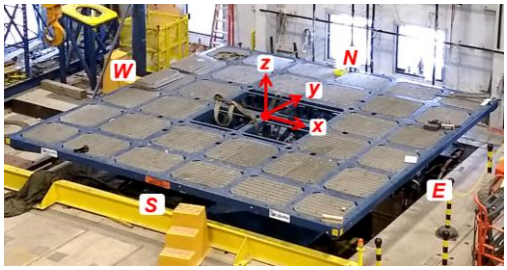

(c) earthquake simulator, coordinates (x, y, z) and cardinal directions (N, S, E, W)

Figure 6.1. Earthquake-simulator tests, base-supported steel tank filled with water: radius of 0.79 m, height of 2 m, wall thickness of 7.92 mm, and water height of 1.6 m

A two-phase program of experiments was performed: 1) Phase I involved the test tank, and 2) Phase II involved the tank sealed with a head, which supported central and off-center internal components immersed in the contained fluid (Mir et al. 2019; 2020a; 2020b)[51]. Two test setups (TSs) were used in Phase I: 1) TS-1, the base plate of the tank was directly attached to the earthquake simulator; and 2) TS-2, load cells were installed between the earthquake simulator and the base plate. These load cells were used to measure five degree-of-freedom reactions (i.e., three translational forces and two moments) at the base of the tank. Hydrodynamic pressures on the tank wall, reactions at the base, and wave heights generated using TS-2 data from Phase I are used herein for validation of numerical models. Test data generated using TS-1 is not used here because reactions were not measured. Test data from Phase II will be used in Mir (in progress) for validation of numerical models of a fluid-filled tank including internal components.

[51] Test data generated in Phases I and II support multiple purposes, including 1) validation of numerical models for a tank, which is presented in this report, 2) validation of numerical models for internal components (Mir, in progress), and 3) demonstration of the merits of seismic isolation for equipment in nuclear power plants. More information on the uses of the test data can be found in Mir et al. (2019, 2020a, 2020b).

The instrumentation used for TS-2 is presented in Figure 6.2, including pressure transducers, load cells, Temposonic gauges, and accelerometers. (The instrumentation for TS-1 was by-and-large identical to that for TS-2, but the load cells and the accelerometers on the base plate were not used for TS-1.) Figure 6.2a presents the names and locations of the pressure transducers, which are arranged at three different heights and in arrays of four: $+x$ (east), $-x$ (west), $+y$ (north), and $-y$ (south) faces of the tank wall. The transducers measure absolute pressures, including hydrostatic and hydrodynamic. Figure 6.2b presents the four load cells, named LNE, LNW, LSE and LSW, denoting their locations around the north-east, north-west, south-east, and south-west corners of the base plate, respectively. Each load cell is capable of measuring axial force, shear forces in two horizontal directions, and moments about two horizontal axes at its center. Figure 6.2c presents two Temposonic gauges, TE and TW, used to measure wave heights at distances of 51 mm (2.5") from the $+x$ (east) and $-x$ (west) faces of the tank wall. The design of the wave measurement consists of a float attached to a lightweight tube that is mounted onto the waveguide of a Temposonic gauge. A magnet is attached to the top of the tube. The Temposonic gauge records the vertical motion of the magnet, which is driven by the motion of the float. Figure 6.2d presents the names and locations of the accelerometers used to measure three-directional acceleration responses of the tank. The accelerometers on the tank wall are in arrays of four (i.e., east, west, north, and south faces of the wall) at the top and around the mid-height of the wall. The accelerometers on the base plate are located near the four corners and at the center. Each accelerometer measures motions in one direction, and so three accelerometers are used at each location shown using a triangle in Figure 6.2d to measure three-directional responses. Other instruments, including strain gauges on the tank wall and cameras supporting image processing for wave actions, are not used in this report and not presented here. More information on the arrangement and instrumentation can be found in Mir et al. (2019; 2020a; 2020b).

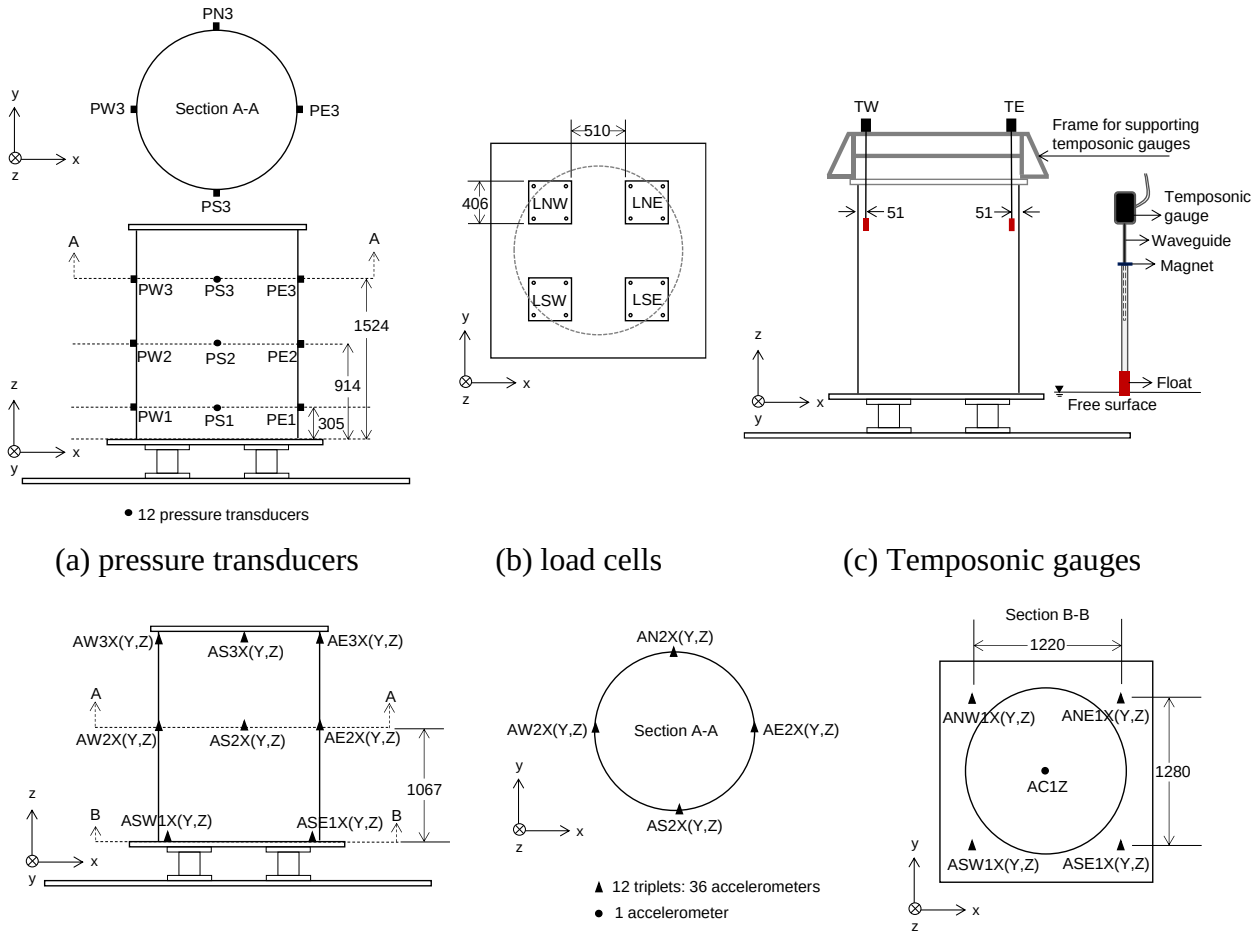

(a) pressure transducers (b) load cells (c) Temposonic gauges

(d) accelerometers

Figure 6.2. Instrumentation for the tank used in TS-2 and Phase I, unit: mm

Phase I of the earthquake-simulator tests involved 138 sets of input motions, including 68 sets for TS-1 and 70 sets for TS-2. The input motions include white noise, sine waves, and uni-, two-, and three-directional earthquake time series extracted from ground motion records. Consistent with a length scale of 1/10, the time scale of each earthquake motion is compressed by a factor of $\sqrt{10}$. A list of the input motions is presented in Appendix D.

Responses generated by motions #30, #35, and #42 listed in Table D.3 are used here for the validation, including 1) one horizontal component of the El Centro Earthquake (1940), 2) the two horizontal components of the Hualien Earthquake (2018), and 3) the three components of the Chi-Chi Earthquake (1999), termed hereafter ES-1, ES-2, and ES-3, respectively, where ES denotes earthquake-simulator inputs. They are five-second time series, extracted from the

earthquake records, after time compression by $\sqrt{10}$, but including their strong motions. Table 6.1 presents information on the three earthquake simulator (ES) inputs, and Figure 6.3 presents their time series after the time and amplitude scaling. Figure 6.4 presents acceleration response spectra for these time series calculated using a damping of 2% of critical. The peak ground accelerations (PGAs) of the x-components of ES-1, ES-2, and ES-3 are scaled to 1 g, 0.1 g, and 0.1 g, respectively: see the x-direction in Figure 6.1c and the columns of Direction and Scaled PGA (g) of Table 6.1. The y-component of ES-2 and the y- and z-components of ES-3 are scaled using the corresponding scale factors for their x-components. The scaling intensifies ES-1 and represents a strong motion, and diminishes ES-2 and ES-3 to prevent the overflow of the contained water due to waves: see the columns of Original PGA (g) and Scaled PGA (g) of Table 6.1.

Table 6.1. Input motion time series[1] used for earthquake-simulator tests

	Event	Year	Station	Direction[2]	Original PGA (g)	Scaled PGA (g)	Time scale
ES-1	El Centro Earthquake (Imperial Valley-02)	1940	El Centro Array #9	180 (x)	0.28	1.0	$1/\sqrt{10}$
ES-2	Hualien Earthquake	2018	HWA019	EW (x)	0.39	0.1	$1/\sqrt{10}$
				NS (y)	0.37	0.09	
ES-3	Chi-Chi Earthquake	1999	TCU052	EW (x)	0.36	0.1	$1/\sqrt{10}$
				NS (y)	0.45	0.13	
				Up (z)	0.19	0.06	

1. Ground motion records of the El Centro and Chi-Chi Earthquakes are extracted from the PEER Ground Motion Database (http://ngawest2.berkeley.edu/, accessed on March 18, 2019), and those of the Hualien Earthquake are provided by the National Center for Research on Earthquake Engineering, Taiwan
2. Directions based on the coordinates described in the dataset of the ground motion records; x, y, and z shown in the parentheses representing the input directions of the earthquake simulator (see Figure 6.1c)

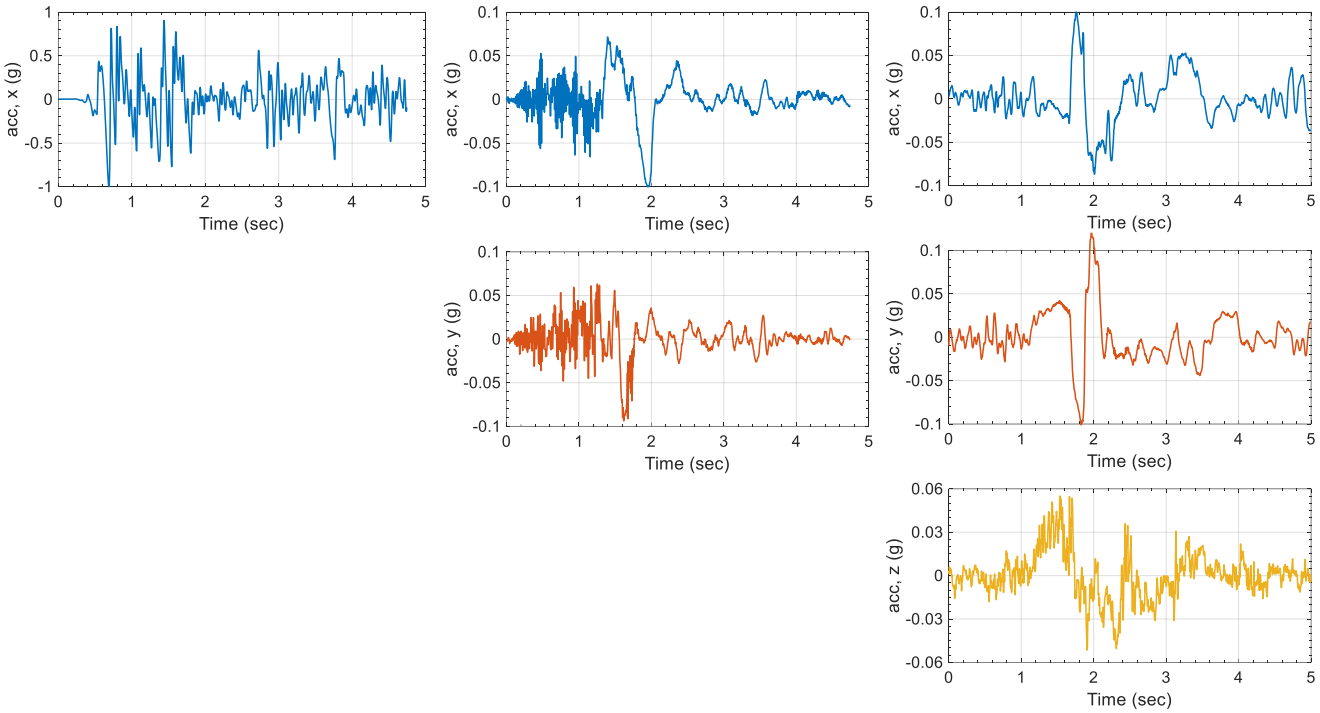

(a) ES-1 (b) ES-2 (c) ES-3

Figure 6.3. Time series for earthquake simulator inputs, PGA scaled to the values presented in Table 6.1, time scale compressed by $\sqrt{10}$.

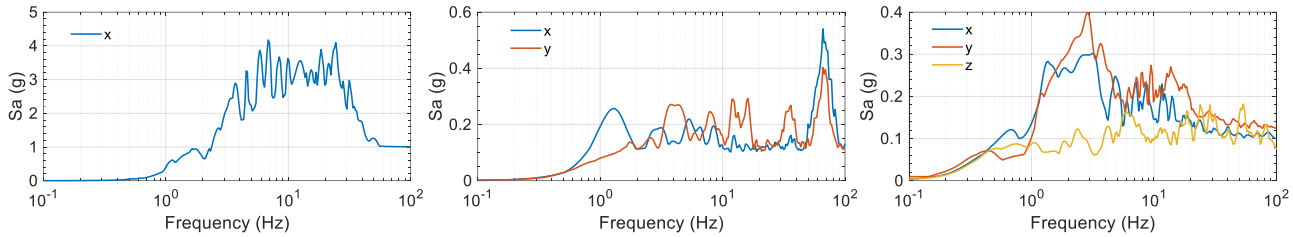

(a) ES-1 (b) ES-2 (c) ES-3

Figure 6.4. Acceleration response spectra of the amplitude- and time-scaled motions shown in Figure 6.3, damping ratio of 2%

6.3 Numerical models

Numerical models for the ALE and ICFD solvers are constructed for the test tank shown in Figures 6.1a and b. The tank is composed of a square base plate and a cylindrical pipe served as a tank wall. The dimensions of the wall (i.e., pipe) are $H_s = 2$ m, $R = 0.76$ m, and $h = 7.92$ mm. The width of the square base plate is 2 m, and the thickness is 45 mm. The tank is filled with tap water to a height of $H = 1.6$ m. The flange at the top of the tank and the four load cells, which supports the tank on the earthquake simulator, are not included in the models. The ALE and

ICFD models presented here are modified from those partially verified in Section 4, with improvement in the accuracy of calculating or outputting wave heights.

Figure 6.5 presents the ALE model for the test tank and global coordinates (x, y, z). Figure 6.5a shows the elements of the tank wall (blue) and the base plate (red). Figure 6.5b shows the elements of the fluid domain: water (yellow) topped by a vacuum space (grey). Air is not included in the model. The sizes of the elements shown in Figures 6.5a and b are optimized, resulting in smaller elements for the fluid domain adjacent to the tank wall and around the boundary between the water and the vacuum (i.e., free surface). The tank wall and the base plate are modeled using 3360 and 2748 Lagrangian, four-node, shell elements, respectively. The water and the vacuum are modeled using 63360 and 17280 Eulerian, eight-node, solid elements, respectively. The tank and the fluid domain (including the water and vacuum) share nodes at their interfaces. Figure 6.5c presents the water in the tank at the first step of the analysis (i.e., time $t = 0$). One hundred twenty-four floating points (black dots in Figure 6.5c) are used to track waves and located on or near the free surface, along the x direction, and near the $\pm x$ faces of the tank wall. There are sixty-two points assigned around each side and placed in two layers (i.e., 31 points in each layer), as shown in the magnified view of a part of the fluid and floating points in Figure 6.5c. The two layers are located on or 10 mm below the free surface. Since the two layers are very close to each other, wave heights output using points in both layers are expected to be identical or similar. The floating points span $x = R$ (0.76 m) to 0.62 m and -0.62 m to -0.76 m, and cover the measuring locations of the Temposonic gauges TE and TW, which are 51 mm away from the $\pm x$ faces of the wall (see Figure 6.2c). The dense distribution and double-layer arrangement of these floating points in the ALE model mitigate the issues presented in Appendix C and improves the predictions for wave heights. Results are presented and discussed in Sections 6.5.3 and 6.5.4.

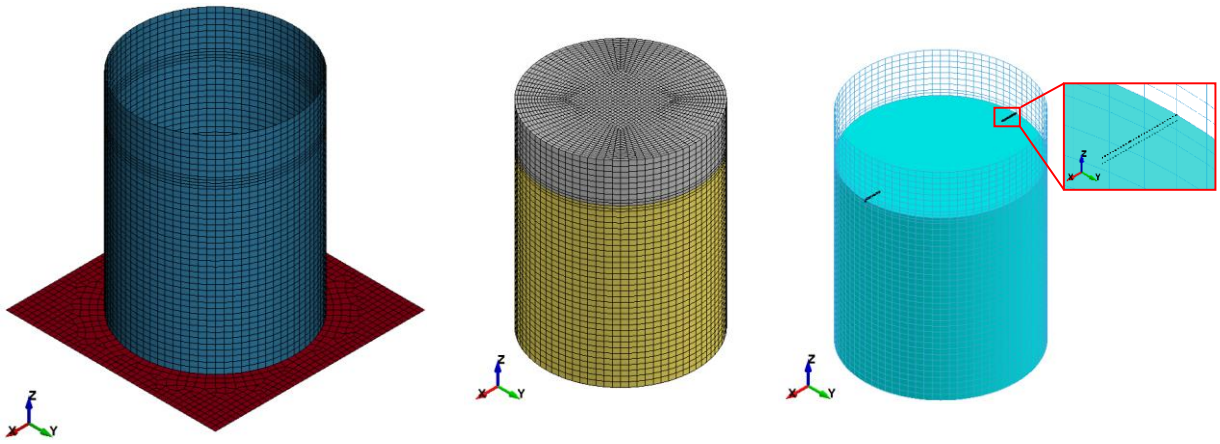

(a) tank wall and base plate (b) water and vacuum (c) water in the tank, floating points, $t = 0$

Figure 6.5. ALE model of the test tank with $R = 0.76$ m, $H_s = 2$ m, and $H = 1.6$ m, isometric view

Figure 6.6 presents the ICFD model for the test tank and global coordinates (x, y, z). Figure 6.6a shows the elements of the tank wall (blue) and the base plate (red), identical to those used for the ALE model shown in Figure 6.6a. Figure 6.6b presents a half domain for the fluid, which is defined using three surfaces: 1) adjacent to the tank base (shown in pink), 2) adjacent to the tank wall (shown in yellow), and 3) horizontally closing the top of the domain (shown in grey). The height of the fluid domain is 1.8 m, providing a sufficient freeboard of 0.2 m to prevent overtopping by waves. (The vertical displacement of the free surface in the tank is less than 0.2 m; see results presented in Figures 6.26 to 6.28.) As presented in Figure 6.6b, a finer fluid mesh is used along the x and y directions across the diameter of the grey surface and in the top 0.4 m of the yellow surface, where wave actions are expected to be relatively significant. The tank wall and the base plate are modeled using 3360 and 2748 Lagrangian, four-node, shell elements, respectively. The fluid surfaces are modeled using 13840 Lagrangian, three/four-node, shell elements. The tank and the fluid surfaces do not share nodes at their interfaces. The interaction between the tank and water is activated by the *ICFD_BOUNDARY_FSI card in the LS-DYNA deck.

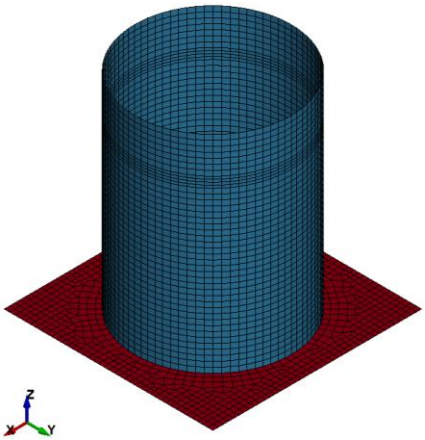

(a) tank

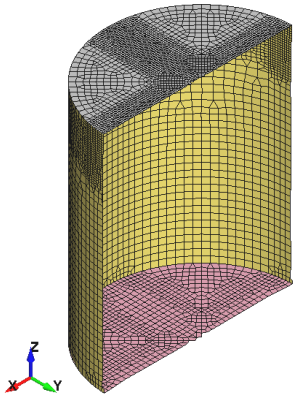

(b) surfaces for a half fluid domain with a height of 1.8 m

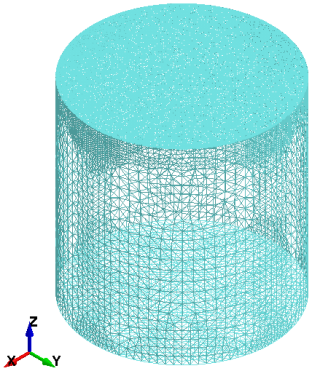

(c) water, $t = 0$

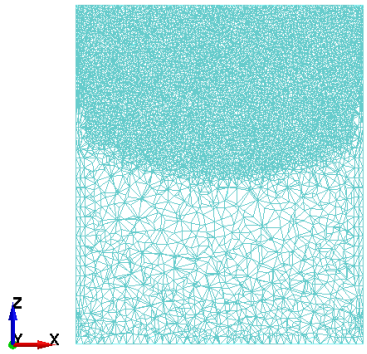

(d) fluid domain, $t = 0$, $x - z$ cross section

Figure 6.6. ICFD model of the test tank with $R = 0.76$ m, $H_s = 2$ m, and $H = 1.6$ m

The elements of the fluid enclosed by the three surfaces in Figure 6.6b are automatically generated by the ICFD solver at the first step of the analysis (i.e., $t = 0$). The initial height of the free surface, $H = 1.6$ m, is defined using the *ICFD_INITIAL_LEVELSET card. Figure 6.6c presents the model of the water, constructed using four-node solid elements. The *MESH_BL and *MESH_SIZE_SHAPE cards are used to generate finer elements adjacent to the tank wall and around the free surface, respectively, as shown in a $x - z$ cross section of the fluid domain of Figure 6.6d. A finer mesh around the free surface is expected to improve the ICFD predictions of wave height.

The elements of the tank wall and the base plate are assigned elastic and rigid materials, respectively, with mechanical properties consistent with carbon steel, including a density ρ_s of

7880 kg/m^3, an elastic modulus E_s of 2×10^{11} N/m^2, and Poisson's ratio υ_s of 0.27. (The values of E_s and υ_s do not affect the responses of the rigid base but must be defined in the models.) A damping ratio of 2% is assigned to the elements of the wall for a frequency range of 20 to 300 Hz using the *DAMPING_FREQUENCY_RANGE_DEFORM card. (Since the flexibility of the base plate is not considered in the numerical model, test data associated with the frequency of the out-of-phase deformation (i.e., vertical motion) of the plate are removed using a filter, to enable comparison of numerical and test results. More information is presented in Sections 6.4 and 6.5.)

The mechanical properties consistent with water at 25°C are used for the elements of the water in the numerical models. A density ρ_w of 1000 kg/m^3, a viscosity μ_w of 10^{-3} N/m^2-s, and a bulk modulus, K_w, of 2.15×10^9 N/m^2 are assigned to the water elements in the ALE model (shown in yellow in Figure 6.5b). Identical values of ρ_w and μ_w are used for the elements of the fluid surfaces adjacent to the tank wall and base plate in the ICFD model (shown in yellow and pink in Figure 6.6b), but the bulk modulus is not used because the solver can accommodate only an incompressible fluid. The elements of the vacuum space in the ALE model shown as grey in Figure 6.5b are assigned void properties through the *INITIAL_VOID card. The elements of the top surface of the fluid domain in the ICFD model, shown as grey in Figure 6.6b, are assigned *vacuum properties* with zero density and viscosity (i.e., $\rho_a = 0$ and $\mu_a = 0$).

The mechanical properties assigned to the elements in the numerical models of the tank, water, and vacuum are listed in Table 6.2. The masses of the numerical models are listed in Table 6.3, and the total mass is 4929 kg. The gravitational acceleration g of 9.81 m/s^2 is assigned to the z direction.

Table 6.2. Mechanical properties assigned to the elements of the tank, water, and vacuum, ALE and ICFD models

		ALE	ICFD
Tank	Density, ρ_s	7880 kg/m^3	
	Elastic modulus, E_s	2×10^{11} N/m^2	
	Poisson's ratio, υ_s	0.27	
Water	Density, ρ_w	1000 kg/m^3	
	Viscosity, μ_w	10^{-3} N/m^2-s	
	Bulk modulus, K_w	2.15×10^9 N/m^2	--[1]
Vacuum	Density, ρ_a	--[2]	0
	Viscosity, μ_a		0

1. The ICFD solver analyzes only incompressible fluids, and so K_w is not used in the models.
2. The vacuum in the ALE model is assigned void properties through the *INITIAL_VOID card.

Table 6.3. Masses of the tank wall, base plate, and water, ALE and ICFD models

Component	Mass (kg)
Tank wall	593
Base plate	1418
Water	2918
Total	4929

6.4 Input motions for numerical models

Accelerations of the base plate measured in the experiments are used as input motions for the response-history analysis of the numerical models. As shown in Figure 6.2d, twelve accelerometers are placed around the four corners of the base plate. Each triangle in the figure indicates three accelerometers that measure respective motions in the x, y, and z directions, based on the coordinates shown in Figure 6.1c. The twelve accelerometers on the plate are denoted as $ANE1X(Y,Z)$, $ANW1X(Y,Z)$, $ASE1X(Y,Z)$, and $ASW1X(Y,Z)$, in which the X, Y, and Z indicate the directions of the measurement. Earthquake simulator inputs used for the

experiments, as presented in Figure 6.3, are not directly used for the numerical models because the four load cells supporting the test tank on the simulator are neither rigid nor included in the models. The four load cells introduced flexibility at the base in the tests, and rocking motions were observed for horizontal excitations. An earthquake simulator input in the x (y) direction generated a translational motion in the x (y) direction and a rocking motion about the y (x) axis on the base plate. An earthquake simulator input in the z direction generated a translational motion in the z direction and out-of-phase (vertical) deformation on the base plate. The base plate is assumed to be rigid in the numerical models, and the out-of-phase deformation is not included in the analysis. To enable comparisons of numerical and test results, the measured accelerations associated with the frequency of the out-of-phase deformation of 37 Hz[52] is removed. A band-stop filter designed for 32 to 42 Hz is used to process the base plate acceleration data. A MATLAB script, OpenSeismoMatlab (Papazafeiropoulos and Plevris 2018), is used to correct the baseline of the accelerations of the base plate generated in the tests to avoid unrealistic and significant displacements due to measuring errors. The translational and rocking motions are derived using the filtered and baseline corrected accelerations, and are used as input time series at the center of the rigid base plate in the numerical models.

Figure 6.7 presents the calculation of the input motions for the numerical models, including three translational components, x, y, and z, and two rocking components, rx and ry, together with coordinates (x, y, z) and cardinal directions (N, S, E, W). The black square in each panel is the plan view of the base plate, and the back solid circles are accelerometers located around the four corners. The red arrows and text represent the accelerations measured by the accelerometers, and the blue arrows and text represent the accelerations used as inputs for the numerical models. As shown in Figure 6.7a, the x-component input motion for the numerical models, acc_x, is derived using the average accelerations measured by $ANE1X$, $ANW1X$, $ASE1X$, and $ASW1X$. Identically, acc_y (acc_z) is derived using the average accelerations measured by $ANE1Y$ (Z), $ANW1Y$ (Z), $ASE1Y$ (Z), and $ASW1Y$ (Z), as shown in Figure 6.7b (c).

[52] The empty tank was tested using white noise in the vertical direction, and the vertical motion at the center of the base plate was measured using $AC1Z$ shown in Figure 6.1d. The Fourier amplitude spectrum of the motion shows a peak at 58 Hz, which is the frequency of the out-of-phase motion of the base plate, f_{out}, when the tank is empty. Considering that f_{out} is proportional to $1/\sqrt{m}$ ($m = 2011$ kg, if empty, and 4929 kg, if $H = 1.6$ m; see Table 4.6), the value of f_{out} involving the tank with a water depth of 1.6 m is expected to be 37 Hz.

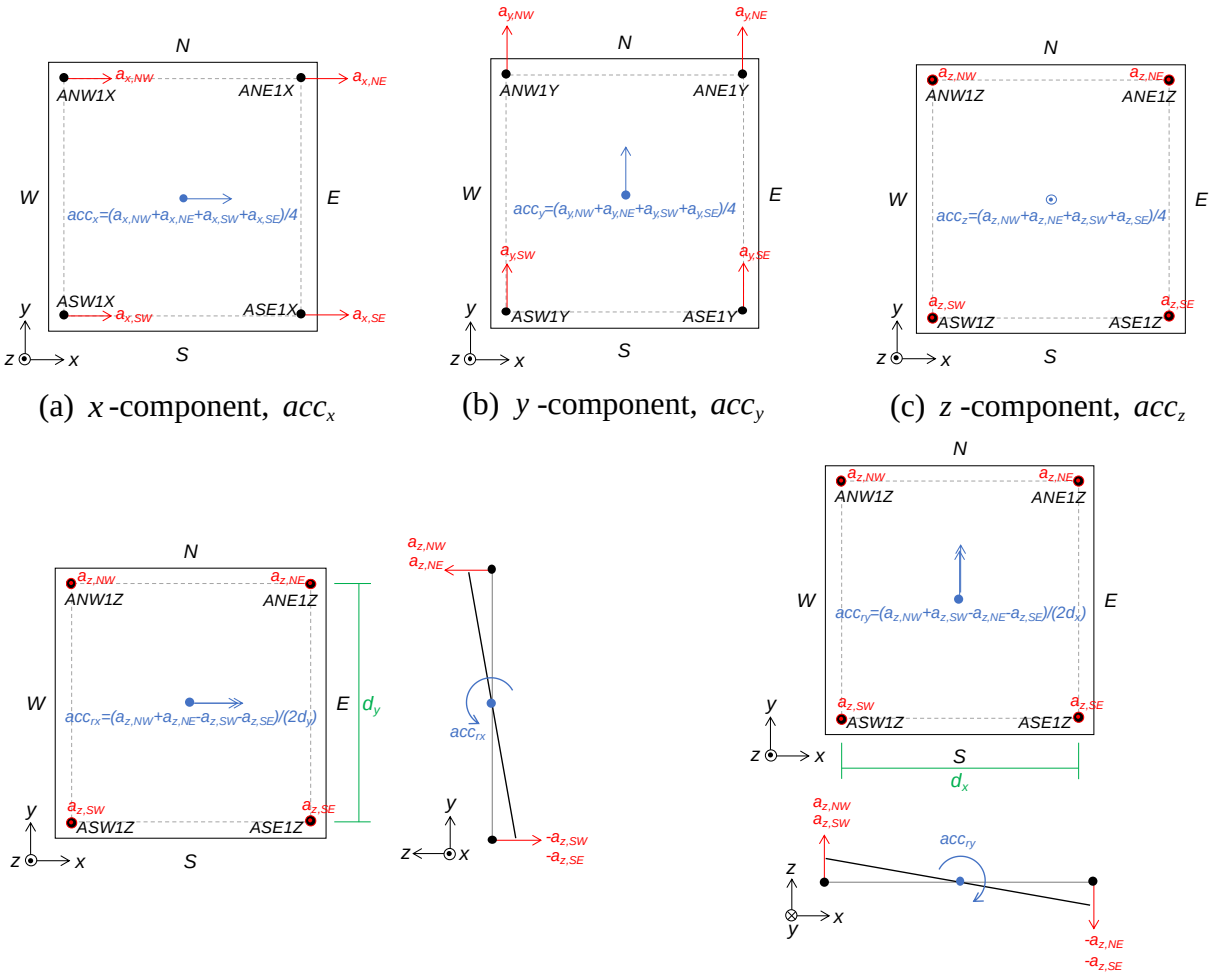

(a) x-component, acc_x (b) y-component, acc_y (c) z-component, acc_z

(d) rx-component, acc_{rx} (e) ry-component, acc_{ry}

Figure 6.7. Motions at the center of the rigid base plate used in the numerical models, three translational and two rocking components, calculated using accelerations measured around the four corners

Figures 6.7d and e present the rocking motions about the x and y axes, respectively, both of which are derived using the accelerations in the z direction measured by $ANE1Z$, $ANW1Z$, $ASE1Z$, and $ASW1Z$. Assuming that the base plate is rigid, per Figure 6.7d, the $x-$directional rocking motion is calculated using the sum of the *relative* vertical accelerations on the north face ($ANE1Z$, $ANW1Z$), with respect to those on the south face ($ASE1Z$, $ASW1Z$), divided by twice the distance between the sets of accelerometers in the y direction (d_y). Similarly, per Figure 6.7e, the $y-$directional rocking motion is calculated using the sum of the relative vertical accelerations on the west face ($ANW1Z$, $ASW1Z$), with respect to those on the east face

($ANE1Z$, $ASE1Z$), divided by twice the distance between the sets of accelerometers in the x direction (d_x).

Three sets of multi-directional time series, NM-1, NM-2, and NM-3, are used for analysis of the numerical models. These motions are derived using accelerometer data on the base plate per Figure 6.7 for input motions ES-1, E-2, and ES-3, presented in Figure 6.3. (The "NM" denotes numerical-model inputs whereas "ES" denotes earthquake-simulator inputs.) Table 6.4 presents information for the numerical model inputs, NM-1, NM-2, NM-3, and their associated earthquake simulator inputs, ES-1, ES-2, and ES-3, respectively. Figure 6.8 presents the time series of NM-1, NM-2, and NM-3, including the three translational components, x , y , z , and two rocking components, rx , ry . Figure 6.9 presents acceleration response spectra for these time series, calculated using a damping of 2% of critical.

Table 6.4. Input motion time series used for the numerical models and their associated earthquake simulator inputs used in the experiments

Numerical model inputs at the rigid base plate	Direction[1]	Earthquake simulator inputs[2]
NM-1	x , ry	ES-1: El Centro Earthquake, x
NM-2	x , y , rx , ry	ES-2: Hualien Earthquake, x , y
NM-3	x , y , z , rx , ry	ES-3: Chi-Chi Earthquake, x , y , z

1. Directions are based on the coordinates used for the numerical models (Figures 6.5 and 6.6) and the earthquake simulator (Figure 6.1)
2. More information presented in Table 6.1

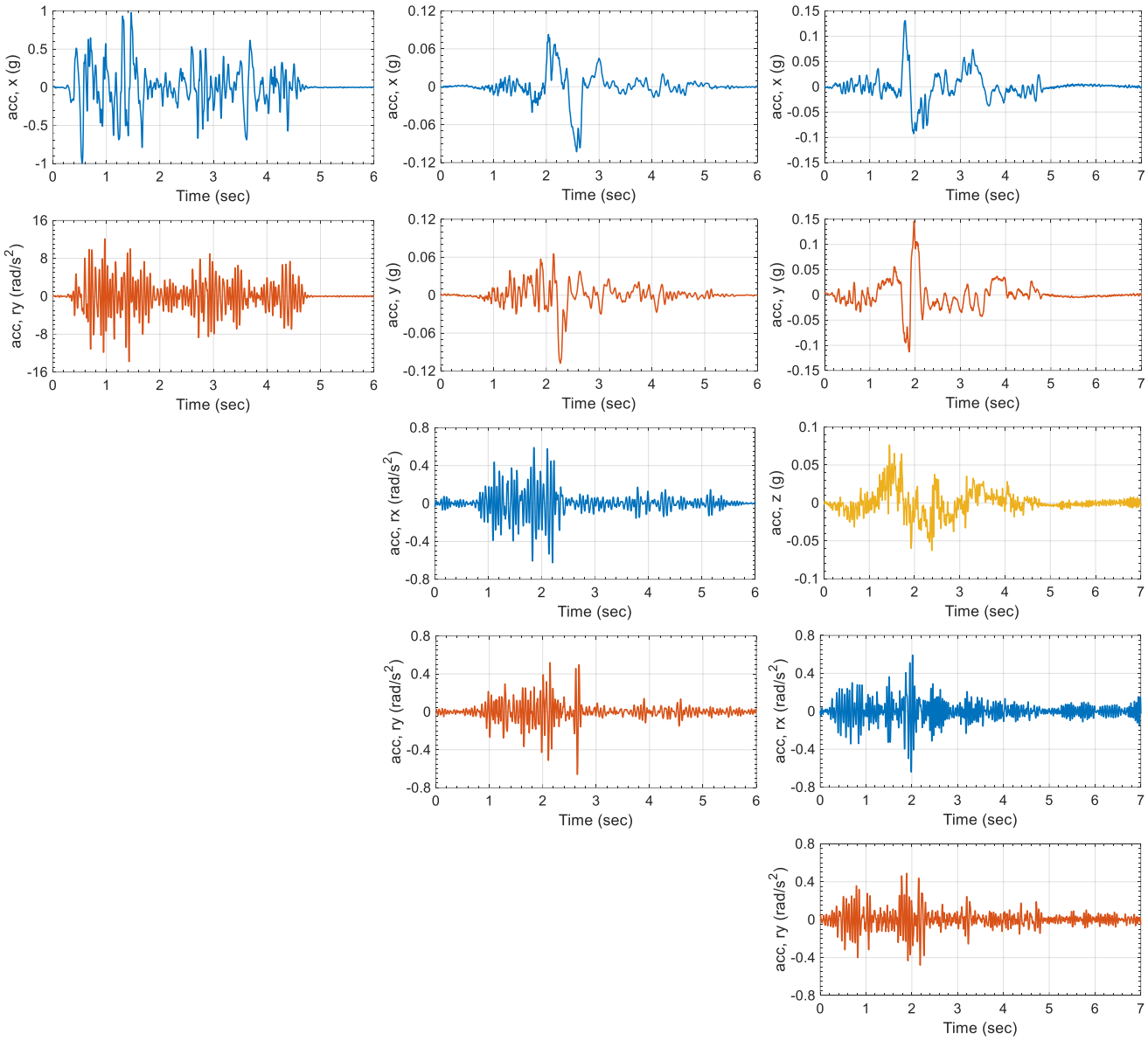

(a) NM-1 (b) NM-2 (c) NM-3

Figure 6.8. Input motion time series for numerical models, derived using filtered and baseline corrected motions of the base plate measured using the twelve accelerometers

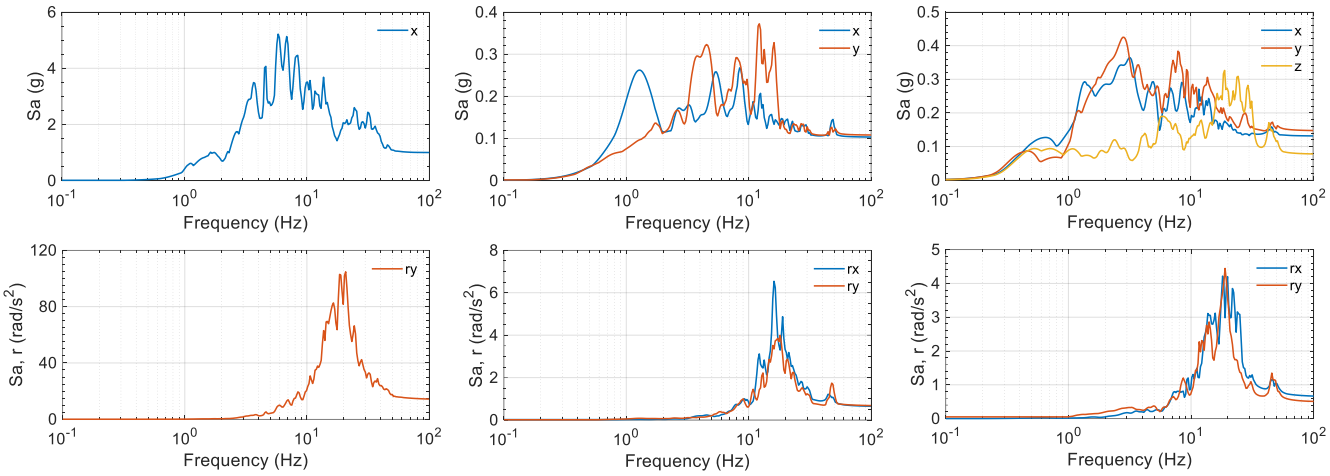

(a) NM-1 (b) NM-2 (c) NM-3

Figure 6.9. Acceleration response spectra of the input motion time series shown in Figure 6.8, damping ratio of 2%

6.5 Results and validation

Fluid-structure responses calculated using the numerical models for inputs NM-1, NM-2, and NM-3 are compared with those measured in the earthquake-simulator tests for ES-1, ES-2, and ES-3. (See the relationships of input motions NM and ES in Table 6.4.) The reported responses include hydrodynamic pressures on the tank wall, forces and the moments at the tank base, and wave heights of the contained water. Again, the base plate is assumed to be rigid in the models, and a band-stop filter is used to remove motion associated with the out-of-phase deformation of the plate (see footnote 52 on page 197), in the frequency range between 32 and 42 Hz.

6.5.1 Hydrodynamic pressure

The hydrodynamic pressures on the tank wall, p_w, measured by the twelve pressure transducers $PN1(2,3)$, $PS1(2,3)$, $PE1(2,3)$, and $PW1(2,3)$ shown in Figure 6.2a are presented with those calculated using the numerical models in Figures 6.10 to 6.15. Figures 6.10 to 6.12 enable a comparison of the ALE results for NM-1, NM-2, and NM-3 and the test results for ES-1, ES-2, and ES-2, respectively. Figures 6.13 to 6.15 present companion data for the ICFD model. Since NM-1 (ES-1) does not include a y-component motion, responses along the y axis are tiny. Consequently, the pressures for NM-1 on the $\pm y$ faces of the tank wall at the locations of $PN1(2,3)$ and $PS1(2,3)$ are not presented in Figures 6.10 and 6.13.

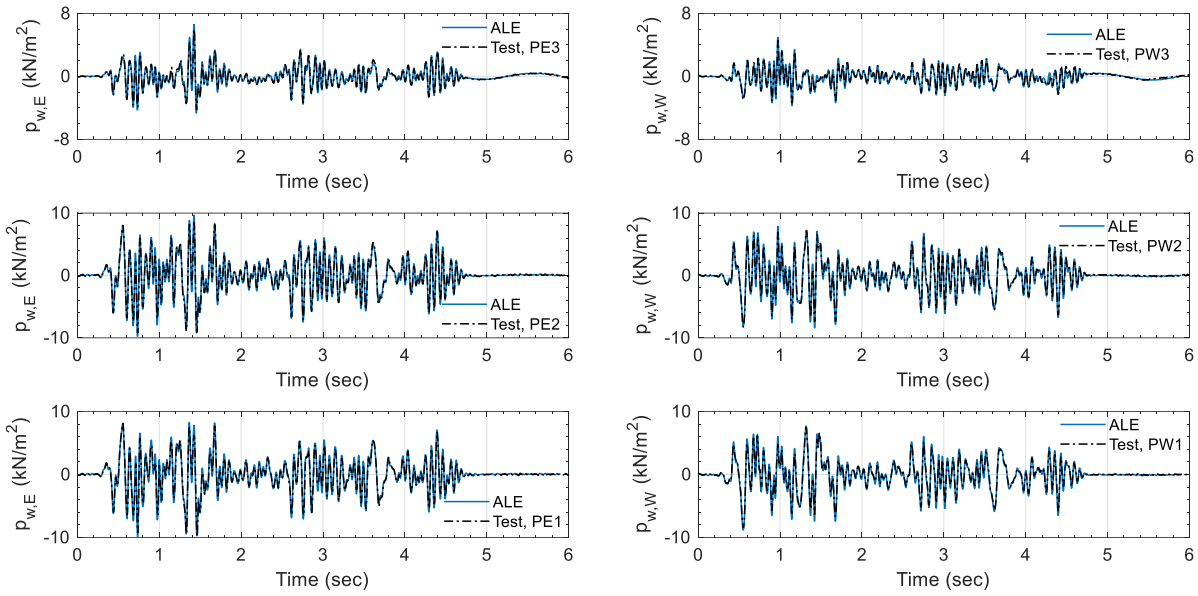

(a) East face (b) West face

Figure 6.10. Time series of hydrodynamic pressure of the tank wall, ALE model for NM-1 and earthquake-simulator test for ES-1

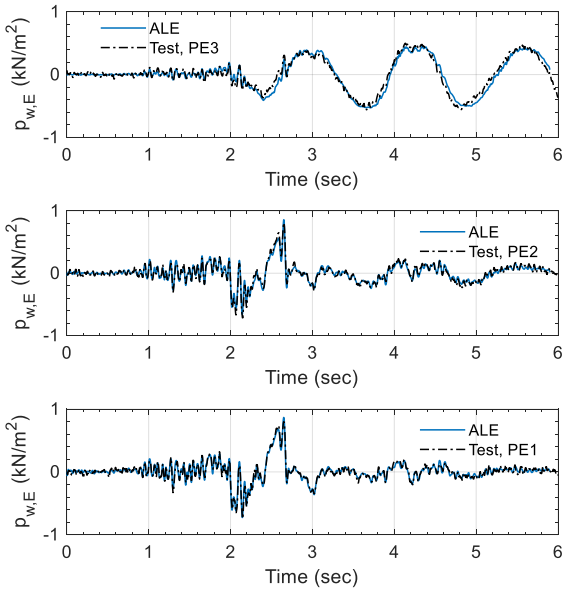

(a) East face

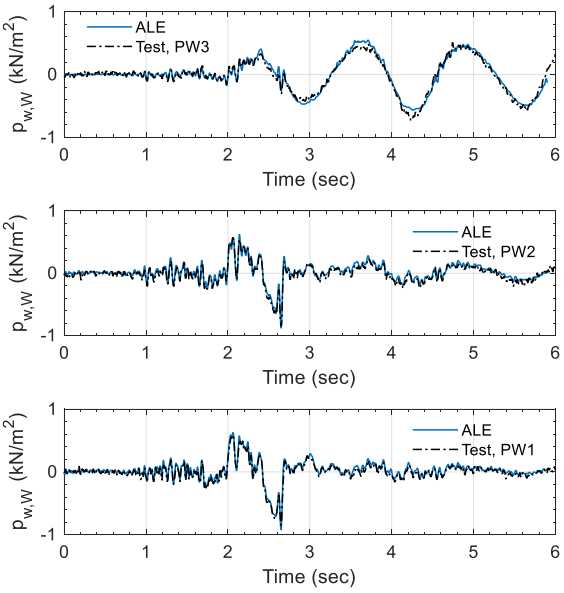

(b) West face

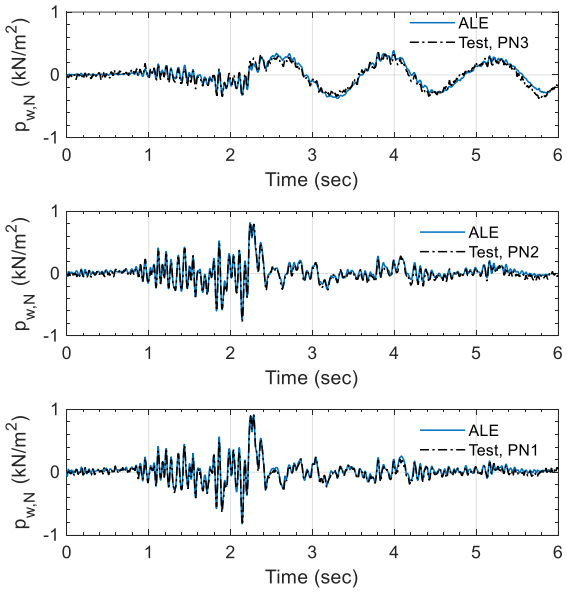

(c) North face

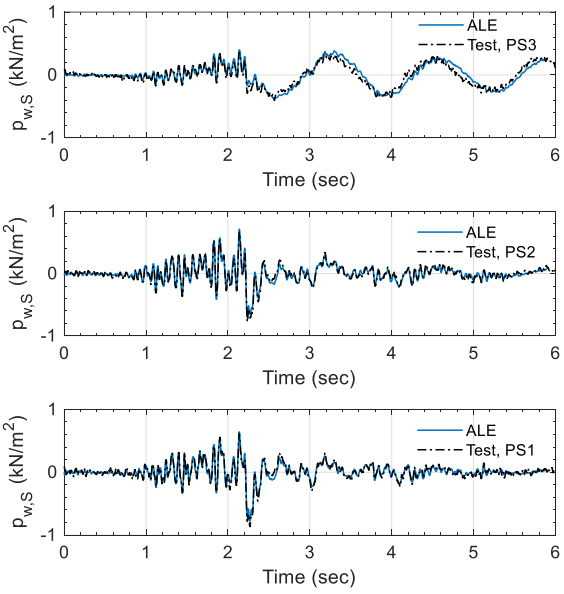

(d) South face

Figure 6.11. Time series of hydrodynamic pressure of the tank wall, ALE model for NM-2 and earthquake-simulator test for ES-2

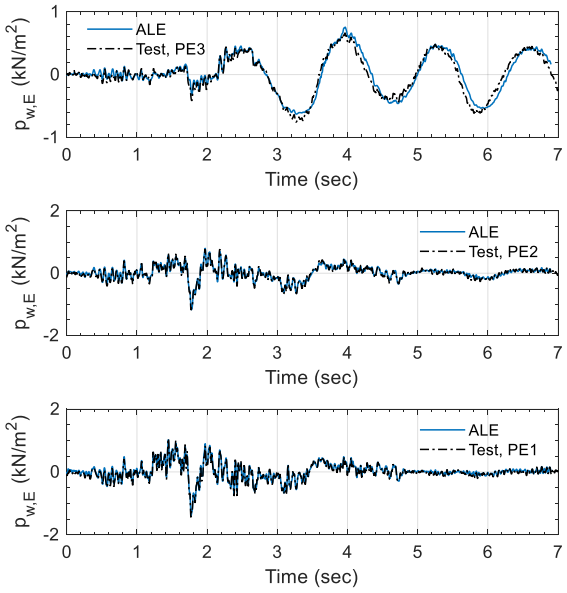

(a) East face

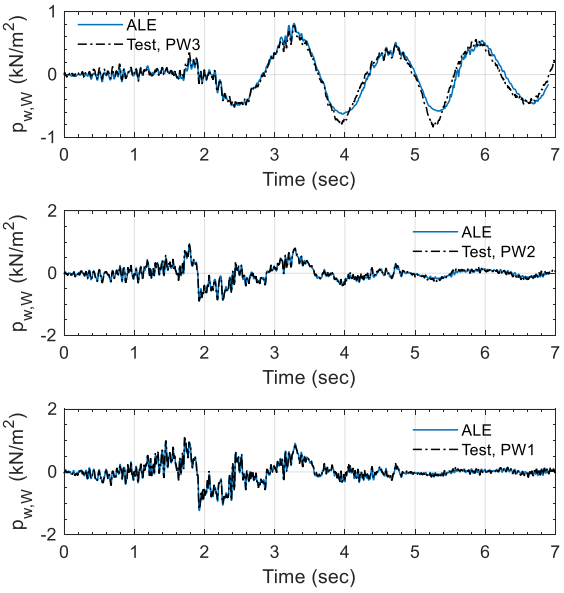

(b) West face

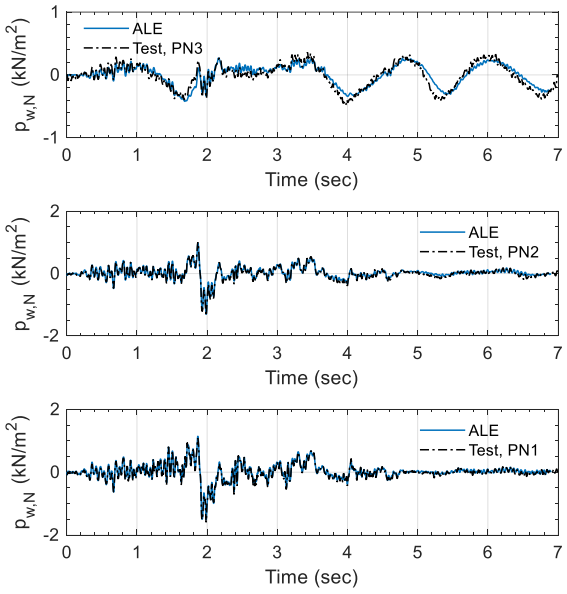

(c) North face

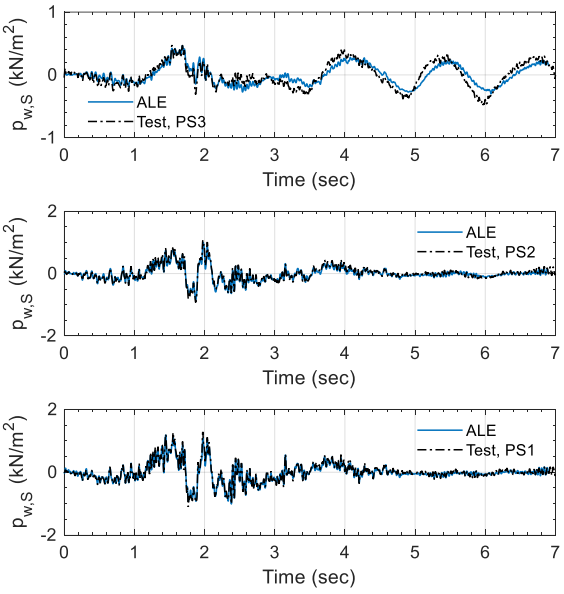

(d) South face

Figure 6.12. Time series of hydrodynamic pressure of the tank wall, ALE model for NM-3 and earthquake-simulator test for ES-3

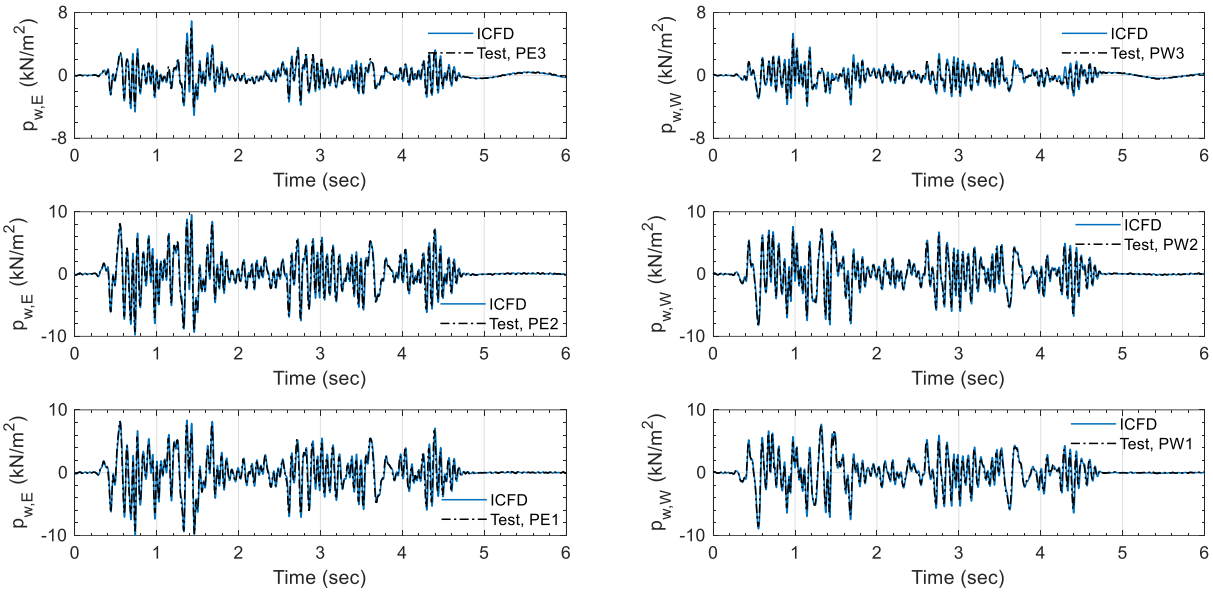

(a) East face (b) West face

Figure 6.13. Time series of hydrodynamic pressure of the tank wall, ICFD model for NM-1 and earthquake-simulator test for ES-1

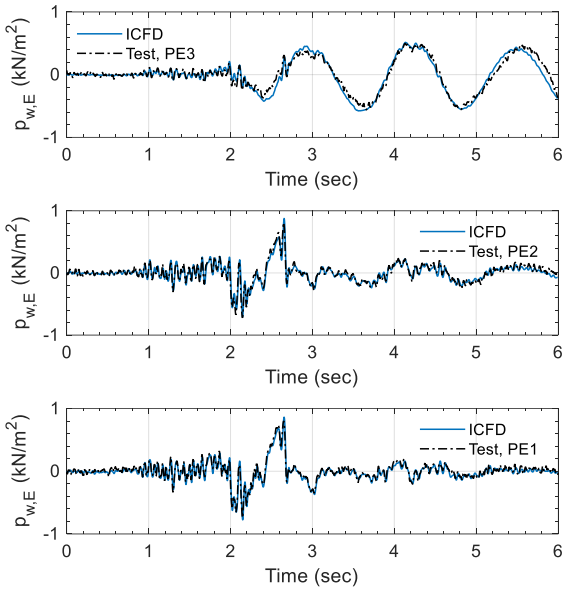

(a) East face

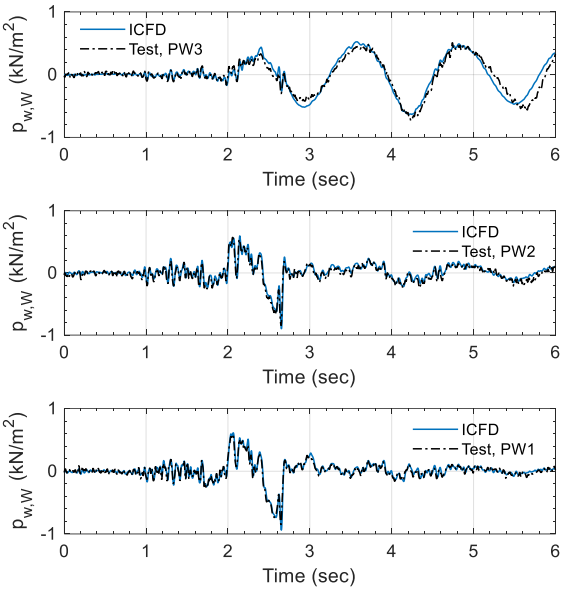

(b) West face

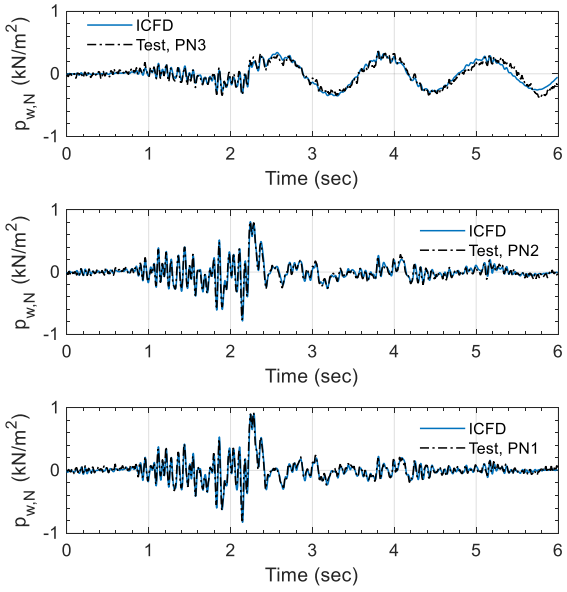

(c) North face

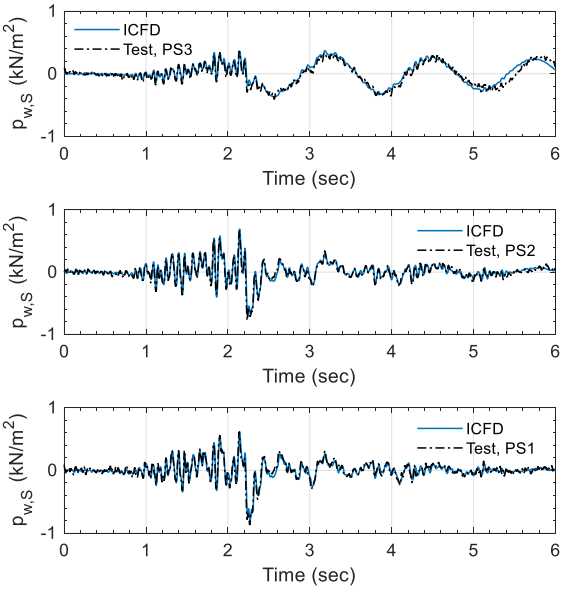

(d) South face

Figure 6.14. Time series of hydrodynamic pressure of the tank wall, ICFD model for NM-2 and earthquake-simulator test for ES-2

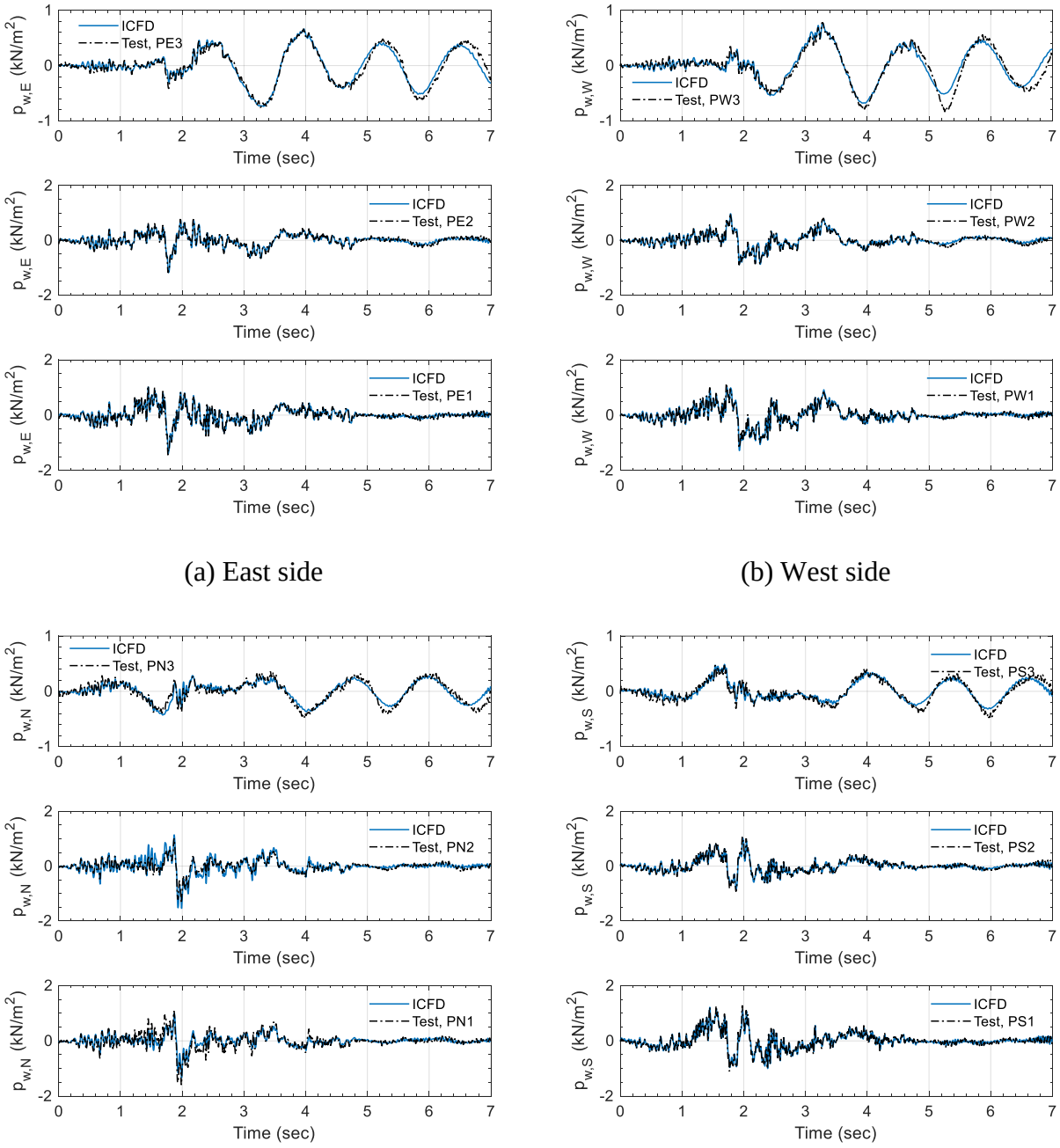

(a) East side

(b) West side

(c) North side

(d) South side

Figure 6.15. Time series of hydrodynamic pressure of the tank wall, ICFD model for NM-3 and earthquake-simulator test for ES-3

6.5.2 Reactions: shear force and moment at the base

The reactions at the base of the tank calculated using the numerical models and measured in the tests are presented in Figures 6.16 to 6.21. The reactions include translational forces in the x, y, and z directions (i.e., F_x, F_y, and F_z) and moments with respect to the x and y axes (i.e., M_x and M_y). Test results for these reactions are derived using output data from the load cells, LNE, LNW, LSE and LSW, shown in Figure 6.2b. The output data of each load cell include x- and y- directional shear forces, an axial (z- directional) force, and x- and y-axis moments, with respect to the center of the load cell (i.e., level of its mid-height). Notations for the output data of the four load cells are: 1) $F_{LNE,x}$, $F_{LNW,x}$, $F_{LSE,x}$, and $F_{LSW,x}$ for x-directional forces, 2) $F_{LNE,y}$, $F_{LNW,y}$, $F_{LSE,y}$, and $F_{LSW,y}$ for y-directional forces, 3) $F_{LNE,z}$, $F_{LNW,z}$, $F_{LSE,z}$, and $F_{LSW,z}$ for axial forces, 4) $M_{LNE,x}$, $M_{LNW,x}$, $M_{LSE,x}$, and $M_{LSW,x}$ for x-axis moments, and 5) $M_{LNE,y}$, $M_{LNW,y}$, $M_{LSE,y}$, and $M_{LSW,y}$ for y-axis moments. The reaction forces F_x, F_y, and F_z at the tank base are the summations of the force data output by the load cells in the given directions, $\sum_{i=1}^{4} F_{L_i,x}$, $\sum_{i=1}^{4} F_{L_i,y}$, and $\sum_{i=1}^{4} F_{L_i,z}$, respectively, where $L_1 = LNE$, $L_2 = LNW$, $L_3 = LSE$, and $L_4 = LSW$. The reaction moments, M_x and M_y, at the tank base are derived using load cell data for moments (at the mid-height of each the load cell), shear forces, and axial forces, as indicated in Figure 6.22. Figure 6.22a presents a plan view of the base plate (which is the tank base here), the four load cells, and the reaction moments, M_x and M_y, at the center of the base (shown in blue), together with coordinates (x, y, z) and cardinal directions (N, S, E, W). Figures 6.22b and c present sections N-S and E-W, respectively, and forces and moments (shown in black) at the interface of the base plate and the four load cells. On section N-S, per the black arrows and text in Figure 6.22b, there are axial forces $F_{N,z}$ and $F_{S,z}$, shear forces $F_{N,y}$ and $F_{S,y}$, and moments $M_{N,x}$ and $M_{S,x}$ on the top of the load cells on the north (LNE and LNW) and the south (LSE and LSW). The reaction M_x at the tank base (shown in blue in Figure 6.22b) relates to the moments and axial forces at the interface (shown in black in Figure 6.22b) as the following:

$$M_x = (M_{N,x} + M_{S,x}) + (F_{N,z} - F_{S,z}) \cdot (d_y / 2) \tag{6.1}$$

where d_y is the distance between the centers of two load cells in the y direction (0.91 m; shown in green), $F_{N,z} = F_{LNE,z} + F_{LNW,z}$, and $F_{S,z} = F_{LSE,z} + F_{LSW,z}$. The shear forces and moments at the interface (black solid circles in Figure 6.22b) are transferred to and create a moment at the center of each load cell (red solid circle). Load-cell data for the x-axis moments, $M_{LNE,x}$, $M_{LNW,x}$, $M_{LSE,x}$, and $M_{LSW,x}$, are output with respect to the centers. Equation (6.2) presents the relationship between the summation of the load cell data for the x-axis moments (with respect to the red solid circles) and the moments and shear forces at the interface (black solid circles) shown on section N-S of Figure 6.22b.

$$M_{LNE,x} + M_{LNW,x} + M_{LSE,x} + M_{LSW,x} = \sum_{i=1}^{4} M_{L_i,x} = (M_{N,x} + M_{S,x}) - (F_{N,y} + F_{S,y}) \cdot (h_z / 2) \qquad (6.2)$$

where h_z is the height of the load cells (0.35 m; shown in orange), and $(F_{N,y} + F_{S,y})$ is equal to the reaction force $F_y = \sum_{i=1}^{4} F_{L_i,y}$ at the tank base.

Given Eqs. (6.1) and (6.2), the moment about the x axis at the tank base, M_x, is a function of the load-cell outputs:

$$M_x = \sum_{i=1}^{4} M_{L_i,x} + \sum_{i=1}^{4} F_{L_i,y} \cdot (h_z / 2) + (F_{LNE,z} + F_{LNW,z} - F_{LSE,z} - F_{LSW,z}) \cdot (d_y / 2) \qquad (6.3)$$

where $L_1 = LNE$, $L_2 = LNW$, $L_3 = LSE$, and $L_4 = LSW$. Similarly, M_y at the tank base (shown in blue in Figure 6.22a) relates to the moments and axial forces at the interface shown in the cross section E-W of Figure 6.22c (black solid circles) as the following:

$$M_y = (M_{E,y} + M_{W,y}) + (F_{W,z} - F_{E,z}) \cdot (d_x / 2) \qquad (6.4)$$

where d_x is the distance between the centers of two load cells in the x direction (0.91 m; marked as green), $F_{W,z} = F_{LNW,z} + F_{LSW,z}$, and $F_{E,z} = F_{LNE,z} + F_{LSE,z}$. The shear forces and moments at the interface (black solid circles in Figure 6.22c) are transformed to the center of each load cell (red solid circle), and data for the y-axis moment are output with respect to the centers:

$$M_{LNE,y} + M_{LNW,y} + M_{LSE,y} + M_{LSW,y} = \sum_{i=1}^{4} M_{L_i,y} = (M_{E,y} + M_{W,y}) + (F_{E,x} + F_{W,x}) \cdot (h_z / 2) \qquad (6.5)$$

where $(F_{E,x}+F_{W,x})$ is equal to the reaction force $F_x=\sum_{i=1}^{4}F_{L_i,x}$ at the tank base. Given Eqs. (6.4) and (6.5), the moment about the y axis at the tank base, M_y, relates to the load cell data as the following:

$$M_y=\sum_{i=1}^{4}M_{L_i,y}-\sum_{i=1}^{4}F_{L_i,x}\cdot(h_z/2)+(F_{LNW,z}+F_{LSW,z}-F_{LNE,z}-F_{LSE,z})\cdot(d_x/2) \tag{6.6}$$

Figures 6.16 to 6.18 enable comparison of ALE results for NM-1, NM-2, and NM-3 and test data for ES-1, ES-2, and ES-3, respectively. Figures 6.19 to 6.21 present companion data for the ICFD model. Since NM-1 (ES-1) does not include y- and z-component motions, the forces in the y and z directions and the moment with respect to the x axis (i.e., F_y, F_z, and M_x) are tiny and not presented in Figures 6.16 and 6.19. Motion NM-2 (ES-2) does not include a z component, and so F_z is not presented in Figures 6.17 and 6.20.

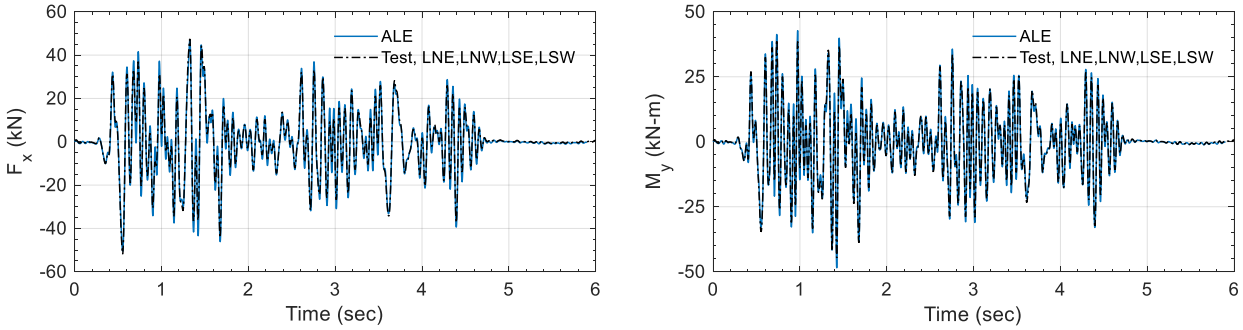

(a) force, x direction (b) moment, y axis

Figure 6.16. Time series of the reactions at the tank base, ALE model for NM-1 and earthquake-simulator test for ES-1

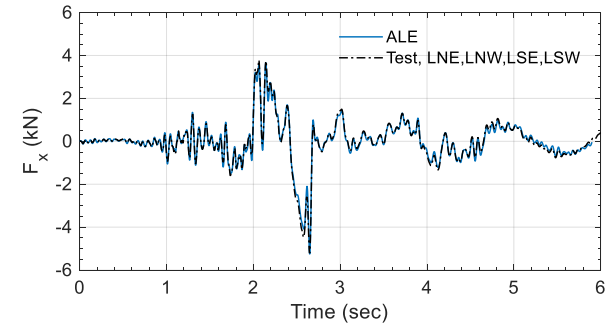

(a) force, x direction

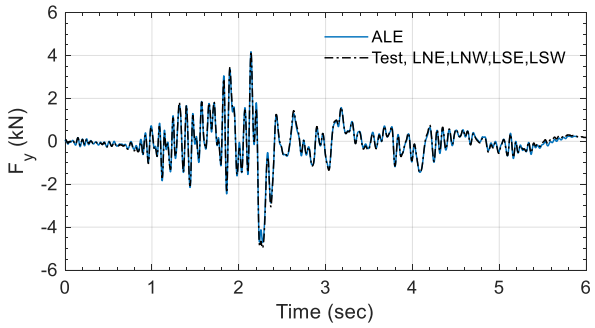

(b) force, y direction

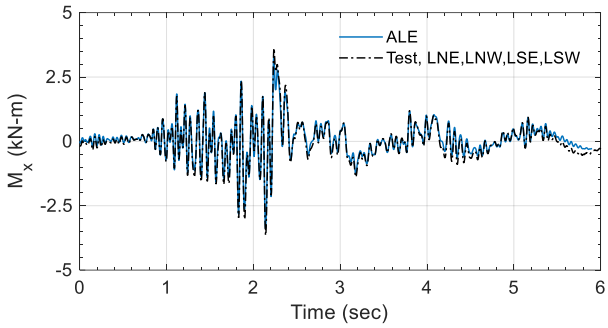

(c) moment, x axis

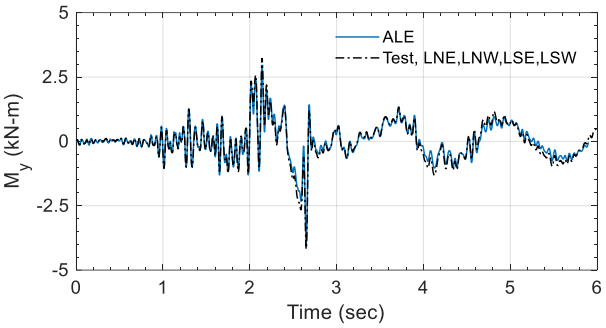

(d) moment, y axis

Figure 6.17. Time series of the reactions at the tank base, ALE model for NM-2 and earthquake-simulator test for ES-2

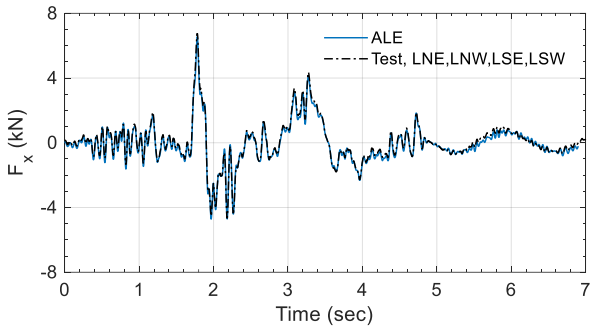

(a) force, x direction

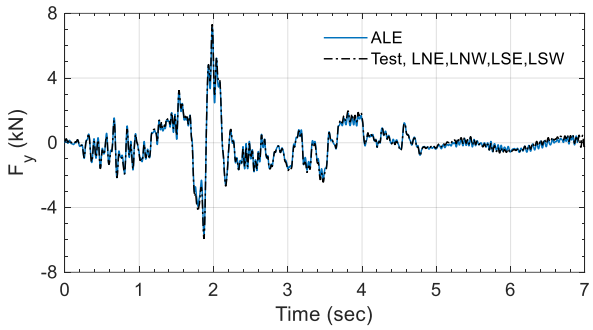

(b) force, y direction

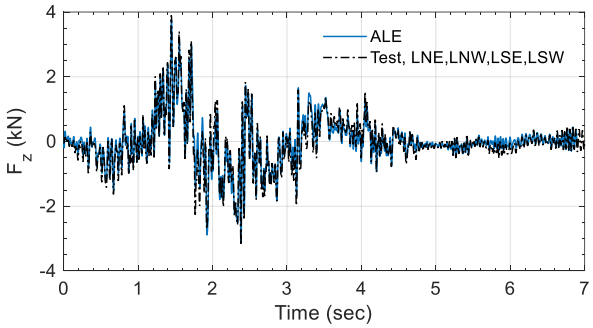

(c) force, z direction

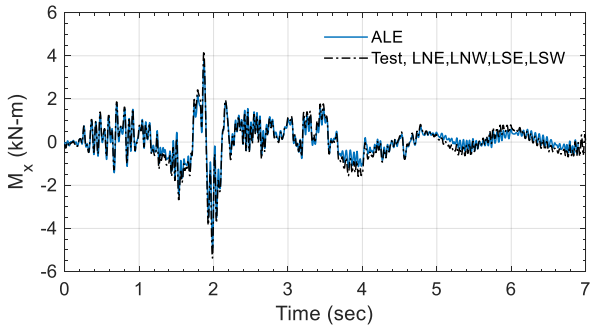

(d) moment, x axis

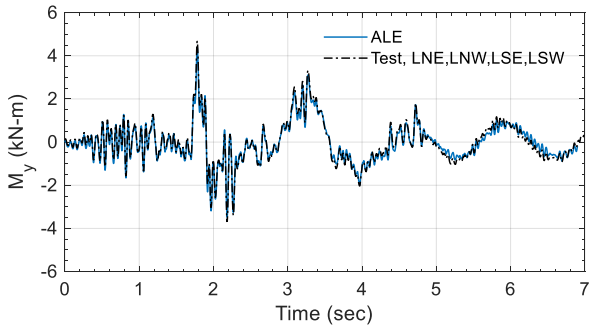

(e) moment, y axis

Figure 6.18. Time series of the reactions at the tank base, ALE model for NM-3 and earthquake-simulator test for ES-3

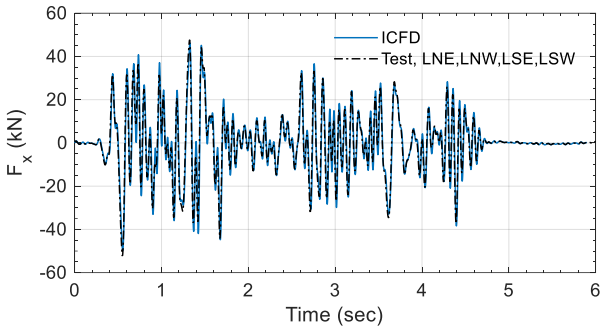

(a) force, x direction

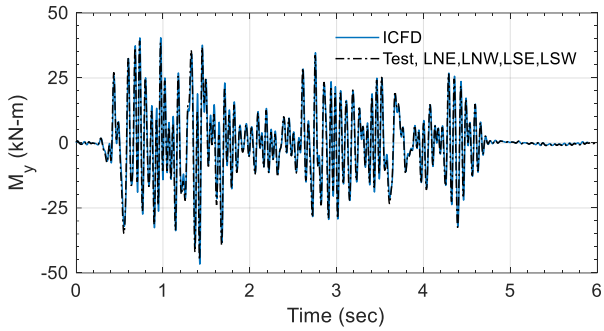

(b) moment, y axis

Figure 6.19. Time series of the reactions at the tank base, ICFD model for NM-1 and earthquake-simulator test for ES-1

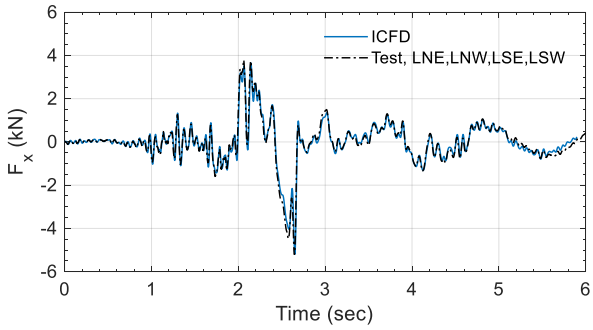

(a) force, x direction

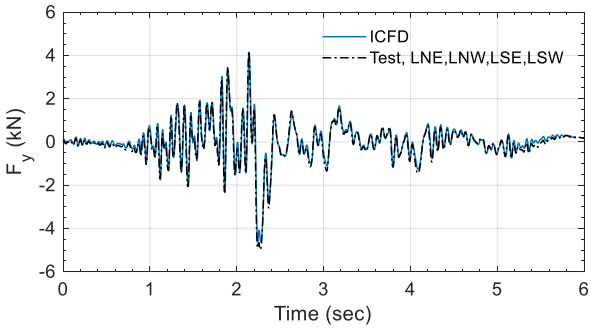

(b) force, y direction

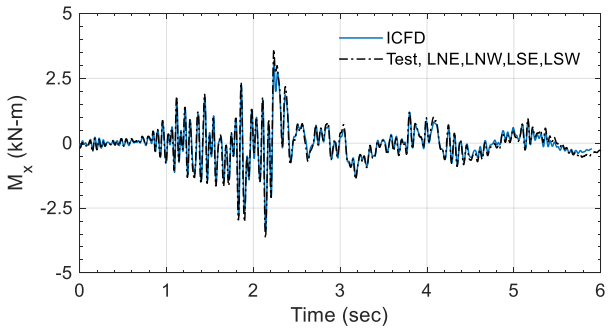

(c) moment, x axis

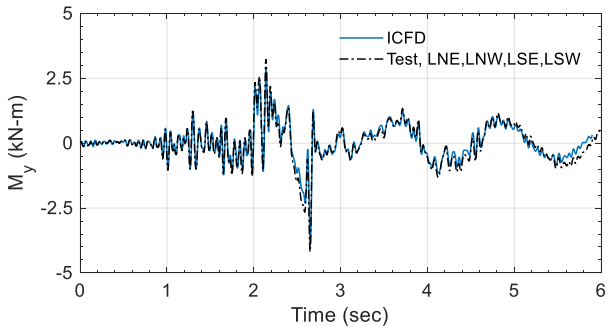

(d) moment, y axis

Figure 6.20. Time series of the reactions at the tank base, ICFD model for NM-2 and earthquake-simulator test for ES-2

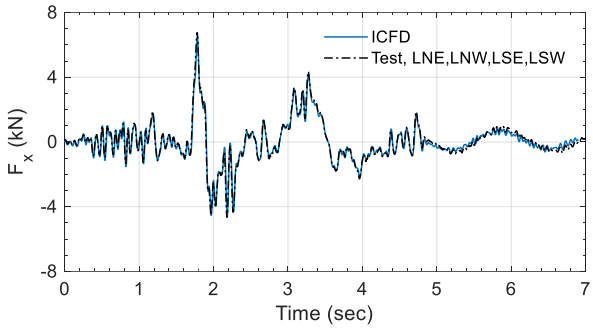

(a) force, x direction

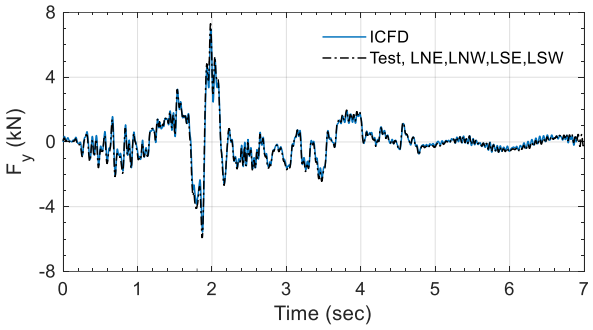

(b) force, y direction

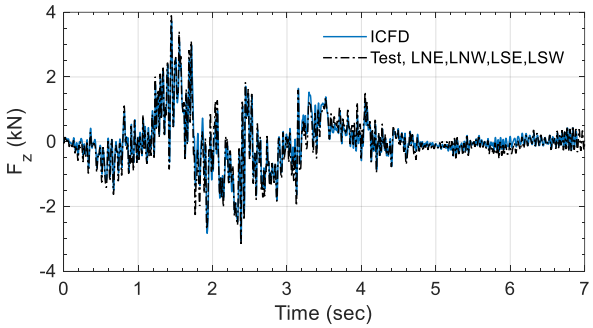

(c) force, z direction

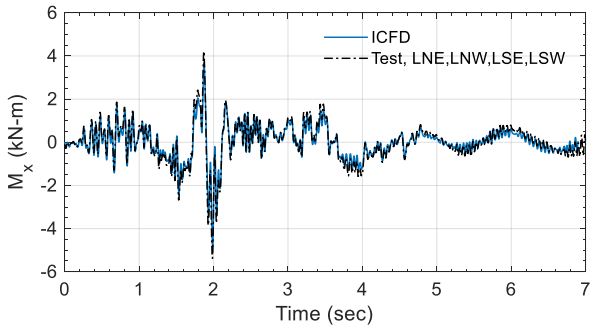

(d) moment, x axis

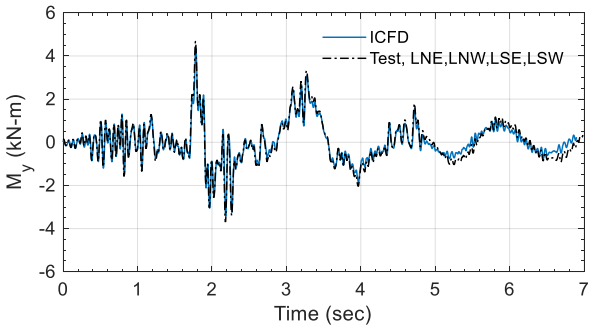

(e) moment, y axis

Figure 6.21. Time series of the reactions at the tank base, ICFD model for NM-3 and earthquake-simulator test for ES-3

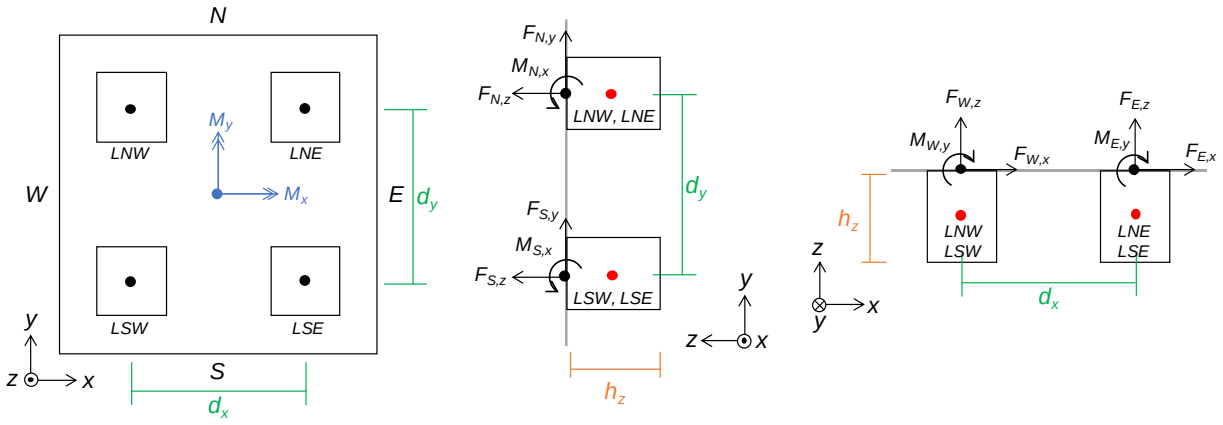

(a) plan view (b) section N - S (c) section E - W

Figure 6.22. Moments on the base plate, forces and moments at the interface of the plate and the four load cells LNE, LNW, LSE and LSW

6.5.3 Vertical displacement of the free surface, wave height

The vertical displacements of the free surface (i.e., wave height with respect to the initial free surface) in the tank measured by the Temposonic gauges, TE and TW, shown in Figure 6.2c, are presented with those calculated using the numerical models in Figures 6.23 to 6.28. Wave heights in the ALE and ICFD models are calculated using the z coordinates of a set of floating points assigned around the measuring locations of TE and TW. (The floating points in the ALE model are arranged in two layers and shown as black dots in Figure 6.5c. Wave heights presented here are output data of the floating points in the upper layer (i.e., on the free surface). For the ICFD analysis, the *Floater* option in the graphical user interface (GUI) of LS-Prepost (2018c) is used to output the z coordinates of assigned points, as described in Section 4.2.3.1.) Figures 6.23 to 6.25 enable comparison between ALE results for NM-1, NM-2, and NM-3 and test data for ES-1, ES-2, and ES-3, respectively. Figures 6.26 to 6.28 present companion data for the ICFD model.

As noted in Section 6.3, the poor predictions of wave heights presented in Section 4 are addressed in the ALE and ICFD models here. As presented in Figure 4.16, the ALE models of Section 4 underestimate wave heights, and the amplitudes diverge further from the analytical results as time increases, due to limitations with the use of floating points, as discussed in Appendix C. By using very dense lines of floating points (124 points) around the measuring

locations of *TE* and *TW*, the issues presented in Appendix C are resolved here, and underestimation is not seen in the ALE results presented in Figures 6.23 to 6.25. The ICFD models in Section 4, as presented in Figure 4.17, underestimate both amplitudes and periods of waves. However, the time series presented in Figures 6.26 to 6.28 are reasonable because *MESH_SIZE_SHAPE card is used in the ICFD model to generate a very fine fluid mesh around the free surface, as shown in Figure 6.6d. (Although the numerical results of wave heights are improved by comparison with those presented in Section 4, the ALE and ICFD models here are not validated. More details on the validation exercise are presented in Section 6.5.4).

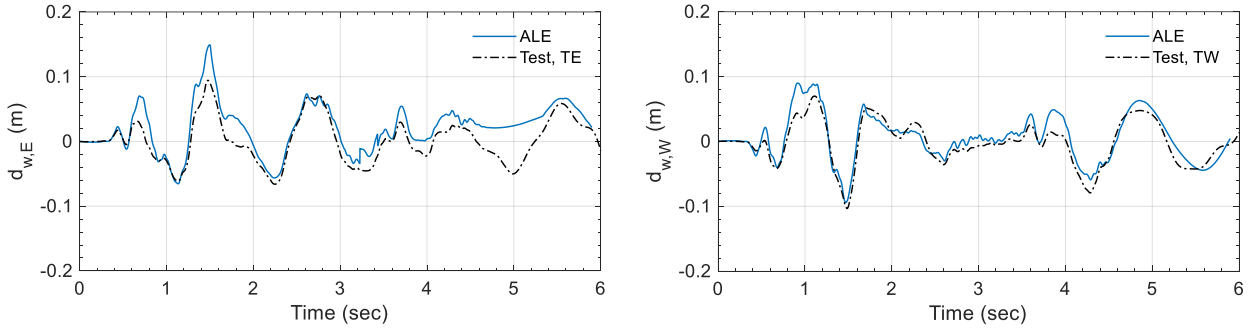

(a) East side (b) West side

Figure 6.23. Time series of wave height adjacent to the tank wall, ALE model for NM-1 and earthquake-simulator test for ES-1

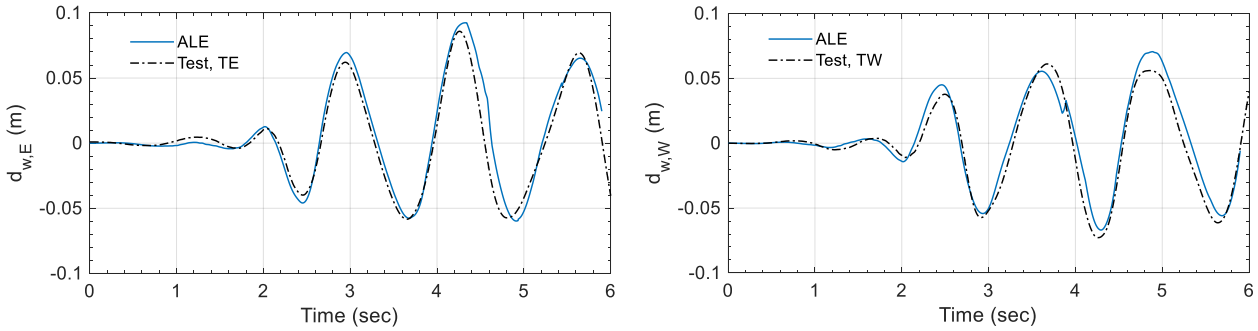

(a) East side (b) West side

Figure 6.24. Time series of wave height adjacent to the tank wall, ALE model for NM-2 and earthquake-simulator test for ES-2

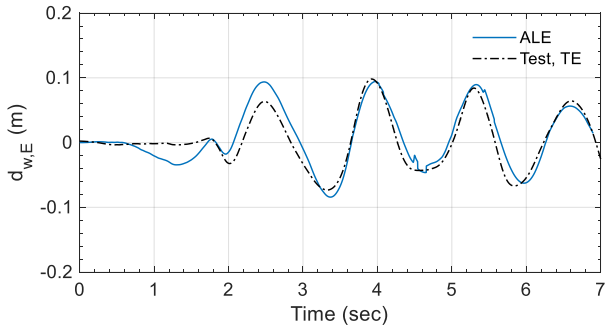

(a) East side

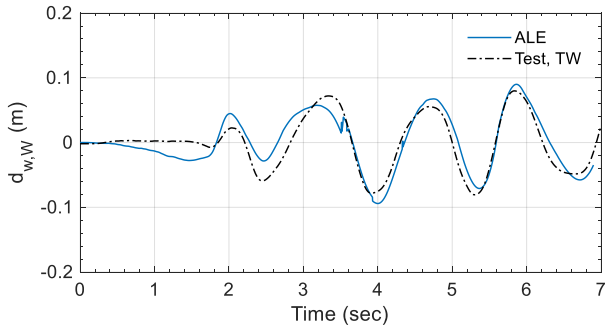

(b) West side

Figure 6.25. Time series of wave height adjacent to the tank wall, ALE model for NM-3 and earthquake-simulator test for ES-3

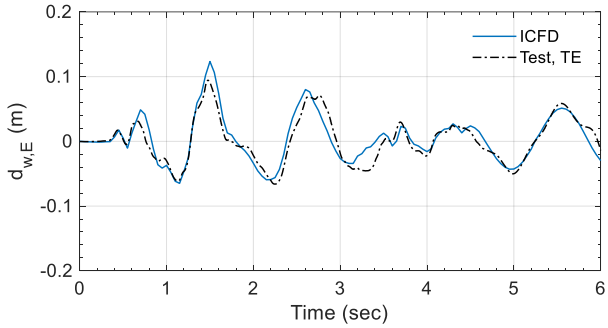

(a) East side

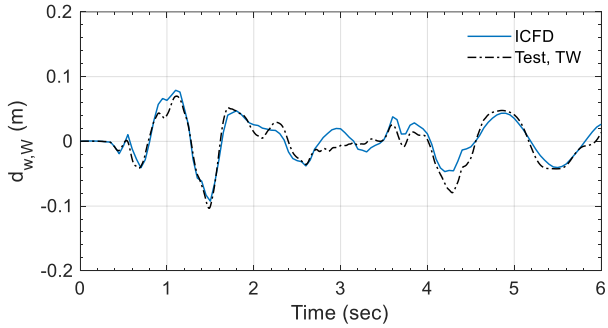

(b) West side

Figure 6.26. Time series of wave height adjacent to the tank wall, ICFD model for NM-1 and earthquake-simulator test for ES-1

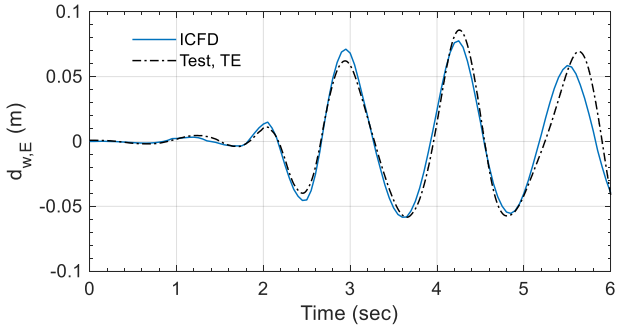

(a) East side

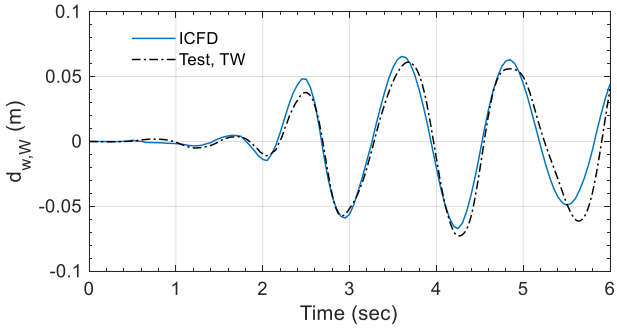

(b) West side

Figure 6.27. Time series of wave height adjacent to the tank wall, ICFD model for NM-2 and earthquake-simulator test for ES-2

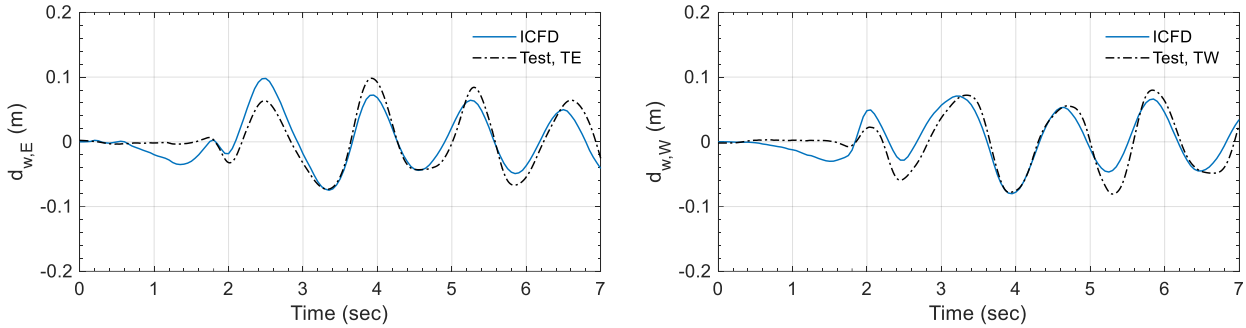

(a) East side (b) West side

Figure 6.28. Time series of wave height adjacent to the tank wall, ICFD model for NM-3 and earthquake-simulator test for ES-3

6.5.4 Discussion

Figures 6.10 to 6.21 and 6.23 to 6.28 enable comparisons of numerical and test results for FSI response time series of a base-supported, cylindrical tank ($R = 0.762$ m, $H_s = 2$ m, and $h = 7.92$ mm), filled with water to a depth of $H = 1.6$ m. The test results of the tank were physically generated using an earthquake simulator for motions ES-1, ES-2, and ES-3 presented in Figure 6.3. The numerical results are calculated in this section using the ALE and ICFD solvers in LS-DYNA for motions NM-1, NM-2, and NM-3 presented in Figure 6.8, input at the base plate of the tank. The input motions of the numerical models, NM-1, NM-2, and NM-3, are derived using data from accelerometers located on the base plate of the tank tested for ES-1, ES-2, and ES-3, respectively. Accordingly, the motions at the base plate of the tank in the numerical models and of the test specimen are essentially identical. The input motions of the numerical model and the tests are not distinguished hereafter, and are both characterized using NM-1, NM-2, and NM-3.

The fluid-structure responses presented in Sections 6.5.1 to 6.5.3 include hydrodynamic pressures on the tank wall, p_w; translational forces at the tank base in the three directions, F_x, F_y, and F_z; moments at the tank base about the two horizontal directions, M_x and M_y; and wave heights, d_w. Results of p_w are reported at the locations of the twelve pressure transducers shown in Figure 6.2a: *PE*1 (2,3), *PW*1 (2,3), *PN*1 (2,3), and *PS*1 (2,3). Results for reactions (i.e., translational forces and moments) are output at the center of the tank base in the numerical models and derived using data from the four load cells used in the tests, as shown in Figure 6.2b:

LNE , *LNW* , *LSE* , and *LSW* . Results for d_w are reported at the locations of the two Temposonic gauges shown in Figure 6.2c: *TE* and *TW* .

Table 6.5 presents the maximum absolute values (amplitudes) of the test, ALE, and ICFD results extracted from the time series presented in Figures 6.10 to 6.21 and 6.23 to 6.28. The percentage differences between the ALE (and ICFD) and test results are presented in parentheses in Table 6.5. The differences greater than $\pm 10\%$ are bolded. If the differences in a response are less than $\pm 10\%$, the model is considered to be validated for calculating the response.

Table 6.5. Maximum absolute FSI responses of the test tank calculated using the numerical models and measured in the earthquake-simulator tests, extracted from Figures 6.10 to 6.21 and 6.23 to 6.28

(a) input motions: NM-1 for numerical analysis and ES-1 for earthquake simulator

Response	Test		ALE	ICFD
	Instrument	Measured response	Calculated response (diff[1])	Calculated response (diff[1])
$p_{w,E}$ (kN/m^2)	*PE*3	6.0	6.5 (9%)	7.0 **(17%)**
	*PE*2	9.2	9.8 (6%)	9.8 (6%)
	*PE*1	9.9	10.2 (3%)	10.2 (3%)
$p_{w,W}$ (kN/m^2)	*PW*3	4.6	5.0 (9%)	5.4 **(18%)**
	*PW*2	8.3	8.4 (2%)	8.2 (-1%)
	*PW*1	8.4	8.8 (4%)	8.9 (6%)
F_x (kN)	*LNE* , *LNW* , *LSE* , *LSW*	51.9	50.4 (-3%)	49.4 (-5%)
M_y (kN-m)		44.7	48.5 (9%)	46.7 (4%)
$d_{w,E}$ (m)	*TE*	94	149 **(58%)**	123 **(31%)**
$d_{w,W}$ (m)	*TW*	103	94 (-9%)	92 **(-11%)**

Table 6.5. Maximum absolute FSI responses of the test tank calculated using the numerical models and measured in the earthquake-simulator tests, extracted from Figures 6.10 to 6.21 and 6.23 to 6.28 (continued)

(b) input motions: NM-2 for numerical analysis and ES-2 for earthquake simulator

Response	Test		ALE	ICFD
	Instrument	Measured response	Calculated response (diff[1])	Calculated response (diff[1])
$p_{w,E}$ (kN/m^2)	*PE*3	0.56	0.53 (-6%)	0.58 (3%)
	*PE*2	0.81	0.86 (6%)	0.88 (8%)
	*PE*1	0.80	0.87 (9%)	0.86 (8%)
$p_{w,W}$ (kN/m^2)	*PW*3	0.74	0.57 **(-23%)**	0.63 **(-14%)**
	*PW*2	0.84	0.88 (4%)	0.90 (6%)
	*PW*1	0.85	0.92 (8%)	0.94 (10%)
$p_{w,N}$ (kN/m^2)	*PN*3	0.39	0.39 (-1%)	0.36 (-8%)
	*PN*2	0.81	0.82 (1%)	0.81 (0%)
	*PN*1	0.92	0.91 (-2%)	0.90 (-2%)
$p_{w,S}$ (kN/m^2)	*PS*3	0.41	0.40 (-1%)	0.37 (-9%)
	*PS*2	0.78	0.71 (-8%)	0.72 (-8%)
	*PS*1	0.87	0.78 (-10%)	0.80 (-8%)
F_x (kN)	*LNE*, *LNW*, *LSE*, *LSW*	5.21	5.25 (1%)	5.19 (0%)
F_y (kN)		4.99	4.71 (-5%)	4.64 (-7%)
M_x (kN-m)		3.65	3.38 (-8%)	3.31 (-9%)
M_y (kN-m)		4.19	3.98 (-5%)	3.93 (-6%)
$d_{w,E}$ (mm)	*TE*	86	92 (8%)	78 (-10%)
$d_{w,W}$ (mm)	*TW*	73	71 (-3%)	67 (-8%)

Table 6.5. Maximum absolute FSI responses of the test tank calculated using the numerical models and measured in the earthquake-simulator tests, extracted from Figures 6.10 to 6.21 and 6.23 to 6.28 (continued)

(c) input motions: NM-3 for numerical analysis and ES-3 for earthquake simulator

Response	Test		ALE	ICFD
	Instrument	Measured response	Calculated response (diff[1])	Calculated response (diff[1])
$p_{w,E}$ (kN/m^2)	*PE*3	0.76	0.75 (0%)	0.74 (-2%)
	*PE*2	1.18	1.17 (-1%)	1.18 (0%)
	*PE*1	1.44	1.39 (-3%)	1.39 (-3%)
$p_{w,W}$ (kN/m^2)	*PW*3	0.83	0.81 (-3%)	0.77 (-8%)
	*PW*2	0.99	0.92 (-6%)	0.98 (-1%)
	*PW*1	1.19	1.23 (3%)	1.28 (8%)
$p_{w,N}$ (kN/m^2)	*PN*3	0.49	0.42 **(-14%)**	0.43 **(-12%)**
	*PN*2	1.36	1.31 (-4%)	1.34 (-1%)
	*PN*1	1.59	1.51 (-5%)	1.54 (-3%)
$p_{w,S}$ (kN/m^2)	*PS*3	0.47	0.47 (-2%)	0.49 (3%)
	*PS*2	1.06	1.00 (-6%)	1.03 (-3%)
	*PS*1	1.28	1.18 (-8%)	1.22 (-5%)
F_x (kN)	*LNE* , *LNW* , *LSE* , *LSW*	6.76	6.58 (-3%)	6.54 (-3%)
F_y (kN)		7.31	7.08 (-3%)	6.97 (-5%)
F_z (kN)		3.90	3.77 (-3%)	3.72 (-4%)
M_x (kN-m)		5.38	4.90 (-9%)	4.83 (-10%)
M_y (kN-m)		4.68	4.39 (-6%)	4.35 (-7%)
$d_{w,E}$ (m)	*TE*	98	94 (-4%)	98 (0%)
$d_{w,W}$ (m)	*TW*	81	91 **(12%)**	80 (-1%)

1. Percentage difference of FSI responses calculated using the numerical models with respect to test results, to the nearest 1%; differences greater than 10% bolded.

Per Table 6.5, the differences of the ALE and test results in hydrodynamic pressures on the tank wall (i.e., $p_{w,E}$, $p_{w,E}$, $p_{w,N}$, and $p_{w,S}$), for the three input motions, are generally less than $\pm 10\%$, except for those at $PW3$ for NM-2 and at $PN3$ for NM-3: -23% and -14%, respectively. Similarly, the differences for the ICFD results are also generally less than $\pm 10\%$, but results at $PE3$ and $PW3$ for NM-1, at $PW3$ for NM-2, and at $PN3$ for NM-3 show greater differences: -14% to 18%. These greater differences (i.e., >10%) between the ALE (or ICFD) and test results are all presented at a height of 1524 mm above the tank base (see $PE3$, $PW3$, and $PN3$ in Figure 6.2a) and close to the free surface of the contained water ($H = 1.6$ m). Two reasons explain these differences. First, hydrodynamic pressures around the free surface are significantly affected by wave actions, of which the calculations are challenging using the ALE and ICFD solvers. (The numerical inaccuracy of waves is described in the *Discussion* in Section 4.2.3.1 and later in this Section 6.5.4.) Second, the test results at the height of 1524 mm above the tank base, where pressures are relatively small, would not be necessarily accurate. The pressure transducers (PXM309-3.5A10V, Omega Engineering Inc.) used here are designed and tested for measuring absolute pressures ranging between 7 and 350 kN/m^2 (70 m Bar to 3.5 Bar). The absolute pressure is the sum of the hydrostatic and hydrodynamic pressures. Per the specifications provided by Omega[53], measuring errors at the lower bound (7 kN/m^2) is $\pm 4.5\%$ and at the higher bound (350 kN/m^2) is $\pm 1.5\%$, namely, greater errors are presented in lower pressures. (Pressures below and beyond the designed range, 7 to 350 kN/m^2, can be measured, but the efficacy of the results are not tested or reported by Omega.) At $z = 1524$ mm, where $PE3$, $PW3$, $PN3$, and $PS3$ are located, the hydrostatic pressure is 0.75 kN/m^2 (i.e., $p_s = \rho_w g(H - z)$; fluid depth $(H - z) = 76$ mm), and the hydrodynamic pressures range between 0.39 and 6 kN/m^2, per test results presented in Table 6.5. Accordingly, the absolute pressures at $PE3$, $PW3$, $PN3$, and $PS3$ are between 1.14 and 6.75 kN/m^2, and below the lower bound of the designed range (i.e., 7 kN/m^2): errors in the test results could be significant. Table 6.6 presents the hydrodynamic pressures at the locations of $PE3$, $PW3$, $PN3$, and $PS3$, calculated using the ALE and ICFD models, and their percentage differences. The differences are insignificant ($\leq \pm 10\%$), which

[53] Specifications of PXM309-3.5A10V: https://www.omega.com/en-us/sensors-and-sensing-equipment/pressure-and-strain/pressure-transducers/p/PXM309 (Omega Engineering Inc, access on Jun 4, 2020)

indicates that the results of the hydrodynamic pressures calculated using the numerical models would be reasonable, and errors in the test results would be more significant.

Table 6.6. Maximum hydrodynamic pressures of the test tank, at the locations of $PE3$, $PW3$, $PN3$, and $PS3$, ALE and ICFD models, extracted from Figures 6.10 to 6.15

Motion	Location	ALE	ICFD	Difference (%)
NM-1	$PE3$	6.5	7.0	-7
	$PW3$	5.0	5.4	-8
NM-2	$PE3$	0.53	0.58	-8
	$PW3$	0.57	0.63	-10
	$PN3$	0.39	0.36	8
	$PS3$	0.4	0.37	9
NM-3	$PE3$	0.75	0.74	2
	$PW3$	0.81	0.77	6
	$PN3$	0.42	0.43	-2
	$PS3$	0.47	0.49	-5

1. Percentage difference of the ALE results with respect to the ICFD results, to the nearest 1%

As seen in Figures 6.16 to 6.21, the numerical (i.e., ALE and ICFD) and test results for reactions at the tank base (i.e., F_x, F_y, F_z, M_x, and M_y) for each motion are in excellent agreement. Per Table 6.5, the differences of the ALE (and ICFD) and test results in these responses are all less than $\pm 10\%$.

As seen in Figures 6.23 to 6.28, the time series of wave heights calculated using numerical models (i.e., ALE and ICFD) are in-phase with the test results, but the amplitudes are not in close agreement. Per Table 6.5, the differences in the amplitude between the ALE and test results range between -9% and 58%, and those for the ICFD model range between -10% and 31%. The most significant differences are in $d_{w,E}$, at TE for NM-1 (Table 6.5a): 58% for the ALE model and 31% for the ICFD model. Differences between the numerical and test results of wave heights for NM-2 and NM-3 are either less than $\pm 10\%$ or insignificant (i.e., 12% for the ALE model, at TW, for NM-3).

The difference of 58% in the ALE and test results, at TE and for motion NM-1, is attributed to errors in 1) numerical calculations, 2) method for outputting numerical results, and 3) measurement in the tests. First, the ALE solver cannot calculate wave heights accurately near the tank wall due to the boundary effect: the vertical fluid velocity adjacent to the wall is zero and so waves cannot form there. Per the ALE results in Figure 4.18, the wave height is zero at $r = R$ and fluctuates in $\pm 0.9 \le r / R \le \pm 1$. Per Figure 6.2c, the Temposonic gauge TE is located 51 mm from the east face of the tank wall, at $r / R = 0.93$ ($R = 762$ mm, $r = R$-51 mm=711 mm), where wave height in the ALE model is not calculated accurately. Second, the points used for outputting wave heights do not necessarily float on the free surface. Figure 6.29 presents the tank, contained fluid (shown in blue), and floating points (black dots) in the ALE model for NM-1 at the time of peak wave height at the location of TE, namely, 1.5 seconds, as shown in Figure 6.23a. A portion of the free surface and floating points around TE are magnified in the figure. The radial coordinate, r, of the monitoring location of TE and five z coordinates are denoted: $r = 711$ mm and $z = 1600$ (i.e., original free surface, $H = 1.6$ m), 1700, 1725, 1749, and 1750 mm. As shown in Figure 6.29, for $r \ge 711$ mm, the floating points in the two layers converge. At $r = 711$ mm, the level of the free surface (i.e., top of the blue part) is at $z = 1725$ mm, whereas the level of the floating point that is identified with a green line is at $z = 1749$ mm. Accordingly, $d_{w,E}$ calculated using the ALE model presented in Table 6.5a is 149 mm (i.e., $d_{w,E} = z - H$ =1749-1600=149 mm). Although the floating point should float on the free surface, it lies above the surface by 24 mm (i.e., 1749-1725=24) at 1.5 seconds, which contributes to an overestimation of 26%, by comparison with the test results of 94 mm measured by TE per Table 6.5a (i.e., 24/94=26%).

The third reason for the differences between the ALE and test results, at TE and for motion NM-1, is associated with errors of measurement in the tests. Figure 6.30 presents snapshots of a video recorded for NM-1, showing TE and its attached float (purple), at $t = 0$, 0.7, and 1.5 seconds. As shown in Figure 6.30a, the float rests on the free surface at $t = 0$. Per Figure 6.30b, at $t = 0.7$ second (the first peak shown in Figure 6.23a), the free surface is higher than its original level seen in Figure 6.30a and is deformed around the boundary of the float. Accordingly, the presence of the float disturbs the wave action. Figure 6.30c presents the water and the float at the time of

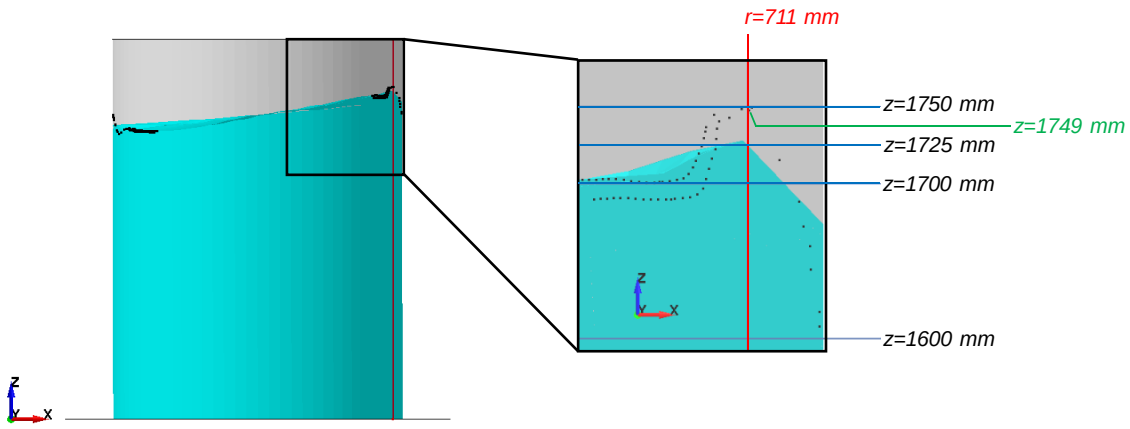

Figure 6.29. Floating points (black dots) used to output vertical displacements of the free surface in the ALE model, for NM-1, at $t = 1.5$ seconds; magnified around *TE*

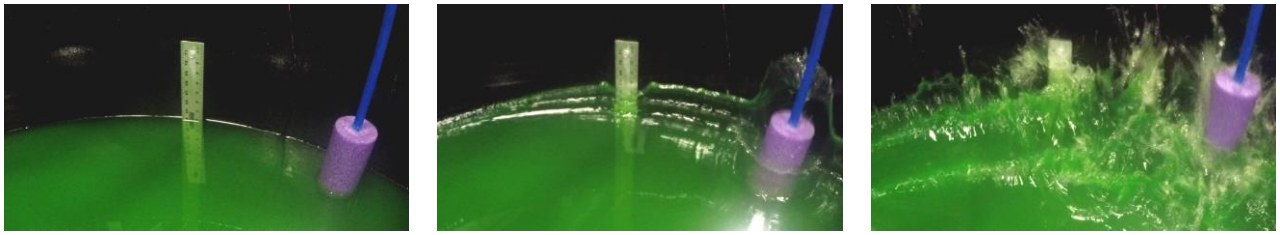

(a) $t = 0$ (b) $t = 0.7$ sec (c) $t = 1.5$ sec

Figure 6.30. Snapshots of a video recorded for NM-1 (ES-1) showing the Temposonic gauge *TW*, its attached float (purple), and surrounding water

maximum wave height: $t = 1.5$ seconds. As seen in the figure, the water splashes, the wave is deformed and broken significantly, and the free surface cannot be defined. The wave height cannot be measured properly by the Temposonic gauge *TE*. This challenge in measurement for NM-1 contributes not only to the difference between the ALE and test results, but also to that for the ICFD results, which is 31%. Consequently, it is not possible to quantify the accuracy (or inaccuracy) of the numerical analysis (ALE and ICFD) for NM-1. The broken wave of Figure 6.30c is not shown in the ALE and ICFD results: see the water in Figure 6.29 for the ALE model and Figure 6.31 for the ICFD model, at $t = 1.5$ seconds. Accordingly, waves generated in the test and those predicted using the ALE and ICFD models are qualitatively different for NM-1. The water splashing and broken waves shown in Figure 6.30c are high-frequency responses and not those of *linear* wave actions (i.e., convective frequencies): 0.8, 1.3, and 1.7 Hz for the first three

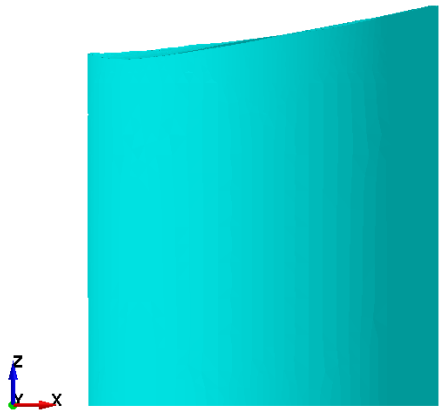

Figure 6.31. Water in the ICFD model, for NM-1, at $t = 1.5$ seconds

modes, estimated using Eq. (3.73) (Veletsos 1984). Such a broken wave is neither shown in the tests nor in the numerical responses for NM-2 and NM-3, of which the spectral accelerations in high frequencies (e.g., 20 to 50 Hz) are relatively small, as presented in Figure 6.9.

Accordingly, the authors concludes that both ALE and ICFD models of the tank and the contained fluid are validated for calculating reactions at the tank base, and hydrodynamic pressures on the tank wall but away from the free surface (i.e., below the mid-height of the tank). The numerical results for hydrodynamic pressures near the free surface cannot be validated here using the test data since the pressures are too small to be measured accurately. However, the hydrodynamic pressures (near the free surface) calculated using the ALE and ICFD models are in reasonable agreement. Neither model is validated for calculating wave heights due to errors in both numerical analysis and measurement in the tests. The accuracy (or inaccuracy) of numerical analysis for calculating waves cannot be identified here using the ALE and ICFD models and test data.

6.6 Closing remarks

Verified and validated numerical models for fluid-structure-interaction (FSI) analysis will be required for the seismic design and qualification of fluid-filled advanced reactors. A verification study should be performed for models of: 1) fluid-structure responses of the vessel (tank) per Section 4 (excluding the internal components), and 2) interaction responses of the tank and its internal components per Section 5. A validation study should be performed for the verified models using data generated from physical testing.

This section validates numerical models, which are modified from those partially verified in Section 4, using data generated from earthquake-simulator tests on a base-supported cylindrical tank. An ALE model and an ICFD model is developed based on the realistic geometries, dimensions, mechanical properties, and boundary conditions of the test tank. Three sets of seismic inputs are used in the analysis, including uni-, two-, or three-directional motions, and rocking motions that are associated with horizontal inputs and the flexibility of the tank support. The intensity of the motions is relatively strong, with PGAs ranging between 0.1 g and 1 g. Hydrodynamic pressures on the tank wall, reactions at the tank base, and wave heights, generated using the tests and numerical models are compared. According to the comparisons presented in Section 6.5, both ALE and ICFD models are validated for calculating reactions and hydrodynamic pressures away from the free surface (e.g., below the mid-height of the tank). Given that the test results for hydrodynamic pressures near the free surface and wave heights involved measuring errors, the models cannot be validated here for calculating these responses, and the accuracy of numerical results cannot be identified. However, hydrodynamic pressures near the free surface are tiny, by comparison with those at a greater fluid depth, and so would not play an important role in either seismic design or qualification.

To validate a verified numerical model of a fluid-filled advanced reactor, the fluid-structure responses critical to the design and qualification should be compared with test data on a specimen representing the reactor. Test results can be generated by performing experiments or extracted from available databases. This report supports an APRA-E project that performs earthquake-simulator tests associated with FSI of nuclear facilities. Model 1, which is in part used in this section, include a base-supported tank and internal components that represent a liquid metal reactor. Model 2 is a cylindrical tank supported near its center of gravity, representing a steam generator. Additional tests are planned. Datasets will be archived in DesignSafe (https://www.designsafe-ci.org/), and can be used by analysts and engineers to validate numerical models for seismic FSI analysis.

After verification and validation, a numerical model for the reactor could be developed using realistic boundary conditions, geometries, dimensions, and mechanical properties. Although the verification and validation studies provide high confidence in the capability of the numerical solver used and the modeling approach, a sensitivity analysis is required to optimize the mesh

and the analysis time step (if an implicit solver is used) for the model of the reactor. The mesh and time step shall be capable of producing responses in a frequency range of interest, depending on the dynamic characteristics of the reactor and its supporting structure and the seismic motions of the site.

SECTION 7
SUMMARY, CONCLUSIONS, AND RECOMMENDATIONS

7.1 Introduction

The Generation IV International Forum (GIF) (2002, 2014) selected six next-generation nuclear reactors for development (Abram and Ion 2008), including two liquid metal reactors, namely, the sodium-cooled fast reactor (SFR) and the lead-cooled fast reactor (LFR). Both the SFR and the LFR use liquid metals as their primary coolants for the removal of heat from the reactor core and the subsequent generation of electricity. The vessel for a liquid metal reactor is substantially thinner than its large-light-water counterparts (and some high temperature gas reactors) because the metal coolant (i.e., liquid sodium or lead-bismuth) does not need to be pressurized since its boiling point is much higher than the operating temperature of the reactor. The greater the internal operating pressure, the thicker the wall of the reactor vessel.

Thin-walled vessels and components, although operationally efficient, lack the seismic robustness of their thick-walled counterparts, necessitating the use of mitigating technologies such as seismic isolation.

Modern reactors must be designed to resist the effects of earthquake shaking. Seismic probabilistic risk assessment must be performed to confirm that the mean annual frequency of core damage or large early release of radiation is sufficiently small. Earthquake shaking of a liquid metal reactor will trigger motion of and interaction between the vessel, the contained fluid, and the internal components. Analytical solutions for seismic fluid-structure interaction (FSI) cannot accommodate the geometries, support conditions, and all internal components in an advanced reactor, simultaneous input motions in three directions, and nonlinear response of the contained liquid. Physical testing of reactor vessels and internal components for seismic qualification is also not feasible because of large size (i.e., simulator payload) and costs. Although seismic design, qualification, and risk assessment of the advanced reactors will require numerical models for FSI analysis, none exist. Importantly, these models will be needed, regardless of whether seismic mitigation strategies such as base isolation are deployed.

To provide the numerical tools needed for seismic FSI analysis of fluid-filled advanced reactors, and meet the goal of Section 1.3, this report: 1) verifies and validates numerical models for rigid and flexible, cylindrical vessels (tanks), supported at either the base or the top (head), analyzed using two solvers capable of predicting nonlinear fluid responses; and 2) verifies numerical models for flexible, submerged internal components. The Arbitrary Lagrangian-Eulerian (ALE) and Incompressible Computational Fluid Dynamics (ICFD) solvers in LS-DYNA (Livermore Software Technology Corporation (LSTC) 2018a) are used to perform the seismic FSI analysis[54]. The numerical models are verified using analytical solutions, available in prior studies and corrected in this report if needed, or derived in this report, and validated using data generated from earthquake-simulator tests on a base-supported, cylindrical, steel tank filled with water.

Section 1.3 lists the six objectives of this report. Objective 1 is addressed in Sections 2 and 3. Objective 2, the development of analytical solutions for FSI analysis of a head-supported tank, is met in Section 3. The verification of numerical models in LS-DYNA for base- and head-supported, fluid-filled tanks, objective 3, is presented in Section 4. The verification of numerical models in LS-DYNA for components submerged in fluid, objective 5, is presented in Section 5. Objective 4, the validation of verified models of a base-supported, fluid-filled vessel, is met in Section 6. Recommendations for developing verified and validated numerical models for fluid-filled, advanced nuclear reactors, objective 6, are provided in Section 7.4.

Section 7.2 summarizes the work performed in Sections 2 to 6. Section 7.3 presents conclusions of the verification and validation studies drawn from the work summarized in Section 7.2. Section 7.4 presents recommendations for developing verified and validated numerical models for fluid-filled advanced reactors.

7.2 Summary

Section 2 reviews the literature on analytical, numerical, and experimental studies related to seismic fluid-structure-interaction (FSI) analysis of fluid-filled tanks and reactors. Studies on seismic FSI of tanks began in the 1930s at the Vibration Laboratory at Stanford University (Hoskins and Jacobsen 1934; Morris 1938; Jacobsen 1949; Jacobsen and Ayre 1951), including

[54] Solvers capable of predicting linear fluid responses were not investigated in this study, in part because the threshold for nonlinear fluid response, which will vary as a function of vessel geometry, boundary conditions, and frequency content and intensity of earthquake inputs, is not known a priori.

the development of analytical solutions and the earliest earthquake-simulator tests on fluid-filled tanks. The products of these studies were used subsequently extended and/or modified by others, including Housner (1957), and used to design first- (Thomas et al. 1963) and second-generation nuclear reactors.

Section 3 reviews analytical studies on the seismic FSI response of base-supported cylindrical tanks developed by Jacobsen (1949), Chalhoub and Kelly (1988), Housner (1957, 1954), and Veletsos (1984a). Simplifying assumptions were made for the analytical solutions: rigid or elastic tanks, ideal and irrotational fluids, and unidirectional horizontal seismic motion of a small amplitude. The FSI responses are parsed into impulsive and convective components. The section summarizes analytical solutions that addressed impulsive frequencies (i.e., lateral frequencies of a flexible tank), convective frequencies (i.e., frequencies of waves), hydrodynamic pressures, wave heights, and reactions at the base support. The derivations or solutions presented in Jacobsen, Chalhoub and Kelly, and Housner involved calculation errors, and are re-worked and corrected here. The FSI responses are calculated for a range of tank dimensions and compared using the different analytical solutions, after correction, as needed.

Analytical solutions for seismic FSI analysis of head-supported tanks are developed in this section, with application to the boundary conditions and geometries similar to those proposed for fluid-filled advanced reactor vessels (Yu and Whittaker 2020). The solutions are derived using the methodologies and assumptions of Jacobsen (1949) and Veletsos (1984), and address the change in support condition, namely, base to head. Impulsive and convective frequencies and FSI responses (i.e., hydrodynamic pressures, wave heights, and reactions) generated by small-amplitude unidirectional horizontal motion are calculated for a head-supported tank using the analytical solutions developed here. The analytical results are normalized to be unitless, and can be used for the preliminary design of tanks and vessels with different dimensions and mechanical properties, and subjected to different input motions.

Section 4 verifies ALE and ICFD models of base- and head-supported cylindrical tanks using analytical solutions presented in Section 3. The models accommodate the assumptions made for the analytical solutions, namely, rigid or elastic tanks, ideal fluids, and small-amplitude, unidirectional, horizontal seismic input. Two fluid heights are used for the rigid tank, and the

elastic (flexible) tank is full. Four input motions are used for response-history analysis, including two sinusoidal motions with a low and a high frequency (i.e., 0.5 and 20 Hz) and two earthquake motions with distinct frequency contents. The numerical results for impulsive frequencies (for the flexible tank only), convective frequencies, hydrodynamic pressures on the tank wall, wave heights, and reactions at the support (base or head), are compared with the analytical solutions.

Section 5 reviews the analytical solutions derived by Chen and Rosenberg (1975), and then verifies ALE and ICFD models of submerged internal components using the solutions. Chen and Rosenberg derived solutions for frequencies of two concentric pipes, with fluid filling the inner pipe and the annulus between the two pipes. The outer and inner pipes map here to a tank wall and a submerged internal component, respectively. The derivations and solutions of Chen and Rosenberg are re-worked herein to correct calculation errors. Numerical models for two sets of two fluid-filled concentric pipes with different dimensions are constructed. To accommodate the assumptions used for the analytical solutions, the lengths of the two pipes in each model are identical, and they are both supported at their tops. The lateral frequencies of the inner pipe in the ALE and ICFD models are identified from free-vibration displacement histories. The numerical results for the frequencies are compared with those calculated using the corrected analytical solutions.

Section 6 validates ALE and ICFD numerical models using data from earthquake-simulator tests on a base-supported cylindrical tank filled with water. The numerical models in Section 6 are modified from those in Section 4 to better understand and capture sloshing responses measured in the earthquake-simulator experiments. The measured dimensions, mechanical properties, and boundary conditions of the test tank are used to build the numerical models. The translational and rotational accelerations measured at the base of the tank in the experiments are used as the inputs to the models. The intensity of the input motions is relatively strong, with peak ground accelerations ranging between 0.1 g and 1 g. Hydrodynamic pressures on the tank wall, reactions at the tank base, and wave heights calculated using the numerical models are compared with the values measured in the experiments.

7.3 Conclusions

Section 7.3.1 presents the conclusions of the verification and validation studies on numerical models of cylindrical tanks, drawn from Sections 3, 4, and 6. Section 7.3.2 presents the conclusions of the verification study on numerical models of submerged internal components, drawn from Section 5.

7.3.1 Verification and validation of numerical models for cylindrical tanks

The ALE and ICFD numerical models of cylindrical tanks, presented in Section 4, are partially verified by comparing numerical results with those calculated using analytical solutions of Section 3. If the difference between the numerical and analytical results for a peak response is less than or equal to $\pm 10\%$, the model is considered to be verified for calculating that response. The ALE models are verified for calculating impulsive and convective frequencies, hydrodynamic pressures on the tank wall, and reactions at the support. Wave heights are underestimated by the ALE models and diverge further from the analytical results with the passage of time due to challenges the code has in outputting results, as described in Appendix C. The ICFD models are verified for calculating impulsive frequencies, hydrodynamic pressures on the tank wall and reactions at the support, if the wave action of the contained fluid is insignificant. The ICFD models do not predict wave action accurately, in both amplitude and phase, by comparison with the analytical results. Accordingly, these ICFD models should be limited to seismic FSI analysis with little-to-no wave action or for input motions with negligible frequency content at the first convective mode. The capability of the ICFD solver for calculating wave actions on the free surface is a subject of on-going LSTC development at the time of this writing (Caldichoury 2020)

The numerical models of Section 4 are modified for use in Section 6 to improve the predictions of wave heights: additional monitoring locations on the free surface in the ALE model to output wave heights, and a finer fluid mesh near the free surface in the ICFD model. The modified models are validated by comparing numerical results with test data for a base-supported tank. If the difference between the numerical and test results for a peak response is less than or equal to $\pm 10\%$, the model is considered to be validated for calculating that response. Both ALE and ICFD models are validated for calculating reactions at the base, and hydrodynamic pressures on the tank wall away from the free surface (e.g., below the mid-height of the tank). Given that the

test results for hydrodynamic pressure near the free surface and wave height involved measurement errors, it is not possible to validate the models for calculating these responses. Accordingly, the modified numerical models of this section were not used to update the verification studies of Section 4.

In conclusion, the LS-DYNA ALE and ICFD models of fluid-filled tanks are verified and validated for calculating reactions at the support and hydrodynamic pressures on the tank wall (away from the free surface). The predictions of wave height are not sufficiently accurate. Further code development on simulating wave action and outputting wave height data is needed, and that work is underway, prompted by the studies described in this report.

7.3.2 Verification of numerical models for submerged internal components

The ALE and ICFD models for submerged internal components are verified in Section 5: the differences in the lateral frequencies calculated using the numerical models and the analytical solutions of Chen and Rosenberg are less than 5%. The frequencies of a submerged component depend on the hydrodynamic pressures on its perimeter. Accordingly, if the numerical results for the frequencies of the component are accurate, the hydrodynamic pressures on its perimeter (and by extension the reactions at its support) are correct. The verified models are not validated in this report. (A validation study for models of submerged internal components is underway, by others.)

7.4 Recommendations for developing verified and validated numerical models for fluid-filled advanced reactors

Numerical models for seismic fluid-structure interaction (FSI) can be verified using analytical solutions and validated using data from physical testing. Recommendations for developing verified and validated numerical models for fluid-filled advanced reactors are presented below, drawn from the studies performed in Sections 3 to 6.

To the knowledge of the authors, none of the analytical studies for FSI responses of a vessel (tank) that address responses critical to seismic design (e.g., pressures, wave heights, and reactions) consider interaction with internal components. Consequently, verification studies would have to be performed separately for models of: 1) FSI responses of the vessel (excluding the internal components), and 2) frequencies and/or interaction responses of internal components in the vessel. Verification for 1) and 2) could follow the work of Sections 4 and 5, respectively.

The dimensions and materials of the reactor vessel and the internal component in the models (to be verified) must be idealized to accommodate the assumptions of the analytical solutions. The models would have to be constructed using a rigid or elastic material assigned the mechanical properties of the metal used for fabricating the reactor vessel and internal components (e.g., stainless steel) and use an ideal fluid with the density of the coolant (e.g., liquid sodium or lead-bismuth) at the assumed operating temperature. A constant radius and wall thickness should be used for the idealized vessel and internal component since analytical solutions are generally developed for prismatic structures. Figure 7.1 demonstrates the idealization for the geometries, dimensions, and boundary conditions using a sample nuclear reactor. Figure 7.1a presents the prototype fast reactor (PFR) in Dounreay, Scotland, with green, red, and blue lines indicating the vessel, reactor jacket (see footnote 48 on page 249 for information), and coolant to be idealized for the verification. Figure 7.1b presents an idealized vessel in the model for calculating FSI responses, with dimensions extracted from Figure 7.1a: the radius at the head support, the wall thickness, the maximum height of the vessel, and the greatest depth of coolant. The model could be verified using the analytical solutions for head-supported tanks (Yu and Whittaker 2020) developed in Section 3. Figure 7.1c presents a model of an idealized component (i.e., the reactor jacket) submerged in a fluid confined by the vessel wall, with radial dimensions at their supports, wall thicknesses, and maximum height of the vessel per Figure 7.1a. The model could be verified using the (corrected) analytical solutions of Chen and Rosenberg (1975) presented in Section 5. Other analytical studies associated with submerged internal components could also be used for the verification study but the numerical model must reflect the assumptions made. Examples are 1) Chung and Chen (1977), who derived frequencies of internal components eccentric to a tank, used for verifying a model for the intermediate heat exchanger and vessel of Figure 7.1a; and 2) Chen (1975a), who derived frequencies of an array of submerged cylindrical beams, used for verifying a model for nuclear fuel rods. If the difference between the numerical and analytical results is less than or equal to $\pm$ 10%, the models should be considered to be verified.

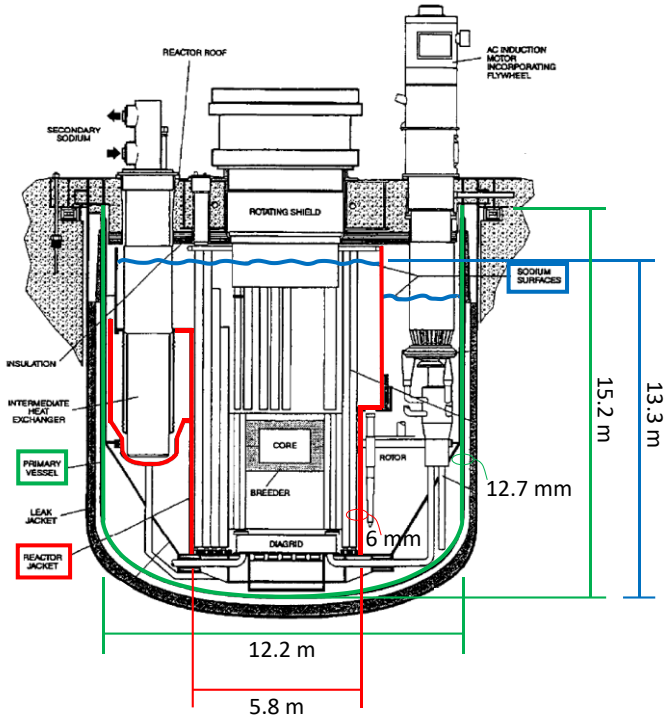

(a) prototype fast reactor (PFR), Dounreay, Scotland (Figure 2.44 in IAEA (2012)), and dimensions extracted from Jensen and Ølgaard (1995) or estimated based on the drawing

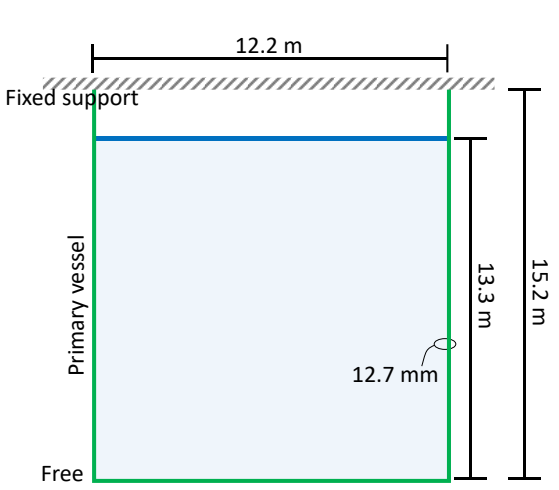

(b) idealized reactor vessel and coolant

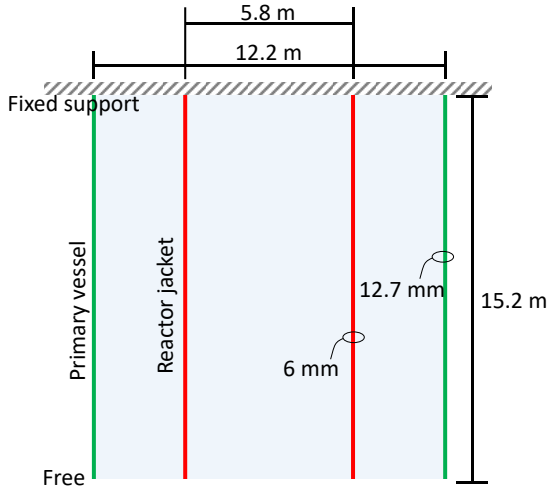

(c) idealized reactor vessel and reactor jacket

Figure 7.1. Sample nuclear reactor and idealized geometries, dimensions, and support conditions

To validate a verified numerical model for a fluid-filled advanced reactor, the responses calculated using the model should be compared with test data on a specimen representing the reactor. The validation study could follow the work of Section 6. Test results could be generated by either performing earthquake-simulator experiments or extracting information from available databases (e.g., DesignSafe, https://www.designsafe-ci.org/). The dimensions, materials, support conditions, and seismic inputs used for the numerical model (to be validated) should be identical to those of the test specimen. Three-component seismic motions with a range of intensities should be used for analysis to maximize the utility of the validation exercise. If the site of the reactor is known, motions consistent with the design-basis seismic hazard at the site should be used. Responses critical to the design and qualification (e.g., hydrodynamic pressures, wave heights, and reactions) are recorded and compared with the numerical predictions. If the difference in peak response for a given response parameter is less than or equal to $\pm 10\%$, the numerical model should be considered to be validated.

After verification and validation, a numerical model for the reactor could be developed using realistic support conditions, geometries, dimensions, and mechanical properties. This model could then be used for calculating FSI responses to three-directional seismic inputs for design, qualification, and probabilistic risk assessment.

SECTION 8

REFERENCES

Abram, T., and Ion, S. (2008). "Generation-IV nuclear power: a review of the state of the science." *Energy Policy*, 36(12), 4323-4330.

Abramson, H. N. (1966). "The dynamic behavior of liquids in moving containers: with applications to space vehicle technology." *NASA SP-106*, National Aeronautics and Space Administration (NASA), Washington DC.

American Concrete Institute (ACI) (2006). "Seismic design of liquid-containing concrete structures and commentary." *350.3-06*, ACI, Farmington Hills, MI.

American Institute of Steel Construction (AISC) (2011). *Steel construction manual*, 14th Ed., Chicago, IL.

American Petroleum Institute (API) (2012). "Welded tanks for oil storage." *API 650*, API, Washington D.C.

American Society of Civil Engineers (ASCE) (2017). "Seismic analysis of safety-related nuclear structures and commentary." *ASCE/SEI 4-16*, Reston, VA.

American Society of Mechanical Engineers (ASME) (1979). "A national historic mechanical engineering landmark - Experimental Breeder Reactor I." ASME, New York, NY.

ANSYS Inc. (2005). "ANSYS 10.0 user's manual." Cecil Township, PA.

Atomic Heritage Foundation (AHF) (2016). "Chicago Pile-1." <https://www.atomicheritage.org/history/chicago-pile-1>. (Sep. 28, 2018).

Bandyopadhyay, K., Cornell, C. A., Costantino, C., Kennedy, R., Miller, C., and Veletsos, A. S. (1995). "Seismic design and evaluation guidelines for the Department of Energy high-level waste storage tanks and appurtenances." *BNL 52361(REV. 10/95)/UC-406/UC-510*, Brookhaven National Laboratory, Associated Universities, Inc., Upton, NY.

Bleich, H. H., and DiMaggio, F. (1952). "A strain-energy expression for thin cylindrical shells." *Technical Report No. 6 for the Office of Naval Research*, Columbia University, New York, NY.

Caldichoury, I. (2020, Jan 3). Personal communication, Email <support@lstc.com>, LSTC Technical Support.

Carr, A. (2004). "RUAUMOKO user's manual." University of Canterbury, Christchurch, New Zealand.

Chalhoub, M. S., and Kelly, J. M. (1988). "Theoretical and experimental studies of cylindrical water tanks in base isolated structures." *UCB/EERC-88/07*, Earthquake Engineering Research Center, University of California at Berkeley, Berkeley, CA.

Chalhoub, M. S., and Kelly, J. M. (1990). "Shake table test of cylindrical water tanks in base-isolated structures." *Journal of Engineering Mechanics*, 116(7), 1451-1472.

Chellapandi, P., Chetal, S., and Raj, B. (2010). "Application of advanced mechanics for the structural design of sodium cooled fast reactor components." *Structural Longevity*, 3(1-2), 1-36.

Chellapandi, P., Chetal, S. C., and Raj, B. (2008). "Investigation on buckling of FBR vessels under seismic loadings with fluid-structure interactions." *Nuclear Engineering and Design*, 238(12), 3208-3217.

Chellapandi, P., Chetal, S. C., and Raj, B. (2012). "Numerical simulation of fluid-structure interaction dynamics under seismic loadings between main and safety vessels in a sodium fast reactor." *Nuclear Engineering and Design*, 253, 125-141.

Chen, S. (1975a). "Vibration of nuclear fuel bundles." *Nuclear Engineering and Design*, 35(3), 399-422.

Chen, S. (1975b). "Vibrations of a row of circular cylinders in a liquid." *Journal of Engineering for Industry*, 97(4), 1212-1218.

Chen, S. (1977). "Dynamics of heat exchanger tube banks." *Journal of Fluids Engineering*, 99(3), 462-467.

Chen, S., and Chung, H. (1976). "Design guide for calculating hydrodynamic mass. Part 1. circular cylindrical structures." *ANL-CT-76-45*, Argonne National Laboratory (ANL), Lemont, IL.

Chen, S., and Rosenberg, G. (1975). "Dynamics of a coupled shell-fluid system." *Nuclear Engineering and Design*, 32(3), 302-310.

Chen, S., Wambsganss, M., and Jendrzejczyk, J. (1976). "Added mass and damping of a vibrating rod in confined viscous fluids." *Journal of Applied Mechanics*, 43(2), 325-329.

Chopra, A. K. (2012). *Dynamics of structures: theory and applications to earthquake engineering*, 4th Ed., Prentice Hall, Upper Saddle River, NJ.

Christovasilis, I. P., and Whittaker, A. S. (2008). "Seismic analysis of conventional and isolated LNG tanks using mechanical analogs." *Earthquake Spectra*, 24(3), 599-616.

Chung, H., and Chen, S. (1976). "Vibration of a group of circular cylinders in a confined fluid." *ANL-CT-76-25*, Argonne National Laboratory (ANL), Lemont, IL.

Chung, H., and Chen, S. (1977). "Vibration of a group of circular cylinders in a confined fluid." *Journal of Applied Mechanics*, 44(2), 213-217.

Chung, H., and Chen, S. (1984). "Hydrodynamic mass." *CONF-840647-9*, Argonne National Laboratory (ANL), Lemont, IL.

Cochran, T. B., Feiveson, H. A., Patterson, W., Pshakin, G., Ramana, M., Schneider, M., Suzuki, T., and von Hippel, F. (2010). "Fast breeder reactor programs: history and status." *Research Report 8*, International Panel on Fissile Materials (IPFM), Princeton University, Princeton, NJ.

Commissariat Français à l'Energie Atomique (CEA) (2003). "CAST3M user's manual." Gif-sur-Yvette, France.

Dassault Systèmes (2018). "ABAQUS 2018-unified FEA products." Vélizy-Villacoublay, France.

Do, I. (2019, Apr 3). Personal communication, Email <support@lstc.com>, LSTC Technical Support.

Dong, R. G. (1978). "Effective mass and damping of submerged structures." *UCRL-52342*, Lawrence Livermore Laboratory, Livermore, CA.

Flugge, W. (1960). *Stresses in shells*, 1st Ed., Springer-Verlag OHG., Berlin/Gottingen/Heidelberg, Germany.

Fujita, K., Ito, T., Shimomura, T., and Morishita, M. (1984). "Aseismic study on the reactor vessel of a fast breeder reactor." *Nuclear Engineering and Design*, 83(1), 47-61.

Generation IV International Forum (GIF) (2002). "A technology roadmap for Generation IV nuclear energy systems." *GIF-002-00*, GIF and U.S. Department of Energy, Washington D.C.

Generation IV International Forum (GIF) (2014). "Technology roadmap update for Generation IV nuclear energy systems." Nuclear Energy Agency (NEA) of Organisation for Economic Co-operation and Development (OECD), Paris, France.

Gluekler, E. L. (1997). "U.S. advanced liquid metal reactor (ALMR)." *Progress in Nuclear Energy*, 31(1-2), 43-61.

Graham, E., and Rodriquez, A. (1951). "The characteristics of fuel motion which affect airplane dynamics." *SM-14212*, Douglas Aircraft Co. Inc., Santa Monica, CA.

Haroun, M. A. (1980a). "Dynamic analyses of liquid storage tanks." Dissertation, presented to California Institute of Technology, Pasadena, CA, in partial fulfillment of the requirements for the degree of Doctor of Philosophy.

Haroun, M. A. (1980b). "Dynamic analyses of liquid storage tanks." *EERL 80-04*, Earthquake Engineering Research Laboratory, California Institute of Technology, Pasadena, CA.

Haroun, M. A. (1983). "Vibration studies and tests of liquid storage tanks." *Earthquake Engineering and Structural Dynamics*, 11(2), 179-206.

Haroun, M. A., and Housner, G. W. (1981a). "Earthquake response of deformable liquid storage tanks." *Journal of Applied Mechanics*, 48(2), 411-418.

Haroun, M. A., and Housner, G. W. (1981b). "Seismic design of liquid storage tanks." *Journal of the Technical Councils of American Society of Civil Engineers (ASCE)*, 107(1), 191-207.

Haroun, M. A., and Housner, G. W. (1982a). "Complications in free vibration analysis of tanks." *Journal of the Engineering Mechanics Division*, 108(5), 801-818.

Haroun, M. A., and Housner, G. W. (1982b). "Dynamic characteristics of liquid storage tanks." *Journal of the Engineering Mechanics Division*, 108(5), 783-800.

Harvey, D. W., McGehee, E. D., Garcia, K. L. M., Ronquillo, J., Towery, K., Loomis, E., Naranjo, N., and Isaacson, J. (2004). "Historical context of the Omega Reactor Facility - Technical Area 2." *LA-UR-04-6681/ Historic Building Report No. 234*, Los Alamos National Laboratory (LANL), Los Alamos, NM.

Hjelmstad, K. D. (2010). *Fundamentals of structural mechanics*, 2nd Ed., Springer Publishing, New York City, NY.

Hoskins, L. M., and Jacobsen, L. S. (1934). "Water pressure in a tank caused by a simulated earthquake." *Bulletin of the Seismological Society of America*, 24(1), 1-32.

Housner, G. W. (1954). "Earthquake pressures on fluid containers." *NR-081-095*, Office of Naval Research, Arlington, VA.

Housner, G. W. (1957). "Dynamic pressures on accelerated fluid containers." *Bulletin of the Seismological Society of America*, 47(1), 15-35.

Housner, G. W. (1963). "The dynamic behavior of water tanks." *Bulletin of the Seismological Society of America*, 53(2), 381-387.

Housner, G. W., and Haroun, M. A. (1980). "Dynamic analyses of liquid storage tanks." *Proc., 7th World Conference on Earthquake Engineering (7WCEE)*, Istanbul, Turkey.

Huang, Y. (2019, Apr 17). Personal communication, Email <yuli.huang@arup.com>, Arup, San Francisco, CA.

Huang, Y., Sturt, R., and Willford, M. (2019). "A damping model for nonlinear dynamic analysis providing uniform damping over a frequency range." *Computers and Structures*, 212, 101-109.

International Atomic Energy Agency (IAEA) (2012). "Status of fast reactor research and technology development." *IAEA-TECDOC-1691*, IAEA, Vienna, Austria.

Jacobsen, L. S. (1949). "Impulsive hydrodynamics of fluid inside a cylindrical tank and of fluid surrounding a cylindrical pier." *Bulletin of the Seismological Society of America*, 39(3), 189-204.

Jacobsen, L. S., and Ayre, R. S. (1951). "Hydrodynamic experiments with rigid cylindrical tanks subjected to transient motions." *Bulletin of the Seismological Society of America*, 41(4), 313-346.

Jeffreys, H. (1925). "The free oscillations of water in an elliptical lake." *Proceedings of the London Mathematical Society*, 2(1), 455-476.

Jensen, S., and Ølgaard, P. (1995). "Description of the prototype fast reactor at Dounreay." *NKS/RAK-2(95)TR-C1*, Rise National Laboratory, Roskilde, Denmark.

Kelly, J. E. (2014). "Generation IV International Forum: a decade of progress through international cooperation." *Progress in Nuclear Energy*, 77, 240-246.

Lamb, H. (1932). *Hydrodynamics*, 6th Ed., Cambridge University Press, Cambridge, England, United Kingdom.

Liu, W. K. (1980). "Development of finite element procedures for fluid-structure interaction." *EERL 80-06*, Earthquake Engineering Research Laboratory, California Institute of Technology, Pasadena, CA.

Liu, W. K. (1981). "Finite element procedures for fluid-structure interactions and application to liquid storage tanks." *Nuclear Engineering and Design*, 65(2), 221-238.

Liu, W. K., and Belytschko, T. (1982). "Mixed-time implicit-explicit finite elements for transient analysis." *Computers and Structures*, 15(4), 445-450.

Livermore Software Technology Corporation (LSTC) (2018a). "LS-DYNA keyword user's manual-R11." Livermore, CA.

Livermore Software Technology Corporation (LSTC) (2018b). "LS-DYNA SMP_d_Dev_126632." Livermore, CA.

Livermore Software Technology Corporation (LSTC) (2018c). "LS-PrePost V4.7." Livermore, CA.

Livermore Software Technology Corporation (LSTC) (2019). "LS-DYNA SMP_d_R11_139066." Livermore, CA.

Ma, D. C. (1985a). "Seismic interactions between primary tank and core barrel." *Tran., 8th International Conference on Structural Mechanics in Reactor Technology (SMiRT-8)*, Brussels, Belgium.

Ma, D. C. (1985b). "Seismic interactions between primary tank and core barrel." *CONF-850809-39*, Argonne National Laboratory (ANL), Lemont, IL.

Ma, D. C., and Chang, Y. W. (1985a). "Analysis of seismic sloshing of reactor tanks considering submerged components and seismic isolation." *CONF-850670-14*, Argonne National Laboratory (ANL), Lemont, IL.

Ma, D. C., and Chang, Y. W. (1985b). "Analysis of seismic sloshing of reactor tanks considering submerged components and seismic isolation." *Proc., ASME/JSME 1985 Pressure Vessels and Piping Conference (1985 PVP)*, New Orleans, LA.

Ma, D. C., Chang, Y. W., and Gvildys, J. (1983a). "Seismic response of large suspended tanks." *Proc., ASME/JSME 1983 Pressure Vessels and Piping Conference (1983 PVP)*, Portland, OR.

Ma, D. C., Gvildys, J., and Chang, Y. W. (1983b). "Dynamic analysis of large suspended LMFBR reactor vessels." *CONF-830805-14*, Argonne National Laboratory (ANL), Lemont, IL.

Ma, D. C., Gvildys, J., and Chang, Y. W. (1983c). "Effects of core barrel on vessel seismic loadings." *Tran., 7th International Conference on Structural Mechanics in Reactor Technology (SMiRT-7)*, Chicago, IL.

Ma, D. C., Gvildys, J., and Chang, Y. W. (1983d). "Effects of core barrel on vessel seismic loadings [LMFBE]." *CONF-830805-27*, Argonne National Laboratory (ANL), Lemont, IL.

Ma, D. C., Gvildys, J., and Chang, Y. W. (1985a). "Effects of deck-mounted components on the sloshing response of a pool-type LMFBR." *Tran., 8th International Conference on Structural Mechanics in Reactor Technology (SMiRT-8)*, Brussels, Belgium.

Ma, D. C., Gvildys, J., and Chang, Y. W. (1985b). "Effects of deck-mounted components on the sloshing response of a pool-type LMFBR." *CONF-850809-34*, Argonne National Laboratory (ANL), Lemont, IL.

Ma, D. C., Gvildys, J., Chang, Y. W., and Liu, W. K. (1982a). "Seismic behavior of liquid-filled shells." *Nuclear Engineering and Design*, 70(3), 437-455.

Ma, D. C., Liu, W. K., Gvildys, J., and Chang, Y. W. (1982b). "Seismically-induced sloshing phenomena in LMFBR reactor tanks." *CONF-820705-13*, Argonne National Laboratory (ANL), Lemont, IL.

Malhotra, P. K. (1997). "New method for seismic isolation of liquid-storage tanks." *Earthquake Engineering and Structural Dynamics*, 26(8), 839-847.

Malhotra, P. K., Wenk, T., and Wieland, M. (2000). "Simple procedure for seismic analysis of liquid-storage tanks." *Structural Engineering International*, 10(3), 197-201.

Mazzoni, S., McKenna, F., Scott, M. H., and Fenves, G. L. (2009). "Open system for earthquake engineering simulation user manual, version 2.0." Pacific Earthquake Engineering Research Center (PEER), University of California, Berkeley, CA.

Mir, F. U. H. (in progress). "Physical and numerical simulations of fluid-structure interaction effects in advanced reactors." Dissertation, presented to University at Buffalo, Buffalo, NY, in partial fulfillment of the requirements for the degree of Doctor of Philosophy.

Mir, F. U. H., Yu, C.-C., Charkas, H., and Whittaker, A. S. (2020a). "Validation of numerical models for seismic fluid-structure interaction analysis of advanced reactors." *Tran., International Congress on Advances in Nuclear Power Plants (ICAPP 2020)*, Abu Dhabi, United Arab Emirates.

Mir, F. U. H., Yu, C.-C., Cohen, M., Bardet, P., Coleman, J. L., and Whittaker, A. S. (2019). "Dataset generation for validation of fluid-structure interaction models." *Tran., 25th International Conference on Structural Mechanics in Reactor Technology (SMiRT-25)*, Charlotte, NC.

Mir, F. U. H., Yu, C.-C., and Whittaker, A. S. (2020b). "Experiments for validation of FSI models for seismic response of advanced reactor internals." *Tran., 17th World Conference on Earthquake Engineering (17WCEE)*, Sendai, Japan.

Morris, B. T. (1938). "A laboratory model study of the behavior of liquid-filled tanks in earthquakes." Dissertation, presented to Standford University, in partial fulfillment of the requirements for the degree of Doctor of Philosophy.

Omega Engineering Inc. "All stainless steel transducer." <https://www.omega.com/en-us/sensors-and-sensing-equipment/pressure-and-strain/pressure-transducers/p/PXM309>. (Jun 4, 2020).

Pacific Earthquake Engineering Research (PEER) "PEER ground motion database." <http://peer.berkeley.edu/peer_ground_motion_database>. (Jan. 12, 2019).

Padmanaban, S. (1996). "Dynamic response of hazardous liquid-waste storage tanks used in nuclear facilities." Dissertation, presented to Rice University, Houston, Texas, in partial fulfillment of the requirements for the degree of Doctor of Philosophy.

Papazafeiropoulos, G., and Plevris, V. (2018). "OpenSeismoMatlab: a new open-source software for strong ground motion data processing." *Heliyon*, 4(9), e00784.

Patton, K. T. (1965). "Tables of hydrodynamic mass factors for translational motion." *ASME Winter Annual Meeting 65-WA/UNT-2*, American Society of Mechanical Engineers (ASME), New York, NY.

Risk and Safety Working Group (RSWG) (2012). "An Integrated Safety Assessment Methodology (ISAM) for Generation IV nuclear systems." *Version 1.1*, 14th RSWG Meeting, Union Gap, WA.

Sakurai, A., Masuko, Y., Kurihara, C., Ishihama, K., Yashiro, T., Chang, Y. W., and Rodwell, E. (1989). "Seismic sloshing experiments of large pool-type fast breeder reactors." *Nuclear Engineering and Design*, 113(3), 423-433.

Soules, J. G. (2018, Nov 23). Personal communication, Email < Greg.Soules@mcdermott.com>.

Tang, Y. (1986). "Studies of dynamic response of liquid storage tanks." Dissertation, presented to Rice University, Houston, TX, in partial fulfillment of the requirements for the degree of Doctor of Philosophy.

Tang, Y., and Chang, Y. (1994). "Free vibration analysis of partially filled liquid storage tanks." *ANL/RE/CP-82143; CONF-940613-20*, Argonne National Laboratory (ANL), Lemont, IL.

Thomas, T. H., Yasui, G., Graham, R. H., Williamson, R. A., Lowe, R. E., and Hoak, W. (1963). "Nuclear reactors and earthquakes." *TID-7024*, Division of Reactor Development, United States Atomic Energy Commission, Washington DC.

Timoshenko, S. (1937). *Vibration problems in engineering*, 1st Ed., D. Van Nostrand Company, Inc, New York, NY.

Tsopelas, P., Nagarajaiah, S., Constantinou, M., and Reinhorn, A. (1991). "3D-BASIS-M: nonlinear dynamic analysis of multiple building base isolated structures." *NCEER 91-0014*, National Center for Earthquake Engineering Research, University at Buffalo, The State University of New York, Buffalo, NY.

United States Geological Survey (USGS) "Earthquake hazards program: unified hazard tool." <https://earthquake.usgs.gov/hazards/interactive/>. (Dec 11, 2018).

Veletsos, A. (1974). "Seismic effects in flexible liquid storage tanks." *Proc., 5th World Conference on Earthquake Engineering (5WCEE)*, Rome, Italy.

Veletsos, A. (1984). "Seismic response and design of liquid storage tanks." *Guidelines for the seismic design of oil and gas pipeline systems*, Committee on Gas and Liquid Fuel Lifelines, American Society of Civil Engineers (ASCE), Reston, VA, 255-370.

Veletsos, A., and Tang, Y. (1986). "Dynamics of vertically excited liquid storage tanks." *Journal of Structural Engineering*, 112(6), 1228-1246.

Veletsos, A., and Tang, Y. (1987). "Rocking response of liquid storage tanks." *Journal of Engineering Mechanics*, 113(11), 1774-1792.

Veletsos, A., and Tang, Y. (1990). "Soil-structure interaction effects for laterally excited liquid storage tanks." *Earthquake Engineering and Structural Dynamics*, 19(4), 473-496.

Veletsos, A., and Yang, J. (1977). "Earthquake response of liquid storage tanks." *Proc., Second Annual Engineering Mechanics Division Specialty Conference*, Raleigh, NC.

Westergaard, H. M. (1933). "Water pressures on dams during earthquakes." *Transactions of the American Society of Civil Engineers*, 95, 418-433.

Yang, J. (1976). "Dynamic behavior of fluid-tank systems." Dissertation, presented to Rice University, Houston, TX, in partial fulfillment of the requirements for the degree of Doctor of Philosophy.

Young, D., and Felgar, R. P. (1949). "Tables of characteristic functions representing normal modes of vibration of a beam." *Engineering Research Series No. 44*, University of Texas, Austin, TX.

Yu, C.-C., and Whittaker, A. S. (2020). "Analytical solutions for seismic fluid-structure interaction of head-supported cylindrical tanks." In press, *Engineering Mechanics*.

Yu, Y. T. (1945). "Virtual masses of rectangular plates and parallelepipeds in water." *Journal of Applied Physics*, 16(11), 724-729.

Zhu, M., McKenna, F., and Scott, M. H. (2018). "OpenSeesPy: python library for the OpenSees finite element framework." *SoftwareX*, 7, 6-11.

APPENDIX A. SUMMARY OF DERIVATIONS AND ANALYTICAL SOLUTIONS FOR FSI ANALYSIS OF CYLINDRICAL TANKS

A.1 Introduction

This appendix summarizes the derivations and analytical solutions for FSI responses of base- and head-supported cylindrical tanks presented in Section 3. The variables for the analytical solutions denoted in Figures 3.2 and 3.31 are used herein, including the dimensions of a cylindrical tank shown in two cut-away views, a Cartesian coordinate system (x , y , z), and a cylindrical coordinate system (r , θ, z). The radius of the tank is R and the height is H_s. The height of the contained fluid is H and its density is ρ. The tank moves with the rigid support (i.e., base or head) at a horizontal displacement, velocity, and acceleration, $u_0(t)$, $u_0'(t)$, and $u_0''(t)$, in the x direction.

Sections A.2 and A.3 summarize the derivations and analytical solutions for base- and head-supported cylindrical tanks, respectively. The summary includes the governing equations and boundary conditions of the fluid used for the derivations, and the methods of separation of variables used for developing the governing equations that were differential equations. Variables are defined once.

A.2 Base-supported tank

The analytical solutions presented in Section 3 for base-supported tanks were derived by Jacobsen (1949), Chalhoub and Kelly (1988), Housner (1954, 1957), and Veletsos (1984). Jacobsen and Housner parsed the FSI responses in a rigid tank into impulsive and convective components (see Section 3 for more information), and derived solutions for the two components separately. Chalhoub and Kelly (1988) did not parse the responses and derived solutions with the consideration of both impulsive and convective components. Veletsos (1984) accounted for the flexibility of the tank wall in deriving impulsive responses, but considered the tank to be rigid for convective responses, which were assumed to be independent of the deformation of the tank wall.

Jacobsen (1949)

Table A.1 lists the governing equation, boundary conditions, separation of variables for deriving the governing equation, and the analytical solutions for impulsive responses of Jacobsen (1949). The governing equation is the potential velocity Φ_{imp} of the fluid associated with impulsive responses. The solutions address the pressures on the tank wall and base, $p_{imp,w}$ and $p_{imp,b}$, and the shear force, F_{imp}, and moments, $M_{imp,w}$ and $M_{imp,b}$, at the tank base. The moment $M_{imp,w}$ is associated with $p_{imp,w}$ on the tank wall, and $M_{imp,b}$ is associated with $p_{imp,w}$ on the base (see Section 3 for more information). The governing equation Φ_{imp} and analytical solutions, as written in Jacobsen (1949), involved calculation errors, and those presented in Table A.1 are corrected per Section 3.

Table A.1. Governing equation, boundary conditions, separation of variables, and analytical solutions for impulsive responses of base-supported rigid tanks (Jacobsen 1949)

Governing equation	Per Eq. (3.8), $$\Phi_{imp} = u_0'(t) H \cos\theta \sum_{i=1}^{\infty} \frac{8(-1)^{i+1}}{\left[(2i-1)\pi\right]^2} \frac{I_1\left[(2i-1)\frac{\pi}{2}\frac{r}{H}\right]}{I_1'\left[(2i-1)\frac{\pi}{2}\frac{R}{H}\right]} \cos\left[(2i-1)\frac{\pi}{2}\frac{z}{H}\right]$$ where I_1 is the modified Bessel function of the first kind with an integer order of 1, and I_1' is the first derivative of I_1 with respect to $(2i-1)\pi R/(2H)$.

Table A.1. Governing equation, boundary conditions, separation of variables, and analytical solutions for impulsive responses of base-supported rigid tanks (Jacobsen 1949) (continued)

Boundary conditions	1. On the initial free surface, at $z = H$, the impulsive pressure is zero per Eq. (3.5): $$-\rho \left. \frac{\partial \Phi_{imp}}{\partial t} \right|_{z=H} = 0$$ 2. On the tank wall, at $r = R$, the radial velocities of the tank wall and the adjacent fluid are equal per Eq. (3.6): $$\left. \frac{\partial \Phi_{imp}}{\partial r} \right|_{r=R} = u_0'(t) \cos\theta$$ 3. On the tank base, at $z = 0$, the vertical velocity of the fluid is zero per Eq. (3.7): $$\left. \frac{\partial \Phi_{imp}}{\partial z} \right|_{z=0} = 0$$ The following equations are obtained using the assumed form of Φ_{imp} per Eq. (3.3) for Eqs. (3.5), (3.6), and (3.7), respectively: $$\tilde{Z}|_{z=H} = 0 \quad \text{(A.1)}$$ $$\tilde{R}|_{r=R} \cdot \tilde{\Theta} \cdot \tilde{Z} \cdot \tilde{T} = u_0'(t) \cos\theta \quad \text{(A.2)}$$ $$\tilde{Z}'|_{z=0} = 0 \quad \text{(A.3)}$$ where $\tilde{R}$, $\tilde{\Theta}$, $\tilde{Z}$, and $\tilde{T}$ are four unknown functions associated with variables r, θ, z, and t, respectively.

Table A.1. Governing equation, boundary conditions, separation of variables, and analytical solutions for impulsive responses of base-supported rigid tanks (Jacobsen 1949) (continued)

Separation of variables	Given Eq. (A.2), $\tilde{\Theta}$ and $\tilde{T}$ are: $$\tilde{\Theta} = \cos\theta \quad \text{(A.4)}$$ $$\tilde{T} = u_0'(t) \quad \text{(A.5)}$$ Given Eq. (3.4), $\tilde{Z}''/\tilde{Z}$ is assumed to be a constant $-\lambda^2$, and so the form of $\tilde{Z}$ is: $$\tilde{Z} = A\cos\lambda z + B\sin\lambda z \quad \text{(A.6)}$$ where A and B are constants, and $B = 0$ per Eq. (A.3). Substituting Eqs. (A.4) and (A.6) for $\tilde{\Theta}$ and $\tilde{Z}$ in Eq. (3.4), respectively, $\tilde{R}$ is solved using the form: $$\tilde{R} = CI_1(\lambda r) \quad \text{(A.7)}$$ where C is a constant. The constants A, C, and λ are solved for using the three boundary conditions per Eqs. (A.1), (A.2), and (A.3). The governing equation Φ_{imp} per Eq. (3.3) is solved using solutions for $\tilde{R}$, $\tilde{\Theta}$, $\tilde{Z}$, and $\tilde{T}$ per Eqs. (A.4) to (A.7).
Analytical solutions	$$p_{imp,w} = -u_0''(t)\rho H\cos\theta\sum_{i=1}^{\infty}\frac{8(-1)^{i+1}}{\left[(2i-1)\pi\right]^2}\frac{I_1\left[(2i-1)\pi R/(2H)\right]}{I_1'\left[(2i-1)\pi R/(2H)\right]}\cos\left[(2i-1)\frac{\pi}{2}\frac{z}{H}\right]$$ $$p_{imp,b} = -u_0''(t)\rho H\cos\theta\sum_{i=1}^{\infty}\frac{8(-1)^{i+1}}{\left[(2i-1)\pi\right]^2}\frac{I_1\left[(2i-1)\pi r/(2H)\right]}{I_1'\left[(2i-1)\pi R/(2H)\right]}$$ $$F_{imp} = u_0''(t)m_l\frac{H}{R}\sum_{i=1}^{\infty}\frac{16}{\left[(2i-1)\pi\right]^3}\frac{I_1\left[(2i-1)\pi R/(2H)\right]}{I_1'\left[(2i-1)\pi R/(2H)\right]}$$ $$M_{imp,w} = u_0''(t)m_l\frac{H^2}{R}\sum_{i=1}^{\infty}\frac{16}{\left[(2i-1)\pi\right]^3}\frac{I_1\left[(2i-1)\pi R/(2H)\right]}{I_1'\left[(2i-1)\pi R/(2H)\right]}\left[1-\frac{2(-1)^{i+1}}{(2i-1)\pi}\right]$$ $$M_{imp,b} = u_0''(t)m_l H\sum_{i=1}^{\infty}\frac{16(-1)^{i+1}}{\left[(2i-1)\pi\right]^3}\frac{I_2\left[(2i-1)\pi R/(2H)\right]}{I_1'\left[(2i-1)\pi R/(2H)\right]}$$ where I_2 is the modified Bessel function of the first kind with an integer order of 2

Chalhoub and Kelly (1988)

Table A.2 lists the governing equation, boundary conditions, separation of variables for deriving the governing equation, and the analytical solutions for FSI responses of Chalhoub and Kelly (1988). The governing equation is the potential velocity Φ_h of the fluid, with consideration of both impulsive and convective components. The solutions address the convective frequency $f_{con,j}$ in the j th mode, and the hydrodynamic pressure of the fluid p_d and wave height d_w.

Table A.2. Governing equation, boundary conditions, separation of variables, and analytical solutions for FSI responses of base-supported rigid tanks (Chalhoub and Kelly 1988)

Governing equation	Per Eq. (3.18) $$\Phi_h = \sum_{i=1}^{\infty} \chi_i \left[\int_0^t u_0''(t) \cos \lambda_i (t-\tau) d\tau \right] \cdot J_1(n_i \frac{r}{R}) \frac{\cosh n_i \frac{z}{R}}{\cosh n_i \frac{H}{R}} \cos\theta + u_0'(t) r \cos\theta$$ where χ_i is per Eq. (3.19), λ_i is per Eq. (3.20), J_1 is the Bessel function of the first kind with an integer order of 1, and n_i is a root of $J_1'(n_i) = 0$.
Boundary conditions	1. On the initial free surface, at $z = H$, the height of the wave generates hydrostatic pressure at $z = H$ per Eq. (3.17): $$g \frac{\partial \Phi_h}{\partial z} \Big|_{z=H} = -\frac{\partial^2 \Phi_h}{\partial t^2} \Big|_{z=H}$$ 2. On the tank wall, at $r = R$, the radial velocities of the tank wall and the adjacent fluid are equal per Eq. (3.6): $$\left. \frac{\partial \Phi_h}{\partial r} \right|_{r=R} = u_0'(t) \cos\theta$$ 3. On the tank base, at $z = 0$, the vertical velocity of the fluid is zero per Eq. (3.7): $$\left. \frac{\partial \Phi_h}{\partial z} \right|_{z=0} = 0$$

Table A.2. Governing equation, boundary conditions, separation of variables, and analytical solutions for FSI responses of base-supported rigid tanks (Chalhoub and Kelly 1988) (continued)

Separation of variables	Given Eq. (3.4), $\tilde{\Theta}''/\tilde{\Theta}$ and $\tilde{Z}''/\tilde{Z}$ are assumed to be constants $-k^2$ and n^2, respectively, and so the forms of $\tilde{\Theta}$ and $\tilde{Z}$ are: $\tilde{\Theta} = K_1 \cos kz + K_2 \sin kz$ (A.8) $\tilde{Z}_0 = K_3 Z + K_4$, if $n = 0$ (A.9) $\tilde{Z}_n = K_7 \cosh nz + K_8 \sinh nz$, if $n \neq 0$ (A.10) where K_1, K_2, K_3, K_4, K_7, K_8 are functions of time t. Using solutions of $\tilde{\Theta}$ and $\tilde{Z}$ per Eqs. (A.8) to (A.10) for Eq. (3.4), $\tilde{R}$ is solved per the form: $\tilde{R}_0 = K_5 r^k + K_6 r^{-k}$, if $n = 0$ (A.11) $\tilde{R}_n = K_9 J_1(nr)$, if $n \neq 0$ (A.12) where J_1 is the Bessel function of the first kind with an integer order of 1, and K_5, K_6, and K_9 are functions of time t. Per the form of Eq. (3.14), the general solution for the governing equation, $\Phi_h = \Phi_{h,0} + \Phi_{h,n}$, is calculated using $\tilde{R}$, $\tilde{\Theta}$, and $\tilde{Z}$ per Eqs. (A.8) to (A.12). The component $\Phi_{h,0}$ is associated with $\tilde{Z}_0$ and $\tilde{R}_0$ for $n = 0$, and $\Phi_{h,n}$ is associated with $\tilde{Z}_n$ and $\tilde{R}_n$ for $n \neq 0$. For a given t, the constants k, n, and K_1 to K_9 are solved for using the general solution of Φ_h and the three boundary conditions per Eqs. (3.17), (3.6), and (3.7).
Analytical solutions	$$f_{con,j} = \frac{1}{2\pi}\sqrt{\frac{n_j g}{R} \cdot \tanh(n_j \frac{H}{R})}$$ $$p_d = -u_0''(t)\rho \cos\theta \cdot \left[\sum_{j=1}^{\infty} B_j + r\right] + \rho \cos\theta \sum_{j=1}^{\infty} B_j \lambda_j \int_0^t u_0''(\tau) \sin\lambda_j (t-\tau) d\tau$$ where B_j is per Eq. (3.22). $$d_w = -\sum_{j=1}^{\infty} A_j(t) \cdot \frac{R}{g} \cos\theta \frac{2}{{n_j}^2 - 1} \frac{J_1(n_j r/R)}{J_1(n_j)}$$ where A_j is per Eq. (3.78).

Housner (1954, 1957)

Tables A.3 and A.4 list the governing equation, boundary conditions, and analytical solutions for impulsive and convective responses, respectively, of Housner (1954, 1957). The impulsive responses are calculated using the vertically discretized fluid presented in Figure 3.3. The governing equations are drawn from Newton's second law, describing the equilibrium of the resultant force of the pressure of the fluid and its inertial force. The solutions address the pressures on the tank wall and base, $p_{imp,w}$ and $p_{imp,b}$, and the shear force, F_{imp}, and moments, $M_{imp,w}$ and $M_{imp,b}$, at the tank base. The convective responses are calculated using the horizontally discretized fluid presented in Figure 3.21. The governing equations are drawn from Hamilton's Principle, describing the balance of the kinetic and potential energies of the fluid. The solutions address the pressures on the tank wall and base, $p_{con,w,1}$ and $p_{con,b,1}$, and wave height, $d_{w,1}$, in the first convective mode, and the convective frequency, $f_{con,j}$, shear force, $F_{con,j}$, and moments, $M_{con,w,j}$ and $M_{con,b,j}$, at the tank base in the jth mode ($j \geq 1$). The analytical solutions for the impulsive and convective responses, as written in Housner, involved calculation errors, and those equations presented in Tables A.3 and A.4 are corrected per Section 3.

Table A.3. Governing equations, boundary conditions, and analytical solutions for impulsive responses of base-supported rigid tanks (Housner 1954, 1957)

Governing equations	The conservation of the volume of the contained fluid per Eq. (3.25): $$u_z'' \cdot dx = \frac{\partial u_x''}{\partial x} dx \cdot z$$ where u_x'' and u_z'' are the fluid velocities in the $x-$ and $z-$directions, respectively. The balance of the resultant force of the pressure and the inertial force of the fluid in the x direction, per Eqs. (3.28) and (3.29), using Newton's second law gives: $$\int_0^H p_{imp} dz = -\rho H dx \cdot u_x''$$ The balance of the resultant force of the pressure and the inertial force of the fluid in the z direction, per Eq. (3.26), using Newton's second law gives: $$\frac{\partial p_{imp}}{\partial z} dz \cdot dx = \rho dx dz \cdot u_z''$$

Table A.3. Governing equations, boundary conditions, and analytical solutions for impulsive responses of base-supported rigid tanks (Housner 1954, 1957) (continued)

Boundary conditions	1. On the initial free surface, at $z = H$, the impulsive pressure is zero: $$p_{imp}(z = H) = 0$$ 2. On the tank wall, at $x = \pm R\cos\theta$, the horizontal velocities of the tank wall and the adjacent fluid are equal: $$u_x''(x = \pm R\cos\theta) = u_0''(t)$$
Analytical solutions	$$p_{imp,w} = -u_0''(t)\frac{\sqrt{3}}{2}\frac{\rho}{H}(H^2 - z^2)\tanh(\sqrt{3}R\cos\theta / H)$$ $$p_{imp,b} = p_{imp}(z = 0) = -u_0''(t)\frac{\sqrt{3}}{2}\rho H\frac{\sinh(\sqrt{3}r\cos\theta / H)}{\cosh(\sqrt{3}r\cos\theta / H)}$$ $$F_{imp} = u_0''(t)\frac{1}{\sqrt{3}}\rho\pi RH^2\tanh(\sqrt{3}\frac{R}{H})$$ $$M_{imp,w} = F_{imp}\frac{3}{8}H$$ $$M_{imp,b} = F_{imp}\frac{1}{2}\left(\frac{\sqrt{3}R / H}{\tanh(\sqrt{3}R / H)} - 1\right)H$$

Table A.4. Governing equations, boundary conditions, and analytical solutions for convective responses of base-supported rigid tanks (Housner 1954; 1957)

Governing equations	The conservation of the volume of the contained fluid per Eq. (3.97): $$\frac{\partial u_x'}{\partial x}+\frac{\partial u_y'}{\partial y}+\frac{\partial u_z'}{\partial z}=0$$ where u_x'', u_y'', and u_z'' are the fluid velocities in the $x-$, $y-$, and $z-$directions, respectively. The balance of the kinetic and potential energies of the contained fluid, K_l and P_l per Eqs. (3.91) to (3.93), using Hamilton's principle: $$\int (K_l - P_l)dt = 0$$ where $K_l = \frac{1}{2}\iiint_{V_l}(u_x'^2 + u_y'^2 + u_z'^2)dV_l$, $P_l = \iiint_{V_l}\rho g u_z dV_l$, and V_l is the volume of the contained fluid.
Boundary conditions	1. On the tank wall, at $x=\pm R\cos\theta$, the fluid velocity in the $x-$direction is zero per Eq. (3.88): $$u_x'(x=\pm R\cos\theta)=0$$ 2. On the tank base, at $z=0$, the rotation of the horizontal fluid layer is zero per Eq. (3.89): $$\varphi(z=0)=0$$ 3. On the $x-z$ cross section (i.e., $y=0$), the fluid velocity in the $y-$direction is zero per Eq. (3.90): $$u_y'(y=0)=0$$

Table A.4. Governing equations, boundary conditions, and analytical solutions for convective responses of base-supported rigid tanks (Housner 1954; 1957) (continued)

Analytical solutions	$$p_{con,w,1} = -\varphi_{H,a} \cdot \sin(\omega_{con,1} \cdot t) \cdot \sqrt{\frac{3}{8}} \rho R^2 (1 - \frac{1}{3}\cos^2\theta)\cos\theta \frac{\cosh(\sqrt{\frac{27}{8}}\frac{z}{R})}{\sinh(\sqrt{\frac{27}{8}}\frac{H}{R})}$$ where $\varphi_{H,a} = \sqrt{\frac{27}{8}}\frac{A_m(2j-1)}{R}\tanh\sqrt{\frac{27}{8}}\frac{H(2j-1)}{R}$, and A_m is the amplitude of the acceleration of a single-degree-of-freedom system in the first convective mode. $$p_{con,b,1} = -\varphi_{H,a} \cdot \sin(\omega_{con,1} \cdot t) \cdot \sqrt{\frac{3}{8}} \rho R^2 (\frac{r}{R} - \frac{1}{3}\frac{r^3}{R^3}\cos^2\theta)\cos\theta \frac{1}{\sinh(\sqrt{\frac{27}{8}}\frac{H}{R})}$$ $$d_{w,1} = \frac{p_{con,1}(z=H)}{\rho g}$$ $$f_{con,j} = \frac{1}{2\pi}\left[\frac{g(2j-1)}{R}\sqrt{\frac{27}{8}}\tanh(\sqrt{\frac{27}{8}}\frac{H(2j-1)}{R})\right]^{\frac{1}{2}}$$ $$F_{con,j} = \varphi_{H,a} \cdot \sin(\omega_{con,j} \cdot t)\frac{1}{4}\sqrt{\frac{27}{8}}\rho(\frac{R}{2j-1})^4$$ $$M_{con,w,j} = F_{con,j} \cdot \left(H + \frac{R}{2j-1}\sqrt{\frac{8}{27}}\frac{1-\cosh\sqrt{\frac{27}{8}}\frac{H(2j-1)}{R}}{\sinh\sqrt{\frac{27}{8}}\frac{H(2j-1)}{R}}\right)$$ $$M_{con,b,j} = F_{con,j}\frac{\frac{5}{6}\sqrt{\frac{3}{8}}\frac{R}{2j-1}}{\sinh(\sqrt{\frac{27}{8}}\frac{H(2j-1)}{R})}$$

Veletsos (1984)

Tables A.5 and A.6 list the governing equations, boundary conditions, separation of variables for deriving the governing equations, and analytical solutions for impulsive and convective responses, respectively, of Veletsos (1984). For the impulsive responses, the governing equations are the equation of motion of the flexible tank and the potential velocity Φ_{imp} of the fluid. The solutions address the impulsive frequency in the k th mode, and the modal pressures on the tank wall and base, $p_{imp,w,k}$ and $p_{imp,b,k}$, and shear force, $F_{imp,k}$, and moments, $M_{imp,w,k}$ and $M_{imp,b,k}$, at the tank base. For the convective responses, the governing equation is the potential velocity Φ_{con} of the fluid. The solutions address the convective frequency $f_{con,j}$ in the j th mode, and the modal pressures on the tank wall and base, $p_{con,w,j}$ and $p_{con,b,j}$, shear force, $F_{con,j}$, and moments, $M_{con,w,j}$ and $M_{con,b,j}$, at the tank base, and wave height, $d_{w,j}$.

Table A.5. Governing equations, boundary conditions, separation of variables, and analytical solutions for impulsive responses of base-supported flexible tanks (Veletsos 1984)

Governing equations	The equation of motion of the tank per Eq. (3.51) is: $$\left[\begin{array}{c} M \end{array}\right]_{N\times N}\left\{\begin{array}{c} U_i'' \\ V_i'' \\ W_i'' \end{array}\right\}_{N\times 1}+\left[\begin{array}{c} K \end{array}\right]_{N\times N}\left\{\begin{array}{c} U_i \\ V_i \\ W_i \end{array}\right\}_{N\times 1}=u_0''(t)\left\{\begin{array}{c} P_{ext} \end{array}\right\}_{N\times 1}$$ where $[M]$ and $[K]$ are the mass and stiffness matrices of the tank, $u_0''(t)\{P_{ext}\}$ is the external force vector associated with the ground motion, and U_i, V_i, and W_i are the degrees of freedom of the tank in the radial, tangential and axial directions, respectively. Per Eq. (3.45), $$\Phi_{imp}=H\cos\theta\sum_{i=1}^{\infty}U_i''(t)\sum_{j=1}^{\infty}\frac{4}{(2j-1)\pi}\frac{I_1\left[(2j-1)\frac{\pi}{2}\frac{r}{H}\right]}{I_1'\left[(2j-1)\frac{\pi}{2}\frac{R}{H}\right]}\cos\left[(2j-1)\frac{\pi}{2}\frac{z}{H}\right]\cdot\alpha_{ij}$$ where α_{ij} is calculated per Eq. (3.46) using the modal shapes of a base-supported cantilever $\psi_i(z)$, I_1 is the modified Bessel function of the first kind with an integer order of 1, and I_1' is the first derivative of I_1 with respect to $(2i-1)\pi R/(2H)$.

Table A.5. Governing equations, boundary conditions, separation of variables, and analytical solutions for impulsive responses of base-supported flexible tanks (Veletsos 1984) (continued)

Boundary conditions	1. On the initial free surface, at $z = H$, the impulsive pressure is zero per Eq. (3.5): $$-\rho \left.\frac{\partial \Phi_{imp}}{\partial t}\right|_{z=H} = 0$$ 2. On the tank wall, at $r = R$, the radial velocities of the tank wall and the adjacent fluid are equal per Eq. (3.44): $$u'(r=R) = \left.\frac{\partial \Phi_{imp}}{\partial r}\right|_{r=R} = U_i'(t)\psi_i(z)\cos\theta$$ 3. On the tank base, at $z = 0$, the vertical velocity of the fluid is zero per Eq. (3.7): $$\left.\frac{\partial \Phi_{imp}}{\partial z}\right|_{z=0} = 0$$ The following equations are obtained using the assumed form of Φ_{imp} per Eq. (3.3) for Eqs. (3.5), (3.44), and (3.7), respectively: $$\tilde{Z}|_{z=H} = 0 \quad \text{(A.13)}$$ $$\tilde{R}|_{r=R} \cdot \tilde{\Theta} \cdot \tilde{Z} \cdot \tilde{T} = U_i'(t)\psi_i(z)\cos\theta \quad \text{(A.14)}$$ $$\tilde{Z}'|_{z=0} = 0 \quad \text{(A.15)}$$
Separation of variables	Given Eq. (A.14), $\tilde{\Theta}$ and $\tilde{T}$ are solved: $$\tilde{\Theta} = \cos\theta \quad \text{(A.16)}$$ $$\tilde{T} = u_0'(t) \quad \text{(A.17)}$$ Given Eq. (3.4), $\tilde{Z}''/\tilde{Z}$ is assumed to be a constant $-\lambda^2$, and so the form of $\tilde{Z}$ is: $$\tilde{Z} = A\cos\lambda z + B\sin\lambda z \quad \text{(A.18)}$$ where A and B are constants, and $B = 0$ per Eq. (A.15). Substituting Eqs. (A.16) and (A.18) for $\tilde{\Theta}$ and $\tilde{Z}$ in Eq. (3.4), respectively, $\tilde{R}$ is solved using the form: $$\tilde{R} = CI_1(\lambda r) \quad \text{(A.19)}$$ where C is a constant. The constants A, C, and λ are solved for using the three boundary conditions per Eqs. (A.13), (A.14), and (A.15). The governing equation Φ_{imp} per Eq. (3.3) is solved using solutions for $\tilde{R}$, $\tilde{\Theta}$, $\tilde{Z}$, and $\tilde{T}$ per Eqs. (A.16) to (A.19).

Table A.5. Governing equations, boundary conditions, separation of variables, and analytical solutions for impulsive responses of base-supported flexible tanks (Veletsos 1984) (continued)

Analytical solutions	$$[K]\{\phi_k\} = \left(\frac{f_{imp,k}}{2\pi}\right)^2 [M]\{\phi_k\}$$ where $f_{imp,k}$ and $\{\phi_k\}$ are the frequency and modal shape in the k th impulsive mode. $$p_{imp,w,k} = -A_k(t)\cdot\rho H\cos\theta e_k \cdot\sum_{i=1}^{N_1}\phi_{ik}\sum_{j=1}^{\infty}\frac{4}{(2j-1)\pi}\frac{I_1\left[(2j-1)\frac{\pi}{2}\frac{R}{H}\right]}{I_1'\left[(2j-1)\frac{\pi}{2}\frac{R}{H}\right]}\cdot\cos\left[(2j-1)\frac{\pi}{2}\frac{z}{H}\right]\cdot\alpha_{ij}$$ where α_{ij}, e_k, and $A_k(t)$ are per Eqs. (3.46), (3.55) and (3.57), respectively. $$p_{imp,b,k} = -A_k(t)\cdot\rho H\cos\theta e_k\sum_{i=1}^{N_1}\phi_{ik}\sum_{j=1}^{\infty}\frac{4}{(2j-1)\pi}\frac{I_1\left[(2j-1)\frac{\pi}{2}\frac{r}{H}\right]}{I_1'\left[(2j-1)\frac{\pi}{2}\frac{R}{H}\right]}\cdot\alpha_{ij}$$ $$F_{imp,k} = A_k(t)\cdot m_l\frac{H}{R}e_k\sum_{i=1}^{N_1}\phi_{ik}\sum_{j=1}^{\infty}\frac{8(-1)^{j+1}}{\left[(2j-1)\pi\right]^2}\frac{I_1\left[(2j-1)\frac{\pi}{2}\frac{R}{H}\right]}{I_1'\left[(2j-1)\frac{\pi}{2}\frac{R}{H}\right]}\cdot\alpha_{ij}$$ $$M_{imp,w,k} = A_k(t)\cdot m_l\frac{H^2}{R}e_k\sum_{i=1}^{N_1}\phi_{ik}\sum_{j=1}^{\infty}\frac{8(-1)^{j+1}}{\left[(2j-1)\pi\right]^2}\frac{I_1\left[(2j-1)\frac{\pi}{2}\frac{R}{H}\right]}{I_1'\left[(2j-1)\frac{\pi}{2}\frac{R}{H}\right]}\left[1-\frac{2(-1)^{j+1}}{(2j-1)\pi}\right]\cdot\alpha_{ij}$$ $$M_{imp,b,k} = A_k(t)\cdot m_l He_k\sum_{i=1}^{N_1}\phi_{ik}\sum_{j=1}^{\infty}\frac{8}{\left[(2j-1)\pi\right]^2}\frac{I_2\left[(2j-1)\frac{\pi}{2}\frac{R}{H}\right]}{I_1'\left[(2j-1)\frac{\pi}{2}\frac{R}{H}\right]}\cdot\alpha_{ij}$$ where I_2 is the modified Bessel function of the first kind with an integer order of 2

Table A.6. Governing equation, boundary conditions, separation of variables, and analytical solutions for convective responses of base-supported rigid tanks (Veletsos 1984)

Governing equation	Per Eq. (3.71): $$\Phi_{con} = \frac{g}{i\omega} e^{i\omega t} \cos\theta \frac{2}{\frac{n_j g}{R}\tanh(n_j \frac{H}{R}) - \omega^2} \frac{n_j}{{n_j}^2 - 1} \frac{J_1(n_j \frac{r}{R})}{J_1(n_j)} \frac{\cosh(n_j \frac{z}{R})}{\cosh(n_j \frac{H}{R})} \tanh(n_j \frac{H}{R})$$ where g is the gravitational acceleration, J_1 is the Bessel function of the first kind with an integer order of 1, n_j is a root of $J_1'(n_j) = 0$, and ω is the frequency of an assumed harmonic motion.
Boundary conditions	1. On the initial free surface, at $z = H$, the height of the wave generates hydrostatic pressure at $z = H$ per Eq. (3.68): $$g \left.\frac{\partial(\Phi_{imp} + \Phi_{con})}{\partial z}\right|_{z=H} = -\left.\frac{\partial^2 \Phi_{con}}{\partial t^2}\right|_{z=H}$$ 2. On the tank wall, at $r = R$, the radial velocity of the fluid is zero per Eq. (3.69): $$\left.\frac{\partial \Phi_{con}}{\partial r}\right|_{r=R} = 0$$ 3. On the tank base, at $z = 0$, the vertical velocity of the fluid is zero per Eq. (3.70): $$\left.\frac{\partial \Phi_{con}}{\partial z}\right|_{z=0} = 0$$ The following equations are obtained using the assumed form of Φ_{con} per Eq. (3.65) and Φ_{imp} per Eq. (3.8) with $u_0'(t) = (1/i\omega)e^{i\omega t}$ for Eqs. (3.68), (3.69), and (3.70), respectively: $$\tilde{R}\cdot\tilde{\Theta}\cdot\tilde{Z}\cdot\tilde{T}''|_{z=H} + g\cdot\tilde{R}\cdot\tilde{\Theta}\cdot\tilde{Z}'\cdot\tilde{T}|_{z=H} = -\frac{g e^{i\omega t}}{i\omega}\cos\theta \cdot\sum_{i=1}^{\infty}\frac{4}{(2n-1)\pi}\frac{I_1[(2n-1)\pi r/(2H)]}{I_1'[(2n-1)\pi r/(2H)]} \quad \text{(A.20)}$$ $$\tilde{R}'|_{r=R} = 0 \quad \text{(A.21)}$$ $$\tilde{Z}'|_{z=0} = 0 \quad \text{(A.22)}$$

Table A.6. Governing equation, boundary conditions, separation of variables, and analytical solutions for convective responses of base-supported rigid tanks (Veletsos 1984) (continued)

Separation of variables	Given Eq. (A.20), $\tilde{\Theta}$ and $\tilde{T}$ are solved: $$\tilde{\Theta} = \cos\theta \quad \text{(A.23)}$$ $$\tilde{T} = e^{i\omega t} \quad \text{(A.24)}$$ Given Eq. (3.4), $\tilde{Z}''/\tilde{Z}$ is assumed to be a constant $(\lambda/R)^2$, and so the form of $\tilde{Z}$ is: $$\tilde{Z} = A\cosh(\lambda z/R) + B\sinh(\lambda z/R) \quad \text{(A.25)}$$ where A and B are constants, and $B = 0$ per Eq. (A.22). Substituting Eqs. (A.23) and (A.25) for $\tilde{\Theta}$ and $\tilde{Z}$ in Eq. (3.4), respectively, $\tilde{R}$ is solved using the form: $$\tilde{R} = CJ_1(\lambda r/R) \quad \text{(A.26)}$$ where C is a constant. The constants A, C, and λ are solved for using the three boundary conditions per Eqs. (A.20), (A.21), and (A.22). The governing equation Φ_{con} per Eq. (3.65) is solved using solutions for $\tilde{R}$, $\tilde{\Theta}$, $\tilde{Z}$, and $\tilde{T}$ per Eqs. (A.23) to (A.26).
Analytical solutions	$$f_{con,j} = \frac{1}{2\pi}\sqrt{\frac{n_j g}{R}\tanh(n_j\frac{H}{R})}$$ $$p_{con,w,j} = -A_j(t)\cdot\rho R\cos\theta\frac{2}{n_j{}^2-1}\frac{\cosh(n_j z/R)}{\cosh(n_j H/R)}$$ where $A_j(t)$ is per Eq. (3.78). $$p_{con,b,j} = -A_j(t)\cdot\rho R\cos\theta\frac{2}{n_j{}^2-1}\frac{J_1(n_j r/R)}{J_1(n_j)}\frac{1}{\cosh(n_j H/R)}$$ $$d_{w,j} = -A_j(t)\cdot\frac{R}{g}\cos\theta\frac{2}{n_j{}^2-1}\frac{J_1(n_j r/R)}{J_1(n_j)}$$ $$F_{con,j} = A_j(t)\cdot m_l\frac{R}{H}\frac{2}{n_j(n_j{}^2-1)}\tanh(n_j\frac{H}{R})$$ $$M_{con,w,j} = A_j(t)\cdot m_l R\frac{2}{n_j(n_j{}^2-1)}\tanh(n_j\frac{H}{R})\left[1-\frac{R}{n_j H}\tanh(n_j\frac{H}{2R})\right]$$ $$M_{con,b,j} = A_j(t)\cdot m_l\frac{R^2}{H}\frac{2}{n_j(n_j{}^2-1)}\frac{J_2(n_j)}{J_1(n_j)}\frac{1}{\cosh(n_j H/R)}$$ where J_2 is the Bessel function of the first kind with an integer order of 2.

A.3 Head-supported tank

The solutions for head-supported tanks are developed in this report. The solutions for impulsive responses are derived for both rigid and flexible tanks using the methodologies of Jacobsen (Table A.1) and Veletsos (Table A.5), respectively. The solutions for convective responses are derived for rigid tanks using the method of Veletsos (Table A.6). Tables A.7 and A.8 present information for impulsive responses of rigid and flexible head-supported tanks, respectively, including the governing equations, boundary conditions of the fluid, separation of variables used for deriving the governing equations, and analytical solutions. Companion information for convective responses of rigid head-supported tanks is presented in Table A.9.

Table A.7. Governing equation, boundary conditions, separation of variables, and analytical solutions for impulsive responses of head-supported rigid tanks

Governing equation	Per Eq. (3.8), $$\Phi_{imp} = u_0'(t) H \cos\theta \sum_{i=1}^{\infty} \frac{8(-1)^{i+1}}{\left[(2i-1)\pi\right]^2} \frac{I_1\left[(2i-1)\frac{\pi}{2}\frac{r}{H}\right]}{I_1'\left[(2i-1)\frac{\pi}{2}\frac{R}{H}\right]} \cos\left[(2i-1)\frac{\pi}{2}\frac{z}{H}\right]$$ where I_1 is the modified Bessel function of the first kind with an integer order of 1, and I_1' is the first derivative of I_1 with respect to $(2i-1)\pi R/(2H)$.

Table A.7. Governing equation, boundary conditions, separation of variables, and analytical solutions for impulsive responses of head-supported rigid tanks (continued)

Boundary conditions	1. On the initial free surface, at $z = H$, the impulsive pressure is zero per Eq. (3.5): $$-\rho \left. \frac{\partial \Phi_{imp}}{\partial t} \right|_{z=H} = 0$$ 2. On the tank wall, at $r = R$, the radial velocities of the tank wall and the adjacent fluid are equal per Eq. (3.6): $$\left. \frac{\partial \Phi_{imp}}{\partial r} \right|_{r=R} = u_0'(t) \cos\theta$$ 3. On the tank base, at $z = 0$, the vertical velocity of the fluid is zero per Eq. (3.7): $$\left. \frac{\partial \Phi_{imp}}{\partial z} \right|_{z=0} = 0$$ The following equations are obtained using the assumed form of Φ_{imp} per Eq. (3.3) for Eqs. (3.5), (3.6), and (3.7), respectively: $$\tilde{Z}|_{z=H} = 0 \quad \text{(A.27)}$$ $$\tilde{R}|_{r=R} \cdot \tilde{\Theta} \cdot \tilde{Z} \cdot \tilde{T} = u_0'(t) \cos\theta \quad \text{(A.28)}$$ $$\tilde{Z}'|_{z=0} = 0 \quad \text{(A.29)}$$

Table A.7. Governing equation, boundary conditions, separation of variables, and analytical solutions for impulsive responses of head-supported rigid tanks (continued)

Separation of variables	Given Eq. (A.28), $\tilde{\Theta}$ and $\tilde{T}$ are solved: $\tilde{\Theta} = \cos\theta$ (A.30) $\tilde{T} = u_0'(t)$ (A.31) Given Eq. (3.4), $\tilde{Z}''/\tilde{Z}$ is assumed to be a constant $-\lambda^2$, and so the form of $\tilde{Z}$ is: $\tilde{Z} = A\cos\lambda z + B\sin\lambda z$ (A.32) where A and B are constants, and $B = 0$ per Eq. (A.29). Substituting Eqs. (A.30) and (A.32) for $\tilde{\Theta}$ and $\tilde{Z}$ in Eq. (3.4), respectively, $\tilde{R}$ is solved using the form: $\tilde{R} = CI_1(\lambda r)$ (A.33) where C is a constant. The constants A, C, and λ are solved for using the three boundary conditions per Eqs. (A.27), (A.28), and (A.29). The governing equation Φ_{imp} per Eq. (3.3) is solved using solutions for $\tilde{R}$, $\tilde{\Theta}$, $\tilde{Z}$, and $\tilde{T}$ per Eqs. (A.30) to (A.33).
Analytical solutions	$p_{imp,w} = -u_0''(t)\rho H\cos\theta\sum_{i=1}^{\infty}\frac{8(-1)^{i+1}}{\left[(2i-1)\pi\right]^2}\frac{I_1\left[(2i-1)\pi R/(2H)\right]}{I_1'\left[(2i-1)\pi R/(2H)\right]}\cos\left[(2i-1)\frac{\pi}{2}\frac{z}{H}\right]$ $p_{imp,b} = -u_0''(t)\rho H\cos\theta\sum_{i=1}^{\infty}\frac{8(-1)^{i+1}}{\left[(2i-1)\pi\right]^2}\frac{I_1\left[(2i-1)\pi r/(2H)\right]}{I_1'\left[(2i-1)\pi R/(2H)\right]}$ $F_{imp} = u_0''(t)m_l\frac{H}{R}\sum_{i=1}^{\infty}\frac{16}{\left[(2i-1)\pi\right]^3}\frac{I_1\left[(2i-1)\pi R/(2H)\right]}{I_1'\left[(2i-1)\pi R/(2H)\right]}$ $M_{imp,w} = u_0''(t)m_l\frac{H^2}{R}\sum_{i=1}^{\infty}\frac{16}{\left[(2i-1)\pi\right]^3}\frac{I_1\left[(2i-1)\pi R/(2H)\right]}{I_1'\left[(2i-1)\pi R/(2H)\right]}\cdot\left[-\frac{H_s}{H}+1-\frac{2(-1)^{i+1}}{(2i-1)\pi}\right]$ $M_{imp,b} = u_0''(t)m_l H\sum_{i=1}^{\infty}\frac{16(-1)^{i+1}}{\left[(2i-1)\pi\right]^3}\frac{I_2\left[(2i-1)\pi R/(2H)\right]}{I_1'\left[(2i-1)\pi R/(2H)\right]}$ where I_2 is the modified Bessel function of the first kind with an integer order of 2

Table A.8. Governing equations, boundary conditions, separation of variables, and analytical solutions for impulsive responses of head-supported flexible tanks

Governing equations	The equation of motion of the tank per Eq. (3.51): $$\left[\begin{array}{c} M \end{array}\right]_{N\times N}\left\{\begin{matrix} U_i'' \\ V_i'' \\ W_i'' \end{matrix}\right\}_{N\times 1}+\left[\begin{array}{c} K \end{array}\right]_{N\times N}\left\{\begin{matrix} U_i \\ V_i \\ W_i \end{matrix}\right\}_{N\times 1}=u_0''(t)\left\{\begin{matrix} P_{ext} \end{matrix}\right\}_{N\times 1}$$ Where $[M]$ and $[K]$ are the mass and stiffness matrices of the tank, $u_0''(t)\{P_{ext}\}$ is the external force vector associated with the ground motion, and U_i, V_i, and W_i are the degrees of freedom of the tank in the radial, tangential and axial directions. Per Eq. (3.126), $$\Phi_{imp}=H\cos\theta\sum_{i=1}^{\infty}U_i''(t)\sum_{j=1}^{\infty}\frac{4}{(2j-1)\pi}\frac{I_1\left[(2j-1)\frac{\pi}{2}\frac{r}{H}\right]}{I_1'\left[(2j-1)\frac{\pi}{2}\frac{R}{H}\right]}\cos\left[(2j-1)\frac{\pi}{2}\frac{z}{H}\right]\cdot\alpha_{ij}$$ where α_{ij} is per Eq. (3.127) using the modal shapes of a top-supported cantilever $\psi_i(H_s-z)$, I_1 is the modified Bessel function of the first kind with an integer order of 1, and I_1' is the first derivative of I_1 with respect to $(2i-1)\pi R/(2H)$.

Table A.8. Governing equations, boundary conditions, separation of variables, and analytical solutions for impulsive responses of head-supported flexible tanks (continued)

Boundary conditions	1. On the initial free surface, at $z = H$, the impulsive pressure is zero per Eq. (3.5): $$-\rho \left. \frac{\partial \Phi_{imp}}{\partial t} \right|_{z=H} = 0$$ 2. On the tank wall, at $r = R$, the radial velocities of the tank wall and the adjacent fluid are equal per Eq. (3.125): $$u'(r=R) = \left. \frac{\partial \Phi_{imp}}{\partial r} \right|_{r=R} = U_i'(t)\psi_i(H_s - z)\cos\theta$$ 3. On the tank base, at $z = 0$, the vertical velocity of the fluid is zero per Eq. (3.7): $$\left. \frac{\partial \Phi_{imp}}{\partial z} \right|_{z=0} = 0$$ The following equations are obtained using the assumed form of Φ_{imp} per Eq. (3.3) for Eqs. (3.5), (3.125), and (3.7), respectively: $$\tilde{Z}|_{z=H} = 0 \quad \text{(A.34)}$$ $$\tilde{R}|_{r=R} \cdot \tilde{\Theta} \cdot \tilde{Z} \cdot \tilde{T} = U_i'(t)\psi_i(H_s - z)\cos\theta \quad \text{(A.35)}$$ $$\tilde{Z}'|_{z=0} = 0 \quad \text{(A.36)}$$
Separation of variables	Given Eq. (A.35), $\tilde{\Theta}$ and $\tilde{T}$ are solved: $$\tilde{\Theta} = \cos\theta \quad \text{(A.37)}$$ $$\tilde{T} = u_0'(t) \quad \text{(A.38)}$$ Given Eq. (3.4), $\tilde{Z}''/\tilde{Z}$ is assumed to be a constant $-\lambda^2$, and so the form of $\tilde{Z}$ is: $$\tilde{Z} = A\cos\lambda z + B\sin\lambda z \quad \text{(A.39)}$$ where A and B are constants, and $B = 0$ per Eq. (A.36). Substituting Eqs. (A.37) and (A.38) for $\tilde{\Theta}$ and $\tilde{Z}$ in Eq. (3.4), respectively, $\tilde{R}$ is solved using the form: $$\tilde{R} = CI_1(\lambda r) \quad \text{(A.40)}$$ where C is a constant. The constants A, C, and λ are solved using the three boundary conditions per Eqs. (A.34), (A.35), and (A.36). The governing equation Φ_{imp} per Eq. (3.3) is solved using solutions for $\tilde{R}$, $\tilde{\Theta}$, $\tilde{Z}$, and $\tilde{T}$ per Eqs. (A.37) to (A.40).

Table A.8. Governing equations, boundary conditions, separation of variables, and analytical solutions for impulsive responses of head-supported flexible tanks (continued)

Analytical solutions	$$[K]\{\phi_k\} = \left(\frac{f_{imp,k}}{2\pi}\right)^2 [M]\{\phi_k\}$$ where $f_{imp,k}$ and $\{\phi_k\}$ are the frequency and modal shape in the k th impulsive mode. $$p_{imp,w,k} = -A_k(t)\cdot \rho H \cos\theta e_k \cdot \sum_{i=1}^{N_1}\phi_{ik}\sum_{j=1}^{\infty}\frac{4}{(2j-1)\pi}\frac{I_1\left[(2j-1)\frac{\pi}{2}\frac{R}{H}\right]}{I_1'\left[(2j-1)\frac{\pi}{2}\frac{R}{H}\right]}\cdot\cos\left[(2j-1)\frac{\pi}{2}\frac{z}{H}\right]\cdot\alpha_{ij}$$ where α_{ij}, e_k, and $A_k(t)$ are per Eqs. (3.127), (3.130) and (3.133), respectively. $$p_{imp,b,k} = -A_k(t)\cdot \rho H \cos\theta e_k \sum_{i=1}^{N_1}\phi_{ik}\sum_{j=1}^{\infty}\frac{4}{(2j-1)\pi}\frac{I_1\left[(2j-1)\frac{\pi}{2}\frac{r}{H}\right]}{I_1'\left[(2j-1)\frac{\pi}{2}\frac{R}{H}\right]}\cdot\alpha_{ij}$$ $$F_{imp,k} = A_k(t)\cdot m_l \frac{H}{R} e_k \sum_{i=1}^{N_1}\phi_{ik}\sum_{j=1}^{\infty}\frac{8(-1)^{j+1}}{\left[(2j-1)\pi\right]^2}\frac{I_1\left[(2j-1)\frac{\pi}{2}\frac{R}{H}\right]}{I_1'\left[(2j-1)\frac{\pi}{2}\frac{R}{H}\right]}\cdot\alpha_{ij}$$ $$M_{imp,w,k} = A_k(t)\cdot m_l \frac{H^2}{R} e_k \cdot \sum_{i=1}^{N_1}\phi_{ik}\sum_{j=1}^{\infty}\frac{8(-1)^{j+1}}{\left[(2j-1)\pi\right]^2}\frac{I_1\left[(2j-1)\frac{\pi}{2}\frac{R}{H}\right]}{I_1'\left[(2j-1)\frac{\pi}{2}\frac{R}{H}\right]}\cdot\alpha_{ij}\cdot\left[-\frac{H_s}{H}+1-\frac{2(-1)^{j+1}}{(2j-1)\pi}\right]$$ $$M_{imp,b,k} = A_k(t)\cdot m_l H e_k \sum_{i=1}^{N_1}\phi_{ik}\sum_{j=1}^{\infty}\frac{8}{\left[(2j-1)\pi\right]^2}\frac{I_2\left[(2j-1)\frac{\pi}{2}\frac{R}{H}\right]}{I_1'\left[(2j-1)\frac{\pi}{2}\frac{R}{H}\right]}\cdot\alpha_{ij}$$ where I_2 is the modified Bessel function of the first kind with an integer order of 2

Table A.9. Governing equation, boundary conditions, separation of variables, and analytical solutions for convective responses of head-supported rigid tanks

Governing equation	Per Eq. (3.71): $$\Phi_{con} = \frac{g}{i\omega} e^{i\omega t} \cos\theta \frac{2}{\frac{n_j g}{R}\tanh(n_j \frac{H}{R}) - \omega^2} \frac{n_j}{{n_j}^2 - 1} \frac{J_1(n_j \frac{r}{R})}{J_1(n_j)} \frac{\cosh(n_j \frac{z}{R})}{\cosh(n_j \frac{H}{R})} \tanh(n_j \frac{H}{R})$$ where g is the gravitational acceleration, J_1 is the Bessel function of the first kind with an integer order of 1, n_j is a root (solution) of $J_1'(n_j) = 0$, and ω is the frequency of an assumed harmonic motion.
Boundary conditions	1. On the initial free surface, at $z = H$, the height of the wave generates hydrostatic pressure at $z = H$ per Eq. (3.68): $$g \left.\frac{\partial(\Phi_{imp} + \Phi_{con})}{\partial z}\right|_{z=H} = -\left.\frac{\partial^2 \Phi_{con}}{\partial t^2}\right|_{z=H}$$ 2. On the tank wall, at $r = R$, the radial velocity of the fluid is zero per Eq. (3.69): $$\left.\frac{\partial \Phi_{con}}{\partial r}\right|_{r=R} = 0$$ 3. On the tank base, at $z = 0$, the vertical velocity of the fluid is zero per Eq. (3.70): $$\left.\frac{\partial \Phi_{con}}{\partial z}\right|_{z=0} = 0$$ The following equations are obtained using the assumed form of Φ_{con} per Eq. (3.65) and Φ_{imp} per Eq. (3.8) with $u_0'(t) = (1/i\omega)e^{i\omega t}$ for Eqs. (3.68), (3.69), and (3.70), respectively: $$\tilde{R}\cdot\tilde{\Theta}\cdot\tilde{Z}\cdot\tilde{T}''|_{z=H} + g\cdot\tilde{R}\cdot\tilde{\Theta}\cdot\tilde{Z}'\cdot\tilde{T}|_{z=H} = -\frac{g e^{i\omega t}}{i\omega}\cos\theta \cdot\sum_{i=1}^{\infty}\frac{4}{(2n-1)\pi}\frac{I_1[(2n-1)\pi r/(2H)]}{I_1'[(2n-1)\pi r/(2H)]} \quad \text{(A.41)}$$ $$\tilde{R}'|_{r=R} = 0 \quad \text{(A.42)}$$ $$\tilde{Z}'|_{z=0} = 0 \quad \text{(A.43)}$$

Table A.9. Governing equation, boundary conditions, separation of variables, and analytical solutions for convective responses of head-supported rigid tanks (continued)

<table>
<tr>
<td>Separation of variables</td>
<td>
Given Eq. (A.41), $\tilde{\Theta}$ and $\tilde{T}$ are solved:
$$\tilde{\Theta} = \cos\theta \quad \text{(A.44)}$$
$$\tilde{T} = e^{i\omega t} \quad \text{(A.45)}$$
Given Eq. (3.4), $\tilde{Z}''/\tilde{Z}$ is assumed to be a constant $(\lambda/R)^2$, and so the form of $\tilde{Z}$ is:
$$\tilde{Z} = A\cosh(\lambda z/R) + B\sinh(\lambda z/R) \quad \text{(A.46)}$$
where A and B are constants, and $B = 0$ per Eq. (A.43).
Substituting Eqs. (A.44) and (A.46) for $\tilde{\Theta}$ and $\tilde{Z}$ in Eq. (3.4), respectively, $\tilde{R}$ is solved using the form:
$$\tilde{R} = CJ_1(\lambda r/R) \quad \text{(A.47)}$$
where C is a constant. The constants A, C, and λ are solved using the three boundary conditions per Eqs. (A.41), (A.42), and (A.43).
The governing equation Φ_{con} per Eq. (3.65) is solved using solutions for $\tilde{R}$, $\tilde{\Theta}$, $\tilde{Z}$, and $\tilde{T}$ per Eqs. (A.44) to (A.47).
</td>
</tr>
<tr>
<td>Analytical solutions</td>
<td>
$$f_{con,j} = \frac{1}{2\pi}\sqrt{\frac{n_j g}{R}\tanh(n_j\frac{H}{R})}$$
$$p_{con,w,j} = -A_j(t)\cdot\rho R\cos\theta\frac{2}{{n_j}^2-1}\frac{\cosh(n_j z/R)}{\cosh(n_j H/R)}$$
where $A_j(t)$ is per Eq. (3.133).
$$p_{con,b,j} = -A_j(t)\cdot\rho R\cos\theta\frac{2}{{n_j}^2-1}\frac{J_1(n_j r/R)}{J_1(n_j)}\frac{1}{\cosh(n_j H/R)}$$
$$d_{w,j} = -A_j(t)\cdot\frac{R}{g}\cos\theta\frac{2}{{n_j}^2-1}\frac{J_1(n_j r/R)}{J_1(n_j)}$$
$$F_{con,j} = A_j(t)\cdot m_l\frac{R}{H}\frac{2}{n_j({n_j}^2-1)}\tanh(n_j\frac{H}{R})$$
$$M_{con,w,j} = A_j(t)\cdot m_l R\frac{2}{n_j({n_j}^2-1)}\tanh(n_j\frac{H}{R})\left[-\frac{H_s}{H}+1-\frac{R}{n_j H}\tanh(n_j\frac{H}{2R})\right]$$
$$M_{con,b,j} = A_j(t)\cdot m_l\frac{R^2}{H}\frac{2}{n_j({n_j}^2-1)}\frac{J_2(n_j)}{J_1(n_j)}\frac{1}{\cosh(n_j H/R)}$$
</td>
</tr>
</table>

A.4 References

Chalhoub, M. S., and Kelly, J. M. (1988). "Theoretical and experimental studies of cylindrical water tanks in base isolated structures." *UCB/EERC-88/07*, Earthquake Engineering Research Center, University of California at Berkeley, Berkeley, CA.

Housner, G. W. (1954). "Earthquake pressures on fluid containers." *NR-081-095*, Office of Naval Research, Arlington, VA.

Housner, G. W. (1957). "Dynamic pressures on accelerated fluid containers." *Bulletin of the Seismological Society of America*, 47(1), 15-35.

Jacobsen, L. S. (1949). "Impulsive hydrodynamics of fluid inside a cylindrical tank and of fluid surrounding a cylindrical pier." *Bulletin of the Seismological Society of America*, 39(3), 189-204.

Veletsos, A. (1984). "Seismic response and design of liquid storage tanks." *Guidelines for the seismic design of oil and gas pipeline systems*, Committee on Gas and Liquid Fuel Lifelines, American Society of Civil Engineers (ASCE), Reston, VA, 255-370.

APPENDIX B. SEISMIC FLUID-STRUCTURE-INTERACTION ANALYSIS OF FLEXIBLE BASE-SUPPORTED CYLINDRICAL TANKS USING ANALYTICAL SOLUTIONS AND A SIMPLIFIED PROCEDURE

B.1 Introduction

Veletsos (1984) developed analytical solutions for the impulsive and convective[55] responses of flexible, base-supported cylindrical tanks, subjected to unidirectional horizontal motion of a small amplitude. The impulsive and convective responses were decoupled into modal contributions and solutions were provided for each mode, as presented in Sections 3.2.1.3 and 3.2.2.2 of this report.

Malhotra et al. (2000) modified the analytical solutions of Veletsos to develop a simplified analysis procedure, using only one impulsive mode and one convective mode: a two-degree-of-freedom (2-DOF) system. The simplified procedure provided global reactions at the base of the tank and vertical displacements of the free surface of the contained fluid (i.e., the height of the waves with respect to the initial free surface) for engineering applications. Eurocode 8 (European Committee for Standardization (CEN) 1998) and API 650 (American Petroleum Institute (API) 2012) both include the simplified procedure for the seismic design and analysis of base-supported cylindrical tanks.

This appendix has three goals: 1) introduce the simplified procedure of Malhotra et al.; 2) present analysis of base-supported cylindrical tanks using both the simplified procedure and the analytical solutions; and 3) characterize the appropriateness of the simplified procedure.

Section B.2 describes the development of the simplified procedure, based in part on a discussion with Malhotra (2018). The 2-DOF system and the procedure for calculating seismic FSI responses of tanks are introduced. Section B.3 presents and compares FSI responses calculated using the simplified procedure and the analytical solutions, for three flexible, base-supported cylindrical tanks with practical dimensions, subjected to small-amplitude, unidirectional, horizontal earthquake histories. FSI responses were previously calculated using the analytical solutions in Section 3, but were normalized. The normalization made the results unitless and

[55] Veletsos (1984) derived analytical solutions of convective responses with no consideration of the flexibility of the wall of the tank. However, these solutions can be applied to flexible tanks since the convective responses are independent of the deformations of the wall. See Section 3.2.2 for more information.

independent/insensitive (footnote 25 on page 75) of the dimensions and the mechanical properties of the tank and the fluid, and independent of the acceleration response of the tank. The results presented in Section B.3 are not normalized, presenting realistic FSI responses for the three tanks.

B.2 Simplified procedure of Malhotra et al.

The simplified procedure of Malhotra et al. calculates the seismic response of a flexible, base-supported cylindrical tank using a 2-DOF system with one impulsive mode and one convective mode. The impulsive responses include: 1) shear force at the base of the tank, F_{imp}, 2) moment immediately above the base of the tank, $M_{imp,w}$, and 3) moment immediately below the base of the tank, $M_{imp,wb}$. The moment $M_{imp,w}$ balances the resultant moment at the center of the base generated by the impulsive pressure on the wall. The moment $M_{imp,wb}$ balances the resultant moment at the center of the base generated by both the impulsive pressures on the wall and the base. Accordingly, $M_{imp,wb}$ is the sum of two components: 1) $M_{imp,w}$, associated with the pressure on the wall and 2) $M_{imp,b}$, associated with the pressure on the base. The convective responses include the shear force and moments at the base, F_{con}, $M_{con,w}$, and $M_{con,wb}$ (counterparts of F_{imp}, $M_{imp,w}$, and $M_{imp,wb}$, respectively), and the maximum vertical displacement of the free surface, $d_{w,\max}$.

Figure B.1 presents the 2-DOF system subjected to ground motion, $u_0''(t)$, in the x direction. In the figure, m_{imp} and m_{con} are the parts of the mass of the contained fluid associated with the impulsive and the convective modes, hereafter termed the impulsive and convective fluid masses, respectively. The sum of the two masses, $(m_{imp} + m_{con})$, is the mass of the contained fluid, m_l. The two fluid masses, m_{imp} and m_{con}, are located at heights of H_{imp} and H_{con}, respectively, above the (rigid) foundation of the 2-DOF system. The foundation represents the base of the tank.

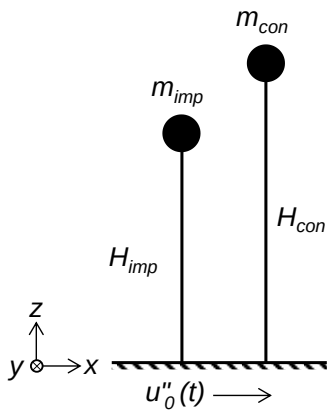

Figure B.1. Two-degree-of-freedom system used in the simplified procedure (Malhotra et al.), including one impulsive mode and one convective mode

Table B.1 presents properties provided by Malhotra et al. for the 2-DOF system, for eight ratios of fluid height-to-tank radius H/R: 0.3, 0.5, 0.7, 1, 1.5, 2, 2.5, and 3. The data needed to calculate impulsive responses include the coefficient of the impulsive period, D_{imp}^{M}; the impulsive fluid mass, m_{imp}; and the heights, $H_{imp,w}$ and $H_{imp,wb}$. The data needed to calculate convective responses include the coefficient of the convective period, D_{con}^{M}; the convective fluid mass, m_{con}; and the heights, $H_{con,w}$ and $H_{con,wb}$.

Table B.1. Properties of the 2-DOF system shown in Figure B.1 used for the simplified procedure to calculate impulsive and convective responses (Malhotra et al.)

	Impulsive				Convective			
H/R	D_{imp}^{M}	m_{imp} $(\times m_l)$	H_{imp} $(\times H)$		D_{con}^{M} $(s/\sqrt{m})$	m_{con} $(\times m_l)$	H_{con} $(\times H)$	
			$H_{imp,w}$	$H_{imp,wb}$			$H_{con,w}$	$H_{con,wb}$
0.3	9.28	0.18	0.40	2.64	2.09	0.82	0.52	3.41
0.5	7.74	0.30	0.40	1.46	1.74	0.70	0.54	1.52
0.7	6.97	0.41	0.40	1.01	1.60	0.59	0.57	1.01
1.0	6.36	0.55	0.42	0.72	1.52	0.45	0.62	0.79
1.5	6.06	0.69	0.44	0.56	1.48	0.31	0.69	0.73
2.0	6.21	0.76	0.45	0.50	1.48	0.24	0.75	0.76
2.5	6.56	0.81	0.45	0.48	1.48	0.19	0.79	0.80
3.0	7.03	0.84	0.45	0.47	1.48	0.16	0.83	0.83

Malhotra et al. derived the values listed in Table B.1 with the goal of calculating responses *similar* to those analytically derived by Veletsos. The impulsive period, T_{imp}, and the convective period, T_{con}, of the 2-DOF system are related to the coefficients D_{imp}^{M} and D_{con}^{M}, respectively:

$$T_{imp} = D_{imp}^{M} H \sqrt{\frac{\rho R}{Eh}} \tag{B.1}$$

$$T_{con} = D_{con}^{M} \sqrt{R} \tag{B.2}$$

where E is the elastic modulus of the material used to construct the tank; ρ is the density of the contained fluid; and h is the thickness of the wall of the tank. Malhotra et al. assumed the frequencies of the 2-DOF system (i.e., $1/T_{imp}$ and $1/T_{con}$) to be equal to the first impulsive and convective frequencies derived by Veletsos: $f_{imp,1}$ and $f_{con,1}$. Figure B.2a duplicates the data for $f_{imp,1}$ in Figure 3.11a, calculated per Veletsos for a tank with $R = 30$ m, $h = 0.001\,R$, $0.2 \le H/R \le 3$, and the mechanical properties listed in Table 3.5, together with the corresponding $1/T_{imp}$ per Eq. (B.1). Similarly, Figure B.2b shows $f_{con,1}$ (repeated from Figure 3.24a) and $1/T_{con}$ calculated per Eq. (B.2) for the same tank analyzed in Figure B.2a. The results of Malhotra et al. and Veletsos are identical, as expected.

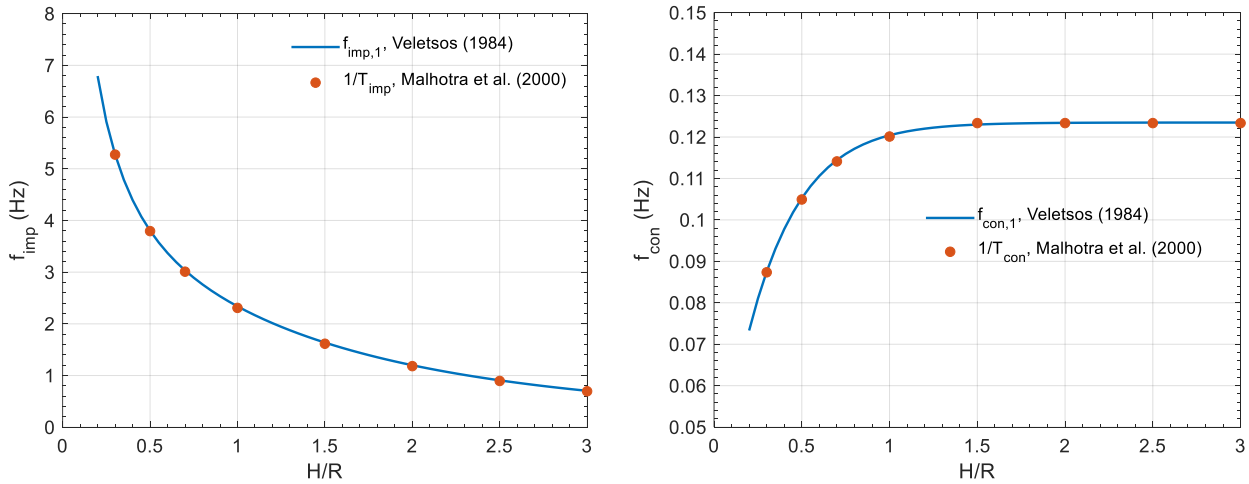

(a) $1/T_{imp}$ and $f_{imp,1}$ (b) $1/T_{con}$ and $f_{con,1}$

Figure B.2. Impulsive and convective frequencies (i.e., $1/T_{imp}$ and $1/T_{con}$) of the 2-DOF system calculated using data provided by Malhotra et al., the first impulsive and convective frequencies (i.e., $f_{imp,1}$ and $f_{con,1}$) calculated using the solutions of Veletsos, $R = 30$ m, $h = 0.001\,R$, $0.2 \le H/R \le 3$, and the mechanical properties listed in Table 3.5

Maximum global reactions at the base of the tank analyzed per the 2-DOF system are calculated using the inertial forces associated with m_{imp} and m_{con} with their respective spectral accelerations (i.e., maximum accelerations), $Sa(f_{imp,1})$ and $Sa(f_{con,1})$. Malhotra et al. recommended damping ratios of 2% and 5% of critical for calculating $Sa(f_{imp,1})$ for steel and concrete tanks, respectively, and a damping ratio of 0.5% for $Sa(f_{con,1})$ for both steel and concrete tanks.

The shear force at the base of the tank, F, in the x direction (i.e., the direction of seismic input) is the sum of the impulsive and convective components, F_{imp} and F_{con}, which are calculated using the inertial forces associated with m_{imp} and m_{con}, respectively:

$$F = F_{imp} + F_{con} = m_{imp} \cdot Sa(f_{imp,1}) + m_{con} \cdot Sa(f_{con,1}) \tag{B.3}$$

The moment immediately above the base of the tank, M_w, about the y axis, is calculated as the sum of the impulsive and convective components, $M_{imp,w}$ and $M_{con,w}$. The moments, $M_{imp,w}$ and $M_{con,w}$, are calculated using the inertial forces per Eq. (B.3) and their respective heights above the foundation, $H_{imp,w}$ and $H_{con,w}$:

$$M_w = M_{imp,w} + M_{con,w} = m_{imp} \cdot Sa(f_{imp,1}) \cdot H_{imp,w} + m_{con} \cdot Sa(f_{con,1}) \cdot H_{con,w} \tag{B.4}$$

Similar to M_w, the moment immediately below the base of the tank, M_{wb}, about the y axis, is the sum of the impulsive and convective components, $M_{imp,wb}$ and $M_{con,wb}$. The moments, $M_{imp,wb}$ and $M_{con,wb}$, are calculated using the inertial forces per Eq. (B.3) and their respective heights above the foundation, $H_{imp,wb}$ and $H_{con,wb}$:

$$M_{wb} = M_{imp,wb} + M_{con,wb} = m_{imp} \cdot Sa(f_{imp,1}) \cdot H_{imp,wb} + m_{con} \cdot Sa(f_{con,1}) \cdot H_{con,wb} \tag{B.5}$$

Although the technical basis for the procedure is not documented, the coefficients for the impulsive modal mass and modal heights in Table B.1 were derived assuming the fluid in each mode derived by Veletsos moved together at respective spectral accelerations in the first mode, $Sa(f_{imp,1})$ and $Sa(f_{con,1})$. Accordingly, the values of m_{imp}, m_{con}, $H_{imp,w}$, $H_{con,w}$, $H_{imp,wb}$, and, $H_{con,wb}$ (in Table B.1) were derived by equating the global reactions per Eqs. (B.3), (B.4), and

(B.5) to the algebraic sums of the corresponding reactions in different modes (Veletsos) with the replacement of $A_k(t)$ by $Sa(f_{imp,1})$:

$$F_{imp} = m_{imp} \cdot Sa(f_{imp,1}) = \sum_{k=1}^{N} \frac{F_{imp,k}}{A_k(t)} \cdot Sa(f_{imp,1}) \tag{B.6}$$

$$M_{imp,w} = m_{imp} \cdot Sa(f_{imp,1}) \cdot H_{imp,w} = \sum_{k=1}^{N} \frac{M_{imp,w,k}}{A_k(t)} \cdot Sa(f_{imp,k}) \tag{B.7}$$

$$M_{imp,wb} = m_{imp} \cdot Sa(f_{imp,1}) \cdot H_{imp,wb} = \sum_{k=1}^{N} \frac{M_{imp,w,k} + M_{imp,b,k}}{A_k(t)} \cdot Sa(f_{imp,k}) \tag{B.8}$$

where the third terms of the above three equations are the algebraic sums of the modal reactions per Eqs. (3.61), (3.62), and (3.62) derived by Veletsos. The values of m_{imp}, $H_{imp,w}$, and $H_{imp,wb}$ were calculated per Eqs. (B.6), (B.7), and (B.8):

$$m_{imp} = \sum_{k=1}^{N} \frac{F_{imp,k}}{A_k(t)} \tag{B.9}$$

$$H_{imp,w} = \frac{1}{m_{imp}} \cdot \sum_{k=1}^{N} \frac{M_{imp,w,k}}{A_k(t)} \tag{B.10}$$

$$H_{imp,wb} = \frac{1}{m_{imp}} \cdot \sum_{k=1}^{N} \frac{M_{imp,w,k} + M_{imp,b,k}}{A_k(t)} \tag{B.11}$$

where N is the number of the modes included in the algebraic summation, which was not described in Malhotra et al. The values of m_{imp}, $H_{imp,w}$, and $H_{imp,wb}$ provided by Malhotra et al. (Table B.1) are compared in Figure B.3a with those calculated using Eqs. (B.9), (B.10), and (B.11), respectively, which are associated with the solutions of Veletsos. The first ten modes (i.e., $N = 10$) are included in the calculations since the contributions of the eleventh and higher modes are negligible. Figure B.3a indicates that two sets of data, 1) from Table B.1 per Malhotra et al. and 2) calculated using the analytical solutions with the replacement of $A_k(t)$ by $Sa(f_{imp,1})$, are almost identical, as ten modes are involved.

An identical process was used to derived values for the convective properties, m_{con}, $H_{con,w}$, and $H_{con,wb}$:

$$m_{con} = \sum_{j=1}^{N} \frac{F_{con,j}}{A_j(t)} \tag{B.12}$$

$$H_{con,w} = \frac{1}{m_{con}} \cdot \sum_{j=1}^{N} \frac{M_{con,w,j}}{A_j(t)} \tag{B.13}$$

$$H_{con,wb} = \frac{1}{m_{con}} \cdot \sum_{j=1}^{N} \frac{M_{con,w,j} + M_{con,b,j}}{A_j(t)} \tag{B.14}$$

where the right-hand sides of the above three equations are the analytical solutions per Eqs. (3.82), (3.83), and (3.84). The values of m_{con}, $H_{con,w}$, and $H_{con,wb}$ provided by Malhotra et al. (Table B.1) are compared in Figure B.3b with those calculated using Eqs. (B.12), (B.13), and (B.14) with $N = 10$, respectively, which are associated with the analytical solutions. The two sets of data are essentially identical.

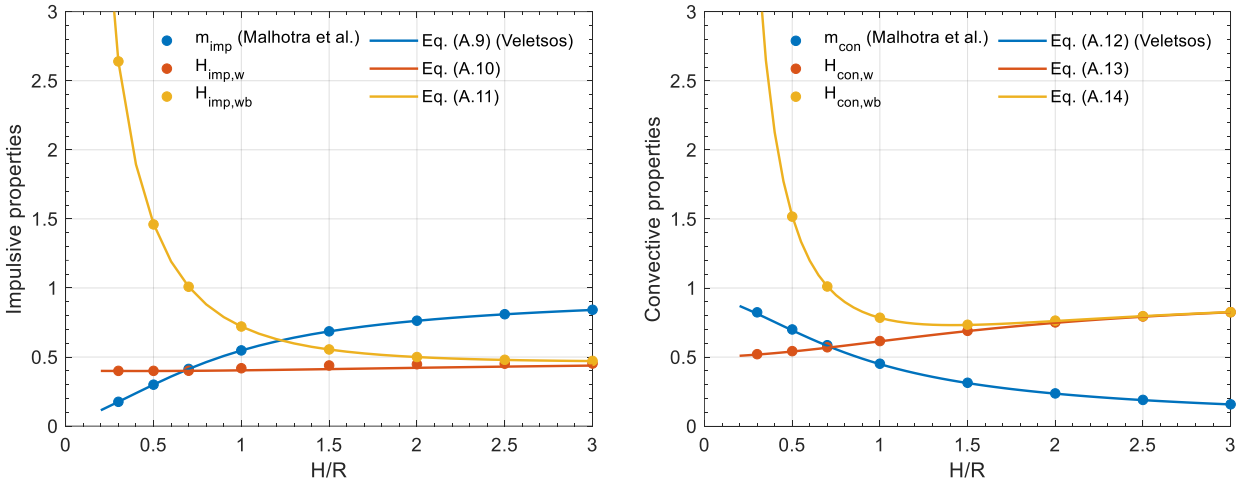

(a) impulsive properties (b) convective properties

Figure B.3. Properties of the 2-DOF system of Figure B.1 provided by Malhotra et al. and calculated using the analytical solutions of Veletsos with the replacement of acceleration time series, $A_k(t)$ and $A_j(t)$, by respective spectral accelerations $Sa(f_{imp,1})$ and $Sa(f_{con,1})$

The simplified procedure provides the maximum vertical displacement of the free surface, $d_{w,\max}$. Following the same process, $d_{w,\max}$ was derived as the algebraic sum of the vertical displacements of the free surface in different convective modes, at $r = R$ and $\theta = 0$ on the cylindrical coordinate system shown in Figure 3.2:

$$d_{w,\max} = \sum_{j=1}^{N} \frac{d_{w,j}(r=R,\theta=0)}{A_j(t)} \cdot Sa(f_{con,1}) \approx \frac{R}{g} \cdot Sa(f_{con,1}) \tag{B.15}$$

where the second term is the sum of the modal vertical displacement of the free surface per Eq. (3.81), in which the time series $A_j(t)$ is replaced by $Sa(f_{con,1})$. With a sufficient number of modes (e.g., $N = 10$), $d_{w,\max}$ is almost identical to the third term in Eq. (B.15), which was the equation given in Malhotra et al.

B.3 Comparisons of Malhotra et al. and Veletsos results

Results of the analysis using the simplified procedure of Malhotra et al. and the analytical solutions of Veletsos are compared in this section. Carbon-steel, base-supported, cylindrical tanks filled with water are analyzed. To ensure that the conclusions drawn from this study are applicable to a wide range of tanks with practical dimensions, the seismic analysis is performed for three sample tanks and three ground motion time series with distinctly different frequency contents.

B.3.1 Description of the sample tanks

The three carbon-steel, base-supported cylindrical tanks are shown in Figure B.4, with a radius $R = 30$ m, a wall thickness $h = 30$ mm, and respective tank heights $H_s = 15$ m, 30 m, and 60 m. Per Table K-1a of API 650, a radius, R, between 25 m to 60 m and a ratio of wall thickness to radius, h/R, of the order of 0.001 are practical for a steel, base-supported cylindrical tank (footnote 23 on page 66). All three tanks are full of water since the two analysis methods (i.e., Malhotra and Veletsos) do not consider freeboards (i.e., $H = H_s$), and so $H/R = 0.5$, 1, and 2. The mechanical properties of the carbon-steel tanks and the contained water are listed in Table B.2, including the elastic modulus, E, Poisson's ratio, υ, and density, ρ_s, of the carbon steel, and the density of the water, ρ. The first three impulsive and convective frequencies and periods of each tank are listed in Table B.3. The values of $f_{imp,k}$ are calculated per Eq. (3.64) with $C_{imp,k}$, shown in Figure 3.11b. The values of $f_{con,j}$ are calculated per Eq. (3.119) with $C_{con,j}$, shown in Figure 3.24b. (Note that $f_{imp,1}$ can be also calculated as the reciprocal of T_{imp} per Eq. (B.1) with

D_{imp}^{M} listed in Table B.1; $f_{con,1}$ can be also calculated as the reciprocal of T_{con} per Eq. (B.2) with D_{con}^{M} listed in Table B.1.)

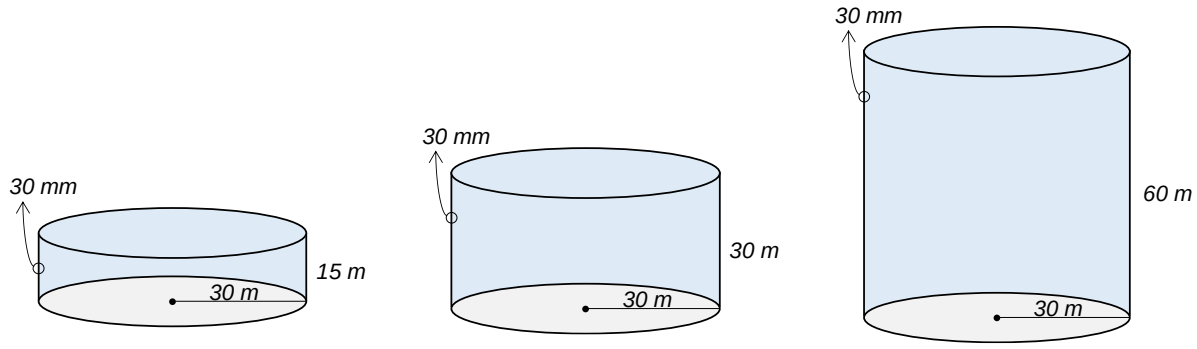

(a) $H/R=0.5$ (b) $H/R=1$ (c) $H/R=2$

Figure B.4. Carbon-steel, base-supported cylindrical tanks for the seismic analysis, $R=30$ m, $h=30$ mm, and $H/R=0.5$, 1, and 2

Table B.2. Mechanical properties of the material used to construct the carbon-steel tanks and the contained water for the seismic analysis

Carbon steel	Elastic modulus, E	1.94×10^{11} (N/m^2)
	Poisson's ratio, υ	0.27
	Density, ρ_s	7875 (kg/m^3)
Water	Density, ρ	1000 (kg/m^3)

Table B.3. First three impulsive and convective frequencies and periods of the three tanks shown in Figure B.4, $R=30$ m, $h=30$ mm

		$H/R=0.5$	$H/R=1$	$H/R=2$
$f_{imp,k}$ (Hz) / $T_{imp,k}$ (sec)	$k=1$	3.8 / 0.26	2.3 / 0.43	1.2 / 0.84
	$k=2$	6.8 / 0.15	4.3 / 0.23	2.8 / 0.36
	$k=3$	8.8 / 0.11	6.1 / 0.16	3.9 / 0.25
$f_{con,j}$ (Hz) / $T_{con,j}$ (sec)	$j=1$	0.11 / 9.5	0.12 / 8.3	0.12 / 8.1
	$j=2$	0.21 / 4.8	0.21 / 4.8	0.21 / 4.8
	$j=3$	0.27 / 3.8	0.27 / 3.8	0.27 / 3.8

B.3.2 Ground motion time series

Table B.4 identifies the three unidirectional, horizontal ground motion time series (i.e., ground motions #1, #2, and #3) used for the seismic analysis of the tanks shown in Figure B.4. These ground motions have very different frequency contents and their peak spectral accelerations are well separated. The peak ground acceleration (PGA) of each ground motion is scaled to 0.1 g for analysis since the two methods (i.e., Malhotra and Veletsos) are strictly applicable to small amplitude motions. Figure B.5 presents the time series for the three scaled motions. Figures B.6a and b (Figures B.6c and d) present spectral accelerations with a damping ratio of 2% (0.5%) for each scaled motion with respect to the period in a linear format and with respect to the frequency in a linear-logarithmic format, respectively. As noted previously, the damping ratios of 2% and 0.5% used here were values suggested by Malhotra et al. to calculate the impulsive and convective responses of steel tanks.

Table B.4. Information of the unidirectional, horizontal ground motion time series[1] for the seismic analysis of the tanks shown in Figure B.4

	Event	Year	Station	Direction	Original PGA (g)	Scaled PGA (g)
#1	Hualien Earthquake	2018	HWA019	EW	0.39	0.1
#2	Chi-Chi Earthquake	1999	TCU052	EW	0.36	0.1
#3	El Centro Earthquake (Imperial Valley-02)	1940	El Centro Array #9	180	0.28	0.1

1. Ground motion #1 is provided by the National Center for Research on Earthquake Engineering, Taiwan. Ground motions #2 and #3 are extracted from the PEER Ground Motion Database (http://ngawest2.berkeley.edu/, accessed on March 18, 2019), Pacific Earthquake Engineering Research (PEER) Center, University of California, Berkeley, CA.

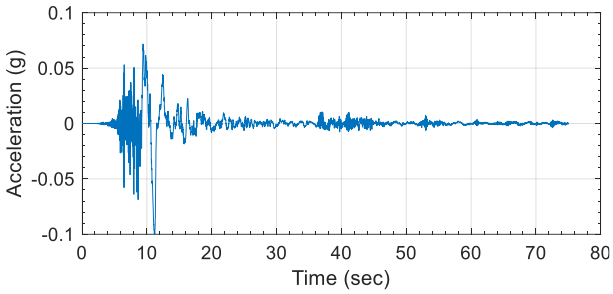

(a) ground motion #1

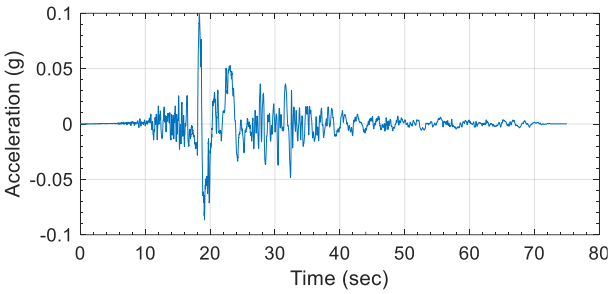

(b) ground motion #2

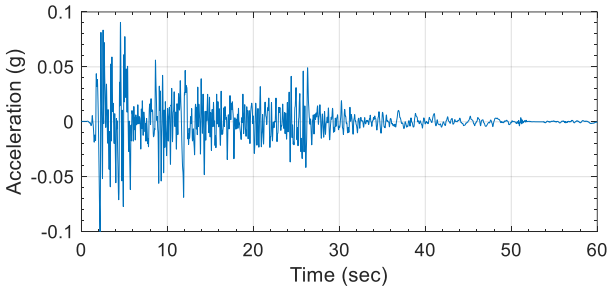

(c) ground motion #3

Figure B.5. Scaled, unidirectional, horizontal ground motion time series for the seismic analysis of the tanks shown in Figure B.4, PGA=0.1g

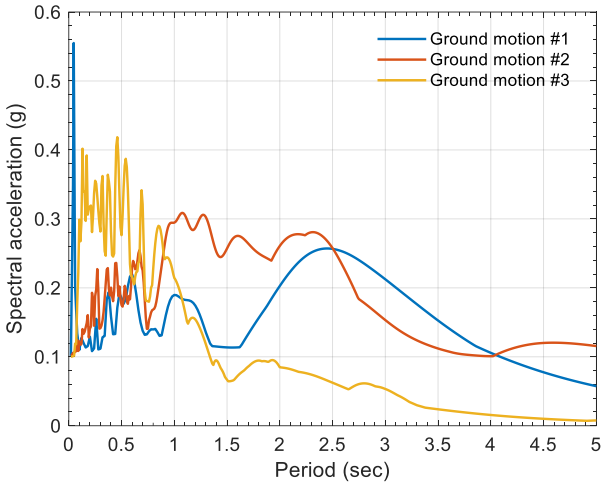

(a) 2%-damped, period, linear scale

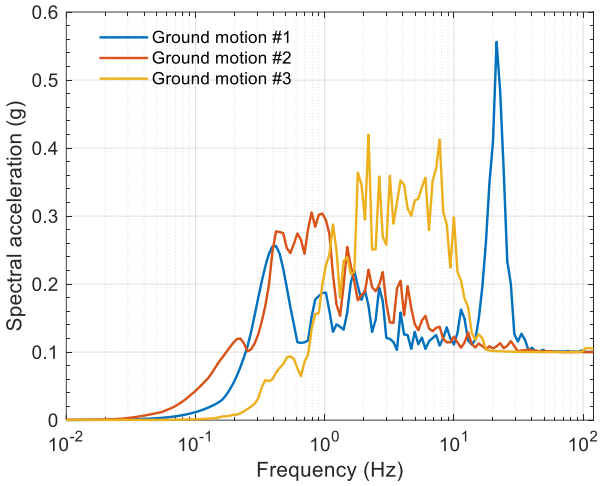

(b) 2%-damped, frequency, linear-logarithmic scale

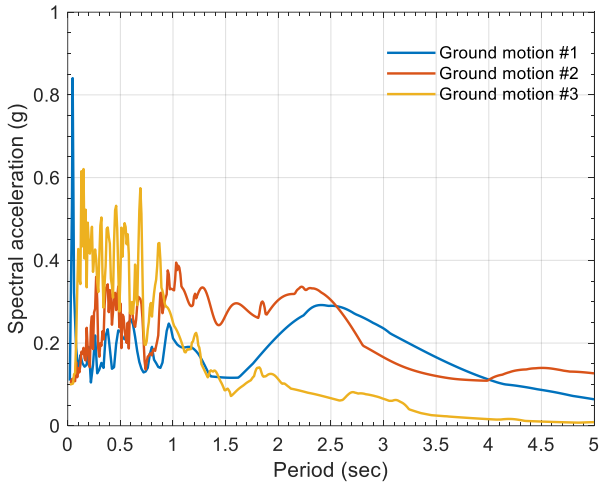

(c) 0.5%-damped, period, linear scale

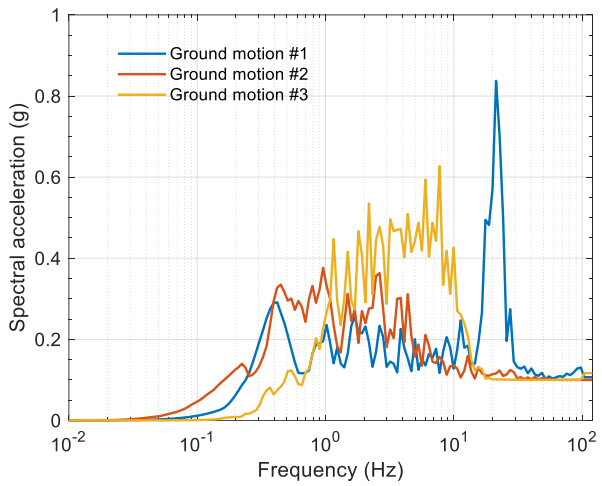

(d) 0.5%-damped, frequency, linear-logarithmic scale

Figure B.6. Spectral accelerations of the scaled ground motion time series shown in Figure B.5, PGA=0.1g, damping ratios of 2% and 0.5%

B.3.3 Calculations of FSI responses

Simplified procedure of Malhotra et al.

Table B.5 presents data used for the analysis, including m_{imp}, $H_{imp,w}$, $H_{imp,wb}$, m_{con}, $H_{con,w}$, and, $H_{con,wb}$ extracted from Table B.1, for the tanks in Figure B.4, and $Sa(f_{imp,1})$ and $Sa(f_{con,1})$ for the scaled motions in Figures B.5 and B.6. Using these data, the maximum responses of each tank are calculated per Eqs. (B.3) to (B.5) and (B.15). Table B.6 presents the maximum responses, including the impulsive and convective components of the shear force, F; the moments, M_w and M_{wb}, at the base of each tank, and the maximum vertical displacement of the free surface, $d_{w,\max}$.

Table B.5. Data for seismic analysis using the simplified procedure for the tanks shown in Figure B.4 (i.e., $H/R = 0.5$, 1, and 2) and the scaled ground motions shown in Figures B.5 and B.6 (i.e., ground motions #1, #2, and #3)

		Impulsive				Convective			
H/R	Ground motion	$Sa(f_{imp,1})$[1] (g)	m_{imp} $(\times m_l)$	$H_{imp,w}$ $(\times H)$	$H_{imp,wb}$ $(\times H)$	$Sa(f_{con,1})$[2] (g)	m_{con} $(\times m_l)$	$H_{con,w}$ $(\times H)$	$H_{con,wb}$ $(\times H)$
0.5	#1	0.16	0.30	0.40	1.46	0.01	0.70	0.54	1.52
	#2	0.20				0.05			
	#3	0.35				0.001			
1.0	#1	0.13	0.55	0.42	0.72	0.02	0.45	0.62	0.79
	#2	0.20				0.06			
	#3	0.25				0.002			
2.0	#1	0.14	0.76	0.45	0.50	0.02	0.24	0.75	0.76
	#2	0.19				0.07			
	#3	0.29				0.002			

1. Spectral acceleration with a damping ratio of 2% shown in Figures B.6a and b
2. Spectral acceleration with a damping ratio of 0.5% shown in Figures B.6c and d

Table B.6. Maximum FSI responses calculated using the simplified procedure per Eqs. (B.3) to (B.5) and (B.15) for the tanks shown in Figure B.4 and the scaled ground motions shown in Figures B.5 and B.6

H/R	0.5			1			2		
Ground motion	#1	#2	#3	#1	#2	#3	#1	#2	#3
F_{imp} (10^4 kN)	1.9	2.5	4.4	5.9	8.9	11.4	17.2	24.0	36.3
F_{con} (10^4 kN)	0.4	1.5	0.0	0.6	2.4	0.1	0.7	2.6	0.1
$F = F_{imp} + F_{con}$ (10^4 kN)	2.3	3.9	4.4	6.5	11.3	11.5	17.9	26.6	36.4
$M_{imp,w}$ (10^5 kN-m)	1.2	1.5	2.6	7.4	11.2	14.3	46.3	64.5	97.6
$M_{con,w}$ (10^5 kN-m)	0.3	1.2	0.0	1.2	4.5	0.1	3.2	11.9	0.4
$M_w = M_{imp,w} + M_{con,w}$ (10^5 kN-m)	1.5	2.7	2.7	8.6	15.7	14.4	49.5	76.4	98.0
$M_{imp,wb}$ (10^5 kN-m)	4.2	5.4	9.6	12.8	19.2	24.6	51.7	72.0	108.9
$M_{con,wb}$ (10^5 kN-m)	0.9	3.4	0.1	1.5	5.7	0.2	3.2	12.1	0.4
$M_{wb} = M_{imp,wb} + M_{con,wb}$ (10^5 kN-m)	5.1	8.8	9.7	14.3	24.9	24.8	54.9	84.1	109.3
$d_{w,\max}$ (m)	0.39	1.52	0.04	0.51	1.94	0.06	0.54	2.01	0.06

Analytical solutions of Veletsos

The reactions at the base of the three tanks in Figure B.4 and the vertical displacements of their free surface are calculated using the analytical solutions of Veletsos. The results are compared with those calculated using the simplified procedure. The solutions for the impulsive component were presented in Section 3.2.1.3, including the frequency, $f_{imp,k}$, and the shear force, $F_{imp,k}$, and two moments, $M_{imp,w,k}$ and $M_{imp,b,k}$, at the base of the tank in the kth mode. The solutions for the convective component were presented in Section 3.2.2.2, including the frequency, $f_{con,j}$, the shear force, $F_{con,j}$, and two moments, $M_{con,w,j}$ and $M_{con,b,j}$, at the base of the tank, and the vertical displacement of the free surface, $d_{w,j}$, in the jth mode. Their equations are not repeated in this appendix. To generate responses for comparison with those of Malhotra et al., the modal

impulsive and convective moments at the base of the tank, $M_{imp,wb,k}$ and $M_{con,wb,j}$, balancing the resultant moments generated by both the pressures on the wall and the base, are calculated as:

$$M_{imp,wb,k} = M_{imp,w,k} + M_{imp,b,k} \tag{B.16}$$

$$M_{con,wb,j} = M_{con,w,j} + M_{con,b,j} \tag{B.17}$$

Unlike the simplified procedure that used spectral accelerations to calculate responses, the analytical solution for each modal impulsive response involves the acceleration time series $A_k(t)$ per Eq. (3.57), and each modal convective response involves $A_j(t)$ per Eq. (3.78). Consequently, the product of each analytical solution is a modal response time series. Both Eqs. (3.57) and (3.78) assume zero damping in the impulsive and convective modes. To compare responses calculated using the simplified procedure and the analytical solutions, identical damping ratios must be used. Accordingly, Eqs. (3.57) and (3.78) are replaced here by equations for non-zero damping (per Chapter 6 of Chopra (2012)):

$$A_k(t) = \frac{\omega_{imp,k}^2}{\omega_{imp,d,k}} \int_0^t u_0''(\tau) \cdot e^{-\zeta \cdot \omega_{imp,k} \cdot (t-\tau)} \cdot \sin \omega_{imp,d,k}(t-\tau) d\tau \tag{B.18}$$

$$A_j(t) = \frac{\omega_{con,j}^2}{\omega_{con,d,j}} \int_0^t u_0''(\tau) \cdot e^{-\zeta \cdot \omega_{con,d,j} \cdot (t-\tau)} \cdot \sin \omega_{con,d,j}(t-\tau) d\tau \tag{B.19}$$

where the damping ratio ζ is 2% for the impulsive response and 0.5% for the convective response of a steel tank; the radial frequencies are $\omega_{imp,k} = 2\pi f_{imp,k}$ and $\omega_{con,j} = 2\pi f_{con,j}$; and the damped radial frequencies are $\omega_{imp,d,k} = \omega_{imp,k}\sqrt{1-\zeta^2}$ and $\omega_{con,d,j} = \omega_{con,j}\sqrt{1-\zeta^2}$.

Theoretically, each of the impulsive and convective responses is the infinite algebraic sum of multiple time series of the corresponding modal responses (i.e., $k = 1$ to ∞ and $j = 1$ to ∞). However, only three impulsive modes and three convective modes are included in the calculations presented here since the contributions of the fourth and higher modes are negligible for the tanks of Figure B.4 and the ground motions of Figure B.5.

Figure B.7 presents the first fifty seconds of the global reaction histories at the base of the tank, including shear forces and moments, for $H/R = 0.5$ subjected to ground motion #1 in the x

direction. Each panel of Figure B.7 presents 1) the impulsive component (i.e., F_{imp}, $M_{imp,w}$, and $M_{imp,wb}$), 2) the convective component (i.e., F_{con}, $M_{con,w}$, and $M_{con,wb}$), and 3) the algebraic sum of the two components (i.e., F, M_w, and M_{wb}). In each panel, the result in each of the upper two figures (i.e., the impulsive and convective components) is the sum of the response time series in the first three modes, and the result in the bottom figure is the sum of the results in the upper two figures. Figure B.8 presents the first fifty seconds of the vertical displacement histories for the free surface, $d_{w,\max}$, at $r = R$ and $\theta = 0$. Identically, the result is composed of the response time series in the first three convective modes.

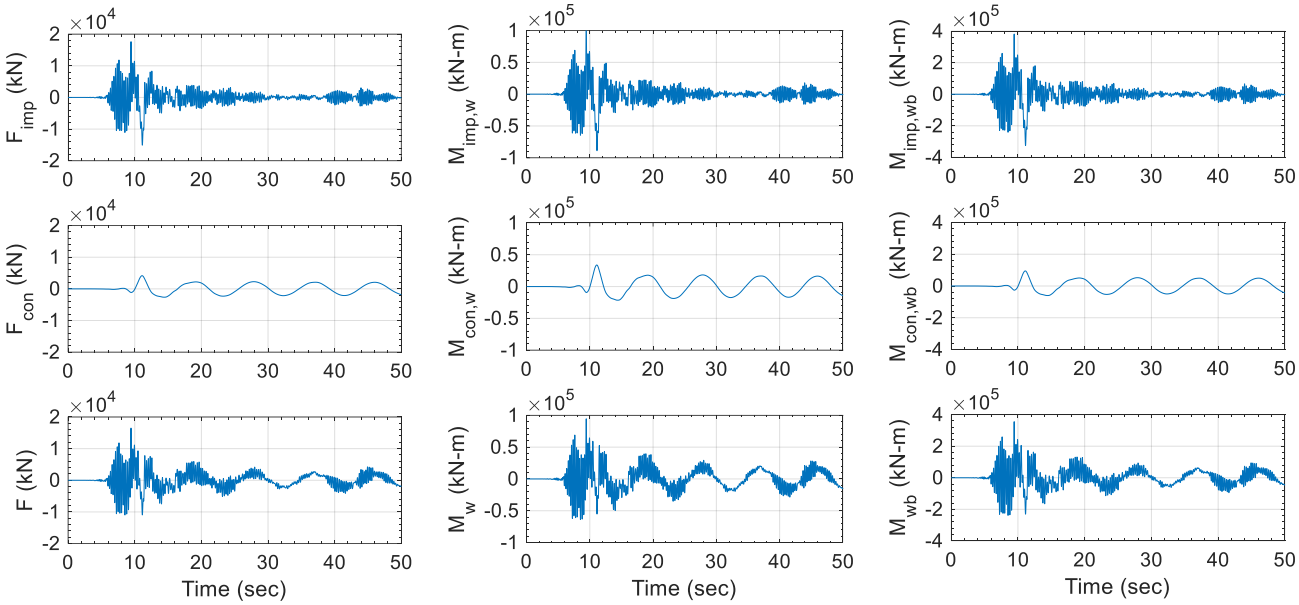

(a) shear forces

(b) moments associated with pressures on the wall

(c) moments associated with pressures on the wall and the base

Figure B.7. Global reactions at the base of the tank, three impulsive and three convective modes, $H/R = 0.5$, ground motion #1, calculated using the analytical solutions of Veletsos

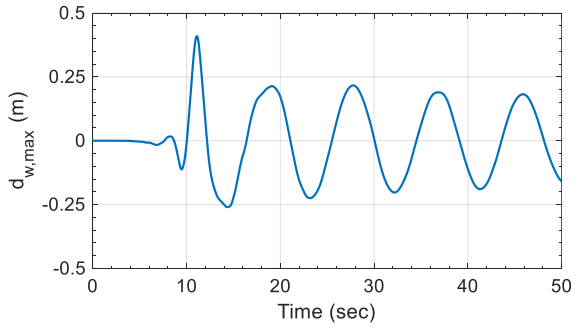

Figure B.8. Vertical displacements of the free surface at $r = R$ and $\theta = 0$, three convective modes, $H/R = 0.5$, ground motion #1, calculated using the analytical solution of Veletsos

Table B.7 presents the maximum values of the response time series, including F_{imp}, F_{con}, F, $M_{imp,w}$, $M_{con,w}$, M_w, $M_{imp,wb}$, $M_{con,wb}$, M_{wb}, and $d_{w,\max}$, for each tank subjected to each ground motion. The maximum value of $F(t)$ is not the sum of the maximum values of $F_{imp}(t)$ and $F_{con}(t)$ because their peak responses occur at different time steps or in different directions (i.e., signs of data, positive or negative). Rather, the maximum value of $F(t)$ is calculated from the sum of $F_{imp}(t)$ and $F_{con}(t)$. Identically, the maximum value of $M_w(t)$ is calculated from the sum of $M_{imp,w}(t)$ and $M_{con,w}(t)$; and the maximum value of $M_{wb}(t)$ is calculated from the sum of $M_{imp,wb}(t)$ and $M_{con,wb}(t)$.

Modal contributions to each of the impulsive and convective responses are calculated for the three tanks subjected to the three scaled ground motions. The contributions are calculated at the time steps of the peak responses. For example, the modal contributions to F_{imp}, $M_{imp,w}$, and $M_{imp,wb}$ of Figure B.7 are calculated at 9.3 seconds, and those to F_{con}, $M_{con,w}$, and $M_{con,wb}$ of Figure B.7 and $d_{w,\max}$ of Figure B.8 are calculated at 11 seconds. Figure B.9 presents the percentage contributions in the first three modes to F_{imp}, F_{con}, $M_{imp,w}$, $M_{con,w}$, $M_{imp,wb}$, $M_{con,wb}$, and $d_{w,\max}$ in respective panels a to g. Each panel presents contributions to includes three bar charts, presenting results for tanks with $H/R = 0.5$, 1, and 2, respectively. Each bar chart shows results for ground motions #1, #2, and #3. Results in Figure B.9 indicate that the first modes are the greatest contributors to all FSI responses for the three tanks and the three ground motions. The contributions shown in each bar chart generally decrease as the order of the mode increases. The contributions of the second and the third modes, although small, generally increase with increasing H/R, with greater percentage contributions to the convective responses (i.e., F_{con}, $M_{con,w}$, $M_{con,wb}$, and $d_{w,\max}$).

Table B.7. Maximum FSI responses, three impulsive and three convective modes, calculated using the analytical solutions of Veletsos for the tanks shown in Figure B.4 and the ground motions shown in Figure B.5

H / R	0.5			1			2		
Ground motion	#1	#2	#3	#1	#2	#3	#1	#2	#3
F_{imp} (10^4 kN)	1.8	2.3	4.3	5.9	9.4	12.6	15.6	21.9	33.6
F_{con} (10^4 kN)	0.4	1.6	0.0	0.7	2.5	0.1	0.7	2.6	0.1
F (10^4 kN)	1.6	2.4	4.2	5.8	9.5	12.5	15.0	21.9	33.6
$M_{imp,w}$ (10^5 kN-m)	1.0	1.3	2.5	7.3	11.8	15.3	45.4	63.3	94.3
$M_{con,w}$ (10^5 kN-m)	0.3	1.3	0.0	1.3	4.7	0.2	3.4	11.8	0.4
M_w (10^5 kN-m)	0.9	1.8	2.4	7.3	12.7	15.2	43.5	62.8	94.2
$M_{imp,wb}$ (10^5 kN-m)	3.8	4.9	9.3	12.5	20.0	26.8	50.1	69.8	105.6
$M_{con,wb}$ (10^5 kN-m)	0.9	3.6	0.1	1.6	5.8	0.2	3.4	12.0	0.4
M_{wb} (10^5 kN-m)	3.6	5.4	9.2	12.5	20.5	26.6	48.2	69.3	105.5
$d_{w,\max}$ (m)	0.41	1.55	0.04	0.59	1.89	0.07	0.59	1.89	0.07

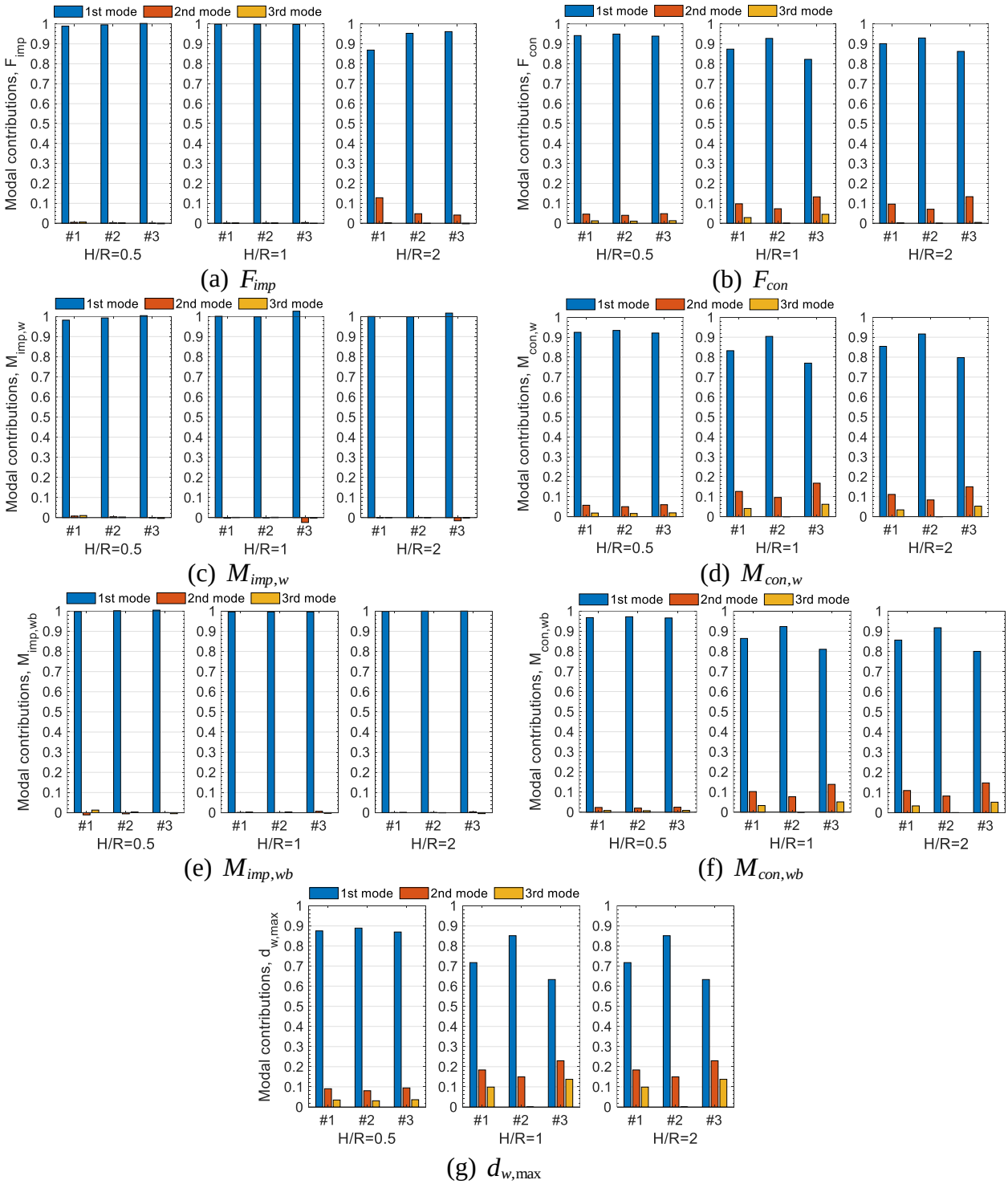

Figure B.9. Modal contributions to the impulsive and convective responses, at the time step of each peak response, calculated using the analytical solutions of Veletsos, for the tanks in Figure B.4 and the ground motions in Figure B.5

Discussion

This section compares the maximum responses calculated using the simplified procedure of Malhotra et al. to the analytical solutions of Veletsos for the three tanks subjected to the three scaled ground motions. The maximum values for F, M_w, M_{wb}, and $d_{w,\max}$ were presented in the fifth, eighth, eleventh, and twelfth rows, respectively, of Tables B.6 and B.7 for the two analysis methods, and presented together here in Figure B.10. Three bar charts are included in each panel of Figure B.10, showing results for tanks with $H/R =$ 0.5, 1, and 2; each bar chart presents data for ground motions #1, #2, and #3. The vertical ranges in the three figures in each panel are different. Table B.8 presents the percentage differences in the maximum responses calculated using the two analysis methods. The simplified procedure significantly overestimates responses in some cases (e.g., F, M_w, and M_{wb} for $H/R = 0.5$ and ground motions #1 and #2) and underestimates responses in others (e.g., the majority of the results for $d_{w,\max}$; M_{wb} for $H/R = 1$ and ground motion #3), compared to the results calculated using the analytical solutions of Veletsos. Although conclusive statements cannot be drawn based on a small number of analyses, the simplified procedure, which is included in Eurocode 8 and API 650 may not be sufficiently accurate for design.

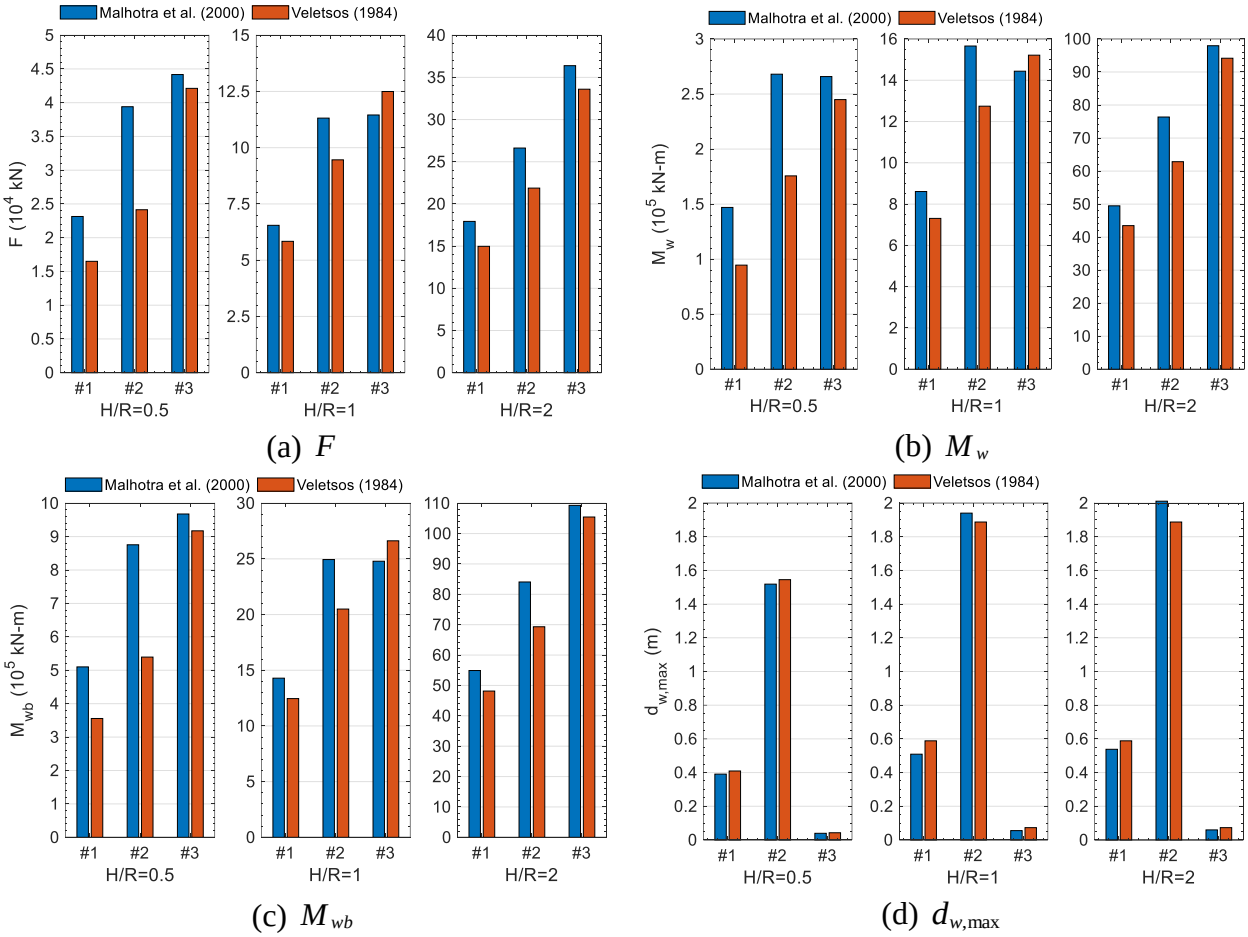

(a) F (b) M_w

(c) M_{wb} (d) $d_{w,\max}$

Figure B.10. Maximum FSI responses, composed of impulsive and convective components, calculated using the simplified procedure (Malhotra et al.) and the analytical solutions (Veletsos), for the tanks in Figure B.4 and the ground motions in Figure B.5.

Table B.8. Percentage differences of the maximum FSI responses shown in Figure B.10, for the tanks in Figure B.4 and the ground motions in Figure B.5.

H/R		0.5			1			2		
Ground motion		#1	#2	#3	#1	#2	#3	#1	#2	#3
Percentage difference[1] (%)	F	40	63	5	12	20	-8	20	22	8
	M_w	55	53	9	18	23	-5	14	22	4
	M_{wb}	43	62	5	15	22	-7	14	21	4
	$d_{w,\max}$	-5	-2	-7	-13	3	-24	-9	7	-18

1. Percentage difference of FSI responses calculated using the simplified procedure (Malhotra et al.) with respect to those calculated using the analytical solutions (Veletsos)

B.4 References

American Petroleum Institute (API) (2012). "Welded tanks for oil storage." *API 650*, API, Washington D.C.

Chopra, A. K. (2012). *Dynamics of structures: theory and applications to earthquake engineering*, 4th Ed., Prentice Hall, Upper Saddle River, NJ.

European Committee for Standardization (CEN) (1998). "Soils, tanks and pipelines." *Eurocode 8: design provision of earthquake resistance of structures*, CEN, Brussels, Belgium.

Malhotra, P. K. (2018), Personal communication, Email <spraveen.malhotra@strongmotions.com>.

Malhotra, P. K., Wenk, T., and Wieland, M. (2000). "Simple procedure for seismic analysis of liquid-storage tanks." *Structural Engineering International*, 10(3), 197-201.

Pacific Earthquake Engineering Research (PEER) "PEER ground motion database." <http://peer.berkeley.edu/peer_ground_motion_database>. (Jan. 12, 2019).

Veletsos, A. (1984). "Seismic response and design of liquid storage tanks." *Guidelines for the seismic design of oil and gas pipeline systems*, Committee on Gas and Liquid Fuel Lifelines, American Society of Civil Engineers (ASCE), Reston, VA, 255-370.

APPENDIX C. CHALLENGES IN OUTPUTTING ALE RESULTS FOR WAVE HEIGHTS IN A TANK SUBJECTED TO SEISMIC MOTION

C.1 Introduction

Seismic fluid-structure interaction (FSI) analysis of a liquid-filled tank can be performed using the Arbitrary Lagrangian-Eulerian (ALE) solver of LS-DYNA (Livermore Software Technology Corporation (LSTC) 2018a). Wave heights of the contained fluid, calculated using the ALE solver, are output by tracking the vertical displacement of the free surface through the *DATABASE_TRACER card. The card records the time series of the coordinates of the assigned points that float on the free surface and move with the velocities of the fluid in the three directions. These floating points not only move vertically with waves but also horizontally with transverse flows. However, information on wave action at a *fixed* location with respect to the tank (i.e., local coordinate system that moves horizontally with the tank) is needed for seismic design (e.g., freeboard of tanks and vessels).

This appendix discusses the challenges and limitations with the use of floating points to output wave heights. An ALE model is constructed in Section C.2 for a rigid, base-supported cylindrical tank filled with water. Seismic FSI analysis is performed for a sinusoidal motion in the x direction defined in Figure C.1. A number of floating points are assigned for the contained fluid to track waves. Section C.3 reports the motions of the floating points and the calculated wave heights at three locations with fixed distances to the tank wall. The results of ALE analysis for wave height are compared with those calculated using an analytical solution per Eq. (3.81) (Veletsos 1984a). Errors in the ALE results associated with the motions of the floating points are discussed. Section C.4 presents closing remarks and recommendations to mitigate errors in wave-height predictions using the ALE solver.

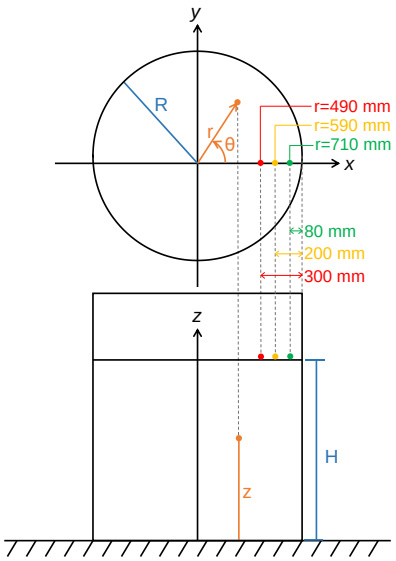

Figure C.1. Cartesian coordinate system and cylindrical coordinate system defined on two cut-away views of a base-supported cylindrical tank, three locations for reporting wave heights shown in green, yellow, and red solid circles

C.2 Numerical model and input motion

Figure 4.3 presents the ALE model of the rigid base-supported cylindrical tank used here for FSI analysis, together with the Cartesian coordinates consistent with those defined in Figure C.1. The radius R is 0.79 m, the height of the tank H_s is 2 m, and the wall thickness h is 0.5 mm. The tank is filled with water to a height H of 1.2 m. In Figure 4.3, the tank is shown in blue, the water is shown in yellow, and a vacuum space built above the water is shown in grey. The tank is modeled using Lagrangian shell elements assigned a rigid material, and the water and the vacuum are modeled using Eulerian solid elements. This model is identical to one of the ALE models used in Section 4.2.1 and presented in Figures 4.3a to c. Section 4.2.1 describes the construction of the model. Table C.1 presents the dimensions, mechanical properties, and masses of the tank and water in the ALE model. The mechanical properties include elastic modulus E, density ρ_s, and Poisson's ratio υ of for the tank, and water density ρ_w. (Section 4.2.1 verifies the ALE model by comparing numerical and analytical results, including reactions at the base that are due to the hydrodynamic response of the fluid but not inertial response of the tank. To ensure that the inertial response of the rigid tank is negligible, it is assigned a thickness h of 0.5 mm and a density ρ_s of 100 kg/m^3 is used for the tank.) No damping is applied to the rigid

material of the tank (i.e., damping ratio=0). Gravitational acceleration is assigned in the z direction. More details on the ALE model can be found in Section 4.2.1.

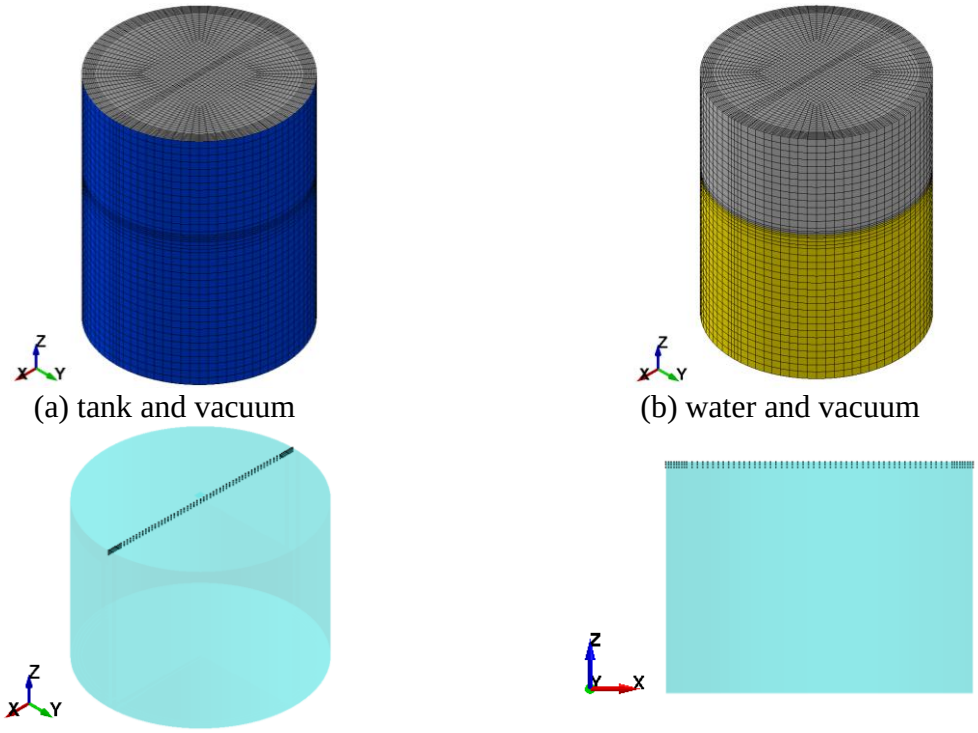

(a) tank and vacuum

(b) water and vacuum

(c) water and floating points, $t = 0$

(d) water and floating points, $t = 0$, $x - z$ cross section

Figure C.2. ALE model of a rigid cylindrical tank with $R = 0.79$ m, $H_s = 2$ m, and $H = 1.2$ m

Table C.1. Dimensions, mechanical properties, and masses of the tank and contained water in the ALE model

	Dimension	Mechanical property	Mass (kg)
Tank, carbon steel	$R = 0.79$ m	$E = 2 \times 10^{11}$ N/m^2	0.6
	$H_s = 2$ m	$\upsilon = 0.27$	
	$h = 0.5$ mm	$\rho_s = 100$ kg/m^3	
Contained fluid, water	$H = 1.2$ m	$\rho_w = 1000$ kg/m^3	2352

Figures C.3c and d present the contained water at the first step of the analysis (i.e., time $t = 0$). Two hundred and one floating points (shown as black dots) are assigned per the *DATABASE_TRACER card, on or near the free surface, along the x direction (direction of seismic input), and across the diameter of the tank. The floating points are placed in three layers of 67. The upper layer is located on the free surface, and the middle and lower layers are in the water, located 15 and 30 mm below the surface, respectively. Wave heights in the tank are calculated using the floating points of the upper layer that provides vertical displacements of the free surface. The floating points in the middle and lower layers are used here to investigate the flow of the water near the free surface.

A 20-Hz sinusoidal motion presented in Figure C.3a is used for the response-history analysis for the ALE model in the x direction. A small amplitude of 0.2 g is used for the input motion to avoid nonlinear or unstable sloshing. The duration of the shaking is 10 seconds, and the analysis continues for 20 seconds after the shaking has ended to investigate wave action under free vibration. Accordingly, the analysis is performed for 30 seconds. Figure C.3b magnifies the first second of the input motion, showing the sinusoidal input.

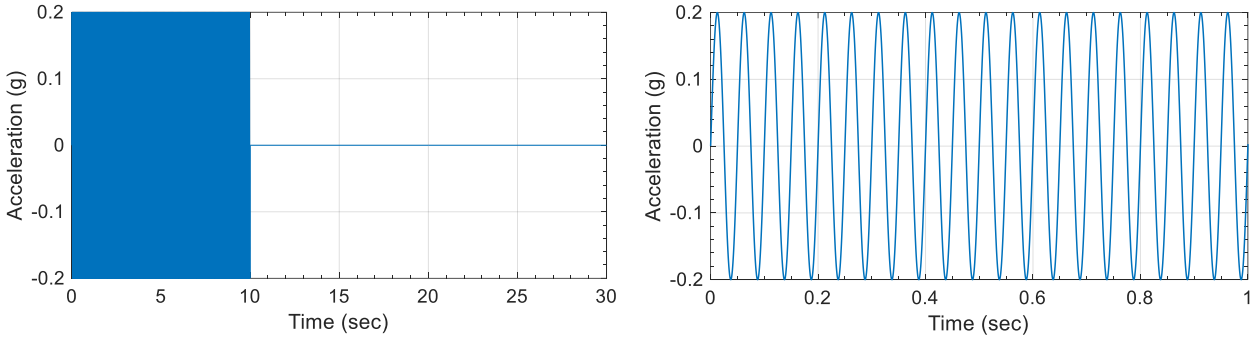

(a) analysis of 30 seconds (b) first second

Figure C.3. Input motion in the x direction, sinusoidal waves with a frequency of 20 Hz and an amplitude of 0.2 g

C.3 Results: motions of the floating points and wave heights

The floating points move with the fluid velocities in the three directions, and wave heights can be determined using their z coordinates. Figure C.4 presents the water and the floating points in the ALE model at 5, 10, 20, and 30 seconds, in an isometric view and on a $x-z$ cross section.

(Figures C.3c and d present the water and floating points at $t = 0$.) Three layers of floating points are seen at 5 seconds. At 10 seconds, the three layers are not clearly distinguishable. For $t \geq 20$ seconds, the middle and lower layers converge to the upper layer. Since the middle and lower layers gradually move upwards (to converge to the upper layer), their z coordinates should not be used to calculate wave heights: the upper layer should be used. As time increases, the floating points move in the x direction to the center of the free surface and downwards near the z axis (see the coordinates in Figure C.1). Figure C.5 presents the $x-$ and $z-$coordinates of the three floating points (one from each layer) that are *initially* ($t = 0$) located at 80 mm away from the $+x$ face of the tank wall. Their $x-$coordinates are 710 mm (i.e., $x = R - 80$=710 mm) at $t = 0$ and all trend toward $x = 0$, which is at the center of the free surface. The initial $z-$coordinates of the layers are $z = 1200$, 1185, and 1700 mm, which are on the free surface ($z = 1200$ mm), and 15 and 30 mm below the surface, respectively, as noted in Section C.2. As seen in Figure C.5b for $0 \leq t \leq 15$ seconds, all three points oscillate in the z direction (vertically) with a period of around 1.3 seconds[56] due to wave action. The points in the middle and lower layers (orange and yellow lines) gradually move upwards and converge to that of the upper layer (blue line) at around 15 to 20 seconds, and so the three layers cannot be seen in Figures C.4c and d. Thereafter, the $z-$coordinates of all three points move downwards. Per Figure C.5, the x and z coordinates of the blue lines move faster than those of the orange and yellow lines: the upper layer moves faster, in the x direction to the center of the free surface and downwards along the z axis, than the other two layers. The velocity field of the fluid is presented in Figure C.6 to explain the motion of the floating points. This figure presents fringes and vectors (shown as arrows) of the fluid velocity at 30 seconds: the $x-$component on the free surface and the $xz-$component on a $x-z$ cross section. The fluid at the free surface shown in Figure C.6a flows toward the y axis (noted as $x = 0$) at the center of the tank. On the $x-z$ cross section of Figure C.6b, the fluid near the free surface flows horizontally (x direction) and then downwards near the z axis. A greater fluid velocity (shown as red) is seen closer to the free surface, which is consistent with the results presented in Figure C.5: the upper layer moves faster than the other two layers. The fluid on the

[56] The period of 1.3 seconds is approximated using the average duration of every two consecutive crests of each layer for $0 \leq t \leq 15$ seconds, presented in Figure C.5b. The first convective period of the tank estimated using Eq. (3.73) (Veletsos 1984) is 1.32 seconds, and so the approximation made for Figure C.5b is reasonable.

$+x$ and $-x$ sides circulates counter-clockwise and clockwise, respectively. The vector fields presented in Figure C.6 confirm that the floating points follow the fluid to the center of the free surface and downwards around the z axis, as shown in Figures C.4 and C.5.

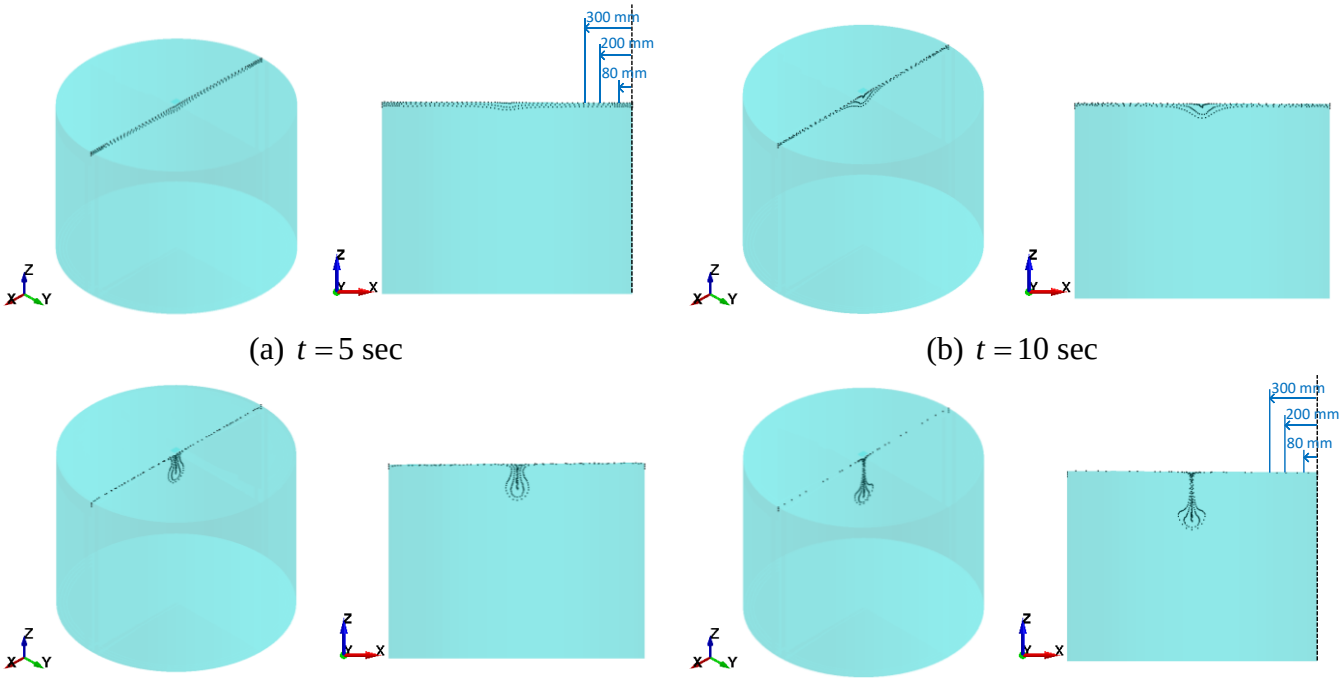

(a) $t = 5$ sec (b) $t = 10$ sec

(c) $t = 20$ sec (d) $t = 30$ sec

Figure C.4. Snapshots of the water and floating points in the ALE model at different time steps, isometric view and $x-z$ cross section

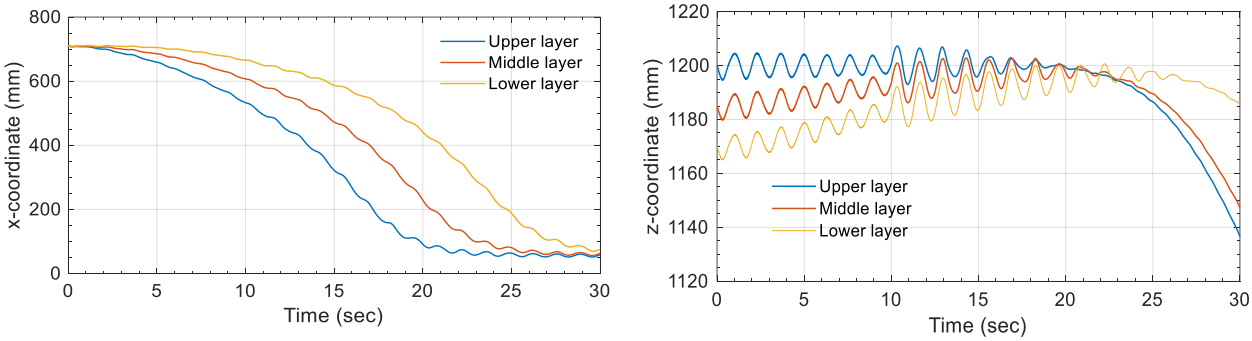

(a) $x-$coordinate (b) $z-$coordinate

Figure C.5. Coordinates of the floating points initially located 80 mm away from the $+x$ side of the tank wall, three layers

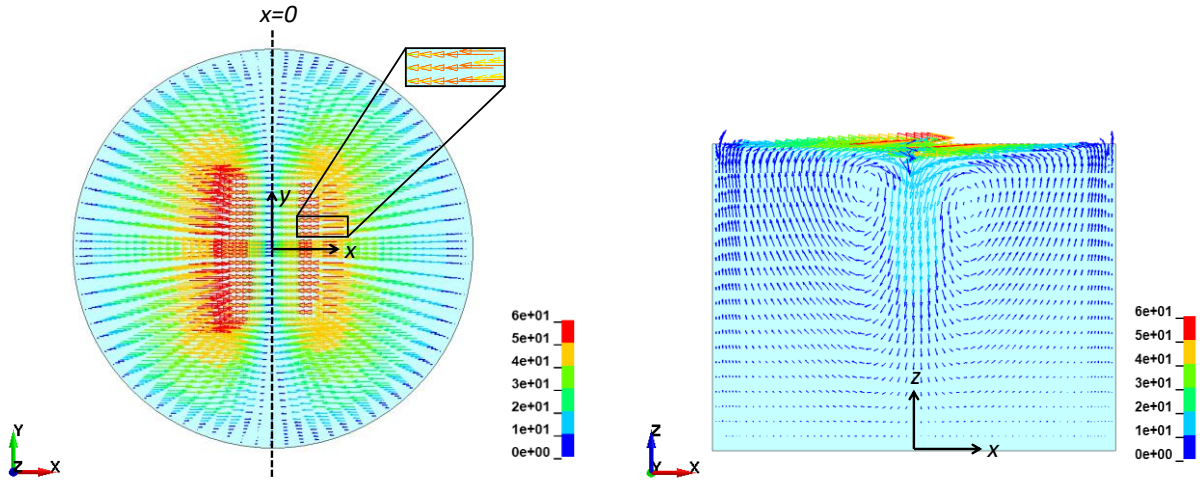

(a) $x-$ component on the free surface (b) $xz-$component on the $x-z$ cross section

Figure C.6. Vectors fields of the fluid velocities at 30 seconds, unit: mm/s

Figure C.7 enables a comparison of vertical displacements of the free surface, namely, wave heights d_w, calculated using the ALE model and an analytical solution per Eq. (3.81) (Veletsos 1984a). The results are reported at locations 80, 200, and 300 mm from the $+x$ face of the tank wall in the ALE model, namely, $r = 710$, 590, 490 mm, respectively. The three monitoring locations are indicated as green, yellow, and red solid circles in Figure C.1. The wave heights are calculated by interpolating the z coordinates of two floating points in the upper layer adjacent to the monitoring locations at each time step. Different pairs of two floating points may be used in different time steps because the points move, as seen in Figure C.4, but the monitoring locations are fixed, with respect to the tank. As presented in Figure C.7, the phases of the time series calculated using the ALE model and the analytical solution are in good agreement. The amplitudes of d_w are underestimated by the ALE model and diverge further from the analytical results as time increases, at all three locations.

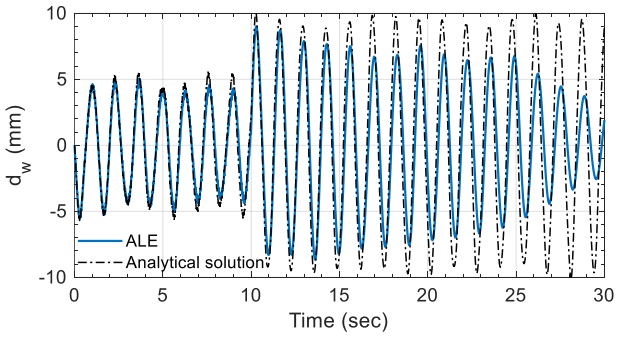

(a) 80 mm from the $+x$ face, $r = 710$ mm

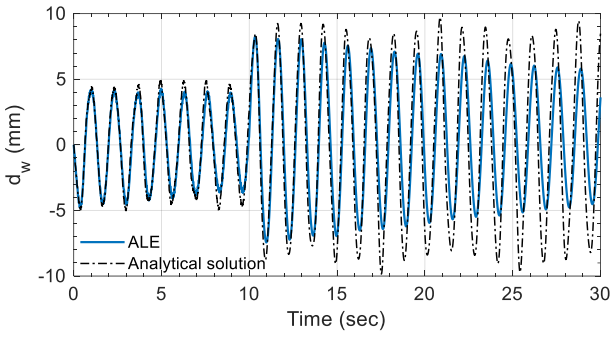

(b) 200 mm from the $+x$ face, $r = 590$ mm

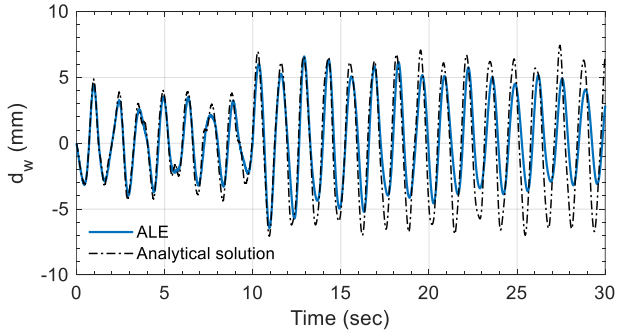

(c) 300 mm from the $+x$ face, $r = 490$ mm

Figure C.7. Wave height at 80, 200, 300 mm away from the $+x$ face of the tank wall, indicated as green, yellow, and red solid circles in Figure C.1, floating points in the upper layer in the ALE model and Eq. (3.81)

Table C.2 presents the maximum amplitudes of d_w in every 5 seconds of each time series shown in Figure C.7, and identifies the differences between the ALE and analytical results. The ALE results in the first 5 or 10 seconds are in reasonable agreement with the analytical results: differences are less than or equal to 15%. The underprediction of the ALE model increases with time, which is associated with the use of floating points to output wave heights. As indicated using blue text and arrows in Figures C.4a and d, the distance between the two floating points adjacent to each monitoring location increases with time, from $t = 5$ to 30 seconds. Wave heights calculated using linear interpolation with the z coordinates of the two points are likely inaccurate if they are distant from each other because 1) the free surface between the two points is not necessarily linear, and 2) the point closer to the center of the free surface tends to move downwards and not be on the surface, as shown in Figure C.4 and Figure C.5b.

Table C.2. Maximum wave heights at the three locations in every 5 seconds, ALE model and Eq. (3.81), extracted from Figure C.7

	d_w (mm)					
	80 mm from $+x$ face, $r = 710$ mm		200 mm from $+x$ face, $r = 590$ mm		300 mm from $+x$ face, $r = 490$ mm	
Time (sec)	Analytical solution	ALE (diff)[1]	Analytical solution	ALE (diff)[1]	Analytical solution	ALE (diff)[1]
0 to 5	5.8	5.6 (-3%)	5.0	4.8 (-4%)	5.2	4.5 (-14%)
5 to 10	5.6	5.1 (-10%)	5.0	4.2 (-15%)	5.2	3.9 (-24%)
10 to 15	10.1	9.0 (-11%)	9.3	8.3 (-11%)	9.1	7.7 (-15%)
15 to 20	9.8	7.9 (-20%)	9.8	7.6 (-23%)	8.9	6.8 (-23%)
20 to 25	9.8	7.2 (-27%)	9.7	6.9 (-29%)	8.9	6.4 (-28%)
25 to 30	10.1	5.4 (-46%)	9.7	6.0 (-38%)	8.6	5.7 (-33%)

1. Percentage differences of ALE results with respect to those calculated using the analytical solution, to the nearest 1%

C.4 Closing remarks and recommendations

This appendix discusses the challenges and limitations with the use of floating points to output wave heights in a tank subjected to horizontal seismic motion, analyzed using the ALE solver. An ALE model of a rigid base-supported tank filled with water is constructed and response-history analysis is performed using a horizontal sinusoidal input. A number of floating points are assigned on the free surface to investigate the motion of the fluid and the capability of outputting wave heights at fixed locations relative to the tank (i.e., local locations). The wave heights are derived using the vertical coordinates of the floating points. As presented in Section C.3, the floating points move toward the center of the free surface and then downwards near the vertical (z) axis of the tank, following the velocities of the contained water. The wave heights output using the floating points are underestimated, and the underestimation increases with time because the points gradually move downwards.

The errors in outputting wave heights can be mitigated by using a very dense line of floating points around the monitoring location. Although all points gradually move to the center of the

free surface, sufficient points would be available around the monitoring location for outputting wave heights. This method is used in Section 6 to improve the ALE results. The most effective solution to the errors is the development of tracking points that can float on the free surface, but be fixed in the horizontal directions or move with the horizontal seismic input to maintain a constant distance to the tank. An example of the use of horizontally fixed points is the *Floater* option in the graphical user interface (GUI) of LS-Prepost (2018c) for outputting wave heights calculated using the Incompressible Computational Fluid Dynamics (ICFD) solver. This option is not available for ALE analysis at the time of this writing.

C.5 References

Livermore Software Technology Corporation (LSTC) (2018a). "LS-DYNA keyword user's manual-R11." Livermore, CA.

Livermore Software Technology Corporation (LSTC) (2018b). "LS-PrePost V4.7." Livermore, CA.

Veletsos, A. (1984). "Seismic response and design of liquid storage tanks." *Guidelines for the seismic design of oil and gas pipeline systems*, Committee on Gas and Liquid Fuel Lifelines, American Society of Civil Engineers (ASCE), Reston, VA, 255-370.

APPENDIX D. SEISMIC MOTIONS FOR EARTHQUAKE-SIMULATOR TESTS OF A CYLINDRICAL TANK

D.1 Introduction

A base-supported cylindrical tank was tested using a six-degree-of-freedom earthquake simulator at the University at Buffalo. The simulator is shown in Figure D.1. The tank is a model of an advanced reactor vessel, at a length scale of approximately 1/10. A two-phase program of experiments was performed to support validation of numerical models and demonstrate the merits of seismic isolation for equipment in nuclear power plants. The Phase I involved the tank, and the Phase II involved the tank sealed with a head, supporting central and off-center internal components immersed in the contained fluid. Two test setups (TSs) were used in the Phase I: 1) TS-1, the base of the tank was directly attached to the earthquake simulator; and 2) TS-2, load cells were installed between the earthquake simulator and the base. The Phase I tests were performed for 138 sets of input motions, including 68 sets for TS-1 and 70 sets for TS-2. Information on the input motions is provided in the next section. Details on the specimen design, test setups, instrumentation, and use of test data can be found in Mir et al. (2019; 2020a; 2020b).

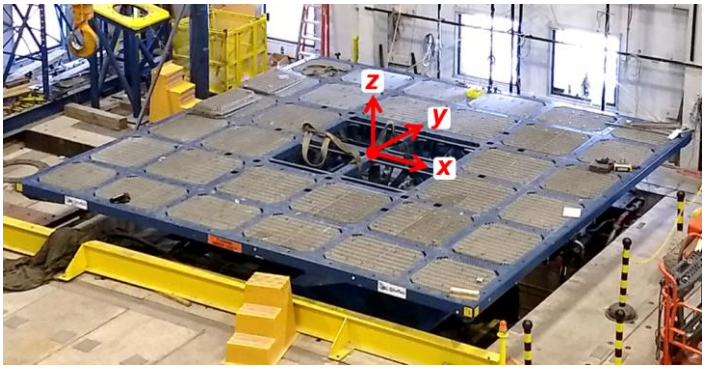

Figure D.1. Earthquake simulator and coordinates (x , y , z)

D.2 Seismic inputs and test sequence

White noise, sine waves, and earthquake records were used as input motions in the Phase I tests. Information on the earthquake records is presented in Table D.1, including the earthquake events, the components used for the tests, and their peak ground acceleration (PGAs). Consistent with a length scale of 1/10, the time scale of each earthquake motion was compressed by a factor of $\sqrt{10}$. Figure D.2 shows 2%-damped acceleration response spectra of the earthquake motions,

with time compression of $\sqrt{10}$. In these spectra, the PGA of the x-component of each earthquake is scaled to 1 g. The y- and z-components of the earthquake are scaled using the factor for the x-component. Five-second input motions were extracted from the earthquake records, after time compression by $\sqrt{10}$, which included the strong motion.

Tables D.1 and D.3 list the inputs used for TS-1 and TS-2, respectively, including white noise, sine waves, and full and five-second earthquake motions. (The five-second motions are denoted with "5s" after the names of the earthquakes.) The PGAs of the earthquake records were scaled to different intensities, with a maximum of 1 g. The PGAs and input directions at the earthquake simulator are identified, based on the coordinates defined in Figure D.1. Motions #30, #35, and #42, which are bolded in Table D.3, are used in Section 6 for a validation study on numerical models.

Table D.1. Input motion time series[1] used for earthquake-simulator tests

Event	Year	Station	Direction[2]	Original PGA (g)	Scaled PGA[3] (g)	Time scale
El Centro Earthquake (Imperial Valley-02)	1940	El Centro Array #9	180 (x)	0.28	1	$1/\sqrt{10}$
			270 (y)	0.21	0.56	
			Up (z)	0.18	0.42	
Hualien Earthquake	2018	HWA019	EW (x)	0.39	1	$1/\sqrt{10}$
			NS (y)	0.37	0.88	
			Up (z)	0.23	0.81	
Chi-Chi Earthquake	1999	TCU052	EW (x)	0.36	1	$1/\sqrt{10}$
			NS (y)	0.45	1.25	
			Up (z)	0.19	0.55	
Tohoku Earthquake (a)	2011	AKT014	EW (x)	0.07	1	$1/\sqrt{10}$
Tohoku Earthquake (b)	2011	MYG014	NS (x)	0.5	1	$1/\sqrt{10}$

1. Ground motion records of the El Centro and Chi-Chi Earthquakes are extracted from the PEER Ground Motion Database (http://ngawest2.berkeley.edu/, accessed on Jan. 12, 2019); records of the Hualien Earthquake are provided by the National Center for Research on Earthquake Engineering, Taiwan; and records of the Tohoku Earthquake are extracted from Strong-motion Seismograph Networks (K-NET, KiK-net) (https://www.kyoshin.bosai.go.jp/, accessed on Mar. 18, 2019).
2. Directions based on the coordinates described in the dataset of the ground motion records; x, y, and z shown in the parentheses representing the input directions of the earthquake simulator (see Figure D.1)
3. Used in Figure D.2

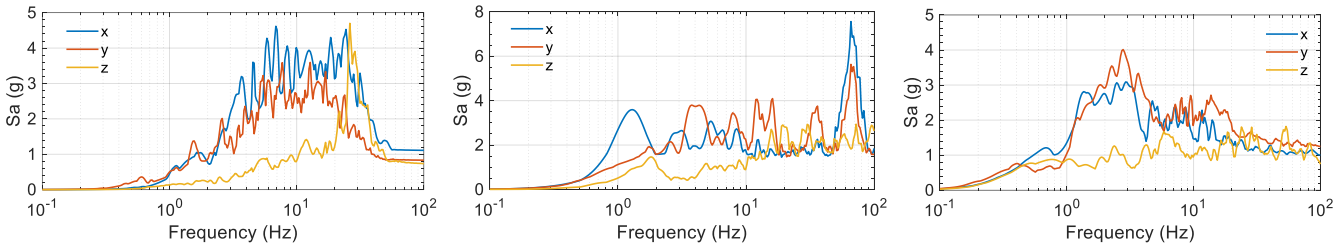

(a) El Centro Earthquake (b) Hualien Earthquake (c) Chi-Chi Earthquake

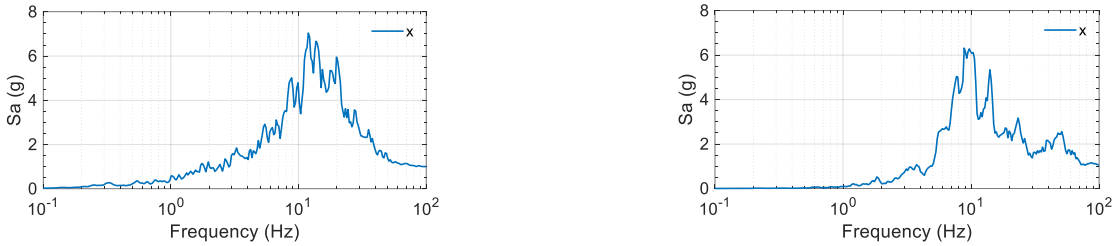

(d) Tohoku Earthquake (AKT014_NS) (e) Tohoku Earthquake (MYG014_NS)

Figure D.2. Acceleration response spectra of input motions used for the earthquake-simulator tests, time scale compressed by $\sqrt{10}$, PGA scaled to the values presented in the sixth column of Table D.1, damping ratio of 2%

Table D.2. Input motions for TS-1

Run #	Motion	x-direction PGA (g)	y-direction PGA (g)	z-direction PGA (g)
1	White noise 1	0.1	-	-
2	White noise 2	0.1	-	-
3	Sine ($f = 0.5$ Hz)	0.01	-	-
4	Sine ($f = 1$ Hz)	0.04	-	-
5	Sine ($f = 10$ Hz)	0.1	-	-
6	Sine ($f = 10$ Hz)	0.2	-	-
7	Sine ($f = 10$ Hz)	0.4	-	-
8	Sine ($f = 10$ Hz)	1	-	-
9	Sine ($f = 1$ Hz)	0.4	-	-
10	Sine ($f = 10$ Hz)	1	-	-
11	Sine ($f = 20$ Hz)	0.1	-	-
12	Sine ($f = 20$ Hz)	0.2	-	-
13	Hualien Earthquake	0.1	-	-
14	Chi-Chi Earthquake	0.1	-	-
15	Chi-Chi Earthquake	0.15	-	-
16	El Centro Earthquake	0.1	-	-
17	El Centro Earthquake	0.2	-	-
18	El Centro Earthquake	0.4	-	-
19	Tohoku Earthquake (a)	0.05	-	-
20	Tohoku Earthquake (a)	0.075	-	-
21	Tohoku Earthquake (b)	0.1	-	-
22	Tohoku Earthquake (b)	0.2	-	-
23	Tohoku Earthquake (b)	0.4	-	-
24	Tohoku Earthquake (b)	0.6	-	-
25	Hualien Earthquake 5s	0.1	-	-
26	Chi-Chi Earthquake 5s	0.15	-	-
27	El Centro Earthquake 5s	0.2	-	-

Table D.2. Input motions for TS-1 (continued)

Run #	Motion	x-direction PGA (g)	y-direction PGA (g)	z-direction PGA (g)
28	El Centro Earthquake 5s	0.4	-	-
29	Tohoku Earthquake (b) 5s	0.2	-	-
30	Tohoku Earthquake (b) 5s	0.6	-	-
31	Tohoku Earthquake (b) 5s	0.2	-	-
32	Tohoku Earthquake (b) 5s	0.6	-	-
33	El Centro Earthquake 5s	1	-	-
34	El Centro Earthquake	1	-	-
35	Sine (f = 20 Hz)	1	-	-
36	Sine (f = 20 Hz)	1	-	-
37	Hualien Earthquake	0.1	0.094	-
38	Chi-Chi Earthquake	0.1	0.125	-
39	Hualien Earthquake	0.1	0.047	-
40	Chi-Chi Earthquake	0.1	0.0625	-
41	Hualien Earthquake	0.1	0.0235	-
42	Chi-Chi Earthquake	0.1	0.0313	-
43	Hualien Earthquake 5s	0.1	0.094	-
44	Chi-Chi Earthquake 5s	0.1	0.125	-
45	Hualien Earthquake 5s	0.1	0.047	-
46	Chi-Chi Earthquake 5s	0.1	0.0625	-
47	Hualien Earthquake 5s	0.1	0.0235	-
48	Chi-Chi Earthquake 5s	0.1	0.0313	-
49	Hualien Earthquake	0.1	0.094	0.058
50	Chi-Chi Earthquake	0.1	0.125	0.055
51	Hualien Earthquake 5s	0.1	0.094	0.058
52	Chi-Chi Earthquake 5s	0.1	0.125	0.055
53	El Centro Earthquake	0.13	0.097	-
54	El Centro Earthquake	0.25	0.187	-

Table D.2. Input motions for TS-1 (continued)

Run #	Motion	x-direction PGA (g)	y-direction PGA (g)	z-direction PGA (g)
55	El Centro Earthquake	0.5	0.375	-
56	El Centro Earthquake	1	0.751	-
57	El Centro Earthquake	1	0.375	-
58	El Centro Earthquake	1	0.187	-
59	El Centro Earthquake 5s	1	0.751	-
60	El Centro Earthquake 5s	1	0.375	-
61	El Centro Earthquake 5s	1	0.187	-
62	El Centro Earthquake	1	0.751	0.637
63	El Centro Earthquake 5s	1	0.751	0.637
64	Sine ($f = 0.77$ Hz)	0.03	-	-
65	Sine ($f = 1.95$ Hz)	0.04	-	-
66	Sine ($f = 1.67$ Hz)	0.03	-	-
67	Sine ($f = 1.32$ Hz)	0.03	-	-
68	Sine ($f = 0.77$ Hz)	0.03	-	-

Table D.3. Input motions for TS-2

Run #	Motion	x-direction PGA (g)	y-direction PGA (g)	z-direction PGA (g)
1	White noise 1	0.1	-	-
2	White noise 2	0.1	-	-
3	Sine ($f = 0.5$ Hz)	0.01	-	-
4	Sine ($f = 1$ Hz)	0.04	-	-
5	Sine ($f = 10$ Hz)	0.2	-	-
6	Sine ($f = 10$ Hz)	1	-	-
7	Sine ($f = 20$ Hz)	0.1	-	-
8	Sine ($f = 20$ Hz)	0.4	-	-
9	Sine ($f = 0.77$ Hz)	0.01	-	-
10	Sine ($f = 1.32$ Hz)	0.04	-	-
11	Sine ($f = 1.67$ Hz)	0.05	-	-
12	Sine ($f = 1.95$ Hz)	0.06	-	-
13	Hualien Earthquake	0.1	-	-
14	Chi-Chi Earthquake	0.1	-	-
15	Chi-Chi Earthquake	0.15	-	-
16	El Centro Earthquake	0.1	-	-
17	El Centro Earthquake	0.2	-	-
18	El Centro Earthquake	0.4	-	-
19	Tohoku Earthquake (a)	0.05	-	-
20	Tohoku Earthquake (a)	0.075	-	-
21	Tohoku Earthquake (b)	0.1	-	-
22	Tohoku Earthquake (b)	0.2	-	-
23	Tohoku Earthquake (b)	0.4	-	-
24	Tohoku Earthquake (b)	0.6	-	-
25	Hualien Earthquake 5s	0.1	-	-
26	Chi-Chi Earthquake 5s	0.1	-	-
27	Hualien Earthquake 5s	-	0.1	-

Table D.3. Input motions for TS-2 (continued)

Run #	Motion	*x* -direction PGA (g)	*y* -direction PGA (g)	*z* -direction PGA (g)
28	Chi-Chi Earthquake 5s	-	0.1	-
29	El Centro Earthquake	1	-	-
30	**El Centro Earthquake 5s**	**1**	**-**	**-**
31	Hualien Earthquake	0.1	0.094	-
32	Chi-Chi Earthquake	0.1	0.125	-
33	Hualien Earthquake	0.1	0.047	-
34	Chi-Chi Earthquake	0.1	0.0625	-
35	**Hualien Earthquake 5s**	**0.1**	**0.094**	**-**
36	Chi-Chi Earthquake 5s	0.1	0.125	-
37	Hualien Earthquake 5s	0.1	0.047	-
38	Chi-Chi Earthquake 5s	0.1	0.0625	-
39	Hualien Earthquake	0.1	0.094	0.058
40	Chi-Chi Earthquake	0.1	0.125	0.055
41	Hualien Earthquake 5s	0.1	0.094	0.058
42	**Chi-Chi Earthquake 5s**	**0.1**	**0.125**	**0.055**
43	El Centro Earthquake	1	0.751	-
44	El Centro Earthquake	1	0.375	-
45	El Centro Earthquake 5s	1	0.751	-
46	El Centro Earthquake 5s	1	0.375	-
47	El Centro Earthquake	1	0.751	0.637
48	El Centro Earthquake 5s	1	0.751	0.637
49	Hualien Earthquake	0.1	-	-
50	Hualien Earthquake 5s	0.1	-	-
51	Hualien Earthquake	0.1	0.094	-
52	Hualien Earthquake	0.1	0.047	-
53	Hualien Earthquake 5s	0.1	0.094	-
54	Hualien Earthquake 5s	0.1	0.047	-

Table D.3. Input motions for TS-2 (continued)

Run #	Motion	*x* -direction PGA (g)	*y* -direction PGA (g)	*z* -direction PGA (g)
55	Hualien Earthquake	0.1	0.094	0.058
56	Hualien Earthquake 5s	0.1	0.094	0.058
57	Hualien Earthquake	-	-	0.058
58	Hualien Earthquake 5s	-	-	0.058
59	Chi-Chi Earthquake	0.1	0.125	0.055
60	Chi-Chi Earthquake 5s	0.1	0.125	0.055
61	Chi-Chi Earthquake	-	-	0.055
62	Chi-Chi Earthquake 5s	-	-	0.055
63	El Centro Earthquake	1	0.751	0.637
64	El Centro Earthquake 5s	1	0.751	0.637
65	El Centro Earthquake	-	-	0.637
66	El Centro Earthquake 5s	-	-	0.637
67	El Centro Earthquake 5s	1	0.751	0.637
68	El Centro Earthquake 5s	1	0.751	-
69	El Centro Earthquake 5s	1	0.385	-
70	El Centro Earthquake 5s	-	-	0.637

D.3 References

Livermore Software Technology Corporation (LSTC) (2018). "LS-DYNA SMP_d_Dev_126632." Livermore, CA.

Livermore Software Technology Corporation (LSTC) (2019). "LS-DYNA SMP_d_R11_139066." Livermore, CA.

Mir, F. U. H., Yu, C.-C., Charkas, H., and Whittaker, A. S. (2020a). "Validation of numerical models for seismic fluid-structure interaction analysis of advanced reactors." *Tran., International Congress on Advances in Nuclear Power Plants (ICAPP 2020)*, Abu Dhabi, United Arab Emirates.

Mir, F. U. H., Yu, C.-C., Cohen, M., Bardet, P., Coleman, J. L., and Whittaker, A. S. (2019). "Dataset generation for validation of fluid-structure interaction models." *Tran., 25th International Conference on Structural Mechanics in Reactor Technology (SMiRT-25)*, Charlotte, NC.

Mir, F. U. H., Yu, C.-C., and Whittaker, A. S. (2020b). "Experiments for validation of FSI models for seismic response of advanced reactor internals." *Tran., 17th World Conference on Earthquake Engineering (17WCEE)*, Sendai, Japan.

National Research Institute for Earth Science and Disaster Resilience (NIED) "Strong-motion Seismograph Networks (K-NET, KiK-net)." <https://www.kyoshin.bosai.go.jp/>. (Mar. 18, 2019).

Pacific Earthquake Engineering Research (PEER) "PEER ground motion database." <http://peer.berkeley.edu/peer_ground_motion_database>. (Jan. 12, 2019).

MCEER Technical Reports

MCEER publishes technical reports on a variety of subjects written by authors funded through MCEER. These reports can be downloaded from the MCEER website at http://www.buffalo.edu/mceer. They can also be requested through NTIS, P.O. Box 1425, Springfield, Virginia 22151. NTIS accession numbers are shown in parenthesis, if available.

NCEER-87-0001 "First-Year Program in Research, Education and Technology Transfer," 3/5/87, (PB88-134275, A04, MF-A01).

NCEER-87-0002 "Experimental Evaluation of Instantaneous Optimal Algorithms for Structural Control," by R.C. Lin, T.T. Soong and A.M. Reinhorn, 4/20/87, (PB88-134341, A04, MF-A01).

NCEER-87-0003 "Experimentation Using the Earthquake Simulation Facilities at University at Buffalo," by A.M. Reinhorn and R.L. Ketter, not available.

NCEER-87-0004 "The System Characteristics and Performance of a Shaking Table," by J.S. Hwang, K.C. Chang and G.C. Lee, 6/1/87, (PB88-134259, A03, MF-A01). This report is available only through NTIS (see address given above).

NCEER-87-0005 "A Finite Element Formulation for Nonlinear Viscoplastic Material Using a Q Model," by O. Gyebi and G. Dasgupta, 11/2/87, (PB88-213764, A08, MF-A01).

NCEER-87-0006 "Symbolic Manipulation Program (SMP) - Algebraic Codes for Two and Three Dimensional Finite Element Formulations," by X. Lee and G. Dasgupta, 11/9/87, (PB88-218522, A05, MF-A01).

NCEER-87-0007 "Instantaneous Optimal Control Laws for Tall Buildings Under Seismic Excitations," by J.N. Yang, A. Akbarpour and P. Ghaemmaghami, 6/10/87, (PB88-134333, A06, MF-A01). This report is only available through NTIS (see address given above).

NCEER-87-0008 "IDARC: Inelastic Damage Analysis of Reinforced Concrete Frame - Shear-Wall Structures," by Y.J. Park, A.M. Reinhorn and S.K. Kunnath, 7/20/87, (PB88-134325, A09, MF-A01). This report is only available through NTIS (see address given above).

NCEER-87-0009 "Liquefaction Potential for New York State: A Preliminary Report on Sites in Manhattan and Buffalo," by M. Budhu, V. Vijayakumar, R.F. Giese and L. Baumgras, 8/31/87, (PB88-163704, A03, MF-A01). This report is available only through NTIS (see address given above).

NCEER-87-0010 "Vertical and Torsional Vibration of Foundations in Inhomogeneous Media," by A.S. Veletsos and K.W. Dotson, 6/1/87, (PB88-134291, A03, MF-A01). This report is only available through NTIS (see address given above).

NCEER-87-0011 "Seismic Probabilistic Risk Assessment and Seismic Margins Studies for Nuclear Power Plants," by Howard H.M. Hwang, 6/15/87, (PB88-134267, A03, MF-A01). This report is only available through NTIS (see address given above).

NCEER-87-0012 "Parametric Studies of Frequency Response of Secondary Systems Under Ground-Acceleration Excitations," by Y. Yong and Y.K. Lin, 6/10/87, (PB88-134309, A03, MF-A01). This report is only available through NTIS (see address given above).

NCEER-87-0013 "Frequency Response of Secondary Systems Under Seismic Excitation," by J.A. HoLung, J. Cai and Y.K. Lin, 7/31/87, (PB88-134317, A05, MF-A01). This report is only available through NTIS (see address given above).

NCEER-87-0014 "Modelling Earthquake Ground Motions in Seismically Active Regions Using Parametric Time Series Methods," by G.W. Ellis and A.S. Cakmak, 8/25/87, (PB88-134283, A08, MF-A01). This report is only available through NTIS (see address given above).

NCEER-87-0015 "Detection and Assessment of Seismic Structural Damage," by E. DiPasquale and A.S. Cakmak, 8/25/87, (PB88-163712, A05, MF-A01). This report is only available through NTIS (see address given above).

NCEER-87-0016 "Pipeline Experiment at Parkfield, California," by J. Isenberg and E. Richardson, 9/15/87, (PB88-163720, A03, MF-A01). This report is available only through NTIS (see address given above).

NCEER-87-0017 "Digital Simulation of Seismic Ground Motion," by M. Shinozuka, G. Deodatis and T. Harada, 8/31/87, (PB88-155197, A04, MF-A01). This report is available only through NTIS (see address given above).

NCEER-87-0018 "Practical Considerations for Structural Control: System Uncertainty, System Time Delay and Truncation of Small Control Forces," J.N. Yang and A. Akbarpour, 8/10/87, (PB88-163738, A08, MF-A01). This report is only available through NTIS (see address given above).

NCEER-87-0019 "Modal Analysis of Nonclassically Damped Structural Systems Using Canonical Transformation," by J.N. Yang, S. Sarkani and F.X. Long, 9/27/87, (PB88-187851, A04, MF-A01).

NCEER-87-0020 "A Nonstationary Solution in Random Vibration Theory," by J.R. Red-Horse and P.D. Spanos, 11/3/87, (PB88-163746, A03, MF-A01).

NCEER-87-0021 "Horizontal Impedances for Radially Inhomogeneous Viscoelastic Soil Layers," by A.S. Veletsos and K.W. Dotson, 10/15/87, (PB88-150859, A04, MF-A01).

NCEER-87-0022 "Seismic Damage Assessment of Reinforced Concrete Members," by Y.S. Chung, C. Meyer and M. Shinozuka, 10/9/87, (PB88-150867, A05, MF-A01). This report is available only through NTIS (see address given above).

NCEER-87-0023 "Active Structural Control in Civil Engineering," by T.T. Soong, 11/11/87, (PB88-187778, A03, MF-A01).

NCEER-87-0024 "Vertical and Torsional Impedances for Radially Inhomogeneous Viscoelastic Soil Layers," by K.W. Dotson and A.S. Veletsos, 12/87, (PB88-187786, A03, MF-A01).

NCEER-87-0025 "Proceedings from the Symposium on Seismic Hazards, Ground Motions, Soil-Liquefaction and Engineering Practice in Eastern North America," October 20-22, 1987, edited by K.H. Jacob, 12/87, (PB88-188115, A23, MF-A01). This report is available only through NTIS (see address given above).

NCEER-87-0026 "Report on the Whittier-Narrows, California, Earthquake of October 1, 1987," by J. Pantelic and A. Reinhorn, 11/87, (PB88-187752, A03, MF-A01). This report is available only through NTIS (see address given above).

NCEER-87-0027 "Design of a Modular Program for Transient Nonlinear Analysis of Large 3-D Building Structures," by S. Srivastav and J.F. Abel, 12/30/87, (PB88-187950, A05, MF-A01). This report is only available through NTIS (see address given above).

NCEER-87-0028 "Second-Year Program in Research, Education and Technology Transfer," 3/8/88, (PB88-219480, A04, MF-A01).

NCEER-88-0001 "Workshop on Seismic Computer Analysis and Design of Buildings With Interactive Graphics," by W. McGuire, J.F. Abel and C.H. Conley, 1/18/88, (PB88-187760, A03, MF-A01). This report is only available through NTIS (see address given above).

NCEER-88-0002 "Optimal Control of Nonlinear Flexible Structures," by J.N. Yang, F.X. Long and D. Wong, 1/22/88, (PB88-213772, A06, MF-A01).

NCEER-88-0003 "Substructuring Techniques in the Time Domain for Primary-Secondary Structural Systems," by G.D. Manolis and G. Juhn, 2/10/88, (PB88-213780, A04, MF-A01).

NCEER-88-0004 "Iterative Seismic Analysis of Primary-Secondary Systems," by A. Singhal, L.D. Lutes and P.D. Spanos, 2/23/88, (PB88-213798, A04, MF-A01).

NCEER-88-0005 "Stochastic Finite Element Expansion for Random Media," by P.D. Spanos and R. Ghanem, 3/14/88, (PB88-213806, A03, MF-A01).

NCEER-88-0006 "Combining Structural Optimization and Structural Control," by F.Y. Cheng and C.P. Pantelides, 1/10/88, (PB88-213814, A05, MF-A01).

NCEER-88-0007 "Seismic Performance Assessment of Code-Designed Structures," by H.H-M. Hwang, J-W. Jaw and H-J. Shau, 3/20/88, (PB88-219423, A04, MF-A01). This report is only available through NTIS (see address given above).

NCEER-88-0008 "Reliability Analysis of Code-Designed Structures Under Natural Hazards," by H.H-M. Hwang, H. Ushiba and M. Shinozuka, 2/29/88, (PB88-229471, A07, MF-A01). This report is only available through NTIS (see address given above).

NCEER-88-0009 "Seismic Fragility Analysis of Shear Wall Structures," by J-W Jaw and H.H-M. Hwang, 4/30/88, (PB89-102867, A04, MF-A01).

NCEER-88-0010 "Base Isolation of a Multi-Story Building Under a Harmonic Ground Motion - A Comparison of Performances of Various Systems," by F-G Fan, G. Ahmadi and I.G. Tadjbakhsh, 5/18/88, (PB89-122238, A06, MF-A01). This report is only available through NTIS (see address given above).

NCEER-88-0011 "Seismic Floor Response Spectra for a Combined System by Green's Functions," by F.M. Lavelle, L.A. Bergman and P.D. Spanos, 5/1/88, (PB89-102875, A03, MF-A01).

NCEER-88-0012 "A New Solution Technique for Randomly Excited Hysteretic Structures," by G.Q. Cai and Y.K. Lin, 5/16/88, (PB89-102883, A03, MF-A01).

NCEER-88-0013 "A Study of Radiation Damping and Soil-Structure Interaction Effects in the Centrifuge," by K. Weissman, supervised by J.H. Prevost, 5/24/88, (PB89-144703, A06, MF-A01).

NCEER-88-0014 "Parameter Identification and Implementation of a Kinematic Plasticity Model for Frictional Soils," by J.H. Prevost and D.V. Griffiths, not available.

NCEER-88-0015 "Two- and Three- Dimensional Dynamic Finite Element Analyses of the Long Valley Dam," by D.V. Griffiths and J.H. Prevost, 6/17/88, (PB89-144711, A04, MF-A01).

NCEER-88-0016 "Damage Assessment of Reinforced Concrete Structures in Eastern United States," by A.M. Reinhorn, M.J. Seidel, S.K. Kunnath and Y.J. Park, 6/15/88, (PB89-122220, A04, MF-A01). This report is only available through NTIS (see address given above).

NCEER-88-0017 "Dynamic Compliance of Vertically Loaded Strip Foundations in Multilayered Viscoelastic Soils," by S. Ahmad and A.S.M. Israil, 6/17/88, (PB89-102891, A04, MF-A01).

NCEER-88-0018 "An Experimental Study of Seismic Structural Response With Added Viscoelastic Dampers," by R.C. Lin, Z. Liang, T.T. Soong and R.H. Zhang, 6/30/88, (PB89-122212, A05, MF-A01). This report is available only through NTIS (see address given above).

NCEER-88-0019 "Experimental Investigation of Primary - Secondary System Interaction," by G.D. Manolis, G. Juhn and A.M. Reinhorn, 5/27/88, (PB89-122204, A04, MF-A01).

NCEER-88-0020 "A Response Spectrum Approach For Analysis of Nonclassically Damped Structures," by J.N. Yang, S. Sarkani and F.X. Long, 4/22/88, (PB89-102909, A04, MF-A01).

NCEER-88-0021 "Seismic Interaction of Structures and Soils: Stochastic Approach," by A.S. Veletsos and A.M. Prasad, 7/21/88, (PB89-122196, A04, MF-A01). This report is only available through NTIS (see address given above).

NCEER-88-0022 "Identification of the Serviceability Limit State and Detection of Seismic Structural Damage," by E. DiPasquale and A.S. Cakmak, 6/15/88, (PB89-122188, A05, MF-A01). This report is available only through NTIS (see address given above).

NCEER-88-0023 "Multi-Hazard Risk Analysis: Case of a Simple Offshore Structure," by B.K. Bhartia and E.H. Vanmarcke, 7/21/88, (PB89-145213, A05, MF-A01).

NCEER-88-0024 "Automated Seismic Design of Reinforced Concrete Buildings," by Y.S. Chung, C. Meyer and M. Shinozuka, 7/5/88, (PB89-122170, A06, MF-A01). This report is available only through NTIS (see address given above).

NCEER-88-0025 "Experimental Study of Active Control of MDOF Structures Under Seismic Excitations," by L.L. Chung, R.C. Lin, T.T. Soong and A.M. Reinhorn, 7/10/88, (PB89-122600, A04, MF-A01).

NCEER-88-0026 "Earthquake Simulation Tests of a Low-Rise Metal Structure," by J.S. Hwang, K.C. Chang, G.C. Lee and R.L. Ketter, 8/1/88, (PB89-102917, A04, MF-A01).

NCEER-88-0027 "Systems Study of Urban Response and Reconstruction Due to Catastrophic Earthquakes," by F. Kozin and H.K. Zhou, 9/22/88, (PB90-162348, A04, MF-A01).

NCEER-88-0028 "Seismic Fragility Analysis of Plane Frame Structures," by H.H-M. Hwang and Y.K. Low, 7/31/88, (PB89-131445, A06, MF-A01).

NCEER-88-0029 "Response Analysis of Stochastic Structures," by A. Kardara, C. Bucher and M. Shinozuka, 9/22/88, (PB89-174429, A04, MF-A01).

NCEER-88-0030 "Nonnormal Accelerations Due to Yielding in a Primary Structure," by D.C.K. Chen and L.D. Lutes, 9/19/88, (PB89-131437, A04, MF-A01).

NCEER-88-0031 "Design Approaches for Soil-Structure Interaction," by A.S. Veletsos, A.M. Prasad and Y. Tang, 12/30/88, (PB89-174437, A03, MF-A01). This report is available only through NTIS (see address given above).

NCEER-88-0032 "A Re-evaluation of Design Spectra for Seismic Damage Control," by C.J. Turkstra and A.G. Tallin, 11/7/88, (PB89-145221, A05, MF-A01).

NCEER-88-0033 "The Behavior and Design of Noncontact Lap Splices Subjected to Repeated Inelastic Tensile Loading," by V.E. Sagan, P. Gergely and R.N. White, 12/8/88, (PB89-163737, A08, MF-A01).

NCEER-88-0034 "Seismic Response of Pile Foundations," by S.M. Mamoon, P.K. Banerjee and S. Ahmad, 11/1/88, (PB89-145239, A04, MF-A01).

NCEER-88-0035 "Modeling of R/C Building Structures With Flexible Floor Diaphragms (IDARC2)," by A.M. Reinhorn, S.K. Kunnath and N. Panahshahi, 9/7/88, (PB89-207153, A07, MF-A01).

NCEER-88-0036 "Solution of the Dam-Reservoir Interaction Problem Using a Combination of FEM, BEM with Particular Integrals, Modal Analysis, and Substructuring," by C-S. Tsai, G.C. Lee and R.L. Ketter, 12/31/88, (PB89-207146, A04, MF-A01).

NCEER-88-0037 "Optimal Placement of Actuators for Structural Control," by F.Y. Cheng and C.P. Pantelides, 8/15/88, (PB89-162846, A05, MF-A01).

NCEER-88-0038 "Teflon Bearings in Aseismic Base Isolation: Experimental Studies and Mathematical Modeling," by A. Mokha, M.C. Constantinou and A.M. Reinhorn, 12/5/88, (PB89-218457, A10, MF-A01). This report is available only through NTIS (see address given above).

NCEER-88-0039 "Seismic Behavior of Flat Slab High-Rise Buildings in the New York City Area," by P. Weidlinger and M. Ettouney, 10/15/88, (PB90-145681, A04, MF-A01).

NCEER-88-0040 "Evaluation of the Earthquake Resistance of Existing Buildings in New York City," by P. Weidlinger and M. Ettouney, 10/15/88, not available.

NCEER-88-0041 "Small-Scale Modeling Techniques for Reinforced Concrete Structures Subjected to Seismic Loads," by W. Kim, A. El-Attar and R.N. White, 11/22/88, (PB89-189625, A05, MF-A01).

NCEER-88-0042 "Modeling Strong Ground Motion from Multiple Event Earthquakes," by G.W. Ellis and A.S. Cakmak, 10/15/88, (PB89-174445, A03, MF-A01).

NCEER-88-0043 "Nonstationary Models of Seismic Ground Acceleration," by M. Grigoriu, S.E. Ruiz and E. Rosenblueth, 7/15/88, (PB89-189617, A04, MF-A01).

NCEER-88-0044 "SARCF User's Guide: Seismic Analysis of Reinforced Concrete Frames," by Y.S. Chung, C. Meyer and M. Shinozuka, 11/9/88, (PB89-174452, A08, MF-A01).

NCEER-88-0045 "First Expert Panel Meeting on Disaster Research and Planning," edited by J. Pantelic and J. Stoyle, 9/15/88, (PB89-174460, A05, MF-A01).

NCEER-88-0046 "Preliminary Studies of the Effect of Degrading Infill Walls on the Nonlinear Seismic Response of Steel Frames," by C.Z. Chrysostomou, P. Gergely and J.F. Abel, 12/19/88, (PB89-208383, A05, MF-A01).

NCEER-88-0047 "Reinforced Concrete Frame Component Testing Facility - Design, Construction, Instrumentation and Operation," by S.P. Pessiki, C. Conley, T. Bond, P. Gergely and R.N. White, 12/16/88, (PB89-174478, A04, MF-A01).

NCEER-89-0001 "Effects of Protective Cushion and Soil Compliancy on the Response of Equipment Within a Seismically Excited Building," by J.A. HoLung, 2/16/89, (PB89-207179, A04, MF-A01).

NCEER-89-0002 "Statistical Evaluation of Response Modification Factors for Reinforced Concrete Structures," by H.H-M. Hwang and J-W. Jaw, 2/17/89, (PB89-207187, A05, MF-A01).

NCEER-89-0003 "Hysteretic Columns Under Random Excitation," by G-Q. Cai and Y.K. Lin, 1/9/89, (PB89-196513, A03, MF-A01).

NCEER-89-0004 "Experimental Study of `Elephant Foot Bulge' Instability of Thin-Walled Metal Tanks," by Z-H. Jia and R.L. Ketter, 2/22/89, (PB89-207195, A03, MF-A01).

NCEER-89-0005 "Experiment on Performance of Buried Pipelines Across San Andreas Fault," by J. Isenberg, E. Richardson and T.D. O'Rourke, 3/10/89, (PB89-218440, A04, MF-A01). This report is available only through NTIS (see address given above).

NCEER-89-0006 "A Knowledge-Based Approach to Structural Design of Earthquake-Resistant Buildings," by M. Subramani, P. Gergely, C.H. Conley, J.F. Abel and A.H. Zaghw, 1/15/89, (PB89-218465, A06, MF-A01).

NCEER-89-0007 "Liquefaction Hazards and Their Effects on Buried Pipelines," by T.D. O'Rourke and P.A. Lane, 2/1/89, (PB89-218481, A09, MF-A01).

NCEER-89-0008 "Fundamentals of System Identification in Structural Dynamics," by H. Imai, C-B. Yun, O. Maruyama and M. Shinozuka, 1/26/89, (PB89-207211, A04, MF-A01).

NCEER-89-0009 "Effects of the 1985 Michoacan Earthquake on Water Systems and Other Buried Lifelines in Mexico," by A.G. Ayala and M.J. O'Rourke, 3/8/89, (PB89-207229, A06, MF-A01).

NCEER-89-R010 "NCEER Bibliography of Earthquake Education Materials," by K.E.K. Ross, Second Revision, 9/1/89, (PB90-125352, A05, MF-A01). This report is replaced by NCEER-92-0018.

NCEER-89-0011 "Inelastic Three-Dimensional Response Analysis of Reinforced Concrete Building Structures (IDARC-3D), Part I - Modeling," by S.K. Kunnath and A.M. Reinhorn, 4/17/89, (PB90-114612, A07, MF-A01). This report is available only through NTIS (see address given above).

NCEER-89-0012 "Recommended Modifications to ATC-14," by C.D. Poland and J.O. Malley, 4/12/89, (PB90-108648, A15, MF-A01).

NCEER-89-0013 "Repair and Strengthening of Beam-to-Column Connections Subjected to Earthquake Loading," by M. Corazao and A.J. Durrani, 2/28/89, (PB90-109885, A06, MF-A01).

NCEER-89-0014 "Program EXKAL2 for Identification of Structural Dynamic Systems," by O. Maruyama, C-B. Yun, M. Hoshiya and M. Shinozuka, 5/19/89, (PB90-109877, A09, MF-A01).

NCEER-89-0015 "Response of Frames With Bolted Semi-Rigid Connections, Part I - Experimental Study and Analytical Predictions," by P.J. DiCorso, A.M. Reinhorn, J.R. Dickerson, J.B. Radziminski and W.L. Harper, 6/1/89, not available.

NCEER-89-0016 "ARMA Monte Carlo Simulation in Probabilistic Structural Analysis," by P.D. Spanos and M.P. Mignolet, 7/10/89, (PB90-109893, A03, MF-A01).

NCEER-89-P017 "Preliminary Proceedings from the Conference on Disaster Preparedness - The Place of Earthquake Education in Our Schools," Edited by K.E.K. Ross, 6/23/89, (PB90-108606, A03, MF-A01).

NCEER-89-0017 "Proceedings from the Conference on Disaster Preparedness - The Place of Earthquake Education in Our Schools," Edited by K.E.K. Ross, 12/31/89, (PB90-207895, A012, MF-A02). This report is available only through NTIS (see address given above).

NCEER-89-0018 "Multidimensional Models of Hysteretic Material Behavior for Vibration Analysis of Shape Memory Energy Absorbing Devices, by E.J. Graesser and F.A. Cozzarelli, 6/7/89, (PB90-164146, A04, MF-A01).

NCEER-89-0019 "Nonlinear Dynamic Analysis of Three-Dimensional Base Isolated Structures (3D-BASIS)," by S. Nagarajaiah, A.M. Reinhorn and M.C. Constantinou, 8/3/89, (PB90-161936, A06, MF-A01). This report has been replaced by NCEER-93-0011.

NCEER-89-0020 "Structural Control Considering Time-Rate of Control Forces and Control Rate Constraints," by F.Y. Cheng and C.P. Pantelides, 8/3/89, (PB90-120445, A04, MF-A01).

NCEER-89-0021 "Subsurface Conditions of Memphis and Shelby County," by K.W. Ng, T-S. Chang and H-H.M. Hwang, 7/26/89, (PB90-120437, A03, MF-A01).

NCEER-89-0022 "Seismic Wave Propagation Effects on Straight Jointed Buried Pipelines," by K. Elhmadi and M.J. O'Rourke, 8/24/89, (PB90-162322, A10, MF-A02).

NCEER-89-0023 "Workshop on Serviceability Analysis of Water Delivery Systems," edited by M. Grigoriu, 3/6/89, (PB90-127424, A03, MF-A01).

NCEER-89-0024 "Shaking Table Study of a 1/5 Scale Steel Frame Composed of Tapered Members," by K.C. Chang, J.S. Hwang and G.C. Lee, 9/18/89, (PB90-160169, A04, MF-A01).

NCEER-89-0025 "DYNA1D: A Computer Program for Nonlinear Seismic Site Response Analysis - Technical Documentation," by Jean H. Prevost, 9/14/89, (PB90-161944, A07, MF-A01). This report is available only through NTIS (see address given above).

NCEER-89-0026 "1:4 Scale Model Studies of Active Tendon Systems and Active Mass Dampers for Aseismic Protection," by A.M. Reinhorn, T.T. Soong, R.C. Lin, Y.P. Yang, Y. Fukao, H. Abe and M. Nakai, 9/15/89, (PB90-173246, A10, MF-A02). This report is available only through NTIS (see address given above).

NCEER-89-0027 "Scattering of Waves by Inclusions in a Nonhomogeneous Elastic Half Space Solved by Boundary Element Methods," by P.K. Hadley, A. Askar and A.S. Cakmak, 6/15/89, (PB90-145699, A07, MF-A01).

NCEER-89-0028 "Statistical Evaluation of Deflection Amplification Factors for Reinforced Concrete Structures," by H.H.M. Hwang, J-W. Jaw and A.L. Ch'ng, 8/31/89, (PB90-164633, A05, MF-A01).

NCEER-89-0029 "Bedrock Accelerations in Memphis Area Due to Large New Madrid Earthquakes," by H.H.M. Hwang, C.H.S. Chen and G. Yu, 11/7/89, (PB90-162330, A04, MF-A01).

NCEER-89-0030 "Seismic Behavior and Response Sensitivity of Secondary Structural Systems," by Y.Q. Chen and T.T. Soong, 10/23/89, (PB90-164658, A08, MF-A01).

NCEER-89-0031 "Random Vibration and Reliability Analysis of Primary-Secondary Structural Systems," by Y. Ibrahim, M. Grigoriu and T.T. Soong, 11/10/89, (PB90-161951, A04, MF-A01).

NCEER-89-0032 "Proceedings from the Second U.S. - Japan Workshop on Liquefaction, Large Ground Deformation and Their Effects on Lifelines, September 26-29, 1989," Edited by T.D. O'Rourke and M. Hamada, 12/1/89, (PB90-209388, A22, MF-A03).

NCEER-89-0033 "Deterministic Model for Seismic Damage Evaluation of Reinforced Concrete Structures," by J.M. Bracci, A.M. Reinhorn, J.B. Mander and S.K. Kunnath, 9/27/89, (PB91-108803, A06, MF-A01).

NCEER-89-0034 "On the Relation Between Local and Global Damage Indices," by E. DiPasquale and A.S. Cakmak, 8/15/89, (PB90-173865, A05, MF-A01).

NCEER-89-0035 "Cyclic Undrained Behavior of Nonplastic and Low Plasticity Silts," by A.J. Walker and H.E. Stewart, 7/26/89, (PB90-183518, A10, MF-A01).

NCEER-89-0036 "Liquefaction Potential of Surficial Deposits in the City of Buffalo, New York," by M. Budhu, R. Giese and L. Baumgrass, 1/17/89, (PB90-208455, A04, MF-A01).

NCEER-89-0037 "A Deterministic Assessment of Effects of Ground Motion Incoherence," by A.S. Veletsos and Y. Tang, 7/15/89, (PB90-164294, A03, MF-A01).

NCEER-89-0038 "Workshop on Ground Motion Parameters for Seismic Hazard Mapping," July 17-18, 1989, edited by R.V. Whitman, 12/1/89, (PB90-173923, A04, MF-A01).

NCEER-89-0039 "Seismic Effects on Elevated Transit Lines of the New York City Transit Authority," by C.J. Costantino, C.A. Miller and E. Heymsfield, 12/26/89, (PB90-207887, A06, MF-A01).

NCEER-89-0040 "Centrifugal Modeling of Dynamic Soil-Structure Interaction," by K. Weissman, Supervised by J.H. Prevost, 5/10/89, (PB90-207879, A07, MF-A01).

NCEER-89-0041 "Linearized Identification of Buildings With Cores for Seismic Vulnerability Assessment," by I-K. Ho and A.E. Aktan, 11/1/89, (PB90-251943, A07, MF-A01).

NCEER-90-0001 "Geotechnical and Lifeline Aspects of the October 17, 1989 Loma Prieta Earthquake in San Francisco," by T.D. O'Rourke, H.E. Stewart, F.T. Blackburn and T.S. Dickerman, 1/90, (PB90-208596, A05, MF-A01).

NCEER-90-0002 "Nonnormal Secondary Response Due to Yielding in a Primary Structure," by D.C.K. Chen and L.D. Lutes, 2/28/90, (PB90-251976, A07, MF-A01).

NCEER-90-0003 "Earthquake Education Materials for Grades K-12," by K.E.K. Ross, 4/16/90, (PB91-251984, A05, MF-A05). This report has been replaced by NCEER-92-0018.

NCEER-90-0004 "Catalog of Strong Motion Stations in Eastern North America," by R.W. Busby, 4/3/90, (PB90-251984, A05, MF-A01).

NCEER-90-0005 "NCEER Strong-Motion Data Base: A User Manual for the GeoBase Release (Version 1.0 for the Sun3)," by P. Friberg and K. Jacob, 3/31/90 (PB90-258062, A04, MF-A01).

NCEER-90-0006 "Seismic Hazard Along a Crude Oil Pipeline in the Event of an 1811-1812 Type New Madrid Earthquake," by H.H.M. Hwang and C-H.S. Chen, 4/16/90, (PB90-258054, A04, MF-A01).

NCEER-90-0007 "Site-Specific Response Spectra for Memphis Sheahan Pumping Station," by H.H.M. Hwang and C.S. Lee, 5/15/90, (PB91-108811, A05, MF-A01).

NCEER-90-0008 "Pilot Study on Seismic Vulnerability of Crude Oil Transmission Systems," by T. Ariman, R. Dobry, M. Grigoriu, F. Kozin, M. O'Rourke, T. O'Rourke and M. Shinozuka, 5/25/90, (PB91-108837, A06, MF-A01).

NCEER-90-0009 "A Program to Generate Site Dependent Time Histories: EQGEN," by G.W. Ellis, M. Srinivasan and A.S. Cakmak, 1/30/90, (PB91-108829, A04, MF-A01).

NCEER-90-0010 "Active Isolation for Seismic Protection of Operating Rooms," by M.E. Talbott, Supervised by M. Shinozuka, 6/8/9, (PB91-110205, A05, MF-A01).

NCEER-90-0011 "Program LINEARID for Identification of Linear Structural Dynamic Systems," by C-B. Yun and M. Shinozuka, 6/25/90, (PB91-110312, A08, MF-A01).

NCEER-90-0012 "Two-Dimensional Two-Phase Elasto-Plastic Seismic Response of Earth Dams," by A.N. Yiagos, Supervised by J.H. Prevost, 6/20/90, (PB91-110197, A13, MF-A02).

NCEER-90-0013 "Secondary Systems in Base-Isolated Structures: Experimental Investigation, Stochastic Response and Stochastic Sensitivity," by G.D. Manolis, G. Juhn, M.C. Constantinou and A.M. Reinhorn, 7/1/90, (PB91-110320, A08, MF-A01).

NCEER-90-0014 "Seismic Behavior of Lightly-Reinforced Concrete Column and Beam-Column Joint Details," by S.P. Pessiki, C.H. Conley, P. Gergely and R.N. White, 8/22/90, (PB91-108795, A11, MF-A02).

NCEER-90-0015 "Two Hybrid Control Systems for Building Structures Under Strong Earthquakes," by J.N. Yang and A. Danielians, 6/29/90, (PB91-125393, A04, MF-A01).

NCEER-90-0016 "Instantaneous Optimal Control with Acceleration and Velocity Feedback," by J.N. Yang and Z. Li, 6/29/90, (PB91-125401, A03, MF-A01).

NCEER-90-0017 "Reconnaissance Report on the Northern Iran Earthquake of June 21, 1990," by M. Mehrain, 10/4/90, (PB91-125377, A03, MF-A01).

NCEER-90-0018 "Evaluation of Liquefaction Potential in Memphis and Shelby County," by T.S. Chang, P.S. Tang, C.S. Lee and H. Hwang, 8/10/90, (PB91-125427, A09, MF-A01).

NCEER-90-0019 "Experimental and Analytical Study of a Combined Sliding Disc Bearing and Helical Steel Spring Isolation System," by M.C. Constantinou, A.S. Mokha and A.M. Reinhorn, 10/4/90, (PB91-125385, A06, MF-A01). This report is available only through NTIS (see address given above).

NCEER-90-0020 "Experimental Study and Analytical Prediction of Earthquake Response of a Sliding Isolation System with a Spherical Surface," by A.S. Mokha, M.C. Constantinou and A.M. Reinhorn, 10/11/90, (PB91-125419, A05, MF-A01).

NCEER-90-0021 "Dynamic Interaction Factors for Floating Pile Groups," by G. Gazetas, K. Fan, A. Kaynia and E. Kausel, 9/10/90, (PB91-170381, A05, MF-A01).

NCEER-90-0022 "Evaluation of Seismic Damage Indices for Reinforced Concrete Structures," by S. Rodriguez-Gomez and A.S. Cakmak, 9/30/90, PB91-171322, A06, MF-A01).

NCEER-90-0023 "Study of Site Response at a Selected Memphis Site," by H. Desai, S. Ahmad, E.S. Gazetas and M.R. Oh, 10/11/90, (PB91-196857, A03, MF-A01).

NCEER-90-0024 "A User's Guide to Strongmo: Version 1.0 of NCEER's Strong-Motion Data Access Tool for PCs and Terminals," by P.A. Friberg and C.A.T. Susch, 11/15/90, (PB91-171272, A03, MF-A01).

NCEER-90-0025 "A Three-Dimensional Analytical Study of Spatial Variability of Seismic Ground Motions," by L-L. Hong and A.H.-S. Ang, 10/30/90, (PB91-170399, A09, MF-A01).

NCEER-90-0026 "MUMOID User's Guide - A Program for the Identification of Modal Parameters," by S. Rodriguez-Gomez and E. DiPasquale, 9/30/90, (PB91-171298, A04, MF-A01).

NCEER-90-0027 "SARCF-II User's Guide - Seismic Analysis of Reinforced Concrete Frames," by S. Rodriguez-Gomez, Y.S. Chung and C. Meyer, 9/30/90, (PB91-171280, A05, MF-A01).

NCEER-90-0028 "Viscous Dampers: Testing, Modeling and Application in Vibration and Seismic Isolation," by N. Makris and M.C. Constantinou, 12/20/90 (PB91-190561, A06, MF-A01).

NCEER-90-0029 "Soil Effects on Earthquake Ground Motions in the Memphis Area," by H. Hwang, C.S. Lee, K.W. Ng and T.S. Chang, 8/2/90, (PB91-190751, A05, MF-A01).

NCEER-91-0001 "Proceedings from the Third Japan-U.S. Workshop on Earthquake Resistant Design of Lifeline Facilities and Countermeasures for Soil Liquefaction, December 17-19, 1990," edited by T.D. O'Rourke and M. Hamada, 2/1/91, (PB91-179259, A99, MF-A04).

NCEER-91-0002 "Physical Space Solutions of Non-Proportionally Damped Systems," by M. Tong, Z. Liang and G.C. Lee, 1/15/91, (PB91-179242, A04, MF-A01).

NCEER-91-0003 "Seismic Response of Single Piles and Pile Groups," by K. Fan and G. Gazetas, 1/10/91, (PB92-174994, A04, MF-A01).

NCEER-91-0004 "Damping of Structures: Part 1 - Theory of Complex Damping," by Z. Liang and G. Lee, 10/10/91, (PB92-197235, A12, MF-A03).

NCEER-91-0005 "3D-BASIS - Nonlinear Dynamic Analysis of Three Dimensional Base Isolated Structures: Part II," by S. Nagarajaiah, A.M. Reinhorn and M.C. Constantinou, 2/28/91, (PB91-190553, A07, MF-A01). This report has been replaced by NCEER-93-0011.

NCEER-91-0006 "A Multidimensional Hysteretic Model for Plasticity Deforming Metals in Energy Absorbing Devices," by E.J. Graesser and F.A. Cozzarelli, 4/9/91, (PB92-108364, A04, MF-A01).

NCEER-91-0007 "A Framework for Customizable Knowledge-Based Expert Systems with an Application to a KBES for Evaluating the Seismic Resistance of Existing Buildings," by E.G. Ibarra-Anaya and S.J. Fenves, 4/9/91, (PB91-210930, A08, MF-A01).

NCEER-91-0008 "Nonlinear Analysis of Steel Frames with Semi-Rigid Connections Using the Capacity Spectrum Method," by G.G. Deierlein, S-H. Hsieh, Y-J. Shen and J.F. Abel, 7/2/91, (PB92-113828, A05, MF-A01).

NCEER-91-0009 "Earthquake Education Materials for Grades K-12," by K.E.K. Ross, 4/30/91, (PB91-212142, A06, MF-A01). This report has been replaced by NCEER-92-0018.

NCEER-91-0010 "Phase Wave Velocities and Displacement Phase Differences in a Harmonically Oscillating Pile," by N. Makris and G. Gazetas, 7/8/91, (PB92-108356, A04, MF-A01).

NCEER-91-0011 "Dynamic Characteristics of a Full-Size Five-Story Steel Structure and a 2/5 Scale Model," by K.C. Chang, G.C. Yao, G.C. Lee, D.S. Hao and Y.C. Yeh," 7/2/91, (PB93-116648, A06, MF-A02).

NCEER-91-0012 "Seismic Response of a 2/5 Scale Steel Structure with Added Viscoelastic Dampers," by K.C. Chang, T.T. Soong, S-T. Oh and M.L. Lai, 5/17/91, (PB92-110816, A05, MF-A01).

NCEER-91-0013 "Earthquake Response of Retaining Walls; Full-Scale Testing and Computational Modeling," by S. Alampalli and A-W.M. Elgamal, 6/20/91, not available.

NCEER-91-0014 "3D-BASIS-M: Nonlinear Dynamic Analysis of Multiple Building Base Isolated Structures," by P.C. Tsopelas, S. Nagarajaiah, M.C. Constantinou and A.M. Reinhorn, 5/28/91, (PB92-113885, A09, MF-A02).

NCEER-91-0015 "Evaluation of SEAOC Design Requirements for Sliding Isolated Structures," by D. Theodossiou and M.C. Constantinou, 6/10/91, (PB92-114602, A11, MF-A03).

NCEER-91-0016 "Closed-Loop Modal Testing of a 27-Story Reinforced Concrete Flat Plate-Core Building," by H.R. Somaprasad, T. Toksoy, H. Yoshiyuki and A.E. Aktan, 7/15/91, (PB92-129980, A07, MF-A02).

NCEER-91-0017 "Shake Table Test of a 1/6 Scale Two-Story Lightly Reinforced Concrete Building," by A.G. El-Attar, R.N. White and P. Gergely, 2/28/91, (PB92-222447, A06, MF-A02).

NCEER-91-0018 "Shake Table Test of a 1/8 Scale Three-Story Lightly Reinforced Concrete Building," by A.G. El-Attar, R.N. White and P. Gergely, 2/28/91, (PB93-116630, A08, MF-A02).

NCEER-91-0019 "Transfer Functions for Rigid Rectangular Foundations," by A.S. Veletsos, A.M. Prasad and W.H. Wu, 7/31/91, not available.

NCEER-91-0020 "Hybrid Control of Seismic-Excited Nonlinear and Inelastic Structural Systems," by J.N. Yang, Z. Li and A. Danielians, 8/1/91, (PB92-143171, A06, MF-A02).

NCEER-91-0021 "The NCEER-91 Earthquake Catalog: Improved Intensity-Based Magnitudes and Recurrence Relations for U.S. Earthquakes East of New Madrid," by L. Seeber and J.G. Armbruster, 8/28/91, (PB92-176742, A06, MF-A02).

NCEER-91-0022 "Proceedings from the Implementation of Earthquake Planning and Education in Schools: The Need for Change - The Roles of the Changemakers," by K.E.K. Ross and F. Winslow, 7/23/91, (PB92-129998, A12, MF-A03).

NCEER-91-0023 "A Study of Reliability-Based Criteria for Seismic Design of Reinforced Concrete Frame Buildings," by H.H.M. Hwang and H-M. Hsu, 8/10/91, (PB92-140235, A09, MF-A02).

NCEER-91-0024 "Experimental Verification of a Number of Structural System Identification Algorithms," by R.G. Ghanem, H. Gavin and M. Shinozuka, 9/18/91, (PB92-176577, A18, MF-A04).

NCEER-91-0025 "Probabilistic Evaluation of Liquefaction Potential," by H.H.M. Hwang and C.S. Lee," 11/25/91, (PB92-143429, A05, MF-A01).

NCEER-91-0026 "Instantaneous Optimal Control for Linear, Nonlinear and Hysteretic Structures - Stable Controllers," by J.N. Yang and Z. Li, 11/15/91, (PB92-163807, A04, MF-A01).

NCEER-91-0027 "Experimental and Theoretical Study of a Sliding Isolation System for Bridges," by M.C. Constantinou, A. Kartoum, A.M. Reinhorn and P. Bradford, 11/15/91, (PB92-176973, A10, MF-A03).

NCEER-92-0001 "Case Studies of Liquefaction and Lifeline Performance During Past Earthquakes, Volume 1: Japanese Case Studies," Edited by M. Hamada and T. O'Rourke, 2/17/92, (PB92-197243, A18, MF-A04).

NCEER-92-0002 "Case Studies of Liquefaction and Lifeline Performance During Past Earthquakes, Volume 2: United States Case Studies," Edited by T. O'Rourke and M. Hamada, 2/17/92, (PB92-197250, A20, MF-A04).

NCEER-92-0003 "Issues in Earthquake Education," Edited by K. Ross, 2/3/92, (PB92-222389, A07, MF-A02).

NCEER-92-0004 "Proceedings from the First U.S. - Japan Workshop on Earthquake Protective Systems for Bridges," Edited by I.G. Buckle, 2/4/92, (PB94-142239, A99, MF-A06).

NCEER-92-0005 "Seismic Ground Motion from a Haskell-Type Source in a Multiple-Layered Half-Space," A.P. Theoharis, G. Deodatis and M. Shinozuka, 1/2/92, not available.

NCEER-92-0006 "Proceedings from the Site Effects Workshop," Edited by R. Whitman, 2/29/92, (PB92-197201, A04, MF-A01).

NCEER-92-0007 "Engineering Evaluation of Permanent Ground Deformations Due to Seismically-Induced Liquefaction," by M.H. Baziar, R. Dobry and A-W.M. Elgamal, 3/24/92, (PB92-222421, A13, MF-A03).

NCEER-92-0008 "A Procedure for the Seismic Evaluation of Buildings in the Central and Eastern United States," by C.D. Poland and J.O. Malley, 4/2/92, (PB92-222439, A20, MF-A04).

NCEER-92-0009 "Experimental and Analytical Study of a Hybrid Isolation System Using Friction Controllable Sliding Bearings," by M.Q. Feng, S. Fujii and M. Shinozuka, 5/15/92, (PB93-150282, A06, MF-A02).

NCEER-92-0010 "Seismic Resistance of Slab-Column Connections in Existing Non-Ductile Flat-Plate Buildings," by A.J. Durrani and Y. Du, 5/18/92, (PB93-116812, A06, MF-A02).

NCEER-92-0011 "The Hysteretic and Dynamic Behavior of Brick Masonry Walls Upgraded by Ferrocement Coatings Under Cyclic Loading and Strong Simulated Ground Motion," by H. Lee and S.P. Prawel, 5/11/92, not available.

NCEER-92-0012 "Study of Wire Rope Systems for Seismic Protection of Equipment in Buildings," by G.F. Demetriades, M.C. Constantinou and A.M. Reinhorn, 5/20/92, (PB93-116655, A08, MF-A02).

NCEER-92-0013 "Shape Memory Structural Dampers: Material Properties, Design and Seismic Testing," by P.R. Witting and F.A. Cozzarelli, 5/26/92, (PB93-116663, A05, MF-A01).

NCEER-92-0014 "Longitudinal Permanent Ground Deformation Effects on Buried Continuous Pipelines," by M.J. O'Rourke, and C. Nordberg, 6/15/92, (PB93-116671, A08, MF-A02).

NCEER-92-0015 "A Simulation Method for Stationary Gaussian Random Functions Based on the Sampling Theorem," by M. Grigoriu and S. Balopoulou, 6/11/92, (PB93-127496, A05, MF-A01).

NCEER-92-0016 "Gravity-Load-Designed Reinforced Concrete Buildings: Seismic Evaluation of Existing Construction and Detailing Strategies for Improved Seismic Resistance," by G.W. Hoffmann, S.K. Kunnath, A.M. Reinhorn and J.B. Mander, 7/15/92, (PB94-142007, A08, MF-A02).

NCEER-92-0017 "Observations on Water System and Pipeline Performance in the Limón Area of Costa Rica Due to the April 22, 1991 Earthquake," by M. O'Rourke and D. Ballantyne, 6/30/92, (PB93-126811, A06, MF-A02).

NCEER-92-0018 "Fourth Edition of Earthquake Education Materials for Grades K-12," Edited by K.E.K. Ross, 8/10/92, (PB93-114023, A07, MF-A02).

NCEER-92-0019 "Proceedings from the Fourth Japan-U.S. Workshop on Earthquake Resistant Design of Lifeline Facilities and Countermeasures for Soil Liquefaction," Edited by M. Hamada and T.D. O'Rourke, 8/12/92, (PB93-163939, A99, MF-E11).

NCEER-92-0020 "Active Bracing System: A Full Scale Implementation of Active Control," by A.M. Reinhorn, T.T. Soong, R.C. Lin, M.A. Riley, Y.P. Wang, S. Aizawa and M. Higashino, 8/14/92, (PB93-127512, A06, MF-A02).

NCEER-92-0021 "Empirical Analysis of Horizontal Ground Displacement Generated by Liquefaction-Induced Lateral Spreads," by S.F. Bartlett and T.L. Youd, 8/17/92, (PB93-188241, A06, MF-A02).

NCEER-92-0022 "IDARC Version 3.0: Inelastic Damage Analysis of Reinforced Concrete Structures," by S.K. Kunnath, A.M. Reinhorn and R.F. Lobo, 8/31/92, (PB93-227502, A07, MF-A02).

NCEER-92-0023 "A Semi-Empirical Analysis of Strong-Motion Peaks in Terms of Seismic Source, Propagation Path and Local Site Conditions, by M. Kamiyama, M.J. O'Rourke and R. Flores-Berrones, 9/9/92, (PB93-150266, A08, MF-A02).

NCEER-92-0024 "Seismic Behavior of Reinforced Concrete Frame Structures with Nonductile Details, Part I: Summary of Experimental Findings of Full Scale Beam-Column Joint Tests," by A. Beres, R.N. White and P. Gergely, 9/30/92, (PB93-227783, A05, MF-A01).

NCEER-92-0025 "Experimental Results of Repaired and Retrofitted Beam-Column Joint Tests in Lightly Reinforced Concrete Frame Buildings," by A. Beres, S. El-Borgi, R.N. White and P. Gergely, 10/29/92, (PB93-227791, A05, MF-A01).

NCEER-92-0026 "A Generalization of Optimal Control Theory: Linear and Nonlinear Structures," by J.N. Yang, Z. Li and S. Vongchavalitkul, 11/2/92, (PB93-188621, A05, MF-A01).

NCEER-92-0027 "Seismic Resistance of Reinforced Concrete Frame Structures Designed Only for Gravity Loads: Part I - Design and Properties of a One-Third Scale Model Structure," by J.M. Bracci, A.M. Reinhorn and J.B. Mander, 12/1/92, (PB94-104502, A08, MF-A02).

NCEER-92-0028 "Seismic Resistance of Reinforced Concrete Frame Structures Designed Only for Gravity Loads: Part II - Experimental Performance of Subassemblages," by L.E. Aycardi, J.B. Mander and A.M. Reinhorn, 12/1/92, (PB94-104510, A08, MF-A02).

NCEER-92-0029 "Seismic Resistance of Reinforced Concrete Frame Structures Designed Only for Gravity Loads: Part III - Experimental Performance and Analytical Study of a Structural Model," by J.M. Bracci, A.M. Reinhorn and J.B. Mander, 12/1/92, (PB93-227528, A09, MF-A01).

NCEER-92-0030 "Evaluation of Seismic Retrofit of Reinforced Concrete Frame Structures: Part I - Experimental Performance of Retrofitted Subassemblages," by D. Choudhuri, J.B. Mander and A.M. Reinhorn, 12/8/92, (PB93-198307, A07, MF-A02).

NCEER-92-0031 "Evaluation of Seismic Retrofit of Reinforced Concrete Frame Structures: Part II - Experimental Performance and Analytical Study of a Retrofitted Structural Model," by J.M. Bracci, A.M. Reinhorn and J.B. Mander, 12/8/92, (PB93-198315, A09, MF-A03).

NCEER-92-0032 "Experimental and Analytical Investigation of Seismic Response of Structures with Supplemental Fluid Viscous Dampers," by M.C. Constantinou and M.D. Symans, 12/21/92, (PB93-191435, A10, MF-A03). This report is available only through NTIS (see address given above).

NCEER-92-0033 "Reconnaissance Report on the Cairo, Egypt Earthquake of October 12, 1992," by M. Khater, 12/23/92, (PB93-188621, A03, MF-A01).

NCEER-92-0034 "Low-Level Dynamic Characteristics of Four Tall Flat-Plate Buildings in New York City," by H. Gavin, S. Yuan, J. Grossman, E. Pekelis and K. Jacob, 12/28/92, (PB93-188217, A07, MF-A02).

NCEER-93-0001 "An Experimental Study on the Seismic Performance of Brick-Infilled Steel Frames With and Without Retrofit," by J.B. Mander, B. Nair, K. Wojtkowski and J. Ma, 1/29/93, (PB93-227510, A07, MF-A02).

NCEER-93-0002 "Social Accounting for Disaster Preparedness and Recovery Planning," by S. Cole, E. Pantoja and V. Razak, 2/22/93, (PB94-142114, A12, MF-A03).

NCEER-93-0003 "Assessment of 1991 NEHRP Provisions for Nonstructural Components and Recommended Revisions," by T.T. Soong, G. Chen, Z. Wu, R-H. Zhang and M. Grigoriu, 3/1/93, (PB93-188639, A06, MF-A02).

NCEER-93-0004 "Evaluation of Static and Response Spectrum Analysis Procedures of SEAOC/UBC for Seismic Isolated Structures," by C.W. Winters and M.C. Constantinou, 3/23/93, (PB93-198299, A10, MF-A03).

NCEER-93-0005 "Earthquakes in the Northeast - Are We Ignoring the Hazard? A Workshop on Earthquake Science and Safety for Educators," edited by K.E.K. Ross, 4/2/93, (PB94-103066, A09, MF-A02).

NCEER-93-0006 "Inelastic Response of Reinforced Concrete Structures with Viscoelastic Braces," by R.F. Lobo, J.M. Bracci, K.L. Shen, A.M. Reinhorn and T.T. Soong, 4/5/93, (PB93-227486, A05, MF-A02).

NCEER-93-0007 "Seismic Testing of Installation Methods for Computers and Data Processing Equipment," by K. Kosar, T.T. Soong, K.L. Shen, J.A. HoLung and Y.K. Lin, 4/12/93, (PB93-198299, A07, MF-A02).

NCEER-93-0008 "Retrofit of Reinforced Concrete Frames Using Added Dampers," by A. Reinhorn, M. Constantinou and C. Li, not available.

NCEER-93-0009 "Seismic Behavior and Design Guidelines for Steel Frame Structures with Added Viscoelastic Dampers," by K.C. Chang, M.L. Lai, T.T. Soong, D.S. Hao and Y.C. Yeh, 5/1/93, (PB94-141959, A07, MF-A02).

NCEER-93-0010 "Seismic Performance of Shear-Critical Reinforced Concrete Bridge Piers," by J.B. Mander, S.M. Waheed, M.T.A. Chaudhary and S.S. Chen, 5/12/93, (PB93-227494, A08, MF-A02).

NCEER-93-0011 "3D-BASIS-TABS: Computer Program for Nonlinear Dynamic Analysis of Three Dimensional Base Isolated Structures," by S. Nagarajaiah, C. Li, A.M. Reinhorn and M.C. Constantinou, 8/2/93, (PB94-141819, A09, MF-A02).

NCEER-93-0012 "Effects of Hydrocarbon Spills from an Oil Pipeline Break on Ground Water," by O.J. Helweg and H.H.M. Hwang, 8/3/93, (PB94-141942, A06, MF-A02).

NCEER-93-0013 "Simplified Procedures for Seismic Design of Nonstructural Components and Assessment of Current Code Provisions," by M.P. Singh, L.E. Suarez, E.E. Matheu and G.O. Maldonado, 8/4/93, (PB94-141827, A09, MF-A02).

NCEER-93-0014 "An Energy Approach to Seismic Analysis and Design of Secondary Systems," by G. Chen and T.T. Soong, 8/6/93, (PB94-142767, A11, MF-A03).

NCEER-93-0015 "Proceedings from School Sites: Becoming Prepared for Earthquakes - Commemorating the Third Anniversary of the Loma Prieta Earthquake," Edited by F.E. Winslow and K.E.K. Ross, 8/16/93, (PB94-154275, A16, MF-A02).

NCEER-93-0016 "Reconnaissance Report of Damage to Historic Monuments in Cairo, Egypt Following the October 12, 1992 Dahshur Earthquake," by D. Sykora, D. Look, G. Croci, E. Karaesmen and E. Karaesmen, 8/19/93, (PB94-142221, A08, MF-A02).

NCEER-93-0017 "The Island of Guam Earthquake of August 8, 1993," by S.W. Swan and S.K. Harris, 9/30/93, (PB94-141843, A04, MF-A01).

NCEER-93-0018 "Engineering Aspects of the October 12, 1992 Egyptian Earthquake," by A.W. Elgamal, M. Amer, K. Adalier and A. Abul-Fadl, 10/7/93, (PB94-141983, A05, MF-A01).

NCEER-93-0019 "Development of an Earthquake Motion Simulator and its Application in Dynamic Centrifuge Testing," by I. Krstelj, Supervised by J.H. Prevost, 10/23/93, (PB94-181773, A-10, MF-A03).

NCEER-93-0020 "NCEER-Taisei Corporation Research Program on Sliding Seismic Isolation Systems for Bridges: Experimental and Analytical Study of a Friction Pendulum System (FPS)," by M.C. Constantinou, P. Tsopelas, Y-S. Kim and S. Okamoto, 11/1/93, (PB94-142775, A08, MF-A02).

NCEER-93-0021 "Finite Element Modeling of Elastomeric Seismic Isolation Bearings," by L.J. Billings, Supervised by R. Shepherd, 11/8/93, not available.

NCEER-93-0022 "Seismic Vulnerability of Equipment in Critical Facilities: Life-Safety and Operational Consequences," by K. Porter, G.S. Johnson, M.M. Zadeh, C. Scawthorn and S. Eder, 11/24/93, (PB94-181765, A16, MF-A03).

NCEER-93-0023 "Hokkaido Nansei-oki, Japan Earthquake of July 12, 1993, by P.I. Yanev and C.R. Scawthorn, 12/23/93, (PB94-181500, A07, MF-A01).

NCEER-94-0001 "An Evaluation of Seismic Serviceability of Water Supply Networks with Application to the San Francisco Auxiliary Water Supply System," by I. Markov, Supervised by M. Grigoriu and T. O'Rourke, 1/21/94, (PB94-204013, A07, MF-A02).

NCEER-94-0002 "NCEER-Taisei Corporation Research Program on Sliding Seismic Isolation Systems for Bridges: Experimental and Analytical Study of Systems Consisting of Sliding Bearings, Rubber Restoring Force Devices and Fluid Dampers," Volumes I and II, by P. Tsopelas, S. Okamoto, M.C. Constantinou, D. Ozaki and S. Fujii, 2/4/94, (PB94-181740, A09, MF-A02 and PB94-181757, A12, MF-A03).

NCEER-94-0003 "A Markov Model for Local and Global Damage Indices in Seismic Analysis," by S. Rahman and M. Grigoriu, 2/18/94, (PB94-206000, A12, MF-A03).

NCEER-94-0004 "Proceedings from the NCEER Workshop on Seismic Response of Masonry Infills," edited by D.P. Abrams, 3/1/94, (PB94-180783, A07, MF-A02).

NCEER-94-0005 "The Northridge, California Earthquake of January 17, 1994: General Reconnaissance Report," edited by J.D. Goltz, 3/11/94, (PB94-193943, A10, MF-A03).

NCEER-94-0006 "Seismic Energy Based Fatigue Damage Analysis of Bridge Columns: Part I - Evaluation of Seismic Capacity," by G.A. Chang and J.B. Mander, 3/14/94, (PB94-219185, A11, MF-A03).

NCEER-94-0007 "Seismic Isolation of Multi-Story Frame Structures Using Spherical Sliding Isolation Systems," by T.M. Al-Hussaini, V.A. Zayas and M.C. Constantinou, 3/17/94, (PB94-193745, A09, MF-A02).

NCEER-94-0008 "The Northridge, California Earthquake of January 17, 1994: Performance of Highway Bridges," edited by I.G. Buckle, 3/24/94, (PB94-193851, A06, MF-A02).

NCEER-94-0009 "Proceedings of the Third U.S.-Japan Workshop on Earthquake Protective Systems for Bridges," edited by I.G. Buckle and I. Friedland, 3/31/94, (PB94-195815, A99, MF-A06).

NCEER-94-0010 "3D-BASIS-ME: Computer Program for Nonlinear Dynamic Analysis of Seismically Isolated Single and Multiple Structures and Liquid Storage Tanks," by P.C. Tsopelas, M.C. Constantinou and A.M. Reinhorn, 4/12/94, (PB94-204922, A09, MF-A02).

NCEER-94-0011 "The Northridge, California Earthquake of January 17, 1994: Performance of Gas Transmission Pipelines," by T.D. O'Rourke and M.C. Palmer, 5/16/94, (PB94-204989, A05, MF-A01).

NCEER-94-0012 "Feasibility Study of Replacement Procedures and Earthquake Performance Related to Gas Transmission Pipelines," by T.D. O'Rourke and M.C. Palmer, 5/25/94, (PB94-206638, A09, MF-A02).

NCEER-94-0013 "Seismic Energy Based Fatigue Damage Analysis of Bridge Columns: Part II - Evaluation of Seismic Demand," by G.A. Chang and J.B. Mander, 6/1/94, (PB95-18106, A08, MF-A02).

NCEER-94-0014 "NCEER-Taisei Corporation Research Program on Sliding Seismic Isolation Systems for Bridges: Experimental and Analytical Study of a System Consisting of Sliding Bearings and Fluid Restoring Force/Damping Devices," by P. Tsopelas and M.C. Constantinou, 6/13/94, (PB94-219144, A10, MF-A03).

NCEER-94-0015 "Generation of Hazard-Consistent Fragility Curves for Seismic Loss Estimation Studies," by H. Hwang and J-R. Huo, 6/14/94, (PB95-181996, A09, MF-A02).

NCEER-94-0016 "Seismic Study of Building Frames with Added Energy-Absorbing Devices," by W.S. Pong, C.S. Tsai and G.C. Lee, 6/20/94, (PB94-219136, A10, A03).

NCEER-94-0017 "Sliding Mode Control for Seismic-Excited Linear and Nonlinear Civil Engineering Structures," by J. Yang, J. Wu, A. Agrawal and Z. Li, 6/21/94, (PB95-138483, A06, MF-A02).

NCEER-94-0018 "3D-BASIS-TABS Version 2.0: Computer Program for Nonlinear Dynamic Analysis of Three Dimensional Base Isolated Structures," by A.M. Reinhorn, S. Nagarajaiah, M.C. Constantinou, P. Tsopelas and R. Li, 6/22/94, (PB95-182176, A08, MF-A02).

NCEER-94-0019 "Proceedings of the International Workshop on Civil Infrastructure Systems: Application of Intelligent Systems and Advanced Materials on Bridge Systems," Edited by G.C. Lee and K.C. Chang, 7/18/94, (PB95-252474, A20, MF-A04).

NCEER-94-0020 "Study of Seismic Isolation Systems for Computer Floors," by V. Lambrou and M.C. Constantinou, 7/19/94, (PB95-138533, A10, MF-A03).

NCEER-94-0021 "Proceedings of the U.S.-Italian Workshop on Guidelines for Seismic Evaluation and Rehabilitation of Unreinforced Masonry Buildings," Edited by D.P. Abrams and G.M. Calvi, 7/20/94, (PB95-138749, A13, MF-A03).

NCEER-94-0022 "NCEER-Taisei Corporation Research Program on Sliding Seismic Isolation Systems for Bridges: Experimental and Analytical Study of a System Consisting of Lubricated PTFE Sliding Bearings and Mild Steel Dampers," by P. Tsopelas and M.C. Constantinou, 7/22/94, (PB95-182184, A08, MF-A02).

NCEER-94-0023 “Development of Reliability-Based Design Criteria for Buildings Under Seismic Load,” by Y.K. Wen, H. Hwang and M. Shinozuka, 8/1/94, (PB95-211934, A08, MF-A02).

NCEER-94-0024 “Experimental Verification of Acceleration Feedback Control Strategies for an Active Tendon System,” by S.J. Dyke, B.F. Spencer, Jr., P. Quast, M.K. Sain, D.C. Kaspari, Jr. and T.T. Soong, 8/29/94, (PB95-212320, A05, MF-A01).

NCEER-94-0025 “Seismic Retrofitting Manual for Highway Bridges,” Edited by I.G. Buckle and I.F. Friedland, published by the Federal Highway Administration (PB95-212676, A15, MF-A03).

NCEER-94-0026 “Proceedings from the Fifth U.S.-Japan Workshop on Earthquake Resistant Design of Lifeline Facilities and Countermeasures Against Soil Liquefaction,” Edited by T.D. O’Rourke and M. Hamada, 11/7/94, (PB95-220802, A99, MF-E08).

NCEER-95-0001 “Experimental and Analytical Investigation of Seismic Retrofit of Structures with Supplemental Damping: Part 1 - Fluid Viscous Damping Devices,” by A.M. Reinhorn, C. Li and M.C. Constantinou, 1/3/95, (PB95-266599, A09, MF-A02).

NCEER-95-0002 “Experimental and Analytical Study of Low-Cycle Fatigue Behavior of Semi-Rigid Top-And-Seat Angle Connections,” by G. Pekcan, J.B. Mander and S.S. Chen, 1/5/95, (PB95-220042, A07, MF-A02).

NCEER-95-0003 “NCEER-ATC Joint Study on Fragility of Buildings,” by T. Anagnos, C. Rojahn and A.S. Kiremidjian, 1/20/95, (PB95-220026, A06, MF-A02).

NCEER-95-0004 “Nonlinear Control Algorithms for Peak Response Reduction,” by Z. Wu, T.T. Soong, V. Gattulli and R.C. Lin, 2/16/95, (PB95-220349, A05, MF-A01).

NCEER-95-0005 “Pipeline Replacement Feasibility Study: A Methodology for Minimizing Seismic and Corrosion Risks to Underground Natural Gas Pipelines,” by R.T. Eguchi, H.A. Seligson and D.G. Honegger, 3/2/95, (PB95-252326, A06, MF-A02).

NCEER-95-0006 “Evaluation of Seismic Performance of an 11-Story Frame Building During the 1994 Northridge Earthquake,” by F. Naeim, R. DiSulio, K. Benuska, A. Reinhorn and C. Li, not available.

NCEER-95-0007 “Prioritization of Bridges for Seismic Retrofitting,” by N. Basöz and A.S. Kiremidjian, 4/24/95, (PB95-252300, A08, MF-A02).

NCEER-95-0008 “Method for Developing Motion Damage Relationships for Reinforced Concrete Frames,” by A. Singhal and A.S. Kiremidjian, 5/11/95, (PB95-266607, A06, MF-A02).

NCEER-95-0009 “Experimental and Analytical Investigation of Seismic Retrofit of Structures with Supplemental Damping: Part II - Friction Devices,” by C. Li and A.M. Reinhorn, 7/6/95, (PB96-128087, A11, MF-A03).

NCEER-95-0010 “Experimental Performance and Analytical Study of a Non-Ductile Reinforced Concrete Frame Structure Retrofitted with Elastomeric Spring Dampers,” by G. Pekcan, J.B. Mander and S.S. Chen, 7/14/95, (PB96-137161, A08, MF-A02).

NCEER-95-0011 “Development and Experimental Study of Semi-Active Fluid Damping Devices for Seismic Protection of Structures,” by M.D. Symans and M.C. Constantinou, 8/3/95, (PB96-136940, A23, MF-A04).

NCEER-95-0012 “Real-Time Structural Parameter Modification (RSPM): Development of Innervated Structures,” by Z. Liang, M. Tong and G.C. Lee, 4/11/95, (PB96-137153, A06, MF-A01).

NCEER-95-0013 “Experimental and Analytical Investigation of Seismic Retrofit of Structures with Supplemental Damping: Part III - Viscous Damping Walls,” by A.M. Reinhorn and C. Li, 10/1/95, (PB96-176409, A11, MF-A03).

NCEER-95-0014 “Seismic Fragility Analysis of Equipment and Structures in a Memphis Electric Substation,” by J-R. Huo and H.H.M. Hwang, 8/10/95, (PB96-128087, A09, MF-A02).

NCEER-95-0015 “The Hanshin-Awaji Earthquake of January 17, 1995: Performance of Lifelines,” Edited by M. Shinozuka, 11/3/95, (PB96-176383, A15, MF-A03).

NCEER-95-0016 “Highway Culvert Performance During Earthquakes,” by T.L. Youd and C.J. Beckman, available as NCEER-96-0015.

NCEER-95-0017 “The Hanshin-Awaji Earthquake of January 17, 1995: Performance of Highway Bridges,” Edited by I.G. Buckle, 12/1/95, not available.

NCEER-95-0018 “Modeling of Masonry Infill Panels for Structural Analysis,” by A.M. Reinhorn, A. Madan, R.E. Valles, Y. Reichmann and J.B. Mander, 12/8/95, (PB97-110886, MF-A01, A06).

NCEER-95-0019 “Optimal Polynomial Control for Linear and Nonlinear Structures,” by A.K. Agrawal and J.N. Yang, 12/11/95, (PB96-168737, A07, MF-A02).

NCEER-95-0020 "Retrofit of Non-Ductile Reinforced Concrete Frames Using Friction Dampers," by R.S. Rao, P. Gergely and R.N. White, 12/22/95, (PB97-133508, A10, MF-A02).

NCEER-95-0021 "Parametric Results for Seismic Response of Pile-Supported Bridge Bents," by G. Mylonakis, A. Nikolaou and G. Gazetas, 12/22/95, (PB97-100242, A12, MF-A03).

NCEER-95-0022 "Kinematic Bending Moments in Seismically Stressed Piles," by A. Nikolaou, G. Mylonakis and G. Gazetas, 12/23/95, (PB97-113914, MF-A03, A13).

NCEER-96-0001 "Dynamic Response of Unreinforced Masonry Buildings with Flexible Diaphragms," by A.C. Costley and D.P. Abrams," 10/10/96, (PB97-133573, MF-A03, A15).

NCEER-96-0002 "State of the Art Review: Foundations and Retaining Structures," by I. Po Lam, not available.

NCEER-96-0003 "Ductility of Rectangular Reinforced Concrete Bridge Columns with Moderate Confinement," by N. Wehbe, M. Saiidi, D. Sanders and B. Douglas, 11/7/96, (PB97-133557, A06, MF-A02).

NCEER-96-0004 "Proceedings of the Long-Span Bridge Seismic Research Workshop," edited by I.G. Buckle and I.M. Friedland, not available.

NCEER-96-0005 "Establish Representative Pier Types for Comprehensive Study: Eastern United States," by J. Kulicki and Z. Prucz, 5/28/96, (PB98-119217, A07, MF-A02).

NCEER-96-0006 "Establish Representative Pier Types for Comprehensive Study: Western United States," by R. Imbsen, R.A. Schamber and T.A. Osterkamp, 5/28/96, (PB98-118607, A07, MF-A02).

NCEER-96-0007 "Nonlinear Control Techniques for Dynamical Systems with Uncertain Parameters," by R.G. Ghanem and M.I. Bujakov, 5/27/96, (PB97-100259, A17, MF-A03).

NCEER-96-0008 "Seismic Evaluation of a 30-Year Old Non-Ductile Highway Bridge Pier and Its Retrofit," by J.B. Mander, B. Mahmoodzadegan, S. Bhadra and S.S. Chen, 5/31/96, (PB97-110902, MF-A03, A10).

NCEER-96-0009 "Seismic Performance of a Model Reinforced Concrete Bridge Pier Before and After Retrofit," by J.B. Mander, J.H. Kim and C.A. Ligozio, 5/31/96, (PB97-110910, MF-A02, A10).

NCEER-96-0010 "IDARC2D Version 4.0: A Computer Program for the Inelastic Damage Analysis of Buildings," by R.E. Valles, A.M. Reinhorn, S.K. Kunnath, C. Li and A. Madan, 6/3/96, (PB97-100234, A17, MF-A03).

NCEER-96-0011 "Estimation of the Economic Impact of Multiple Lifeline Disruption: Memphis Light, Gas and Water Division Case Study," by S.E. Chang, H.A. Seligson and R.T. Eguchi, 8/16/96, (PB97-133490, A11, MF-A03).

NCEER-96-0012 "Proceedings from the Sixth Japan-U.S. Workshop on Earthquake Resistant Design of Lifeline Facilities and Countermeasures Against Soil Liquefaction, Edited by M. Hamada and T. O'Rourke, 9/11/96, (PB97-133581, A99, MF-A06).

NCEER-96-0013 "Chemical Hazards, Mitigation and Preparedness in Areas of High Seismic Risk: A Methodology for Estimating the Risk of Post-Earthquake Hazardous Materials Release," by H.A. Seligson, R.T. Eguchi, K.J. Tierney and K. Richmond, 11/7/96, (PB97-133565, MF-A02, A08).

NCEER-96-0014 "Response of Steel Bridge Bearings to Reversed Cyclic Loading," by J.B. Mander, D-K. Kim, S.S. Chen and G.J. Premus, 11/13/96, (PB97-140735, A12, MF-A03).

NCEER-96-0015 "Highway Culvert Performance During Past Earthquakes," by T.L. Youd and C.J. Beckman, 11/25/96, (PB97-133532, A06, MF-A01).

NCEER-97-0001 "Evaluation, Prevention and Mitigation of Pounding Effects in Building Structures," by R.E. Valles and A.M. Reinhorn, 2/20/97, (PB97-159552, A14, MF-A03).

NCEER-97-0002 "Seismic Design Criteria for Bridges and Other Highway Structures," by C. Rojahn, R. Mayes, D.G. Anderson, J. Clark, J.H. Hom, R.V. Nutt and M.J. O'Rourke, 4/30/97, (PB97-194658, A06, MF-A03).

NCEER-97-0003 “Proceedings of the U.S.-Italian Workshop on Seismic Evaluation and Retrofit,” Edited by D.P. Abrams and G.M. Calvi, 3/19/97, (PB97-194666, A13, MF-A03).

NCEER-97-0004 "Investigation of Seismic Response of Buildings with Linear and Nonlinear Fluid Viscous Dampers," by A.A. Seleemah and M.C. Constantinou, 5/21/97, (PB98-109002, A15, MF-A03).

NCEER-97-0005 "Proceedings of the Workshop on Earthquake Engineering Frontiers in Transportation Facilities," edited by G.C. Lee and I.M. Friedland, 8/29/97, (PB98-128911, A25, MR-A04).

NCEER-97-0006 "Cumulative Seismic Damage of Reinforced Concrete Bridge Piers," by S.K. Kunnath, A. El-Bahy, A. Taylor and W. Stone, 9/2/97, (PB98-108814, A11, MF-A03).

NCEER-97-0007 "Structural Details to Accommodate Seismic Movements of Highway Bridges and Retaining Walls," by R.A. Imbsen, R.A. Schamber, E. Thorkildsen, A. Kartoum, B.T. Martin, T.N. Rosser and J.M. Kulicki, 9/3/97, (PB98-108996, A09, MF-A02).

NCEER-97-0008 "A Method for Earthquake Motion-Damage Relationships with Application to Reinforced Concrete Frames," by A. Singhal and A.S. Kiremidjian, 9/10/97, (PB98-108988, A13, MF-A03).

NCEER-97-0009 "Seismic Analysis and Design of Bridge Abutments Considering Sliding and Rotation," by K. Fishman and R. Richards, Jr., 9/15/97, (PB98-108897, A06, MF-A02).

NCEER-97-0010 "Proceedings of the FHWA/NCEER Workshop on the National Representation of Seismic Ground Motion for New and Existing Highway Facilities," edited by I.M. Friedland, M.S. Power and R.L. Mayes, 9/22/97, (PB98-128903, A21, MF-A04).

NCEER-97-0011 "Seismic Analysis for Design or Retrofit of Gravity Bridge Abutments," by K.L. Fishman, R. Richards, Jr. and R.C. Divito, 10/2/97, (PB98-128937, A08, MF-A02).

NCEER-97-0012 "Evaluation of Simplified Methods of Analysis for Yielding Structures," by P. Tsopelas, M.C. Constantinou, C.A. Kircher and A.S. Whittaker, 10/31/97, (PB98-128929, A10, MF-A03).

NCEER-97-0013 "Seismic Design of Bridge Columns Based on Control and Repairability of Damage," by C-T. Cheng and J.B. Mander, 12/8/97, (PB98-144249, A11, MF-A03).

NCEER-97-0014 "Seismic Resistance of Bridge Piers Based on Damage Avoidance Design," by J.B. Mander and C-T. Cheng, 12/10/97, (PB98-144223, A09, MF-A02).

NCEER-97-0015 “Seismic Response of Nominally Symmetric Systems with Strength Uncertainty,” by S. Balopoulou and M. Grigoriu, 12/23/97, (PB98-153422, A11, MF-A03).

NCEER-97-0016 “Evaluation of Seismic Retrofit Methods for Reinforced Concrete Bridge Columns,” by T.J. Wipf, F.W. Klaiber and F.M. Russo, 12/28/97, (PB98-144215, A12, MF-A03).

NCEER-97-0017 “Seismic Fragility of Existing Conventional Reinforced Concrete Highway Bridges,” by C.L. Mullen and A.S. Cakmak, 12/30/97, (PB98-153406, A08, MF-A02).

NCEER-97-0018 “Loss Asssessment of Memphis Buildings,” edited by D.P. Abrams and M. Shinozuka, 12/31/97, (PB98-144231, A13, MF-A03).

NCEER-97-0019 “Seismic Evaluation of Frames with Infill Walls Using Quasi-static Experiments,” by K.M. Mosalam, R.N. White and P. Gergely, 12/31/97, (PB98-153455, A07, MF-A02).

NCEER-97-0020 “Seismic Evaluation of Frames with Infill Walls Using Pseudo-dynamic Experiments,” by K.M. Mosalam, R.N. White and P. Gergely, 12/31/97, (PB98-153430, A07, MF-A02).

NCEER-97-0021 “Computational Strategies for Frames with Infill Walls: Discrete and Smeared Crack Analyses and Seismic Fragility,” by K.M. Mosalam, R.N. White and P. Gergely, 12/31/97, (PB98-153414, A10, MF-A02).

NCEER-97-0022 "Proceedings of the NCEER Workshop on Evaluation of Liquefaction Resistance of Soils," edited by T.L. Youd and I.M. Idriss, 12/31/97, (PB98-155617, A15, MF-A03).

MCEER-98-0001 "Extraction of Nonlinear Hysteretic Properties of Seismically Isolated Bridges from Quick-Release Field Tests," by Q. Chen, B.M. Douglas, E.M. Maragakis and I.G. Buckle, 5/26/98, (PB99-118838, A06, MF-A01).

MCEER-98-0002 "Methodologies for Evaluating the Importance of Highway Bridges," by A. Thomas, S. Eshenaur and J. Kulicki, 5/29/98, (PB99-118846, A10, MF-A02).

MCEER-98-0003 "Capacity Design of Bridge Piers and the Analysis of Overstrength," by J.B. Mander, A. Dutta and P. Goel, 6/1/98, (PB99-118853, A09, MF-A02).

MCEER-98-0004 "Evaluation of Bridge Damage Data from the Loma Prieta and Northridge, California Earthquakes," by N. Basoz and A. Kiremidjian, 6/2/98, (PB99-118861, A15, MF-A03).

MCEER-98-0005 "Screening Guide for Rapid Assessment of Liquefaction Hazard at Highway Bridge Sites," by T. L. Youd, 6/16/98, (PB99-118879, A06, not available on microfiche).

MCEER-98-0006 "Structural Steel and Steel/Concrete Interface Details for Bridges," by P. Ritchie, N. Kauhl and J. Kulicki, 7/13/98, (PB99-118945, A06, MF-A01).

MCEER-98-0007 "Capacity Design and Fatigue Analysis of Confined Concrete Columns," by A. Dutta and J.B. Mander, 7/14/98, (PB99-118960, A14, MF-A03).

MCEER-98-0008 "Proceedings of the Workshop on Performance Criteria for Telecommunication Services Under Earthquake Conditions," edited by A.J. Schiff, 7/15/98, (PB99-118952, A08, MF-A02).

MCEER-98-0009 "Fatigue Analysis of Unconfined Concrete Columns," by J.B. Mander, A. Dutta and J.H. Kim, 9/12/98, (PB99-123655, A10, MF-A02).

MCEER-98-0010 "Centrifuge Modeling of Cyclic Lateral Response of Pile-Cap Systems and Seat-Type Abutments in Dry Sands," by A.D. Gadre and R. Dobry, 10/2/98, (PB99-123606, A13, MF-A03).

MCEER-98-0011 "IDARC-BRIDGE: A Computational Platform for Seismic Damage Assessment of Bridge Structures," by A.M. Reinhorn, V. Simeonov, G. Mylonakis and Y. Reichman, 10/2/98, (PB99-162919, A15, MF-A03).

MCEER-98-0012 "Experimental Investigation of the Dynamic Response of Two Bridges Before and After Retrofitting with Elastomeric Bearings," by D.A. Wendichansky, S.S. Chen and J.B. Mander, 10/2/98, (PB99-162927, A15, MF-A03).

MCEER-98-0013 "Design Procedures for Hinge Restrainers and Hinge Sear Width for Multiple-Frame Bridges," by R. Des Roches and G.L. Fenves, 11/3/98, (PB99-140477, A13, MF-A03).

MCEER-98-0014 "Response Modification Factors for Seismically Isolated Bridges," by M.C. Constantinou and J.K. Quarshie, 11/3/98, (PB99-140485, A14, MF-A03).

MCEER-98-0015 "Proceedings of the U.S.-Italy Workshop on Seismic Protective Systems for Bridges," edited by I.M. Friedland and M.C. Constantinou, 11/3/98, (PB2000-101711, A22, MF-A04).

MCEER-98-0016 "Appropriate Seismic Reliability for Critical Equipment Systems: Recommendations Based on Regional Analysis of Financial and Life Loss," by K. Porter, C. Scawthorn, C. Taylor and N. Blais, 11/10/98, (PB99-157265, A08, MF-A02).

MCEER-98-0017 "Proceedings of the U.S. Japan Joint Seminar on Civil Infrastructure Systems Research," edited by M. Shinozuka and A. Rose, 11/12/98, (PB99-156713, A16, MF-A03).

MCEER-98-0018 "Modeling of Pile Footings and Drilled Shafts for Seismic Design," by I. PoLam, M. Kapuskar and D. Chaudhuri, 12/21/98, (PB99-157257, A09, MF-A02).

MCEER-99-0001 "Seismic Evaluation of a Masonry Infilled Reinforced Concrete Frame by Pseudodynamic Testing," by S.G. Buonopane and R.N. White, 2/16/99, (PB99-162851, A09, MF-A02).

MCEER-99-0002 "Response History Analysis of Structures with Seismic Isolation and Energy Dissipation Systems: Verification Examples for Program SAP2000," by J. Scheller and M.C. Constantinou, 2/22/99, (PB99-162869, A08, MF-A02).

MCEER-99-0003 "Experimental Study on the Seismic Design and Retrofit of Bridge Columns Including Axial Load Effects," by A. Dutta, T. Kokorina and J.B. Mander, 2/22/99, (PB99-162877, A09, MF-A02).

MCEER-99-0004 "Experimental Study of Bridge Elastomeric and Other Isolation and Energy Dissipation Systems with Emphasis on Uplift Prevention and High Velocity Near-source Seismic Excitation," by A. Kasalanati and M. C. Constantinou, 2/26/99, (PB99-162885, A12, MF-A03).

MCEER-99-0005 "Truss Modeling of Reinforced Concrete Shear-flexure Behavior," by J.H. Kim and J.B. Mander, 3/8/99, (PB99-163693, A12, MF-A03).

MCEER-99-0006 "Experimental Investigation and Computational Modeling of Seismic Response of a 1:4 Scale Model Steel Structure with a Load Balancing Supplemental Damping System," by G. Pekcan, J.B. Mander and S.S. Chen, 4/2/99, (PB99-162893, A11, MF-A03).

MCEER-99-0007 "Effect of Vertical Ground Motions on the Structural Response of Highway Bridges," by M.R. Button, C.J. Cronin and R.L. Mayes, 4/10/99, (PB2000-101411, A10, MF-A03).

MCEER-99-0008 "Seismic Reliability Assessment of Critical Facilities: A Handbook, Supporting Documentation, and Model Code Provisions," by G.S. Johnson, R.E. Sheppard, M.D. Quilici, S.J. Eder and C.R. Scawthorn, 4/12/99, (PB2000-101701, A18, MF-A04).

MCEER-99-0009 "Impact Assessment of Selected MCEER Highway Project Research on the Seismic Design of Highway Structures," by C. Rojahn, R. Mayes, D.G. Anderson, J.H. Clark, D'Appolonia Engineering, S. Gloyd and R.V. Nutt, 4/14/99, (PB99-162901, A10, MF-A02).

MCEER-99-0010 "Site Factors and Site Categories in Seismic Codes," by R. Dobry, R. Ramos and M.S. Power, 7/19/99, (PB2000-101705, A08, MF-A02).

MCEER-99-0011 "Restrainer Design Procedures for Multi-Span Simply-Supported Bridges," by M.J. Randall, M. Saiidi, E. Maragakis and T. Isakovic, 7/20/99, (PB2000-101702, A10, MF-A02).

MCEER-99-0012 "Property Modification Factors for Seismic Isolation Bearings," by M.C. Constantinou, P. Tsopelas, A. Kasalanati and E. Wolff, 7/20/99, (PB2000-103387, A11, MF-A03).

MCEER-99-0013 "Critical Seismic Issues for Existing Steel Bridges," by P. Ritchie, N. Kauhl and J. Kulicki, 7/20/99, (PB2000-101697, A09, MF-A02).

MCEER-99-0014 "Nonstructural Damage Database," by A. Kao, T.T. Soong and A. Vender, 7/24/99, (PB2000-101407, A06, MF-A01).

MCEER-99-0015 "Guide to Remedial Measures for Liquefaction Mitigation at Existing Highway Bridge Sites," by H.G. Cooke and J. K. Mitchell, 7/26/99, (PB2000-101703, A11, MF-A03).

MCEER-99-0016 "Proceedings of the MCEER Workshop on Ground Motion Methodologies for the Eastern United States," edited by N. Abrahamson and A. Becker, 8/11/99, (PB2000-103385, A07, MF-A02).

MCEER-99-0017 "Quindío, Colombia Earthquake of January 25, 1999: Reconnaissance Report," by A.P. Asfura and P.J. Flores, 10/4/99, (PB2000-106893, A06, MF-A01).

MCEER-99-0018 "Hysteretic Models for Cyclic Behavior of Deteriorating Inelastic Structures," by M.V. Sivaselvan and A.M. Reinhorn, 11/5/99, (PB2000-103386, A08, MF-A02).

MCEER-99-0019 "Proceedings of the 7th U.S.- Japan Workshop on Earthquake Resistant Design of Lifeline Facilities and Countermeasures Against Soil Liquefaction," edited by T.D. O'Rourke, J.P. Bardet and M. Hamada, 11/19/99, (PB2000-103354, A99, MF-A06).

MCEER-99-0020 "Development of Measurement Capability for Micro-Vibration Evaluations with Application to Chip Fabrication Facilities," by G.C. Lee, Z. Liang, J.W. Song, J.D. Shen and W.C. Liu, 12/1/99, (PB2000-105993, A08, MF-A02).

MCEER-99-0021 "Design and Retrofit Methodology for Building Structures with Supplemental Energy Dissipating Systems," by G. Pekcan, J.B. Mander and S.S. Chen, 12/31/99, (PB2000-105994, A11, MF-A03).

MCEER-00-0001 "The Marmara, Turkey Earthquake of August 17, 1999: Reconnaissance Report," edited by C. Scawthorn; with major contributions by M. Bruneau, R. Eguchi, T. Holzer, G. Johnson, J. Mander, J. Mitchell, W. Mitchell, A. Papageorgiou, C. Scaethorn, and G. Webb, 3/23/00, (PB2000-106200, A11, MF-A03).

MCEER-00-0002 "Proceedings of the MCEER Workshop for Seismic Hazard Mitigation of Health Care Facilities," edited by G.C. Lee, M. Ettouney, M. Grigoriu, J. Hauer and J. Nigg, 3/29/00, (PB2000-106892, A08, MF-A02).

MCEER-00-0003 "The Chi-Chi, Taiwan Earthquake of September 21, 1999: Reconnaissance Report," edited by G.C. Lee and C.H. Loh, with major contributions by G.C. Lee, M. Bruneau, I.G. Buckle, S.E. Chang, P.J. Flores, T.D. O'Rourke, M. Shinozuka, T.T. Soong, C-H. Loh, K-C. Chang, Z-J. Chen, J-S. Hwang, M-L. Lin, G-Y. Liu, K-C. Tsai, G.C. Yao and C-L. Yen, 4/30/00, (PB2001-100980, A10, MF-A02).

MCEER-00-0004 "Seismic Retrofit of End-Sway Frames of Steel Deck-Truss Bridges with a Supplemental Tendon System: Experimental and Analytical Investigation," by G. Pekcan, J.B. Mander and S.S. Chen, 7/1/00, (PB2001-100982, A10, MF-A02).

MCEER-00-0005 "Sliding Fragility of Unrestrained Equipment in Critical Facilities," by W.H. Chong and T.T. Soong, 7/5/00, (PB2001-100983, A08, MF-A02).

MCEER-00-0006 "Seismic Response of Reinforced Concrete Bridge Pier Walls in the Weak Direction," by N. Abo-Shadi, M. Saiidi and D. Sanders, 7/17/00, (PB2001-100981, A17, MF-A03).

MCEER-00-0007 "Low-Cycle Fatigue Behavior of Longitudinal Reinforcement in Reinforced Concrete Bridge Columns," by J. Brown and S.K. Kunnath, 7/23/00, (PB2001-104392, A08, MF-A02).

MCEER-00-0008 "Soil Structure Interaction of Bridges for Seismic Analysis," I. PoLam and H. Law, 9/25/00, (PB2001-105397, A08, MF-A02).

MCEER-00-0009 "Proceedings of the First MCEER Workshop on Mitigation of Earthquake Disaster by Advanced Technologies (MEDAT-1), edited by M. Shinozuka, D.J. Inman and T.D. O'Rourke, 11/10/00, (PB2001-105399, A14, MF-A03).

MCEER-00-0010 "Development and Evaluation of Simplified Procedures for Analysis and Design of Buildings with Passive Energy Dissipation Systems, Revision 01," by O.M. Ramirez, M.C. Constantinou, C.A. Kircher, A.S. Whittaker, M.W. Johnson, J.D. Gomez and C. Chrysostomou, 11/16/01, (PB2001-105523, A23, MF-A04).

MCEER-00-0011 "Dynamic Soil-Foundation-Structure Interaction Analyses of Large Caissons," by C-Y. Chang, C-M. Mok, Z-L. Wang, R. Settgast, F. Waggoner, M.A. Ketchum, H.M. Gonnermann and C-C. Chin, 12/30/00, (PB2001-104373, A07, MF-A02).

MCEER-00-0012 "Experimental Evaluation of Seismic Performance of Bridge Restrainers," by A.G. Vlassis, E.M. Maragakis and M. Saiid Saiidi, 12/30/00, (PB2001-104354, A09, MF-A02).

MCEER-00-0013 "Effect of Spatial Variation of Ground Motion on Highway Structures," by M. Shinozuka, V. Saxena and G. Deodatis, 12/31/00, (PB2001-108755, A13, MF-A03).

MCEER-00-0014 "A Risk-Based Methodology for Assessing the Seismic Performance of Highway Systems," by S.D. Werner, C.E. Taylor, J.E. Moore, II, J.S. Walton and S. Cho, 12/31/00, (PB2001-108756, A14, MF-A03).

MCEER-01-0001 "Experimental Investigation of P-Delta Effects to Collapse During Earthquakes," by D. Vian and M. Bruneau, 6/25/01, (PB2002-100534, A17, MF-A03).

MCEER-01-0002 "Proceedings of the Second MCEER Workshop on Mitigation of Earthquake Disaster by Advanced Technologies (MEDAT-2)," edited by M. Bruneau and D.J. Inman, 7/23/01, (PB2002-100434, A16, MF-A03).

MCEER-01-0003 "Sensitivity Analysis of Dynamic Systems Subjected to Seismic Loads," by C. Roth and M. Grigoriu, 9/18/01, (PB2003-100884, A12, MF-A03).

MCEER-01-0004 "Overcoming Obstacles to Implementing Earthquake Hazard Mitigation Policies: Stage 1 Report," by D.J. Alesch and W.J. Petak, 12/17/01, (PB2002-107949, A07, MF-A02).

MCEER-01-0005 "Updating Real-Time Earthquake Loss Estimates: Methods, Problems and Insights," by C.E. Taylor, S.E. Chang and R.T. Eguchi, 12/17/01, (PB2002-107948, A05, MF-A01).

MCEER-01-0006 "Experimental Investigation and Retrofit of Steel Pile Foundations and Pile Bents Under Cyclic Lateral Loadings," by A. Shama, J. Mander, B. Blabac and S. Chen, 12/31/01, (PB2002-107950, A13, MF-A03).

MCEER-02-0001 "Assessment of Performance of Bolu Viaduct in the 1999 Duzce Earthquake in Turkey" by P.C. Roussis, M.C. Constantinou, M. Erdik, E. Durukal and M. Dicleli, 5/8/02, (PB2003-100883, A08, MF-A02).

MCEER-02-0002 "Seismic Behavior of Rail Counterweight Systems of Elevators in Buildings," by M.P. Singh, Rildova and L.E. Suarez, 5/27/02. (PB2003-100882, A11, MF-A03).

MCEER-02-0003 "Development of Analysis and Design Procedures for Spread Footings," by G. Mylonakis, G. Gazetas, S. Nikolaou and A. Chauncey, 10/02/02, (PB2004-101636, A13, MF-A03, CD-A13).

MCEER-02-0004 "Bare-Earth Algorithms for Use with SAR and LIDAR Digital Elevation Models," by C.K. Huyck, R.T. Eguchi and B. Houshmand, 10/16/02, (PB2004-101637, A07, CD-A07).

MCEER-02-0005 "Review of Energy Dissipation of Compression Members in Concentrically Braced Frames," by K.Lee and M. Bruneau, 10/18/02, (PB2004-101638, A10, CD-A10).

MCEER-03-0001 "Experimental Investigation of Light-Gauge Steel Plate Shear Walls for the Seismic Retrofit of Buildings" by J. Berman and M. Bruneau, 5/2/03, (PB2004-101622, A10, MF-A03, CD-A10).

MCEER-03-0002 "Statistical Analysis of Fragility Curves," by M. Shinozuka, M.Q. Feng, H. Kim, T. Uzawa and T. Ueda, 6/16/03, (PB2004-101849, A09, CD-A09).

MCEER-03-0003 "Proceedings of the Eighth U.S.-Japan Workshop on Earthquake Resistant Design f Lifeline Facilities and Countermeasures Against Liquefaction," edited by M. Hamada, J.P. Bardet and T.D. O'Rourke, 6/30/03, (PB2004-104386, A99, CD-A99).

MCEER-03-0004 "Proceedings of the PRC-US Workshop on Seismic Analysis and Design of Special Bridges," edited by L.C. Fan and G.C. Lee, 7/15/03, (PB2004-104387, A14, CD-A14).

MCEER-03-0005 "Urban Disaster Recovery: A Framework and Simulation Model," by S.B. Miles and S.E. Chang, 7/25/03, (PB2004-104388, A07, CD-A07).

MCEER-03-0006 "Behavior of Underground Piping Joints Due to Static and Dynamic Loading," by R.D. Meis, M. Maragakis and R. Siddharthan, 11/17/03, (PB2005-102194, A13, MF-A03, CD-A00).

MCEER-04-0001 "Experimental Study of Seismic Isolation Systems with Emphasis on Secondary System Response and Verification of Accuracy of Dynamic Response History Analysis Methods," by E. Wolff and M. Constantinou, 1/16/04 (PB2005-102195, A99, MF-E08, CD-A00).

MCEER-04-0002 "Tension, Compression and Cyclic Testing of Engineered Cementitious Composite Materials," by K. Kesner and S.L. Billington, 3/1/04, (PB2005-102196, A08, CD-A08).

MCEER-04-0003 "Cyclic Testing of Braces Laterally Restrained by Steel Studs to Enhance Performance During Earthquakes," by O.C. Celik, J.W. Berman and M. Bruneau, 3/16/04, (PB2005-102197, A13, MF-A03, CD-A00).

MCEER-04-0004 "Methodologies for Post Earthquake Building Damage Detection Using SAR and Optical Remote Sensing: Application to the August 17, 1999 Marmara, Turkey Earthquake," by C.K. Huyck, B.J. Adams, S. Cho, R.T. Eguchi, B. Mansouri and B. Houshmand, 6/15/04, (PB2005-104888, A10, CD-A00).

MCEER-04-0005 "Nonlinear Structural Analysis Towards Collapse Simulation: A Dynamical Systems Approach," by M.V. Sivaselvan and A.M. Reinhorn, 6/16/04, (PB2005-104889, A11, MF-A03, CD-A00).

MCEER-04-0006 "Proceedings of the Second PRC-US Workshop on Seismic Analysis and Design of Special Bridges," edited by G.C. Lee and L.C. Fan, 6/25/04, (PB2005-104890, A16, CD-A00).

MCEER-04-0007 "Seismic Vulnerability Evaluation of Axially Loaded Steel Built-up Laced Members," by K. Lee and M. Bruneau, 6/30/04, (PB2005-104891, A16, CD-A00).

MCEER-04-0008 "Evaluation of Accuracy of Simplified Methods of Analysis and Design of Buildings with Damping Systems for Near-Fault and for Soft-Soil Seismic Motions," by E.A. Pavlou and M.C. Constantinou, 8/16/04, (PB2005-104892, A08, MF-A02, CD-A00).

MCEER-04-0009 "Assessment of Geotechnical Issues in Acute Care Facilities in California," by M. Lew, T.D. O'Rourke, R. Dobry and M. Koch, 9/15/04, (PB2005-104893, A08, CD-A00).

MCEER-04-0010 "Scissor-Jack-Damper Energy Dissipation System," by A.N. Sigaher-Boyle and M.C. Constantinou, 12/1/04 (PB2005-108221).

MCEER-04-0011 "Seismic Retrofit of Bridge Steel Truss Piers Using a Controlled Rocking Approach," by M. Pollino and M. Bruneau, 12/20/04 (PB2006-105795).

MCEER-05-0001 "Experimental and Analytical Studies of Structures Seismically Isolated with an Uplift-Restraint Isolation System," by P.C. Roussis and M.C. Constantinou, 1/10/05 (PB2005-108222).

MCEER-05-0002 "A Versatile Experimentation Model for Study of Structures Near Collapse Applied to Seismic Evaluation of Irregular Structures," by D. Kusumastuti, A.M. Reinhorn and A. Rutenberg, 3/31/05 (PB2006-101523).

MCEER-05-0003 "Proceedings of the Third PRC-US Workshop on Seismic Analysis and Design of Special Bridges," edited by L.C. Fan and G.C. Lee, 4/20/05, (PB2006-105796).

MCEER-05-0004 "Approaches for the Seismic Retrofit of Braced Steel Bridge Piers and Proof-of-Concept Testing of an Eccentrically Braced Frame with Tubular Link," by J.W. Berman and M. Bruneau, 4/21/05 (PB2006-101524).

MCEER-05-0005 "Simulation of Strong Ground Motions for Seismic Fragility Evaluation of Nonstructural Components in Hospitals," by A. Wanitkorkul and A. Filiatrault, 5/26/05 (PB2006-500027).

MCEER-05-0006 "Seismic Safety in California Hospitals: Assessing an Attempt to Accelerate the Replacement or Seismic Retrofit of Older Hospital Facilities," by D.J. Alesch, L.A. Arendt and W.J. Petak, 6/6/05 (PB2006-105794).

MCEER-05-0007 "Development of Seismic Strengthening and Retrofit Strategies for Critical Facilities Using Engineered Cementitious Composite Materials," by K. Kesner and S.L. Billington, 8/29/05 (PB2006-111701).

MCEER-05-0008 "Experimental and Analytical Studies of Base Isolation Systems for Seismic Protection of Power Transformers," by N. Murota, M.Q. Feng and G-Y. Liu, 9/30/05 (PB2006-111702).

MCEER-05-0009 "3D-BASIS-ME-MB: Computer Program for Nonlinear Dynamic Analysis of Seismically Isolated Structures," by P.C. Tsopelas, P.C. Roussis, M.C. Constantinou, R. Buchanan and A.M. Reinhorn, 10/3/05 (PB2006-111703).

MCEER-05-0010 "Steel Plate Shear Walls for Seismic Design and Retrofit of Building Structures," by D. Vian and M. Bruneau, 12/15/05 (PB2006-111704).

MCEER-05-0011 "The Performance-Based Design Paradigm," by M.J. Astrella and A. Whittaker, 12/15/05 (PB2006-111705).

MCEER-06-0001 "Seismic Fragility of Suspended Ceiling Systems," H. Badillo-Almaraz, A.S. Whittaker, A.M. Reinhorn and G.P. Cimellaro, 2/4/06 (PB2006-111706).

MCEER-06-0002 "Multi-Dimensional Fragility of Structures," by G.P. Cimellaro, A.M. Reinhorn and M. Bruneau, 3/1/06 (PB2007-106974, A09, MF-A02, CD A00).

MCEER-06-0003 "Built-Up Shear Links as Energy Dissipators for Seismic Protection of Bridges," by P. Dusicka, A.M. Itani and I.G. Buckle, 3/15/06 (PB2006-111708).

MCEER-06-0004 "Analytical Investigation of the Structural Fuse Concept," by R.E. Vargas and M. Bruneau, 3/16/06 (PB2006-111709).

MCEER-06-0005 "Experimental Investigation of the Structural Fuse Concept," by R.E. Vargas and M. Bruneau, 3/17/06 (PB2006-111710).

MCEER-06-0006 "Further Development of Tubular Eccentrically Braced Frame Links for the Seismic Retrofit of Braced Steel Truss Bridge Piers," by J.W. Berman and M. Bruneau, 3/27/06 (PB2007-105147).

MCEER-06-0007 "REDARS Validation Report," by S. Cho, C.K. Huyck, S. Ghosh and R.T. Eguchi, 8/8/06 (PB2007-106983).

MCEER-06-0008 "Review of Current NDE Technologies for Post-Earthquake Assessment of Retrofitted Bridge Columns," by J.W. Song, Z. Liang and G.C. Lee, 8/21/06 (PB2007-106984).

MCEER-06-0009 "Liquefaction Remediation in Silty Soils Using Dynamic Compaction and Stone Columns," by S. Thevanayagam, G.R. Martin, R. Nashed, T. Shenthan, T. Kanagalingam and N. Ecemis, 8/28/06 (PB2007-106985).

MCEER-06-0010 "Conceptual Design and Experimental Investigation of Polymer Matrix Composite Infill Panels for Seismic Retrofitting," by W. Jung, M. Chiewanichakorn and A.J. Aref, 9/21/06 (PB2007-106986).

MCEER-06-0011 "A Study of the Coupled Horizontal-Vertical Behavior of Elastomeric and Lead-Rubber Seismic Isolation Bearings," by G.P. Warn and A.S. Whittaker, 9/22/06 (PB2007-108679).

MCEER-06-0012 "Proceedings of the Fourth PRC-US Workshop on Seismic Analysis and Design of Special Bridges: Advancing Bridge Technologies in Research, Design, Construction and Preservation," Edited by L.C. Fan, G.C. Lee and L. Ziang, 10/12/06 (PB2007-109042).

MCEER-06-0013 "Cyclic Response and Low Cycle Fatigue Characteristics of Plate Steels," by P. Dusicka, A.M. Itani and I.G. Buckle, 11/1/06 06 (PB2007-106987).

MCEER-06-0014 "Proceedings of the Second US-Taiwan Bridge Engineering Workshop," edited by W.P. Yen, J. Shen, J-Y. Chen and M. Wang, 11/15/06 (PB2008-500041).

MCEER-06-0015 "User Manual and Technical Documentation for the REDARS™ Import Wizard," by S. Cho, S. Ghosh, C.K. Huyck and S.D. Werner, 11/30/06 (PB2007-114766).

MCEER-06-0016 "Hazard Mitigation Strategy and Monitoring Technologies for Urban and Infrastructure Public Buildings: Proceedings of the China-US Workshops," edited by X.Y. Zhou, A.L. Zhang, G.C. Lee and M. Tong, 12/12/06 (PB2008-500018).

MCEER-07-0001 "Static and Kinetic Coefficients of Friction for Rigid Blocks," by C. Kafali, S. Fathali, M. Grigoriu and A.S. Whittaker, 3/20/07 (PB2007-114767).

MCEER-07-0002 "Hazard Mitigation Investment Decision Making: Organizational Response to Legislative Mandate," by L.A. Arendt, D.J. Alesch and W.J. Petak, 4/9/07 (PB2007-114768).

MCEER-07-0003 "Seismic Behavior of Bidirectional-Resistant Ductile End Diaphragms with Unbonded Braces in Straight or Skewed Steel Bridges," by O. Celik and M. Bruneau, 4/11/07 (PB2008-105141).

MCEER-07-0004 "Modeling Pile Behavior in Large Pile Groups Under Lateral Loading," by A.M. Dodds and G.R. Martin, 4/16/07(PB2008-105142).

MCEER-07-0005 "Experimental Investigation of Blast Performance of Seismically Resistant Concrete-Filled Steel Tube Bridge Piers," by S. Fujikura, M. Bruneau and D. Lopez-Garcia, 4/20/07 (PB2008-105143).

MCEER-07-0006 "Seismic Analysis of Conventional and Isolated Liquefied Natural Gas Tanks Using Mechanical Analogs," by I.P. Christovasilis and A.S. Whittaker, 5/1/07, not available.

MCEER-07-0007 "Experimental Seismic Performance Evaluation of Isolation/Restraint Systems for Mechanical Equipment – Part 1: Heavy Equipment Study," by S. Fathali and A. Filiatrault, 6/6/07 (PB2008-105144).

MCEER-07-0008 "Seismic Vulnerability of Timber Bridges and Timber Substructures," by A.A. Sharma, J.B. Mander, I.M. Friedland and D.R. Allicock, 6/7/07 (PB2008-105145).

MCEER-07-0009 "Experimental and Analytical Study of the XY-Friction Pendulum (XY-FP) Bearing for Bridge Applications," by C.C. Marin-Artieda, A.S. Whittaker and M.C. Constantinou, 6/7/07 (PB2008-105191).

MCEER-07-0010 "Proceedings of the PRC-US Earthquake Engineering Forum for Young Researchers," Edited by G.C. Lee and X.Z. Qi, 6/8/07 (PB2008-500058).

MCEER-07-0011 "Design Recommendations for Perforated Steel Plate Shear Walls," by R. Purba and M. Bruneau, 6/18/07, (PB2008-105192).

MCEER-07-0012 "Performance of Seismic Isolation Hardware Under Service and Seismic Loading," by M.C. Constantinou, A.S. Whittaker, Y. Kalpakidis, D.M. Fenz and G.P. Warn, 8/27/07, (PB2008-105193).

MCEER-07-0013 "Experimental Evaluation of the Seismic Performance of Hospital Piping Subassemblies," by E.R. Goodwin, E. Maragakis and A.M. Itani, 9/4/07, (PB2008-105194).

MCEER-07-0014 "A Simulation Model of Urban Disaster Recovery and Resilience: Implementation for the 1994 Northridge Earthquake," by S. Miles and S.E. Chang, 9/7/07, (PB2008-106426).

MCEER-07-0015 "Statistical and Mechanistic Fragility Analysis of Concrete Bridges," by M. Shinozuka, S. Banerjee and S-H. Kim, 9/10/07, (PB2008-106427).

MCEER-07-0016 "Three-Dimensional Modeling of Inelastic Buckling in Frame Structures," by M. Schachter and AM. Reinhorn, 9/13/07, (PB2008-108125).

MCEER-07-0017 "Modeling of Seismic Wave Scattering on Pile Groups and Caissons," by I. Po Lam, H. Law and C.T. Yang, 9/17/07 (PB2008-108150).

MCEER-07-0018 "Bridge Foundations: Modeling Large Pile Groups and Caissons for Seismic Design," by I. Po Lam, H. Law and G.R. Martin (Coordinating Author), 12/1/07 (PB2008-111190).

MCEER-07-0019 "Principles and Performance of Roller Seismic Isolation Bearings for Highway Bridges," by G.C. Lee, Y.C. Ou, Z. Liang, T.C. Niu and J. Song, 12/10/07 (PB2009-110466).

MCEER-07-0020 "Centrifuge Modeling of Permeability and Pinning Reinforcement Effects on Pile Response to Lateral Spreading," by L.L Gonzalez-Lagos, T. Abdoun and R. Dobry, 12/10/07 (PB2008-111191).

MCEER-07-0021 "Damage to the Highway System from the Pisco, Perú Earthquake of August 15, 2007," by J.S. O'Connor, L. Mesa and M. Nykamp, 12/10/07, (PB2008-108126).

MCEER-07-0022 "Experimental Seismic Performance Evaluation of Isolation/Restraint Systems for Mechanical Equipment – Part 2: Light Equipment Study," by S. Fathali and A. Filiatrault, 12/13/07 (PB2008-111192).

MCEER-07-0023 "Fragility Considerations in Highway Bridge Design," by M. Shinozuka, S. Banerjee and S.H. Kim, 12/14/07 (PB2008-111193).

MCEER-07-0024 “Performance Estimates for Seismically Isolated Bridges,” by G.P. Warn and A.S. Whittaker, 12/30/07 (PB2008-112230).

MCEER-08-0001 “Seismic Performance of Steel Girder Bridge Superstructures with Conventional Cross Frames,” by L.P. Carden, A.M. Itani and I.G. Buckle, 1/7/08, (PB2008-112231).

MCEER-08-0002 “Seismic Performance of Steel Girder Bridge Superstructures with Ductile End Cross Frames with Seismic Isolators,” by L.P. Carden, A.M. Itani and I.G. Buckle, 1/7/08 (PB2008-112232).

MCEER-08-0003 “Analytical and Experimental Investigation of a Controlled Rocking Approach for Seismic Protection of Bridge Steel Truss Piers,” by M. Pollino and M. Bruneau, 1/21/08 (PB2008-112233).

MCEER-08-0004 “Linking Lifeline Infrastructure Performance and Community Disaster Resilience: Models and Multi-Stakeholder Processes,” by S.E. Chang, C. Pasion, K. Tatebe and R. Ahmad, 3/3/08 (PB2008-112234).

MCEER-08-0005 “Modal Analysis of Generally Damped Linear Structures Subjected to Seismic Excitations,” by J. Song, Y-L. Chu, Z. Liang and G.C. Lee, 3/4/08 (PB2009-102311).

MCEER-08-0006 “System Performance Under Multi-Hazard Environments,” by C. Kafali and M. Grigoriu, 3/4/08 (PB2008-112235).

MCEER-08-0007 “Mechanical Behavior of Multi-Spherical Sliding Bearings,” by D.M. Fenz and M.C. Constantinou, 3/6/08 (PB2008-112236).

MCEER-08-0008 “Post-Earthquake Restoration of the Los Angeles Water Supply System,” by T.H.P. Tabucchi and R.A. Davidson, 3/7/08 (PB2008-112237).

MCEER-08-0009 “Fragility Analysis of Water Supply Systems,” by A. Jacobson and M. Grigoriu, 3/10/08 (PB2009-105545).

MCEER-08-0010 “Experimental Investigation of Full-Scale Two-Story Steel Plate Shear Walls with Reduced Beam Section Connections,” by B. Qu, M. Bruneau, C-H. Lin and K-C. Tsai, 3/17/08 (PB2009-106368).

MCEER-08-0011 “Seismic Evaluation and Rehabilitation of Critical Components of Electrical Power Systems,” S. Ersoy, B. Feizi, A. Ashrafi and M. Ala Saadeghvaziri, 3/17/08 (PB2009-105546).

MCEER-08-0012 “Seismic Behavior and Design of Boundary Frame Members of Steel Plate Shear Walls,” by B. Qu and M. Bruneau, 4/26/08 . (PB2009-106744).

MCEER-08-0013 “Development and Appraisal of a Numerical Cyclic Loading Protocol for Quantifying Building System Performance,” by A. Filiatrault, A. Wanitkorkul and M. Constantinou, 4/27/08 (PB2009-107906).

MCEER-08-0014 “Structural and Nonstructural Earthquake Design: The Challenge of Integrating Specialty Areas in Designing Complex, Critical Facilities,” by W.J. Petak and D.J. Alesch, 4/30/08 (PB2009-107907).

MCEER-08-0015 “Seismic Performance Evaluation of Water Systems,” by Y. Wang and T.D. O’Rourke, 5/5/08 (PB2009-107908).

MCEER-08-0016 “Seismic Response Modeling of Water Supply Systems,” by P. Shi and T.D. O’Rourke, 5/5/08 (PB2009-107910).

MCEER-08-0017 “Numerical and Experimental Studies of Self-Centering Post-Tensioned Steel Frames,” by D. Wang and A. Filiatrault, 5/12/08 (PB2009-110479).

MCEER-08-0018 “Development, Implementation and Verification of Dynamic Analysis Models for Multi-Spherical Sliding Bearings,” by D.M. Fenz and M.C. Constantinou, 8/15/08 (PB2009-107911).

MCEER-08-0019 “Performance Assessment of Conventional and Base Isolated Nuclear Power Plants for Earthquake Blast Loadings,” by Y.N. Huang, A.S. Whittaker and N. Luco, 10/28/08 (PB2009-107912).

MCEER-08-0020 "Remote Sensing for Resilient Multi-Hazard Disaster Response – Volume I: Introduction to Damage Assessment Methodologies," by B.J. Adams and R.T. Eguchi, 11/17/08 (PB2010-102695).

MCEER-08-0021 "Remote Sensing for Resilient Multi-Hazard Disaster Response – Volume II: Counting the Number of Collapsed Buildings Using an Object-Oriented Analysis: Case Study of the 2003 Bam Earthquake," by L. Gusella, C.K. Huyck and B.J. Adams, 11/17/08 (PB2010-100925).

MCEER-08-0022 "Remote Sensing for Resilient Multi-Hazard Disaster Response – Volume III: Multi-Sensor Image Fusion Techniques for Robust Neighborhood-Scale Urban Damage Assessment," by B.J. Adams and A. McMillan, 11/17/08 (PB2010-100926).

MCEER-08-0023 "Remote Sensing for Resilient Multi-Hazard Disaster Response – Volume IV: A Study of Multi-Temporal and Multi-Resolution SAR Imagery for Post-Katrina Flood Monitoring in New Orleans," by A. McMillan, J.G. Morley, B.J. Adams and S. Chesworth, 11/17/08 (PB2010-100927).

MCEER-08-0024 "Remote Sensing for Resilient Multi-Hazard Disaster Response – Volume V: Integration of Remote Sensing Imagery and VIEWS^{TM} Field Data for Post-Hurricane Charley Building Damage Assessment," by J.A. Womble, K. Mehta and B.J. Adams, 11/17/08 (PB2009-115532).

MCEER-08-0025 "Building Inventory Compilation for Disaster Management: Application of Remote Sensing and Statistical Modeling," by P. Sarabandi, A.S. Kiremidjian, R.T. Eguchi and B. J. Adams, 11/20/08 (PB2009-110484).

MCEER-08-0026 "New Experimental Capabilities and Loading Protocols for Seismic Qualification and Fragility Assessment of Nonstructural Systems," by R. Retamales, G. Mosqueda, A. Filiatrault and A. Reinhorn, 11/24/08 (PB2009-110485).

MCEER-08-0027 "Effects of Heating and Load History on the Behavior of Lead-Rubber Bearings," by I.V. Kalpakidis and M.C. Constantinou, 12/1/08 (PB2009-115533).

MCEER-08-0028 "Experimental and Analytical Investigation of Blast Performance of Seismically Resistant Bridge Piers," by S.Fujikura and M. Bruneau, 12/8/08 (PB2009-115534).

MCEER-08-0029 "Evolutionary Methodology for Aseismic Decision Support," by Y. Hu and G. Dargush, 12/15/08.

MCEER-08-0030 "Development of a Steel Plate Shear Wall Bridge Pier System Conceived from a Multi-Hazard Perspective," by D. Keller and M. Bruneau, 12/19/08 (PB2010-102696).

MCEER-09-0001 "Modal Analysis of Arbitrarily Damped Three-Dimensional Linear Structures Subjected to Seismic Excitations," by Y.L. Chu, J. Song and G.C. Lee, 1/31/09 (PB2010-100922).

MCEER-09-0002 "Air-Blast Effects on Structural Shapes," by G. Ballantyne, A.S. Whittaker, A.J. Aref and G.F. Dargush, 2/2/09 (PB2010-102697).

MCEER-09-0003 "Water Supply Performance During Earthquakes and Extreme Events," by A.L. Bonneau and T.D. O'Rourke, 2/16/09 (PB2010-100923).

MCEER-09-0004 "Generalized Linear (Mixed) Models of Post-Earthquake Ignitions," by R.A. Davidson, 7/20/09 (PB2010-102698).

MCEER-09-0005 "Seismic Testing of a Full-Scale Two-Story Light-Frame Wood Building: NEESWood Benchmark Test," by I.P. Christovasilis, A. Filiatrault and A. Wanitkorkul, 7/22/09 (PB2012-102401).

MCEER-09-0006 "IDARC2D Version 7.0: A Program for the Inelastic Damage Analysis of Structures," by A.M. Reinhorn, H. Roh, M. Sivaselvan, S.K. Kunnath, R.E. Valles, A. Madan, C. Li, R. Lobo and Y.J. Park, 7/28/09 (PB2010-103199).

MCEER-09-0007 "Enhancements to Hospital Resiliency: Improving Emergency Planning for and Response to Hurricanes," by D.B. Hess and L.A. Arendt, 7/30/09 (PB2010-100924).

MCEER-09-0008 "Assessment of Base-Isolated Nuclear Structures for Design and Beyond-Design Basis Earthquake Shaking," by Y.N. Huang, A.S. Whittaker, R.P. Kennedy and R.L. Mayes, 8/20/09 (PB2010-102699).

MCEER-09-0009 "Quantification of Disaster Resilience of Health Care Facilities," by G.P. Cimellaro, C. Fumo, A.M Reinhorn and M. Bruneau, 9/14/09 (PB2010-105384).

MCEER-09-0010 "Performance-Based Assessment and Design of Squat Reinforced Concrete Shear Walls," by C.K. Gulec and A.S. Whittaker, 9/15/09 (PB2010-102700).

MCEER-09-0011 "Proceedings of the Fourth US-Taiwan Bridge Engineering Workshop," edited by W.P. Yen, J.J. Shen, T.M. Lee and R.B. Zheng, 10/27/09 (PB2010-500009).

MCEER-09-0012 "Proceedings of the Special International Workshop on Seismic Connection Details for Segmental Bridge Construction," edited by W. Phillip Yen and George C. Lee, 12/21/09 (PB2012-102402).

MCEER-10-0001 "Direct Displacement Procedure for Performance-Based Seismic Design of Multistory Woodframe Structures," by W. Pang and D. Rosowsky, 4/26/10 (PB2012-102403).

MCEER-10-0002 "Simplified Direct Displacement Design of Six-Story NEESWood Capstone Building and Pre-Test Seismic Performance Assessment," by W. Pang, D. Rosowsky, J. van de Lindt and S. Pei, 5/28/10 (PB2012-102404).

MCEER-10-0003 "Integration of Seismic Protection Systems in Performance-Based Seismic Design of Woodframed Structures," by J.K. Shinde and M.D. Symans, 6/18/10 (PB2012-102405).

MCEER-10-0004 "Modeling and Seismic Evaluation of Nonstructural Components: Testing Frame for Experimental Evaluation of Suspended Ceiling Systems," by A.M. Reinhorn, K.P. Ryu and G. Maddaloni, 6/30/10 (PB2012-102406).

MCEER-10-0005 "Analytical Development and Experimental Validation of a Structural-Fuse Bridge Pier Concept," by S. El-Bahey and M. Bruneau, 10/1/10 (PB2012-102407).

MCEER-10-0006 "A Framework for Defining and Measuring Resilience at the Community Scale: The PEOPLES Resilience Framework," by C.S. Renschler, A.E. Frazier, L.A. Arendt, G.P. Cimellaro, A.M. Reinhorn and M. Bruneau, 10/8/10 (PB2012-102408).

MCEER-10-0007 "Impact of Horizontal Boundary Elements Design on Seismic Behavior of Steel Plate Shear Walls," by R. Purba and M. Bruneau, 11/14/10 (PB2012-102409).

MCEER-10-0008 "Seismic Testing of a Full-Scale Mid-Rise Building: The NEESWood Capstone Test," by S. Pei, J.W. van de Lindt, S.E. Pryor, H. Shimizu, H. Isoda and D.R. Rammer, 12/1/10 (PB2012-102410).

MCEER-10-0009 "Modeling the Effects of Detonations of High Explosives to Inform Blast-Resistant Design," by P. Sherkar, A.S. Whittaker and A.J. Aref, 12/1/10 (PB2012-102411).

MCEER-10-0010 "L'Aquila Earthquake of April 6, 2009 in Italy: Rebuilding a Resilient City to Withstand Multiple Hazards," by G.P. Cimellaro, I.P. Christovasilis, A.M. Reinhorn, A. De Stefano and T. Kirova, 12/29/10.

MCEER-11-0001 "Numerical and Experimental Investigation of the Seismic Response of Light-Frame Wood Structures," by I.P. Christovasilis and A. Filiatrault, 8/8/11 (PB2012-102412).

MCEER-11-0002 "Seismic Design and Analysis of a Precast Segmental Concrete Bridge Model," by M. Anagnostopoulou, A. Filiatrault and A. Aref, 9/15/11.

MCEER-11-0003 'Proceedings of the Workshop on Improving Earthquake Response of Substation Equipment," Edited by A.M. Reinhorn, 9/19/11 (PB2012-102413).

MCEER-11-0004 "LRFD-Based Analysis and Design Procedures for Bridge Bearings and Seismic Isolators," by M.C. Constantinou, I. Kalpakidis, A. Filiatrault and R.A. Ecker Lay, 9/26/11.

MCEER-11-0005 "Experimental Seismic Evaluation, Model Parameterization, and Effects of Cold-Formed Steel-Framed Gypsum Partition Walls on the Seismic Performance of an Essential Facility," by R. Davies, R. Retamales, G. Mosqueda and A. Filiatrault, 10/12/11.

MCEER-11-0006 "Modeling and Seismic Performance Evaluation of High Voltage Transformers and Bushings," by A.M. Reinhorn, K. Oikonomou, H. Roh, A. Schiff and L. Kempner, Jr., 10/3/11.

MCEER-11-0007 "Extreme Load Combinations: A Survey of State Bridge Engineers," by G.C. Lee, Z. Liang, J.J. Shen and J.S. O'Connor, 10/14/11.

MCEER-12-0001 "Simplified Analysis Procedures in Support of Performance Based Seismic Design," by Y.N. Huang and A.S. Whittaker.

MCEER-12-0002 "Seismic Protection of Electrical Transformer Bushing Systems by Stiffening Techniques," by M. Koliou, A. Filiatrault, A.M. Reinhorn and N. Oliveto, 6/1/12.

MCEER-12-0003 "Post-Earthquake Bridge Inspection Guidelines," by J.S. O'Connor and S. Alampalli, 6/8/12.

MCEER-12-0004 "Integrated Design Methodology for Isolated Floor Systems in Single-Degree-of-Freedom Structural Fuse Systems," by S. Cui, M. Bruneau and M.C. Constantinou, 6/13/12.

MCEER-12-0005 "Characterizing the Rotational Components of Earthquake Ground Motion," by D. Basu, A.S. Whittaker and M.C. Constantinou, 6/15/12.

MCEER-12-0006 "Bayesian Fragility for Nonstructural Systems," by C.H. Lee and M.D. Grigoriu, 9/12/12.

MCEER-12-0007 "A Numerical Model for Capturing the In-Plane Seismic Response of Interior Metal Stud Partition Walls," by R.L. Wood and T.C. Hutchinson, 9/12/12.

MCEER-12-0008 "Assessment of Floor Accelerations in Yielding Buildings," by J.D. Wieser, G. Pekcan, A.E. Zaghi, A.M. Itani and E. Maragakis, 10/5/12.

MCEER-13-0001 "Experimental Seismic Study of Pressurized Fire Sprinkler Piping Systems," by Y. Tian, A. Filiatrault and G. Mosqueda, 4/8/13.

MCEER-13-0002 "Enhancing Resource Coordination for Multi-Modal Evacuation Planning," by D.B. Hess, B.W. Conley and C.M. Farrell, 2/8/13.

MCEER-13-0003 "Seismic Response of Base Isolated Buildings Considering Pounding to Moat Walls," by A. Masroor and G. Mosqueda, 2/26/13.

MCEER-13-0004 "Seismic Response Control of Structures Using a Novel Adaptive Passive Negative Stiffness Device," by D.T.R. Pasala, A.A. Sarlis, S. Nagarajaiah, A.M. Reinhorn, M.C. Constantinou and D.P. Taylor, 6/10/13.

MCEER-13-0005 "Negative Stiffness Device for Seismic Protection of Structures," by A.A. Sarlis, D.T.R. Pasala, M.C. Constantinou, A.M. Reinhorn, S. Nagarajaiah and D.P. Taylor, 6/12/13.

MCEER-13-0006 "Emilia Earthquake of May 20, 2012 in Northern Italy: Rebuilding a Resilient Community to Withstand Multiple Hazards," by G.P. Cimellaro, M. Chiriatti, A.M. Reinhorn and L. Tirca, June 30, 2013.

MCEER-13-0007 "Precast Concrete Segmental Components and Systems for Accelerated Bridge Construction in Seismic Regions," by A.J. Aref, G.C. Lee, Y.C. Ou and P. Sideris, with contributions from K.C. Chang, S. Chen, A. Filiatrault and Y. Zhou, June 13, 2013.

MCEER-13-0008 "A Study of U.S. Bridge Failures (1980-2012)," by G.C. Lee, S.B. Mohan, C. Huang and B.N. Fard, June 15, 2013.

MCEER-13-0009 "Development of a Database Framework for Modeling Damaged Bridges," by G.C. Lee, J.C. Qi and C. Huang, June 16, 2013.

MCEER-13-0010 "Model of Triple Friction Pendulum Bearing for General Geometric and Frictional Parameters and for Uplift Conditions," by A.A. Sarlis and M.C. Constantinou, July 1, 2013.

MCEER-13-0011 "Shake Table Testing of Triple Friction Pendulum Isolators under Extreme Conditions," by A.A. Sarlis, M.C. Constantinou and A.M. Reinhorn, July 2, 2013.

MCEER-13-0012 "Theoretical Framework for the Development of MH-LRFD," by G.C. Lee (coordinating author), H.A Capers, Jr., C. Huang, J.M. Kulicki, Z. Liang, T. Murphy, J.J.D. Shen, M. Shinozuka and P.W.H. Yen, July 31, 2013.

MCEER-13-0013 "Seismic Protection of Highway Bridges with Negative Stiffness Devices," by N.K.A. Attary, M.D. Symans, S. Nagarajaiah, A.M. Reinhorn, M.C. Constantinou, A.A. Sarlis, D.T.R. Pasala, and D.P. Taylor, September 3, 2014.

MCEER-14-0001 "Simplified Seismic Collapse Capacity-Based Evaluation and Design of Frame Buildings with and without Supplemental Damping Systems," by M. Hamidia, A. Filiatrault, and A. Aref, May 19, 2014.

MCEER-14-0002 "Comprehensive Analytical Seismic Fragility of Fire Sprinkler Piping Systems," by Siavash Soroushian, Emmanuel "Manos" Maragakis, Arash E. Zaghi, Alicia Echevarria, Yuan Tian and Andre Filiatrault, August 26, 2014.

MCEER-14-0003 "Hybrid Simulation of the Seismic Response of a Steel Moment Frame Building Structure through Collapse," by M. Del Carpio Ramos, G. Mosqueda and D.G. Lignos, October 30, 2014.

MCEER-14-0004 "Blast and Seismic Resistant Concrete-Filled Double Skin Tubes and Modified Steel Jacketed Bridge Columns," by P.P. Fouche and M. Bruneau, June 30, 2015.

MCEER-14-0005 "Seismic Performance of Steel Plate Shear Walls Considering Various Design Approaches," by R. Purba and M. Bruneau, October 31, 2014.

MCEER-14-0006 "Air-Blast Effects on Civil Structures," by Jinwon Shin, Andrew S. Whittaker, Amjad J. Aref and David Cormie, October 30, 2014.

MCEER-14-0007 "Seismic Performance Evaluation of Precast Girders with Field-Cast Ultra High Performance Concrete (UHPC) Connections," by G.C. Lee, C. Huang, J. Song, and J. S. O'Connor, July 31, 2014.

MCEER-14-0008 "Post-Earthquake Fire Resistance of Ductile Concrete-Filled Double-Skin Tube Columns," by Reza Imani, Gilberto Mosqueda and Michel Bruneau, December 1, 2014.

MCEER-14-0009 "Cyclic Inelastic Behavior of Concrete Filled Sandwich Panel Walls Subjected to In-Plane Flexure," by Y. Alzeni and M. Bruneau, December 19, 2014.

MCEER-14-0010 "Analytical and Experimental Investigation of Self-Centering Steel Plate Shear Walls," by D.M. Dowden and M. Bruneau, December 19, 2014.

MCEER-15-0001 "Seismic Analysis of Multi-story Unreinforced Masonry Buildings with Flexible Diaphragms," by J. Aleman, G. Mosqueda and A.S. Whittaker, June 12, 2015.

MCEER-15-0002 "Site Response, Soil-Structure Interaction and Structure-Soil-Structure Interaction for Performance Assessment of Buildings and Nuclear Structures," by C. Bolisetti and A.S. Whittaker, June 15, 2015.

MCEER-15-0003 "Stress Wave Attenuation in Solids for Mitigating Impulsive Loadings," by R. Rafiee-Dehkharghani, A.J. Aref and G. Dargush, August 15, 2015.

MCEER-15-0004 "Computational, Analytical, and Experimental Modeling of Masonry Structures," by K.M. Dolatshahi and A.J. Aref, November 16, 2015.

MCEER-15-0005 "Property Modification Factors for Seismic Isolators: Design Guidance for Buildings," by W.J. McVitty and M.C. Constantinou, June 30, 2015.

MCEER-15-0006 "Seismic Isolation of Nuclear Power Plants using Sliding Bearings," by Manish Kumar, Andrew S. Whittaker and Michael C. Constantinou, December 27, 2015.

MCEER-15-0007 "Quintuple Friction Pendulum Isolator Behavior, Modeling and Validation," by Donghun Lee and Michael C. Constantinou, December 28, 2015.

MCEER-15-0008 "Seismic Isolation of Nuclear Power Plants using Elastomeric Bearings," by Manish Kumar, Andrew S. Whittaker and Michael C. Constantinou, December 29, 2015.

MCEER-16-0001 "Experimental, Numerical and Analytical Studies on the Seismic Response of Steel-Plate Concrete (SC) Composite Shear Walls," by Siamak Epackachi and Andrew S. Whittaker, June 15, 2016.

MCEER-16-0002 "Seismic Demand in Columns of Steel Frames," by Lisa Shrestha and Michel Bruneau, June 17, 2016.

MCEER-16-0003 "Development and Evaluation of Procedures for Analysis and Design of Buildings with Fluidic Self-Centering Systems" by Shoma Kitayama and Michael C. Constantinou, July 21, 2016.

MCEER-16-0004 "Real Time Control of Shake Tables for Nonlinear Hysteretic Systems," by Ki Pung Ryu and Andrei M. Reinhorn, October 22, 2016.

MCEER-16-0006 "Seismic Isolation of High Voltage Electrical Power Transformers," by Kostis Oikonomou, Michael C. Constantinou, Andrei M. Reinhorn and Leon Kemper, Jr., November 2, 2016.

MCEER-16-0007 "Open Space Damping System Theory and Experimental Validation," by Erkan Polat and Michael C. Constantinou, December 13, 2016.

MCEER-16-0008 "Seismic Response of Low Aspect Ratio Reinforced Concrete Walls for Buildings and Safety-Related Nuclear Applications," by Bismarck N. Luna and Andrew S. Whittaker.

MCEER-16-0009 "Buckling Restrained Braces Applications for Superstructure and Substructure Protection in Bridges," by Xiaone Wei and Michel Bruneau, December 28, 2016.

MCEER-16-0010 "Procedures and Results of Assessment of Seismic Performance of Seismically Isolated Electrical Transformers with Due Consideration for Vertical Isolation and Vertical Ground Motion Effects," by Shoma Kitayama, Michael C. Constantinou and Donghun Lee, December 31, 2016.

MCEER-17-0001 "Diagonal Tension Field Inclination Angle in Steel Plate Shear Walls," by Yushan Fu, Fangbo Wang and Michel Bruneau, February 10, 2017.

MCEER-17-0002 "Behavior of Steel Plate Shear Walls Subjected to Long Duration Earthquakes," by Ramla Qureshi and Michel Bruneau, September 1, 2017.

MCEER-17-0003 "Response of Steel-plate Concrete (SC) Wall Piers to Combined In-plane and Out-of-plane Seismic Loadings," by Brian Terranova, Andrew S. Whittaker, Siamak Epackachi and Nebojsa Orbovic, July 17, 2017.

MCEER-17-0004 "Design of Reinforced Concrete Panels for Wind-borne Missile Impact," by Brian Terranova, Andrew S. Whittaker and Len Schwer, July 18, 2017.

MCEER-17-0005 "A Simple Strategy for Dynamic Substructuring and its Application to Soil-Foundation-Structure Interaction," by Aikaterini Stefanaki and Metttupalayam V. Sivaselvan, December 15, 2017.

MCEER-17-0006 "Dynamics of Cable Structures: Modeling and Applications," by Nicholas D. Oliveto and Mettupalayam V. Sivaselvan, December 1, 2017.

MCEER-17-0007 "Development and Validation of a Combined Horizontal-Vertical Seismic Isolation System for High-Voltage-Power Transformers," by Donghun Lee and Michael C. Constantinou, November 3, 2017.

MCEER-18-0001 "Reduction of Seismic Acceleration Parameters for Temporary Bridge Design," by Conor Stucki and Michel Bruneau, March 22, 2018.

MCEER-18-0002 "Seismic Response of Low Aspect Ratio Reinforced Concrete Walls," by Bismarck N. Luna, Jonathan P. Rivera, Siamak Epackachi and Andrew S. Whittaker, April 21, 2018.

MCEER-18-0003 "Seismic Damage Assessment of Low Aspect Ratio Reinforced Concrete Shear Walls," by Jonathan P. Rivera, Bismarck N. Luna and Andrew S. Whittaker, April 16, 2018.

MCEER-18-0004 "Seismic Performance Assessment of Seismically Isolated Buildings Designed by the Procedures of ASCE/ SEI 7," by Shoma Kitayama and Michael C. Constantinou, April 14, 2018.

MCEER-19-0001 MCEER-19-0001 "Development and Validation of a Seismic Isolation System for Lightweight Residential Construction," by Huseyin Cisalar and Michael C. Constantinou, March 24, 2019.

MCEER-20-0001 "A Multiscale Study of Reinforced Concrete Shear Walls Subjected to Elevated Temperatures," by Alok Deshpande and Andrew S. Whittaker, June 26, 2020.

MCEER-20-0002 "Further Results on the Assessment of Performance of Seismically Isolated Electrical Transformers," by Shoma Kitayama and Michael C. Constantinou, June 30, 2020.

MCEER-20-0003 "Analytical and Numerical Studies of Seismic Fluid-Structure Interaction in Liquid-Filled Vessels," by Ching-Ching Yu and Andrew S. Whittaker, August 1, 2020.

MCEER: Earthquake Engineering to Extreme Events

University at Buffalo, The State University of New York
133A Ketter Hall | Buffalo, NY 14260
mceer@buffalo.edu; buffalo.edu/mceer

ISSN 1520-295X